博士論文

Study of the Oscillation of Neutrinos and Anti-Neutrinos and of Non-Standard Neutrino Interactions with the Atmospheric Data in Super-Kamiokande

(スーパーカミオカンデの大気ニュートリノデータによる ニュートリノと反ニュートリノ振動の研究と 非標準ニュートリノ相互作用の研究)

平成２７年３月博士(理学)申請

東京大学大学院理学系研究科
物理学専攻

マクラクラン・福英・トーマス
Mclachlan Fukuei Thomas

March 2015

Abstract

In atmospheric neutrinos, there has been a long established deficit of ν_μ events that enter from below the detector after traversing long distances. This phenomena has been well described by a theory called Neutrino Oscillations, which allows neutrinos to oscillate from one flavour to another. The probability of these transitions is characterised by the ratio of the flight path of the neutrino to its energy, L/E. The L/E Analysis aims to accurately determine the oscillation parameters by reconstructing the L/E dependence of the flavour transitions. It achieves this by selecting events with a high resolution in L/E.

Atmospheric neutrino experiments have typically measured oscillations with combined neutrino and anti-neutrino data. In recent years, accelerator experiments have been reversing the polarity of their focussing magnets, greatly increasing the $\bar{\nu}$ composition in their beams. Early oscillation analyses of this $\bar{\nu}$ data by MINOS (2011) resulted in a much larger Δm^2 measurement than the established value for neutrinos. This lead to experiments checking if distinct anti-neutrino oscillation parameters can be measured by oscillating $\bar{\nu}$ independently from ν. In addition, Neutral-Current (NC) Non-Standard Interactions (NSI) of neutrinos with matter have been proposed to explain the anomaly. In the years following 2011, MINOS reported on ν and $\bar{\nu}$ oscillation parameters that were in agreement.

However, it is important to make independent checks of any physical phenomena, particularly with an experiment with a different scope of sensitivity. Super-Kamiokande (SK) covers a wider range of the parameter space with baselines extending from $\sim$10 km to over 10^4 km; and energies ranging from 30 MeV to 50 GeV in this analysis. These baselines traverse extensive amounts of matter, crossing the entire Earth and include the mantle and core. While SK cannot distinguish between ν and $\bar{\nu}$ on an event-by-event basis, it has the potential for discovery of unexpected effects and unparalleled sensitivity to matter effects, such as in NC NSI.

In this thesis, both of the above hypotheses have been investigated. After extending the Standard L/E Analysis to cover over 10 years of atmospheric neutrino data, further improvements were made to increase the sensitivity to $\bar{\nu}$ parameters and sub-dominant NSI. These included a separately binned second resolution sample to considerably increase the available statistics, and an improved χ^2 calculation with greater stability in bins with few events. The standard analysis was in 2-flavours, which was extended to a 3-flavour model and then again to include $\mu\tau$–sector NSI. Included in this thesis is the first L/E analysis performed with 3-flavour oscillations, and the first analysis of atmospheric neutrino data with 3-flavour oscillations and NSI in the $\mu\tau$–sector.

No distinction could be observed between ν and $\bar{\nu}$ parameters, and the results were consistent with no observation of NSI. The 90% C.L. limits on the NSI parameters were $-1.97 \times 10^{-2} < \varepsilon_{\mu\tau} < 1.45 \times 10^{-2}$ and $-4.54 \times 10^{-2} < \varepsilon' \equiv (\varepsilon_{\tau\tau} - \varepsilon_{\mu\mu}) < 4.47 \times 10^{-2}$, assuming a normalisation of neutrino NSI with down-quarks in the matter traversed, and $\varepsilon_{\mu\mu} = \varepsilon_{e\tau} = 0$. With proper consideration of 3-flavour effects, and the best sensitivity to matter effects, these constraints are currently the best in the world. The oscillation parameters measured in the 3-flavour L/E Analysis for Normal (Inverted) Hierarchy were $\sin^2\theta_{23} = 0.55^{+0.07}_{-0.13}$ $\left(0.54^{+0.07}_{-0.12}\right)$ and $\Delta m^2_{31} = 2.60^{+0.22}_{-0.21}$ $\left(2.45^{+0.25}_{-0.16}\right) \times 10^{-3}\,\text{eV}^2$. The data showed no preference between Normal and Inverted Hierarchy.

Acknowledgements

It has been a true challenge seeing this thesis through to completion, and there are surely too many people to be named in fully extending my gratitude. Firstly, I would like to thank Prof. Takaaki Kajita, who provided the wonderful opportunity to carry out my post-graduate studies at the University of Tokyo and to work in a historical international collaboration, Super-Kamiokande. He has been more kind, patient, and supportive beyond any reasonable expectation for a supervisor. For giving me the freedom to explore the many possibilities for an interesting topic of study, and for helping me find my way again when things did not go so well. His guidance has continued beyond duty, allowing this thesis to finally reach a satisfying conclusion. I know I have not been an easy student, so for everything written here, and much more, I am truly grateful.

I must thank my family for their perseverance and unending patience with me, especially through the final years of my PhD. This thesis has survived through some trying circumstances, and surely would not exist without the support of my family. In particular to my mother, who provided persistent motivation whenever my own was weak. This gratitude is extended to my childhood friend, Kenny, who is like a brother and has been incredibly patient and supportive through the many difficult moments I have faced. For always being there, for our rejuvenating long walks in nature, and for helping me find my way again when I stray off-course.

I am forever thankful to the amazing friends I met on this journey, who have made my time in Japan an unforgettable experience. There are too many wonderful people to mention, but particularly I would like to thank Sarah A. for being so inspirational, for her acceptance and companionship, and for helping me believe I can tackle the most challenging dreams. Thank you to Rie I. for our many open-minded conversations, for her belief and support, and for being there during the most difficult times I have ever faced. My thanks to Farid S. for our explorations in culture and technology, for constantly challenging my opinions, and for being one of the most caring friends I have ever had. Cheers to Sebastian, Tony and Elliot for our many conversations as we faced the wonders and challenges of being a student in Japan. Thanks also to Mayuko, Sekine, Yukina, Yanju, Saki, Rie K., Megumi, Magdalenda, and Akabane for making me feel at home.

On campus, my gratitude goes to Yamamoto-san for running a wonderful homely cafe, where I have enjoyed many conversations and fun times. And to the friends I met there, particularly Yoshi, Eiji, Sasha, Grace, Bruno, Shashank, Fid, Regi, Hui, Yoon Lin, Koji, Yuuka, Mariko, Nick, Mark, Paul, Goran, Will and Sourav for making campus life enjoyable. I am also very thankful to Yoshida-san, Nishikawa-san, Yamaguchi-san, Kitsugi-san, and Watanabe-san for their kindness and support.

I am grateful to the Osaka group, where I had my first taste of neutrino research. In particular to Prof. Y. Kuno, Yoshida-san, Prof. Sato, Prof. Aoki, Itahashi-san, Nori, Naosuke, Zono, Yano,

Nakanishi, Taichou, Kyapuchin, Atsushi, and Wakako who taught me much about research and the wonders of life in Japan. Also to Dr. Soler who gave me the opportunity to continue to work with neutrinos in Glasgow.

I am thankful to the students who helped me get started when I arrived at RCCN, in particular I would like to thank C. Ishihara, who introduced me to research life in the collaboration, and to H. Nishino, G. Mitsuka, M. Ikeda for their help early on.

I am tremendously grateful to Prof. S. Moriyama who brought me up to speed with research in the collaboration, and who was always happy to answer my many questions. I would like to thank Prof. M. Nakahata, who often answered my curiosities while working in the SKDETSIM group. And to Prof. K. Kaneyuki and Dr. J. Kameda who helped me get started in analysis.

I would like to thank the many ICRR and Kamioka staff who have assisted me at various times, including Prof. M. Shiozawa, Prof. Y. Hayato, Dr. Y. Obayashi, Dr. M. Miura, Dr. Y. Koshio, and Kai. Particularly, I would like to thank Jan and Lluis, for their many discussions and 3 a.m. coffee breaks while working night-shifts.

I am indebted to the members of the RCCN group, for their company, conversation and advice, in particular to Okumura-san, Honda-san, Andrew, Maggie, Tristan, Euan, Kaji-san, Tanimoto-san, Shimizu-san, Shinohara-san, and Nishimura-san. Thank you for everything you have taught me, for our chats; coffee, lunch and dinner breaks; and for making research much more pleasant. I know I can be difficult to work with, so thank you also for your patience and understanding.

I am grateful for the comments and advice from the atmospheric neutrino analysis group, including Prof. E. Kearns, Prof. C. Walter, Prof. K. Sholberg, Dr. J. Raff, Dr. S. Mine, Piotr, Tarek, and particularly to Dr. R. Wendell and Okumura-san for their advice and assistance for solving challenging problems during analysis. Of course, my thanks go to Dr. M. Ishitsuka and Dr. F. Dufour for their previous work on the Standard L/E Analysis.

I am grateful to the other students S. Hazama, Y. Kozuma, T. Yokozawa, A. Shinozaki, H. Nishiie, K. Iyogi, T. Tanaka, D. Motoki, K. Ueshima, T. Iida, Byeongsu, Josh, Patrick, Michael D., Koun, Haibing, and Yang who helped make research life more enjoyable.

I am especially indebted to all those who helped me during the final stretch of my thesis. I am very grateful to Watanabe-san, who went out of her way to assist me when I could not be present in Japan, and for her ever-present encouragement. Thank you to Yamamoto-san and her husband for their exceptional compassion and care, and for helping me stay in Japan to finalise my thesis. I am truly humbled by the compassion of Kana and Scott, Sei-chan and Chi-tan, Sibylle and Roger, as well as Farid for accommodating and supporting me during this time. I will pass on this compassion to others, whenever I have the chance. I am very grateful to Nakazawa-sensei, for his patience and kindness, and for helping me raise the standard of this thesis considerably to reach its final form. Of course, any remaining errors are my own.

I am thankful also to the countless others who have made each moment interesting, delightful, and a learning experience.

Finally, I am eternally thankful to my father, who could not see the completion of this thesis, but has subtly guided me throughout my life.

Contents

List of Figures

List of Tables

Chapter 1

Introduction

1.1 Introduction to Neutrinos

The neutrino is one of the more mysterious of the elementary particles. It is the only, currently known, particle that solely interacts by the Weak Force, and it is the second most abundant substance in the universe after the photon. This means that a neutrino will very readily transverse the whole Earth without interacting! Indeed, ten thousand billion neutrinos from the sun pass through an area the size of your hand every second, [1] and that is not including the many other neutrino sources!

The neutrino first came into our awareness to explain the continuous energy distribution of emitted electrons from β-decay. In 1930, Wolfgang Pauli [2] postulated that a ghostly particle, the neutrino, was carrying off some of the energy the β-electron was expected to have. He was worried because the particle he had postulated, at that time, would have been very difficult to detect. It took a further 26 years until the neutrino was finally discovered in 1956 by Cowan and Reines [3, 4]. Their experiment made use of a highly distinctive delayed-coincidence signal from inverse β-decay, $\bar{\nu}_e + p \rightarrow n + e^+$, where the positron was detected promptly followed by a delayed γ signal from the neutron capture a few μs later.

Of course there have since been many more experiments, employing massive detectors to better catch neutrinos and gradually establishing our knowledge of them. Super-Kamiokande is a modern experiment, weighing at 50 kton, that can detect as many as 20–30 neutrinos per day. We know that there are 3 flavours of active neutrinos, one for each flavour of lepton, with the ν_μ discovered in 1962 [5] and the ν_τ in 2000 [6]. However the flavour ratios of neutrinos detected from the sun and the atmosphere were not as expected, and so multiple theories were proposed to account for the deficit of the expected neutrino events measured.

After years of experimentation, a theory known as "Neutrino Oscillations" [7, 8] is thought to be the most likely explanation for the anomaly in flavour ratios observed. This theory proposes that the flavour of a neutrino detected may change from the flavour at its creation. The probability for the change depends on the flight path length, L (km), and the energy of the neutrino, E_ν (GeV). More precisely, how frequently the neutrino flavours cycle between each other, or oscillate, has an L/E dependence. The Super-Kamiokande L/E analysis [9] excluded the other proposed theories.

In recent years, since 2009, the MINOS experiment has been collecting data with an anti-neutrino beam produced by a particle accelerator. Surprisingly, when they applied the standard

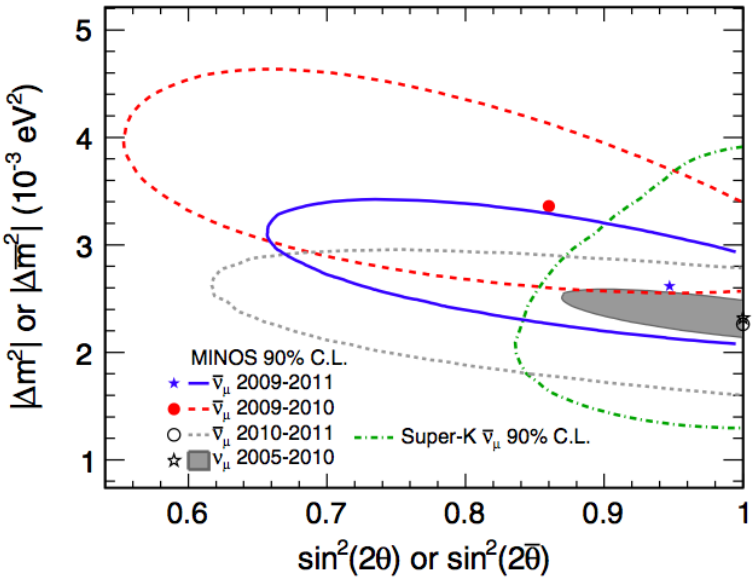

Figure 1.1: Neutrino and Anti-neutrino parameter 90% C.L. allowed regions from MINOS [11]. The initial anti-neutrino result reported in 2011 [10] can be seen as the dashed-red line. This region was distinct from the neutrino parameters (gray shaded area), which formed part of the motivation of the topics in this thesis. The updated anti-neutrino result reported in 2012 [11] can be seen as the blue solid contour. Clearly, the neutrino and anti-neutrino parameters are now in agreement. The anti-neutrino search at SK with the Zenith analysis [12] is shown by the dash-dotted green contour.

neutrino oscillation analysis to their initial data in 2010, the oscillation parameters they measured were considerably different from that of the best fits to their neutrino-beam data [10]. Specifically, a much larger $\Delta\bar{m}^2$ was reported in 2011 compared with the neutrino case, which can be seen in the dashed red contour (2009-2010 data taking period) in Figure 1.1. At this time the ν and $\bar{\nu}$ oscillation parameters measured at MINOS were consistent only at the 2% C.L. These surprising results were an early inspiration for the analyses in this thesis.

It should be noted that MINOS continued to improve their statistics with a beam optimised for $\bar{\nu}_\mu$, as well as performing additional checks. After running the $\bar{\nu}_\mu$ beam from 2009 to 2011, MINOS reported on an improved analysis in 2012 that had an allowed region that overlapped with the neutrino measurement [11], which can be seen in solid blue in Figure 1.1.

However, are the flavour transitions of neutrinos and anti-neutrinos truly governed by the same mechanism? Until recently, this property was simply assumed. As the foundation of Neutrino Oscillations depends on this holding true, it is crucial to have independent confirmations that neutrinos and anti-neutrinos oscillate in the same way. Although the MINOS experiment has shown consistency among the ν and $\bar{\nu}$ oscillation parameters, another confirmation by an experiment with a different scope of sensitivity is important. This question has also opened the possibility for alternative explanations, such as sub-dominant Non-Standard Neutrino Interactions (NSI) acting in the background together with Neutrino Oscillations. These scenarios also must be investigated.

1.2 Thesis Motivations

If nature is such that through an oscillation analysis we are able to measure differing parameters for neutrinos and anti-neutrinos, could this effect be seen at Super-Kamiokande (SK)? Theoretically, Neutrino Oscillations should be CPT symmetric and so the parameters measured for ν and $\bar{\nu}$ should be the same. CPT symmetry is a fundamental characteristic of the Standard Model, however the apparent discrepancies in 2011 lead to considerations that this property should be checked in neutrinos, rather than assumed.

The data at SK are composed of neutrino and anti-neutrino constituents, however these were not separated as SK has very little power to distinguish the charge of outgoing leptons. So a direct check on independent particle and anti-particle oscillation parameters would have to involve oscillating neutrinos and anti-neutrinos independently in the simulation and compare the output with the data. Such an analysis was carried out at SK with distributions for the incoming neutrino direction with respect to the vertical axis of the detector (a *Zenith analysis*) [12], which can be seen in the dash-dotted green line in Figure 1.1. The analyses in this thesis aim to reconstruct the L/E pattern expected for oscillations, and use these distributions to investigate neutrino oscillations accurately or deviations from pure oscillations. If no differences in the ν and $\bar{\nu}$ oscillation patterns were found, this would form another confirmation of the CPT symmetry in neutrinos within the sensitivity of SK.

The apparent appearance of a different Δm^2 for neutrinos and anti-neutrinos assuming vacuum oscillations could also be explained by oscillations with one Δm^2 together with Neutral-Current (NC) Non-Standard Neutrino Interactions (NSI) of neutrinos with matter [13]. In an analysis of oscillations in vacuum, the effect of NSI acting in the background[1] would cause the Δm^2 to be measured larger for $\bar{\nu}$ and smaller for ν from the actual Δm^2. So this was a promising explanation for the results reported at MINOS. With this as an initial motivation, an NSI-oscillation analysis with the L/E distributions was also carried out for this thesis.

1.2.1 The L/E Analysis with Atmospheric Neutrinos at Super-Kamiokande

Super-Kamiokande (SK) has collected atmospheric neutrino data for over 10 years, covering a wide range of energies and baselines. This makes the data ideal for checking a variety of oscillation parameters and for observing potentially unexpected effects; compared to an oscillation experiment tuned to a particular range of L/E. SK is also the largest pure water Cherenkov detector in the world, in the GeV range, giving it a respectable neutrino event rate of about 20–30 events per day.

There are two clear figures of merit for performing an L/E analysis of atmospheric neutrino data at SK. Atmospheric neutrinos traverse great distances through matter, from $\sim$10 km to over 10^4 km, with flight paths including the Earth's mantle and core. This gives atmospheric neutrino experiments the best sensitivity to matter effects, such as those expected from NC NSI or from the Mikheyev–Smirnov–Wolfenstein (MSW) effect (Section 1.4.3). In addition, since the L/E Analysis directly reconstructs the characteristic pattern of neutrino oscillations over this wide range of distances, it provides the strongest constraint on the atmospheric Δm^2 from atmospheric neutrinos. This makes it an ideal choice for studies that are highly dependent on the measurement of Δm^2.

[1] Assuming a negative $\varepsilon_{\mu\tau}$ NSI term and normal neutrino mass hierarchy

1.2.2 Neutrino Anti-Neutrino L/E Analysis

The L/E Analysis has the best discrimination of Δm^2 from atmospheric neutrino studies, and so could potentially have the sensitivity to pick out a secondary $\Delta \bar{m}^2$ for anti-neutrinos underlying the data. Since SK cannot distinguish ν from $\bar{\nu}$, this investigation would involve oscillating ν and $\bar{\nu}$ independently, and then fitting an L/E distribution with two Δm^2, and two $\sin^2\theta$. From this, the allowed ranges of these parameters can be found. An equivalent measurement for particle and anti-particle would confirm the CPT symmetry in neutrino oscillations, while a significant difference between these parameters would signify the need for new physics.

1.2.3 3-Flavour L/E Analysis

In 2012, the oscillation parameter θ_{13}, which allows $\nu_\mu \leftrightarrow \nu_e$ mixing, was found to be non-zero and not-so-small [14]. So it is better to do analyses with 3-flavour oscillations rather than only with the 2-flavour approximation. For this reason, a 3-flavour L/E Analysis was performed for the first time. All other L/E analyses with neutrino data from any experiment have relied on the 2-flavour approximation. Whether the L/E distributions are still good for measuring oscillation parameters under the presence of 3-flavour and matter effects will be investigated in this thesis.

The L/E Analysis can provide an independent measurement of the oscillation parameters from the Zenith 3-flavour analysis [15], by the measurement of a different variable and by the use of a sub-sample of data. The analyses in this thesis directly measure the distribution of the L/E variable, a fundamental characteristic of neutrino oscillations. In addition, this measurement is made with selected samples of neutrinos with a precise resolution in L/E. So an independent determination of the oscillation parameters can be made from the same source SK data. Furthermore, this result should be more accurate than any previous L/E analysis since it is free from the approximations of a 2-flavour approach.

1.2.4 NSI L/E Analysis

The observation of neutrino oscillations and the necessary neutrino masses already require an extension to the Standard Model, which originally postulated massless neutrinos. So the properties of neutrinos act as a good probe for potential new physics beyond the Standard Model. Neutral-Current neutrino NSI in matter are a category of possible non-standard effects that can be investigated with atmospheric neutrinos. A 3-Flavour Oscillation and NSI analysis in the $\mu\tau$–sector with atmospheric neutrino data was carried out for the first time. All previous measurements of NSI with atmospheric neutrinos in the $\mu\tau$–sector have made use of 2-flavour hybrid models.

Atmospheric neutrinos traverse great distances through matter, spanning the entire Earth, including the mantle and core. This provides unparalleled sensitivity to potential matter effects, such as in this NC matter NSI measurement. Particularly, sensitivity to the $\varepsilon_{\mu\tau}$ NSI term is dependent on the measurement of Δm^2, making the L/E Analysis a good choice to study NSI.

1.3 Atmospheric Neutrinos

The Earth is constantly bombarded by a massive flux of primary comic rays, ∼90% protons and ∼9% α-particles [17], that interact with nuclei in the atmosphere to produce secondary particles, mostly pions and some kaons, in hadronic showers. The decay of these mesons and subsequent

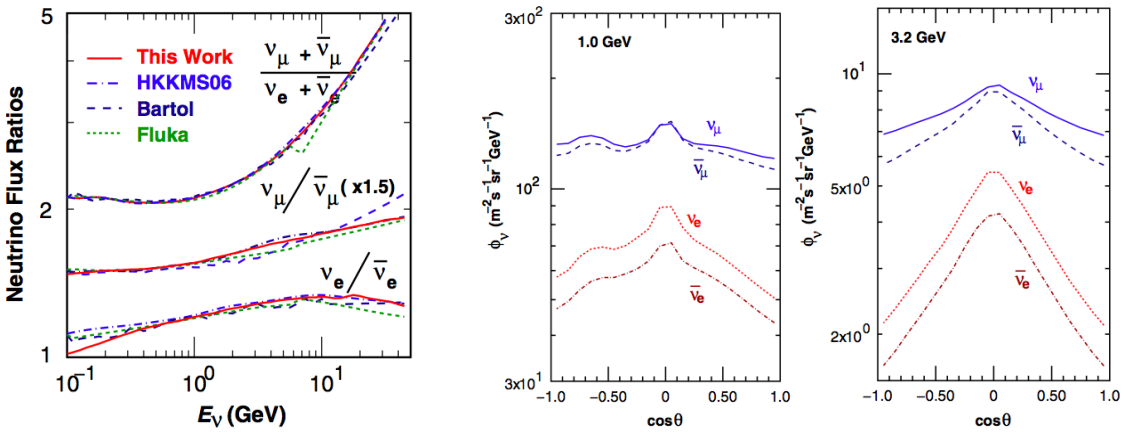

Figure 1.2: Atmospheric neutrino flux ratios on the left, and the zenith distribution of the flux on the right, calculated by Honda et al. in 2011 [16]. The left figure shows muon to electron flavour ratio of atmospheric neutrinos, as well as neutrino to anti-neutrino ratios. The red solid is for the Honda 2011 calculation, while comparisons with other calculations are also shown. The right plot has been averaged over all azimuthal angles and is for the Kamioka site. The neutrinos arrive from directly above the detector for $\cos\theta = 1.0$, and from directly below at $\cos\theta = -1.0$. The flux is nearly up-down symmetric above around ∼3 GeV.

particles produce atmospheric neutrinos. The main contributor to these neutrinos comes from the decay chains of pions:

$$\begin{aligned} \pi^+ &\rightarrow \mu^+ + \nu_\mu \\ &\quad \hookrightarrow e^+ + \nu_e + \overline{\nu}_\mu, \end{aligned} \tag{1.1}$$

$$\begin{aligned} \pi^- &\rightarrow \mu^- + \bar{\nu}_\mu \\ &\quad \hookrightarrow e^- + \bar{\nu}_e + \nu_\mu. \end{aligned} \tag{1.2}$$

As seen in these decay chains, each pion produces two muon neutrinos and one electron neutrino. So from the atmospheric neutrino flux, a $(\nu_\mu + \bar{\nu}_\mu)/(\nu_e + \bar{\nu}_e)$ flavour ratio of 2 is expected. For higher energy cosmic rays, the muons have a greater probability of reaching the ground before decaying. So for neutrinos above a few GeV, there are less electron neutrinos and the flavour ratio increases, which can be seen in Figure 1.2. A nice feature of this ratio is that all the flux calculations essentially agree on its value and variation with energy, leading to a much smaller uncertainty, of around 3%, in the quantity. While the absolute flux of each calculation agree within about 10% for neutrinos below ∼10 GeV.

The zenith dependence of the atmospheric neutrino flux for sample energies is also shown in Figure 1.2. Where $\cos\theta = 1.0$ corresponds to downward going neutrinos relative to the Kamioka site; and $\cos\theta$ = -1.0 to upward going neutrinos. It can be seen that above ∼3 GeV, the distributions are largely up-down symmetric. There is a geomagnetic cutoff rigidity, below which primary comic rays do not make it through the magnetosphere to produce secondary particles in the atmosphere. The cutoff rigidity varies at different locations in the world. Below ∼3 GeV at Kamioka, due to this cutoff, the up-down neutrino fluxes are asymmetric.

Atmospheric neutrino flux calculations show that a $(\nu_\mu + \bar{\nu}_\mu)/(\nu_e + \bar{\nu}_e)$ flavour ratio of 2 or above is expected and that this ratio is a reliable quantity to measure, as well as the fluxes

being up-down symmetric above a few GeV. However experiments have measured a deficit in this ratio, and in particular a deficit in ν_μ or $\bar{\nu}_\mu$ arriving from below the detector. This result can be explained by the theory of Neutrino Oscillations. The atmosphere provides a source of neutrinos that travel between ∼10 km to ∼13,000 km to reach a detector, and so atmospheric experiments are in a good position to probe the neutrino flight path over energy (L/E) dependence of neutrino oscillations.

1.4 Neutrino Oscillations

1.4.1 3-Flavour Oscillations

Many experiments have shown that neutrinos can change from one flavour to another during transit, and the theory which best describes this is Neutrino Oscillations. At production, or after a measurement, a neutrino is in one of three flavour eigenstates: $|\nu_e\rangle$, $|\nu_\mu\rangle$, $|\nu_\tau\rangle$. This flavour eigenstate is defined by the flavour of the lepton associated with the neutrino during creation or detection. During transit, the neutrino is a superposition of three mass eigenstates: $|\nu_1\rangle$, $|\nu_2\rangle$, $|\nu_3\rangle$. The composition of the mixing is described by the 3×3 Unitary Lepton Mixing Matrix, U, also known as the Pontecorvo-Maki-Nakagawa-Sakata (PMNS) Mixing Matrix. The two sets of eigenstates are related by the equation:

$$|\nu_\alpha\rangle = \sum_{i=1}^{3} U^*_{\alpha i} |\nu_i\rangle, \tag{1.3}$$

where $\alpha = e$, μ, or τ label one of the flavour eigenstates, and $i = 1$, 2, or 3 indicate the mass eigenstates. An insightful parameterisation of U for vacuum oscillations is:

$$U = \begin{pmatrix} 1 & 0 & 0 \\ 0 & c_{23} & s_{23} \\ 0 & -s_{23} & c_{23} \end{pmatrix} \begin{pmatrix} c_{13} & 0 & s_{13}e^{-i\delta_{cp}} \\ 0 & 1 & 0 \\ -s_{13}e^{i\delta_{cp}} & 0 & c_{13} \end{pmatrix} \begin{pmatrix} c_{12} & s_{12} & 0 \\ -s_{12} & c_{12} & 0 \\ 0 & 0 & 1 \end{pmatrix}, \tag{1.4}$$

where $s_{ij} \equiv \sin\theta_{ij}$ and $c_{ij} \equiv \cos\theta_{ij}$. U can be seen in Eq. (1.4) as three independent rotations characterised by the mixing angles θ_{12}, θ_{23}, and θ_{13}. While δ_{cp} is a complex phase that allows for CP violations in the neutrino sector[2]. The neutrino in transit will be one of the ν_i mass eigenstates, however since we do not know which mass eigenstate was created, we treat the time evolution as a superposition of each of the mass eigenstates [18].

$$|\nu_\alpha(t)\rangle = \sum_i U^*_{\alpha i} e^{-iE_i t} |\nu_i(t=0)\rangle, \tag{1.5}$$

[2]To allow for the case of Majorana neutrinos in which the neutrino is its own antiparticle, another matrix containing two more complex phases can be multiplied on to U. Since these phases are not of interest in this thesis, they have not been included. Similarly, the case for more sterile mass eigenstates has not been considered.

where E_i is an energy eigenvalue of ν_i. The probability amplitude of detecting a neutrino in the flavour eigenstate $|\nu_\beta\rangle$ at time t, from one created as $|\nu_\alpha\rangle$ at time $t = 0$:

$$\begin{aligned} A(\nu_\alpha \to \nu_\beta)(t) &\equiv \langle \nu_\beta | \nu_\alpha(t) \rangle && (1.6)\\ &= \sum_i \langle \nu_\beta | U^*_{\alpha i} e^{-iE_i t} | \nu_i \rangle && (1.7)\\ &= \sum_i \sum_{\gamma=e,\mu,\tau} \langle \nu_\beta | U^*_{\alpha i} e^{-iE_i t} U_{\gamma i} | \nu_\gamma \rangle && (1.8)\\ &= \sum_i \sum_{\gamma=e,\mu,\tau} U^*_{\alpha i} U_{\gamma i} e^{-iE_i t} \langle \nu_\beta | \nu_\gamma \rangle && (1.9)\\ &= \sum_i U^*_{\alpha i} U_{\beta i} e^{-iE_i t}, && (1.10) \end{aligned}$$

where in the line (1.8), U has been used to express the propagated ν_i back into a superposition of flavour eigenstates, using the sum with label $\gamma = e$, μ or τ. The probability for the flavour transition is then given by:

$$\begin{aligned} P(\nu_\alpha \to \nu_\beta)(t) &= |A(\nu_\alpha \to \nu_\beta)(t)|^2 \\ &= \sum_{i,j} U^*_{\alpha i} U_{\beta i} U_{\alpha j} U^*_{\beta j} e^{-i(E_i - E_j)t}. && (1.11) \end{aligned}$$

Considering natural units ($c = \hbar = 1$) and using the following approximation:

$$E_i = \sqrt{\mathbf{p}_i^2 + m_i^2} = \mathbf{p}_i \sqrt{1 + \frac{m_i^2}{\mathbf{p}_i^2}} \simeq \mathbf{p}_i \left(1 + \frac{m_i^2}{2\mathbf{p}_i^2}\right) = \mathbf{p}_i + \frac{m_i^2}{2\mathbf{p}_i}, \tag{1.12}$$

the energy component of the exponential phase in Equation (1.11) becomes:

$$\begin{aligned} E_i - E_j &= \left(\mathbf{p}_i + \frac{m_i^2}{2\mathbf{p}_i}\right) - \left(\mathbf{p}_j + \frac{m_j^2}{2\mathbf{p}_j}\right) && (1.13)\\ &= \frac{\Delta m^2_{ij}}{2E_\nu}, && (1.14) \end{aligned}$$

where $\Delta m^2_{ij} = m_i^2 - m_j^2$ is the mass squared difference between two mass eigenstates, and the relativistic neutrino energy $E_\nu \simeq |\mathbf{p}_i| = |\mathbf{p}_j|$, neglecting the mass contribution. Experiments typically do not measure the flight time of the neutrino, but the flight path between the source and detector, L_ν. Since $L_\nu \equiv t$ with a factor of c, Equation (1.11) can be written:

$$P(\nu_\alpha \to \nu_\beta)(t) = \sum_{i,j} U^*_{\alpha i} U_{\beta i} U_{\alpha j} U^*_{\beta j} \exp\left(-i \frac{\Delta m^2_{ij} L_\nu}{2E_\nu}\right). \tag{1.15}$$

In the case for anti-neutrinos, assuming that CPT invariance is maintained, the treatment of the flavour transition probability is the same only that the complex conjugate of U would be used in the anti-neutrino case: $P(\nu_\alpha \to \nu_\beta; U^*) \equiv P(\bar{\nu}_\alpha \to \bar{\nu}_\beta; U)$. If U is real, these probabilities are equivalent; and if U is complex, these probabilities differ in general.

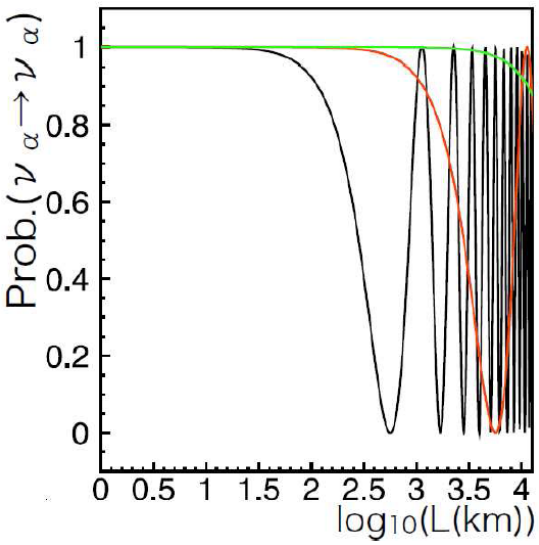

Figure 1.3: Neutrino Oscillations survival probability typical for atmospheric neutrinos, where the following parameters were assumed: $\sin^2 2\theta = 1.0$ and $\Delta m^2 = 2.2 \times 10^{-3}\,\mathrm{eV}^2$. Since oscillations depend on energy, three plots have been shown: $E_\nu = 1\,\mathrm{GeV}$ in black, $E_\nu = 10\,\mathrm{GeV}$ in red, $E_\nu = 100\,\mathrm{GeV}$ in green.

1.4.2 2-Flavour Approximation

The rotation in the 12 plane shown in Eq. (1.4) is associated with solar mixing, whereas the 23 plane rotation is associated with atmospheric experiments. In 1999, CHOOZ set an upper limit on $\theta_{13} \lesssim 12°$, so it was known that θ_{13} is small [19]. This means that the middle rotation in U tends to the identity, and U decouples to two 2×2 mixing phenomena to a good approximation. Since experiments tend to have sensitivity to one of these rotations, as an initial analysis the mixing between two flavours only was usually considered. These rotations can be written as:

$$\begin{pmatrix} \nu_\alpha \\ \nu_\beta \end{pmatrix} = \begin{pmatrix} \cos\theta_{ij} & \sin\theta_{ij} \\ -\sin\theta_{ij} & \cos\theta_{ij} \end{pmatrix} \begin{pmatrix} \nu_i \\ \nu_j \end{pmatrix}, \tag{1.16}$$

where α and β are two of e, μ or τ, whereas i and j correspond to the associated mass states. The time evolution of a neutrino state, $|\nu_\alpha\rangle$ for example, can be treated like so:

$$|\nu_\alpha(t)\rangle \;=\; e^{-iE_i t}\cos\theta_{ij}|\nu_i\rangle \;+\; e^{-iE_j t}\sin\theta_{ij}|\nu_j\rangle. \tag{1.17}$$

Following the same procedure as the 3-flavour case, and the energy approximation in Equation (1.12), the transition probability of a two-flavour oscillation can be shown to be:

$$\begin{aligned} P(\nu_\alpha \to \nu_\beta) &= |\langle\nu_\beta|\nu_\alpha(t)\rangle|^2 \\ &= \sin^2 2\theta_{ij}\sin^2\left(\frac{\Delta m^2_{ji} L_\nu}{4E_\nu}\right) \qquad (1.18) \\ &= \sin^2 2\theta_{ij}\sin^2\left(\frac{1.267\Delta m^2_{ji} L_\nu}{E_\nu}\right), \qquad (1.19) \end{aligned}$$

where $\Delta m^2_{ji} = m^2_j - m^2_i$ is the mass squared difference, L_ν is the baseline, E_ν is the neutrino energy, and making use of the identities $\sin 2x = 2\sin x\cos x$ and $2\sin^2 x = 1 - \cos 2x$. The figure "1.267" in Equation (1.19) allows the use of the units Δm^2_{ji} in eV^2, L_ν in km and E_ν in GeV. Of

course, the survival probability that is normally measured by experiments can be written as:

$$P(\nu_\alpha \to \nu_\alpha) = 1 - \sin^2 2\theta_{ij} \sin^2 \left(\frac{1.27 \Delta m^2_{ji} L_\nu}{E_\nu} \right). \tag{1.20}$$

It can be seen in Equation (1.20) that the magnitude of the effect is determined by θ_{ij}, while the frequency of the oscillations in L/E by Δm^2_{ji}. Some examples of this survival probability can be seen in Figure 1.3. The first oscillation maximum, where the survival probability is at a minimum, occurs at:

$$\frac{\Delta m^2_{ji} L_\nu}{E_\nu} = \frac{\pi}{2.534}. \tag{1.21}$$

This relationship can be considered to tune the sensitivity in Δm^2_{ji} of an experiment. Here are some examples:

CHOOZ	$L = 1\,\text{km}$	$E = 0.0018\,\text{GeV}$	$\longrightarrow \Delta m^2 \sim 2.23 \times 10^{-3}\,\text{eV}^2$,
T2K	$L = 295\,\text{km}$	$E = 0.6\,\text{GeV}$	$\longrightarrow \Delta m^2 \sim 2.52 \times 10^{-3}\,\text{eV}^2$,
KamLAND	$L = 180\,\text{km}$	$E = 0.0018\,\text{GeV}$	$\longrightarrow \Delta m^2 \sim 1.24 \times 10^{-5}\,\text{eV}^2$.

CHOOZ (Section 2.3.1) and KamLAND (Section 2.3.2) were reactor experiments, and they had sensitivity to oscillations above the stated Δm^2 here. T2K (Section 2.4.3) is an accelerator experiment and was tuned to maximise its sensitivity around this Δm^2. Neutrino Oscillations can essentially be defined by two mass square differences, one at $\Delta m^2 \sim 10^{-5}\,\text{eV}^2$ for the oscillations driven by solar parameters; and $\Delta m^2 \sim 10^{-3}\,\text{eV}^2$ for oscillations governed by atmospheric parameters and θ_{13} effects. Since the Δm^2 differ largely in magnitude, oscillation experiments can be approximated by one 2-flavour 2×2 rotation matrix.

1.4.3 Matter Effects

The above discussion of neutrino oscillations was for propagation in vacuum. However, as neutrinos traverse through matter they undergo coherent forward scattering on electrons, protons and neutrons. This leads to oscillation with effective mass square differences and mixing angles, that vary from vacuum oscillations. This is known as the MSW effect [20–22], or the matter effect.

To understand how this effect occurs [18], consider the propagation of neutrinos in matter by the following Schrödinger equation:

$$i \frac{\partial}{\partial t} \Psi(t) = H \Psi(t), \tag{1.22}$$

where $\Psi_\alpha(t)$ is a component of the above wave function that gives the amplitude for a neutrino with flavour α at time t. H is the hamiltonian and a 3×3 matrix for three flavours. This hamiltonian has interaction energies that result from neutrino-matter interactions through W or Z exchange. All neutrino flavours can interact through NC Z exchange, while only electron neutrinos interact via CC W exchange, as matter has a high density of electrons. For standard model interactions, NC interactions result in no flavour change and so Z exchange does not contribute to the oscillation effects observed[3], which depend only on the relative phases of the neutrino eigenstates.

[3] non-standard neutrino interactions could allow NC flavour change, see Section 1.5

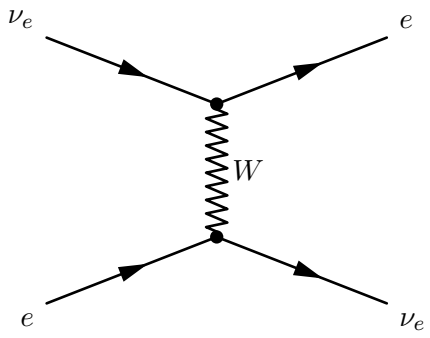

Figure 1.4: Matter effects that have an influence on flavour oscillations occur via the W exchange interaction, shown in this Feynman diagram.

However, ν_e may interact via W exchange, which results in a contribution that does have an effect on the oscillation transitions. A feynman diagram of the W exchange interaction is shown in Figure 1.4. The electron-electron element of H would gain the interaction energy:

$$V = \sqrt{2} G_F N_e, \tag{1.23}$$

where G_F is the Fermi coupling constant, and N_e is the electron number density per unit volume in the neutrinos flight path. For $\bar{\nu}_e$ propagation the interaction energy becomes $-V$.

For an illustration of the effect [18], consider oscillations in matter involving two flavours ν_e and ν_μ, then H becomes:

$$H = \frac{\Delta m^2_M}{4E_\nu} \begin{pmatrix} -\cos 2\theta_M & \sin 2\theta_M \\ \sin 2\theta_M & \cos 2\theta_M \end{pmatrix}, \tag{1.24}$$

where Δm^2_M is the effective mass squared difference, θ_M is the effective mixing angle, and E_ν is the neutrino energy. These effective parameters are defined by:

$$\Delta m^2_M = \Delta m^2 \sqrt{\sin^2 2\theta + (\cos 2\theta - x_\nu)^2}, \tag{1.25}$$

$$\sin^2 2\theta_M = \frac{\sin^2 2\theta}{\sin^2 2\theta + (\cos 2\theta - x_\nu)^2}, \tag{1.26}$$

where x_ν quantifies the degree of the effect and is defined:

$$x_\nu \equiv \frac{2\sqrt{2} G_F N_e E_\nu}{\Delta m^2}. \tag{1.27}$$

It can be seen that these effective parameters reduce to their vacuum equivalent, Δm^2 and θ, when the parameter x_ν vanishes as N_e tends to 0. For anti-neutrinos $x_{\bar{\nu}} (\equiv -x_\nu)$ is used instead. As matter effects (including the non-standard case) have a different effect on neutrinos and anti-neutrinos, they can lead to a difference in the oscillation parameters observed for particles and anti-particles. This should not be confused with CP violations, which need to be distinguished from matter effects. Finally, for an idea of the magnitude of the matter effects [18], consider an accelerator experiment sending neutrinos through the Earth's crust over a baseline of 1000 km, with $\Delta m^2_{31} \simeq 2.4 \times 10^{-3}\,\mathrm{eV}^2$, then:

$$x_\nu \simeq \frac{E}{12\,\mathrm{GeV}}. \tag{1.28}$$

So for $E_\nu = 0.6\,\mathrm{GeV}$, the peak T2K beam energy, the effect is small; for $E_\nu = 2\,\mathrm{GeV}$, the peak beam energy for NOνA, the effect is considerable; and for $E_\nu \sim 17\,\mathrm{GeV}$, as in the case of OPERA, the effect would be large. Note that these mentioned experiments have varying baselines, and were mentioned to provide realistic neutrino energies.

1.4.4 Status of the Oscillation Parameter Research

This a brief discussion of the status of the oscillation parameter search, for an comprehensive review of neutrino oscillation experiments see Chapter 2. Since 1968, solar neutrino experiments [23–26] have measured 30–50% of the flux expected from scrupulously calculated Standard Solar Models (SSM), which was known as the *solar neutrino problem*. A similar deficit in muon atmospheric neutrinos was observed in 1988 by Kamiokande [27, 28] and IMB [29], which was dubbed the *atmospheric anomaly*. These measurements were the first indication for the need of a theory such as Neutrino Oscillations.

The first real evidence for oscillations came from Super-Kamiokande in 1998, from the atmospheric *zenith analysis* [30, 31], favouring the theory of oscillations over alternatives in the 2004 atmospheric *L/E analysis* [9]. Global analyses of the *solar* oscillation parameters, Δm^2_{21} and θ_{12}, from solar neutrino experiments [32] have greatly constrained the allowed regions. The solar experiment SNO measured the total flux of neutrinos coming from the sun with an NC reaction [33], which agreed with the SSMs, confirming the flavour changing interpretation of the deficit. Additionally the reactor experiment, KamLAND, that had sensitivity to solar oscillations, greatly restricted the Δm^2_{21} allowed region [34]. Along with the Super-Kamiokande atmospheric analyses, neutrino accelerator experiments, such as T2K [35] and MINOS [36], have confined the *atmospheric* oscillation parameters, Δm^2_{32} and θ_{23}.

The final mixing angle, θ_{13}, proved to be quite evasive. CHOOZ put an upper limit of around 12° in 1999 [19]. While in 2011, Double CHOOZ [38], T2K [39] and MINOS [40] gave indications of a non-zero θ_{13}. Finally, in 2012 the parameter was measured by the reactor experiments firstly by Daya Bay [14], and confirmed shortly afterwards by RENO [41] and Double CHOOZ [42]. The mass hierarchy, or the ordering of the neutrino mass eigenstates, and the degree of CP violations in neutrinos are still unknown. Accelerator experiments are beginning to confine the allowed values of δ_{cp} [37, 43], and attempting to observe differences between the mass hierarchy assumptions. The resulting parameters from a global fit to the neutrino oscillation data after the Neutrino 2012 conference [44], is shown Table 1.1. Recent oscillation parameter allowed regions are shown in Figures 1.5 and 1.6.

Parameter	Value	
Δm^2_{21}	$7.62^{+0.19}_{-0.19} \times 10^{-5}\,\mathrm{eV}^2$	
Δm^2_{31}	$2.55^{+0.06}_{-0.09} \times 10^{-3}\,\mathrm{eV}^2$	
$\sin^2\theta_{12}$	$0.320^{+0.016}_{-0.017}$	
$\sin^2\theta_{23}$	$0.613^{+0.022}_{-0.040}$	$0.600^{+0.026}_{-0.031}$
$\sin^2\theta_{13}$	$0.0246^{+0.0029}_{-0.0028}$	$0.0250^{+0.0026}_{-0.0027}$

Table 1.1: Global fit of oscillation parameters after the Neutrino 2012 conference [44]. The left figures correspond to normal hierarchy and the right to inverted hierarchy, where these differ. The errors stated are at the $1\,\sigma$ level. Note that in this global analysis there was a local minimum of $\sin^2\theta_{23} = 0.427^{+0.034}_{-0.027}$ with $\Delta\chi^2 = 0.02$ above the global minimum.

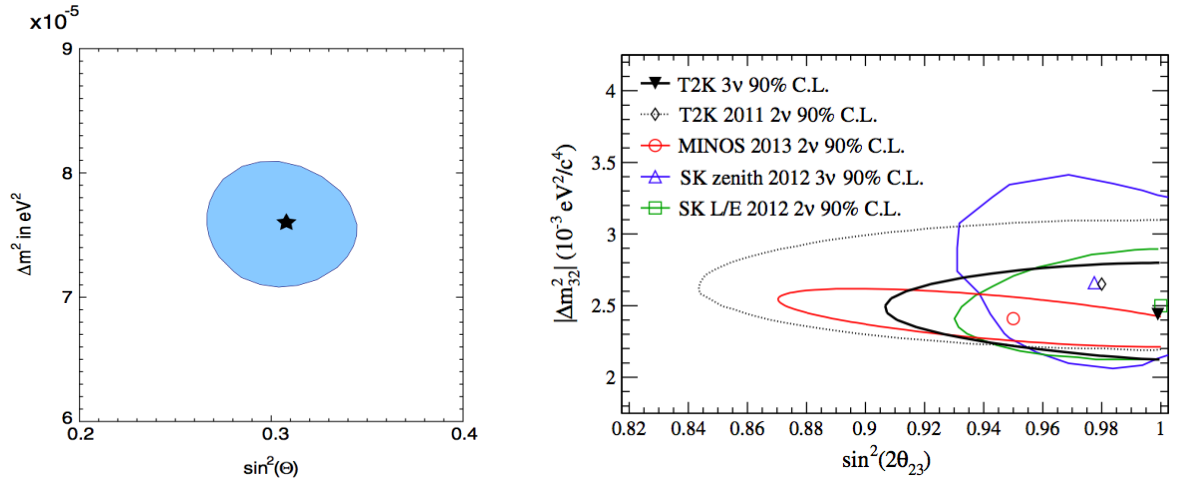

Figure 1.5: Global solar oscillation parameter allowed regions from 2011 [32] on the left, and recent atmospheric allowed regions from 2013 [35] on the right. The left figure came from a combined analysis of the solar experiment data from SNO, Borexino, radiochemical experiments and SK, as well as from KamLAND. The 95% C.L. regions are shown for Δm^2_{21} and θ_{12}. The right figure shows recent results from the accelerator experiments T2K and MINOS, as well as the zenith and L/E analyses from SK, all at the 90% C.L. The L/E allowed region presented in green will be discussed as one of the analyses in this thesis.

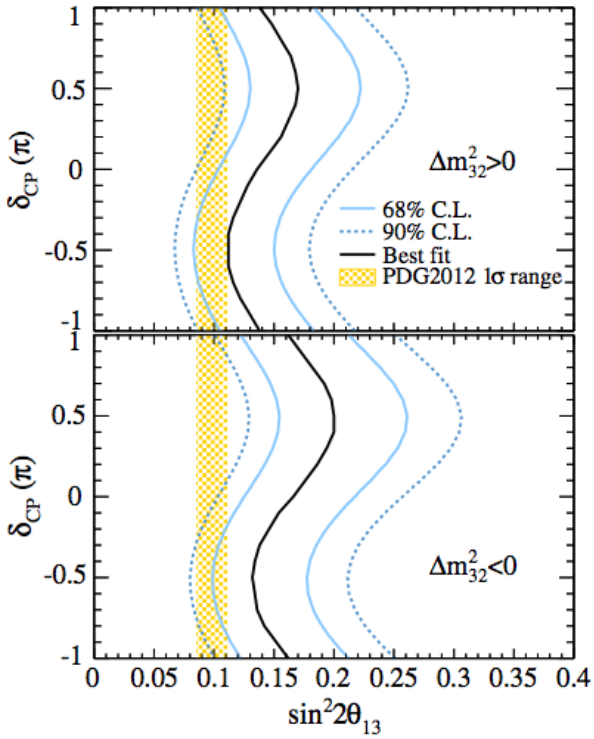

Figure 1.6: T2K 2013 allowed regions for $\sin^2 2\theta_{13}$ for varying δ_{cp} [37]. The top panel is for normal hierarchy and the bottom for inverted. The black solid line gives the best fit and the orange hatched band displays the average θ_{13} value from the PDG, 2012, which largely comes from reactor experiments.

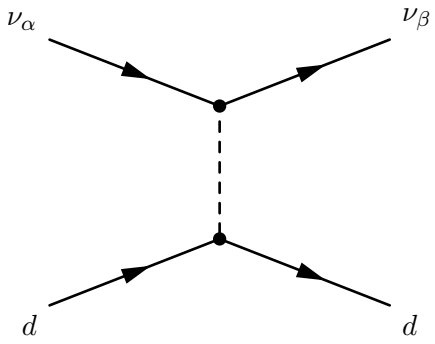

Figure 1.7: An example Feynman diagram for a flavour changing neutral current (FCNC) non-standard neutrino interaction (NSI) on a down quark. The figure illustrates a non-standard process that would allow neutrinos to change flavour as they propagate through matter.

1.5 Non-Standard Neutrino Interactions (NSI)

Non-Standard Neutrino Interactions (NSI) are interactions of neutrinos beyond the Standard Model that are predicted by various theories. The NSIs of interest in this thesis are NSIs of neutrinos with matter. In this case the interaction probability amplitudes are dependent on the density of matter traversed by the neutrino, and therefore the flavour transition probability is dependent on the flight path of the neutrino through matter. This is not necessarily the case, as there also are predicted neutrino NSI that couple to something other than matter, as well producing other properties [45].

Generally, NSI can arise even if neutrinos are massless [46–48], although most models expect neutrinos to have mass [49–56]. For example NSI can be seen in massive neutrinos where their mass is generated by a see-saw mechanism, naturally resulting in a degree of non-diagonality of the neutrino states [49, 57]; or with the breaking of R parity in supersymmetric models [50, 57]. In general, these matter NSIs depend on the density of matter on the neutrino flight path, while not showing the E^{-1} dependence seen in neutrino oscillations [45].

Early fits considering purely NSI were in agreement with the atmospheric data [58]. However, with higher statistics data and particularly with the addition of the high energy upward-going muon sample, NSIs appeared to be at best a sub-dominant effect to oscillations [57, 59, 60]. For this reason, an approach incorporating both neutrino oscillations while allowing for NSI effects was implemented in this thesis.

1.5.1 Treatment of NSI

The main topic of interest regarding neutrino NSI is in how they can generate flavour transitions as a sub-dominant effect. Therefore the flavour transition probabilities were calculated with a model independent approach described by a Hamiltonian including both Neutrino Oscillations and neutrino matter NSI [57].

These NSI can be classified into two categories: Flavour Changing Neutral Current (FCNC) [61–64] and lepton Non-Universality (NU) [65]. FCNC allows flavour transitions by the neutral current forward scattering of neutrinos in matter and take the form $\nu_\alpha + f \rightarrow \nu_\beta + f$. Here the neutrino converts from flavour α to flavour β by the interaction with a fermion, f. An example Feynman diagram for an FCNC interaction on a down quark is shown in Figure 1.7. NU allows the interaction probability amplitude of a neutrino with a fermion to vary depending on the flavour of the neutrino. A common feature of these interactions is that they are independent of the neutrino energy, however as previously stated, they should depend on the density and distance of the matter traversed.

To illustrate how these matter NSI can be incorporated into an oscillation model, consider

the Standard Model weak interaction hamiltonion:

$$H_W = \frac{G_F}{\sqrt{2}}(J_\mu^\dagger J_\mu + \rho J_\mu^{NC} J_\mu^{NC}), \tag{1.29}$$

where J_μ and J_μ^{NC} are the weak current. For neutrino scattering on a fermion, the effective hamiltonion becomes:

$$\begin{aligned} H_W^{eff} &= \frac{G_F}{\sqrt{2}}[\bar{f}\gamma_\mu(1-\gamma_5)\nu_\alpha][\bar{\nu}_\alpha\gamma^\mu(1-\gamma_5)f] \\ &+ \sqrt{2}G_F\rho[\bar{\nu}_\alpha\gamma_\mu\frac{1}{2}(1-\gamma_5)\nu_\alpha][\bar{f}\gamma^\mu(g_V - g_A\gamma_5)f], \end{aligned} \tag{1.30}$$

where $\rho = 1$ and L,R label the left- and right-handed fermions. g_V and g_A are:

$$g_V = g_L + g_R = -\frac{1}{2} + 2\sin^2\theta_W, \tag{1.31}$$

$$g_A = g_L - g_R = -\frac{1}{2}, \tag{1.32}$$

with θ_W as the weak mixing angle, or Weinberg angle. Then applying the Fierz transformation to the first term of Equation (1.30), separating the neutrino and fermion factors:

$$H_W^{eff} = \frac{G_F}{\sqrt{2}}[\bar{\nu}_\alpha\gamma_\mu(1-\gamma_5)\nu_\alpha][\bar{f}\gamma^\mu(c_V - c_A\gamma_5)f], \tag{1.33}$$

where c_V and c_A are corrections to the vector- and axial vector- weak charge, respectively, and are defined:

$$c_V = \begin{cases} g_V + 1 & (\alpha = f), \\ g_V & (\alpha \neq f), \end{cases} \tag{1.34}$$

$$c_A = \begin{cases} g_A + 1 & (\alpha = f), \\ g_A & (\alpha \neq f). \end{cases} \tag{1.35}$$

As neutrinos propagate through and interact with matter, they gain an interaction energy, V, from the fermion f, derived from Equation (1.33):

$$V_{SM} = \sqrt{2}G_F c_V N_f, \tag{1.36}$$

where N_f is the fermion number density in the matter traversed. In the case $\alpha \neq f$, the interaction energy becomes:

$$\begin{aligned} V_{SM} &= \sqrt{2}G_F c_V N_f \\ &= \sqrt{2}G_F g_V N_f \\ &= \sqrt{2}G_F(g_L(f) + g_R(f))N_f. \end{aligned} \tag{1.37}$$

Equation (1.37) shows the interaction energy gained in a standard model neutrino interaction with matter. Extending this to allow us to quantify the effect of NSI in a model independent way, we can redefine V as:

$$V_{NSI} = \sqrt{2}G_F(\varepsilon_{\alpha\beta}^{fL} + \varepsilon_{\alpha\beta}^{fR})N_f, \tag{1.38}$$

where the $\varepsilon^{fP}_{\alpha\beta}$ (P = L,R) parameterise the strength of NSI for an interaction with a left- or right-handed fermion, and correspond to the $g_P(f)$ neutral current coupling in the standard model. However, with atmospheric neutrinos we cannot distinguish interactions with left- and right-handed fermions in the matter propagated, so we consider $\varepsilon^{f}_{\alpha\beta} \equiv \varepsilon^{fL}_{\alpha\beta} + \varepsilon^{fR}_{\alpha\beta}$. Furthermore, the analysis normalisation is set by assuming interactions only with the down quarks in matter, following the convention set by previous analyses [58]. So we can drop the fermion superscript, taking $f = d$, and work with $\varepsilon_{\alpha\beta}$ parameters. NSI cases outside of this assumption can be considered by rescaling the $\varepsilon_{\alpha\beta}$ parameters reported in this thesis.

Considering the 2-flavour case in the ν_α–ν_β sector, the effective potential can be written as:

$$H(r) = H_0 + V_{eff} \tag{1.39}$$

$$= \begin{pmatrix} p & 0 \\ 0 & p \end{pmatrix} + \sqrt{2} G_F N_f(\vec{r}) \begin{pmatrix} \varepsilon_{\alpha\alpha} & \varepsilon^*_{\alpha\beta} \\ \varepsilon_{\alpha\beta} & \varepsilon_{\beta\beta} \end{pmatrix}, \tag{1.40}$$

where p is the momentum of the neutrino, and G_F is the Fermi coupling constant. The $\varepsilon_{\alpha\beta}$ represents the amplitude of the FCNC interactions, while the quantity $\varepsilon_{\beta\beta} - \varepsilon_{\alpha\alpha}$ represents the difference in the amplitude for ν_α or ν_β interactions with matter (NU). $N_f(\vec{r}$ is the fermion (d-quark) density as a function of position, $\vec{r}$, along the flight path of the neutrino. The Schrödinger equation can be written as:

$$|\psi(t)\rangle = \exp\left(-i \int_0^L H(r) dr \right) |\psi(0)\rangle, \tag{1.41}$$

where the integration is carried out along the neutrino flight path and L is the distance travelled. Then the survival probability of ν_α becomes:

$$P(\nu_\alpha \to \nu_\alpha) = 1 - \frac{\varepsilon^2_{\alpha\beta}}{\varepsilon^2_{\alpha\beta} + \frac{(\varepsilon_{\beta\beta} - \varepsilon_{\alpha\alpha})^2}{4}} \sin^2\left(\sqrt{2} G_F X_f \sqrt{\varepsilon^2_{\alpha\beta} + \frac{(\varepsilon_{\beta\beta} - \varepsilon_{\alpha\alpha})^2}{4}} \right), \tag{1.42}$$

where X_f is the column density of fermions, f, integrated over the neutrino flight path:

$$X_f = \int_0^L N_f(\vec{r}) dr. \tag{1.43}$$

It can be seen that the survival probability has an oscillitory magnitude that is a function of the column density of fermions on the neutrino path, but does not depend on the neutrino energy. This survival probability can be seen in Figure 1.8.

Since pure NSI alone cannot simultaneously explain the whole energy range of the atmospheric neutrino data, the effects of both neutrino oscillations and NSI can be included in one effective hamiltonion:

$$H_{\alpha\beta} = \frac{1}{2E} U \begin{pmatrix} 0 & 0 & 0 \\ 0 & \Delta m^2_{21} & 0 \\ 0 & 0 & \Delta m^2_{31} \end{pmatrix} U^\dagger \pm V_{MSW} \pm \sqrt{2} G_F N_f(\vec{r}) \begin{pmatrix} \varepsilon_{ee} & \varepsilon^*_{e\mu} & \varepsilon^*_{e\tau} \\ \varepsilon_{e\mu} & \varepsilon_{\mu\mu} & \varepsilon^*_{\mu\tau} \\ \varepsilon_{e\tau} & \varepsilon_{\mu\tau} & \varepsilon_{\tau\tau} \end{pmatrix}, \tag{1.44}$$

where the additional interaction potentials are positive for neutrinos and negative for anti-neutrinos. The first term is the vacuum oscillation term; the second is from MSW matter effects on electrons; and the third allows for NSI. In this way, the dominant mechanism for the flavour transitions are expected to come from oscillations, while deviations due to NSI could possibly be measured.

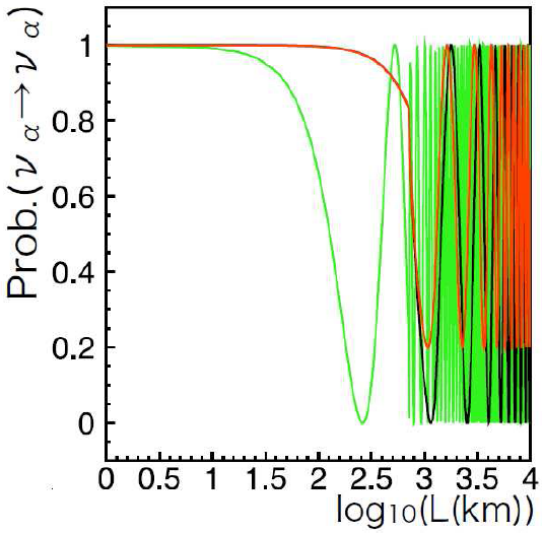

Figure 1.8: NSI survival probability for $\nu_\alpha \to \nu_\alpha$ as a function of the flight path in $\log_{10}(L\,(\mathrm{km}))$. The parameter sets are as follows, $\varepsilon_{\alpha\beta} = 1.0$ and $\varepsilon_{\beta\beta} - \varepsilon_{\alpha\alpha} = 0.01$ in black; $\varepsilon_{\alpha\beta} = 1.0$ and $\varepsilon_{\beta\beta} - \varepsilon_{\alpha\alpha} = 1.0$ in red; and $\varepsilon_{\alpha\beta} = 10.0$ and $\varepsilon_{\beta\beta} - \varepsilon_{\alpha\alpha} = 0.1$ in green. For this calculation, the average fermion density, $\langle N_f(\vec{r})\rangle$, along the flight path of the neutrino was used.

1.5.2 Previous Work with Atmospheric Neutrinos and NSI

With the initial statistics of early atmospheric neutrino data from SK-I, pure NSI could explain the ν_μ deficit as an alternative to neutrino oscillations [58]. However, with the addition of greater statistics and higher energy upward-going muon samples, pure NSI could no longer simultaneously explain the full energy range of atmospheric data [57, 59, 60].

Since the atmospheric data could no longer be explained by pure NSI alone, and with the success of the oscillation description at SK, analyses began to include oscillations and NSI together [45, 57]. This was done by including oscillations and $\mu\tau$–sector matter NSI in a 2-flavour Hamiltonian. The NSI contribution to the Hamiltonian [57] had the form:

$$H_{\mathrm{NSI}} = \pm\sqrt{2}G_F N_f(r) \begin{pmatrix} 0 & \varepsilon \\ \varepsilon & \varepsilon' \end{pmatrix}, \tag{1.45}$$

where N_f was the fermion number density and was taken to be the density of down-quarks as the normalisation for these analyses – the same normalisation used in this thesis. The + (−) sign holds for neutrinos (anti-neutrinos). This allowed for neutral-current-like interactions with matter, with the off-diagonal ε coupling for flavour-changing (FC) interactions; and the diagonal ε' ($\equiv \varepsilon_{\tau\tau} - \varepsilon_{\mu\mu}$) as the flavour conserving non-universality (NU) parameter. The mechanism was similar to the MSW matter interactions.

The first of these analyses was reported in 2002 [57] and made use of the 79 kton yr SK and MACRO data sets. The best-fit was at $\Delta m^2 = 2.4 \times 10^{-3}\,\mathrm{eV}^2$, $\sin^2 2\theta = 0.99$, $\varepsilon = -9.1 \times 10^{-3}$, and $\varepsilon' = -1.9 \times 10^{-3}$. The allowed regions can be seen in the left set of 4 plots in Figure 1.9. The oscillation mechanism was stable with the introduction of the perturbation from NSI. It was concluded that FC at the order of 1% could be present, while ν_μ and ν_τ interactions were likely to be universal. The 99% C.L. limits obtained from marginalising over the other parameters were $-0.03 < \varepsilon < 0.02$ and $|\varepsilon'| < 0.07$.

Another analysis was published in 2004 [45], that looked at oscillations with sub-dominant effects from new physics including matter NSI. In the latter case, the treatment was essentially the same as the 2002 analysis [57], and used the 1489 day SK and K2K data sets. The best-fit points were close to the best-fit for pure oscillations, so it was concluded that there was no

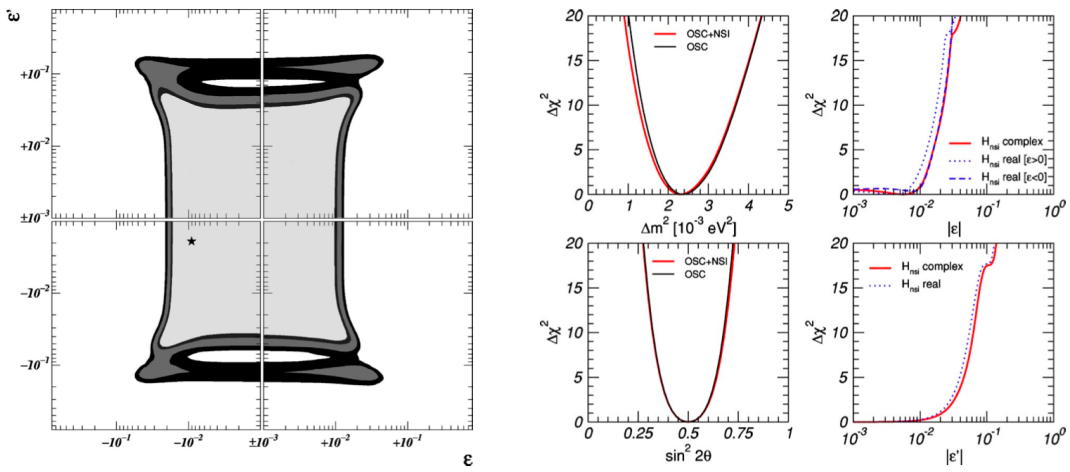

Figure 1.9: NSI allowed regions from the first oscillation+NSI hybrid analyses with atmospheric neutrinos. In the figures, ε represents the FCNC $\varepsilon_{\mu\tau}$ parameter and ε' represents the NU $(\varepsilon_{\tau\tau} - \varepsilon_{\mu\mu})$ parameter. The left four figures were reported in 2001 using the 79 kton yr SK and MACRO data sets [57]. The two oscillation parameters were integrated out, and the shaded regions refer to 90%, 95%, 99% and 99.7% C.L. with two parameters. While the right four figures are from 2004 and used the 1489 day SK and K2K data sets [45]. The undisplayed parameters were marginalised out.

evidence for new physics even as a sub-dominant effect. The allowed regions are shown in the right 4 plots in Figure 1.9. The oscillation mechanism was found to be robust, and the 90% (3σ) bounds on matter NSI were:

$$(-0.021) - 0.013 \leqslant \varepsilon \leqslant 0.010(0.017), \tag{1.46}$$
$$|\varepsilon'| \leqslant 0.029(0.052) \qquad (\mathbf{H}_{\text{NSI}} \text{ real}), \tag{1.47}$$
$$|\varepsilon| \leqslant 0.013(0.021), \tag{1.48}$$
$$|\varepsilon'| \leqslant 0.034(0.060) \qquad (\mathbf{H}_{\text{NSI}} \text{ complex}). \tag{1.49}$$
$$\tag{1.50}$$

These bounds were well-constrained, however it was called into question whether a 2-flavour treatment was sufficient for atmospheric neutrinos [13, 66–68]. In a 2004 analysis of atmospheric neutrinos and ν_e mixing NSI [66, 67], it was shown that at least $\varepsilon_{\tau\tau}$ bounds were significantly relaxed by the addition of non-zero $\varepsilon_{e\tau}$. Values of $\varepsilon_{\tau\tau}$ up to $\mathcal{O}(1)$ were allowed, along the parabola $\varepsilon_{\tau\tau} = |\varepsilon_{e\tau}|^2/(1+\varepsilon_{ee})$ where the oscillations mimic vacuum oscillations with the same dependence on the neutrino flight path and energy. This allowed region can be seen in Figure 1.10. So with the large range of baselines of atmospheric neutrinos, that also traverse the matter densities of the mantle and core, 3-flavour effects become more significant. In this thesis, a 3-flavour approach to NSI was conducted. Accelerator baselines at the order of a couple hundred kilometres, like that of MINOS and T2K, would be less sensitive to these 3-flavour effects and a 2-flavour approach is sufficient [69].

The early results from MINOS running in anti-neutrino mode reported a significantly larger $\Delta\bar{m}^2 = 3.36^{+0.45}_{-0.40} \times 10^{-3}\,\text{eV}^2$ than the value obtained from their neutrino analysis [10], and also

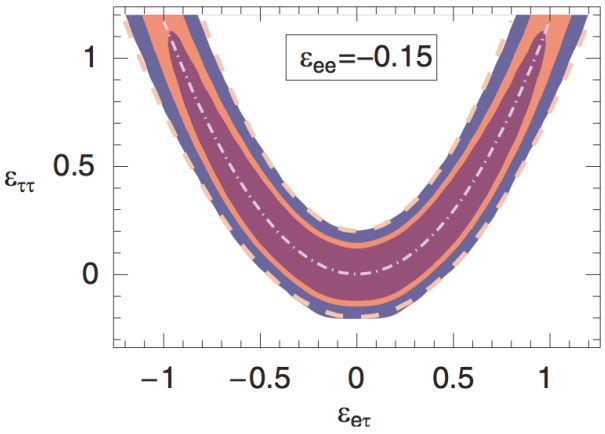

Figure 1.10: Effect of ν_e mixing with electron flavour ε NSI in atmospheric neutrinos [66]. This is a 2-D cross-section at $\varepsilon_{ee} = -0.15$, where the shaded regions represent 95%, 99% and 3.6σ C.L. for 3 degrees of freedom. This is inverted hierarchy where $|\varepsilon_{e\tau}|$ and $|\varepsilon_{\tau\tau}|$ extend up to $\mathcal{O}(1)$ at the 95% C.L. For normal hierarchy this extent is up to ∼0.6. The inner contour represents a condition of zero eigenvalue, where NSI mimics vacuum oscillations along the parabola $\varepsilon_{\tau\tau} = |\varepsilon_{e\tau}|^2/(1+\varepsilon_{ee})$

allowed a larger deviation for $\sin^2 2\bar{\theta} = 0.86 \pm 0.11$. In an attempt to explain these results, a few analyses were carried out in 2010 considering the effect of matter NSIs [13, 70].

The apparent difference in the ν_μ and $\bar{\nu}_\mu$ data could be explained by the oscillation phase receiving a contribution from matter effects that retards (advances) the total phase as ν_μ ($\bar{\nu}_\mu$) propagate through matter [13]. The effect of this shift in phase would cause an analysis assuming vacuum oscillations to measure a Δm^2 of lower (higher) value. A phenomenology involving matter NSI would have one value for Δm^2 in between the vacuum oscillation measurements. For normal hierarchy, this effect could be produced with a negative value for $\varepsilon_{\mu\tau}$; and a positive value for the inverted hierarchy case.

In 2010, the MINOS data for ν_μ and $\bar{\nu}_\mu$ were simultaneously fit by Mann et al. [13] with the best-fit at $(\Delta m^2,\ \sin^2 2\theta_{23},\ \Re(\varepsilon_{\mu\tau})|V_e|) = (2.56^{+0.27}_{-0.24} \times 10^{-3}\,\text{eV}^2,\ 0.90 \pm 0.05,\ -(0.12 \pm 0.21)|V_e|)$ [13]. The allowed regions of the separate and combined fits of this analysis can be seen in Figure 1.11. It can be seen in the separate ν_μ ($\bar{\nu}_\mu$) allowed region that an increase in the magnitude of $|\varepsilon_{\mu\tau}|$ favours a larger (smaller) value for Δm^2. The Δm^2 converge into a single value for the combined fit. In the analysis, electron number density was assumed in the Earth's crust, and so the MINOS data could be explained with matter NSI at around 12% the strength of the MSW effect. This result was not taken as evidence for non-zero $\varepsilon_{\mu\tau}$, as $\varepsilon_{\mu\tau} = 0$ was within 1σ, however the NSI fit worked as well as a pure oscillation fit and could fit the ν_μ and $\bar{\nu}_\mu$ data simultaneously with 3 parameters. Considering the much more significant matter effects in atmospheric neutrinos, the difference in the Δm^2 assuming vacuum oscillations would grow with energy up to ∼20 GeV. However, since ν_μ and $\bar{\nu}_\mu$ cannot be separated on an event-by-event basis, this effect would be averaged over.

Another analysis of the MINOS data by Kopp et al. [70] assumed that NC-like matter NSI were already disfavoured by the 2-flavour atmospheric NSI analyses, but the data could be explained by CC-like NSI at the production or detection of the neutrinos within NSI bounds at the time. However, the paper included an initial analysis with NC matter NSI. The analysis also had an electron number density normalisation, and had the best-fit parameters $(\varepsilon^m_{\mu\tau},\ \varepsilon^m_{\tau\tau},\ \sin^2\theta_{23},\ \Delta m^2_{32}) = (-0.40,\ -2.16,\ 0.38,\ 2.86 \times 10^{-3}\,\text{eV}^2)$. Where the m superscript denoted matter NSI to distinguish from the CC case. The allowed regions can be seen in Figure 1.12.

The $|\varepsilon^m_{\mu\tau}| \sim 0.4$ measured here was considerably larger than the $|\varepsilon^m_{\mu\tau}| \sim 0.1$ measured by Mann et al. [13], which used the same data set and normalisation. The difference was thought to be due to Mann et al. fitting the oscillation probability to the ratio of observed to expected

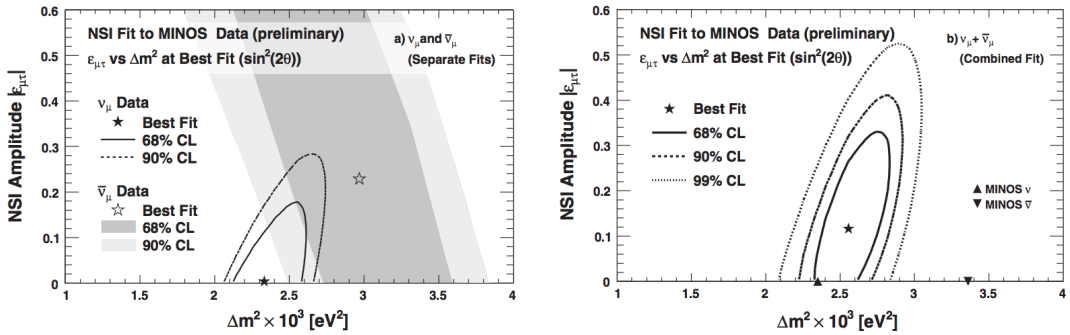

Figure 1.11: Fit of NC-like matter NSI [13] to explain the 2010 MINOS data [10]. The left plot shows the NSI fits to the ν_μ (contours) and $\bar{\nu}_\mu$ (shaded regions) data separately. With increasing $|\varepsilon_{\mu\tau}|$, the Δm^2 increases for neutrinos; while the Δm^2 decreases for anti-neutrinos. The right plot shows the fit to the combined data, and at the best-fit the Δm^2 converge to one value, in between the vacuum oscillation values (triangles).

event numbers from MINOS, while this analysis used a modified version of GLoBES to simulate the energy resolution effects at MINOS, and could reproduce the MINOS results rather well. Despite the large best-fit value for $|\varepsilon^m_{\tau\tau}|$, the result was compatible with $\varepsilon^m_{\tau\tau} = 0$ at the 90% C.L. Interestingly however, pure standard oscillations was ruled out at the 90% C.L (with the MINOS data in 2010).

With the significant results from these matter NSI analyses with MINOS data, there was good motivation to look for differences in vacuum oscillation parameters between neutrinos and anti-neutrinos and to search for sub-dominant NSI with atmospheric neutrinos at SK – the topic of this thesis. There has already been an initial NSI search at SK making use of the zenith distributions, reported in 2011 [73]. The analysis in the $\mu\tau$–sector used a 2-flavour Hamiltonian, and followed the model used in the first NSI+Oscillation analyses of atmospheric data [45], and used the down-quark number density normalisation. The best-fit was at $\sin^2 2\theta_{23} = 1.00$, $\Delta m^2_{32} = 2.2 \times 10^{-3}\,\text{eV}^2$, $\varepsilon = 1.0 \times 10^{-3}$, $\varepsilon' = -2.7 \times 10^{-2}$, $\chi^2_{\text{min}} = 838.9/746.0$ d.o.f. The allowed regions for the oscillation parameters and for the NSI parameters are shown in Figure 1.13. The 90% C.L. limits for the NSI parameters were:

$$|\varepsilon| < 1.1 \times 10^{-2},$$
$$-4.9 \times 10^{-2} < \varepsilon' < 4.9 \times 10^{-2}.$$

From looking at the NSI allowed regions for each of the samples separately, it was found that the ε parameter was mostly constrained by the upward-going muon sample, and the ε' parameter by the partially-contained and stopping muon samples. A 3-flavour oscillation analysis with NSI in the $e\tau$–sector was also carried out (separately from the $\mu\tau$–sector analysis). The NSI analysis in this thesis was conducted with a 3-flavour Oscillation+NSI model focussed mostly on the $\mu\tau$–sector, using high resolution L/E distributions to look for any deviations from standard oscillations. However, since the L/E value cannot be reconstructed with sufficient resolution for the upward-going muon samples, they were not included in the analyses in this thesis.

In 2013, the MINOS collaboration looked for NSI in their data [69]. At the MINOS baseline, the $\mu\tau$–sector NSI are effectively disjoint from the $e\tau$-sector, so a 2-flavour approach was taken. The long propagation path of neutrinos in matter gives an enhanced sensitivity to NC-like matter

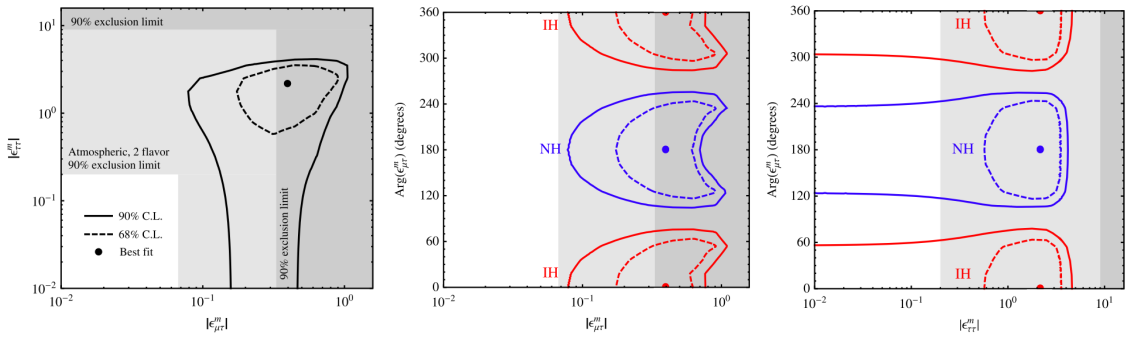

Figure 1.12: NC-like NSI allowed regions in the $\mu\tau$–sector from a modified GLoBES simulation fit by Kopp et al. [70] to the 2010 MINOS ν_μ and $\bar{\nu}_\mu$ data [10]. In each panel the third NSI parameter was marginalised out, as were the oscillation parameters. The best-fit for $\varepsilon^m_{\mu\tau}$ was considerably larger than the other fit to the same data from Mann et al. [13]. While pure standard oscillations were ruled out at the 90% C.L. The stringent 2-flavour atmospheric limits [57, 71] and general limits [72] are shown in the gray shaded regions. The left-most panel shows the $\arg(\varepsilon^m_{\mu\tau})$ parameter marginalised out, while the effect of the parameter is shown in the other two panels.

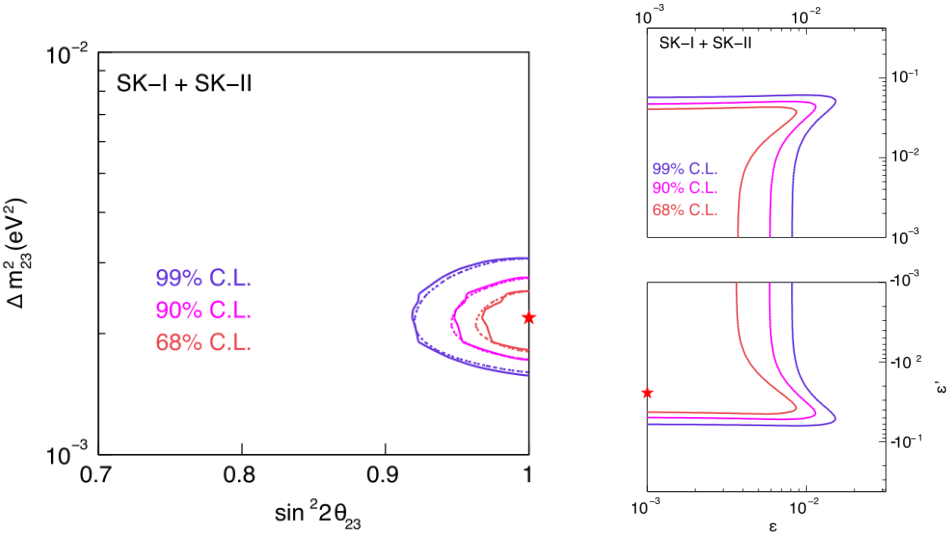

Figure 1.13: Allowed regions from a 2-flavour Oscillation+NSI analysis in the $\mu\tau$–sector with the *Zenith* distributions at SK [73]. The undisplayed parameters were integrated out. In the left panel, the solid contours are for the Oscillation+NSI hybrid model, and the dashed curves for standard 2-flavour Oscillations. The right panels show the NSI allowed regions, where the parameters were defined as $\varepsilon \equiv \varepsilon_{\mu\tau}$ (FCNC) and $\varepsilon' \equiv (\varepsilon_{\tau\tau} - \varepsilon_{\mu\mu})$ (NU). The stars represent the best-fit points.

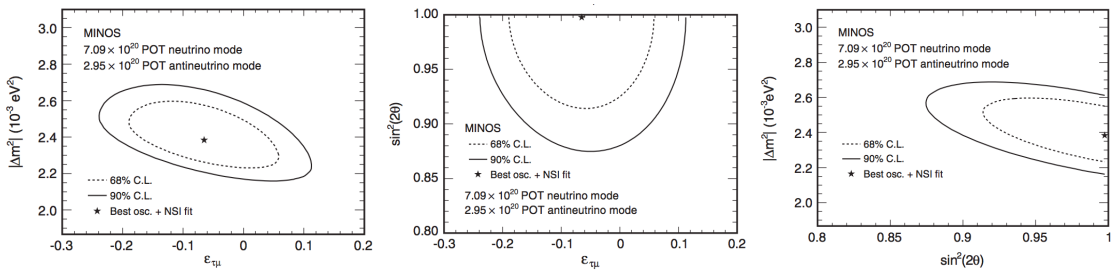

Figure 1.14: Allowed regions for NC-like NSI from the MINOS collaboration [69]. The 68% and 90% C.L. contours are shown for 2D projections of the (Δm^2, $\sin^2 2\theta$, $\varepsilon_{\mu\tau}$) parameter space with the third parameter marginalised out. The left-most panel shows $\varepsilon_{\mu\tau}$ against Δm^2; the middle is of $\varepsilon_{\mu\tau}$ against $\sin^2 2\theta$; and the right shows the oscillation parameter allowed regions for the ν_μ and $\bar{\nu}_\mu$ data combined.

NSI, so the paper focussed on that case. CC-like NSI along the neutrino path would produce an outgoing charged lepton, which gets absorbed by the Earth's matter and would not be observed. On the other hand, NC-like NSI along the neutrino flight path produces a final state neutrino with another flavour, altering the flavour composition of the beam. Three parameters were fit, and the best-fit point was at:

$$\begin{aligned} \Delta m^2 &= 2.39^{+0.14}_{-0.11} \times 10^{-3}\,\mathrm{eV}^2, \\ \sin^2 2\theta &= 1.00^{+0.00}_{-0.06}, \\ \varepsilon_{\mu\tau} &= -0.07^{+0.08}_{-0.08}, \end{aligned}$$

with the allowed region $-0.20 < \varepsilon_{\mu\tau} < 0.07$ (90% C.L.). Note that the analysis assumed the electron number density in matter, as opposed to down-quark normalisation. So the magnitude of these $\varepsilon_{\mu\tau}$ regions are three times larger than for down-quark density normalisation, to describe the same effect. Figure 1.14 shows the 2D allowed regions with the third parameter marginalised out. The oscillation parameter allowed regions were in agreement with previously reported regions by MINOS. Within the errors the fit was consistent with no contribution from flavour changing NSI.

A summary of the bounds on NSI was published in 2009 [72], which also quoted the ε regions assuming electron number density, and so are also 3 times larger than ε regions measured in this thesis to describe the same effect. The 90% C.L. bounds were

$$|\varepsilon^{\bigoplus}_{\alpha\beta}| < \begin{pmatrix} 4.2 & 0.33 & 3.0 \\ 0.33 & 0.068 & 0.33 \\ 3.0 & 0.33 & 21 \end{pmatrix},$$

where the $\bigoplus$ superscript denoted interactions in Earth matter and the columns and rows run through the e, μ and τ flavour. So the $\varepsilon_{\alpha\beta}$ are arranged in the same form as the NSI matrix in Equation (11.3). The constraints on the parameters of interest in this thesis, $\varepsilon_{\mu\tau}$ and $\varepsilon_{\tau\tau}$, were fairly loosely bound. Whether the tighter constraints from 2-flavour atmospheric analyses hold in a 3-flavour framework will be determined in this thesis.

1.6 Outline of Thesis

The aim of this thesis is:

1. To determine if any difference in oscillation parameters can be observed between neutrinos and anti-neutrinos, assuming no matter effects, with an L/E analysis at SK; or to confirm the CPT symmetry of neutrino oscillations.

2. To perform the first 3-flavour L/E Analysis with non-zero θ_{13}, to check that this is still a good method to make oscillation measurements, and to obtain more accurate oscillation parameters free from 2-flavour approximations.

3. To search for NC matter NSI in the $\mu\tau$–sector in the atmospheric neutrino data with a 3-flavour hybrid model of Oscillations and NSI, for the first time. To determine the degree of non-standard neutrino interactions allowed by the data, in a model-independent way.

These searches were initially inspired by the discrepancy in ν_μ and $\bar{\nu}_\mu$ data around 2011, and the interest in the literature that NSI could potentially be acting sub-dominantly behind neutrino mass mixing. However, these analyses are further motivated to confirm the CPT symmetry in neutrinos, and for the search for new non-standard physics. In addition, now that we know θ_{13} is not-so-small, it is better to perform oscillation analyses in 3-flavours. Atmospheric neutrinos cover a large range of energies and baselines and have an enhanced sensitivity to matter effects, such as in NSI or the MSW effect. Moreover, the L/E Analysis has the best discrimination of Δm^2_{31} from atmospheric neutrinos, making it a good analysis to perform these studies.

To this end, the chapters in this thesis are arranged as follows. Chapter 2 covers a comprehensive overview of over 40 years of experimental evidence for neutrino oscillations, including the many ways the ghostly neutrino has been detected, and the unravelling of the anomalies to our present understanding. Chapter 3 describes Super-Kamiokande, the detector that collected the analysis data. Chapter 4 explains details of the simulation, from the determination of the atmospheric neutrino flux, to the interactions and detector simulation. Chapter 5 highlights some of the calibrations to ensure the energy, time and charge accuracy at SK and the extraction of input values to the simulation. Chapter 6 details how the raw data is reduced to neutrino events and Chapter 7 illustrates how physical properties are reconstructed from the data.

For the analyses and the main contributions of the author, Chapter 8 explains the details of the 2-flavour L/E analysis and is relevant to all other analyses in this thesis. Chapter 9 covers an analysis that searches for the difference in neutrino and anti-neutrino oscillation parameters assuming the vacuum condition, while expanding the available data with an additional resolution sample. Chapter 10 describes the extension of the L/E Analysis to 3-flavour oscillations, while the 3-flavour Oscillation and NSI analysis is covered in Chapter 11. Finally, the conclusions of this thesis are written in Chapter 12.

List of Abbreviations:

ADC : Analogue to Digital Converter

ATM : Analogue Timing Module

CC : Charge-Current

FC : Fully-Contained

FCFV : Fully-Contained Fiducial Volume

FV : Fiducial Volume

HE : High Energy. High Energy Trigger

HV : High Voltage

ID : Inner Detector

LE : Low Energy. Low Energy Trigger

L/E : Neutrino Flight Length over Neutrino Energy

MC : Monte Carlo

MSW : Mikheyev–Smirnov–Wolfenstein effect (matter effect)

NC : Neutral-Current

NSI : Non-Standard (Neutrino) Interactions

OD : Outer Detector

PC : Partially-Contained

p.e. : Photo-electrons

PMT : Photo-Multiplier Tube

QAC : Charge to Analogue Converter

QTC : Charge to Time Converter

QE : Quantum Efficiency

SK : Super-Kamiokande

TAC : Time to Analogue Converter

TOF : Time of Flight

UPMU : Upward-Going Muons

Chapter 2

Experimental Evidence for Neutrino Oscillations

The neutrino is difficult to detect, Pauli himself wondered if it could ever be seen. However, over the years experimentalists have managed to detect the neutrino in the laboratory, amass statistics of neutrino fluxes, and find some quite surprising results. One such outcome is that neutrinos are thought to oscillate in such a way that their flavour at detection may differ from their flavour at creation – Neutrino Oscillations. This theory however, requires that neutrinos have mass while the neutrinos in the Standard Model are massless. There has been a wealth of evidence for Neutrino Oscillations collected over the last 40 or so years, and some of the highlights have been collected here.

2.1 Solar Neutrino Experiments

The most obvious source of neutrinos is the sun, producing a tremendous flux of neutrinos during the fusion processes that are the origin of almost all the energy used on Earth today. Since neutrinos easily pass through matter, they can provide a window to study the interactions occurring at the core of the sun. There are a number of chains of interactions at the solar core, fusing nuclei into increasingly heavier elements. Interactions like the following:

$$4\mathrm{p} \rightarrow {}^{4}\mathrm{He} + 2e^{+} + 2\nu_e + \gamma \tag{2.1}$$

where the above equation is an average representative reaction of the proton-proton-chain (pp-chain), and shows the process of four protons, p, fusing into a Helium nucleus, and emitting neutrinos and photons. There are actually multiple steps and several possible branches that the reaction cycle can follow, accurately calculated and tested in the Standard Solar Model (SSM)[74, 75]. Other branches can lead on to produce ^{7}Be or ^{8}B, each also producing neutrinos. A summary of the energy spectrum of the emitted neutrino fluxes at the Suns core, labelled by the parent isotope it is associated with, can be seen in Figure. 2.1. The three main fusion reactions emitting neutrinos are [76]:

$$\text{pp neutrinos} \qquad \mathrm{p} + \mathrm{p} \longrightarrow \mathrm{d} + e^{+} + \nu_e \qquad E_{\max} = 420\,\mathrm{keV} \tag{2.2}$$

$$^{7}\text{Be neutrinos} \qquad {}^{7}\mathrm{Be} + e^{-} \longrightarrow {}^{7}\mathrm{Li} + \nu_e \qquad E = 860\,\mathrm{keV}\ \text{(mainly)} \tag{2.3}$$

$$^{8}\text{B neutrinos} \qquad {}^{8}\mathrm{B} \longrightarrow {}^{8}\mathrm{Be} + e^{+} + \nu_e \qquad E_{\max} = 14\,\mathrm{MeV} \tag{2.4}$$

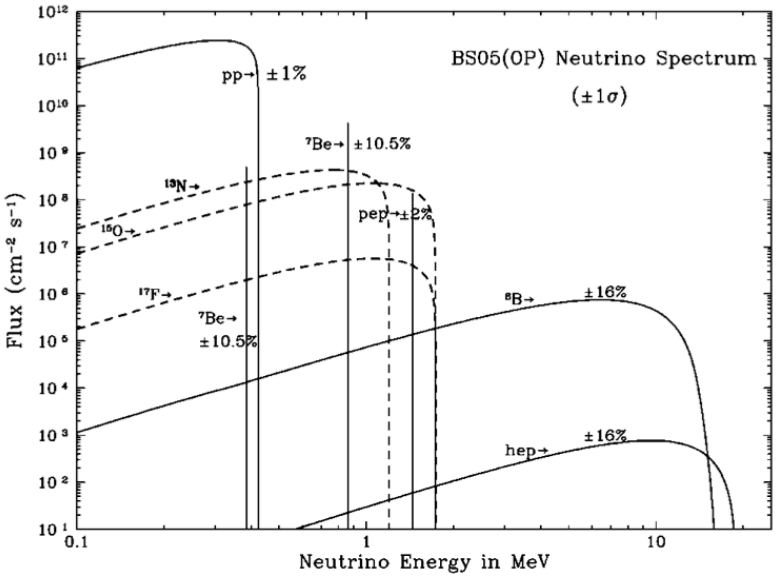

Figure 2.1: Fluxes of solar neutrinos as predicted from the BS05(OP) Standard Solar Model [74] The labels indicate the source reaction of the neutrinos. The relative abundances can be seen. The pp neutrinos have the largest flux, but their low energies made them difficult to detect and were measured in radio-chemical experiments. The ^{7}Be mono-energetic peak was challenging to distinguish and was seen in Borexino. The ^{8}B neutrinos extend to higher energies and could be seen by Cherenkov detectors such as SK and SNO.

where the d is a deuteron and the reactions have the relative fluxes: $\phi_{\mathrm{pp}} : \phi_{^{7}\mathrm{Be}} : \phi_{^{8}\mathrm{B}} \approx 1 : 0.08 : 0001$. The most abundant source of neutrinos is the pp-chain, but the energy of these neutrinos is in the order of a fraction of an MeV and are difficult to detect. There have been a number of solar neutrino experiments, each employing a different detection method and having sensitivity to a different region of the solar neutrino spectrum.

2.1.1 Homestake Chlorine Experiment

The Chlorine experiment conducted by Raymond Davis et al. began in 1967, and reported the first detection of solar neutrinos in 1968 [23, 77–79]. The experiment continued to take data for around 25 years, improving the statistics and accuracy of its initial findings. The detection method made use of 615 metric tons of tetrachloroethylene (perchloroethylene), C_2Cl_4, that captured solar neutrinos by the process $^{37}\mathrm{Cl}(\nu, e^{-})^{37}\mathrm{Ar}$. The reaction has an energy threshold of 0.814 MeV, giving it sensitivity to the ^{7}Be and ^{8}B solar neutrino fluxes. The SSM predicted that 78% of the relevant flux is from ^{8}B neutrinos, while 13% originate from ^{7}Be neutrinos [71]. The detector was a horizontal cylindrical tank and was built 4400 m.w.e.[1] underground, to greatly reduce the background from cosmic rays, in the Homestake gold mine at Lead, South Dakota. The detector facility can be seen in Figure 2.2.

Neutrino detection involved removing the ^{37}Ar from the liquid chlorine and then observing the ^{37}Ar decay (35.0 day half-life) in miniature proportional counters. To achieve this eductors

[1] m.w.e is metres water equivalent, the depth of water in metres that would give the same reduction in flux of Cosmic Rays. 2.650 times the depth of standard rock.

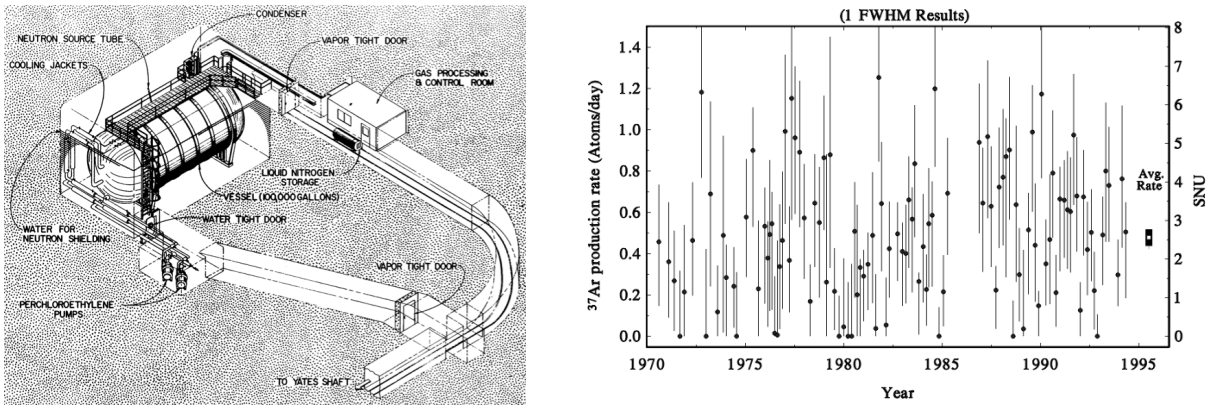

Figure 2.2: The Chlorine Experiment facility on the left and ^{37}Ar production rate on the right [78]. The large tank holding the tetrachloroethylene and helium/argon gas can be seen, as well as the pipes and pumps for circulating and extracting from the gas. The ^{37}Ar production rate from the maximum-likelihood analysis can be seen from the data between 1970 and 1994. The final 'average' point is from an analysis combining all the data.

circulated helium from the gas at the top of the tank into the chlorine liquid, which maintained an equilibrium between dissolved argon in the chlorine and gaseous argon in the gas mixture above. The helium/argon gas was pumped through an argon extraction system that involved 77° K charcoal traps that absorbed the argon. The charcoal was heated to remove the argon/noble gas mixture, and the other noble gasses were removed with two stages of gas chromatography. From tests, it was determined that 95% of the argon can be removed from a helium purge over 22 hours [23].

Afterwards the ^{37}Ar decay events, by electron capture releasing 2.82 keV Auger electrons, was observed in miniature proportional counters over a period of 250-400 days. Most of the background was rejected by selecting for the energy and characteristic pulse rise time. The output of the selection was a time series of events including signal and background. Finally, a maximum-likelihood analysis for the series of events with variables for production rate of ^{37}Ar in the detector, and background rate in the counter, was carried out. The resulting ^{37}Ar production rate was attributed to the solar neutrino flux. The ^{37}Ar production rate from 1970 to 1994 is shown in Figure 2.2, with the last point from a combined analysis of all the data [78].

Over the whole data taking period, a consistently smaller flux than predicted by the SSM was measured [78]. The neutrino capture rate was:

$$R_{\mathrm{Cl}} = 2.56 \pm 0.16 \pm 0.16\,\mathrm{SNU} \tag{2.5}$$

where 1 Solar Neutrino Unit (SNU) is the equivalent to the neutrino flux producing 10^{-36} captures per target atom per second. The neutrino capture rate compared with the SSM prediction was [71]:

$$\frac{R_{\mathrm{Cl}}}{\mathrm{SSM}} = 0.3 \pm 0.03 \tag{2.6}$$

The ratio of ν_e observed was around 30% of that expected. Since this result could not be explained by the Standard Model, this was the beginning of the so-called *solar neutrino problem*. Davis continued the experiment to verify the result for around 25 years, earning him the shared Nobel Prize in Physics in 2002 [79].

2.1.2 Gallium Experiments

Since 1990, there have been more radiochemical solar neutrino experiments using Galium as their detection mass, through the $^{71}\mathrm{Ga}(\nu, e^-)^{71}\mathrm{Ge}$ reaction. It has a low threshold at 233 keV, which gave these experiments sensitivity down to the pp-neutrinos. Gallium allowed for the observation of 93% of the solar neutrino flux, and without these experiments, the majority of the flux would not have been measured. The SAGE experiment began in Russia in 1990 with 30 tons of liquid metallic Gallium (increased to 57 tons since 1991) [25], and the GALLEX experiment ran in Gran Sasso, Italy, from 1991–1997 with 30.3 tons of gallium in the form of $GaCl_3$-HCl [80]. The GALLEX experiment was superseded by GNO from 1998–2003. The expected flux of solar neutrinos from the SSM for gallium was 128^{+9}_{-7} SNU, of which the pp neutrino component was 69.7 SNU [25].

The concept of these experiments were similar to the Chlorine Experiment. The GALLEX (GALLium EXperiment) experiment made use of 30.3 t of gallium containing 12 t of ^{71}Ga in aqueous gallium chloride solution at 101 t. This was contained in a 7 m high 70 m^3 tank. Each exposure began with the addition of ≈1 mg of a stable germanium carrier, and lasted about 3-4 weeks, after which the Ge would be extracted.

The acidity of the solution and the high concentration of chlorine ensured that the germanium would be in the form of the volatile tetrachloride, $GeCl_4$. Which could be separated from the non-volatile $GaCl_3$ by bubbling nitrogen gas through the liquid. The $GeCl_4$ was reabsorbed in water, and chemically converted to germane, GeH_4, which was then counted in specialised miniature very-low-background proportional counters. Tests showed that the extraction efficiency was greater than 99%.

In 1992, GALLEX reported on the first observation of solar pp-neutrinos, with the full expected flux, and reduced fluxes for ^{8}B and ^{7}Be neutrinos [76, 81]. The result in 1999 from GALLEX I-IV [80] was

$$R_{\mathrm{GALLAX}} = 77.5 \pm 6.2(\mathrm{stat.})^{+4.3}_{-4.7}(\mathrm{syst.})\,\mathrm{SNU} \tag{2.7}$$

where the errors were at 1σ. The GALLAX data from the solar runs, together with the GNO data, can be seen in Figure 2.3.

The SAGE (Soviet-American Gallium Experiment) experiment made use of 50 t of gallium in the form of a liquid metal and was distributed over seven 2 m^3 chemical reactors. The runs began with the addition of 700 μg of a germanium carrier uniformly distributed over all the reactors, and lasted 3-4 weeks. The reactors had motors for stirring the liquid metal to thoroughly mix in the Ge carrier and the extraction reagent during an extraction.

To extract the Ge [82], a reagent containing de-ionised water, HCl and H_2O_2 was added to the Ga, which turns it into an emulsion of droplets. The Ge dissolved in Ga migrated to the surface of the droplets where it becomes oxidised. This oxide was dissolved with more HCl, and immediately decanted out.

The Ge was concentrated firstly by evaporating it. More HCl was added to increase the volatility of the $GeCl_4$, and an air flow was used to sweep it from the solution, after which it was absorbed in 1 l of de-ionized water. The Ge in the swept solution was further concentrated by 3 stages of solvent extraction, into 100 ml of low-tritium water. This solution was then synthesised into germane (GeH_4), where it was swept by helium and separated using gas chromatography. The final gas mixture was then inserted into a miniature proportional counter. Since 1997 (SAGE

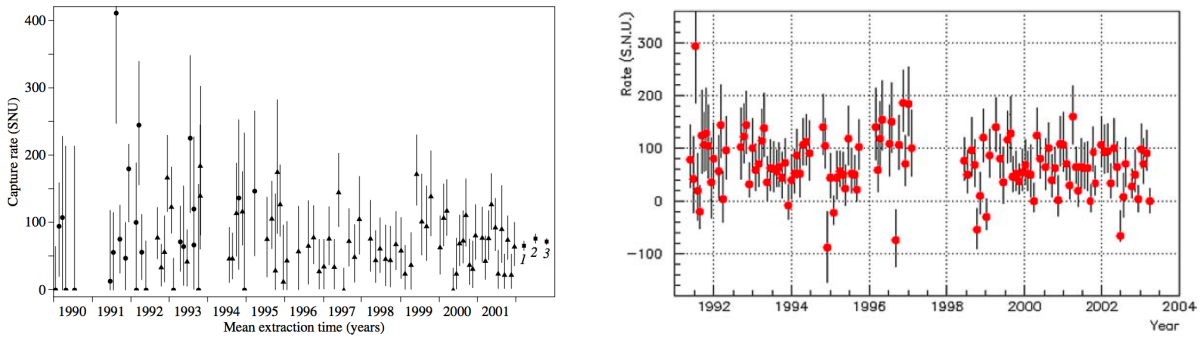

Figure 2.3: The gallium solar neutrino rate from SAGE on the left [25], and the combined result from GALLAX and GNO on the right [24]. In the SAGE data, the triangles represent an analysis with the L and K peaks, and circles for K peaks alone. The final three points show combined analysis points for (1) L Peak, (2) K Peak, and (3) all data. The GALLEX and GNO data span a full solar cycle and side reaction contributions have been subtracted. The error bars on both figures are 1σ statistical.

III), the quantity of the reagents added during an extraction was halved, and two extractions were performed. The extraction efficiency was ∼80% and improved to over 90% by 1997 [82].

In the counters, ^{71}Ge decays only by electron capture to the ground state of ^{71}Ga. These decays resulted in the emission of Auger electrons observed by the proportional counters, and X-rays that were measured with a reduced efficiency. The signal was a nearly point-like ionisation, and a fast pulse rise time. These characteristics allowed separation from the background. The data was put through a selection process, resulting in candidate ^{71}Ge events with both L- and K- peak regions. These were fitted with a likelihood for a decay curve of a fixed number of ^{71}Ge atoms, and two constant backgrounds for each peak. From the fitted parameters the production rate of Ge per day, and the solar neutrino flux was calculated.

In 2002, after taking 12 years of data, SAGE measured the following capture rate of solar neutrinos [25]:

$$R_{\mathrm{SAGE}} = 70.8^{+5.3}_{-5.2}(\mathrm{stat.})\,\mathrm{SNU} \tag{2.8}$$

The systematic errors were not included as they were considerably smaller than the statistical error ($^{+3.7}_{-3.2}$ SNU). Their result was a 6σ deviation from the expectation from the SSM. They concluded that this was strong evidence for a reduced flux of solar neutrinos from the expectation, and that neutrino matter oscillations in the LMA range best described the data (see Section 2.1.4 for details about the Large Mixing Angle solution). The data can be seen in Figure 2.3.

The GNO (Gallium Neutrino Observatory) experiment [24] also at LNGS, Gran Sasso, was the successor to the GALLEX experiment, and ran from 1998 to 2003. The neutrino target was still 100 t of gallium chloride, containing 30.3 t of gallium. The observations of GNO improved the quality of data, and combined with GALLAX cover more than a full solar cycle (1991-2003).

The experimental set-up from GALLEX went through a major overhaul and modernisation for GNO. The extraction procedure was largely the same as that for GALLAX, although the efficiency improved to an average of 95.7% determined from the recovery of the Ge carriers, where ≈1 mg was added per run. The electronics were upgraded. New preamplifiers for improved resolution in the pulses; new data acquisition system that had better pulse discrimination; and a new X-ray calibration source that helped reduce systematic errors [83].

The analysis involved a neural network for the pulse shape selection, replacing the rise-time selection used in GALLEX, and was followed by a maximum likelihood analysis. The neural network had a better noise rejection than the previous method, including the recognition and rejection of fast-rising background pulses.

The result from all the GNO data, and GALLAX+GNO was [24]:

$$R_{\mathrm{GNO}} = 62.9^{+6.0}_{-5.9}\,\mathrm{SNU} \tag{2.9}$$

$$R_{\mathrm{GALLEX+GNO}} = 69.3 \pm 4.1(\mathrm{stat.}) \pm 3.6(\mathrm{syst.})\,\mathrm{SNU} \tag{2.10}$$

With the errors at 1σ and with the GNO errors including both systematic and statistical contributions. The rates were after the 4.55 SNU subtraction from side reactions. The systematic error was dominated by the counting efficiencies. The results from GALLEX and GNO also showed that there was a constant production rate of ^{71}Ge over the whole period. The production rate for the GALLEX and GNO runs can be seen in Figure 2.3.

In gallium, the SSM estimation is that 54% of the flux comes from pp-neutrinos, 26% from ^{7}Be neutrinos and 11% from ^{8}B neutrinos. The combined rate of solar neutrinos measured by these Gallium experiments was [24]:

$$R_{\mathrm{Ga}} = 68.1 \pm 3.75\,\mathrm{SNU} \tag{2.11}$$

When this was compared with the SSM prediction, the following ratio was observed:

$$\frac{R_{\mathrm{Ga}}}{\mathrm{SSM}} = 0.52 \pm 0.03 \tag{2.12}$$

So the Gallium experiments gave a confirmation of the solar neutrino problem, and clearly an explanation was required for the deficit in solar neutrinos observed.

2.1.3 Kamiokande

The Kamioka Nucleon Decay Experiment (KamiokaNDE) was built to search for proton decay, and took analysis data from 1987–1995 [26]. The Kamioka Observatory is located 2700 m.w.e underground in the Kamioka mine, Japan. The detector was a cylindrical tank, 16.1 m tall and 15.6 m in diameter, filled with 2140 tons of pure water with 948 photomultiplier tubes (PMTs) facing inwards from the wall – 20% photodetector coverage. This allowed the measurement of charged particles by their Cherenkov radiation. Interaction particles travelling faster than the speed of light in water would emit Cherenkov radiation forming rings of light on the detector walls. Surrounding the inner volume, there was an optically separated 4π anti-counter equipped with 123 PMTs to cut backgrounds that originated from outside the detector. Kamiokande also had a water purification system to maintain a high level of transparency in the water. The detector setup can be seen in Figure 2.4.

The detector turned out to be an excellent setup for detecting cosmic neutrinos. It was able to measure neutrinos in real-time, largely preserving the directional information of the neutrino trajectory. This allowed Kamiokande to perform studies of time variations of the solar neutrino flux with solar activity, and confirm the origin of the solar neutrinos.

Neutrinos could be detected by the elastic scattering interaction, $\nu + e^- \rightarrow \nu + e^-$. The analysis had a threshold of 7.5 MeV, lowered to 7 MeV at the end of 1991, and was sensitive to

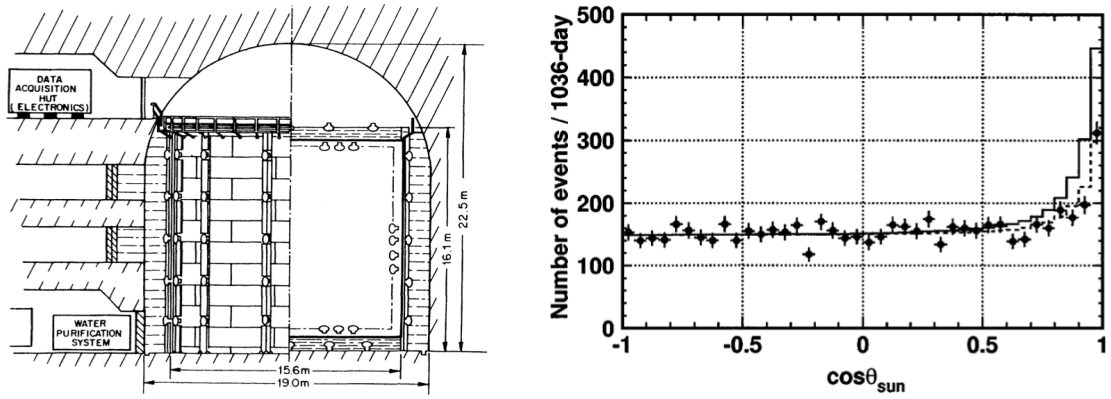

Figure 2.4: The Kamiokande detector on the left [84], and $\cos\theta_{\text{Sun}}$ distribution on the right [26]. In the left figure, the bulb-like shapes represent where the PMTs were distributed and the direction they faced. The right figure shows 1036 days of Kamiokande-III data, with $\cos\theta_{\text{Sun}} = 1$ being the direction of the sun. The black solid line was the BP5 SSM prediction, and the dotted line the best fit to the data assuming a flat background.

approximately half of the ^{8}B neutrino spectrum. The scattering angle, θ_e, of the recoil electron largely preserved the direction of the incoming neutrino:

$$\theta_e^2 \leq \frac{2m_e}{T_e} \tag{2.13}$$

where T_e and m_e are the kinetic energy and mass of the recoil electron. The angular resolution was affected by the multiple scattering of the electron in water and was 28° at 10 MeV. Kamiokande was the first experiment to measure an excess of events[2] in the direction from the sun, confirming the solar origin of the low energy neutrinos. This can be seen in Figure 2.4.

The flux of solar neutrinos measured over 2079 days was [26]:

$$\Phi_{\text{Kamiokande}} = (2.80 \pm 0.19 \pm 0.33) \times 10^6 \text{cm}^{-2}\text{s}^{-1} \tag{2.14}$$

The main systematic error contributions came from uncertainties in the angular resolution, energy scale and the fiducial volume cut. The ratio of the flux to the SSM prediction was:

$$\frac{\Phi_{\text{Kamiokande}}}{\text{SSM}} = 0.492^{+0.034}_{-0.033} \pm 0.058 \tag{2.15}$$

Over the 8 years of data, Kamiokande did not observe any statistically significant correlation between the solar neutrino flux and the solar activity and sun spots. Similarly the daytime and night time flux were not significantly different.

Again, Kamiokande observed a deficit from the flux of solar neutrinos expected, further establishing the solar neutrino problem. It should be noted that the elastic scattering interaction is sensitive to both charge-current (CC) and neutral current (NC) interactions (via Z-boson), which gives it sensitivity to all neutrino flavours. Although only ν_e interact via the CC W-exchange, and so ν_e has a 6 times larger contribution than ν_μ or ν_τ. The radiochemical experiments, on the other hand, only interact by CC interactions.

[2] compared to other directions

In addition to these measurements, 11 neutrino events from Supernova 1987A were also luckily captured [85], and there were significant contributions from analyses of atmospheric neutrinos. These contributions earned Masatoshi Koshiba the shared Nobel Prize in Physics in 2002.

2.1.4 Super-Kamiokande

The Super-Kamiokande (SK) experiment[86] has been running since 1996 and is the successor to Kamiokande. Most of the principles are the same as those mentioned above, however the detector now holds ∼50 ktons of ultra-pure water, with a 22.5 kton fiducial volume, viewed by 11,146 inward facing 20-inch PMTs – with over 40% photodetector coverage. The tank is 41.4 m tall and has a diameter of 39.3 m. The outer detector (OD), anti-counter, now has a completely separate volume surrounding the inner detector (ID) and houses 1885 8-inch PMTs. SK was the detector used in the analyses in this thesis and is described in greater detail in Chapter 3.

The chlorine and gallium experiments and Kamiokande had measured a solar neutrino flux that was half or less than that which was expected from the Standard Solar Models. This firmly established the *solar neutrino problem*. Kamiokande was a real-time detector that could observe solar neutrinos on an event-by-event basis and confirmed the solar origin of the neutrinos. Signals for neutrino oscillation could be a distortion of the neutrino energy spectrum; a difference between daytime and night time fluxes; or seasonal variations on the flux. Kamiokande began searches for these signals, although did not observe any statistically significant differences. SK had ∼25 times the target mass as Kamiokande, and continued the search [87].

The dominant background below 6.5 MeV was from the radioactivity of Radon externally and in the water. To reduce this in SK, the detector area was air-tight with fresh air pumped in from outside the mine, and the rock above the detector was covered with radon-resistant plastic sheets. In the air above the water-level in the tank, purified air was pumped in to maintain positive pressure. This reduced the radon concentration to less than 3 mBq/m^3 [86]. In addition, the water purification system completely filters the 50 ktons of water over a period of 2 months. Further low energy backgrounds were removed by cuts and reconstruction characteristics [87]. Above 6.5 MeV, the main background comes from the decay of muon-induced spallation products, e.g. ^{16}N created by the absorption of cosmic muons on ^{16}O. These events were removed by cuts and likelihoods functions.

The solar neutrino signal was extracted from the $\cos\theta_{\text{sun}}$ distribution, fitting a likelihood function of the signal and background shapes. The signal could be predicted with the known angular resolution between the incoming solar neutrino and outgoing lepton, and a mostly flat background w.r.t. the $\cos\theta_{\text{sun}}$ direction. Some neutrino oscillation parameter values predicted an asymmetry in the flux of solar neutrinos that arrive from above the detector (daytime) and those that pass through the Earth below the detector (night time). This difference would be due to the matter effects in the Earth's mantle and core. For vacuum oscillations, the change of baseline with the eccentricity of the Earth's orbit could create a seasonal variation.

In 1999, SK reported an early day night asymmetry analysis for 504 days of data [88], after already confirming the solar neutrino deficit in 1998. No significant difference was observed, allowing a region of the oscillation parameter space to be excluded. This region was associated with the regeneration of ν_e solar neutrinos through matter effects in the Earth. In 2001, a precision measurement of 18,464 observed solar neutrino events over 1,258 days was reported [87]. The flux was $45.1 \pm 0.5(\text{stat.})^{+1.6}_{-1.4}(\text{stat.})\%$ of the BP2000 SSM prediction. A day night asymmetry of 3.3% from the average flux, and 1.3σ away from zero difference, was observed, providing

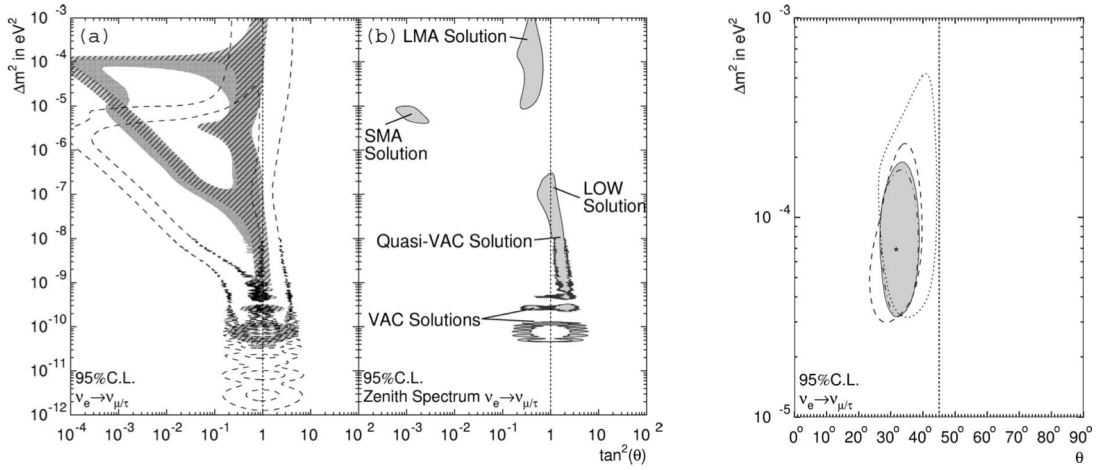

Figure 2.5: In the left figure (a) shows the allowed regions for oscillation parameters from several experiments (2002) [89]. The shaded region was from the Homestake Chlorine experiment, the region in the dashed lines from GALLEX/GNO and SAGE. The hatched area is from the charge-current contribution from SNO (discussed later). The (b) figure shows the multiple solutions that result from combining these results. The right figure shows a zoomed in region for the surviving LMA solution with the addition of SK data (2002) [89] and SNO NC data to the allowed regions in the left figure. The most confined region with a dashed-dotted contour was a global fit of all the data. The dashed contour was with the SNO rates removed, and the dotted contour was with no radio-chemical rates. The shaded region was the result without using the SSM ^{8}B flux calculation.

constraints on neutrino parameters. No seasonal variation beyond the effect from the eccentricity of the Earth's orbit was found.

Early fits to the deficit of solar neutrinos from each of the experiments, resulted in multiple solutions as seen in Figure 2.5. These solutions occurred where the CC allowed regions overlapped. These were the *Large Mixing Angle* (LMA) and *Small Mixing Angle* (SMA) solutions at large Δm^2_{21}; and for smaller Δm^2_{21} there were the *LOW* and *Quasi-Vacuum* (Quasi-VAC) solutions, down to the *Vacuum* (VAC) solutions for Δm^2_{21} below $\sim 10^{-10}\text{eV}^2$.

For $10^{-8}\,\text{eV}^2 < \Delta m^2_{21} < 10^{-3}\,\text{eV}^2$, the matter density in the sun strongly affects the oscillation probability. There was an expected resonant enhancement of the oscillations due to the MSW effect for $\theta_{12} < \frac{\pi}{4}$, and a suppression for $\theta_{12} > \frac{\pi}{4}$ from an anti-resonance effect. This effect can be seen around the $\tan^2\theta_{12} = 1$ line drawn in the figure. For Δm^2_{21} below $10^{-8}\,\text{eV}^2$, the matter effects are negligible and there would be vacuum oscillations that are symmetrical around $\theta_{12} = \frac{\pi}{4}$.

In 2002, SK updated their results for 1496 days of data, including two analyses [89]. One was a "zenith angle spectrum" analysis looking for daily variations and spectrum distortions but found no significant difference. This result was independent of the absolute solar neutrino flux and considerably broke the degeneracy of the previous solutions. When combined with the rate analysis against the SSM prediction, only a part of the LMA and quasi-VAC solutions remained, both were large mixing solutions. When the SNO data was combined, allowing the interpretation of appearance of other active flavours in the SK measurement, the LMA solution was favoured. A zoomed in plot of the surviving solution is also shown in Figure 2.5. In 2004, SK performed a

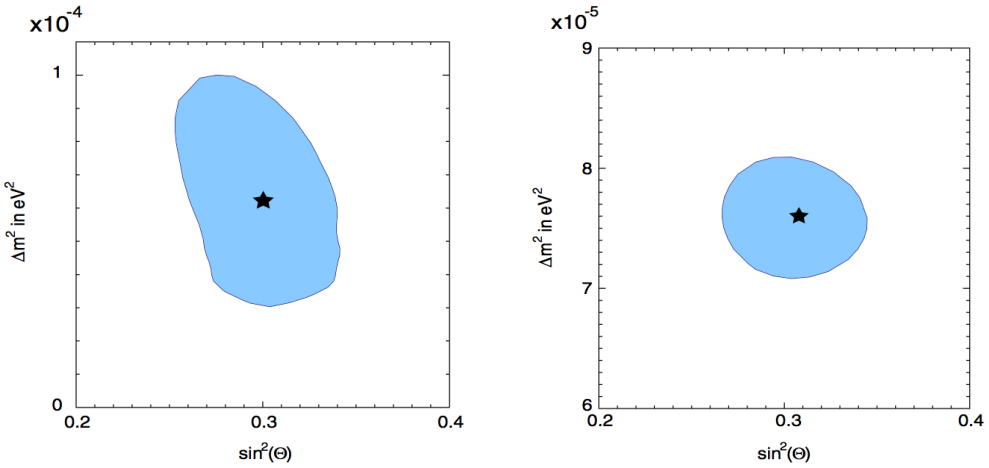

Figure 2.6: The oscillation parameter 95% C.L. allowed regions [32] are shown for the combined solar experiments on the left and with the addition of KamLAND data on the right. The solar allowed regions came from a combined analysis of the SNO, Borexino, radiochemical experiment results and the SK contribution.

precise day-night analysis of the SK-I data using a maximum likelihood method [90]. A variation of $-1.8 \pm 1.6(\text{stat.})^{+1.3}_{-1.2}(\text{syst.})\%$ was observed, where -2.1% was expected from the best-fit LMA solution. This result was still consistent with no variation, and some more of the oscillation parameter space could be excluded.

The greater sensitivity of SK compared to Kamiokande has allowed the solar neutrino analysis threshold to be lowered to 5 MeV. Again, the main flux concerned was from the ^{8}B neutrinos, with a much smaller contribution from the hep-neutrinos. The flux calculation from the SK-I data, and the ratio w.r.t. the SSM was: [71, 86]:

$$\Phi_{\text{SK}} = (2.35 \pm 0.02 \pm 0.08) \times 10^6 \text{cm}^{-2}\text{s}^{-1} \tag{2.16}$$

$$\frac{\Phi_{\text{SK}}}{\text{SSM}} = 0.413 \pm 0.014 \tag{2.17}$$

In 2011, SK released updated results including data from the SK-I to SK-III experimental periods [32]. By constraining the ^{8}B neutrino flux to the SNO NC flux, the analysis of the energy spectrum and time variation at SK, for the first time, favoured only the LMA solution at 95% C.L. A global fit of all the solar results was performed, including results from SNO, Borexino and the radiochemical experiments. The allowed resulting allowed region is shown in Figure 2.6. The addition of KamLAND data greatly constrained the Δm^2 of the allowed region, which is also shown in Figure 2.6. The best-fit parameters were [32]:

$$\sin^2\theta_{12} = 0.30^{+0.02}_{-0.01} \qquad (\tan^2\theta_{12} = 0.42^{+0.04}_{-0.02}) \qquad \text{(All solar)} \tag{2.18}$$

$$\Delta m^2_{21} = 6.2^{+1.1}_{-1.9} \times 10^{-5}\,\text{eV}^2 \tag{2.19}$$

$$\sin^2\theta_{12} = 0.31 \pm 0.01 \qquad (\tan^2\theta_{12} = 0.44 \pm 0.03) \qquad \text{(Solar + KamLAND)} \tag{2.20}$$

$$\Delta m^2_{21} = 7.6 \pm 0.2 \times 10^{-5}\,\text{eV}^2 \tag{2.21}$$

A three flavour analysis was also performed combining all the solar data and KamLAND data. The best fit was $\sin^2\theta_{13} = 0.025^{+0.018}_{-0.016}$ and the upper bound at the 95% C.L. reported was

$\sin^2\theta_{13} < 0.059$. In addition, the absolute fluxes for the SK-II and SK-III periods were consistent with the SK-I measurement.

Recently, in 2013, SK published the first indication of the regeneration of solar electron neutrinos from terrestrial matter effects [91]. The asymmetry measured was $[-3.2 \pm 1.1(\text{stat.}) \pm 0.5(\text{syst.})]\%$ which deviated from zero by 2.7σ. This was the first direct indication that matter effects modify the neutrino oscillation probabilities.

2.1.5 Sudbury Neutrino Observatory

The Sudbury Neutrino Observatory (SNO) experiment began in 1999, at the Creighton mine ~6,000 m.w.e underground near Sudbury, Canada [92]. It was unique in that it had a combination of interaction channels to make a clean observation of the solar ν_e flux, as well as the flux from all active neutrinos originating from the sun. The comparison of these flux measurements could determine if the observed deficit in the solar ν_e flux was due to the oscillations to other active flavours.

SNO achieved this by utilising 1 kt of heavy water, D_2O, as the neutrino target, allowing the following reactions:

$$\nu_e + d \longrightarrow p + p + e^- \qquad \text{(CC)} \tag{2.22}$$

$$\nu_x + d \longrightarrow p + n + \nu_x \qquad \text{(NC)} \tag{2.23}$$

$$\nu_x + e^- \longrightarrow \nu_x + e^- \qquad \text{(ES)} \tag{2.24}$$

where ν_x is one of ν_e, ν_μ, or ν_τ, d is a deuteron and p a proton. The charged-current (CC) interaction in Equation (2.22), is sensitive only to ν_e and produces an electron that can be detected by Cherenkov radiation. Through this interaction the flux of solar neutrinos arriving at the Earth with electron flavour could be determined. The neutral-current (NC) interaction in Equation (2.23), is the disintegration of a deuteron by a neutrino. It has a threshold of 2.2 MeV and is independent of the neutrino flavour. The outgoing neutron was detected by the absorption on deuterium producing a 6.25 MeV photon, or absorption on ^{35}Cl producing photons with a total energy of 8.6 MeV. $MgCl_2$ was added to the D_2O for the enhanced neutron capture probability. These photons Compton scatter, knocking out electrons that can be observed by their Cherenkov light. Finally, the elastic scattering interaction in Equation (2.24), is the same interaction that solar neutrinos are detected at Super-Kamiokande and is primarily sensitive to ν_e, while the cross-section for ν_μ or ν_τ is a factor of $\frac{1}{6}$ smaller than for ν_e. Through the combination of these interactions, SNO could make a measurement of the solar neutrino flux and search for oscillations independent of the SSM predictions.

The detector consisted of a 12 m diameter transparent spherical acrylic vessel that contained 1 kt of ultra pure heavy water. The vessel was supported by 10 rope loops of synthetic fibre, and was surrounded by a 17.8 m diameter geodesic sphere made from stainless steel struts that held the 9,438 inward-facing PMTs, as seen in Figure 2.7. This was all housed in a barrel-shaped cavity, 22 m in diameter and 34 m in height, and was filled with purified light water that provided shielding and support. The water shield attenuated low energy (< 4 MeV) γ rays from radioactivity in the PMT array, as well as high energy γ rays from the cavity. In the main detector volume, the total contribution from all radioactive sources was $< 0.2\%$ for low energy backgrounds and $< 0.8\%$ for the high energy sources.

In 2001, SNO released the first results on the ES and CC measurements of the solar ^8B flux [93]. The ES measurement was consistent with the value measured at SK, however the CC

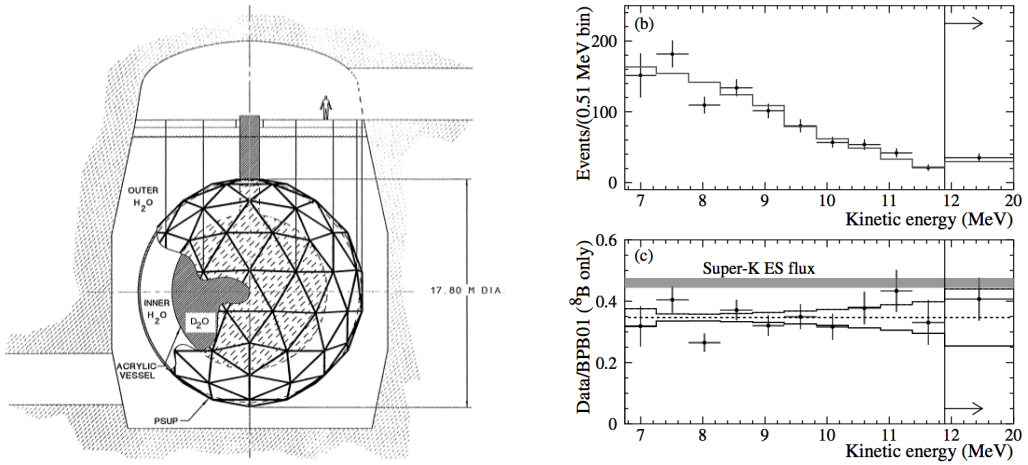

Figure 2.7: The left figure shows the SNO detector [92], and the SNO CC measurement is on the right [93]. The upper right figure shows the kinetic energy distribution of the extracted CC events in the data points. The solid histogram was the ^{8}B flux from the null oscillation prediction, scaled to the data. No deviation from the ^{8}B spectral shape was seen. The lower right plot displays the ratio of the CC events to the prediction. Also shown is the accurate ES rate from SK. The CC distribution was consistently smaller than the ES flux. The bands represent the most significant energy dependent systematic errors.

result, that was sensitive only to ν_e, was considerably smaller. From the discrepancy of these two results, there was good evidence for flavour transitions in solar neutrinos. In addition, this result was inconsistent with the null oscillation hypothesis that all observed solar neutrinos are of electron flavour. The data were taken over a live time of 240.95 days and were divided into two sets: 70% was used to establish analysis techniques and 30% was kept for a blind test of a statistical bias in the analysis. The analysis of the two data sets were statistically consistent. The analysis had a high threshold of 6.75 MeV, cutting out most low energy radioactive backgrounds and most of the neutron capture events.

The data were separated into contributions from CC, ES, and remaining neutron events by probability density functions (pdf) of effective kinetic energy, the event direction relative to the solar direction, and from a volume weighted radial variable. From the 1169 fiducial events above threshold, the maximum likelihood analysis output 975.4 ± 39.7 CC events, 106.1 ± 15.2 ES events and 87.5 ± 24.7 neutron events. The CC spectrum could be extracted by repeating the signal extraction with the constraint on the shape of the CC pdf removed. The resulting distributions are shown in Figure 2.7. The ^{8}B neutrino fluxes assuming standard spectrum shape were measured to be:

$$\phi_{\mathrm{CC}}^{\mathrm{SNO}} = 1.75 \pm 0.07(\mathrm{stat.})^{+0.12}_{-0.11}(\mathrm{syst.}) \quad \times 10^6\,\mathrm{cm}^{-2}\,\mathrm{s}^{-1} \tag{2.25}$$

$$\phi_{\mathrm{ES}}^{\mathrm{SNO}} = 2.39 \pm 0.34(\mathrm{stat.})^{+0.16}_{-0.14}(\mathrm{syst.}) \quad \times 10^6\,\mathrm{cm}^{-2}\,\mathrm{s}^{-1} \tag{2.26}$$

The difference between the ^{8}B flux derived from the SNO ES measurement and CC measurement was $0.64 \pm 0.40 \times 10^6\,\mathrm{cm}^{-2}\,\mathrm{s}^{-1}$, which was a 1.6σ difference. The SNO ES rate was consistent with the accurately measured rate by SK. The difference between the SK ES rate and SNO CC rate was $0.57 \pm 0.17 \times 10^6\,\mathrm{cm}^{-2}\,\mathrm{s}^{-1}$, a deviation of 3.3σ or a probability of 0.04%

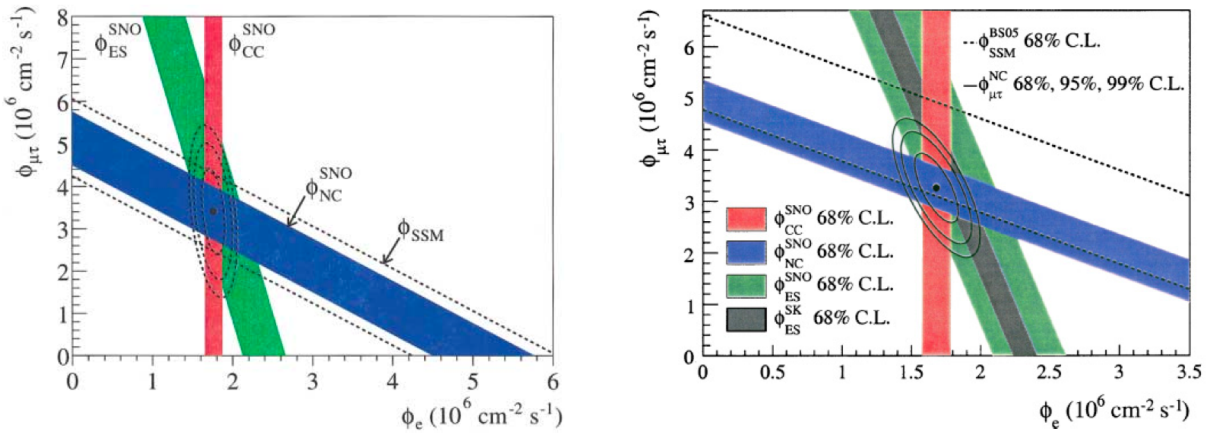

Figure 2.8: The original measurement of the ^{8}B solar neutrino flux from the three reactions at SNO from 2002 [33] on the left, and the updated result from 2005 [94] on the right. The bands show the possible flavour compositions of active neutrinos from the measured information and the $\pm 1\sigma$ uncertainty. The dashed band was the SSM prediction, and the NC measurement in the blue band agrees well with it. The red band shows the CC measurement and the green band for the ES result. The intersection of the bands give the flavour composition in ϕ_e and $\phi_{\mu\tau}$ at the detection point. The 2002 result assumed no distortion in the ^{8}B spectrum, while the 2005 measurement made no assumptions on the neutrino energy spectrum. The grey band shows the SK ES measurement.

that the SK measurement could statistically fluctuate down to the SNO CC measurement. This inconsistency was evidence for non-electron active flavour constituents in the solar neutrino flux. Since the ν_e component was determined with the CC measurement, the $\nu_{\mu\tau}$ component could be inferred from the ES measurements and therefore the total flux. These were determined to be:

$$\phi(\nu_{\mu\tau}) = 3.69 \pm 1.13 \quad \times 10^6\,\mathrm{cm}^{-2}\,\mathrm{s}^{-1} \tag{2.27}$$

$$\phi(\nu_x) = 5.44 \pm 0.99 \quad \times 10^6\,\mathrm{cm}^{-2}\,\mathrm{s}^{-1} \tag{2.28}$$

This inferred total flux was in excellent agreement with the SSM prediction! The additional information from the ν_e component of the solar neutrino flux could give a good indication of the total observed flux.

In 2002, SNO reported on a direct measurement of the total solar neutrino flux from NC reactions on deuterium, which could determine the total flux independent of neutrino flavour [33]. The threshold for the reaction in Equation (2.23) was 2.2 MeV, and the analysis threshold was sensitive to the neutrons at 5 MeV. To reduce backgrounds data with vertices in the fiducial volume of 550 cm from the centre were used. In these conditions the neutron detection efficiency was measured to be 14.4% through calibrations.

The main backgrounds were from low levels of bismuth and thallium, ^{214}Bi and ^{208}Tl, in the detector materials, from uranium and thorium decay daughter chains. The activity of these isotopes caused low energy Cherenkov events and the photodisintegration of D_2O, releasing free neutrons. Several *ex situ* and *in situ* studies were carried out to determine the neutron and background production rate. The expected background rates were 1.0 ± 0.2 neutrons per day in the target region, and $1.3^{+0.4}_{-0.5}$ neutrons per day from external sources. These rates were

approximately 12% of the expected signal from NC interactions from the SSM prediction. In addition, a 250 ms dead time after every event was required to reduce contamination from cosmic ray and atmospheric neutrino induced neutrons, while the background contribution from sub-Cherenkov threshold muons were expected to be small.

Using a maximum likelihood analysis, the fluxes for each reaction were measured to be:

$$\phi_{\mathrm{CC}}^{\mathrm{SNO}} = 1.76^{+0.06}_{-0.05}(\mathrm{stat.})^{+0.09}_{-0.09}(\mathrm{syst.}) \quad \times 10^6\,\mathrm{cm}^{-2}\,\mathrm{s}^{-1} \tag{2.29}$$

$$\phi_{\mathrm{ES}}^{\mathrm{SNO}} = 2.39^{+0.24}_{-0.23}(\mathrm{stat.})^{+0.12}_{-0.12}(\mathrm{syst.}) \quad \times 10^6\,\mathrm{cm}^{-2}\,\mathrm{s}^{-1} \tag{2.30}$$

$$\phi_{\mathrm{NC}}^{\mathrm{SNO}} = 5.09^{+0.44}_{-0.43}(\mathrm{stat.})^{+0.46}_{-0.43}(\mathrm{syst.}) \quad \times 10^6\,\mathrm{cm}^{-2}\,\mathrm{s}^{-1} \tag{2.31}$$

The NC flux, that was independent of neutrino flavour, was considerably larger than the CC flux, that depends on only ν_e, strongly implying neutrino flavour transitions such as those in Neutrino Oscillations. From these fluxes, SNO calculated the components from electron (ϕ_e) and other active flavours ($\phi_{\mu\tau}$):

$$\phi_e = 1.76^{+0.05}_{-0.05}(\mathrm{stat.})^{+0.09}_{-0.09}(\mathrm{syst.}) \quad \times 10^6\,\mathrm{cm}^{-2}\,\mathrm{s}^{-1} \tag{2.32}$$

$$\phi_{\mu\tau} = 3.41^{+0.45}_{-0.45}(\mathrm{stat.})^{+0.48}_{-0.45}(\mathrm{syst.}) \quad \times 10^6\,\mathrm{cm}^{-2}\,\mathrm{s}^{-1} \tag{2.33}$$

This $\phi_{\mu\tau}$ component was 5.3σ above zero. When combined with the SK ES measurement at the time, this component became $\phi_{\mu\tau} = 3.45^{+0.65}_{-0.62}$, which was 5.5σ above zero. So this was strong evidence for flavour transitions of solar neutrinos. The bands for the flavour constituents of the flux are shown in Figure 2.8. The bands came from the unknown flavour composition of each measurement, with the exception of the CC result that was induced by ν_e regardless of a ν_μ or ν_τ component, and from the uncertainty in the measurements.

The other remarkable thing about the SNO NC measurement was that it was consistent with the contemporary SSM prediction for ^{8}B neutrinos at $\phi_{\mathrm{SSM}} = 5.05^{+1.01}_{-0.81}$. Prior to this result, all solar neutrino experiments were reporting a deficit in the solar neutrino flux. These experiments were primarily sensitive to ν_e, and indeed there was a deficit in the electron flavour contribution. SNO has shown that when all flavours were combined, the total solar flux of active ^{8}B neutrinos was in agreement with the theoretical SSM prediction.

Also in 2002, SNO made the first direct measurement of the day-night asymmetry in the ν_e flux and the total solar neutrino flux [95]. The ν_e (CC) events had a day minus night asymmetry of $14.0\% \pm 6.3\%^{+1.5}_{-1.4}\%$. If the total flux of active neutrinos was constrained to have no asymmetry, the ν_e asymmetry reduced to $7.0\% \pm 4.9\%^{+1.3}_{-1.2}\%$. The SNO results constrained a lot of the allowed oscillation parameter space, and when combined in a global analysis with other solar neutrino experiments, the LMA solution was strongly favoured.

SNO began the "salt phase" of their experiment in June 2001 when they added 2 metric tons of NaCl to the D_2O volume, which continued through until October 2003. The addition of NaCl increased the neutron capture efficiency by a factor of three, and the capture on ^{35}Cl created a distinctive isotropic pattern of γ rays with a higher total energy than the single photon from neutron capture on deuteron. The NC events could therefore be more accurately separated statistically, allowing for a more precise measurement of the NC rate. In 2004, SNO released an improved measurement of the total solar neutrino flux with the added NaCl [96]. This measurement had no assumptions about the energy dependence of the ν_e survival probability and was found to be:

$$\phi_{\mathrm{NC}}^{\mathrm{SNO}} = 5.21 \pm 0.27(\mathrm{stat.}) \pm 0.38(\mathrm{syst.}) \quad \times 10^6\,\mathrm{cm}^{-2}\,\mathrm{s}^{-1} \tag{2.34}$$

Maximal mixing was also rejected with a significance of 5.4σ. In 2005, the extracted integral CC rate was consistent with no day-night asymmetry, which was expected for the best fit LMA solution [94]. The updated solar neutrino flux flavour composition bands can also be seen in Figure 2.8. For the oscillation parameters, see the global fits that include SNO data in the SK solar review, Section 2.1.4.

2.1.6 Borexino

The Borexino experiment began taking data in 2007 with a low background liquid scintillator detector 3800 m.w.e. underground at Gran Sasso, Italy [97]. The main aim of the experiment was to make real-time measurements of solar neutrinos below 2 MeV, which accounts for over 99% of the flux. Radiochemical experiments had low thresholds, but the result of their measurements were integrated solar neutrino rates, losing individual event information. Whereas water Cherenkov detectors could measure in real-time, but were limited to thresholds above 5 MeV accounting for 0.01% of the total flux, due to low light yields from cherenkov light and natural radioactive backgrounds.

The real-time measurements prior to Borexino were primarily sensitive to ^{8}B neutrinos. So one of Borexino's first goals was to measure the mono-energetic 0.862 MeV line of the ^{7}Be solar neutrino flux [98, 99], which was expected to constitute ≈10% of the total flux. The data at the time favoured the MSW LMA oscillation solution, which predicted matter enhanced oscillations at the ^{8}B neutrino energies that reduced to vacuum oscillations at low energies in the vicinity of ^{7}Be. The ν_e survival probability increased from ≈0.33 for high energies up to ≈0.6 around the ^{7}Be mono-energetic line. So this measurement could provide a good test of the favoured oscillation solution.

The detection mechanism at Borexino was through the neutrino elastic scattering on electrons in liquid scintillator that produced sufficient light to observe low energy events. The reaction was sensitive to all flavours of neutrinos, although primarily to electron neutrinos. The signal efficiency of the scintillator was ≈50 times greater than water Cerenkov, but no directionality could be observed and the signal electrons could not be distinguished from natural radioactivity. So Borexino relied on producing an environment with extremely low radioactivity.

The detector was made up of layers of concentric spherical containers [97] as seen in Figure 2.9. The Inner Vessel (IV) had a radius of 4.25 m and contained 300 tons of scintillator. The scintillator was pseudocumene (PC) doped with 2,5-diphenyloxazole (PPO) at a concentration of 1.5 g/l. Surrounding this was a 5.5 m radius Outer Vessel (OV) that contained PC and 5.0 g/l of dimethylphthalate (DMP). The DMP quenches the residual scintillation of the PC. So this layer acts as a passive shield against radon and other backgrounds outside the detector. Outside this was a 6.85 m radius stainless steel sphere, which also contained the PC-DMP buffer fluid and held 2212 8" PMTs. The encompassing tank of radius 9 m and height 16.9 m, contained ultra-pure water and acted as a passive shield and comic muon veto. The main signal was observed from the IV, and the outer layers provided ≈5.5 m of m.w.e. passive shielding from external radiation.

Many careful considerations were taken during the preparation, transportation and handling of detector materials to minimise all sources of radioactivity. A fiducial volume was chosen to efficiently remove external backgrounds, in this volume the predicted γ background was less than 0.5 counts/(d · 100 t) in the 250-800 keV range. Backgrounds from Rn daughters from the U decay chain were removed by detecting the delayed coincidence of ^{214}Bi–^{214}Po and vetoing up to 3 hours prior to the coincidence. The ^{14}C intrinsic to the scintillator provides a background

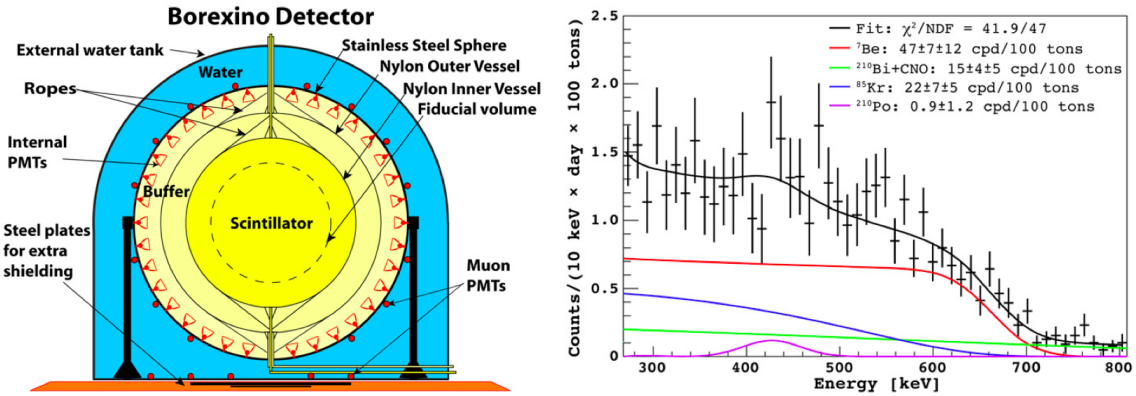

Figure 2.9: The Borexino detector on the left [98], and the ^{7}Be measurement on the right [98]. The detector geometry is shown, a description of each layer is written in the text. The right figure shows the ^{7}Be analysis in which the peak from α particles from ^{210}Po decay was statistically subtracted. The remnant contribution was still considered in the fit shown by the pink line. Background contributions from ^{85}Kr (blue) and ^{210}Bi (green) were considered. Finally the distinctive 'shoulder' contribution from ^{7}Be is shown in red, and the combined fit in black.

from the 156 keV β decay, limiting signal observations to above 200 keV.

In 2008, Borexino reported on its first measurements of the ^{7}Be neutrinos [98, 99]. The signal for the mono-energetic ^{7}Be neutrinos was an electron recoil with a flat energy distribution and a sharp cut-off at 665 keV. This shoulder in the distribution can be seen by following the red curve in Figure 2.9. There was a peak in the distribution due to α particles from ^{210}Po decay, which was statistically subtracted in the figure. After the subtraction, the energy range between 270–800 keV was dominated by ^{7}Be neutrinos. A small bump still remained, around 400 keV, which was fitted with the fuchsia curve. Another analysis was performed without this statistical subtraction, and limited the fit region to above the ^{210}Po peak (560–800 keV). Both methods gave consistent results. Other background contributions, such as from the ^{85}Kr (blue) and ^{210}Bi (green) β decays were also fitted. The best value for the 0.862 MeV ^{7}Be neutrinos was:

$$R_{^{7}\mathrm{Be}} = (47 \pm 7 \pm 12)\mathrm{counts}/\ (\mathrm{day} \cdot 100\,\mathrm{ton}) \tag{2.35}$$

Where the ratio to the SSM was [71]:

$$\frac{R_{^{7}\mathrm{Be}}}{\mathrm{SSM}} = 0.63 \pm 0.18 \tag{2.36}$$

One of the main uncertainties came from the unknown component of the ^{85}Kr β decay spectrum, which was similar in shape to the signal, but could be distinguished in the shoulder region. The hypothesis that the results were explained by ^{85}Kr alone was rejected at $>5\sigma$ level. The main systematic uncertainty came from the determination of the fiducial mass and was estimated to be 25%. Due to the good agreement of the fit in the shoulder region, which could not be explained by any known backgrounds, Borexino concluded that they had detected ^{7}Be solar neutrinos.

In 2010, Borexino reported on a measurement of ^{8}B neutrinos with a 3 MeV threshold [100]. The measurement made use of ^{8}B neutrino induced ν-e elastic scattering that resulted in a solar

flux of $\Phi_{^8\mathrm{B}}^{\mathrm{ES}} = 2.4 \pm 0.4 \pm 0.1 \times 10^6\,\mathrm{cm}^{-2}\mathrm{s}^{-1}$. The survival probability was found to be 0.29 ± 0.10, which was 1.9σ different from the ^{7}Be result and consistent with the MSW-LMA solution that predicted a varying survival probability. In 2012, Borexino made the first measurement of the *pep* solar neutrinos in the 1.0–1.5 MeV range [101]. The solar flux was estimated to be $\Phi_{pep} = (1.6 \pm 0.3) \times 10^8\,\mathrm{cm}^{-2}\mathrm{s}^{-1}$. The absence of the *pep* signal was disfavoured at 98% C.L. This result provided the strongest constraint on the CNO solar neutrinos.

2.1.7 Solar Neutrino Summary

The sun is an abundant source of neutrinos. Their relatively low energy makes them tricky to detect and many experiments have employed widely varying detection mechanisms to study them. The first solar neutrinos were discovered in 1968 by Davis' Chlorine Experiment that captured them with a 0.8 MeV reaction threshold that gave it sensitivity to ^{7}Be and ^{8}B neutrinos. About 30% of the flux expected from the Standard Solar Model (SSM) was observed, which marked the beginning of the *solar neutrino problem*. The Gallium experiments ran between 1990–2003, which had a very low energy threshold of 233 keV, giving sensitvity down to pp-neutrinos. They had complicated procedures for extracting and counting the signal Germanium isotope, and observed about 52% of the flux of the SSM prediction, further evidence for the solar neutrino deficit.

Since 1987 the Kamiokande experiment achieved real-time detection of solar neutrinos, preserving their directional information and confirming their solar origin. The initial analysis threshold of the elastic scattering interaction was ∼7 MeV and was sensitive primarily to the ^{8}B neutrinos. Similarly, approximately 49% of the expected flux was observed. Since 1996, Kamiokande was succeeded by Super-Kamiokande (SK). It had ∼25 times the detector mass and detected solar neutrinos with a threshold of about ∼5 MeV. The early global fits, around 2000, to solar neutrino data had many potential solutions for a Neutrino Oscillation explanation of the flux deficit.

SNO largely helped to solve the puzzle by measuring the electron flavour neutrinos directly with a CC reaction in 2001, and the total solar flux independent of flavour with a NC interaction in 2002. A smaller flux of ν_e was observed compared to other experiments that had some ν_μ and ν_τ in their signal, meanwhile the total flux measured agreed with the SSM! This result showed that the deficit was due to flavour transitions from electron neutrinos to muon and/or tau neutrinos. The constraints from SNO allowed the global analyses to favour the *Large Mixing Angle* (LMA) solution. Since 2007 Borexino has been measuring solar neutrinos below 2 MeV in real-time. The MSW LMA solution predicted that the ν_e survival probability increased from ≈0.33 at high energies to ≈0.6 at lower energies. *Borexino confirmed this with precice measurements of the 0.86 MeV ^{7}Be flux in 2008 and 1.0–1.5 MeV *pep* neutrinos in 2012.

2.2 Atmospheric Neutrino Experiments

The Earth is constantly bombarded by cosmic rays that interact with molecules in the air to produce mainly pions and some kaons. These then decay into neutrinos known as Atmospheric Neutrinos, by chains like those seen in Equations (2.37, 2.38). The first atmospheric neutrinos were detected in the 1960s in South Africa [102] and India [103].

$$\pi^+ \longrightarrow \mu^+ + \nu_\mu \tag{2.37a}$$
$$\mu^+ \longrightarrow e^+ + \nu_e + \bar{\nu}_\mu \tag{2.37b}$$

$$\pi^- \longrightarrow \mu^- + \bar{\nu}_\mu \tag{2.38a}$$
$$\mu^- \longrightarrow e^- + \bar{\nu}_e + \nu_\mu \tag{2.38b}$$

The pions produced decay to give a ν_μ and a muon, which can then decay to give a ν_e and another ν_μ. Naively, two atmospheric ν_μ would be expected for each ν_e, a 2:1 ratio of ν_μ to ν_e. Since the higher energy muons reach the ground before they can decay in flight, an even larger ratio could be expected for higher energy events. However, there was some discrepancy in the measured ratio which lead to the establishment of Neutrino Oscillations as the dominant theory of neutrinos.

There were various calculations of the atmospheric neutrino flux produced by the bombarding cosmic rays. Their absolute fluxes agree within about 20%, however the ratio of flavours is more accurate at the 5% level. So atmospheric neutrino experiments generally quote their results in a ratio like that in Equation (2.39).

$$\mathrm{R} = \frac{\left(\frac{\nu_\mu+\bar{\nu}_\mu}{\nu_e+\bar{\nu}_e}\right)_{obs}}{\left(\frac{\nu_\mu+\bar{\nu}_\mu}{\nu_e+\bar{\nu}_e}\right)_{MC}} \tag{2.39}$$

2.2.1 Kamiokande and IMB

Kamiokande started operation from 1983 and went through several upgrades, including an outer detector veto counter in 1985 (Kamiokande-II) and an electronics upgrade in 1990 (Kamiokande-III) [27, 28]. The detector was able to detect neutrinos by the water cherenkov light emitted by the lepton products of neutrino interactions. It was originally constructed to search for nucleon decay, and studied atmospheric neutrinos as a principle background. The experiment was able to find a significantly smaller ν_μ flux than expected through this research.

The experiment ran 2700 m.w.e. underground near Kamioka, Gifu Prefecture, Japan, where Super-Kamiokande currently runs. The detector was a 4.5 kton cylindrical tank (15.6 m ø × 16 m height) filled with pure water and surrounded by 1000 inward facing Photo-Multiplier Tubes. The detector can be seen in Figure 2.4. In 1988, Kamiokande observed $(59 \pm 7)\%$ muon-like events from that expected at less than 1.33 GeV, which could not be explained by systematic detector effects or uncertainties in the atmospheric neutrino flux [27]. Similarly, in 1994, a flavour double ratio of $0.57^{+0.08}_{-0.07} \pm 0.07$ compared to the expectation was observed for events greater than 1.33 GeV [28].

Some early Zenith distributions can be seen in Figure 2.10. The first results released were for Sub-Gev events (<1.33 GeV), a deficit can be seen in the left most figure, but there appears to be no zenith dependence. Kamiokande later carried out an analysis on Multi-GeV events (>1.33 GeV), which have a greater angular correspondence to the neutrino direction (an RMS of 15-20°, compared to ∼60° for sub-GeV). The middle figure shows that the deficit seems to be

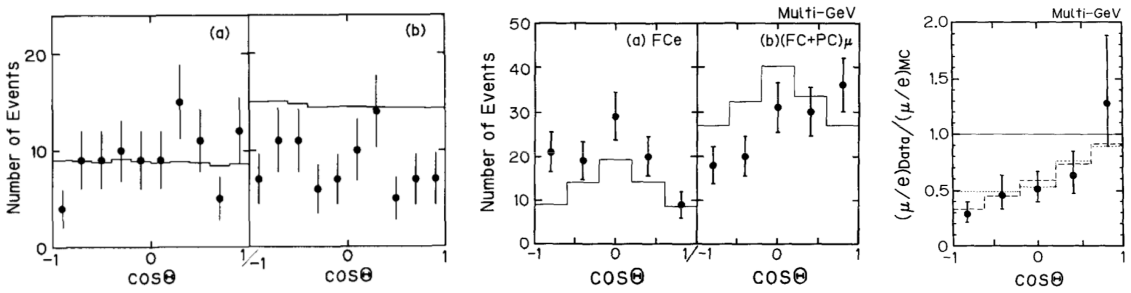

Figure 2.10: Kamiokande Zenith Distributions. The left most figure is for sub-GeV events (<1.33 GeV) [27]; the middle for multi-GeV events (>1.33 GeV) [28]; and the right most figure is the zenith distribution of the flavour ratio for Multi-GeV events [28]. The (a) panels are for electron-like events and the (b) panels for muon-like events. The dashed and dotted lines correspond to early neutrino oscillation monte-carlo.

coming from upward muon neutrino events that have travelled through the Earth. This zenith dependence can be more clearly seen in the flavour ratio.

The IMB experiment ran from 1986 to 1991 and utilised a larger 8-kton cherenkov detector consisting of a cuboid tank (18 m × 17 m × 22.5 m) with 2048 PMTs on the 6 faces, 1570 m.w.e. underground at Cleveland, Ohio, US [29]. Using two independent analyses, one of particle identification and one requiring a muon decay signal, IMB reported a deficit of muon neutrinos (or excess of electron neutrinos) from the expectation. In their final data set, the fraction of muon-like events was $0.36 \pm 0.02(\text{stat.}) \pm 0.02(\text{syst.})$, where $0.51 \pm 0.01(\text{stat.}) \pm 0.05(\text{syst.})$ was expected [29]. The percentage of events with a muon decay signal was $33 \pm 2(\text{stat.})\%$ events while $43 \pm 1(\text{stat.})\%$ were expected [29].

Kamiokande measured about 60% muon-like events compared to the expectation from the Standard Model predictions, and the flavour ratios measured by IMB supported this discrepancy. This unexpected result became known as the *Atmospheric Anomaly*, and both experiments suggested that Neutrino Oscillations could be a possible explanation for these results. The later higher energy Kamiokande analysis also seemed to show a zenith angle correlation of the muon-neutrino deficit, further supporting the Neutrino Oscillation picture.

2.2.2 Fréjus and NUSEX

The Fréjus experiment [104] collected data between 1984 and 1988, in an underground laboratory under the Alps between Italy and France. The detector was a fine grain iron-calorimeter built to better understand the atmospheric neutrino flux and properties, as well as for background studies for nucleon decay and neutrino astronomy. It started with 240 tons, gradually increasing to 900 tons. The detector consisted of 912 flash chambers and iron planes interspersed with 113 planes of geiger tubes. It could reconstruct muon tracks internally (contained), as well as from the surrounding rock (upward going stopping muons and horizontal through-going muons).

The fine granularity of the detector allowed it to measure up to 10 TeV muons and search some of the parameter space not covered by Kamiokande and IMB. However, they found no evidence for neutrino oscillations and their measurement of the ν_μ rate agreed with the expectation.

The NUSEX experiment ran from 1982 to 1988 [105]. The detector was similar in the design concept to Fréjus, but was smaller at 150 tons of active mass and ran from 1982 to 1988. It was

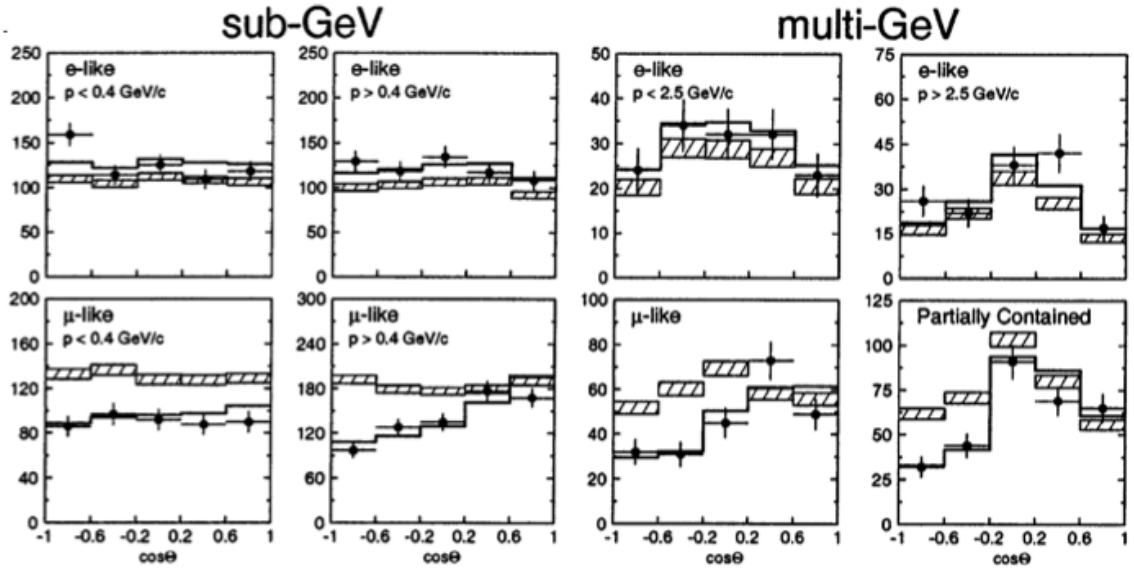

Figure 2.11: Super-Kamiokande Zenith distributions [31]. The top panels show e-like events, and the bottom panels show μ-like events. The left 4 panels contain sub-GeV events ($<$1.33 GeV), and the right 4 panels contain multi-GeV events ($>$1.33 GeV). Partially Contained events are μ-like events where the muon escapes the inner volume of the detector. The zenith angle dependence of the muon neutrino deficit can be seen in the higher energy muon events.

located at the Mont Blanc tunnel in France. Similarly to Fréjus they measured no deficit in the muon neutrino rate from the expectation.

The agreement of these two experiments with the Standard Model prediction suggested that the Atmospheric Anomaly could possibly have been the result of a systematic effect. Later atmospheric experiments provided more evidence in support of Neutrino Oscillations.

2.2.3 Super-Kamiokande Atmospheric Neutrinos

Super-Kamiokande (SK), described in Chapter 3, is also capable of measuring atmospheric neutrinos. The experiment collected high statistics data with greater accuracy than Kamiokande. They measured the neutrino distributions relative to their incoming zenith angle, where a $\cos\theta$ of 1 was directly above the detector and -1 corresponded to neutrinos coming from the other side of the Earth below the detector. In 1998, SK released a measurement that showed the deficit of muon neutrinos had a zenith angle dependence, and that the observed results could be explained well by $\nu_\mu \rightarrow \nu_\tau$ neutrino oscillations [30, 31, 106–109]. They also showed that $\nu_\mu \rightarrow \nu_e$ oscillations were disfavoured and that these observations could not be explained by any known uncertainties. This result was key evidence for neutrino oscillations.

Figure 2.11 shows the zenith distributions presented in 1998. The top panels display the zenith distributions for the electron-like events, which are more or less consistent with the no oscillation prediction in the hashed histograms. However, the zenith dependence of the muon events can be seen in the lower panels. The neutrino energy of the events increases in the figures from left to right. This zenith dependence becomes more apparent as the neutrino energy increases, where there is a greater angular correspondence between the directions of the neutrino

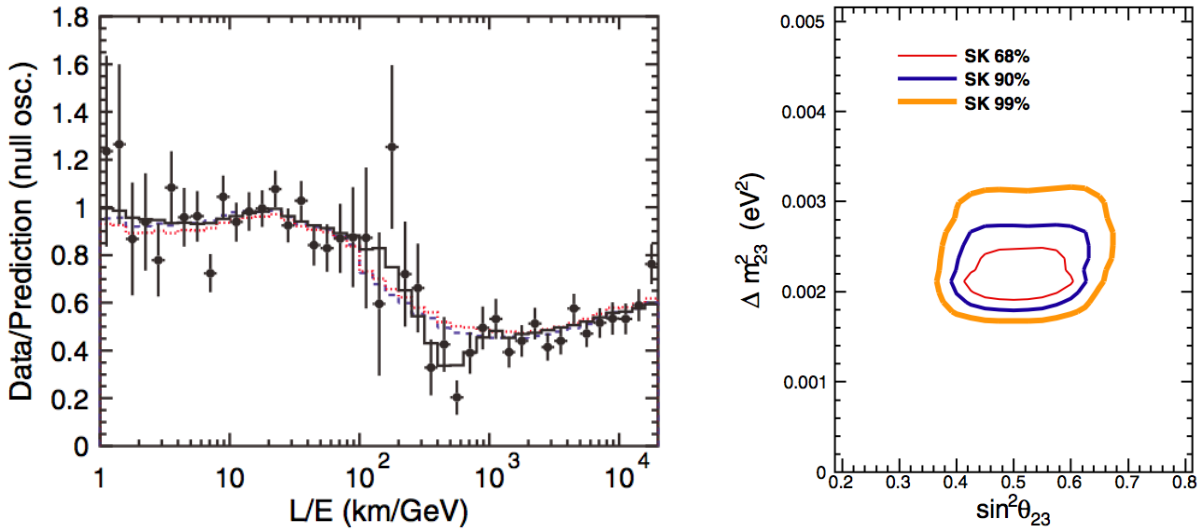

Figure 2.12: Super-Kamiokande L/E distributions on the left [9], and atmospheric oscillation parameter allowed regions from 2010 3-flavour analysis [15]. On the left, the ratio of the data to the null oscillation prediction as a function of the reconstructed L/E is shown. If there were no oscillations, points distributed around 1 would be expected. Best fits for 2-flavour $\nu_\mu \to \nu_\tau$ oscillations (solid line), neutrino decay (dashed line), and neutrino decoherence (dotted line) are shown. On the right, the allowed regions are for the normal mass hierarchy, at 68% C.L. in the thin red line, 90% C.L. in the medium blue line, and 99% C.L. in the thick yellow line.

and the lepton product of the interactions. These results show that the deficit in the muon neutrinos mostly comes from upward going neutrinos that have travelled the order of 10,000 km.

By breaking the events into energy groups, an energy dependence of the deficit can also be probed. The solid lines in Figure 2.11 represented the best-fit $\nu_\mu \to \nu_\tau$ neutrino oscillation prediction. SK showed these oscillations to be in good agreement with the data and reported at the 90% confidence level the oscillation parameters were $\sin^2 2\theta > 0.82$ and $5 \times 10^{-4} < \Delta m^2 < 6 \times 10^{-3}\,\text{eV}^2$.

Prior to the zenith measurement, SK reported on their first measurement of the double flavour ratio of $0.61 \pm 0.03(\text{stat.}) \pm 0.05(\text{syst.})$ for the sub-Gev energy range in early 1998 [107], which was consistent with the Kamiokande, IMB and Soudan-2 experiments. A little later a similar ratio was published for the multi-GeV range, and some zenith asymmetry of the deficit was observed [106]. With an updated data set of 535 days, still in 1998, SK reported on the first evidence for neutrino oscillations visible from the zenith, or flight path, dependence of the deficit of muon neutrinos [30, 31]. This result pointed to neutrino oscillations as a likely explanation for all the anomalies seen in neutrino experiments. This same zenith dependence was seen in the higher energy through-going muon events, in which a high energy neutrino interacts in the rock surrounding the detector and the muon product is observed [110]. In 2000, SK was able to reject the oscillation to sterile neutrinos at the 99% C.L. while the two-flavour $\nu_\mu \leftrightarrow \nu_\tau$ oscillations were consistent with all the data [108].

These results were the first evidence that neutrinos oscillate, something that the later Kamiokande results were also hinting at. Although, there were multiple competing theories that could produce a deficit in the number of muon neutrinos observed with increasing zenith angle. One of

the characteristic features of Neutrino Oscillations, however, is that it has an L/E dependence: a dependence on the ratio of the neutrino flight length to its energy. In 2004, SK released a result from an analysis that aimed to reconstruct the oscillatory L/E signature of neutrino oscillations [9], which can be seen in Figure 2.12. The analysis was able to show a significant dip at L/E = 500 km/GeV in the data, which was reproduced by neutrino oscillations, but not by neutrino decay and neutrino decoherence. The minimum χ^2 best fit for neutrino decay was 3.4σ larger than the neutrino oscillation best fit; and the best fit for neutrino decoherence was 3.8σ larger. This was the first evidence that the neutrino survival probability follows the sinusoidal behaviour of neutrino oscillations.

For more recent analyses, in 2010 there was a report on an investigation into 3-flavour oscillations trying to measure a non-zero θ_{13} from the data, as well as a search for sub-leading effects that could determine the quadrant of θ_{12}, using data from the SK-I to SK-III periods [15]. No evidence for a non-zero θ_{13} or a preferred θ_{12} quadrant was found. The data for both normal and inverted hierarchy were consistent, and neither were preferred. The allowed regions for the atmospheric parameters for normal hierarchy from this analysis can be seen in Figure 2.12. There has also been a statistical approach with a neural network analysis to observe tau neutrino appearance in the SK data, published in 2012 [111]. The result was consistent with the expected number of oscillated τ neutrinos, and excluded the no appearance hypothesis at the 3.8σ level.

2.2.4 Soudan2 and MACRO

The Soudan 2 experiment ran from 1989 to 2001 and used a 963 metric ton iron tracking-calorimeter detector that was originally built to study proton decay. The experiment was located 2070 m.w.e. underground in northern Minnesota, US. Soudan 2 provided the first independent confirmation [112] of the Super-Kamiokande (SK) zenith results.

The detector was a honeycomb structure and acted as a time-projection chamber. The drift tubes were 1.5 cm in diameter and 1 m long, filled with an argon-CO_2 gas mixture and can be seen in Figure 2.13. The tubes were secured in corrugated steel sheets and arranged into a honeycomb matrix. This geometry was chosen for a more isotropic response. Charged particles that passed through the drift tubes ionised the gas producing electrons. An electric field over the tubes caused the electrons to drift at $\sim$0.6 cm/μs to the ends of the tubes. At the tube ends there were vertical anode wires that amplify and collect the electrons, and an induced charge was read from horizontal cathode pads. These two signals matched in time identify which tube the ionisation occurred in. The coordinate along the tube was given by the drift time. The track sampling frequency was about once every 3 cm, and tracks and vertices were reconstructed at $\sim$0.5 cm resolution. The honeycomb structure made up modules with dimensions of about $1 \times 1 \times 2.5\,\mathrm{m}^3$, and these modules were built up to construct the 963 ton detector mass. Surrounding the detector, there were three layers of proportional counters that operated as a comic ray and external background veto.

Soudan 2 was considerably smaller than SK, and so had a lower event rate, however they were able to reconstruct clear particle tracks and the event vertices with centimetre resolution. This enabled them to reconstruct both the lepton and hadronic final state, allowing them to improve the resolution of the L/E value by 2 to 3 times at low energies. Whereas the recoil proton was very difficult to see in SK, so there was a low resolution in L/E for events below $\sim$1 GeV.

Figure 2.14 shows the L/E distributions reconstructed by Soudan 2 in 2003 [112]. No significant deficit or excess was seen in the ν_e distributions, however a deficit in the ν_μ events can be

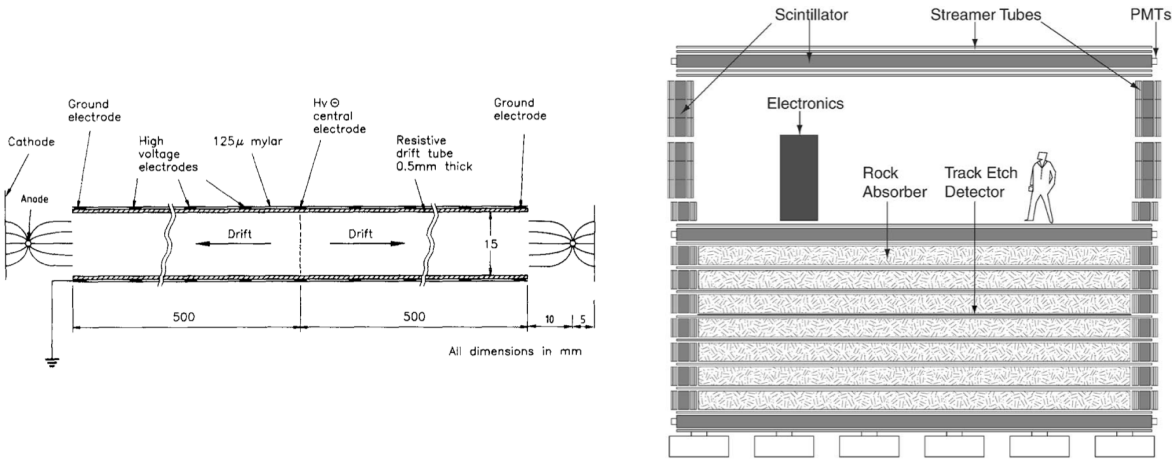

Figure 2.13: The Soudan 2 drift tube on the left [113], and the MACRO detector on the right [114]. In the left figure is a schematic of the main active element in the Soudan 2 detector, a drift tube. An electric field was set up from the centre of the tube to the ends by electrodes embedded in the circumference of the cylinders. This caused the ionisation electrons to drift to the ends and collect on the anode wires, and induce a charge on the cathode pads. A honeycomb matrix of these tubes built up the detector. On the right, the arrangement of the detection mechanisms in a MACRO supermodule is shown. The dark grey planes were scintillator (3 horizontal, 2 vertical), the many light grey planes were streamer tubes, and there were a few Track Etch detectors shown in black.

seen from around $\log_{10}(L/E) > 1.5$. Soudan 2 also reproduced zenith distributions similar to those from SK, and reported an oscillation parameter space that enclosed the SK result, which can also be seen in Figure 2.14.

The MACRO experiment started taking data during construction from 1989 and recorded their main dataset between 1994 and 2000 [115]. The detector used layers of scintillator for timing and streamer tubes for particle tracking, and was located an average of 3800 m.w.e. underground at Gran Sasso, Italy. One of the main goals of the experiment was to study atmospheric neutrino oscillations. The experiment primarily observed upward-going muons that were produced by neutrino interactions in the rock below the detector. Although, they also recorded neutrino events that originated within the detector as well.

The MACRO detector was made up from six supermodules, lined up side-by-side with total dimensions $76.5 \times 12 \times 9.3\,\mathrm{m}^3$, and a total weight of 5.3 kton [114]. A diagram of one of the supermodules can be seen in Figure 2.13. Each module consisted of three independent detection mechanisms: liquid scintillation counters, streamer tubes, and nuclear track (track-etch) detectors. The arrangement of these three sub-detectors can be seen in the figure. The scintillator was a mixture of 96.4% mineral oil, 3.6% pseudocumene, and some PPO and bis-MSB. Each end of the counters were viewed by 8-inch PMTs. The coordinate along the counter could be determined by the time-of-flight, from the relative time difference at each end. The streamer tubes had $3 \times 3\,\mathrm{cm}^2$ cross-sectional area, were filled with a 73% He and 27% n-pentane gas mixture and were read out by anode wires in the centre of the tube. The second coordinate in each plane was given by pick-up strips. The track-etch detectors were mainly for magnetic monopole detection.

The MACRO results were in agreement with $\nu_\mu \to \nu_\tau$ oscillations, and excluded the no-

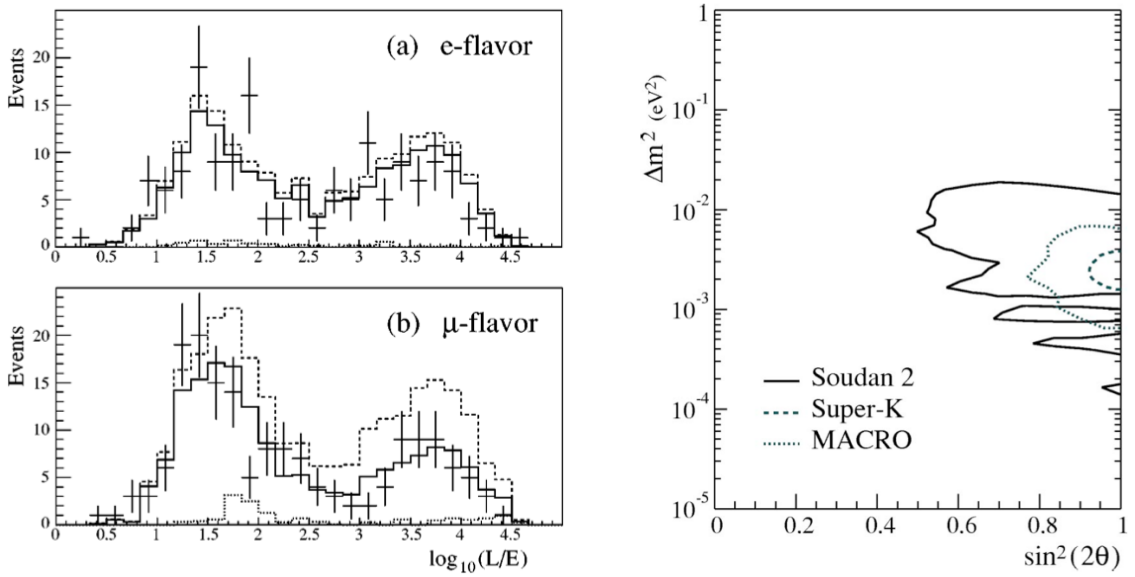

Figure 2.14: Soudan 2 L/E distributions of their high resolution sample on the left [112], and the oscillation parameter allowed regions from MACRO and Soudan2 [112]. The upper plot is for ν_e events, and the lower for ν_μ events. The dashed histogram is the Monte Carlo prediction without oscillations, while the solid histogram is with oscillations. A deficit can be seen from $\log_{10}(L/E) > 1.5$ in the ν_μ L/E distribution. The dotted line is the contribution expected from interactions in the surrounding rock, and is included in the Monte Carlo distributions. In the right figure, the Soudan2 90% allowed region is shown in the solid line, MACRO in the dotted line and the contemporary SK result in the dashed line.

oscillation hypothesis at 5σ. They reported a more constrained oscillation parameter space than Soudan 2, which also encompassed the SK result as seen in Figure 2.14. Although the limited dataset of Fréjus and NUSEX did not observe oscillations, Soudan 2 and MACRO had similar detection methods and reported results in agreement with neutrino oscillations. This confirmation from independent experiments strengthened the evidence for neutrino oscillations, making it very unlikely that the observation was a systematic effect or statistical fluctuation.

2.2.5 Atmospheric Neutrino Summary

Neutrinos are produced by the collision of cosmic rays in the atmosphere across the globe, making an abundant source of neutrinos with largely varying flight-paths from ∼10 km to ∼10,000 km, and a spectrum of energies. This made them an ideal probe into the flight-length and energy dependence predicted by Neutrino Oscillations. In 1988, Kamiokande observed about ∼60% of the ν_μ events from the Standard Model expectation. This was supported by the IMB results observing closer to ∼70% of the expectation. These unexpected measurements were known as the *Atmospheric Anomaly*.

The early iron-calorimeter experiments in the 1980's, Fréjus and NUSEX, measured a ν_μ rate in agreement with the expectation. So it was possible the deficits seen in the first Cherenkov neutrino experiments were due to a systematic effect. However, the first real evidence for Oscillations came from the 50 kton water Cherenkov experiment Super-Kamiokande (SK) in 1998.

A clear zenith angle dependence was observed in the ν_μ events, which showed the deficit grew with flight-path. There were several competing explanations for this and the 2004 L/E Analysis at SK demonstrated that Neutrino Oscillations provided the best interpretation, by reproducing the first dip in the predicted sinusoidal pattern. Around the year ∼2000, the later tracking-calorimeter experiments Soudan 2 and MACRO, which had similar detection methods to Fréjus and NUSEX, gave an independent confirmation of the Neutrino Oscillation evidence observed at SK. These results could not be explained by any known systematic uncertainty, establishing firm evidence for Oscillations from atmospheric neutrino experiments.

2.3 Reactor Neutrino Experiments

Nuclear reactors provide a source of $\bar{\nu}_e$ through the β^- decay of the neutron rich fragments from the nuclear fission reactions of uranium and plutonium. In order for these fission products to be stable, on average 6 neutrons decay to 6 protons releasing 6 $\bar{\nu}_e$ per fission. The energy release in each fission is around 200 MeV, so there are on average about 2×10^{20} $\bar{\nu}_e$/sec for each $\mathrm{GW}_{\mathrm{thermal}}$ of power output. These neutrinos can be used to probe $\bar{\nu}_e \to \bar{\nu}_x$ oscillations, where x is a species of neutrino other than the electron neutrino. Since the energy of neutrinos produced by a reactor is a few MeV, there is insufficient energy to produce a muon or tau lepton at detection. For this reason, only the possibility of a deficit of $\bar{\nu}_e$ flux could be observed and reactor neutrino experiments were therefore known as disappearance experiments.

Typically reactor neutrinos are detected by the inverse β-decay reaction:

$$\bar{\nu}_e + p \to e^+ + n \tag{2.40}$$

The signature for this reaction is the prompt detection of the e^+ from its annihilation with an electron into two 511 keV γ-rays, followed by the delayed neutron capture. The coincidence of these two events can be used to reject the majority of the background. It has a reaction threshold of 1.804 MeV.

There were many reactor experiments that did not observe neutrino oscillations: Gosgen, Krasnoyarsk, Bugey, CHOOZ and Palo Verde. However, they set limits on oscillation parameters, particularly, CHOOZ provided a stringent limit on θ_{13}. The later Reactor experiments were the first to measure θ_{13}.

2.3.1 CHOOZ

The CHOOZ experiment [19, 116, 117] took their main data between March 1997 to July 1998 and was located in a villiage of the same name, in France. The detector was located 1 km away from two pressurized water reactors with a combined thermal power of 8.5 GW. These reactors were just coming online, and only one reactor was on for over 80% of the experiment live time. However, this situation allowed CHOOZ to understand their neutrino source over a range of conditions.

The detector was a cylindrical vessel 5.5 m in diameter, 5.5 m deep, and can be seen in Figure 2.15. The target was a 5-ton plexiglass container filled with hydrogen rich paraffinic liquid scintillator for the "free protons," and 0.09% gadolinium for the high neutron capture cross section and ∼8 MeV γ-ray signal. The target container was observed by 192 8-inch PMTs with 15% coverage, and outside that there was an optically isolated veto region. These regions outside the target region were filled with undoped scintillator.

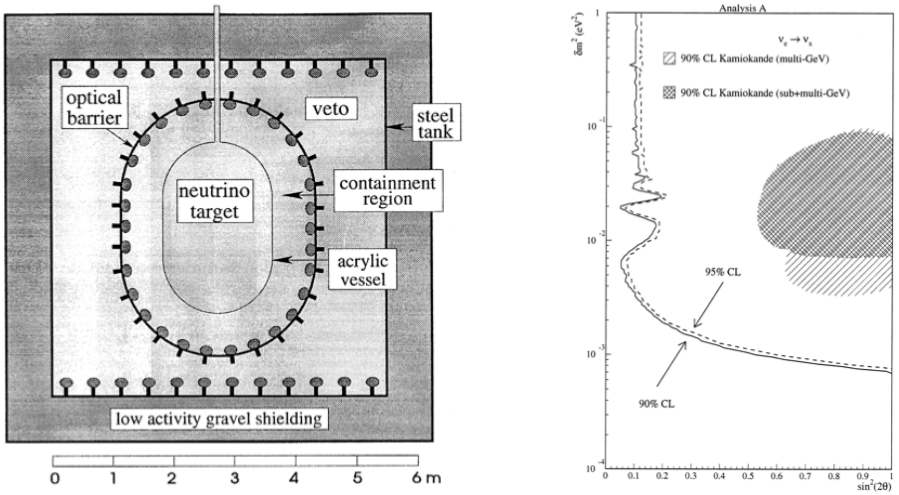

Figure 2.15: The CHOOZ detector [116] on the left and the CHOOZ $\bar{\nu}_e \leftrightarrow \bar{\nu}_x$ oscillation excluded parameter space [19] on the right. This measurement put stringent limits on $\nu_e \leftrightarrow \nu_x$ oscillation. The hashed region shows the Kamiokande 90% allowed oscillation region. This was excluded, supporting the $\nu_\mu \leftrightarrow \nu_\tau$ oscillation hypothesis for atmospheric neutrinos.

The neutrino source flavour composition was nearly pure ($\sim$100% $\bar{\nu}_e$), and the intensity of the flux was known to within 2%. They had a sensitivity down to $10^{-3}\,\mathrm{eV}^2$ in Δm^2, which was an order of magnitude better than previous reactor experiments. The ratio of the measured $\bar{\nu}_e$ flux to the expectation was [19]:

$$R = 1.01 \pm 2.8\%(\mathrm{stat}) \pm 2.7\%(\mathrm{syst}) \tag{2.41}$$

and so no evidence for oscillations was observed. Their oscillation analysis allowed them to exclude some of the parameter space (Figure 2.15), for $\bar{\nu}_e \leftrightarrow \bar{\nu}_x$ transitions, including the allowed region observed at Kamiokande. CHOOZ removed the possibility of explaining the Atmospheric Anomaly with $\nu_\mu \leftrightarrow \nu_e$ oscillations, which supported the $\nu_\mu \leftrightarrow \nu_\tau$ explanation from Kamiokande.

2.3.2 KamLAND

KamLand acquired its primary data between 2002 and 2009 [34, 118–120], and was situated at the old Kamiokande site, near Kamioka, Japan. The detector was located an average distance of $\sim$180 km (138-214 km) from 26 reactors accounting for over 79% of the $\bar{\nu}_e$ flux. The remaining flux originated from one close reactor and many reactors over 295 km away. This considerable $\bar{\nu}_e$ flux concentrated within a narrow range around $\sim$180 km, put the detector in an ideal position to test neutrino oscillations that could explain the solar anomaly.

The detector was a 1 kton sphere of 18 m diameter, containing a 13 m diameter transparent balloon filled with ultra-pure liquid scintillator. The balloon was suspended in non-scintillating oil, and there were 1879 PMTs mounted on the inside of the sphere. Outside the sphere there was a 3.2 kton water cherenkov outer detector, primarily for tagging background events. Electron anti-neutrinos were detected by the inverse β decay interaction, as in Equation (2.40), with the 2.2 MeV γ-ray from neutron capture on hydrogen $\sim$200 μs later.

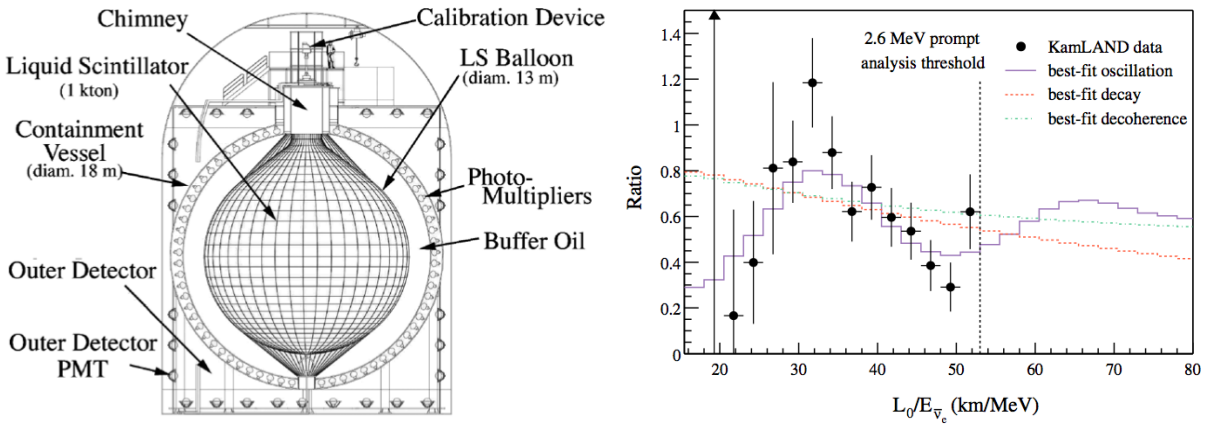

Figure 2.16: The KamLAND detector [119] on the left and the measured spectral distortion L/E [120] on the right. The ratio of the observed $\bar{\nu}_e$ over the no-oscillation expectation, against the reconstructed L/E. Best-fit for neutrino oscillations in the solid purple histogram; decay in the dashed red; and decoherence in the green dot-dashed histogram. The plot assumes all neutrinos follow an $L_0 = 180\,\text{km}$ flight path.

KamLAND's first results in early 2003 clearly showed, for the first time, the disappearance of $\bar{\nu}_e$ [119]. The ratio of measured $\bar{\nu}_e$ to the expectation was:

$$R = 0.611 \pm 0.085(\text{stat}) \pm 0.041(\text{syst}) \tag{2.42}$$

This data helped constrain the solar oscillation parameter space, excluding all but the large-mixing-angle (LMA-MSW) solution.

In a 2005 analysis [120], with increased statistics, $\bar{\nu}_e$ disappearance was observed at the 99.998% significance level, 4σ away from the non-oscillation hypothesis. In this analysis they showed the first evidence for distortion in the energy spectrum of $\bar{\nu}_e$, which was in agreement with oscillations, seen in Figure 2.16.

KamLAND continued to improve the precision of its measurements. In 2008 they released the most precise measurement of Δm^2_{21} and an L/E plot showing almost two cycles of the oscillation pattern [34], which can be seen in Figure 2.17. In a combined analysis of the KamLAND and solar experiment data, the reported oscillation parameters were $\Delta m^2_{21} = 7.59^{+0.21}_{-0.21} \times 10^{-5}\,\text{eV}^2$ and $\tan^2\theta_{12} = 0.47^{+0.06}_{-0.05}$.

Since 2009, the detector was upgraded to KamLAND-Zen, a neutrino-less double beta decay experiment with a world-class sensitivity, but still struggling with backgrounds [121].

2.3.3 Daya Bay

The Daya Bay experiment started taking data at the end of 2011, and in March 2012 it published the first observation of non-zero θ_{13} [14], with a significance of 5.2σ. The data were collected over 55 days, although the result was based on around 10,000 $\bar{\nu}_e$ candidates in the far detectors, and about 80,000 in the near detectors. The experiment was located at the reactor complex at Daya Bay, China.

The Daya Bay experiment was located around six 2.9 GW (thermal) pressurised water nuclear reactors, arranged into three pairs of nuclear power plants. The $\bar{\nu}_e$ flux was measured with 6

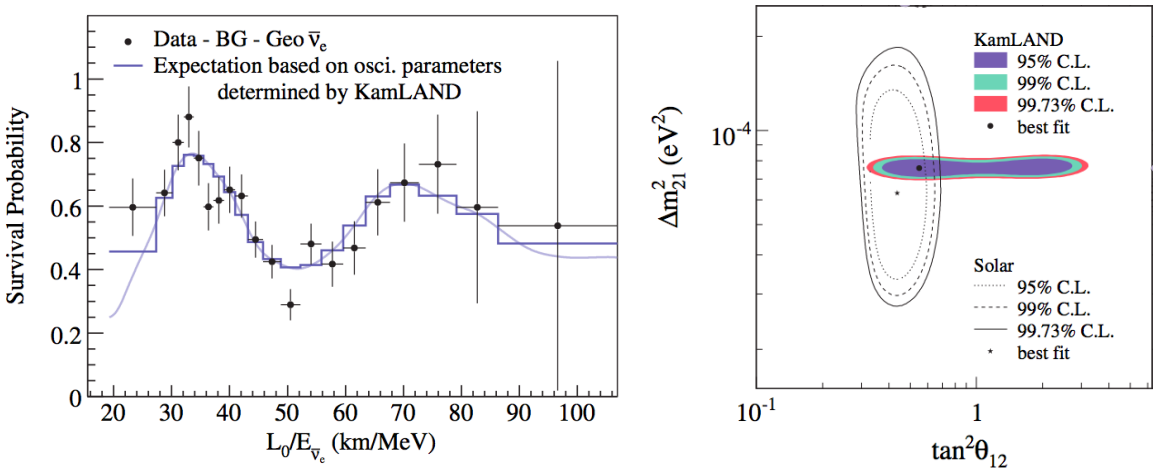

Figure 2.17: KamLAND 2008 Distributions [34] The left plot shows the updated L/E plot, displaying nearly two oscillation cycles. $L_0 = 180\,\text{km}$ is the flux-weighted average distance to the reactors. The right plot shows the neutrino oscillation parameter allowed space from KamLAND and solar neutrino experiments. It can be seen that the KamLAND data puts a large constraint on Δm^2_{21}.

functionally identical anti-neutrino detectors arranged in two near experimental halls (470 m and 576 m) and one far at the oscillation maximum (1648 m). The arrangement can be seen in Figure 2.18. This allowed them to measure the relative differences in the $\bar{\nu}_e$ flux, independent of correlated uncertainties and minimised uncorrelated reactor uncertainties. The analysis used the following survival probability:

$$P_{\text{sur}} \approx 1 - \sin^2 2\theta_{13} \sin^2(1.267\Delta m^2_{31} L/E) \tag{2.43}$$

This can be used for reactor based experiments and gives an unambiguous determination of θ_{13}, as the disappearance of $\bar{\nu}_e$ driven by θ_{12} and Δm^2_{21} is negligible at baselines of around $\sim$1 km.

The detection method made use of inverse β-decay (Equation (2.40)) and consisted of a 3.1 m diameter inner acrylic vessel containing 20 tons of gadolinium-doped liquid scintillator as the target. Outside this there was a 4 m diameter acrylic vessel holding 20 tons of liquid scintillator. These were contained in a 5 m diameter stainless steel cylindrical vessel, filled with 37 tons of mineral oil to shield the inner vessels from radioactivity, and housed 192 PMTs. The detectors were surrounded by a >2.5 m of high-purity water segmented into two water cherenkov detectors to remove spallation neutrons and cosmogenic backgrounds.

The experiment observed a deficit in the $\bar{\nu}_e$ flux in the far experimental hall. The ratio of the measured flux to the expectation was [14]:

$$R = 0.940 \pm 0.011(\text{stat}) \pm 0.004(\text{syst}) \tag{2.44}$$

and the best-fit value was:

$$\sin^2 2\theta_{13} = 0.092 \pm 0.016(\text{stat}) \pm 0.005(\text{syst}) \tag{2.45}$$

with a χ^2/NDF of 4.26/4 for 4 degrees of freedom. The 6.0% rate deficit in the far hall can also be seen in Figure 2.18. The experiment also made an energy spectrum measurement where the

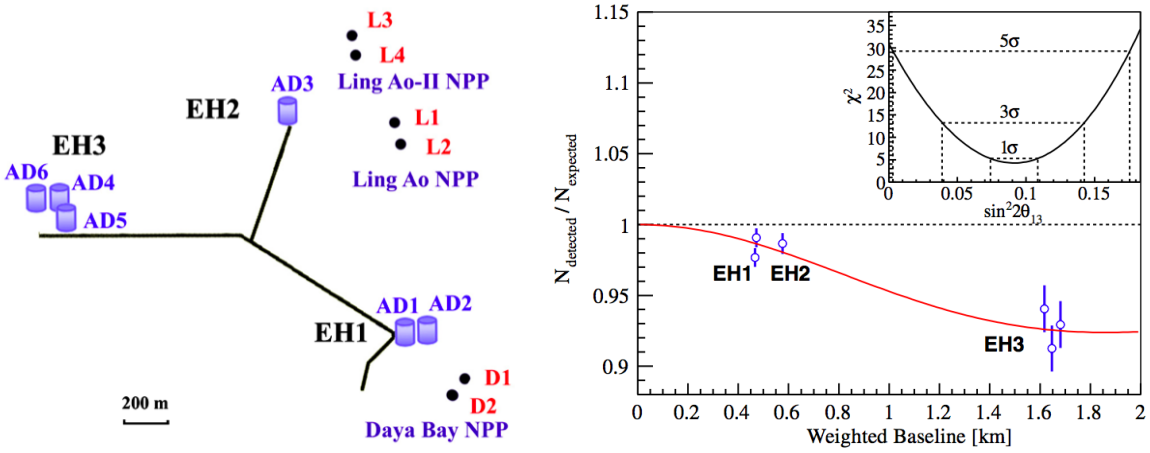

Figure 2.18: The Daya Bay experimental arrangement is shown on the left and the deficit measurement on the right. In the diagram, the reactors are shown by dots in pairs forming nuclear power plants (NPP). Six anti-neutrino detectors (AD) are located in three experimental halls (EH). In the right figure, the ratio of the measured flux over the expected flux assuming no oscillations is shown. The expected signal was corrected with the best-fit normalisation parameter. The detectors in EH3 have been displaced slightly for clarity. The best-fit survival probability is shown by the red curve, and the χ^2 against $\sin^2 2\theta_{13}$ is shown in the top right.

expected spectrum was calculated with the near detectors. The distortion was in agreement with the best-fit θ_{13} measurment, further supporting the non-zero θ_{13} result.

2.3.4 Double CHOOZ

The Double CHOOZ is the successor to the CHOOZ experiment and its aim is to improve the sensitivity to the θ_{13} parameter, reaching down to $\sin^2 2\theta_{13} = 0.03$ after three years of operation with two detectors [122]. A new near detector was planned for construction at the reactor site, identical to the far detector, allowing a relative normalisation systematic error of 0.6%.

Double CHOOZ also had multiple improvements on their detector design to help reduce some uncertainties. The detector was made up of 4 concentric cylindrical tanks, which can be seen in Figure 2.19. The inner most acrylic vessel contained 10.3 m^3 of gadolinium-doped scintillator as the neutrino target. The next acrylic vessel added a 55 cm layer of liquid scintillator as a γ-catcher. Outside this there was a 105 cm thick layer of mineral oil to shield from the radioactivity of the PMTs, and was a major improvement from CHOOZ. All of this was contained in a stainless steel vessel housing 390 10-inch PMTs and was referred to as the Inner Detector. Outside the main detector there was an inner veto with a scintillator layer, and some further outer veto planes above the detector.

In January 2012, Double CHOOZ released an indication for $\bar{\nu}_e$ disappearance at a detector $\sim$1 km from two 4.25 GW (thermal) reactors, and a non-zero value for θ_{13} [38]. In July 2012, they provided evidence for $\bar{\nu}_e$ disappearance, and made a measurment on θ_{13} based on both the rate and energy spectrum [42]:

$$\sin^2 2\theta_{13} = 0.109 \pm 0.030(\text{stat}) \pm 0.025(\text{syst}) \tag{2.46}$$

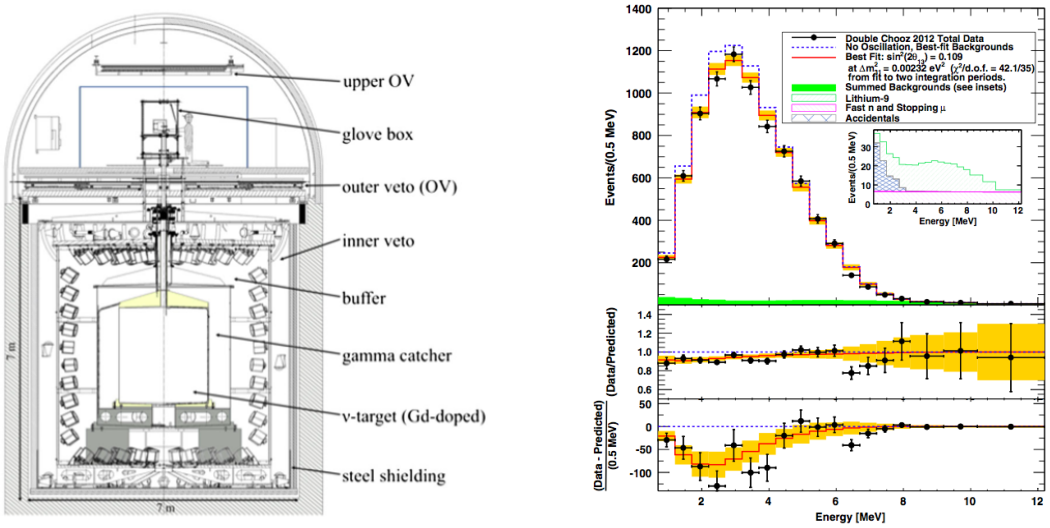

Figure 2.19: Double CHOOZ detector [38] on the left and disappearance measurement on the right [42], with θ_{13} fit. See the text for the detector description. The right figure shows the prompt energy spectrum; the no-oscillation prediction in the blue dotted line; and the best fit in the solid red line at $\sin^2 2\theta_{13} = 0.109$ and $\Delta m^2_{31} = 2.32 \times 10^{-3}\,\text{eV}^2$. The orange bands show the systematic uncertainties on the best-fit. The background contribution is shown in green, and also in the inset. Comparisons with the no-oscillation prediction are shown beneath the main plot.

Their result excluded the no-oscillation hypothesis at 2.9σ. The analysis fit is shown in Figure 2.19. This supported the measurement at Daya Bay published on March 2012, which was primarily a rate-only analysis.

2.3.5 RENO

RENO is an experiment set up around six 2.8 GW (thermal) reactors in Korea. In April 2012, they released their observation of $\bar{\nu}_e$ disappearance, excluding the non-oscillating hypothesis at 4.9σ [41].

RENO had two identical anti-neutrino detectors located at 294 m and 1383 m from the centre of the reactor array. As in the Daya Bay set-up, and the planned set-up for Double CHOOZ, making a relative measurement from two identical detectors considerably reduces the systematic errors.

The detector design can be seen in Figure 2.20. The main components were similar to Daya Bay and Double CHOOZ. The inner most acrylic vessel had 16 t (18.3 m^3) of ∼0.1% Gadolinium doped hydrocarbon liquid scintillator. The outer acrylic vessel was a 60 cm thick layer scintillator γ-catcher. Outside that was a 70 cm thick buffer layer of 65 tons of mineral oil with 354 10-inch inward facing PMTs. The outer detector was a 1.5 m thick volume of highly purified water observed by 67 10-inch PMTs.

The RENO result was based on 229 days of data taking, in which they collected around ∼17,000 $\bar{\nu}_e$ candidates at the far detector and about ∼154,000 at the near detector. The ratio

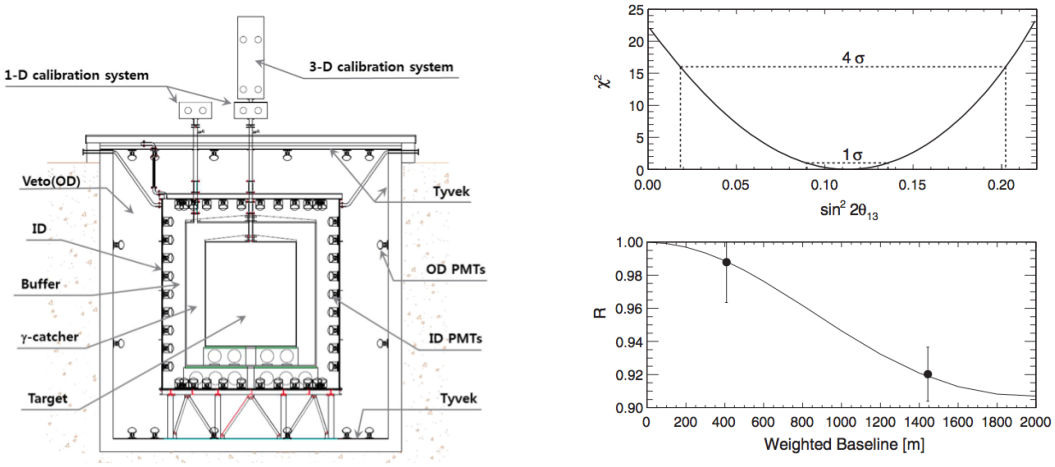

Figure 2.20: The RENO Detector on the left and the θ_{13} measurement from the rate disappearance on the right. The top plot on the right shows the χ^2 distribution as a function of $\sin^2 2\theta_{13}$; and the lower plot shows the ratio of the measured events to the number expected with no-oscillations at the two detectors. The smooth curve is from the best fit.

of $\bar{\nu}_e$ observed to that expected was:

$$R = 0.920 \pm 0.009(\text{stat}) \pm 0.014(\text{syst}) \tag{2.47}$$

and the best-fit value was:

$$\sin^2 2\theta_{13} = 0.113 \pm 0.013(\text{stat}) \pm 0.019(\text{syst}) \tag{2.48}$$

2.3.6 Reactor Neutrino Summary

Reactor neutrino oscillation experiments make use of the nuclear fission reaction as a neutrino source. Many early reactor experiment did not observe oscillations, but they set limits on the θ_{13} parameter. Notably in 1999, CHOOZ with a detector ~1 km from the reactor set the standard limit on the parameter for many years, and excluded the possibility for $\nu_\mu \leftrightarrow \nu_e$ oscillations for atmospheric neutrinos, supporting the $\nu_\mu \leftrightarrow \nu_\tau$ explanation from Kamiokande. In 2003 KamLAND, that had an average baseline of ~180 km, reported on the first measurement of $\bar{\nu}_e$ disappearance driven by the solar parameters θ_{12} and Δm^2_{21}. With their updated results in 2005 and 2008 they were able to greatly constrain the solar Δm^2_{21} in global analyses, as well as showing nearly two oscillation cycles in L/E.

Around 2011, three reactor experiments were all aiming for a measurement of θ_{13}. In January 2012, Double CHOOZ was the first to report anti-neutrino disappearance at around ~1 km from a reactor where the solar parameters are negligible. This result gave an indication for a non-zero value for θ_{13}. Daya Bay released the first measurement of θ_{13} and evidence for $\bar{\nu}_e$-disappearance driven by the parameter, with 5.2σ significance in March 2012. This result was confirmed shortly afterwards at RENO, with 4.9σ significance. A little later Double CHOOZ provided more evidence with an analysis based on both the energy spectrum and rate, but still with one detector and with a 2.9σ significance.

2.4 Accelerator Neutrino Experiments

The first two sources of neutrinos discussed, solar and atmospheric, are a natural flux that can be investigated. Reactor anti-neutrinos were human-made, so the details of the flux could be better understood, however the reactor conditions were outside the control of the experiments. Accelerator neutrinos, on the other hand, were a directed beam of human-made neutrinos with well-understood properties that could be studied. The direction, energy, momentum and composition of the neutrino beams were determined by the experiments. So accelerator experiments could give a controlled test of the natural phenomena observed in other experiments.

Typically the beams were created by accelerating protons up to a few GeV, where the power of the beam was more important for creating an intense beam of neutrinos, rather than achieving very high energies. The protons were then collided into a target mass, resulting in a spray of pions and some kaons (quite like atmospheric neutrinos). The pions were then collected and focussed by magnets in the direction of the detector. This was followed by a region where the pions could decay in flight, and finally a muon dump to stop unwanted penetrating particles. The result was a directed beam of neutrinos, typically with a high purity of muon neutrinos. An example of focusing magnets from K2K can be seen in Figure 2.21, and a beamline from T2K in Figure 2.24.

The earlier short baseline (few hundred metres) accelerator neutrino experiments did not observe any oscillations. The first long baseline (few hundred kilometres) experiments aimed to make a controlled confirmation of the oscillations seen in atmospheric neutrinos, and to constrain the atmospheric Δm^2_{32}. Following this, their aim was to make a measurement of θ_{13}, and then the mass hierarchy and δ_{cp} if θ_{13} was large enough. Whereas the reactor experiments could make a pure measurement of θ_{13}; for accelerator experiments the measurement of θ_{13} also depended on δ_{cp}, θ_{23} and the mass hierarchy. This made a measurement of θ_{13} more difficult, but it also meant these experiments could potentially measure the remaining parameters.

2.4.1 K2K

K2K (KEK To Kamioka) was the first accelerator neutrino long-baseline experiment, that sent a nearly pure ν_μ beam 250 km from the Japanese accelerator facility KEK to the Super Kamiokande (SK) detector in Kamioka [123–125]. This baseline and the mean neutrino energy of 1.3 GeV allowed the atmospheric Δm^2 to be probed by an accelerator based experiment for the first time. The main data was taken from June 1999 to November 2004. The stability of the beam was measured by monitors downstream from the target and beam dump.

A neutrino near detector (ND) was built 300 m from the proton target to verify the stability and direction of the beam, and to determine the energy spectrum and flux normalisation. The neutrino flux at SK was estimated by multiplying a far/near ratio to this spectrum. The ND consisted of a 1 kt water cherenkov detector (1KT) and a fine-grained detector (FGD), which can be seen in Figure 2.21. The 1KT was used to measure the flux normalisation, as it had the same detection method as SK most of the systematic uncertainties cancelled. The 1KT had a high efficiency for reconstructing the muon momentum below 1 GeV/c, while the FGD had a high efficiency above 1 GeV/c. Together, these detection systems measured the energy spectrum. The FGD consisted of a scintillating fiber and water detector (SciFi), a lead-glass calorimeter (LG) and a muon range detector (MRD). The FGD could reconstruct event tracks, and even classify events by using the track reconstructed by the recoil proton when it was visible. The

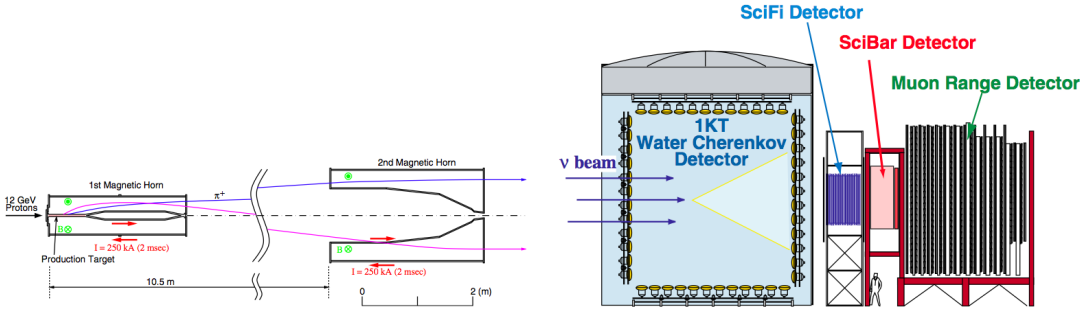

Figure 2.21: The K2K horn magnets on the left and the near detector configuration on the right [125]. The horns each have a 250 kA current that flows through the inside and returns on the outside, setting up a toroidal magnetic field inside. This collects the pions of one polarity, π^+ here, into the forward direction. A second horn further focusses towards the far detector. The production target was a 66 cm aluminium rod that also served as the inner conductor of the horn. The near detector configuration after the lead-glass calorimeter was replaced with SciBar, is shown.

events at SK were selected using GPS timing information to correspond with the beam timing, which almost entirely cut out any atmospheric neutrino events. For details of the far detector, SK, see Sections 2.1.4,2.2.3 or Chapter 3.

The analysis used a maximum-likelihood method that included both the number of events observed (normalisation term) and the energy spectrum (shape term). The presence or absence of neutrino oscillations depended on both of these terms.

In early 2003, K2K reported an indication for neutrino oscillations with disappearance of the ν_μ accelerator neutrino flux [123]. They estimated that the probability the measurement was due to statistical fluctuations in the absence of oscillations was less than 1%. In 2005, K2K reported evidence for neutrino oscillations at the 4σ level [124]. In this second data taking period, there was no LG which was then replaced with SciBar around half-way through the run. SciBar was made of scintillator strips read out by wavelength shifting fibres and multianode PMTs, It was fully active and did not have the aluminium water tanks like SciFi. SK also had half the PMT coverage (SK-II) during this period. The final results from K2K [125] can be seen in Figure 2.22.

2.4.2 MINOS

The Main Injector Neutrino Oscillation Search (MINOS) experiment is an accelerator experiment that sends a neutrino beam from Fermilab to a near detector (ND) at 1 km and a far detector (FD) 735 km away in the Soudan mine in Minnesota, US [10, 36, 40, 43]. MINOS collected data from 2005.

The neutrinos are produced with the NuMI (Neutrino Main Injector) beam at Fermilab. 120 GeV protons are extracted in 10 μs spills, bent 3.3° downwards towards the FD and collide with a 95.4 cm long target. The positively or negatively charged particles produced are focussed by two magnetic horns, 10 m apart, depending on the current polarity. These particles then decay in a 675 m long, 2 m diameter, vacuum decay pipe to produce a ν_μ or $\bar{\nu}_\mu$ beam.

The MINOS detectors were both steel-scintillator tracking calorimeters with 1.3 T toroidal magnetic fields. They were made with octagonal planes of steel plates (2.54 cm thick) and planes

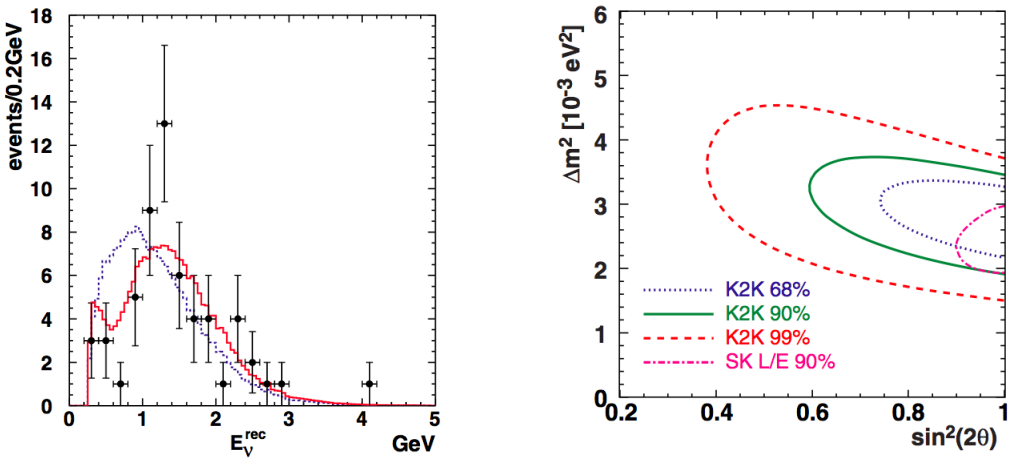

Figure 2.22: K2K reconstructed neutrino energy spectrum on the left and the allowed oscillation parameter space on the right [125]. In the left plot, the best-fit with neutrino oscillations is shown in the solid red histogram; and the no-oscillation expectation in the dashed blue histogram. The right plot shows a comparison of the K2K allowed regions against the 2004 SK L/E analysis allowed region [9].

of scintillating plastic strips (1 cm thick). These strips were arranged 45° to the vertical and 90° relative to their neighbours. The FD was 5.4 kton and 705 m underground with 484 8 m wide planes. It triggered with a hit within a 100 μs window centred on the beam spill timing. The ND was 0.98 kton and 103 m underground with 282 irregular $4\times6\,\mathrm{m}^2$ planes. It had a $\sim10^5$ times larger data rate than the FD and had a continuous 53.1 MHz sampling during the beam spill.

In 2006, MINOS reported disappearance of ν_μ when they observed 215 events at the FD where 336±14 were expected without oscillations [36]. In 2010, MINOS slightly improved the constraint on θ_{13} in their $\nu_\mu \to \nu_e$ oscillation search [126], from the stringent limit set by CHOOZ. In 2011, after running anti-neutrino mode, MINOS published the first direct measurement of $\bar{\nu}_\mu$ disappearance [10]. Surprisingly, the allowed region for $\bar{\nu}_\mu$ oscillation reported had a considerably larger Δm^2 and almost excluded the allowed region for ν_μ oscillation. This result was one of the motivations for the analyses in this thesis. However, an updated result of the anti-neutrino analysis showed an allowed region that overlapped with the allowed region for neutrinos, as seen in Figure 1.1.

MINOS was also continuing to look for ν_e appearance, and their results in July 2011 excluded the $\theta_{13} = 0$ hypothesis at the 89% C.L [40]. The flavour composition of the beam was expected to be 98.7% $\nu_\mu + \bar{\nu}_\mu$ and 1.3% $\nu_e + \bar{\nu}_e$. MINOS was sensitive to θ_{13} through $\nu_\mu \to \nu_e$ oscillations and they searched for an excess of ν_e events. The oscillation probability, to leading order, was given by:

$$P(\nu_\mu \to \nu_e) \approx \sin^2(\theta_{23}) \sin^2(2\theta_{13}) \sin^2(1.27\Delta m^2_{32} L/E) \tag{2.49}$$

The probability varies with matter effects and leptonic CP violation [127], so results were presented as a function of δ_{cp} and mass hierarchy.

The events were classified by spatial patterns of energy deposition. ν_e events were more compact and close to the hadronic shower, typically traversing 6-12 planes. The analysis, firstly, used selection criteria to largely cut out the background events. The main technique to separate

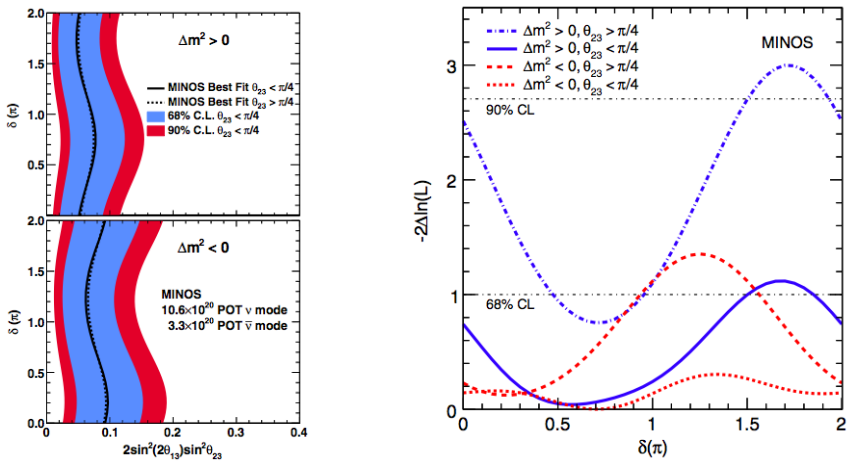

Figure 2.23: MINOS results from 2013, combining ν_μ and $\bar{\nu}_\mu$ beam mode data [43]. The left figure shows the allowed region for $2\sin^2(2\theta_{13})\sin^2(\theta_{23})$ with varying δ_{cp}, with the upper plot for normal mass hierarchy and the lower plot for inverted hierarchy. The right figure shows the difference of the likelihood from the bestfit value, for multiple parameter configurations. The hash-dotted horizontal lines mark the 68% and 90% C.L. indicating the disfavoured values.

the signal from the background was a nearest-neighbour algorithm, "library event matching" (LEM), where each candidate was compared to 5×10^7 simulated signal and background events with a likelihood. The final classification was then made with a neural network. The best-fit of the analysis was $2\sin^2(\theta_{23})\sin^2(2\theta_{13}) = 0.041^{+0.047}_{-0.031}(0.079^{+0.071}_{-0.053})$ for the normal (inverted) hierarchy and at $\delta_{cp} = 0$, which was an improvement on the T2K result at the time. The limit MINOS reported was $2\sin^2(\theta_{23})\sin^2(2\theta_{13}) < 0.12(0.20)$ at 90% confidence level and $\delta_{cp} = 0$. These results from accelerator experiments were hints that θ_{13} was large enough to be measured by the current generation of experiments. Indeed, in 2012 the reactor experiments made the first measurements on θ_{13} (see from Section 2.3.3).

In 2013 MINOS published an analysis that was a first search for $\bar{\nu}_\mu \to \bar{\nu}_e$ oscillations; and they extracted parameters using both the ν_μ and $\bar{\nu}_\mu$ beam mode data [43]. The LEM method was used again to define 3 parameters that were put into a neural network along with the reconstructed neutrino energy. By assuming $\delta_{cp} = 0$, $\theta_{23} < \frac{\pi}{4}$ and a mass hierarchy, they defined the new limits: $0.01 < 2\sin^2(2\theta_{13})\sin^2(\theta_{23}) < 0.12$ at 90% C.L. for normal hierarchy; and $0.03 < 2\sin^2(2\theta_{13})\sin^2(\theta_{23}) < 0.18$ at 90% C.L. for inverted hierarchy. Additionally, by setting $\sin^2(2\theta_{13}) = 0.098 \pm 0.013$ from reactor data they have began to exclude some of the parameter space from δ_{cp}, θ_{23} octant, and the mass hierarchy, as seen in Figure 2.23.

2.4.3 T2K

The T2K (Tokai-to-Kamioka) experiment is the successor to K2K and sends a neutrino beam 295 km from the new MW-class proton synchrotron, J-PARC, at Tokai to Super-Kamiokande (SK) as the far detector (FD) [35, 37, 39, 128–131]. Data collection began in January 2010.

T2K made use of an off-axis method, in which the neutrino beam was intentionally directed 2.5° away from the FD. This created a muon neutrino beam with a narrow-band in energy and a peak energy at ~0.6 GeV, which maximised oscillations for ν_μ-disappearance at 295 km,

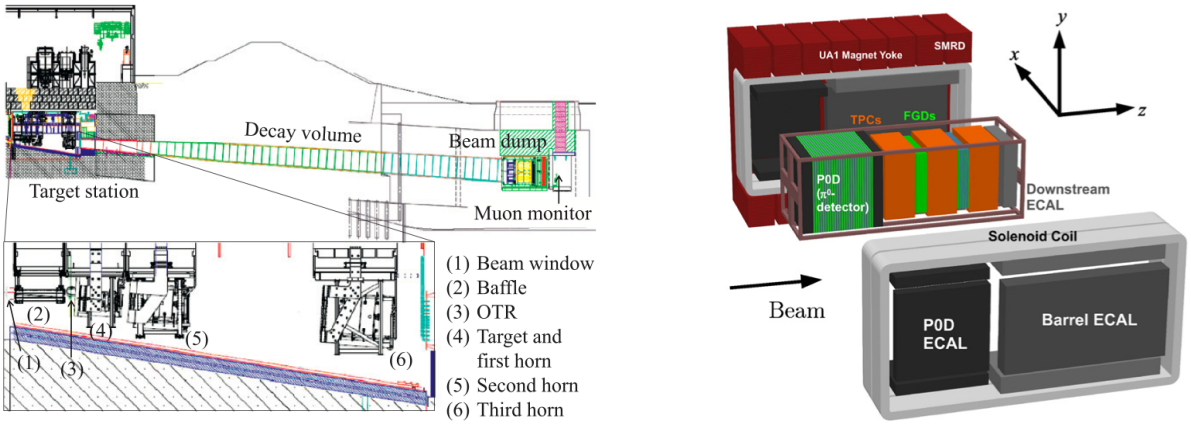

Figure 2.24: T2K beamline on the left and near detector on the right [129]. The neutrino beam is made by colliding 8 bunches of 30 GeV protons into a graphite target. The production target and downstream is shown in the left figure. A blown-out view of the ND280 near detector is shown on the right.

and minimised backgrounds from higher energy neutrino interactions. The beam profile was constantly monitored and the beam steering was within ± 1 mrad. The main physics goals of the experiment was to make precision measurements of the atmospheric oscillation parameters and to achieve a 20 times better sensitivity to θ_{13} compared to the CHOOZ limit [129].

At J-PARC, eight bunches of 30 GeV protons were extracted from the main ring per spill and guided by super-conducting magnets to the 90 cm long graphite production target. Three pulsed 250 kA magnetic horns sign selected the outgoing charged pions and kaons and focussed them in the beam direction. These decayed in flight into neutrinos in the 96 m long decay volume. This was followed by a beam dump and muon monitors. The setup can be seen in Figure 2.24.

The near detector complex (ND280) was located 280 m down-stream from the production target. It consisted of two detectors. The Interactive Neutrino GRID (INGRID) was on-axis and monitored the beam direction, intensity and profile. It was made up of 14 7-ton identical modules arranged into a vertical column and a horizontal row centred on the beam - forming a "+" sign - and two additional modules off-axis. The detectors were constructed with 9 iron plates and 11 tracking scintillator planes sandwiched together. Each tracking plane had 24 horizontal and 24 vertical scintillator bars.

The other near detector was off-axis and was designed to study neutrino interactions and to calculate beam properties at the FD. The configuration can be seen in Figure 2.24. It consisted of a π^0 detector (P0D), 3 large volume time projection chambers (TPCs), 2 fine-grained tracking detectors (FGDs), and all surrounded by electromagnetic calorimeters (ECAL). The detector was encased in the 0.2 T refurbished UA1 magnet, which was also fitted with a side muon range detector (SMRD).

The main backgrounds to the $\nu_\mu \rightarrow \nu_e$ search were intrinsic ν_e contamination in the beam as well as an NC π^0 interaction that could be misidentified as a signal event. Misidentified π^0 events were suppressed by forcing the reconstruction of two rings with the expected light pattern assuming two electromagnetic showers, and cutting on the invariant mass $M_{\text{inv}} < 105\,\text{MeV/c}^2$. The detector uncertainties came mainly from tracking and PID efficiencies, while the main physics systematic errors were related to the interaction modelling. Neutrino interaction simulations used

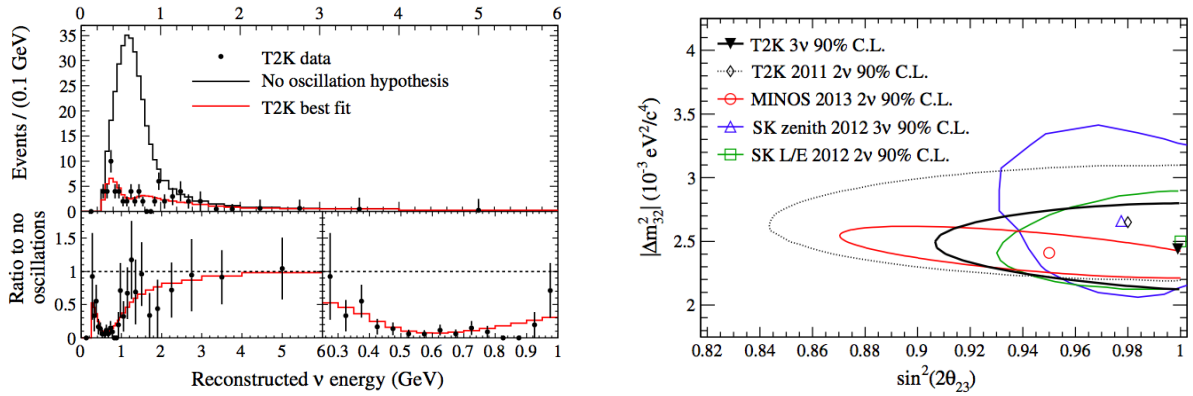

Figure 2.25: T2K ν_μ disappearance energy spectrum on the left and allowed parameter regions on the right compared with other recent results on the right [35]. The bottom panels on the left show the ratio of data and best-fit to the no-oscillation prediction for two energy ranges, 0-6 GeV and 0.3-1.0 GeV. The right plot shows the 90% C.L. allowed regions. The black contour is for the recent T2K result, while the green contour shows one of the analyses in this thesis.

the NEUT event generator, maintained at SK. These predictions were compared with other event generators, such as GENIE and NuWro, as well as against experimental data from SciBooNE, MiniBooNE and K2K.

For the analyses at T2K, comparison of the number of candidate events with the expected number of events without any oscillations was important. A sample of inclusive ν_μ CC-interactions at the ND were compared with the MC prediction at the ND to get a normalisation factor. This factor was applied to the MC at the FD, allowing partial cancellation of the cross-section modelling and flux uncertainties.

In June 2011, T2K reported an indication of $\nu_\mu \rightarrow \nu_e$ appearance with 2.5σ significance, and the first indication for non-zero θ_{13} [39]. From about 11 months beam time (Run 1 and 2), 6 candidate ν_e events were observed with an expectation of $1.5 \pm 0.3(5.5 \pm 1.0)$ events for $\sin^2 2\theta_{13} = 0(0.1)$. The 90% confidence interval observed for $\delta_{cp} = 0$ and $\sin^2 2\theta_{23} = 1.0$ was $0.03(0.04) < \sin^2 2\theta_{13} < 0.28(0.34)$ for normal (inverted) neutrino mass hierarchy. The best fit values were 0.11 (0.14).

In January 2012, T2K submitted the first results for ν_μ disappearance using the off-axis technique [130]. Two analysis methods were used on the data from Run 1 and 2. One compared the number of observed events in bins of reconstructed energy to the expectation using a binned likelihood-ratio method. The other was a maximum likelihood method with a "normalisation" term for the observed events, and a "shape" term for the unbinned likelihood for the reconstructed neutrino energy spectrum. The two analyses were in agreement and the measured parameter allowed regions for two flavour $\nu_\mu \rightarrow \nu_\tau$ oscillations were consistent with those reported by previous experiments.

In 2013, T2K updated their data and analysis to show the first evidence for ν_e appearance in a ν_μ beam, with 3.1σ significance [131]. The data was from Run 1, 2 and 3 and included 11 candidate events over an expectation of 3.3 ± 0.4 background events. Run 3 was taken after T2K and J-Parc recovered from the 2011 Tohoku earthquake, and approximately doubled the size of the overall data set. Over the same data period, a precision oscillation parameter measurement

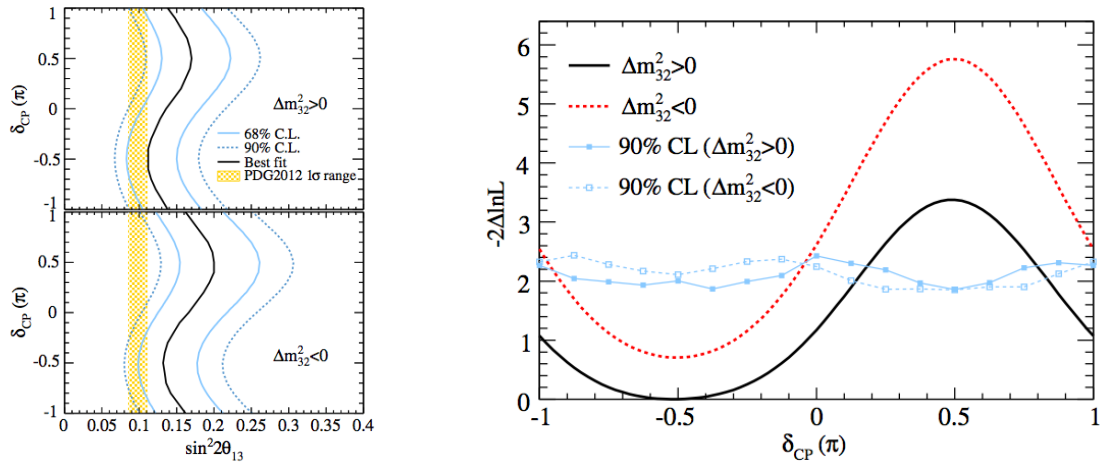

Figure 2.26: T2K allowed regions for $\sin^2 2\theta_{13}$ for varying δ_{cp} on the left and a scan of δ_{cp} on the right [37]. In the left figure, the top panel is for normal hierarchy and the bottom for inverted. The black solid line gives the best fit and the orange hatched band displays the average θ_{13} value from the PDG, 2012. The right figure shows the likelihood for δ_{cp} marginalised over $\sin^2 2\theta_{13}$, $\sin^2 \theta_{23}$, and Δm^2_{32}, while θ_{13} was further constrained by recent results. Solid black is for normal hierarchy and dotted red for inverted. The values above the cyan lines are disfavoured at the 90% C.L.

was made in a ν_μ disappearance analysis [35]. 58 events were observed with 205±17(syst.) events expected in a no-oscillation hypothesis. The survival probability used in the analysis included the effects from θ_{13}, and maximal mixing was observed, $\theta_{23} \approx \frac{\pi}{4}$. The allowed regions can be seen in Figure 2.25, where a comparison with the SK L/E analysis is shown and will be described in this thesis.

At the end of 2013, T2K reported the first observation of electron neutrino appearance in a muon neutrino beam with a significance of 7.2σ over the $\sin^2 2\theta_{13} = 0$ hypothesis [37]. For further background reduction, a new maximum-likelihood method using time and charge probability density functions for every PMT hit was used. The ratio of the background π^0 likelihood to the signal ν_e likelihood and the reconstructed π^0 mass were used to form a 2D cut. This removed 69% more of the π^0 background compared to the previous selection, with only a 2% loss in signal efficiency. In the fit the unmeasured oscillation parameters were fixed, including δ_{cp} and the mass hierarchy. The best-fit value measured was $\sin^2 2\theta_{13} = 0.140^{+0.038}_{-0.032}(0.170^{+0.045}_{-0.037})$ for $\delta_{cp} = 0$ and normal (inverted) neutrino mass hierarchy. The allowed region of $\sin^2 2\theta_{13}$ as a function of δ_{cp} for both mass hierarchy hypotheses can be seen in Figure 2.26.

By using the precisely measured value of θ_{13} from reactor experiments, T2K also began to explore CP violation, which can also be seen in Figure 2.26. The combined reactor and T2K measurements favour $\delta_{cp} = -\frac{\pi}{2}$. The 90% exclusion limits were determined by the Feldman-Cousins method.

2.4.4 MiniBooNE

There has been some evidence for anomalies in short-baseline experiments with oscillations occurring at $L/E_\nu \sim 1\,\mathrm{m/MeV}$. These controversial results began with the evidence for $\bar{\nu}_\mu \to \bar{\nu}_e$

oscillations at the $\Delta m^2 \sim 1\,\mathrm{eV}^2$ at the Liquid Scintillator Neutrino Detector (LSND) experiment, with 3.8σ significance [132]. A compatible effect was seen in a re-analysis of reactor anti-neutrino data with baselines $< 100\,\mathrm{m}$, where an average ratio of 0.943 ± 0.023 for the observed to expected rates was found – the reactor anti-neutrino anomaly [133]. There was further evidence from radioactive source experiments at GALLEX and SAGE, where they observed a deficit of electron neutrinos from radioactive sources inserted into the detectors – the gallium anomaly [134]. These anomalies were often interpreted as oscillations at $\Delta m^2_{\mathrm{new}} > 1.5\,\mathrm{eV}^2$ to a fourth sterile neutrino, ν_{new}, beyond the standard model.

MiniBooNE is a short baseline experiment designed to either confirm or refute the result seen at LSND. The neutrinos were produced at the Fermilab Booster neutrino beam, from 8 GeV protons colliding on to a 71 cm long Beryllium target. The produced particles were focussed with a 174 kA horn, passed through a 60 cm diameter collimater and decayed in a 50 m long air-filled tunnel.

The detector was 541 m from the target, and was a spherical tank with a radius of 610 cm filled with 800 tons of pure mineral oil. This allowed for both the production of directional Cherenkov light and isotropic scintillation light. The tank was optically separated into a 575 cm radius inner volume with 1280 PMTs, and a 35 cm radius outer volume acting as a veto with 240 PMTs.

The ν_μ spectrum peaked at ~600 MeV (~400 MeV for $\bar{\nu}_\mu$) and spanned out to 3000 MeV. CC ν_μ and ν_e events were distinguished by their distinct patterns in Cherenkov and scintillation light. In addition a decay electron was seen from the muon 80% of the time. The main backgrounds were a single electromagnetic shower from ν_μ induced NC π^0 events; single photons from radioactive Δ decays; and photons from ν interactions outside the detector penetrating the veto.

In 2007, MiniBooNE released its initial results and found no significant excess above the background [135]. The data could exclude two-neutrino appearance-only oscillations as an explanation of the anomaly seen at LSND. However, they did observe a little excess below 475 MeV that could not be explained by a two-flavour neutrino model. Later on, a 3.0σ excess of these low-energy electron neutrino events was reported.

In 2010, MiniBooNE searched for $\bar{\nu}_\mu \to \bar{\nu}_e$, which was the same mode as LSND, and observed an excess of $\bar{\nu}_e$ events above 475 MeV [136]. There was only a 0.5% probability that the data could be explained by the backgrounds. Their results were consistent with $\bar{\nu}_\mu \to \bar{\nu}_e$ oscillations in the 0.1 to $1\,\mathrm{eV}^2$ Δm^2 range, and consistent with LSND.

In 2013, MiniBooNE reported on an improved $\bar{\nu}_\mu \to \bar{\nu}_e$ search, and an updated $\nu_\mu \to \nu_e$ result [137]. They improved their understanding of the possible backgrounds, with in situ measurements at both MiniBooNE and SciBooNE (SciBar detector upstream). In anti-neutrino mode, an excess of 78.4 ± 28.5 events, 2.8σ, was observed. The allowed region had some overlap with the LSND result. The data was consistent with $\bar{\nu}_\mu \to \bar{\nu}_e$ oscillations in the 0.01 to 1 eV^2 Δm^2 range. The updated result in neutrino mode also found an excess of 162 ± 47.8 events, 3.8σ, at low energies. Although the energy distribution was not compatible with a simple 2 neutrino model and the resulting allowed region was marginally compatible with LSND. The allowed regions are shown in Figure 2.27.

These inconsistencies could perhaps be explained by some unknown systematic uncertainties or backgrounds, or possibly by models with several sterile neutrinos and allowing CP violating effects. In any case, MiniBooNE has measured some anomalies from the 3ν oscillations seen in other experiments, and these require explanation.

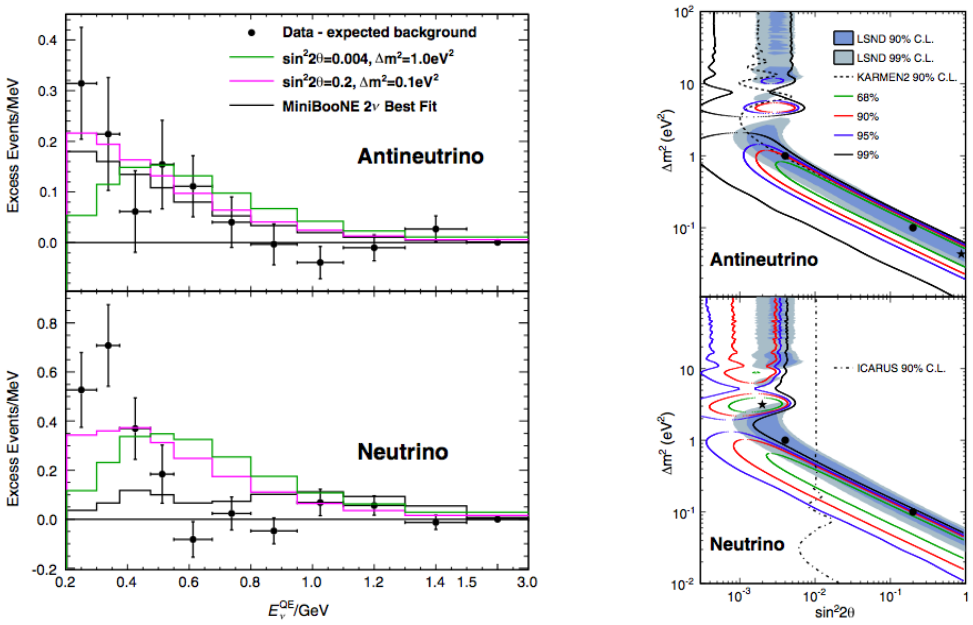

Figure 2.27: MiniBooNE 2013 distributions on the left and the allowed regions on the right [137]. The top panels show anti-neutrino mode and the bottom panels for neutrino mode. The 2ν best-fits are shown in the black histograms on the left figure and by star points on the right. The shaded regions in the right figure show the LSND allowed regions.

2.4.5 OPERA

The OPERA experiment sends neutrinos from the CNGS ν_μ beam at CERN to the LNGS underground laboratory, 730 km away in Gran Sasso, Italy [138–141]. The main goal of the OPERA experiment was to observe an appearance signal from neutrino oscillations and to prove unambiguously that $\nu_\mu \to \nu_\tau$ oscillation is the dominant atmospheric transition channel. The CNGS was a high energy beam optimised for ν_μ CC interactions, producing neutrinos with an average energy of ~17 GeV. The $\bar{\nu}_\mu$ contamination was 2.1%, and ν_e and $\bar{\nu}_e$ less than 1%. OPERA had their first interactions in 2006, and took their main data from 2008 until the end of 2012.

The OPERA detector was an interesting hybrid of detection technologies, allowing it to achieve sub-micrometric resolution. Firstly there was a veto, which was followed by two identical super modules (SM) each containing 625 tons of 75 000 emulsion/lead ECC (emulsion cloud chamber) modules, or "bricks." The SM also consisted of a scintillator target tracker detector (TT) to trigger the read-out and locate interactions in the bricks, and a muon spectrometer. Each brick had 56 1 mm thick lead plates sandwiched with 57 emulsion films.

A dedicated pair of emulsion films, Changeable Sheets (CS), was glued to the downstream face of each brick. The CS and TT were used together by an automated system to locate the hit bricks and extract them. The bricks were exposed to X-Rays and high energy cosmic rays for alignment, before being developed. These bricks were then scanned by automatic scanning microscopes at laboratories at LNGS, Europe and Japan. The scan resulted in a 3D reconstruction of the neutrino interaction, as well as micrometric resolution of possible secondary short-lived decay particles. The bricks and how they relate to the CS and TT can be seen in Figure 2.28.

The τ signal was identified by its characteristic topologies with either one prong (electron,

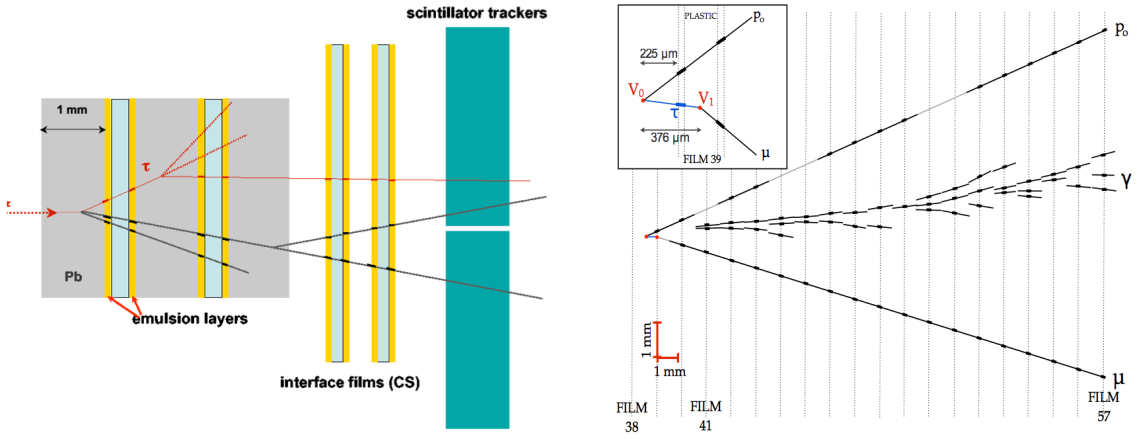

Figure 2.28: Schematic of the OPERA detector elements on the left and the 3rd ν_τ candidate on the right. How the emulsion/lead ECC bricks, CS and TT reconstruct an example ν_τ event is shown in the left figure [138]. The right figure shows the topology of the event reported in the 2014 analysis [141]. The inset is a zoomed in view of the primary and decay vertex. The τ decayed in the plastic, where there was a kink for the outgoing muon. p_0 was a hadron, and the EM shower from the γ can be seen from film 41.

muon or hadron) or three prongs. A software algorithm selected bricks with a high probability of containing the interaction vertex. Contamination from events outside the brick was estimated to be 4.5%. The CS of an extracted brick was developed and used to help reconstruct tracks within the brick. The efficiency of the brick finding procedure was estimated to be 77% for 1-2 brick events and 83% for up to 4 brick events. One characteristic feature of the signal was a kink in the decay topology.

In 2010, OPERA reported on their first ν_τ candidate event [139]. The event was muon-less, and survived after a stringent selection procedure. Each of the tracks were carefully identified to build up the topology. Possible backgrounds were $c - \bar{c}$ pair production with one charm particle not being identified; a primary hadron from an unidentified ν_μ CC-interaction; or ν_μ NC-interaction with no nuclear fragment associated with the secondary interaction. OPERA carried out extensive background studies to understand the probability of the background to the proposed channel, $h^-(\pi^0)\nu_\tau$, fluctuating to one event. The event was found to have 2.36σ significance of not being a background event. When all decay modes were considered, the significance bacame 2.01σ. The expected number of ν_tau events in the 2010 data sample was 0.54 ± 0.13(syst.), and OPERA claimed the observation of their first ν_τ CC interaction.

In 2014, OPERA reported evidence for $\nu_\mu \rightarrow \nu_\tau$ oscillations at the 3.4σ level after observing their 3rd ν_τ candidate in 5 years of data [141]. This included two ν_τ candidate events in the hadronic decay channels (one prong in 2009, three-prong in 2011), and a new candidate in the muonic decay channel. The topology of the new event can be seen in Figure 2.28. The main background for the new candidate was large-angle muon scattering in lead (80%), and charmed particle decays (20%). Although, the event was in a region of the parameter space free from background, considering the τ decay in the low-density low-Z plastic and the 690 MeV/c traverse momentum. As before, OPERA measured the probability for each of the backgrounds, and had an expectation of 1.7 ν_τ events in the analysed data. The absence of a $\nu_\mu \rightarrow \nu_\tau$ oscillation signal was excluded at 3.4σ.

One of the analyses at OPERA was a measurement of the velocity of neutrinos. It became global news in 2011 when they reported neutrinos arriving 60.7 ns earlier than light would have taken to travel the same 730 km. The result had a reported significance of 6σ, and the announcement had followed 6 months of rigorous cross-checking, so it had to be considered seriously. However, in the following year, two substantial systematic effects were discovered. One was a faulty connection in the fibre optic cable between the GPS receiver and the OPERA master clock resulting in a 73 ns earlier arrival time; and the other was a clock on an electronic board ticking faster than the specified 10 MHz, reducing the anomalous result. OPERA has since modified the systematic uncertainties in their paper to be consistent with the speed of light [140].

2.4.6 Accelerator Neutrino Summary

Accelerator neutrino experiments provided a controlled man-made source of neutrinos to closely study the natural phenomena seen in other experiments. The early short-baseline experiments ($\sim$100 m) did not observe any indication for oscillations. In 1999, K2K was the first long-baseline experiment with a 295 km baseline and produced 1.3 GeV neutrinos allowing it to probe the atmospheric oscillations observed. In 2003 they reported on an indication for ν_μ disappearance, which reached 4σ significance by 2005.

MINOS followed from 2005, with a 735 km baseline, and began the search for the remaining oscillation parameters: θ_{13}, δ_{cp}, and the mass hierarchy. In 2010, they slightly improved the constraint on θ_{13} from the CHOOZ limit with their $\nu_\mu \to \nu_e$ search. In 2011, their measured parameter allowed region for anti-neutrinos differed from the region for neutrinos. This result was part of the motivation for this thesis. However, later anti-neutrino results were consistent with the neutrino measurements. T2K was the successor to K2K and had an off-axis beam to narrow the band in energy of the neutrinos reaching the far detector. In June 2011 they reported on the first $\nu_\mu \to \nu_e$ appearance and non-zero θ_{13} indication with 2.5σ significance, with the observation of 6 candidate events over a 1.5 ± 0.3 expectation for $\theta_{13} = 0$. By 2013, T2K measured a non-zero θ_{13} at the 7.2σ level. Both MINOS and T2K have been working to confine the parameter space for θ_{13} and δ_{cp}, and to determine the mass-hierarchy and the octant of the θ_{23} parameter.

There has been an anomalous result in accelerator experiments since 2001 when LSND observed $\bar{\nu}_\mu \to \bar{\nu}_e$ oscillations at $\Delta m^2 \sim 1\,\text{eV}^2$, with 3.8σ significance. The results from MiniBooNE in 2013 were consistent with LSND. These anomalies have to be explained in some way, perhaps by the existence of sterile neutrinos. In 2010 OPERA observed the first $\nu_\mu \to \nu_\tau$ appearance candidate event. By 2014 they had reported on 3 candidate events and evidence for $\nu_\mu \to \nu_\tau$ appearance at the 3.4σ level. OPERA also infamously reported on a 6σ result for faster-than-light neutrinos when they measured neutrinos arriving at the detector 60.7 ns earlier than light would take to travel the same path. This turned out to be a due to a systematic error with a faulty connection of a fibre optic cable.

2.5 Future Neutrino Experiments

Recent experiments have done well to establish a non-zero θ_{13}, providing allowed regions for all the mixing angles and mass square differences in a 3 neutrino framework. With θ_{13} being reasonably large, current experiments can begin to probe for CP violation in the lepton sector; to attempt to determine the nature of the neutrino mass hierarchy; and to resolve the octant of θ_{23}.

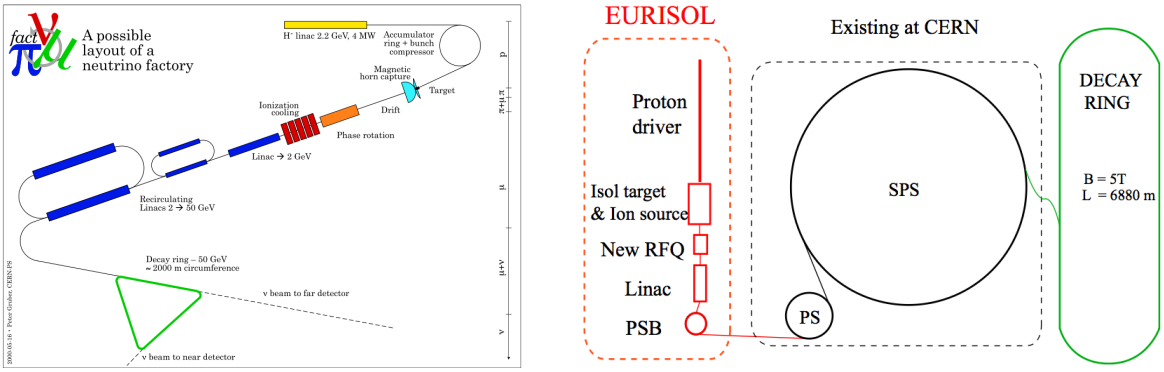

Figure 2.29: Possible Neutrino Factory layout on the left and Beta-Beam Facility Layout on the right [143]. There are many challenges accelerating muons, the left figure shows some of the elements such as phase rotation, ionisation cooling and several stages of acceleration. Shown here is a triangular storage ring with straight sections pointing to detectors. On the right is a potential beta beam set-up using existing facilities at CERN, the beta-beam storage ring pointing to detectors would need to be built.

Many physicists believe that the small masses in neutrinos are related to physics at the extremely high energy-scale, such as in the See-saw Mechanism, that cannot be probed directly. There are also theories, such as Leptogenesis, that suggest CP violation in neutrinos could partially explain why we live in a universe composed of matter, rather than equal quantities of matter and anti-matter. In addition, large scale water cherenkov detectors can also search for nucleon decay which is an important measurement for Grand Unified Theories. There is considerable interest in the further understanding of the properties of neutrinos.

Perhaps the current generation of experiments will be adequate to make these measurements. However, the next generation of experiments are being designed and proposed to make precise and accurate measurements of these evasive parameters, as well as to probe a variety of new physics. Some of these projects are highlighted here.

2.5.1 Neutrino Factory and Beta Beams

The Neutrino Factory and Beta-Beam experiments both propose new ways of creating neutrino beams. The Neutrino Factory could produce a high-intensity high-energy neutrino beam by accelerating muons and allowing them to decay in a storage ring with long straight sections pointing in a desired direction [142]. This differs from the conventional accelerator neutrino experiments that produce their main flux from the decay of charged mesons. A potential Neutrino Factory layout can be seen in Figure 2.29.

Neutrino beams from meson decay have a few limitations. The finite precision that the beam fluxes can be predicted are a significant source of systematic uncertainties; and the wrong-flavour contamination from kaon decays are a nuisance. They are also primarily ν_μ beams making $\nu_e \rightarrow \nu_\tau$ oscillation searches difficult. In addition, high energy beams will also have some ν_τ contamination, which could be a problem for $\nu_\mu \rightarrow \nu_\tau$ oscillation searches.

The advantage of a beam from muon decays is that the absolute flux can easily and precisely be calculated. It also has precisely known composition. Stored μ^- will produce 50% muon neutrinos and 50% electron anti-neutrinos. Only one type of neutrino and one type of anti-

neutrino. For μ^+ decay, the flavours are reversed. So precise measurements can be made from ν_μ, ν_e, $\bar{\nu}_\mu$, and $\bar{\nu}_e$ by selecting the muon charge and monitoring its properties in the accelerator.

There have been discussions of the potential of measuring $\nu_e(\bar{\nu}_e) \rightarrow \nu_\mu(\bar{\nu}_\mu)$ oscillations, known as the golden channel for making precision measurements [144]. Since there is only one type of neutrino and anti-neutrino in the beam composition, the signal would come from a "wrong-sign" muon in a detector with good muon charge identification power. The international design study for the neutrino factory can be seen in Reference [145].

Beta-Beams could be made by accelerating radioactive ions to high energies, and allowing them to decay in storage rings with long straight sections pointing to a detector [146]. For example, this could be achieved by producing ^{6}He ions, which β-decay:

$$^6_2\mathrm{He}^{2+} \longrightarrow {}^6_3\mathrm{Li}^{3+} + e^- + \bar{\nu}_e \tag{2.50}$$

producing a Lorentz boosted collimated $\bar{\nu}_e$ beam of a single flavour, and with a well-known energy spectrum and intensity.

It has already been demonstrated at CERN ISOLDE that it is possible to produce $\approx 10^8$ ^{6}He ions per second, and this method could be used for producing a high intensity neutrino beam. The construction of a storage ring would be similar to the effort involved in building one for a muon-decay Neutrino Factory. Although, shielding on some accelerator components would be needed to protect them from the decay electrons and lithium ions. With technologies that already exist, it could be possible to produce focussed low-energy beams of ν_e or $\bar{\nu}_e$ for precision neutrino physics. A possible Beta-Beam set-up can be seen in Figure 2.29.

2.5.2 Megaton Detectors: Hyper-Kamiokande, DUSEL, and LAGUNA

Hyper-Kamiokande (HK) will be a next-generation water Cherenkov underground detector at the megaton scale with a design based on the proven technology from Super-Kamiokande (SK) [147]. It will have sensitivity far beyond that of SK over a range of physics searches – proton decay, atmospheric neutrinos and astronomical neutrinos. It will be located 8 km south of SK, and also 295 km from Tokai and will act as the far detector for T2HK.

The detector will have a 1,750 m.w.e. of rock overburden, and a total (fiducial) mass will be 20 (25) times larger than SK, at 0.99 (0.56) million metric tons. The design consists of 2 cylindrical tanks 250 m long, 48 m wide and 54 m high, as seen in Figure 2.30. The inner detector will have 20% photo-cathode coverage with 99,000 20-inch PMTs, and the outer detector will have 25,000 8-inch PMTs.

HK would have a rich neutrino physics program. The detector would have unprecedented sensitivity to oscillation parameters. Used with the upgraded J-PARC beamline, T2HK would be able to obtain 3σ significance for 74% of the δ_{cp} parameter space. HK by itself should have the sensitivity to determine the mass hierarchy at 3σ for 46% of the domain of δ_{cp}. If $\sin^2 2\theta_{23} < 0.99$, the octant of θ_{23} could be determined. HK will extend its sensitivity to nucleon decay, for example for the partial lifetime of the decay mode $p \rightarrow e^+\pi^0$ to 1.3×10^{35} years. HK can also make contributions for many other topics, such as supernova neutrinos, supernova relic neutrinos, and search for dark matter WIMPs.

DUSEL (Deep Underground Science and Engineering Laboratory) is a new underground laboratory the US is planning to build with 6,200 m.w.e. of rock overburden at the Homestake Mine at Lead, South Dakota [149]. Several designs for neutrino detectors are being considered. A megaton scale, modular, multi-purpose water Cherenkov detector is one possibility [149]. The

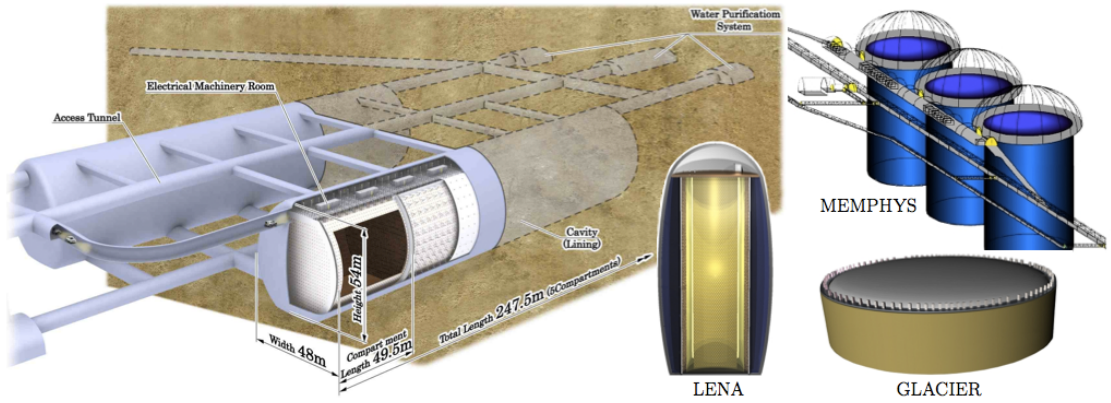

Figure 2.30: Graphic of the Hyper-Kamiokande detector design on the left [147], and the various designs for the LAGUNA detectors towards the right [148]. HK has two horizontal cylindrical tanks at ∼1 MT. LENA is scintillator detector at 50 kT; MEMPHYS has modular water cherenkov shafts at ∼600 kT for three; and GLACIER is a liquid argon TPC Cherenkov detector at ∼100 kT per vessel.

design is an array of 10 individual cylindrical 100 kT water cherenkov detectors with a total mass of 1,000 kT and 800 kT fiducial mass, and a photocathode coverage of 14%. Each module would be 50 m in diameter and 50 m high. The physics topics DUSEL could study would be similar to HK, with similar sensitivities. In addition, the modular design could allow some of the detectors to be filled with a different target material, giving sensitivity to a lower energy threshold than water can achieve. DUSEL are also considering liquid argon detectors for LBNE.

The LAGUNA, or Large Apparatus studying Grand Unification and Neutrino Astrophysics), is a project in Europe to build a detector of ∼50 kT to ∼650 kT for next-generation nucleon decay searches and neutrino physics [148]. Many sites around Europe are being considered for extending or building a new underground laboratory of an appropriate scale and distance from CERN. The project has three candidates for the detector design: GLACIER, LENA, and MEMPHYS. A graphic of the designs can be seen in Figure 2.30.

GLACIER (The Giant Liquid Argon Charge Imaging ExpeRiment) is an underground liquid argon TPC detector of around ∼100 kT [150]. This detector design is very interesting, as it can reconstruct high resolution tracks, produces scintillation light, and cherenkov rings. There are also some studies into magnetising the volume, to provide charge discrimination. LENA (Low Energy Neutrino Astronomy) is a liquid-scintillator detector of around 50 kT [151]. It would be particularly sensitive for supernova, solar, geo- and reactor neutrinos. It could search for dark matter, proton decay and potentially act as a far detector for LAGUNA-LBNO. MEMPHYS (MEgaton Mass PHYSics) is the European design for a water Cherenkov detector at half a megaton, with a modular design of three 215 kT cylindrical tanks [152]. The modular set-up would allow for 100% up-time for supernova neutrinos, and one module could potentially be Gadolinium loaded for improved supernova detection. The baseline design assumes 3 modules, with a total fiducial mass of 440 kT.

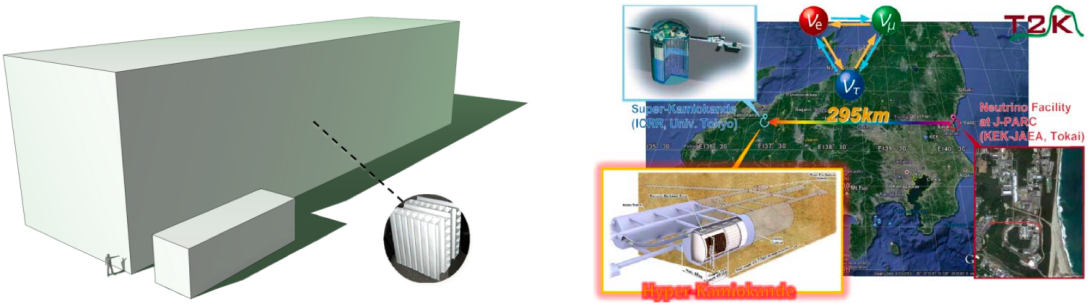

Figure 2.31: The scale of the NOνA detectors on the left and an overview of the T2HK baseline on the right. The NOνA detectors were made up of hundreds of layers of PVC cells filled with mineral oil and liquid scintillator. The T2HK baseline would run from an upgraded J-PARC in Tokai to the proposed Hyper-Kamiokande.

2.5.3 Off-Axis Super-beams: NOνA and T2HK

The NOνA, or NuMI Off-Axis ν_e Appearance, experiment aims to build a new detector that could achieve a factor of 10 times better sensitivity to the $\nu_\mu \to \nu_e$ channel than MINOS [153]. The recent results world-wide suggest that NOνA is in a good position to determine the ordering of neutrino masses and measure the first indications of CP violation in neutrinos [154]. NOνA began taking data with the first modules in 2013, and the construction will be finished in 2014.

The next-generation of accelerator experiments require more intense beams of neutrinos and more massive detectors. The NuMI beamline is being upgraded from 300 kW to 700 kW of beam power, to produce a 10 μs beam spill every 1.33 s with 4.9×10^{13} protons per pulse. The far detector will be a 14 kT, finely segmented 64% active tracking calorimeter. The detector is built up from PVC cells with (6×4) cm cross-section and extending the full 15.6 m height or width of the detector. The cells are filled with mineral oil and liquid scintillator. The scintillation light is transported by wave-length shifting fibres, to 32-channel avalanche photodiodes. The FD is made up of 928 layers of 384 cells. The ND is 329 tons, located at a 1 km baseline and is built with the same components. The ND has 4.1 m width and height, and 206 layers of 96 cells.

The NOνA detectors are being constructed 14 mrad off-axis, with the FD situated in a new laboratory in Northern Minnesota, 810 km away from Fermilab. The off-axis position provides a narrow energy-band at the oscillation maximum, peaked at 2 GeV, while also reducing backgrounds. The plan is to run for 6 years, with the time equally dispersed for neutrino mode and anti-neutrino mode. Within the first year NOνA expects to make a 5σ observation of θ_{13}-driven $\nu_\mu \to \nu_e$ oscillations [154]. The analysis tools have been updated and first results could be released at the end of 2014.

T2HK, or Tokai to Hyper-Kamiokande, is a natural extension of the T2K experiment. The proposition is to upgrade the J-PARC accelerator to 750 kW of beam power and to use the proposed Hyper-Kamiokande (HK) as the far detector [155]. The main goal of the experiment would be the discovery of CP asymmetry, where they expect to measure CP violation with more than 3σ significance over $\frac{3}{4}$ of the domain of δ_{CP}, if the systematic errors are suppressed to 5% and the mass hierarchy is known. The plan is to run for 10 years, 3 years in neutrino mode and 7 in anti-neutrino mode. The proposed construction schedule of HK would take 7 years from 2016, so the T2HK experiment would begin in 2023.

In summer 2013, the LINAC was upgraded from 181 MeV to provide 400 MeV beam energy.

For the 2014 summer shutdown, the peak current will be increased from 30 mA to 50 mA. These LINAC upgrades should bring the beam power up to 450 kW. There would be problems raising the beam energy from 30 GeV to 50 GeV, so they propose to double the repetition rate to obtain a 1.3 s cycle of 30 GeV beam energy and 2.0×10^{14} protons per pulse. With this upgrade scheme, it could be possible to reach 750 kW beam power in 2017 [155].

There are other next-generation projects that have been put forward LBNE, the Long Baseline Neutrino Experiment, to be constructed by 2022 and LAGUNA-LBNO, a Long Baseline Neutrino Oscillations experiment using one of the LAGUNA detectors.

2.6 Neutrino Experiments Summary

There are many sources of neutrinos, from the fusion reactions in the sun; the collision of cosmic rays in the atmosphere; nuclear fission in nuclear reactors; and created at accelerator beamlines; as well as other astronomical sources. The first solar neutrinos were detected in 1968 in the Homestake Chlorine Experiment where 30% of the flux expected by the Standard Solar Models was observed. This was the beginning of the *Solar Neutrino Problem.* These findings were confirmed between 1992 and 2003 by the gallium experiments, GALLEX, SAGE and GNO. From 1987 to 1995, Kamiokande used a water Cherenkov detector and measured solar neutrinos in real-time. They established the solar origin of the neutrinos, while also observing a deficit from the SSM.

Kamiokande, and a similar experiment IMB, also measured a deficit in the flavour ratio of muon to electron in atmospheric neutrinos. They observed about 60% of the muon-like events expected and this was the beginning of the *Atmospheric Anomaly.* These two anomalies were early indications that a theory such as Neutrino Oscillations would be needed to explain these results.

Super-Kamiokande (SK) was the successor to Kamiokande, had ∼25 times the target mass, and ran from 1996. The experiment helped constrain the oscillation parameter space for solar neutrinos, but there were many potential solutions around the year 2000. SK observed a clear zenith dependence in the measured atmospheric neutrinos in 1998, which was key evidence for Neutrino Oscillations. This result showed that the deficit in neutrinos observed was dependent on their flight-path. In 2004, SK disfavoured alternative explanations for the zenith dependence, with an L/E analysis. In 2001, SNO measured the electron flavour component of the solar neutrino flux with their CC reaction and determined that a proportion of the flux was of another flavour. In 2002, SNO reported on a NC measurement that revealed the total solar neutrino flux regardless of flavour, and this was consistent with the SSM! This was clear evidence that solar electron neutrinos were oscillating into muon and tau flavour. The SNO results also allowed global analyses of the solar neutrino parameters to reduce to the MSW Large-mixing Angle (LMA) solution. From 2008 to 2012, Borexino measured low energy solar neutrinos in real-time and was also in support of the MSW LMA solution. In the early 2000s, the atmospheric neutrino results from SK were confirmed by the tracking calorimeter experiments Soudan 2 and MACRO.

In 1999, the reactor experiment CHOOZ set a stringent limit on the remaining mixing angle to be determined, θ_{13}. In 2003, KamLAND was the first reactor experiment to measure disappearance of an $\bar{\nu}_e$ reactor flux. It had an average baseline of ∼180 km from many reactors in Japan and the deficit was driven by the solar neutrino parameters. This allowed their result to greatly confine the solar Δm^2_{21}. They also measured almost two cycles in their L/E analysis.

In 2011, three reactor experiments were all aiming for a measurement of θ_{13}: Double CHOOZ, Daya Bay and RENO. In January 2012, Double CHOOZ gave the first indication of a non-zero θ_{13}. Daya Bay was the first experiment to report on a non-zero θ_{13} in March 2012, with 5.2σ significance. Results shortly afterward from RENO and Double CHOOZ were consistent with the measured value.

Accelerator experiments provide a controlled test of observed phenomena with a precise and directed man-made neutrino source. K2K was the first long-baseline experiment at 250 km, and in 2003 confirmed the atmospheric parameter allowed regions. Similar support was reported by MINOS in 2006 and T2K in 2012. T2K published the first indication of $\nu_\mu \rightarrow \nu_e$ appearance in 2011, with 6 candidate events over an expectation of 1.5 ± 0.3. By the end of 2013, T2K improved the significance of this result to 7.2σ. Both T2K and MINOS have been restricting the parameter space for the remaining parameters, θ_{13} and δ_{cp}, while trying to determine the neutrino mass hierarchy and octant of θ_{23}. In 2013, results from MiniBooNE were in agreement with anomalous oscillations seen at LSND that suggested the existence of sterile neutrinos. While in 2010, OPERA observed their first ν_τ candidate for $\nu_\mu \rightarrow \nu_\tau$ appearance. By 2014 they had 3 candidates and observed appearance at the 3.4σ level.

The challenge for future experiments is to determine the neutrino mass hierarchy, δ_{cp}, and the octant of θ_{23}. A next-generation off-axis beam, NOνA has begun taking data in 2014. T2HK depends on Hyper-Kamiokande, a megaton water-cherenkov detector, so may not begin until 2023. The Neutrino Factory proposes to make a precise well-understood neutrino beam by muon decay in a storage ring. While Beta Beams suggest accelerating ions and letting them decay in a storage ring to create low energy electron neutrino beams. There are many other next-generation proposals, for the DUSEL underground lab in the US, LAGUNA in Europe, and Hyper-Kamiokande in Japan.

Chapter 3

Super-Kamiokande Detector

Super-Kamiokande is a 50 kton water Cherenkov detector located in Gifu Prefecture, Japan. [1] It was constructed in a zinc mine under the peak of Mt. Ikenoyama to reduce contamination from cosmic-ray backgrounds. The mean rock overburden is ∼1000 m (2700 m water equivalent) and acts as a shield, reducing the cosmic ray muon background by 5 orders of magnitude compared with that on the surface of the Earth. The detector is also segmented into a main *Inner Detector* region and a slimmer *Outer Detector* region, hereafter referred to as the ID and OD, respectively. The OD is a principle part of the detector design, allowing the remaining cosmic-ray backgrounds to be eliminated. The combination of the ID and OD allow Super-Kamiokande (SK) to determine which interaction vertices originate from within the detector, and which are due to particles and radiation entering from outside the detector. An illustration of the detector showing its cylindrical structure, and Inner and Outer detector regions, is given in Figure 3.1.

The main physics aims of SK are to search for the existence of nucleon decay and the research of neutrinos. The neutrinos reaching SK are from many sources: the core of the sun; produced by cosmic-rays in the atmosphere; created in accelerators and from astrophysical sources such as supernovae. *Solar neutrinos* have low energies in the order of a few MeV. While *atmospheric neutrinos* arrive at the SK site from the atmosphere surrounding the entire globe and have an energy range from a couple of MeV to multiple TeV. SK has been the *Far Detector* of the first neutrino beamline experiment KEK-to-Kamioka (K2K) [125], which produced *accelerator neutrinos* by the collision of accelerated protons on a target and focusing the interaction and decay products that include neutrinos. At the time of writing, SK is currently acting as the Far Detector of the neutrino beamline experiment Tokai-to-Kamioka (T2K) [128], the successor to K2K and offering a higher intensity and precise neutrino beam.

The Super-Kamiokande experiment started taking data in April 1996 and continued for five years of continuous observation until the detector maintenance in July 2001. This data taking period is referred to as SK-I. While refilling the water after the maintenance, an accident occurred in November 2001 in which more than a half of the PMTs were destroyed. The SK detector was rebuilt after the accident with half of the original PMT density in the ID and resumed observation from October 2002. Continuous data taking continued for three years until October 2005, which is referred to as the SK-II running period. There was a reconstruction effort to restore the ID PMT density back to the original design specification, and observation was restarted in June 2006. SK continued operation until September 2008, which is the SK-III running period. New upgraded

[1] The geographic coordinates of the site are 36°25'N and 137°18'E, and the altitude above sea level is 370 m

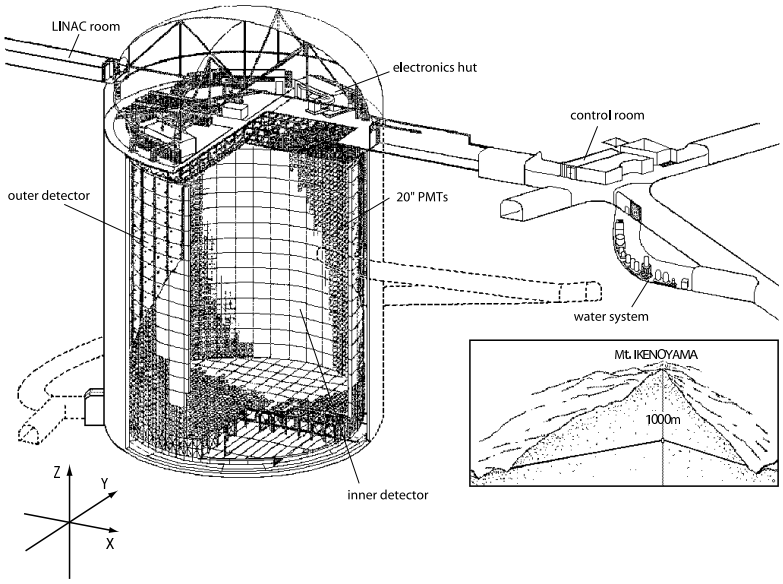

Figure 3.1: The Super-Kamiokande Detector [156] is located under Mt. Ikenoyama to reduce cosmic-ray backgrounds. These backgrounds are further reduced by segmenting the detector into the Inner Dector (ID) and Outer Detector (OD) regions.

electronics were installed, and data taking was resumed in September 2008. This is known as the SK-IV running period and is still continuing at the time of writing.

3.1 Cherenkov Radiation

Super-Kamiokande is able to make physical measurements primarily by observing Cherenkov radiation [157]. When relativistic charged particles have a velocity that exceeds the velocity of light in the medium, Cherenkov photons are emitted:

$$v \geq \frac{c}{n} \tag{3.1}$$

where v is the velocity of the charged particle, c is the velocity of light, and n is the index of refraction of the medium. So there is a velocity threshold before the particle begins to emit Chrenkov photons, which depends on the index of refraction of the medium. It is useful to consider the momentum threshold, which is also dependent on the mass of the particle. The refractive index of water is about 1.34, so the momentum thresholds of Cherenkov radiation for electrons, muons and charged pions are 0.57, 118 and 156 MeV/c, respectively. The proton is much more massive, and has a relatively large momentum threshold of about 1.07 GeV/c.

There is a characteristic angle from the trajectory of the particle to the emission direction of the Cherenkov photons. The half-cone opening angle, Cherenkov angle θ_c, can be calculated:

$$\cos\theta_c = \frac{1}{n\beta} \tag{3.2}$$

where $\beta = \frac{v}{c}$. For highly relativistic particles, with $\beta \approx 1$, the Cherenkov angle in water is about 42°.

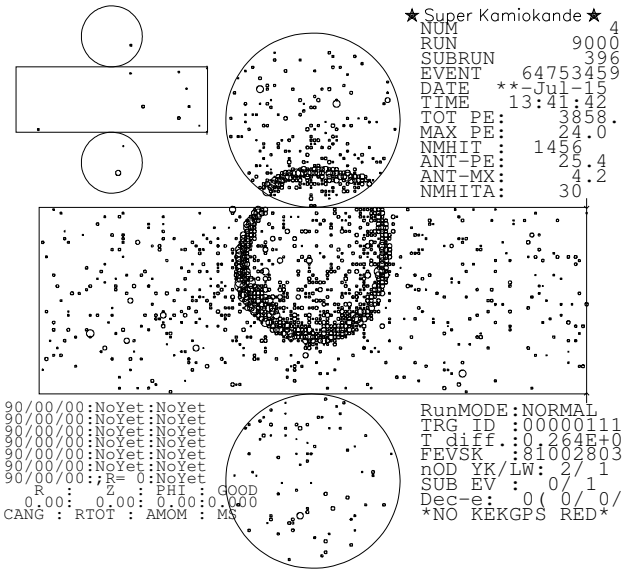

Figure 3.2: A typical neutrino event observed by Super-Kamiokande. The cylindrical structure has been unrolled, and the clear ring is due to a charged particle emitting Cherenkov photons until falling below threshold, resulting in the ring image as opposed to a filled circle.

The number of Cherenkov photons, N, emitted as a double derivative with respect to the wavelength, λ, and charged particle tragectory, x, is given by:

$$\frac{d^2N}{dxd\lambda} = \frac{2\pi\alpha}{\lambda^2}\left(1 - \frac{1}{(n\beta)^2}\right) \tag{3.3}$$

where α is the fine structure constant. The PMTs in SK are sensitive to photons in the wavelength range of around 300 nm to 600 nm, and the number of Cherenkov photons emitted in this range is about 340 photons/cm. The Cherenkov wavelength spectrum in water together with the PMT quantum efficiency is shown in Figure 3.3.

So in a typical event, a charged particle will emit Cherenkov photons at $\theta_c \approx 42^\circ$ while depositing energy in the detector, until its momentum drops below the Cherenkov threshold. The result of this is a ring of photons are projected on to the wall of the tank and detected by the PMTs. In this fashion, SK can detect various charged particles and reconstruct physical variables by the analysis of Cherenkov rings. A typical neutrino event is shown in Figure 3.2, where the ring is created by detecting the lepton product of the neutrino interaction.

3.2 Detector Details

3.2.1 Super-Kamiokande Tank

The Super-Kamiokande detector is 41.4 m high, 39.3 m in diameter and contains 50 kton of highly purified water. In between the inner and outer sensitive regions, there is a PMT support structure that holds the inward-facing PMTs of the ID and the outward-facing PMTs of the OD. The non-sensitive regions of the structure are covered with opaque sheets to optically separate the ID and the OD. The PMT structure is shown in Figure 3.4.

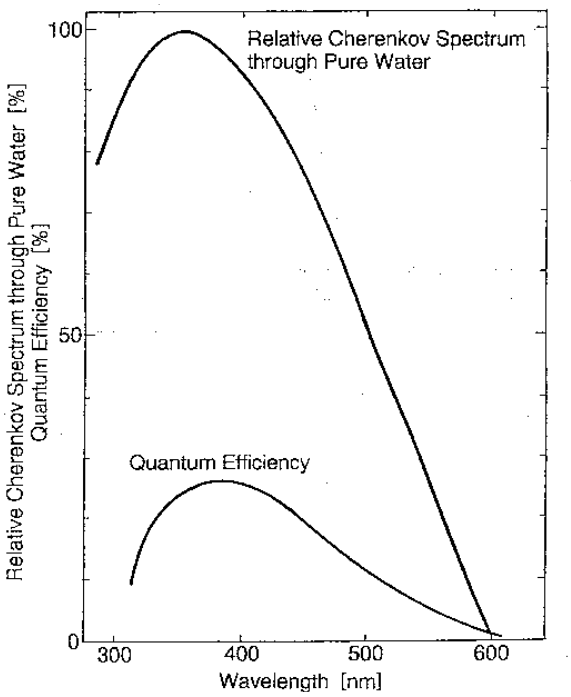

Figure 3.3: The relative Cherenkov spectrum in water as a function of wavelength is shown. The upper curve gives an idea of the wavelength region the Cherenkov photons are emitted in. The lower curve shows the percentage quantum efficiency (QE) of the PMTs. The QE peaks in the same region as the peak of the Cherenkov photon emission.

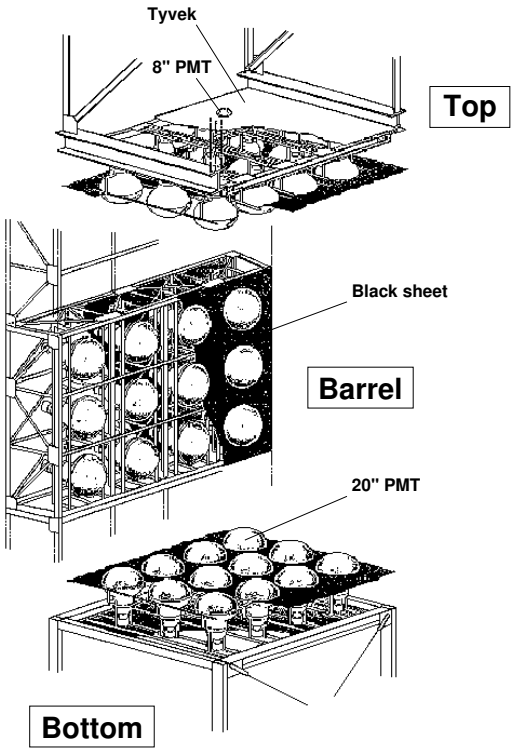

Figure 3.4: Technical drawing of the Super-Kamiokande PMT Support Structure [156]. A segment of each of the detector regions is shown. The inward facing 20" PMTs of the Inner Detector, and an outward facing 8" OD PMT can be seen. The black sheet covers the region between the PMTs in the ID to optically separate it from the OD. The intermediate space between the OD PMTs is covered with highly reflective Tyvek to increase light collection efficiency.

The Inner Detector (ID) is 36.2 m high, 33.8 m in diameter and contains 32 kton of water. It detects photons with 11,146 inward-facing 20-inch PMTs. With the full PMT density, the PMTs are spaced uniformly at intervals of 70 cm giving an effective photocathode coverage of about 40% in the ID. In the SK-II period, the remaining 5,182 20-inch PMTs after the accident were re-distributed such that they were uniformly spaced, with a reduced photocathode coverage of around 20%. To prevent light-leaks between the inner and outer sensitive regions, the space between the PMTs is covered with an opaque *black sheet*.

The Outer Detector (OD) is the outer sensitive region surrounding the ID and has a width of 2.2 m along the barrel wall, and is 2.05 m thick at the top and bottom. It acts as an effective veto to reduce background events in the data, or to tag outgoing charged particles. It detects photons with 1,885 8-inch PMTs outward-facing from the PMT support structure. The photocathode coverage is considerably less than that of the ID, so each OD PMT is attached to a 60 cm × 60 cm wavelength shifting plate to improve the light collection efficiency. This is further improved by covering the walls with a highly reflective (∼90%) *tyvek sheet*. The OD is also a 2 m thick wall of water that surrounds the ID and serves as a shield to attenuate gamma rays and neutrons from radioactivity in the rock.

For SK-III, the top and bottom regions of the OD were optically separated from the barrel regions by running the tyvek sheet directly upward and downward from the barrel region. This allowed Partially-Contained events, which exit the tank usually through either the top/bottom or barrel regions, to be distinguished from cosmic-ray muon *Clipper* events which activate both the top/bottom and barrel regions. This helped improve the reduction of the backgrounds, as discussed in Section 6.3.

There is also a 55 cm thick *dead region* between the ID and OD, which is where the PMT support structure is situated. This stainless steel structure also houses the signal and HV cables of all the PMTs and routes them out of the detector.

3.2.2 Photo-Multiplier Tubes (PMTs)

The ID photo-multiplier tubes (PMTs) are *Hamamatsu R3600* PMTs and have a diameter of 50 cm (20 inch). The 20-inch PMT was originally developed by Hamamatsu in cooperation with the Kamiokande collaboration [158]. For Super-Kamiokande, the dynode structure and bleeder circuit were improved to achieve better collection efficiency, energy resolution and timing response [159]. A technical drawing of the PMT is shown in Figure 3.5.

The photocathode of the PMT is coated with a layer of bialkali (Sb-K-Cs) due to its low thermionic emission and its high spectral sensitivity to the blue of Cherenkov light [159]. Figure 3.3 shows the close match of the quantum efficiency (QE) and Cherenkov emission spectra. The QE peaks at 22% at around 360–400 nm, which can be seen more clearly in Figure 3.6. The collection efficiency at the first dynode averages at 70%, and is uniform across the whole PMT surface within ±7%. The gain through the *venetian blind* dynode structure is 10^7 for the ID PMTs with a supply high voltage of 1500–2000 V. The single photoelectron signal can be clearly discerned, which is also shown in Figure 3.6. The transit time spread of the 1 p.e. signal is about 2.2 nsec and the average dark noise rate is around 3 kHz at the 0.25 p.e. threshold.

The geomagnetic field at the detector site is about 450 mG, while a magnetic field above 100 mG affects the photoelectron trajectories in the PMTs, reducing the timing resolution. To compensate for this, 26 sets of horizontal and vertical Helmholtz coils were set up around the perimeter of the tank reducing the magnetic field in the PMTs to around 50 mG.

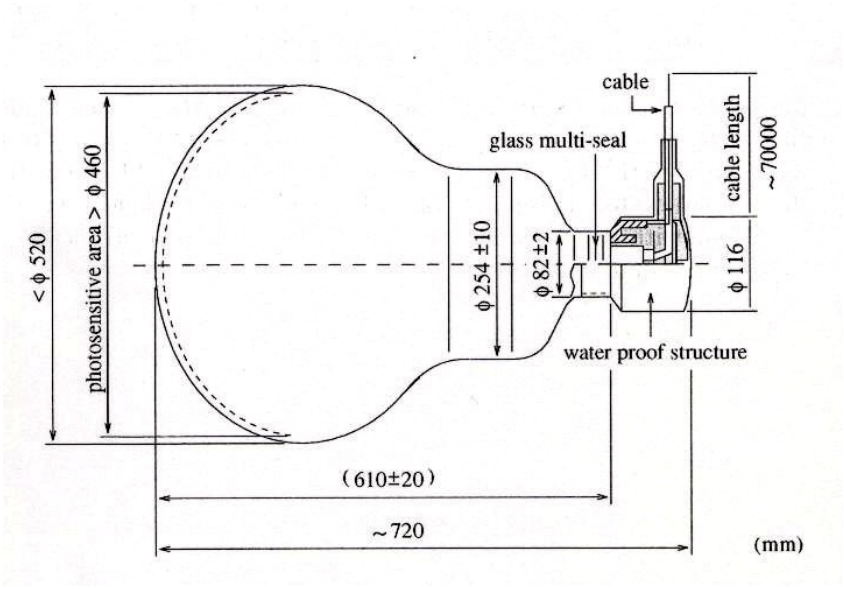

Figure 3.5: Technical drawing of the Inner Detector PMT [156].

After the accident in 2001 where one ID PMT at the bottom of the tank imploded, causing a chain reaction that destroyed around 60% of the ID and OD PMTs, an acrylic cover was designed for the PMTs. The acrylic is 12 mm thick and UV-transparent, while the side of the PMTs are protected with a fiberglass casing. There are also holes in the casing to allow water to flow inside. The PMT acrylic and fiberglass case is shown in Figure 3.7. The transparency of the acrylic can be seen in Figure 3.8, which is more than 94% above 330 nm for photons of normal incidence.

In the OD there are 1,885 8-inch PMTs, which are mostly *Hamamatsu R1408* PMTs and some are reused from the IMB experiment [160]. The effective photocathode coverage in the OD is increased by attaching a 60 cm × 60 cm × 1.3 cm wavelength shifter plate, that collects light that would not have reached the OD PMT directly otherwise. The light collection efficiency is increased by 60%. There is a slight decrease in the timing resolution from 13 nsec → 15 nsec for

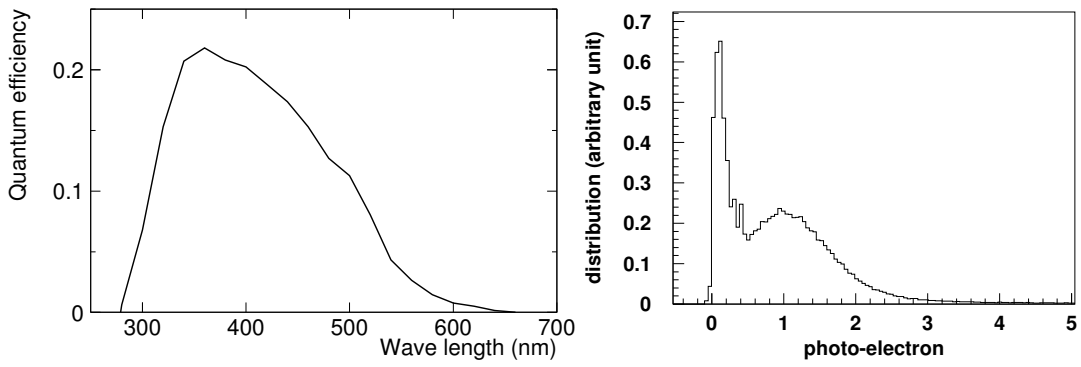

Figure 3.6: The ID PMT quantum efficiency [156], showing a peak of 22% at around 360–400 nm is shown on the left, and the single photoelectron distribution on the right, showing a clear signal at 1 p.e.

Figure 3.7: Cover of PMTs since SK-II

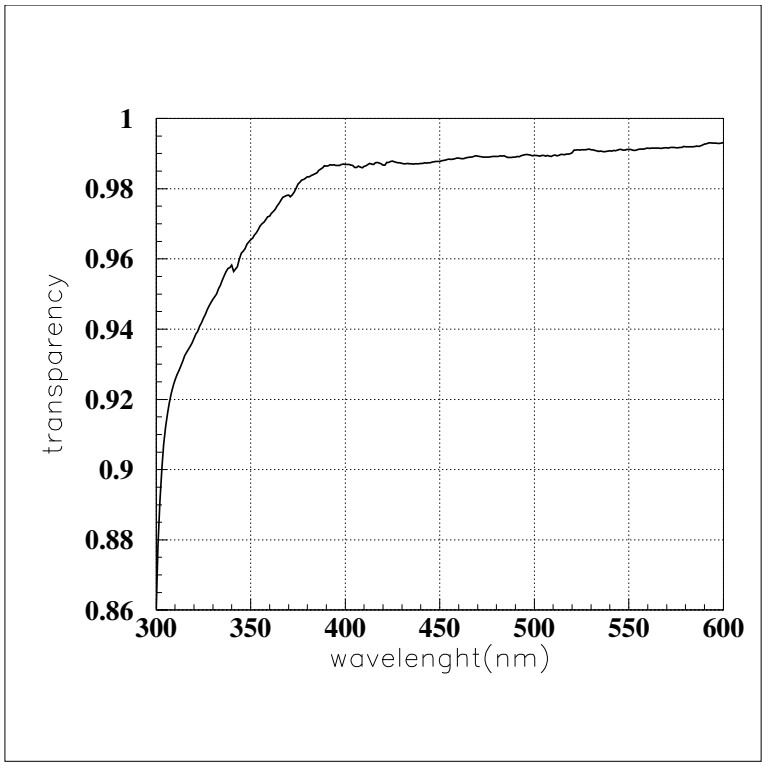

Figure 3.8: PMT cover transparency

Component	Purpose
1 μm Mesh Filter	Removes dust and small particles.
Heat Exchanger	Cools water to reduce PMT dark rate and suppress the growth of bacteria. Detector water is kept at 14 °C.
Cartridge Polisher	Removes over 99% of heavy ions (Na^+, Cl^-, Ca^{2+}).
Ultra-Violet Sterilizer	Kills bacteria.
Rn-Free Air Dissolving Tank	Dissolves Rn-free air into the water, improves efficiency at the vacuum degasifier stage.
Reverse Osmosis Filter	Removes Radium and minute particles of the order of 1 nm
Vacuum Degasifier	Removes dissolved gases in water, such as oxygen and radon.
Ultra Filter	Removes small particles of the order of 10 nm.
Membrane Degasifier	Removes radon dissolved in water.

Table 3.1: Water Purification System components and their purpose.

the single photoelectron signal, by attaching the waveshifter. However, in the OD, observing the extra photons is of much more importance than better timing resolution.

3.3 Water Purification System

The original source of the Super-Kamiokande water is spring water in the mine. This water is highly purified by the water system, shown in Figure 3.9 with each component explained in Table 3.1. The SK water is continuously circulated at a rate of about 35 ton/hour through the purification system to maintain high water transparency and to remove radioactive isotopes such as Radon (Rn) and Radium (Ra). Such isotopes are significant backgrounds for low energy analyses.

The resistivity of the water flowing out of the detector for purification is about 11 MΩ·cm and averages at 18.20 MΩ·cm after purification, approaching the chemical limit. The light attenuation length is about ∼100 m, and particles larger than 0.2 nm are reduced to 6 particles/cc.

3.4 Air Purification System

To minimise the radon level in the detector water, SK also uses an air purification system. The seasonal variation of the radon air in the mine is shown in Figure 3.11. The winter levels, where cool air flows in from outside, are comparably low at ∼100–300 Bq/m^3, however the summer levels, where air flows from deep within the mine, are ∼2,000–3,000 Bq/m^3. Firstly fresh air is pumped into the SK dome area at a rate of 10 m^3/minute, resulting in a typical radon concentration of ∼20–30 mBq/m^3 at the SK dome and control room.

From here radon-free air is produced by the air purification system outlined in Figure 3.10, with the components explained in Table 3.2. This system pumps the purified air into the SK tank, above the water level at a positive pressure to prevent any Radon present in the dome air from dissolving in the highly purified water [161]. The resulting radon concentration in the radon-free air is less than 3 mBq/m^3.

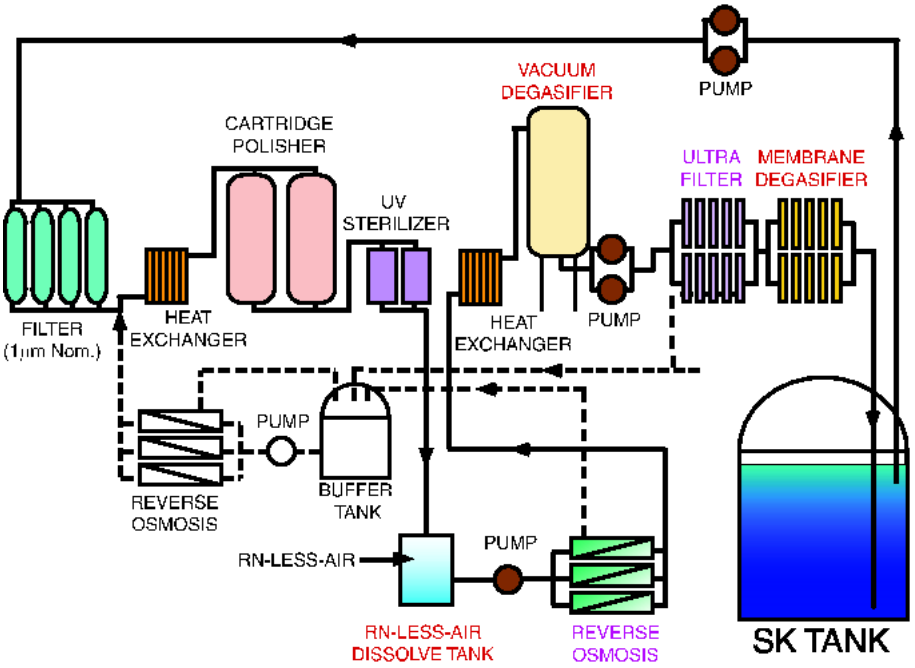

Figure 3.9: Water System [156].

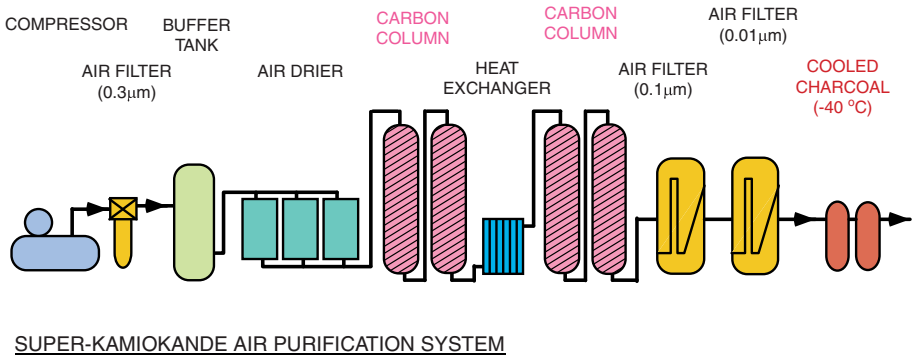

Figure 3.10: Air purification system [156].

Component	Purpose
Compressor	Compresses the air to 7–8.5 atmospheric pressure.
Air Filter	Removes dusts of size $\sim$0.3 μm.
Buffer Tank	Stores the air.
Air Drier	Dries the air and removes CO_2 gas to improve the efficiency of the Carbon Columns.
Carbon Columns	Removes radon gas using activated charcoal.
Air Filter	Further Removes small dust and particles of $\sim$0.01 μm.
Cooled Charcoal	Removes the remaining Rn gas with charcoal at –40°C.

Table 3.2: Air Purification System components and their purpose.

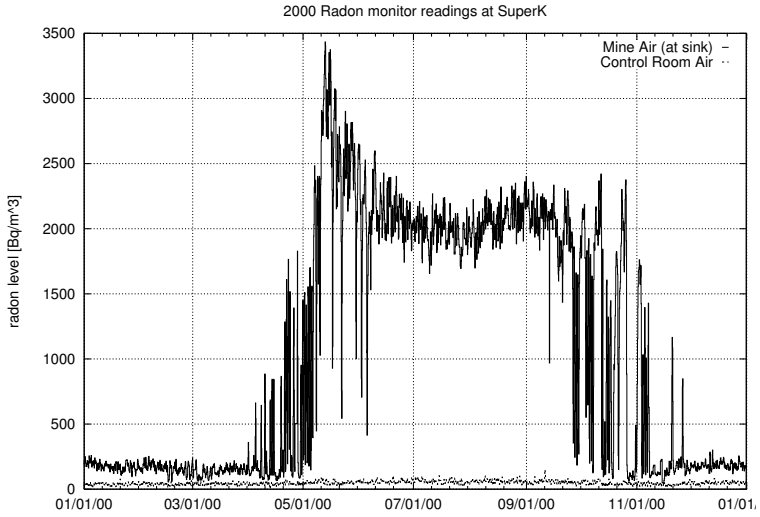

Figure 3.11: Radon levels [156] of the air in the mine is shown by the upper histogram. The lower histogram at the base shows the radon levels in the SK control room.

3.5 Electronics and Data Aquisition System

3.5.1 Electronics and Data Aquisition: SK-I to SK-III

The electronics for the SK-I to SK-III period make use of custom-built ATM (Analogue-Timing-Module) modules of the TKO (TRISTAN KEK Online) standard [162]. The ATM modules receive the integrated charge signal and arrival timing information of each PMT. A block diagram of the ATM is shown in Figure 3.12. There are two pairs of readouts that are used in succession to avoid dead time in the data taking. As an example, this allows both a muon and its decay electron to be recorded. Each of these readouts consist of a QAC (Charge to Analogue Converter) and a TAC (Time to Analogue Converter).

The PMT signal is first amplified 100 times at the ATM, and then divided into four signals that are routed to different components. One is sent to the discriminator, which checks the PMT signal exceeds the threshold of 0.25 p.e.s . If a sufficient signal is received a 400 nsec timing window is opened by a gate signal to the QAC, and a start signal is generated and sent to the TAC. This is for an individual PMT. This *hit* PMT then generates a *HITSUM* signal which is sent to a global trigger module. This trigger module receives HITSUM signals from each of the hit PMTs, if the HITSUM threshold is exceeded, then all the event information is recorded. At the ATM, if there is no global trigger within 1.3 μsec then all the information in the QAC and TAC readouts are cleared. Two of the divided PMT signals are sent to each QAC, and the fourth is an output signal of the ATM without the discriminator threshold and is a PMTSUM signal.

In the case a global trigger is issued, a stop signal is sent to the TAC then the readout information from the QAC and TAC are digitised by an ADC (Analogue to Digital Converter), and stored in the ATM's internal FIFO memory. The ATM has a 450 pC dynamic range with a resolution of 0.2 pC, and 1.3 μsec dynamic range with a resolution of 0.4 nsec.

The DAQ (Data Aquisition) records the event information from all the PMTs when a global trigger is issued. A block diagram of the DAQ is illustrated in Figure 3.13. Each ATM caters to 12 PMTs, with about 20 ATMs housed in each of the 48 TKO crates. Every 16 events, the

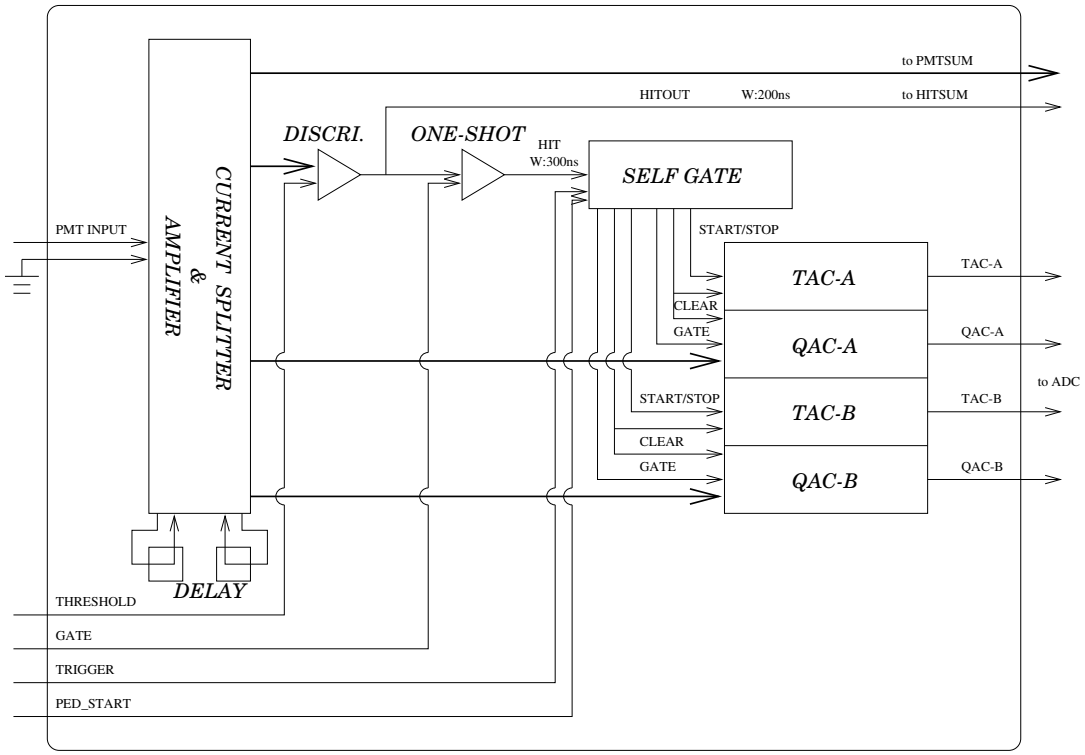

Figure 3.12: Input proportion of the ATM

digitised data in the ATM FIFO memory are sent to the SMP (Super Memory Partner) in the VME. Each SMP looks after the 20 ATMs, and each VME crate houses 6 SMPs. The 8 VME crates hold the SMPs, which are read out by 8 slave computers and send the data to the online host computer.

Outer Detector Electronics and DAQ: SK-I to SK-III

The OD DAQ consists of *paddle cards* that distribute high voltage through coaxial cable to the OD PMTs, and also handle the PMT signals. A block diagram of the OD DAQ can be seen in Figure 3.14. The paddle cards receive the PMT signals through a high voltage capacitor and send them to QTC (Charge to Time Converter) Modules. The OD PMT signals are recorded as a rectangular signal with a width proportional to the charge, and the time given by the leading edge. The QTC modules have a threshold of 0.25 p.e.s, and generate a HITSUM signal which is sent to the global trigger module. If a global trigger is issued, a LeCroy 1877 multi-hit TDC module converts the QTC signal into the charge and timing information. The DPM (Dual Port Memory) modules in VME crates read out the digitised data in the TDC modules, which is sent to a slave computer and then the online host computer. The TDC module can record up to 8 QTC pulses with a resolution of 0.5 nsec. The dynamic range is set to 16 μsec starting from 10 μsec before the global trigger timing.

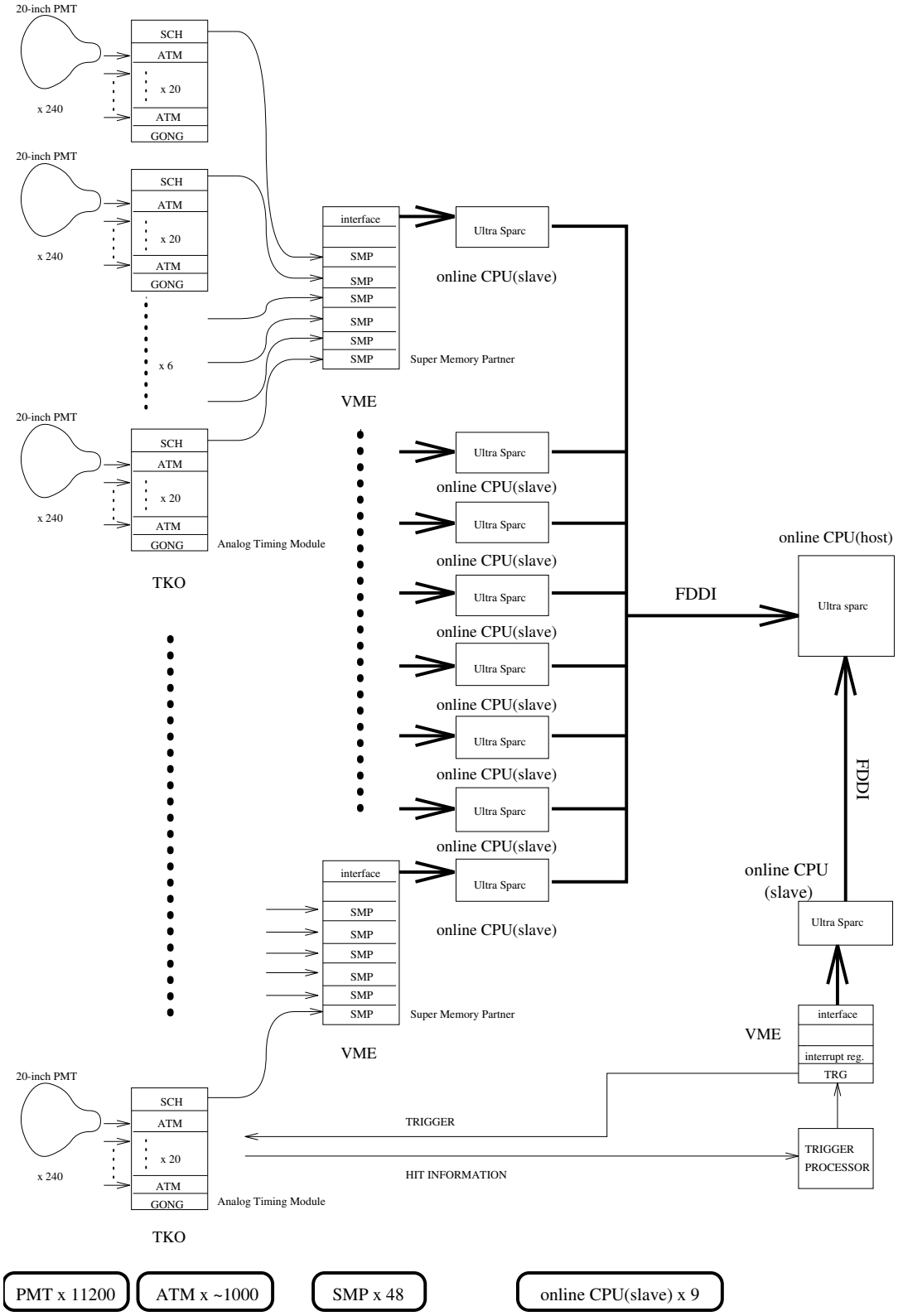

Figure 3.13: Inner Detector DAQ

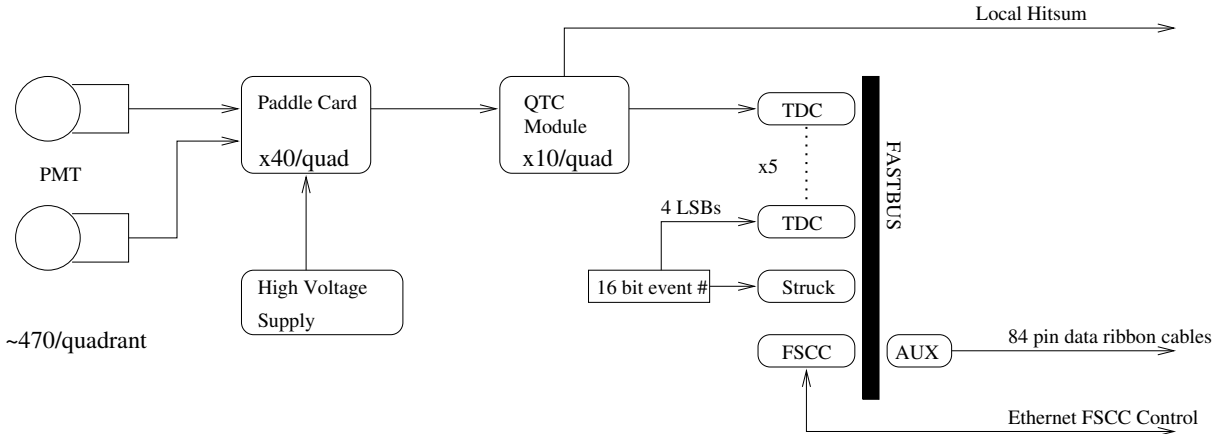

Figure 3.14: Outer Detector DAQ

3.5.2 Hardware Trigger

In the DAQ sections for the ID and OD, HITSUM signals and the global trigger module were mentioned. When an ID PMT is hit, with a charge above the 0.25 p.e. threshold, the ATM generates a rectangular 200 nsec wide 15 mV pulse as a HITSUM signal. The global trigger module receives the HITSUM signals from hit PMTs in the ID, and sums them up to generate an overall ID-HITSUM signal. A diagram of the ID Trigger is shown in Figure 3.15.

There are multiple trigger thresholds for the ID-HITSUM within a 200 nsec window: High Energy (HE) which is –340 mV (31 hits), Low Energy (LE) which is –320 mV (29 hits) and Super Low Energy (SLE). The LE trigger corresponds to the signal expected from a 5.7 MeV electron (with 50% trigger efficiency) and the SLE trigger is equivalent to a 4.6 MeV signal. The trigger rates are ∼5 Hz for HE and ∼11 Hz for LE, with energy thresholds of 10 MeV and 8 MeV, respectively.

The trigger for the OD is similar. When an OD PMT exceeds the 0.25 p.e. threshold, the QTC generates a rectangular 200 nsec wide 20 mV pulse as a HITSUM signal. These are summed to generate the OD-HITSUM signal, with a threshold of 19 hits within a 200 nsec time window.

There are four types of trigger signals in total (HE, LE, SLE and OD) that are fed into the hardware trigger module: TRG. If any one of these trigger signals is received, the TRG module generates a global trigger signal and the event information is recorded.

3.5.3 Upgraded Electronics and Data Aquisition for SK-IV

For SK4, all of the front-end electronics were upgraded in September 2008 [163]. The new electronics are based on a quick charge to time converter and a multi-hit time to digital converter. The new system allows every hit to be processed, and the triggering was changed to be software based, in place of the previous hardware trigger. This removed the down time from the DAQ, and made it necessary to transmit large volumes of data, up to 470 MB/s, which was achieved with Gigabit and 10-Gigabit Ethernet technologies.

In the previous electronics, the bottleneck for the data transfer was the TKO, limited at about 2 MB/s for 20 ATM boards. This corresponded to a data rate of about 1.4 kHz per channel, while the PMT dark rate is typically 4.5 kHz. The new electronics can handle much

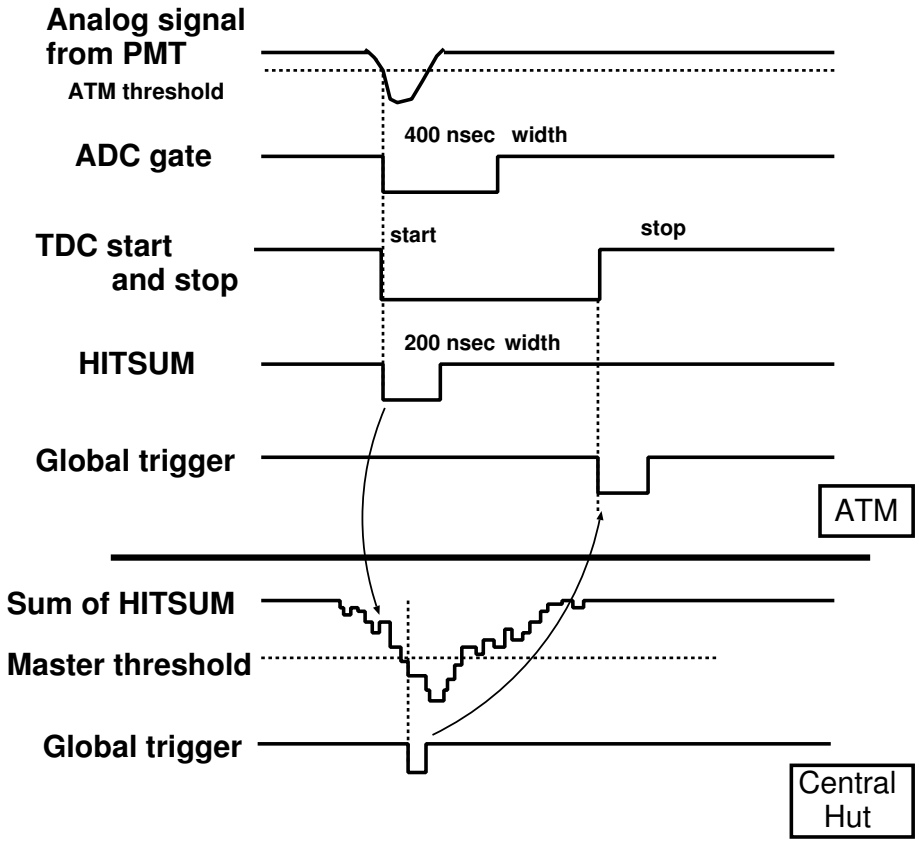

Figure 3.15: Inner Detector Trigger

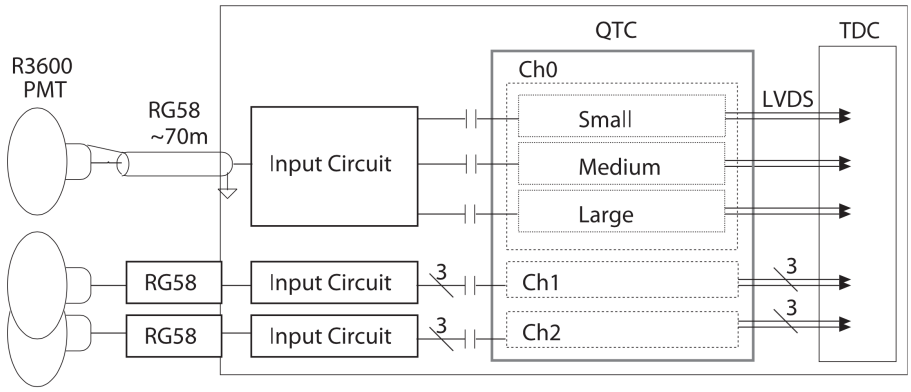

Figure 3.16: SK-IV New Charge to Time Converter (QTC), which were custom Application-Specific Integrated Circuits (ASIC) [164].

larger data throughput, allowing the event trigger threshold to be lowered. This is important for making precise measurements of the low energy solar neutrinos, by observing the energy dependence of the Neutrino Oscillations. The new system also allows the measurement of a greater number of events from a neutrino burst from a supernova. From a supernova at the galactic centre, around 8 thousand events are expected within 10 seconds. The previous DAQ could handle 60,000 events in this time window, while the new DAQ can process 100 times more.

Another advantage is the software-based trigger, making it possible to trigger data recording for more complex conditions. An example of where this would be important is distinguishing relic neutrinos above the atmospheric neutrino background. This can be done by observing a neutron capture by a 2.2 MeV γ emission 200 μs after the initial event. This energy was too small to trigger an event in the previous system. In the new system, the trigger can be configured to keep data for some time period after an event, which could be searched.

3.5.4 SK-IV New Electronics

The new electronics are called QBEEs, short for QTC (Charge to Time Converter) Based Electronics with Ethernet. Primarily, these measure the charge and arrival timing from the PMTs and produce a 6-byte cell per hit and send the data to the online PCs. Each QBEE board was equipped with eight QTC chips, which were custom Application-Specific Integrated Circuits (ASIC) [164]. Each of these QTCs, shown as a block diagram in Figure 3.16, had three inputs (i.e. 24 channels per QBEE) and three measurement ranges per channel (small, medium, and large), to cover a much wider dynamic range than the previous electronics. Previously, charge saturation would occur at 600 pC, while the new QTC can measure over 2000 pC (∼1000 p.e.) without saturation. The QTC produces an output pulse whose width is proportional to the input charge, and leading edge indicates the timing.

The output of the QTC is fed to a multi-hit TDC (Time to Digital Converter), which detects the leading and falling edges. The charge resolution is about 5% at 1 p.e. and less than 2% above 3 p.e., similar to the previous ATM resolution. The digitised signal from one hit is arranged into a 6-byte cell containing charge, timing and input channel information. For more details about the ASIC QTC, see Reference [164].

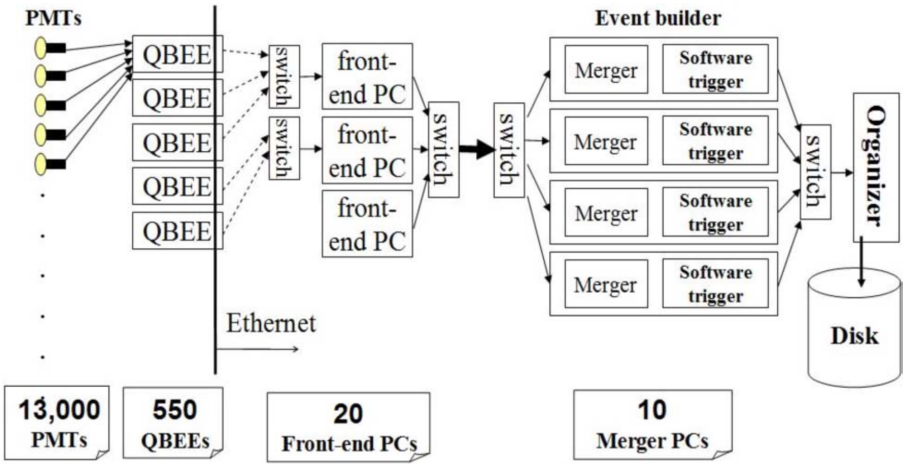

Figure 3.17: SK-IV New Online System [163].

3.5.5 SK-IV New Online System

A block diagram of the new online system can be seen in Figure 3.17. The data from about 550 QBEE boards are transferred as TCP packets to 20 front-end PCs. Data processed from the front-end PCs are sent via 10-Gigabit Ethernet to 10 Merger PCs. Here, the data are merged and the software trigger is applied to select candidate events. The triggered events are then sent to an Organiser PC, which writes merged data onto the disk for offline analysis. The PCs are Linux based, with 2 GB RAM and 3 GHz Intel dual-core CPUs (Xeon 5160).

The software trigger can be used to set conditions for recording data, which can easily be added or modified to the requirements of physics analysis. The basic trigger was set up to reproduce the previous hardware trigger conditions, and depended on the number of hits exceeding a threshold within a 200 ns time window. The software trigger allows for special triggers, such as the neutron trigger that looks for an emitted gamma ray from neutron capture; the T2K trigger for selecting a wide time window around the beam timing; and external triggers for detector calibrations. For more details about the new online system, see Reference [163].

Chapter 4

Monte Carlo Simulation

4.1 Overview

The Monte Carlo (MC) method was used to simulate atmospheric neutrino events in Super-Kamiokande. To be able to simulate events that are just like the data, there were many considerations. Firstly the neutrino flux at the SK site needs to be calculated by considering the global data for primary cosmic-rays, their interactions that produce neutrinos and the following propagation to the SK detector. Once the neutrino flux at SK was estimated, cross-section data collected by many experiments can be used to predict how the neutrinos interact in the detector and the resulting kinematics. The third step was to propagate all the interaction products in a simulated detector geometry, and the Cherenkov photons to the PMTs. The simulation also considered the electronics, such that simulated output similar to the data could be generated. Since the MC also includes all the true physical parameters, it can be compared with the data to understand the physical meaning of what was observed.

4.2 Atmospheric Neutrino Flux

There are several models for estimating the neutrino flux from the primary comic-ray flux. They are referred to here as the Honda flux [16, 165–167] Fluka flux [168], and Bartol flux [169]. The main flux model adopted for the atmospheric data analyses at Super-Kamiokande is the Honda flux, and the others were used to estimate the systematic uncertainties on the Honda calculation. The Honda flux is calculated up to 10 TeV, so the Volkova flux [170] was used above 10 TeV, with the normalisation adjusted to match the Honda flux continuously.

There are many experiments globally that are trying to determine the flux of primary cosmic-rays, which has been summarised in Figure 4.1 together with the fitting used in the Honda flux model. This data serves as the initial input into the atmospheric neutrino flux calculation. The primary comic-ray proton flux up to 100 GeV has been precisely measured by the BESS [171] and AMS [172] experiments. The curve was adjusted slightly to agree with emulsion chamber data above $\sim$10 TeV [166]. The more recent improvements to the Honda flux have been improvements in the interaction models [16, 167].

The variation of the solar wind affects the cosmic-ray flux, particularly at the lower energy range of the spectrum. The flux at the Earth is higher with high solar activity, referred to as the *solar maximum*, and lower with low solar activity, the *solar minimum*. For cosmic-rays of

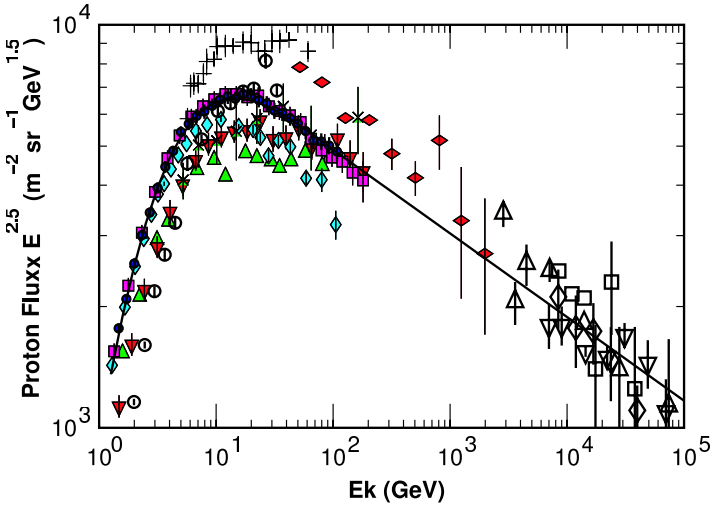

Figure 4.1: Measurements of primary cosmic ray proton flux and the model used in the Honda flux calculation. The data are taken from Webber [173] (crosses), LEAP [174] (upward triangles), MASS1 [175] (open circles), CAPRICE [176] (vertical diamonds), IMAX [177] (downward triangles), BESS98 [171] (circles), AMS [172] (squares), Ryan [178] (horizontal diamonds), JACEE [179] (downward open triangles), Ivanenko [180] (upward open triangles), Kawamura [181] (open squares) and Runjob [182] (open diamonds).

around ∼1 GeV, the difference between the solar maximum and minimum is more than a factor of two. However, the influence decreases to ∼10% at ∼10 GeV. There is also an effect from the geomagnetic field. It deflects cosmic-rays and is characterised by a rigidity (= momentum/charge) cutoff. Cosmic-rays with momentum lower than the cutoff do not arrive at the Earth. The cosmic-ray flux above 100 GeV, which is responsible for ≥ 10 GeV neutrinos, is not affected by the solar activity nor the geomagnetic field.

When the primary cosmic ray protons and nuclei enter that atmosphere and interact with nuclei in the air, secondary particles are produced, which consist mostly of pions and kaons. The density structure of the atmosphere is given by the US Standard Atmosphere model [183], whereas the geomagnetic field model is based on the IGRF2005 model [184].

4.2.1 Hadronic Interaction Models

Two models are used for the hadronic interactions of cosmic-rays with the nuclei in the air. In the case of the Honda 2006 flux [167] and earlier these models were NUCRIN [185] for primary cosmic-ray energies < 5 GeV and DPMJET-III [186] for > 5 GeV. These models determine how the meson products are produced, and the atmospheric neutrinos are produced when they decay. Secondary cosmic-ray muons are also produced in the decay chain, and their flux has been measured by experiments such as BESS [187] and L3+C [188]. The DMPJET-III hadronic model was modified using the measurements of BESS and L3+C, and used in the Honda flux calculation [167]. The ratio of the cosmic-ray muon spectrum after the modification is shown in Figure 4.2. After the modification, the hadronic interaction model agrees with the data within $\lesssim$10% in the 1–100 GeV muon energy range.

The main differences in the Honda 2011 flux [16] was a modification to the hadronic interac-

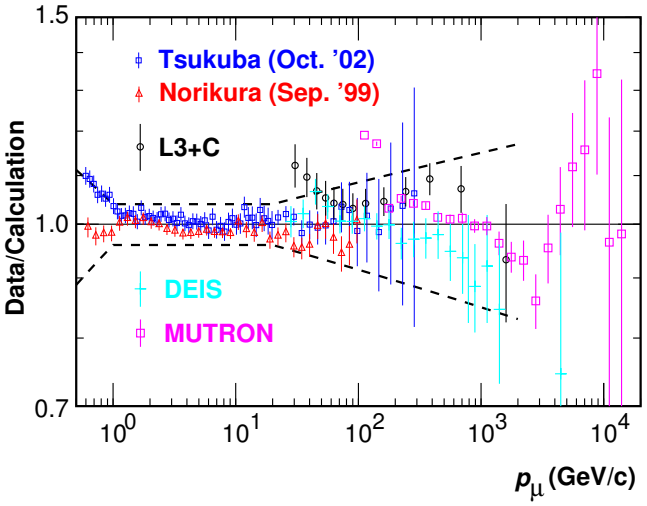

Figure 4.2: Secondary cosmic-ray muon fluxes normalized by the calculation [167]. Data were observed at Tsukuba(open box) and Norikura(open triangle) with the BESS detector [189, 190], and at CERN(open circle) with the L3 detector [188]. For reference, DEIS [191] and MUTRON [192] are plotted. Dashed lines represent the sum of errors in data and calculation. Figure is taken from [167].

tion models, which performed better particularly in the low energy region. To better reproduce the atmospheric muon spectra at lower energies, at sea level and at mountain altitudes, the JAM hadronic interaction model [193] was used. In addition the HARP experiment greatly improved our understanding of hadronic interactions at low energies [194], and in particular by colliding protons on thin N_2 and O_2 targets [195]. The JAM model was found to agree better with the HARP data. In the Honda 2011 calculation, JAM was used between 0.2 GeV to 32 GeV, and for energies above this the modified DPMJET-III model was used as before. Despite these changes, the zenith dependence and flavour ratios of the atmospheric neutrino flux are very similar to before. The main difference is a change of the absolute value of the atmospheric neutrino flux below 1 GeV. A comparison between the low energy HARP data and the JAM and modified DPMJET-III models can be seen in Figure 4.3.

4.2.2 3-Dimensional Flux Calculation

The calculation of the neutrino flux is treated in a 3-dimensional way. The curvature and propagation of charged particles in the geomagnetic field as well as 3-dimensional interaction topologies are considered. Treating the flux in 3-dimensions actually has a significant effect on the directional flux observed at SK, compared with a simpler 1-dimensional treatment. The two main features of the 3D calculation are that there is an increase in the neutrino flux in the near-horizontal direction, and that there is also lower production height of neutrinos, also significant in the near-horizontal direction.

The increase in the near-horizontal neutrino flux is explained by the increased effective area that can generate near-horizontal neutrinos, illustrated in Figure 4.4. The lower energy secondary charged pions and muons, produced from the hadronic interactions of primary cosmic-rays, are also affected. They have an effect from their transverse momentum and also experience curvature

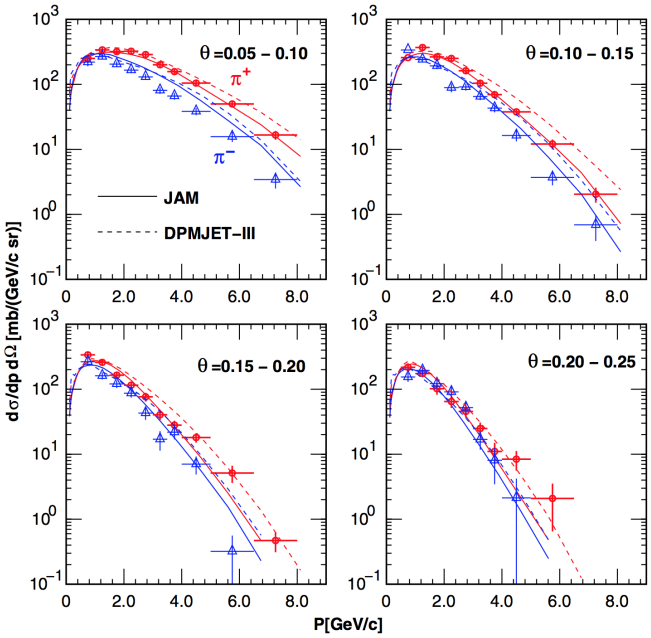

Figure 4.3: Comparison of the HARP data on forward pion production of low energy hadronic interactions [195] with the JAM and modified DPMJET-III model [16]. The HARP data on N_2 and O_2 targets were combined in a ratio of 78.5% N_2 and 21.5% O_2 to simulate an air target.

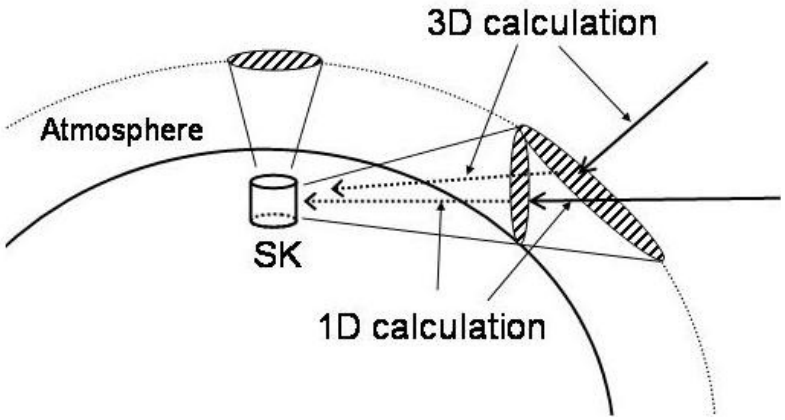

Figure 4.4: A schematic view of the effective areas of primary cosmic rays interacting with air nuclei for 1-dimensional and 3-dimensional calculations. Arrows written by solid lines show the primary cosmic rays and dotted lines show the neutrinos. The 3-dimensional calculation gives larger areas for near-horizontal direction.

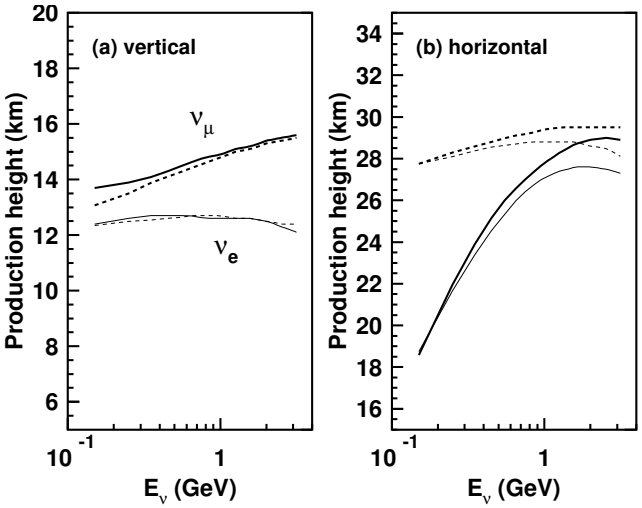

Figure 4.5: 50 % accumulation probability of neutrino production height for (a) near-vertical ($\cos\theta > 0.95$) and (b) near-horizontal ($|\cos\theta| < 0.05$) directions. Thick and thin solid curves are for ν_μ and ν_e by the 3-dimensional calculation, and thick and thin dashed curves are for ν_μ and ν_e by the 1-dimensional calculation, respectively.

in the geomagnetic field. This influences primarily low energy neutrinos at < 1 GeV. Some zenith plots showing the enhancement of the neutrino flux in the horizontal direction for lower energies is shown in Figure 4.6, with the earlier 1D Honda flux and the 3D Fluka flux also drawn for comparison. Due to the stronger than average geomagnetic field above SK, the neutrino flux is predicted to be up-down asymmetric below a few GeV. However, due to the relatively smaller angular correlation of the neutrino and lepton directions at low energies, this up-down asymmetry is smeared.

Neutrinos being produced at lower altitudes in the 3D calculation, than in the 1D calculation, can be explained by the difference in the path length of the primary cosmic-rays. Referring again to Figure 4.4, and considering direct 1D paths, it can be seen that the path taken through the atmosphere is larger at the horizontal zenith direction than for more vertical zenith directions. In the 3D calculation, a primary cosmic-ray that has a more vertical incident angle and then curves to the horizontal direction has a shorter path length than the equivalent horizontal 1D case. This results in neutrinos reaching lower altitudes in the 3D calculation before interacting. Since this effect depends on the curvature of primary cosmic-rays, the influence is most prominent for low energy neutrinos at < 1 GeV. The simulated neutrino production height for the 3D Honda flux and the 1D Honda flux are shown in Figure 4.5. Further details of the differences of the 3D and 1D calculations can be found in Reference [165].

4.2.3 The Neutrino Flux at Super-Kamiokande

The resulting neutrino flux observed at the SK site from the Honda 2011 flux calculation [16] is shown in Figure 4.7, where the flux has been averaged over all directions. The Fluka and Bartol fluxes were also drawn for comparison. The flux of the electron flavour neutrinos drops at a faster rate than the muon flavours with increasing energy. This is explained by the higher energy muons reaching the surface of the Earth before they can decay and produce electron neutrinos.

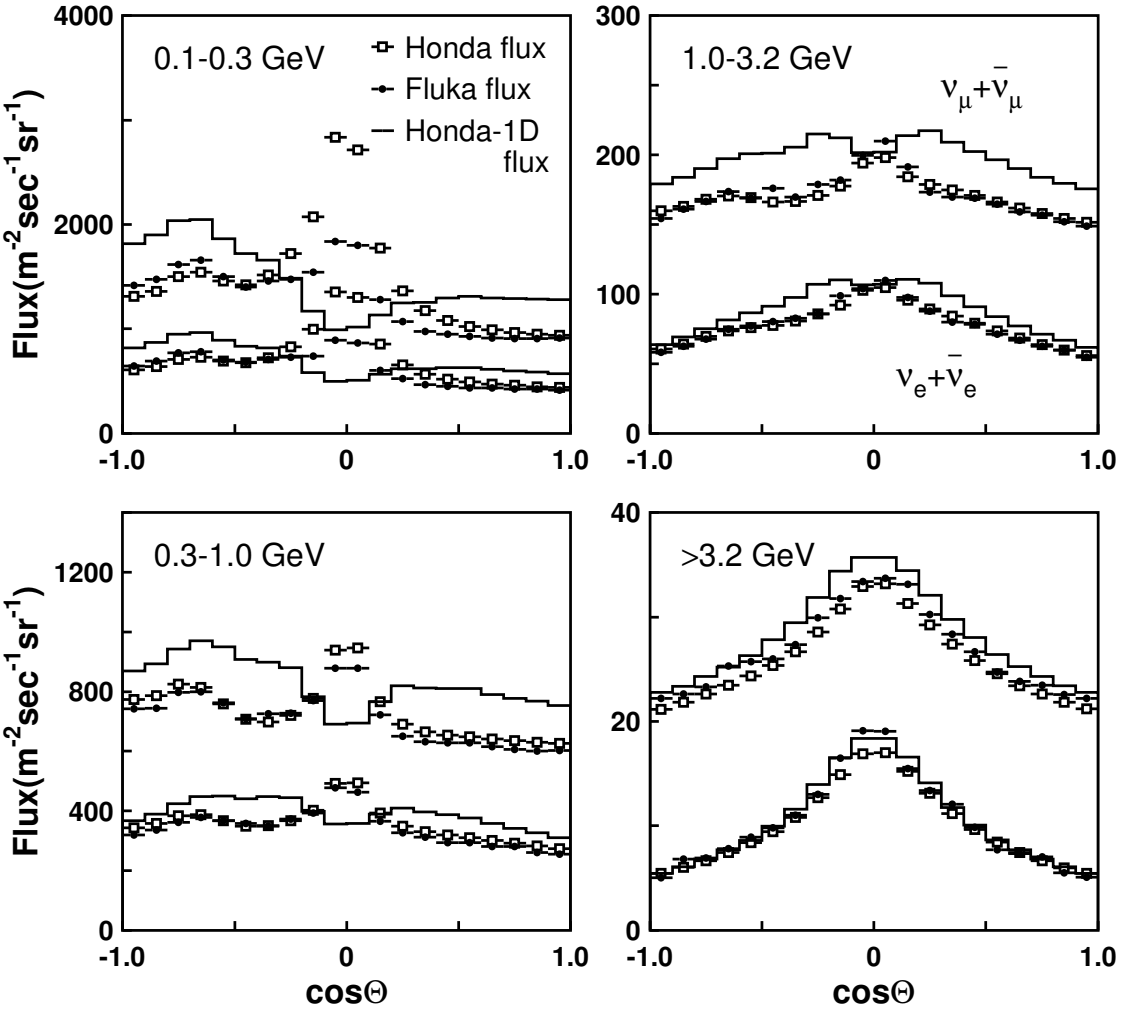

Figure 4.6: Zenith angle dependence of the atmospheric neutrino flux. Boxes show the Honda flux, dots show the Bartol flux and solid lines show the Honda-1D flux. The higher flux is for $\nu_\mu + \bar{\nu}_\mu$ and the lower flux for $\nu_e + \bar{\nu}_e$ in each plot. An enhancement of the neutrino flux is seen for near-horizontal directions at energies below 1 GeV in 3-dimensional calculations, the Honda flux and the Fluka flux. On the other hand, no enhancement is seen in the Honda-1D flux.

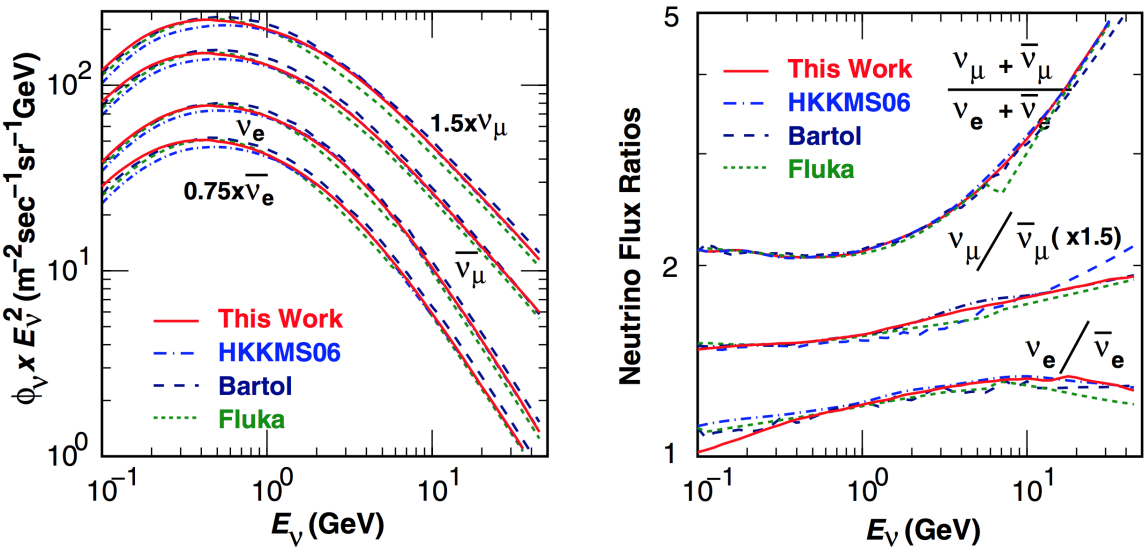

Figure 4.7: Predictions of the direction averaged atmospheric neutrino flux (Left) and the flavour ratio and neutrino anti-neutrino ratios (Right), from Reference [16]. The Honda 2011 flux is shown in solid red [16]; the Honda 2006 calculation in dash-dotted blue [167]; the Bartol flux [169] in dashed navy; and the Fluka flux [168] in dotted green.

The flavour ratio is also shown in Figure 4.7. The $(\nu_\mu+\bar{\nu}_\mu)/(\nu_e+\bar{\nu}_e)$ ratio is around two up until a few GeV, and then increases with energy.

The neutrino anti-neutrino ratios have also been overlaid in the right plot of Figure 4.7. There is a good agreement on these ratios between the flux models. The Bartol flux agrees a little less at higher energies, but this is likely due to an incomplete treatment of the kaon component of the atmospheric neutrino and anti-neutrino fluxes, which becomes increasingly relevant at higher energies. The fact that these ratios are well-understood is important, as the MC was divided into its neutrino and anti-neutrino constituents in the analysis in Chapter 9.

4.3 Neutrino Interactions

The interactions of neutrinos in the simulation are handled by an interaction generator called NEUT [196]. The libraries were originally developed for research into proton decay and neutrinos for the Kamiokande experiment, and then modified for Super-Kamiokande. The following charged current (CC) and neutral current (NC) interactions are simulated:

CC/NC (Quasi-)Elastic Scattering	$\nu + N \rightarrow l + N'$
CC/NC Single Meson Production	$\nu + N \rightarrow l + N' + meson$
CC/NC Single Gamma Production	$\nu + N \rightarrow l + N' + \gamma$
CC/NC Deep Inelastic Scattering	$\nu + N \rightarrow l + N' + hadrons$
CC/NC Coherent Pion Production	$\nu + {}^{16}\mathrm{O} \rightarrow l + {}^{16}\mathrm{O} + \pi$

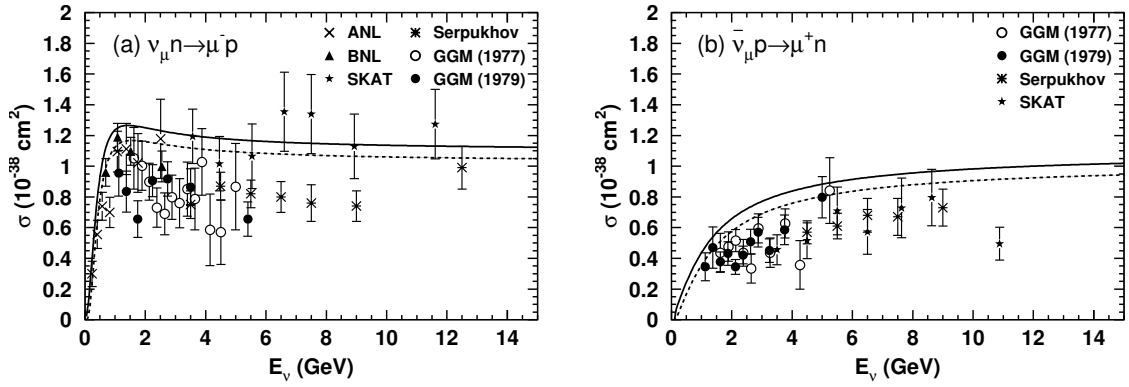

Figure 4.8: Cross-sections for quasi-elastic scattering of (a) ν_μ and (b) $\bar{\nu}_\mu$. The solid line is for NEUT on free nucleons, and the dashed line is for NEUT on bound nuclei. The experimental data are from ANL [200], Gargamelle [201–203], BNL [204], Serpukhov [205] and SKAT [206].

where N and N' are nucleon (proton or neutron) states before and after the interaction and l is a lepton.

Since the cross section of neutrino-electron elastic scattering is about three orders of magnitude smaller than that of the neutrino-nucleon interactions at a neutrino energy of $\sim$1 GeV, this interaction mode is neglected in the simulation. Since the author did not work on the neutrino interactions at Super-Kamiokande, a summary will be written here. For a detailed account from someone who did work on them, see Reference [197].

4.3.1 Quasi-Elastic Neutrino-Nucleon Scattering

In NEUT, the CC Quasi-Elastic Scattering (CCQE) on free protons (the hydrogen atoms in water are essentially free) was based on the Llewellyn Smith Model [198]; while the interactions on bound nucleons in ^{16}O, and the nuclear effects, are treated with the Smith and Moniz [199] model. The characteristic of a quasi-elastic interaction is that the nucleon does not break up from the reaction, and are interactions of the form:

$$\nu_\mu + n \to \mu^- + p \tag{4.1}$$

$$\bar{\nu}_\mu + p \to \mu^+ + n \tag{4.2}$$

$$\overset{(-)}{\nu} + p \to \overset{(-)}{\nu} + p \tag{4.3}$$

where the n is a neutron, p is a proton, and the interaction in Equation (4.3) is an example of NC elastic scattering. A comparison of the cross-sections for quasi-elastic scattering between experimental data and the NEUT calculation can be seen in Figure 4.8.

The elastic scattering on free protons is based on dipole-type form factors, in which the the vector mass M_V is set to be 0.84 GeV and the axial vector mass M_A is set to be 1.21 GeV. These were set from the experimental measurements by the SciFi [207] and SciBar [208] detectors (K2K), as well as MiniBooNE [209]. This M_A value is also used for Single Meson Production. The effect of a larger M_A value is that interactions with larger Q^2 and larger scattering angles are enhanced. The uncertainty in the M_A value was taken to be 10%. The axial vector coupling constant, g_A, is set to 1.232 measured by polarised nucleon beta-decay [210, 211]. Other than

the dipole form factors, mentioned above that are used in NEUT, a few other types of form factor have been put forward [212–214]. The difference in the cross-section from these models and NEUT is estimated to be $< 10\%$.

When considering interactions on bound nucleons in ^{16}O, nuclear effects such as the Pauli exclusion principle or the Fermi motion of the nucleons should be taken into account. The nuclear effects in NEUT are treated with the Smith and Moniz [199] model. To allow quasi-elastic scattering to occur, the outgoing momentum of the nucleons in the interactions is required to be larger than the Fermi surface momentum. NEUT takes the Fermi surface momentum to be 225 MeV, which was determined to reproduce the quasi-elastic peak in electron scattering. The systematic uncertainties on the neutrino interactions and nuclear effects are estimated by considering other models. Other such models have been proposed, for example, by Nieves *et al.* [215] and Nakamura *et al.* [216].

The cross-sections for NC elastic scattering are estimated from the CC cross-sections by the following relations [217, 218]:

$$\sigma(\nu p \to \nu p) = 0.153 \times \sigma(\nu n \to e^- p) \tag{4.4}$$
$$\sigma(\bar{\nu} p \to \bar{\nu} p) = 0.218 \times \sigma(\bar{\nu} p \to e^+ n) \tag{4.5}$$
$$\sigma(\nu n \to \nu n) = 1.5 \times \sigma(\nu p \to \nu p) \tag{4.6}$$
$$\sigma(\bar{\nu} n \to \bar{\nu} n) = 1.0 \times \sigma(\bar{\nu} p \to \bar{\nu} p) \tag{4.7}$$

4.3.2 Single Meson Production

When the hadronic invariant mass (W) is $\lesssim 2\,\mathrm{GeV/c^2}$, single meson production via baryon resonances are the dominant hadron production processes. The model used in NEUT is based on the Rein and Sehgal model [219, 220]. This model considers single pion production, however it was adapted for NEUT to encompass the single meson production of η and K mesons, by altering the decay of the resonances. The meson is produced via intermediate baryon resonances:

$$\begin{aligned} \nu + N \to l + N^* \\ \hookrightarrow N' + \text{meson} \end{aligned} \tag{4.8}$$

where N^* is the baryon resonance, and N and N' are the nucleon states before and after the interaction.

Lepton polarisation and mass effects are considered [221, 222], which results in a suppression of the cross-section at lower Q^2. The angular distribution of the pion in the final state for the $\Delta(1232)$ resonance is given by a method proposed by Rein [220]. The angular distribution of the other resonances are taken as isotropic in the resonance rest frame. In the decay of a baryon resonance, the Pauli blocking effect is considered for interactions off a bound nucleon by requiring the momentum of the nucleon to be greater than the Fermi surface momentum.

The meson-less decay of the baryon resonance is also considered [223], and 20% of the resonances decay in ^{16}O with only a lepton and nucleon in the final state. The process occurs in the presence of other nucleons like so:

$$N^* + N \to N' + N'' \tag{4.9}$$

where N^* is a baryon resonance and N, N', N'' are nucleon states.

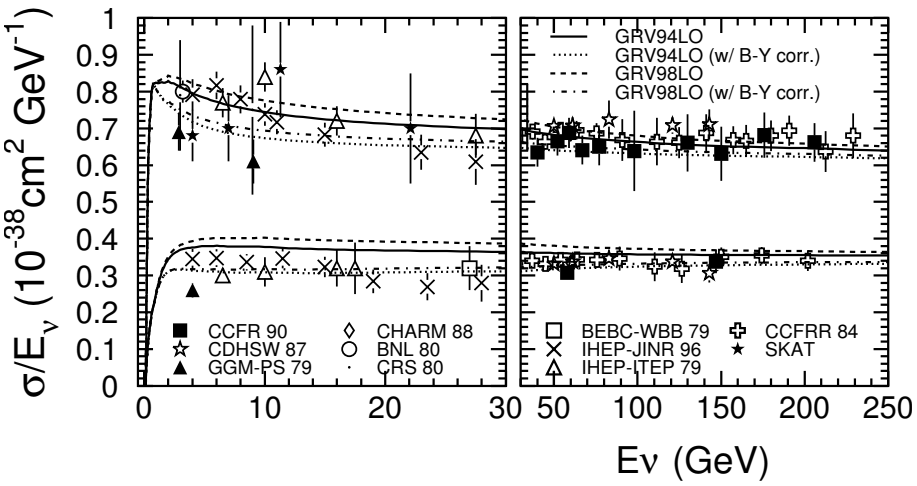

Figure 4.9: Cross-sections for charged current deep inelastic scattering ν_μ and $\bar{\nu}_\mu$ interactions. The upper (lower) curves are for ν_μ ($\bar{\nu}_\mu$).

4.3.3 Deep Ineslastic Scattering

The cross-section of CC Deep Inelastic Scattering (DIS) was determined using nucleon structure functions taken from the parton distribution functions (PDF) calculated by Glück et al. [224]. The PDF in the lower Q^2 region was improved by the corrections of Bodek and Yang [225]. Cross-sections of the CC ν_μ and $\overline{\nu}_\mu$ interactions are plotted in Figure 4.9.

The treatment of neutral current interactions in NEUT for deep inelastic scattering are estimated from the charge-current case by relations determined by experimental measurements [226, 227]:

$$\frac{\sigma(\nu N \to \nu X)}{\sigma(\nu N \to \mu^- X)} = \begin{cases} 0.26 & (E_\nu < 3\,\mathrm{GeV}) \\ 0.26 + 0.04\,(E_\nu/3 - 1) & (3\,\mathrm{GeV} \le E_\nu < 6\,\mathrm{GeV}) \\ 0.30 & (E_\nu \ge 6\,\mathrm{GeV}) \end{cases} \tag{4.10}$$

$$\frac{\sigma(\bar{\nu} N \to \bar{\nu} X)}{\sigma(\bar{\nu} N \to \mu^+ X)} = \begin{cases} 0.39 & (E_\nu < 3\,\mathrm{GeV}) \\ 0.39 - 0.02\,(E_\nu/3 - 1) & (3\,\mathrm{GeV} \le E_\nu < 6\,\mathrm{GeV}) \\ 0.37 & (E_\nu \ge 6\,\mathrm{GeV}) \end{cases} \tag{4.11}$$

Depending on the invariant mass W, the kinematics of the hadronic system is simulated by one of two methods. For the $1.3\,\mathrm{GeV/c^2} < W < 2.0\,\mathrm{GeV/c^2}$ region, only pions are considered as outgoing mesons. For the DIS treatment of pions, NEUT requires $n_\pi \ge 2$ to avoid overlapping with the W region for single pion production. The forward-backward asymmetry in the hadronic centre of mass system of the pion multiplicity is considered using the results from the BEBC experiment [228]. For the $W > 2.0\,\mathrm{GeV/c^2}$ region, the kinematics of the hadronic system are calculated by the CERN Pythia and Jetset package [229], which treats K, η, ρ and so on, as well as π.

4.3.4 Coherent Pion Production

Coherent pion production is a neutrino interaction with a nucleus as a whole (oxygen here), which remains intact as there is only a small momentum transfer to the nucleus. The event is

characterised by an outgoing pion with the same charge as the incoming weak-current, with both the outgoing pion and lepton having a strong forward angular correlation with the neutrino. To simulate this interaction, NEUT makes use of the Rein and Sehgal formalism [230]. There is an upper limit on the cross-section for CC coherent pion production, set by the K2K SciBar detector [231].

4.3.5 Nuclear Effects

To properly understand the interactions observed, it is necessary to consider nuclear effects. These are secondary interactions of the outgoing mesons, while they are still inside the nucleus. All the mesons produced from neutrino interactions inside the ^{16}O nucleus are tracked from production until they are absorbed or leave the nucleus. NEUT employs a cascade model to propagate the π, K and η produced in interactions in the ^{16}O nucleus. At $E_\nu > 1\,\text{GeV}$, the cross-sections for pion production from neutrino interactions, as well as pion-nucleon interaction cross-sections are large. So the secondary interactions of pions are particularly important. The following interactions are considered: inelastic scattering, charge exchange, and absorption. In NEUT, the Wood-Saxon density distribution [232] determines the initial production point of the pion in the nucleus:

$$\rho(r) = \frac{Z}{A}\rho_0 \frac{1}{1+\exp\left(\dfrac{r-c}{a}\right)} \tag{4.12}$$

where Z is the atomic number, A is the mass number, ρ_0 is the average density of the nucleus, and a and c are the density parameters. For the ^{16}O nucleus: $\rho_0 = 0.48\,m_\pi^3$, $a = 0.41\,\text{fm}$, $c = 2.69\,\text{fm}$, $Z = 8$ and $A = 16$ [233]. The mean free path, with momentum and position dependence, of each possible interaction is used to determine which pion interaction takes place [234]. Fermi motion and Pauli blocking are considered. The energy of the outgoing nucleon must be above the Fermi surface momentum:

$$p_F(r) = \left(\frac{3}{2}\pi^2\rho(r)\right)^{\frac{1}{3}}. \tag{4.13}$$

Using the results of a phase shift analysis from π–N scattering experiments [235], the angular and momentum distributions of the outgoing pions are determined. The pion interaction simulation was compared with the experimental data for the following three interactions : $\pi-^{12}$C scattering, $\pi-^{16}$O scattering, and pion photo-production ($\gamma+^{12}\text{C} \to \pi^- + X$) [236, 237], as shown in Figure 4.10.

For kaons, cross-section measurements of $K^\pm - N$ scattering [238–240] were used to develop the elastic scattering and charge exchange treatment in NEUT. For η mesons, η absorption ($\eta N \to N^* \to \pi(\pi)N$) was considered [241], where the pions are tracked as previously described.

Nucleon–nucleon elastic scattering was also considered, using cross-section measurements [242]. These interactions can lead to the production of delta resonances, which decay to produce pions. This effect is considered with the isobar production model proposed by Lindenbaum et al. [243].

4.4 Detector Simulation (SKDETSIM)

After the flux of neutrinos expected at the detector has been calculated, and the interaction generator has predicted how many interact and the interaction topology, the tracking of particles

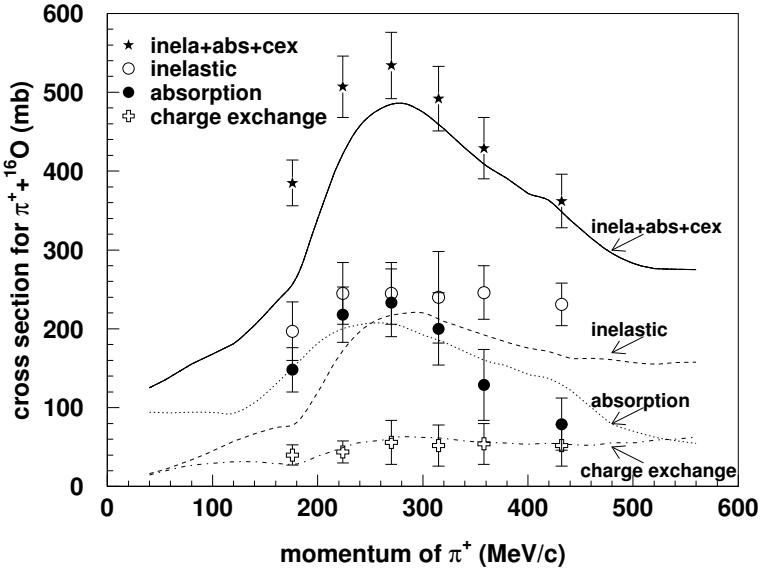

Figure 4.10: The cross-sections of $\pi^+ - {}^{16}\mathrm{O}$ scattering as a function of π^+ momentum. The lines are the cross sections calculated by NEUT for each interaction mode, and the experimental data points are taking from [237].

in the detector itself was simulated. The simulation can be summarised as three steps. The first is the tracking of the outgoing particles through the detector and secondly the generation and propagation of their Cherenkov photons in water. The third is to simulate the PMT response as well as the electronics readout. The Super-Kamiokande Detector Simulator is referred to as SKDETSIM.

4.4.1 Particle Tracking

The detector simulation was developed using the CERN GEANT3 libraries [244]. During the tracking of the particles through the detector, there are multiple processes that can occur depending on the particle type. A list of the processes considered is presented in Table 4.1. For the hadronic interactions in water, the CALOR package was used [245], which reproduces the pion interactions well in the low momentum region ($\sim$1 GeV/c). For the $p_\pi \leq 500\,\mathrm{MeV}/c$ momentum region, a custom program [246] was used that was based on experimental results from $\pi - {}^{16}\mathrm{O}$ scattering [247] and $\pi - p$ scattering [248]. The systematic uncertainty in the hadron interactions was estimated from the difference between CALOR, which was used in SKDETSIM, and the FLUKA model.

For the propagation of charged particles, Cherenkov photons are generated with an opening angle defined by Equation (3.2), and the number and wavelengths by Equation (3.3). Only photons in the range of 300–700 nm are generated because this is the sensitive region of the PMTs, as shown in Figure 3.3.

4.4.2 Cherenkov Photon Tracking

Each of the Cherenkov photons produced by the passage of charged particles are tracked in the detector. The photons can undergo several processes. They can be scattered due to local changes

γ	(e^+, e^-) pair production Compton scattering Photoelectric effect
$e^\pm$	Multiple scattering Ionization and δ-rays production Bremsstrahlung Annihilation of positron Generation of Cherenkov radiation
$\mu^\pm$	Decay in flight Multiple scattering Ionization and δ-rays production Bremsstrahlung Direct (e^+, e^-) pair production Nuclear interactions Generation of Cherenkov radiation
Hadrons	Decay in flight Multiple scattering Ionization and δ-rays production Hadronic interactions Generation of Cherenkov radiation

Table 4.1: List of the simulated processes.

in density in the water, or they can be absorbed. The probability of either of these processes occurring are characterised by parameters that depend on the transparency of the water, and are tuned values. The details on how this calibration is performed are written in Section 5.2.

If the Cherenkov photon is absorbed, tracking of that photon simply stops. Otherwise, there is a possibility that the photon is scattered. If it scatters, there are two angular distributions in which the photon may follow. The primary distribution is symmetric in the forward-backward direction and corresponds to the type of angular distribution expected from Rayleigh Scattering.

There is also a relatively smaller probability that a very forward angular scattering distribution is taken. This corresponds to the asymmetric component expected from Mie Scattering. When the Cherenkov photons scatter on tiny dust particles in the water that are close to the size of the photon wavelength, Mie scattering may occur. The exact angular distribution taken can vary between a symmetric shape and a considerably forward form, depending on the distribution of small particles present in the tank. Since the exact distribution of small particles in the tank is not known, there is an effective treatment in SKDETSIM to account for the possibility of forward scattering.

The probability of the photon being absorbed greatly depends on the transparency of the water, and varies with the water quality. A study into the possibility of a time varying Monte-Carlo to account for the changes in water quality was carried out and is described in Section 5.2. At the time of writing, the MC is not varied with time, but instead the momentum calculation is varied with the water transparency. This variation is determined from the very reliable water transparency measurement from cosmic-ray muons (see Section 5.1.4).

The probability of these processes occurring is described in Section 5.2. The simulation also

accounts for reflections on the *black sheet* and on the PMT surfaces. The probability of this occurring is also a tuned parameter.

4.4.3 PMT Response

Using the measured quantum efficiency, the PMT photocathode surface is simulated as part of the detector geometry. To determine the charge distribution, the single p.e. distribution is summed for each photoelectron emitted and smeared by the timing resolution of the PMT. As well as this, properties of the electronics are simulated like the timing window and charge threshold.

Chapter 5

Calibration

5.1 Detector Calibration

5.1.1 Relative Gain Calibration

Uniformity of the high voltage (HV) gain of each PMT is necessary to accurately reconstruct the momentum of particles without introducing systematic differences due to the particle's vertex position of direction. It is the goal of the Relative Gain Calibration to adjust the HV of each PMT such that the gain is approximately uniform across the whole detector. The remaining differences in gain can then be corrected for in the software.

This calibration is done using a Xe lamp light source and scintillator ball set up as shown in Figure 5.1 (left). The Xe lamp light is passed through an ultraviolet (UV) filter and a neutral density (ND) filter, and then split into four optical fibres. One fibre is routed into the tank and into the scintillator ball, making the light source for the calibration. Another fibre is used to trigger a Xe lamp calibration event, and the others to monitor the intensity of the light flash.

The scintillator ball is made up of a mixture of acrylic resin, BBOT wavelength shifter and MgO powder diffuser. The BBOT wavelength shifter absorbs the UV light and re-emits photons with a peak wavelength of 440 nm, which is a typical wavelength for Cherenkov light produced in water.

The high voltage value of each PMT is adjusted to obtain uniform gain by measuring the relative gain G_i of the i-th PMT:

$$G_i = \frac{Q_i}{Q_0 f(\theta)} \cdot l_i^2 \cdot \exp\left(\frac{l_i}{L}\right) \tag{5.1}$$

where Q_i is the charge detected by the i-th PMT, Q_0 is a normalisation factor, $f(\theta)$ is the PMT acceptance as a function of the photon incidence angle θ, l_i is the distance from the light source to the PMT, and L is the attenuation length. This measurement is performed for several positions of the scintillator ball, changing the voltage.

After adjusting the HV of the PMTs, a relative gain distribution for all the PMTs like that shown in Figure 5.1 (right) is obtained. The one sigma spread of the relative gain is about 7 %. This figure shows the remaining gain difference of each PMT, which is corrected for in the software.

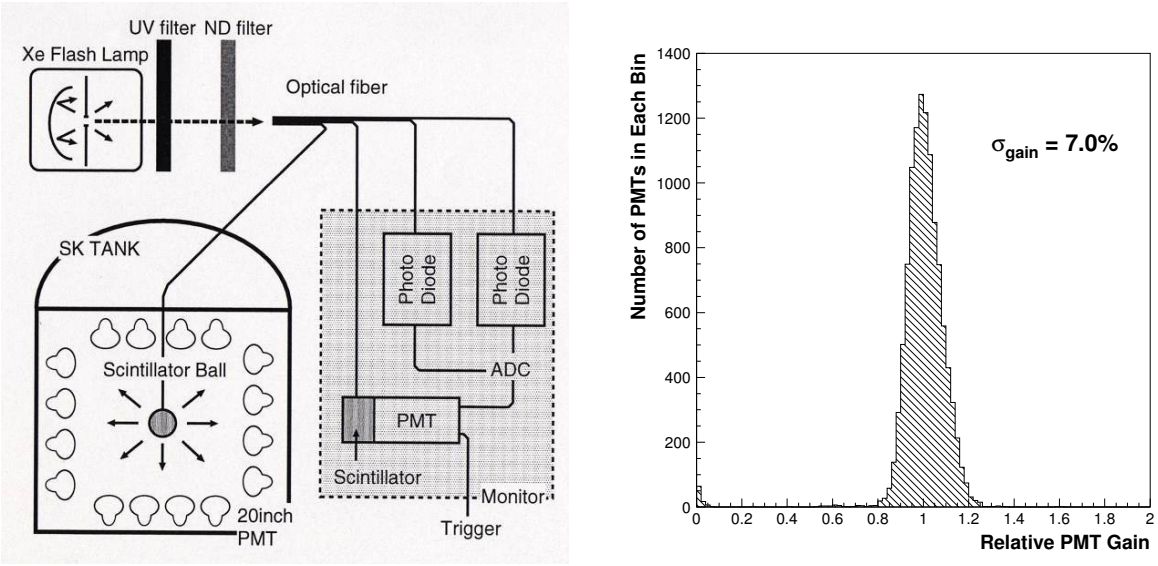

Figure 5.1: Relative Gain Calibration with the Xe lamp. The left figure shows the set-up of the Xe lamp, Scintillator ball and intensity monitoring. The right figure shows the relative gain of all the PMTs after adjusting the HV to obtain approximately uniform gain. The remaining difference in the gain is shown, which is corrected for in the software.

5.1.2 Absolute Gain Calibration

The main unit of charge used in the Super-Kamiokande software is the number of photoelectrons detected. The goal of the Absolute Gain Calibration is to determine the conversion factor from the pico-Coulomb (pC) measured by the PMTs to the equivalent number of photoelectrons. This is done by measuring the single photoelectron charge distribution of the PMTs.

The calibration source is a polyethylene vessel containing Nickel wires and housing a 252-Californium (^{252}Cf) neutron source, as illustrated in Figure 5.2 (left). The spontaneous fission of ^{252}Cf produces neutrons, which are captured in the Nickel wires causing the immediate emission of γ-rays in the 6$\sim$9 MeV region.

The Nickel source is lowered into the tank through one of the calibration portholes. This is a low intensity source leading to 50$\sim$80 PMTs hit in the whole tank, so only one photon is reaching each PMT. This gives the single photoelectron charge distributions, to calibrate the conversion factor. A typical charge distribution measured by this calibration is also shown in Figure 5.2 (right). The sharp peak just above 0 pC is due to emitted photoelectrons that missed the first dynode and therefore receive less amplification. Whereas, the peak at around $\sim$2 pC is the single photoelectron signal. The mean value of 2.055 pC is used as the conversion constant from the PMT charge to the number of photoelectrons.

5.1.3 Relative Timing Calibration

The timing of each individual PMT depends on the length of the signal cable from each PMT and also on the charge detected, due to the *timewalk* effect of larger signals exceeding the threshold earlier than weaker signals. Particularly for accurate vertex position reconstruction, the systematic differences of each PMT timing should be minimised. The goal of the Relative

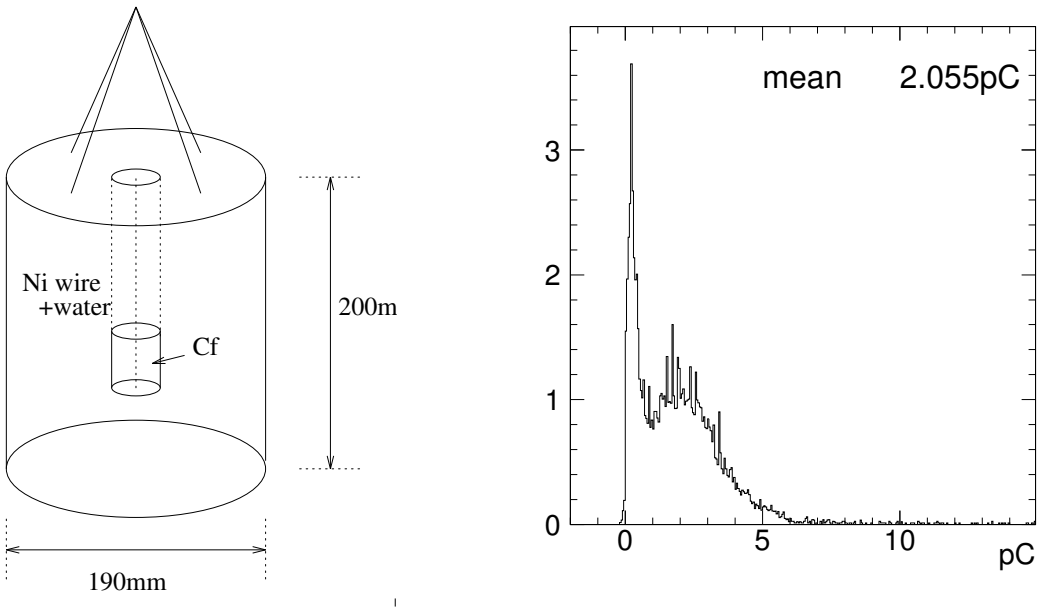

Figure 5.2: Absolute Gain Calibration with the Ni source is shown on the left. The neutrons emitted by ^{252}Cf are captured in the Nickel wires, leading to the emission of γ-rays. The intensity is low such that the single photoelectron signal can be observed as shown on the right. Here, 2.055 pC is taken as the conversion factor from pC→p.e.

Timing Calibration is to measure the timing of each PMT as a function of charge (p.e.), and use this data to correct the differences.

This calibration is performed with a diffuser ball inserted into the tank as shown in Figure 5.3 (left). Firstly a 337 nm wavelength N_2 laser emits a pulse with a time width of 3 nsec. The light is then shifted to 384 nm by a dye laser module, which is the wavelength the PMTs are most sensitive to. The laser light is split into two optical fibres, one is used for monitoring and triggering the Relative Timing Calibration event, and the other is routed into the tank.

This fibre is routed into the diffuser ball, where the light is first diffused by a TiO_2 diffuser tip at the centre, and then further diffused by the encompassing LUXDOX silica gel made of 20 nm glass fragments. The laser light causes the diffuser ball to light up more-or-less uniformly in all directions.

This measurement is repeated for a range of light intensities using an adjustable attenuation filter, corresponding to a charge measurement from 1 p.e. to a few hundred p.e. A scatter plot of the timing against charge, referred to as the *TQ-map*, for each PMT is made, like the one shown in Figure 5.3 (right). The TQ-map is then used to correct the timing of the ID PMTs.

5.1.4 Water Transparency from Cosmic-Ray Muons

A water transparency measurement is made by using abundant downward going cosmic-ray muons as the calibration source. The energy deposit is approximately constant at around $\sim$2 MeV/cm and a stable source of Cherenkov photons. The selected sample is of vertically downward going muons that traverse the full length of the tank. The muon track is reconstructed from the entrance and exit points in the ID. The Cherenkov light is assumed to not

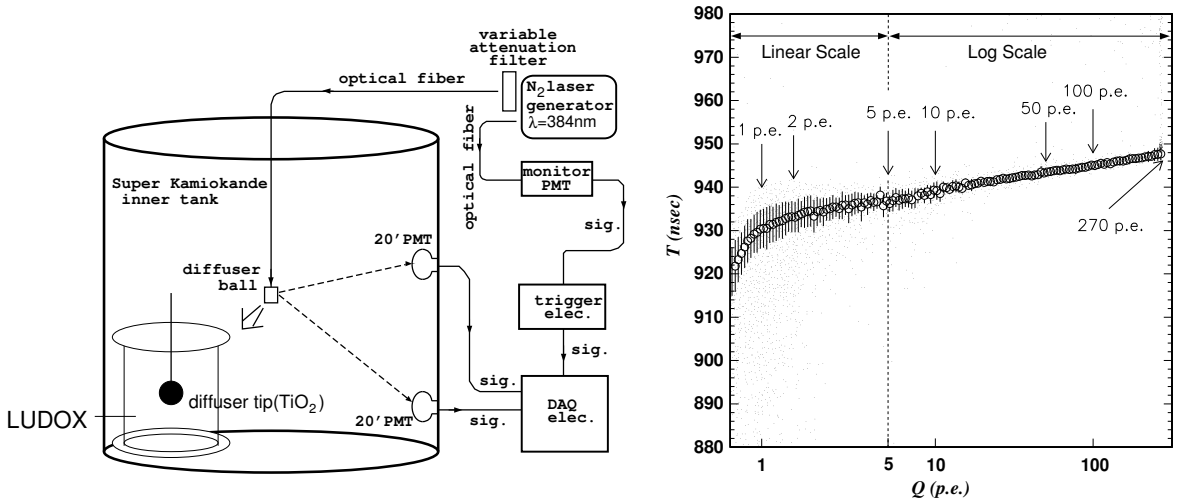

Figure 5.3: Relative Timing Calibration with the diffuser ball. The left figure shows the setup of the laser and the diffuser ball that disperses the light around the tank. The right figure shows the timing distribution against charge for a PMT, which is used to adjust the timing information.

undergo scattering, then the detected charge (p.e.) for the i-th PMT is defined as:

$$Q_i = Q_0 \cdot \frac{f(\theta)}{l_i} \cdot \exp\left(-\frac{l_i}{L}\right) \tag{5.2}$$

where Q_0 is a constant, $f(\theta)$ is the PMT acceptance, l_i is the photon path length to the i-th PMT and L is the attenuation length. The path length l_i is calculated from the muon track by assuming a 42° opening angle. An illustration of the measurement is shown in Figure 5.4 (left). Collecting the charge and length information together for a typical run, $\log\left(Q \cdot l / f(\theta)\right)$ as a function l is also shown in Figure 5.4 (right), where the attenuation length was estimated to be 95 m.

Cosmic-ray muons are continuously measured as part of the recorded data, so they provide a non-invasive method of measuring the water transparency continuously over time. The time variation of the light attenuation length is shown in Figure 5.5. This gives a reliable measurement of the water transparency, which is used to modify the momentum reconstruction in the data.

This measurement is also used to tune the charge scale of the MC. This is done by considering the intersection of the plot on the right of Figure 5.4 where $l \to 0$. The time variation of this quantity against elapsed days is shown in Figure 5.6.

The effective observed charge at $l \sim 0$ is stable during data taking, as the time variation of the attenuation length is neligible as $l \to 0$. The number of Cherenkov photons generated by the passage of charged particles and the acceptance of the PMT is adjusted in the MC to match the charge intersection quantity between MC and data. The adjustment to the PMT acceptance is independent of the photon incident angle. The charge scale is adjusted to within 0.4% of the data.

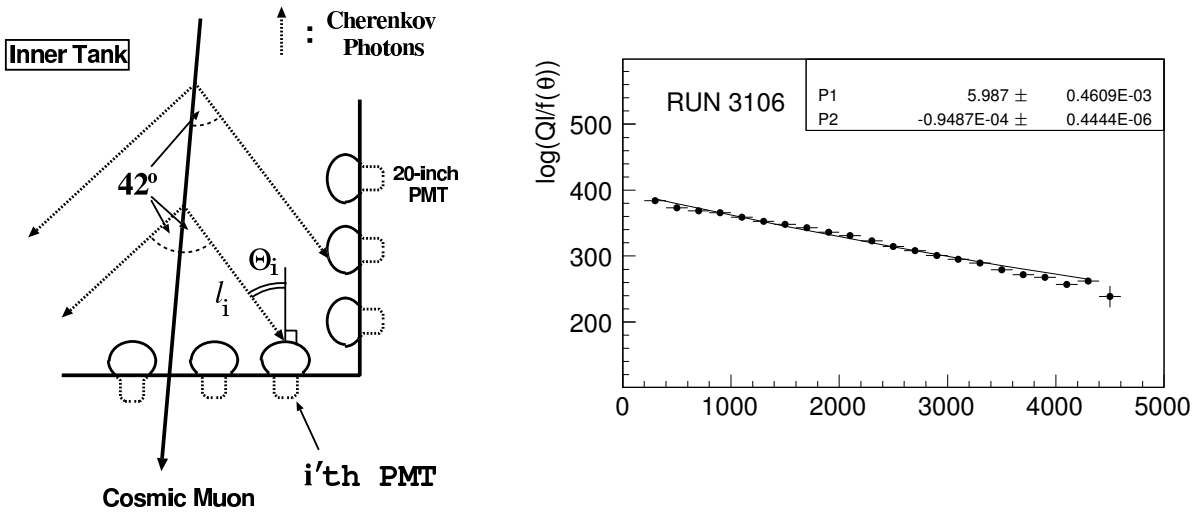

Figure 5.4: Water Transparency from cosmic-ray muons. The left figure shows the muon passing vertically downward through the tank as a stable source of Cherenkov photons. The right plot shows the quantity used to determing the water transparency.

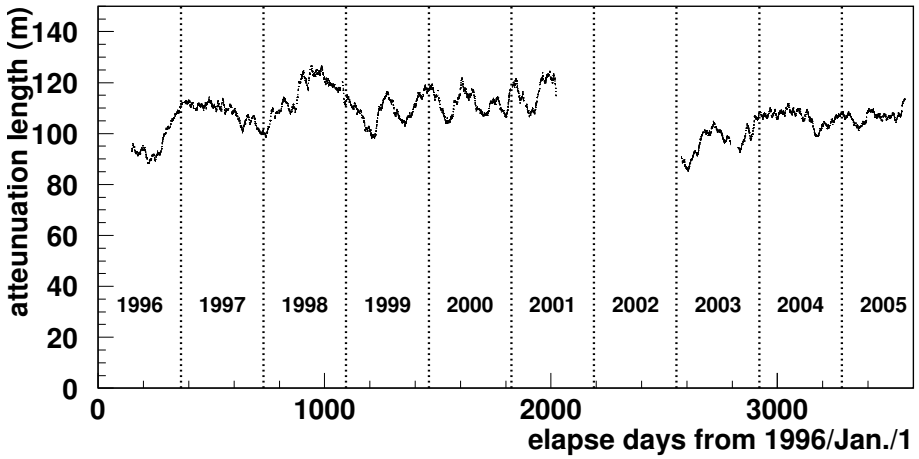

Figure 5.5: Time variation of the water transparency measured from the continuous source of cosmic-ray muons. The attenuation length recorded is used to adjust the momentum calculation of the data. The attenuation length is shown as a running average over around 1 week of data points.

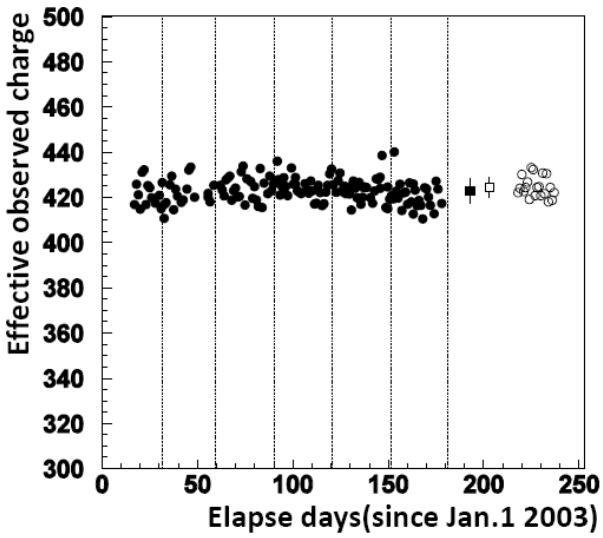

Figure 5.6: Time variation of the water transparency measured from the continuous source of cosmic-ray muons. The attenuation length recorded is used to adjust the momentum calculation of the data. The attenuation length is shown as a running average over around 1 week of data points.

5.2 Water Parameter Tuning

In the Monte Carlo simulation, it is necessary to simulate the processes Cherenkov light undergo during their propagation (see also Section 4.4.3). The photons may be absorbed or scattered, each of which has a wavelength dependence. The goal of this calibration is to obtain wavelength dependent parameters that characterise the probability of the Cherenkov photons interacting by these processes in water. This is often referred to as the *water parameter* calibration.

The light attenuation length in water is due to the absorption of photons and scattering, where the scattering can take a forward-backward symmetric or asymmetric form. The light attenuation length can therefore be described as:

$$L(\lambda) = \frac{1}{\alpha_{abs}(\lambda) + \alpha_{sym}(\lambda) + \alpha_{asy}(\lambda)} \tag{5.3}$$

where $\alpha_{abs}(\lambda)$, $\alpha_{sym}(\lambda)$, and $\alpha_{asy}(\lambda)$ are the wavelength (λ) dependent attenuation coefficients for absorption, symmetric scattering and asymmetric scattering, respectively. The light attenuation length is also measured by cosmic-ray muon data as described in Section 5.1.4. However, the power of this calibration is that it can give an indication of how much each process contributes to $L(\lambda)$, and its wavelength dependence.

The water parameter calibration, therefore, makes use of lasers of several wavelengths. The setup consists of a 337 nm N_2 laser, and system of laser dye modules to create the wavelengths of 371 nm, 400 nm and 420 nm. The configuration is shown in Figure 5.7.

The laser output is then divided into four optical fibres. Two for monitoring, one to trigger the water parameter calibration event and the fourth is routed to a light injector that is permanently fixed to the Inner Detector wall. The light injector gives the laser input an opening angle that creates a spot of direct light about ∼10 m in diameter at the bottom of the tank, illuminating more PMTs. It is preferable to light up more PMTs, as this gives a more accurate measurement of the laser light intensity. Figure 5.7 also shows an event display in which the laser spot on the bottom of the tank can be seen.

For the analysis of the laser data, the tank is divided into six regions: the top and five barrel regions as shown in Figure 5.8. Each time distribution is made up of the PMT hit time with

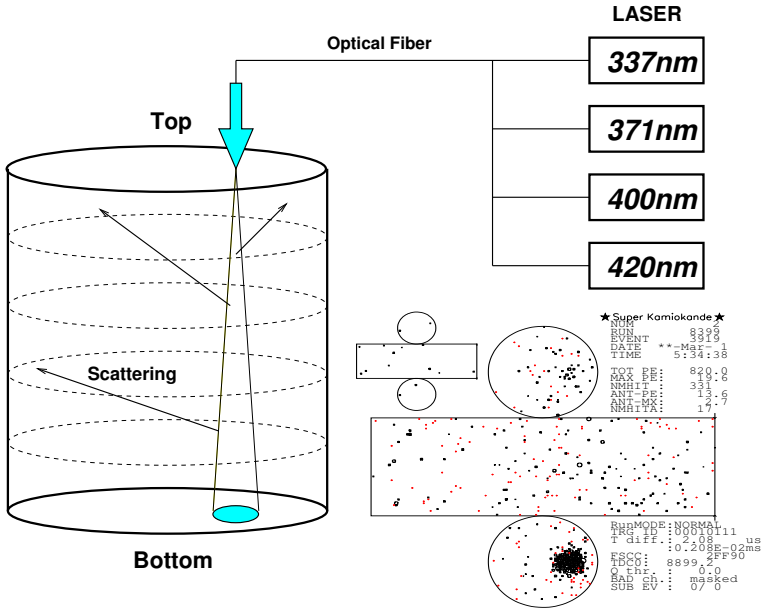

Figure 5.7: Water parameter calibration by laser setup. Multiple wavelengths were prepared such that the wavelength dependence of photon scattering and absorption could be studied. The event display shows the output from the laser firing through the light injector installed at the top of the tank. A ∼10 m spot can be seen at the bottom of the tank, the charge inside is used to normalise the analysis distributions. The hits elsewhere are due to scattering, and reflections for later timing.

the time-of-flight from the centre of the bottom spot subtracted. This causes the distributions to form a peak on the right due to the reflected light. The distributions are also normalised by the charge detected in the bottom spot to account for variations in intensity of the laser source. The first bump in the distribution is due to scattered light. The general shape gives information about the scattering, while the falling slope is influenced by the absorption of photons. The division of the barrel into the different regions also gives some information about the angular distribution of the scattering. The distributions are made for both data and MC.

The simulation uses the SKDETSIM software. The light injector is simulated by generating a virtual particle called a *geantino* at the position of the light injector. The geantino immediately bursts into a large number of photons, with a specified opening angle pointing into the tank. A separate MC is generated for each laser wavelength, and the absorption, symmetric scattering and asymmetric scattering probabilities are varied. By finding the MC with the set of water parameters that minimises the χ^2 with the laser data, the value of each attenuation coefficient can be found for one wavelength. This measurement is repeated for each of the other wavelengths, producing the attenuation coefficient, L^{-1}, plot shown in Figure 5.9.

5.2.1 Rayleigh and Mie Scattering

The primary process by which photons scatter is by Rayleigh Scattering on the local changes in density in the water, which has a forward-backward symmetric angular distribution. When the photons encounter a small dust-like particle in the water comparable in size to the wavelength,

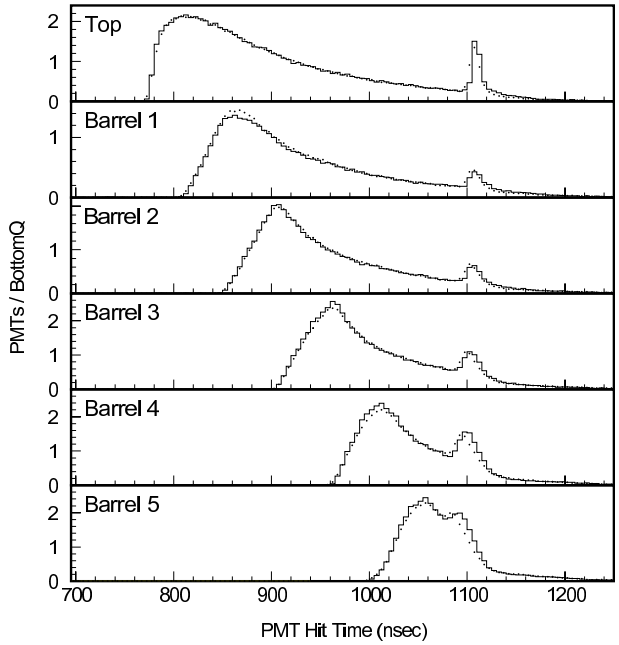

Figure 5.8: The timing distributions used for the water parameter analysis. Here the detector has been divided into the top and five barrel regions. The time-of-flight from the laser spot on the bottom is subtracted. This causes the reflection peak on the right of the distributions. The charge in the spot is used to normalise the distributions to account for differences in the laser intensity. The first bump gives information about the scattering and absorption of photons when the MC is compared with data. Only the first bump region is used in the χ^2 analysis.

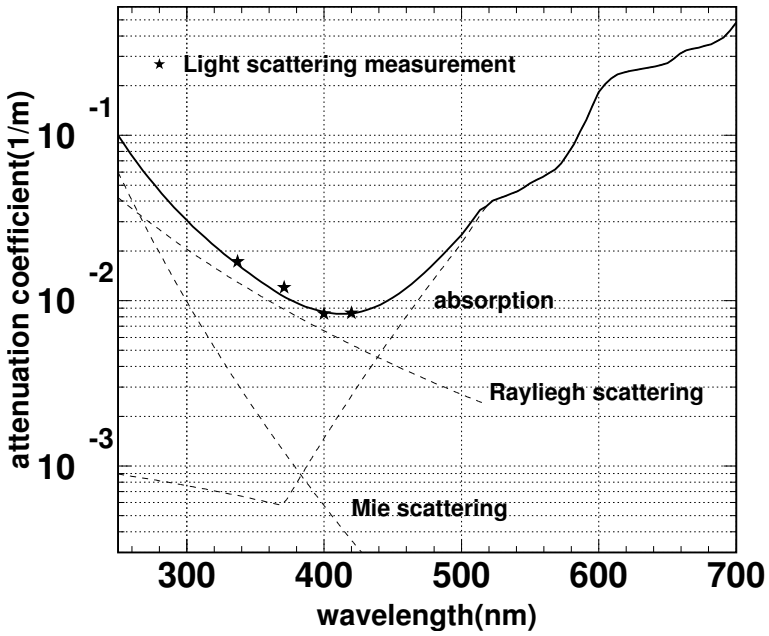

Figure 5.9: Attenuation Coefficient L^{-1} from the water parameter calibration. By comparing the MC and data and minimising the χ^2, absorption and scattering information is extracted for each wavelength. The attenuation coefficients are summed as shown in Equation (5.3).

then Mie Scattering has an increased probability of occurring. The angular distribution of Mie scattering varies from a forward-backward symmetric shape to a considerably forward form, depending on the distribution of small dust-like particles in the detector. Since it is difficult to know the exact size distribution of small particles, there is not a formal treatment of Mie scattering. Instead, the scattering is approximated by a symmetric contribution and an asymmetric forward-scattering component. In this way, the calibration can measure the primary symmetric contribution, while allowing for forward-scattering.

5.3 Energy Calibration

The momentum of detected particles is reconstructed from the charge information collected by the PMTs. It is essential to understand the absolute energy scale as accurately as possible, and to determine the systematic uncertainty of the energy scale for the atmospheric neutrino analyses. To study this, four sources are used, listed from lowest to highest energy:

- Momentum of decay electrons ($\sim$50 MeV/c)
- The invariant mass of π^0 events produced by neutrinos ($\sim$140 MeV/c)
- Cherenkov angle of low energy stopping muons (200$\sim$500 MeV/c)
- Track range of high energy stopping muons (1$\sim$10 GeV/c)

The data from the above sources is compared with the MC prediction to estimate the accuracy of the absolute energy scale.

5.3.1 Decay Electrons

There are many electons detected by Super-Kamiokande from the decay of stopping cosmic-ray muons. The decay electrons have a spectrum of energies below $\sim$53 MeV, known as the Michel spectrum. This energy spectrum is compared between the observed data and MC in order to check the energy scale.

The decay electrons are selected by requiring the following criteria:

1. The time interval from a stopping muon event is 1.5 μsec to 8.0 μsec.
2. The number of hit PMTs in a 50 nsec time window is greater than 60 (30 for SK-II).
3. The goodness of the vertex fit is greater than 0.5 .
4. The vertex position is reconstructed more than 2 m away from the ID wall.

The first criterion selects the timing range where the decay electron search is reliable, while the second criterion rejects $\sim$6 MeV γ-rays from μ^- capture on a nucleon.

The momentum spectra of the decay electrons is shown in Figure 5.10. It can be seen that the tail of the spectra extends up to around $\sim$70 MeV/c, which is a discrepancy from the expected Michel spectrum. This is due to μ^- capture on the K-Shell (1 shell) of an Oxygen atom, resulting in a decay electron that is influenced by the electric potential of the oxygen nuclei and the μ^- orbital motion [249]. The simulation considers this effect, making use of the measured μ^+/μ^- ratio of 1.37 [250].

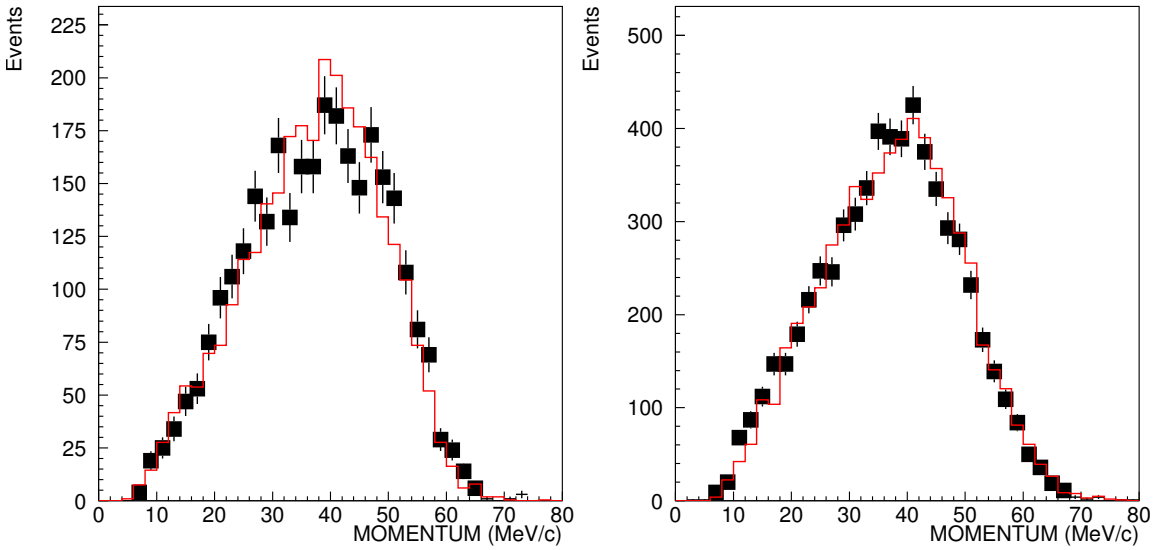

Figure 5.10: Momentum spectra for the decay electrons. The michel spectra is expected to have a momentum distribution up to ∼53 MeV/c, whereas this distribution extends towards ∼70 MeV. This is due to effects from μ^- decaying in orbit of an Oxygen nucleus. The effect is considered in the MC. The left (right) plot shows the distribution for SK-I (SK-II).

The vertex fitter used is one that was developed for low energy neutrino observations for analyses of solar and supernova neutrinos, where the maximum goodness is 1. The mean values of data agree with the MC prediction within 0.6%, 1.6%, and 0.8% for SK-I, SK-II and SK-III, respectively.

5.3.2 Neutrino Induced π^0 Events

There are NC neutrino interactions whereby a single π^0 is produced, immediately decaying into two γ-rays. Checking the combined momentum of the two γ-rays and reconstructing the invariant mass of the π^0 allows the energy scale to be checked in the few hundred MeV energy region. The invariant mass of the π^0 can be reconstructed as:

$$M_{\pi^0} = \sqrt{2P_{\gamma 1}P_{\gamma 2}(1-\cos\theta)} \tag{5.4}$$

where $P_{\gamma 1}$ and $P_{\gamma 2}$ are the momenta of the two γ-rays, and θ is the opening angle between them. The π^0 events are selected from the atmospheric neutrino data by the following criteria:

1. Two Cherenkov rings are reconstructed and both of them are identified as electron-like.
2. No electrons from muon decay were detected.
3. The vertex position is reconstructed more than 2 m away from the ID wall.

The second criterion rejects events where charged pions were also produced with the π^0 (e.g. $\pi^+\pi^0$), or charge current events (i.e. $\mu^\pm\pi^0$). A typical π^0 event, where the two γ-ray rings can be clearly seen is shown in Figure 5.11. The reconstructed momentum of the selected events

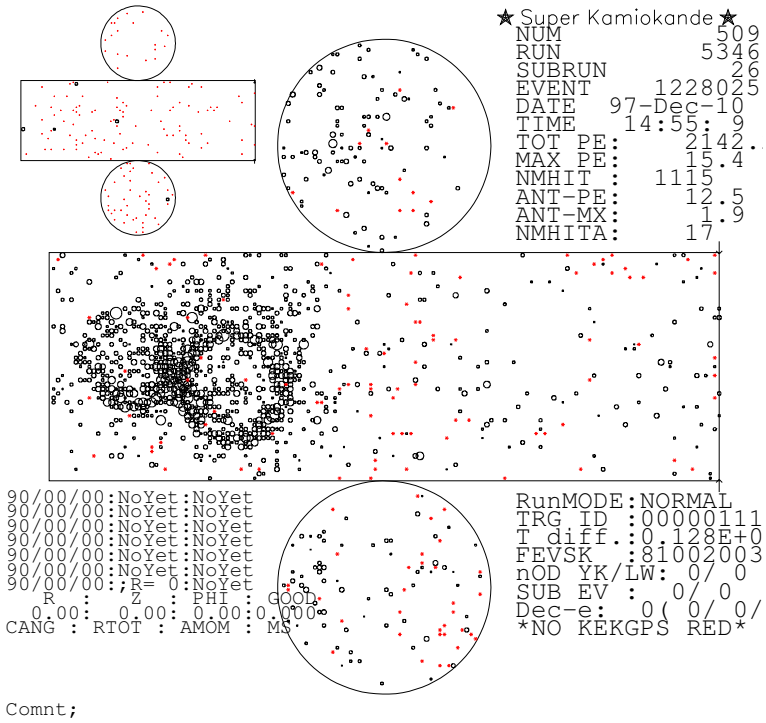

Figure 5.11: A typical π^0 event display clearly showing two rings from the two γ-ray products.

is shown in Figure 5.12. There is a clear peak around $\sim$140 MeV/c^2, confirming that the they originated from the decay of a π^0.

The actual π^0 mass is $\sim$135 MeV/c^2, whereas the mean invariant mass reconstructed is $\sim$139 MeV/c^2. This shift to a slightly larger mass can be explained by mainly two reasons. Firstly, the π^0 is produced with an interaction with an Oxygen nucleus, which is left in an excited state. There are de-excitiation γ-rays that are also included in the interaction that add a few additional MeV to the event. The second is that the γ-rays from the decay of the π^0 propagate for a short distance before breaking into an electromagnetic shower. This results in the vertex being reconstructed slightly in the forward direction, and the opening angle between the γs being reconstructed slightly larger, giving a larger π^0 invariant mass.

The MC considers the de-excitation of the oxygen nucleus, so there is a good agreement between the data and MC. The peak position of the data is higher than that of the MC by 0.6%, 1.6% and 0.8% for SK-I, SK-II and SK-III, respectively.

5.3.3 Low Energy Stopping Muons

There is a close relationship between the Cherenkov opening angle and momentum, if the momentum is not many times larger than the mass of the particle. So using low energy stopping muons ($<$ 400 MeV/c), the momentum can be estimated from the reconstructed opening angle. By comparing the reconstructed momentum from the observed charge ($P_{\text{p.e.}}$) to the momentum estimation from the Cherenkov opening angle (P_θ) for data and MC, the systematic uncertainty in the momentum reconstruction can be estimated. The Cherenkov opening angle expressed as

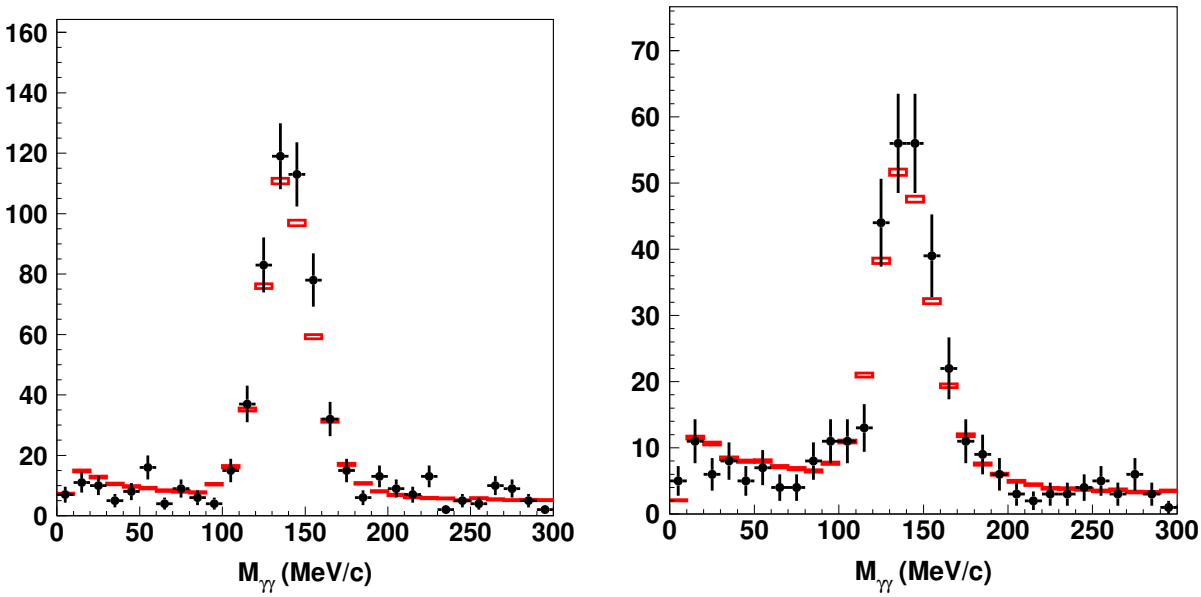

Figure 5.12: Reconstructed invariant π^0 mass from the two detected γ-rays. The π^0 mass is $\sim$135 MeV/c^2, whereas $\sim$139 MeV is observed. This is due to the additional detection of de-excitation γ-rays from the Oxygen, and the slightly forward reconstructed vertex. The left (right) plot shows the distribution for SK-I (SK-II).

a function of the momentum is:

$$\cos\theta_c = \frac{1}{n\beta} = \frac{1}{n}\sqrt{1+\frac{m^2}{p^2}} \tag{5.5}$$

where θ_c is the Cherenkov opening angle, n is the index of refraction for water, $\beta = \frac{v}{c}$, while m and p are the mass and momentum of the ring. Note that electrons and high energy muons are too relativistic, and the Cherenkov opening angle converges to a limit as $\beta \to 1$. Since their momentum is large compared to their mass. In such cases, the momentum cannot be estimated accurately from the Cherenkov angle. The low energy stopping muons are selected by the following criteria:

1. The total charge in the ID is less than 1500 p.e. ($<$750 for SK-II)
2. One cluster of hit PMTs in the outer detector.
3. The entrance point is on the top wall.
4. The direction is downward ($\cos\theta > 0.9$).
5. One decay electron event is detected.

The first criterion selects low energy muons. The second to fourth criteria selects very vertical, downward going stopping muons. The fifth criterion improves the purity for muon events.

Figure 5.13 shows the momentum and Cherenkov opening angle distributions for the selected events. In Figure 5.14 the momentum estimated from the charge is compared with the estimation

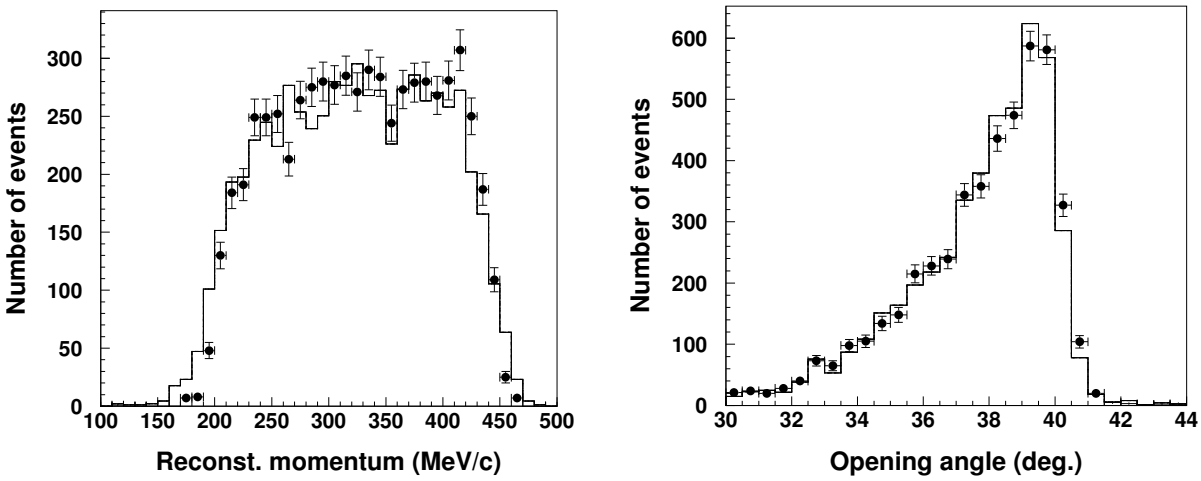

Figure 5.13: Low energy stopping muon reconstructed momentum and Cherenkov angle (SK-II).

from the Cherenkov opening angle, $P_{p.e.}/P_\theta$, on the left. The ratio is compared between data and MC in the right plots, as a function of the expected momentum P_θ. The agreement is within 0.7%, 1.3%, and 2.1% for SK-I, SK-II and SK-III, respectively.

5.3.4 High Energy Stopping Muons

The track length of high energy stopping muons is approximately proportional to the muon momentum. So it can be used to make an independent check of the momentum reconstruction (by observed charge) in the 1 GeV/c to 10 GeV/c momentum range. The following criteria are used to select high energy stopping muons:

1. The entrance point is on the top wall.
2. The direction is downward ($\cos\theta > 0.94$).
3. One decay electron event is detected.
4. The reconstructed range of the muon track is greater than 7 m.

The first three criteria select very vertical downward going muons. The fourth criterion selects high energy events. The range of the muon is determined from the distance between the entrance point of the stopping muon and the vertex position of the following decay electron. Figure 5.15 shows the mean ratio of momentum/range against the range (left), and the MC/Data comparison for this ratio (right). A clear momentum loss of ∼2.3 MeV/c per cm can be seen. There is a slight momentum dependence observed, however the data and MC are in agreement within 0.7%, 1.1%, and 2.0% for SK-I, SK-II and SK-III, respectively.

5.3.5 Time Variation of Energy Scale

The stability of the energy scale is monitored by the time variation of the decay electron and stopping muon measurements. The mean momentum of decay electrons is watched over time as shown in the top panels of Figure 5.16, with the bottom panels showing the difference between

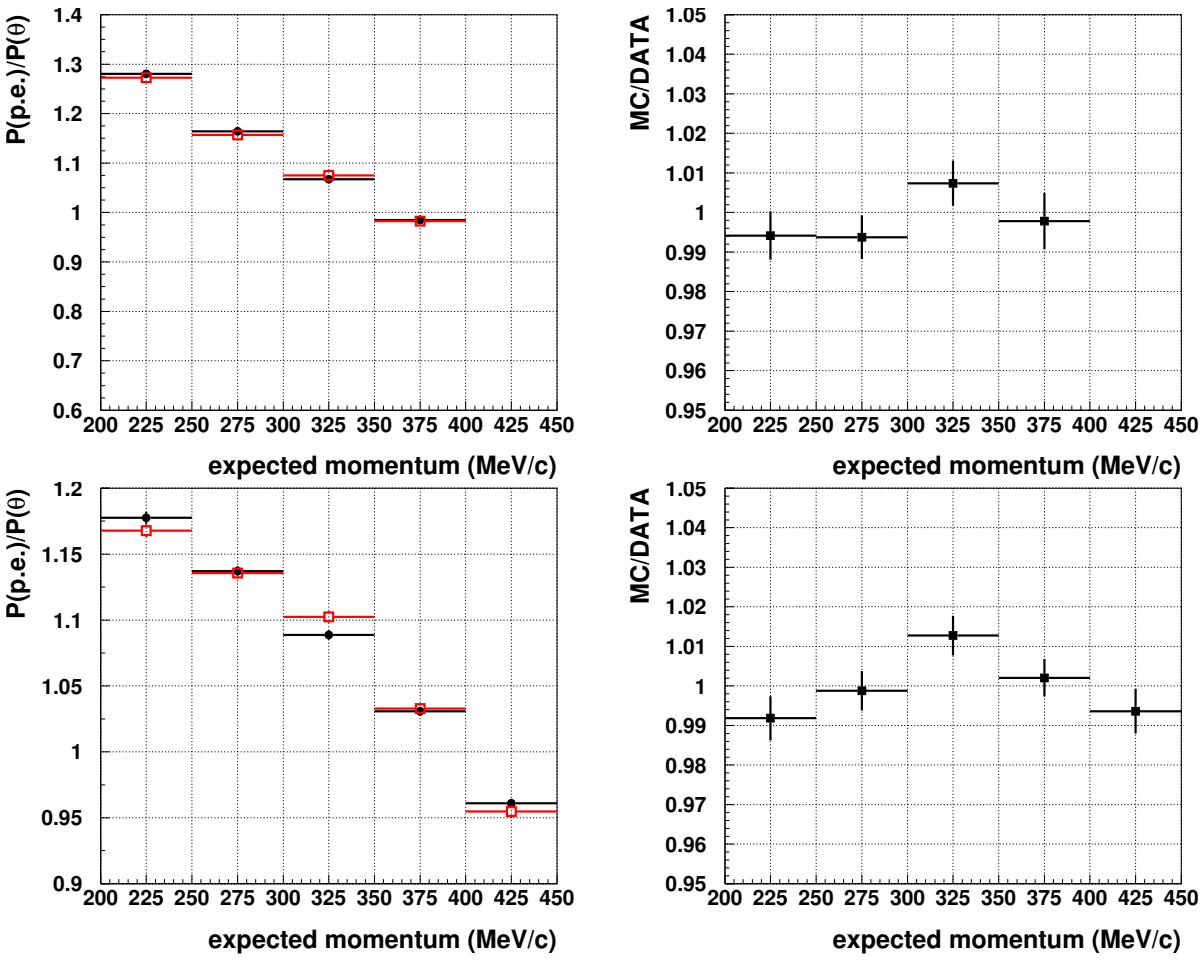

Figure 5.14: Low energy stopping muon distributions. The ratio of the momentum expected from the charge to the momentum estimated from the Cherenkov angle, $P_{p.e.}/P_{\theta}$, is shown on the left. The MC/Data for the $P_{p.e.}/P_{\theta}$ ratio is shown on the right. The top (bottom) plots show the distributions for SK-I (SK-II).

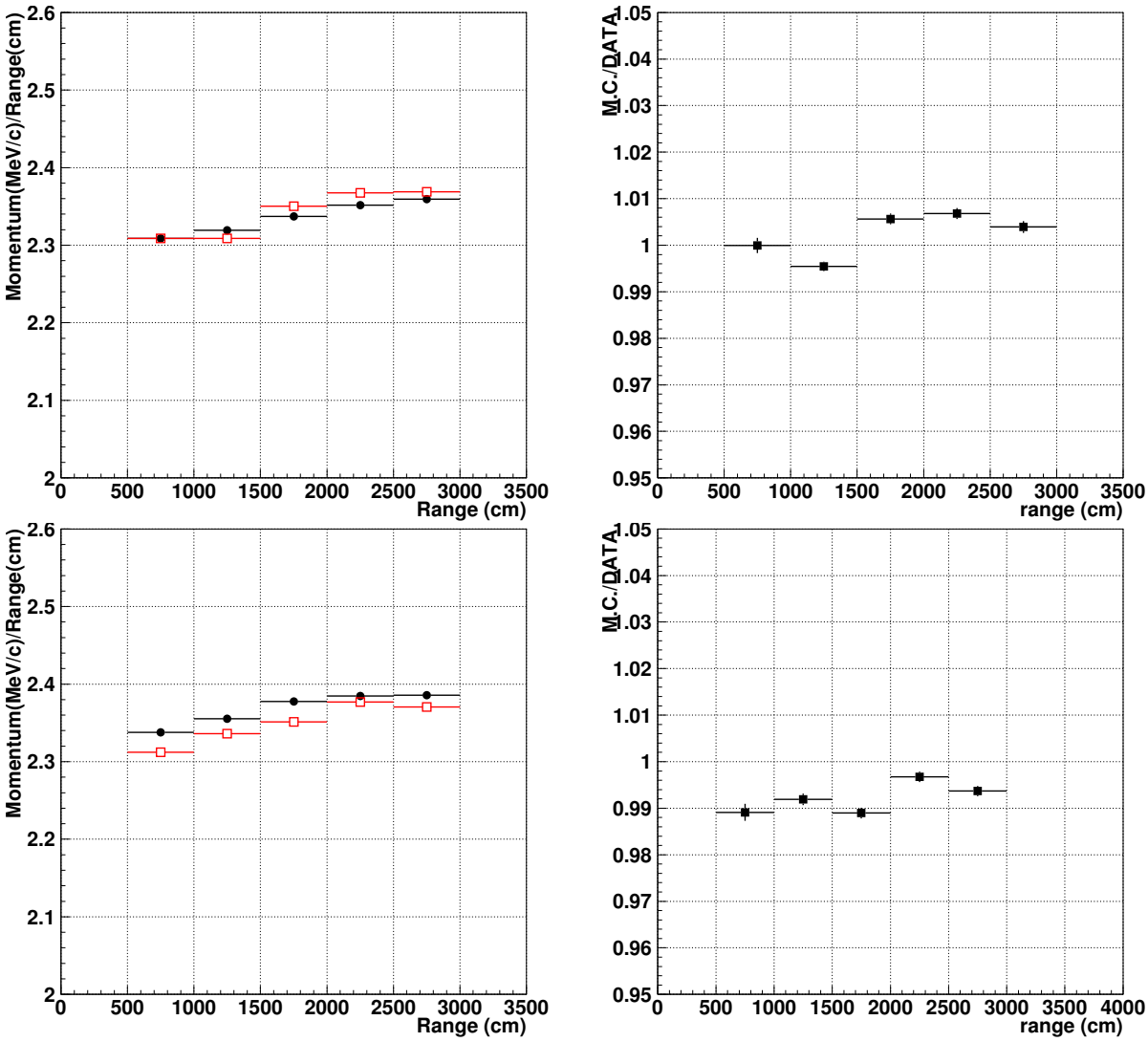

Figure 5.15: High energy stopping muon distributions of the ratio momentum/range against the range (left), and the MC/Data comparison for this ratio (right). A near constant relationship can be seen for momentum and range, ∼2.3 MeV per cm. This ratio slightly increases with range (i.e. momentum), however there is still about a ∼1% agreement between MC and data. The top (bottom) plots show the distributions for SK-I (SK-II).

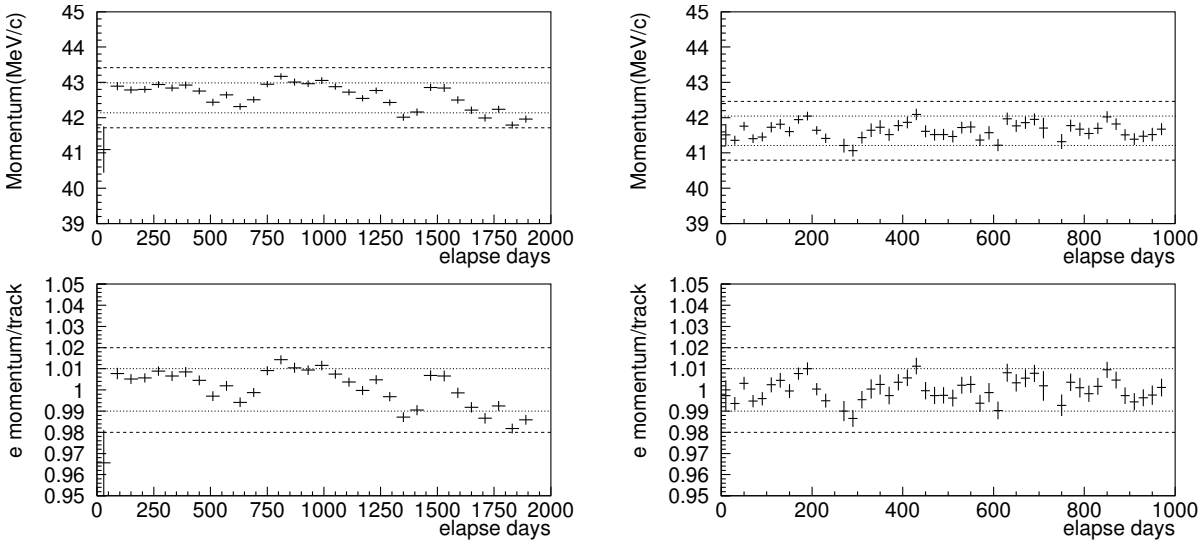

Figure 5.16: Time variation of the decay electron momentum average (top) and the difference between data and MC (bottom). The dotted lines show a 1% variation, and the dashed a 2% variation. The left (right) plots show the time variation in elapsed days since the beginning of SK-I (SK-II).

data and MC. For the stability of the energy scale at high energies, the average momentum/range of stopping muons is monitored as in the top panels of Figure 5.17, while the lower panels show the difference between data and MC. The RMS of the variation is 0.88%, 0.55%, and 1.79% for SK-I, SK-II, and SK-III.

5.3.6 Summary of Energy Scale Calibrations

A summary of the absolute energy scale calibration, showing the contribution from each sample, can be seen in Figure 5.18. A momentum range from a few MeV to about ∼10 GeV is checked which covers the energy range of FC events and low energy PC events well. A good agreement can be seen between the data and MC for the full momentum range, and the variation in the energy scale is estimated to be within 0.74%, 1.60%, and 2.08% for SK-I, SK-II and SK-III, respectively. This absolute variation of the energy scale is combined with the expected variation of the energy scale over time to give an estimation of the systematic error. The systematic uncertainty for the energy scale is estimated to be 1.1%, 1.7% and 2.7% for SK-I, SK-II, and SK-III, respectively.

5.3.7 Uniformity of Energy Scale

The uniformity of the detector is measered using the decay electrons from the cosmic ray muons. They are good calibration sources to check the detector uniformity, because the vertex is distributed uniformly in the fiducial volume and the momentum distribution is almost uniform in all directions. To take into account the muon polarization, only electrons whose direction is perpendicular to the parent muon direction are used. This condition is -0.25< $\cos\Theta_{e\leftrightarrow\mu}$ < 0.25, where $\cos\Theta_{e\leftrightarrow\mu}$ is the opening angle between the electron and muon directions. Figure **??** shows

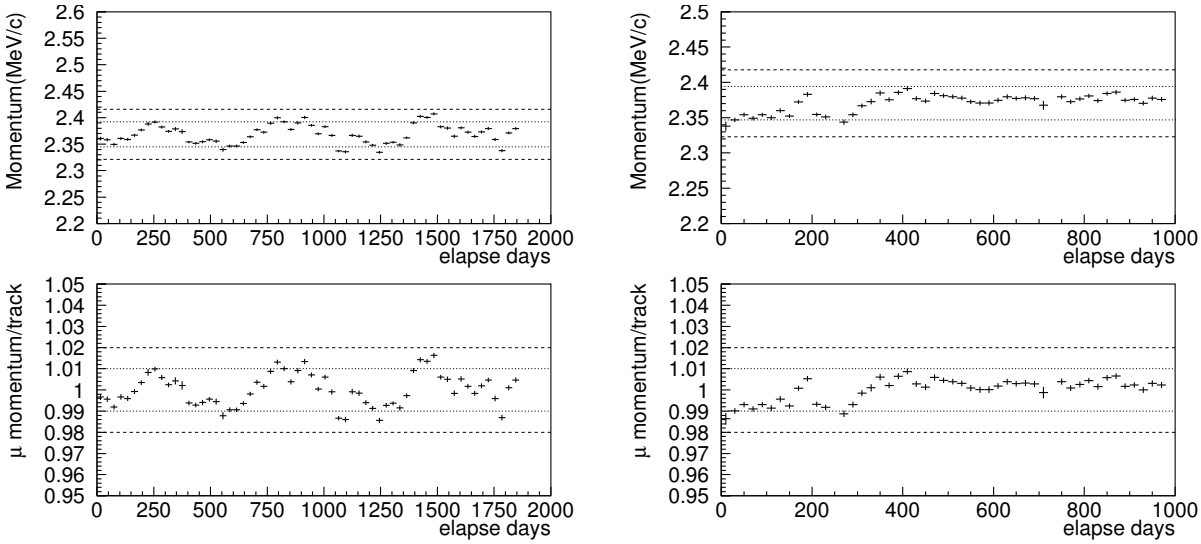

Figure 5.17: Time variation of the stopping muon momentum/range average (top) and the difference between data and MC (bottom). The dotted lines show a 1% variation, and the dashed a 2% variation. The left (right) plots show the time variation in elapsed days since the beginning of SK-I (SK-II).

the averaged momentum of decay electrons for the Monte Carlo events normalized by that for data as a function of the zenith angle of the electrons. From this figure, the detector gain is uniform within $\pm 0.6\,\%$ for SK-I and SK-II.

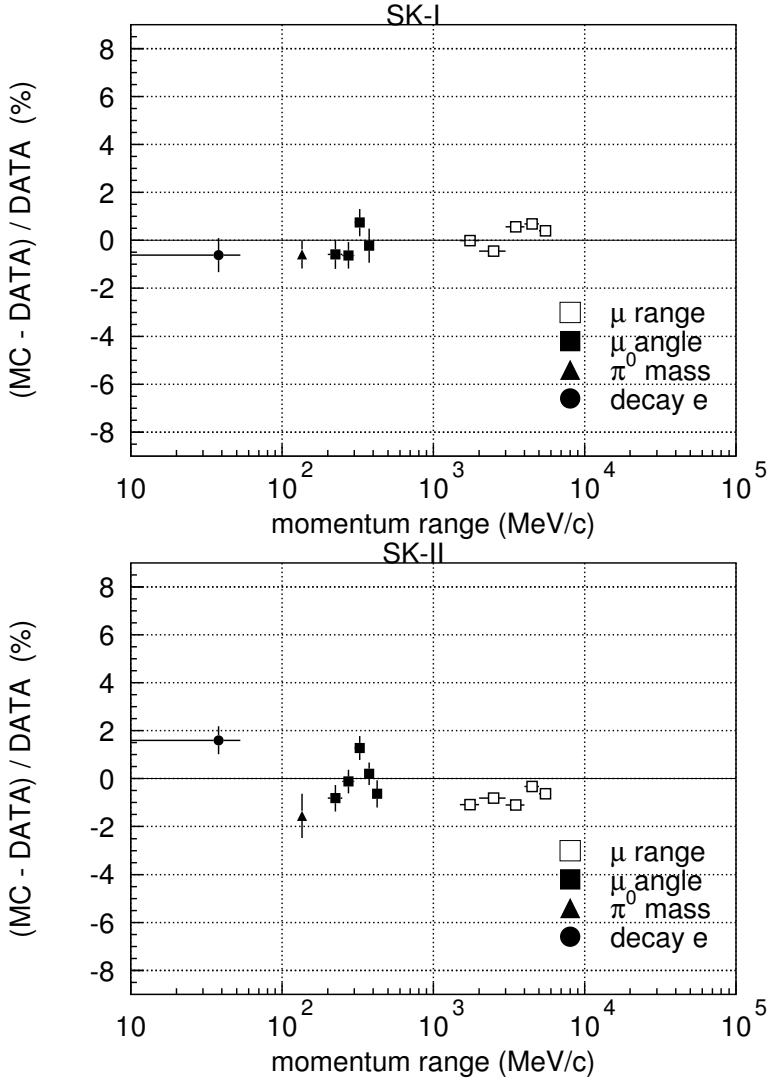

Figure 5.18: Summary of energy scale calibrations. The percentage differences between data and MC are shown for: mean momentum from decay electrons; the peak position of the π^0 invariant mass;

Chapter 6

Data Reduction

6.1 Overview

Super-Kamiokande collects around 10^6 events per day from it's *High Energy* and *Low Energy* triggers. However, only around 10 events per day are expected in the atmospheric neutrino data. Most of the events recorded by the DAQ are expected to be background events originating from cosmic-rays, environmental radiation and their by-products. Therefore an effective procedure is required to select the neutrino events of interest from all the background events.

There are four classifications for the atmospheric neutrino events observed: *Fully-Contained* (*FC*), *Partially-Contained* (*PC*), *Upward Stopping Muons*, and *Upward Through-Going Muons* (the last two collectively referred to as *UPMU*). The events are classified into these categories depending on the location of the original neutrino interaction vertex and the containment of the interaction products, as summerised in Figure 6.1.

The FC and PC events require that the neutrino interaction vertices are inside the *Fiducial Volume* of the Inner Detector (ID). The Fiducial Volume (FV) is typically defined to be 2 m from the ID wall. In the L/E analysis, a slightly larger region is used to increase the statistics. However, the 2 m FV is assumed for the figures in this chapter. The FV is selected such that the events can be reconstructed reliably. When all the interaction products are contained within the ID, then the event is classified as FC. If one of the particles exits the ID and deposits energy in

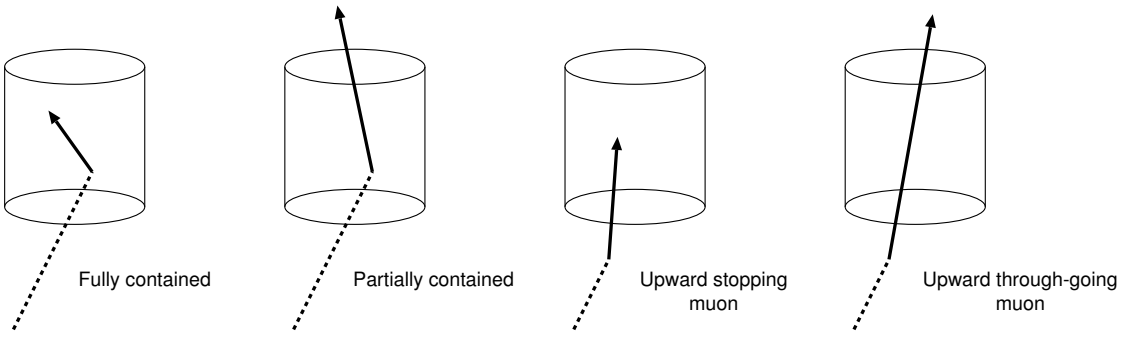

Figure 6.1: Event categorisation of the atmospheric data into FC, PC and the two UPMU selections. The dashed lines represent incoming neutrinos, the solid lines interaction products, and the cylinders the Inner Detector volume.

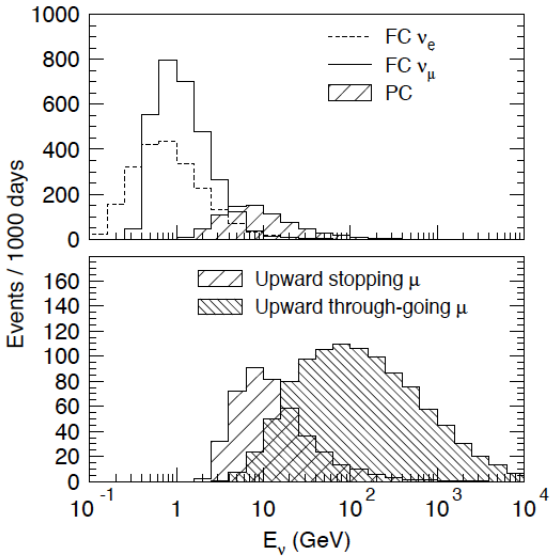

Figure 6.2: The expected energy distributions for each of the event classifications. The upper figure shows the FC and PC events, and UPMU events are shown in the lower figure.

the Outer Detector (OD), then the event is classified as PC.

There is an UPMU sample to study high energy neutrinos. When energetic neutrinos interact in the rock beneath the Super-Kamiokande detector, sometimes the muons will enter the ID volume. Unlike the downward-going muons which consist mostly of cosmic-ray products, these muons are likely to have been induced by neutrino interactions. If these neutrino-induced muons stop in the ID then the event is classified as Upward Stopping Muon; and Upward Through-Going Muon if the muon passes through the ID.

The mean energies of these event categories are ∼1 GeV for FC, ∼10 GeV for PC and Stopping UPMU, and ∼100 GeV for Through-Going UPMU, which can be seen in Figure 6.2. The data reduction procedures are different for each of these categories and are described in this chapter.

6.2 Reduction for Fully-Contained Sample

The FC events are separated from PC events by the activity in the OD. FC events require that the number of PMT hits in the highest charge cluster is less than 16 (10 for SKI):

- NHITAC $<$ 16 (10 for SKI).

There are 5 reduction steps described here. Note that in the SK-II period, the PMT coverage in the ID was around half of that in the other SK periods, so the numbers for SKII are quoted separately.

6.2.1 First Reduction

The First Reduction removes a lot of the basic background events and has the following criteria:

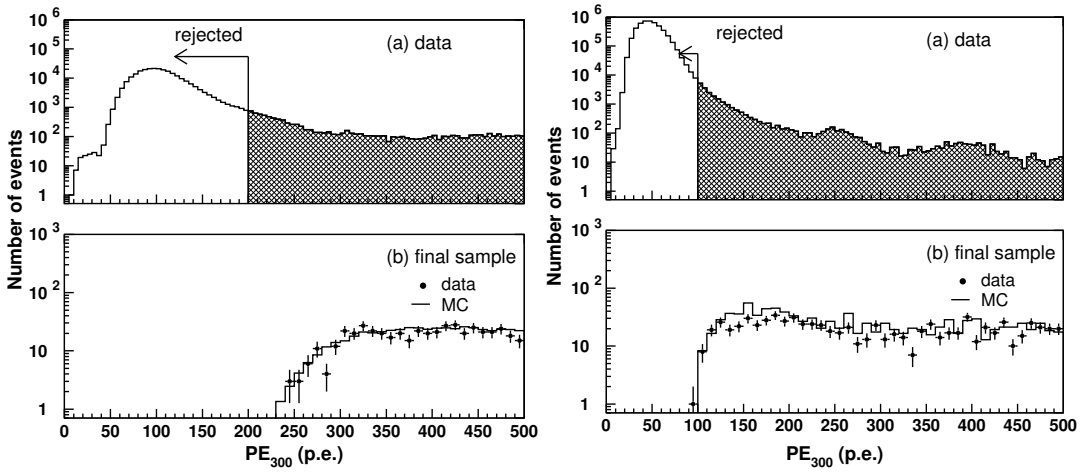

Figure 6.3: FC First Reduction: PE_{300} distributions for (a) raw data and (b) the final sample data and non-oscillated MC normalised to the data. Distributions are for SK-I (left) and SK-II (right). The PE_{300} cut criteria arrows mark the rejected events.

(1) $PE_{300} \geq 200$ p.e.s (> 100 p.e.s for SK-II).
PE_{300} is the maximum number of total p.e.s observed by the ID PMTs in a sliding 300 nsec time window.

(2) $NHITA_{800} \leq 50$ or OD trigger is off.
$NHITA_{800}$ is the number of hit OD PMTs in a fixed 800 nsec time window from -400 nsec to $+400$ nsec before and after the trigger timing.

(3) TDIFF $> 100\,\mu$sec
TDIFF is a time interval to the previous event.

Criterion (1) removes the low energy background events from environmental or induced radioisotopes. Figure 6.3 shows the PE_{300} distributions for the raw data and the FC final events. The 200 p.e.s (100 p.e.s for SK-II) corresponds to 22 MeV/c of electron momentum. Note that in the analyses events with visible energy below 30 MeV are not used. Criterion (2) rejects the cosmic ray muon events. Figure 6.4 shows the $NHITA_{800}$ distributions for the raw data, FC atmospheric neutrino Monte Carlo events and the FC final events. Criterion (3) discards events that could be contaminated by decay electrons from cosmic ray muons that stopped in the ID prior to the event. The events within 30 μsec after the selected events by the above criteria are selected as sub-events to keep any decay electrons. These cuts reduce the data size from 10^6 events/day to $\sim$3000 ($\sim$2200) events/day (for SK-II).

6.2.2 Second Reduction

In the Second Reduction low energy events and cosmic ray muons are rejected by the following critera:

(1) $NHITA_{800} \leq 25$ if $PE_{tot} < 100{,}000$ p.e.s (50,000 for SK-II) or OD trigger is off.

(2) $PE_{max}/PE_{300} < 0.5$.
PE_{max} is the maximum number of p.e.s observed by an ID PMT.

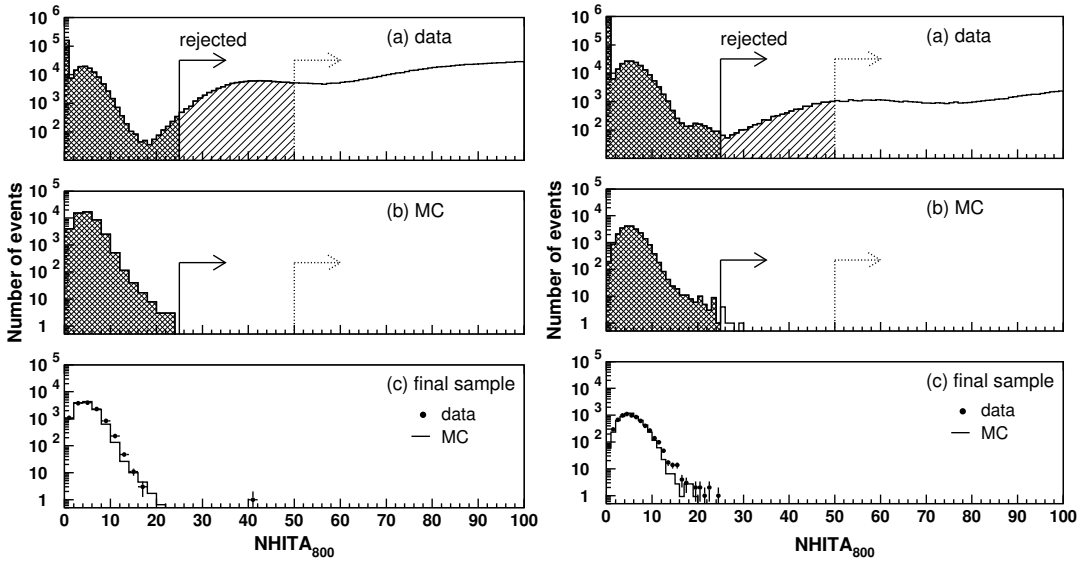

Figure 6.4: FC Reduction: NHITA_{800} distributions for (a) raw data, (b) MC with vertex $> 2\,\mathrm{m}$ from the wall, (c) final sample data and MC normalised to the data. Distributions are for SK-I (left) and SK-II (right). The NHITA_{800} cut criteria dotted (solid) arrows mark the rejected events for FC First (Second) Reduction.

Criterion (1) removes more cosmic ray muons by a tighter threshold than the First Reduction. Figure 6.4 also shows the stricter cut on NHITA_{800} by the solid lines. Criterion (2) rejects low energy and electrical noise events, where most of the recorded charge is from a single PMT. Figure 6.5 shows the $\mathrm{PE}_{\mathrm{max}}/\mathrm{PE}_{300}$ distributions for the data after First Reduction, the FC atmospheric neutrino MC events and the FC final events. This cut also discards some of the *Flasher* events. Sometimes a PMT spontaneously starts flashing due to discharges in the dynode structure, recording a very large charge. Such a background is called a Flasher event. Further Flasher events are reduced at a later stage. After the FC Second Reduction the event rate is $\sim$200 ($\sim$280) events/day (for SK-II).

6.2.3 Third Reduction

After the First and Second Reduction, the remaining background events are mostly electronic noise events and cosmic ray muons which have a small number of OD hits.

Through-Going Muon Cut

There are still some through-going muon events after the basic cuts in the previous reduction steps, which have fewer hits in the OD. To eliminate these events, a through-going muon fitter is applied if the charge in a single PMT is greater than 230 p.e.s. This fitter reconstructs a track by selecting an entrance point and an exit point. The entrance point is selected from the earliest hit PMT together with some neighbouring PMTs and the exit point from the centre of the saturated

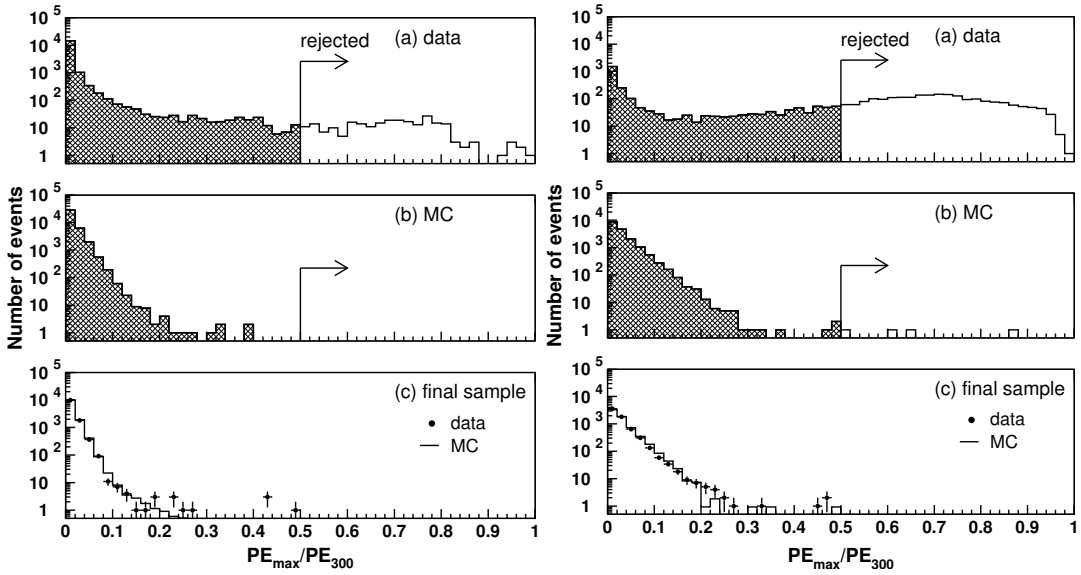

Figure 6.5: FC Second Reduction: PE_{max}/PE_{300} distributions for (a) data after FC1, (b) FC MC, (c) final sample data and MC normalised to the data. Distributions are for SK-I (left) and SK-II (right). The PE_{max}/PE_{300} cut criteria arrows mark the rejected events.

ID PMTs. The goodness of the fit is defined as:

$$Goodness = \frac{1}{\sum_i \frac{1}{\sigma_i^2}} \times \sum_i \frac{1}{\sigma_i^2} \exp\left(-\frac{(t_i - T_i)^2}{2(1.5 \times \sigma_i)^2}\right) \tag{6.1}$$

where t_i and σ_i are the observed hit time of the i-th PMT and its resolution, and T_i is the hit time expected from the entering time of muon and its track.

There is an additional requirment for the SK-II period, that the number of hit ID PMTs exceeds 1000. The rejection criteria for through-going muons are:

(1) $PE_{max} > 230$ p.e.s (and NHIT > 1000 for SK-II)

(2) *Goodness* of the Through-Going Muon Fit > 0.75

(3) $NHITA_{in} \geq 10$ or $NHITA_{out} \geq 10$
$NHITA_{in}$ ($NHITA_{out}$) is the number of hit OD PMTs located within 8 m from the entrance (exit) point in a fixed 800 nsec time window.

Figures 6.6 and 6.7 show the number of hit OD PMTs near the entrance and the exit points for the data after Second Reduction, the FC atmospheric neutrino MC events and the FC final events. satisfying the above criteria (1) and (2).

Stopping Muon Cut

To remove stopping muons a Stopping Muon Fitter is applied, which finds the entrance point in a similar way to the through-going case. Then the rejection criteria for stopping muons are:

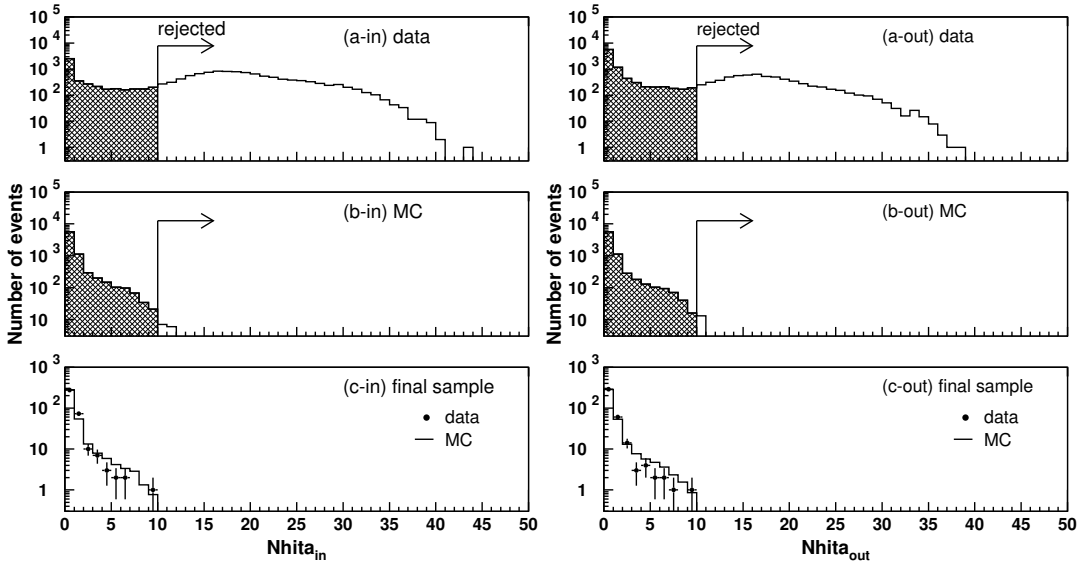

Figure 6.6: FC Third Reduction: through-going muon, SK1 $\mathrm{NHITA_{in}}$ and $\mathrm{NHITA_{out}}$ distributions for (a) data after FC2, (b) FC MC, (c) final sample data and MC normalised to the data. The $\mathrm{NHITA_{in}}$ and $\mathrm{NHITA_{out}}$ cut criteria arrows mark the rejected events.

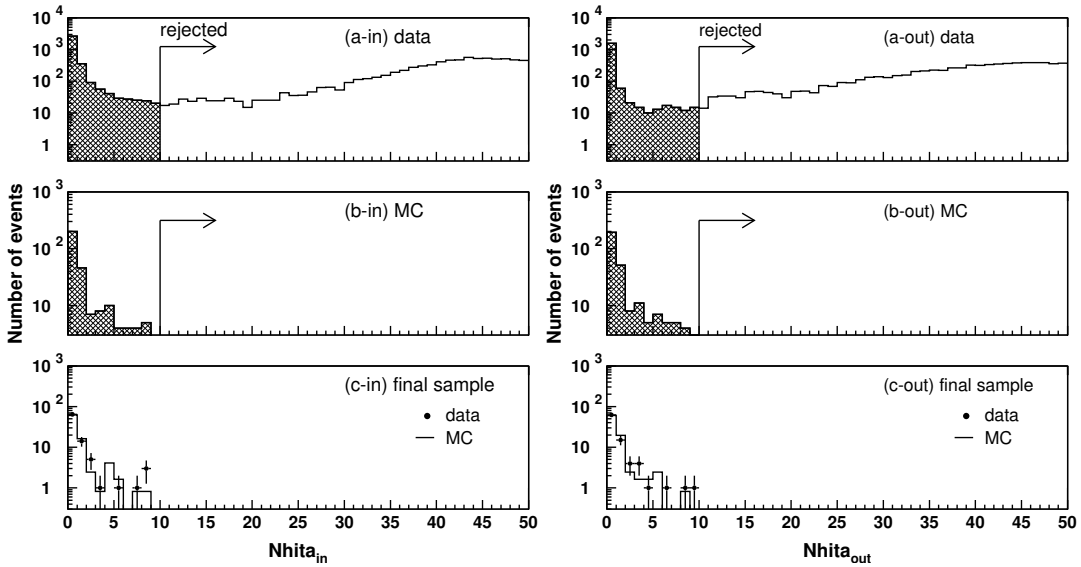

Figure 6.7: FC Third Reduction: through-going muon, SK2 $\mathrm{NHITA_{in}}$ and $\mathrm{NHITA_{out}}$ distributions for (a) data after FC2, (b) FC MC, (c) final sample data and MC normalised to the data. The $\mathrm{NHITA_{in}}$ and $\mathrm{NHITA_{out}}$ cut criteria arrows mark the rejected events.

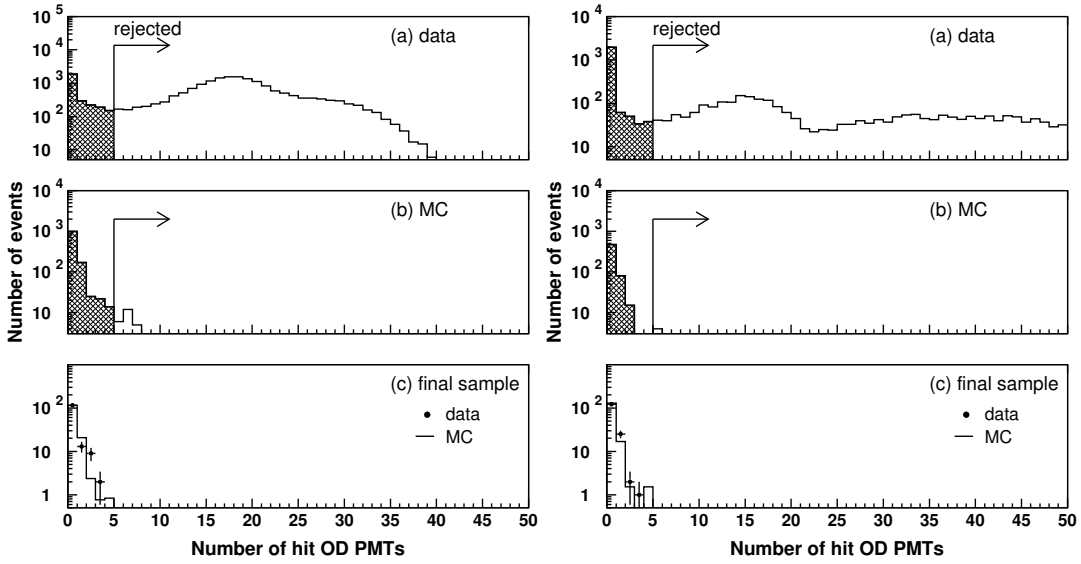

Figure 6.8: FC Third Reduction: stopping muon, $\mathrm{NHITA_{in}}$ distributions for (a) data after FC2, (b) FC MC, (c) final sample data and MC normalised to the data. Events shown have goodness >0.5. Distributions are for SK-I (left) and SK-II (right). The $\mathrm{NHITA_{in}}$ cut criteria arrows mark the rejected events.

(1) $\mathrm{NHITA_{in}} \geq 10$
or
$\mathrm{NHITA_{in}} \geq 5$ if Goodness of Stopping Muon Fit > 0.5
$\mathrm{NHITA_{in}}$ is the number of hit OD PMTs located within 8 m from the entrance point in a fixed 800 nsec time window.

The direction of the muon is reconstructed to maximize the total number of p.e.s inside a cone with a half opening angle of 42°. The goodness definition is same as that of through-going muon fit given in Equation (6.1). Figure 6.8 shows $\mathrm{NHITA_{in}}$ distributions for the data after Second Reduction, the FC atmospheric neutrino MC events and the FC final events. Events shown have goodness > 0.5.

Cable Hole Muons

On top of the detector tank, there are twelve cable holes to route in and out the data and HV supply cables. The passage of four out of the twelve cable holes through the OD form an inactive region, which could allow cosmic-ray muons to pass into the ID without an OD signal to remove them. To account for this scenario, a set of veto counters (2 m $\times$ 2.5 m plastic scintillation counters) were installed in April 1997, as depicted in Figure 6.9. The rejection criteria for the cable hole muons are:

(1) One veto counter hit

(2) $\mathrm{L_{veto}} < 4\,\mathrm{m}$
$\mathrm{L_{veto}}$ is the distance from the cable hole to the the reconstructed vertex.

Figure 6.10 shows the reconstructed vertex distributions for the FC 1-ring μ-like events before and after the installation of the veto counters. The cable hole muons are rejected well by the veto counters. Criteria (2) is there to save events that may have been rejected by electronic noise in the veto counters.

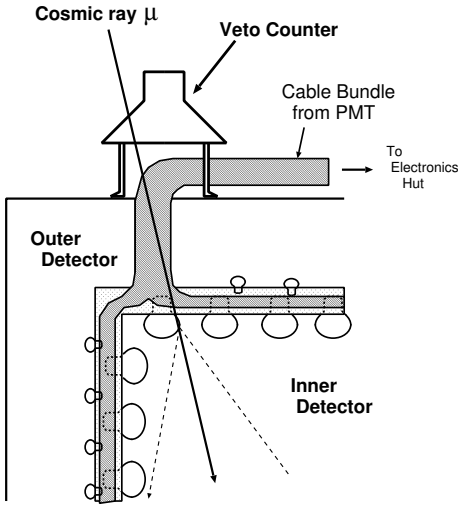

Figure 6.9: Illustration of the cable hole muon veto system, which shows how cosmic-ray muons passing through an inactive region of the OD can still be rejected.

Flasher Event Cut

Flasher events usually have a broad hit timing distribution compared with that of the neutrino events. The flasher events which exhibit this feature are removed by the following cut. The cut criteria are different for SK-I and are as follows:

(1) $\mathrm{NMIN}_{100} \geq 14$
or
$\mathrm{NMIN}_{100} \geq 10$ if the number of hit ID PMTs < 800
NMIN_{100} is the minimum number of hit ID PMTs in a sliding 100 nsec time window from +300 nsec to +800 nsec after the trigger.

From SK-II onwards, the cut criteria are:

(1) $\mathrm{NMIN}_{100} \geq 20$

Figure 6.11 shows the timing distribution and the time window searched for (i) a typical flashing PMT event and (ii) a typical FC neutrino event. NMIN_{100} is checked within the region enclosed by the arrows. Figure 6.12 shows a typical event display of a flasher event. An almost identical event can be seen $\sim$20 mins later. Figures 6.13 and 6.14 show the NMIN_{100} distributions for the data after Second Reduction, the FC atmospheric neutrino MC events and the FC final events.

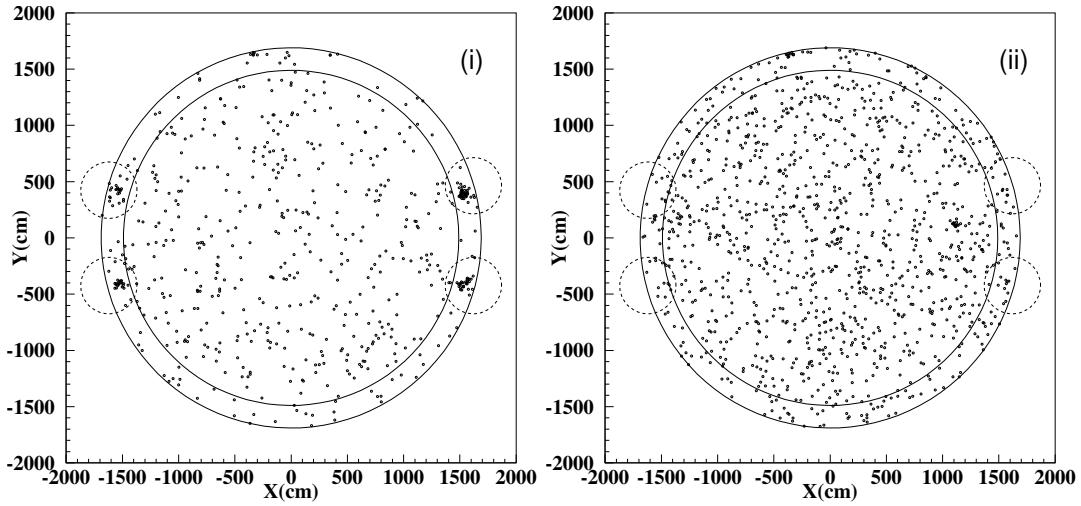

Figure 6.10: Reconstructed vertex distributions for the FC 1-ring μ-like events (i) before the installation of the veto counters and (ii) after the installation. The small dashed circles indicate the positions of the veto counters. Clusters of muon events can clearly be seen before the veto counters were installed, and no excess is seen after the installation. The outer solid circle shows the ID wall and the inner solid circle shows the fiducial volume (2 m from the wall).

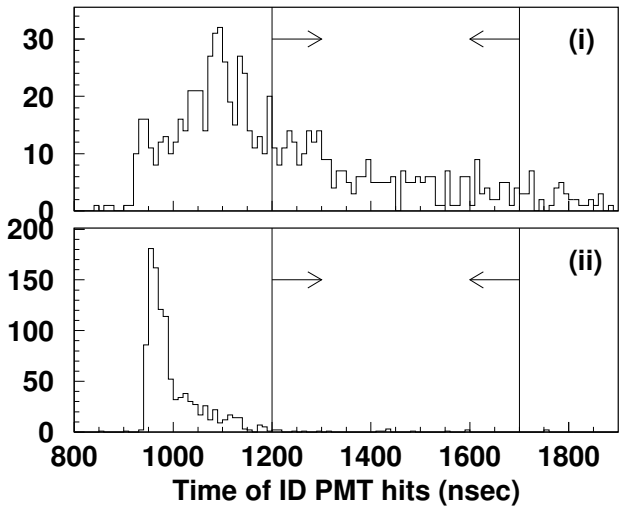

Figure 6.11: A typical timing distribtion for (i) a typical flashing PMT event and (ii) a typical FC neutrino event. The arrows enclose the timing window in which NMIN_{100} is checked. A clear difference in the charge distribution can be seen in this window between (i) and (ii).

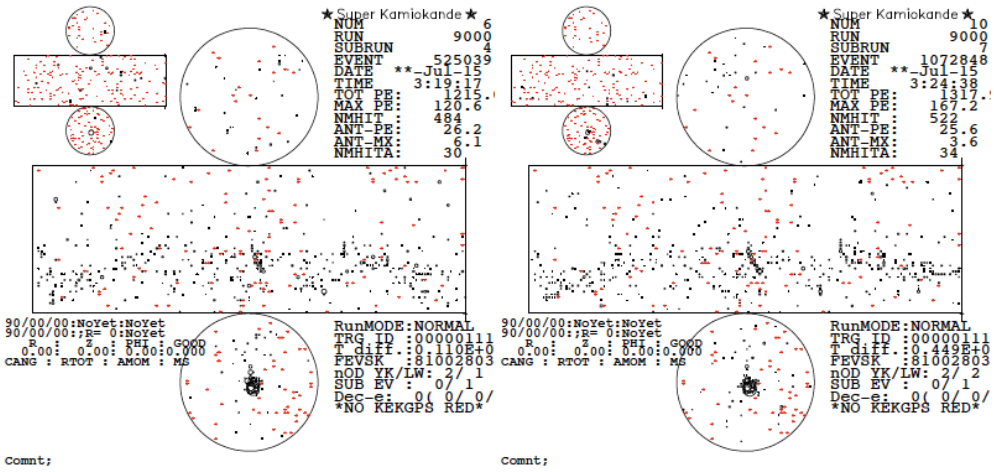

Figure 6.12: Event display of a typical flasher PMT discharging. The time interval between these two events is around ∼20 mins.

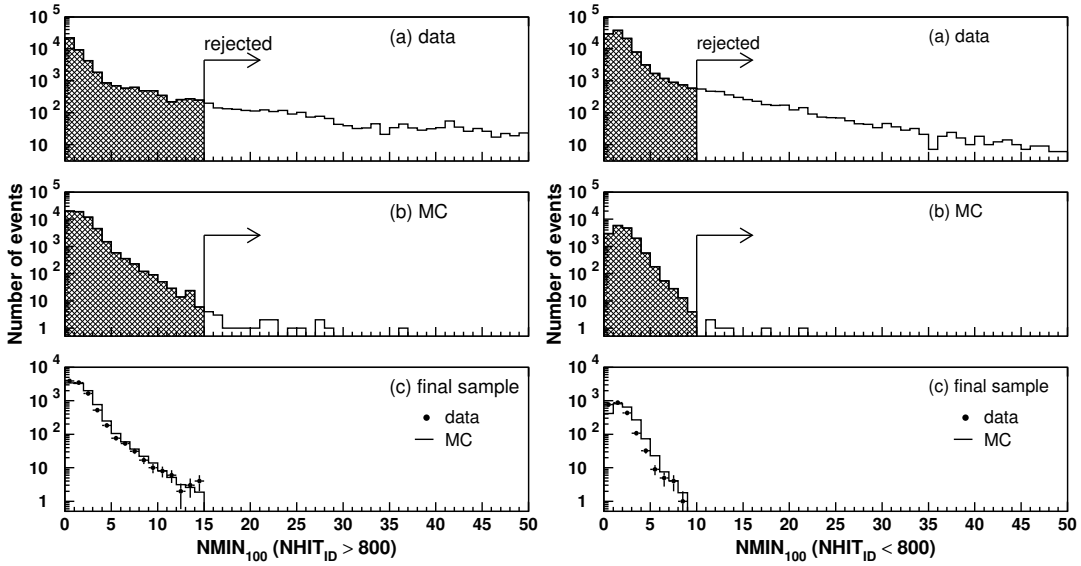

Figure 6.13: FC Third Reduction: flasher SK1 $NMIN_{100}$ distributions for (a) data after FC2, (b) FC MC, (c) final sample data and MC normalised to the data. Distributions are for number of hit ID PMTs > 800 (left) and < 800 (right). The $NMIN_{100}$ cut criteria arrows mark the rejected events.

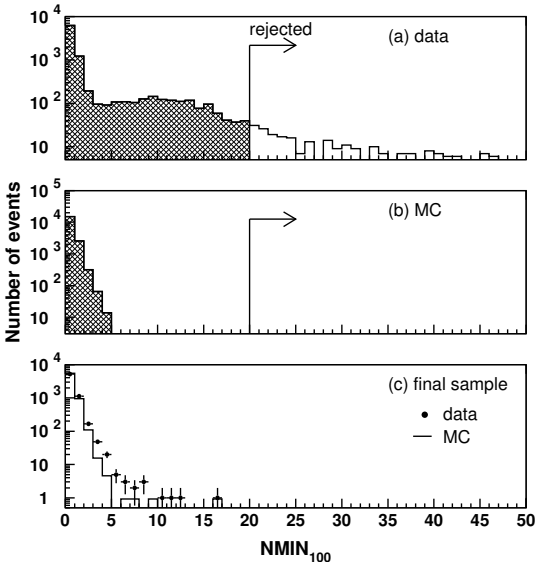

Figure 6.14: FC Third Reduction: flasher SK2 $NMIN_{100}$ distributions for (a) data after FC2, (b) FC MC, (c) final sample data and MC normalised to the data. The $NMIN_{100}$ cut criteria arrows mark the rejected events.

Accidental Coincidence Events Cut

Sometimes there is an accidental coincidence of a low energy event which opens the trigger window with low activity in the OD, and a following cosmic-ray muon event that deposits a lot of charge in the ID. The OD hits in the trigger window from the low energy event pass the earlier $NHITA_{800}$ cuts, and the cosmic-ray muon in the same event window passes the PE_{300} cut. These accidental coincidence events are removed by the following cuts:

(1) $NHITA_{off} \geq 20$
$NHITA_{off}$ is the number of hit OD PMTs in a fixed 500 nsec off-timing window from +400 nsec to +900 nsec after the trigger timing.

(2) $PE_{off} > 5000$ p.e.s (2500 for SK-II)
PE_{off} is the number of p.e.s observed by ID PMTs in a fixed 500 nsec off-timing window from +400 nsec to +900 nsec.

Low Energy Events Cut

The remaining low energy events are from the decay of radio-isotopes and electrical noise. Such events are removed by the following criteria:

(1) $NHIT_{50} < 50$ (25 for SK-II)
$NHIT_{50}$ is the number of hit ID PMTs in a sliding 50 nsec time window.

where $NHIT_{50}$ is counted after subtracting the time of flight (TOF) of each observed photon assuming all photons are generated at a point. The vertex is determined as the position at which

the timing residual distribution is peaked. NHIT_{50}=50 corresponds to visible energy of 9 MeV and is low enough to not lose efficiency for contained neutrino events with $\mathrm{E}_{\mathrm{vis}}$ >30 MeV.

After the FC Third Reduction, the event rate is ∼45 (∼21) events/day (for SK-II).

6.2.4 Fourth Reduction

In the Fourth Reduction, further flasher events are removed by using an intelligent pattern matching algorithm. As shown in Figure 6.12, Flasher events tend to repeat with very similar hit patterns in the detector over the course of hours and days. Repeated events with a similar hit pattern are very unlikely to be due to neutrino events. So an algorithm that looks for matching hit patterns is used to reject repeating Flasher events. The algorithm steps are as follows:

(1) Divide the ID wall into 1450 patches of 2 m×2 m square.

(2) Compute the correlation factor r by comparing the total charge in each patch of two events, A and B. The correlation is defined as :

$$r = \frac{1}{N}\sum_{i}\frac{\left(Q_i^A - \langle Q^A\rangle\right)\times\left(Q_i^B - \langle Q^B\rangle\right)}{\sigma_A \times \sigma_B} \tag{6.2}$$

where N is the number of the patches, and $\langle Q^{A(B)}\rangle$ and $\sigma_{A(B)}$ are the averaged charge and its standard deviation for event A and B, respectively.

(3) Calculate the distance ($\mathrm{DIST}_{\mathrm{max}}$)between the PMTs with the maximum pulse heights in the two compared events

(4) If $\mathrm{DIST}_{\mathrm{max}} < 75$ cm, an offset value is added to r :r=r+0.15.

(5) If r exceeds the threshold(r_{th}), events A and B are recognized as matched events. r_{th} is defined as :

$$r > r_{th} = 0.168 \times \log_{10}((\mathrm{PE}^A_{\mathrm{tot}} + \mathrm{PE}^B_{\mathrm{tot}})/2.) + 0.130, \tag{6.3}$$

where $\mathrm{PE}_{\mathrm{tot}}$ is the total number of p.e.s observed in the ID.

(6) Repeat the above calculation over 10,000 events around the target event and count the number of matched events.

(7) Remove the events with large correlation factor r, or large number of matched events.

The cut criteria showing which events are rejected is shown in Figure 6.15 for the data after FC Third Reduction and the FC atmospheric MC.

The event rate after the FC Fourth Reduction is ∼18 events/day.

6.2.5 Fifth Reduction

After the Fourth Reduction, the number of remaining background events are few and these are removed by criteria specialised for each background event type.

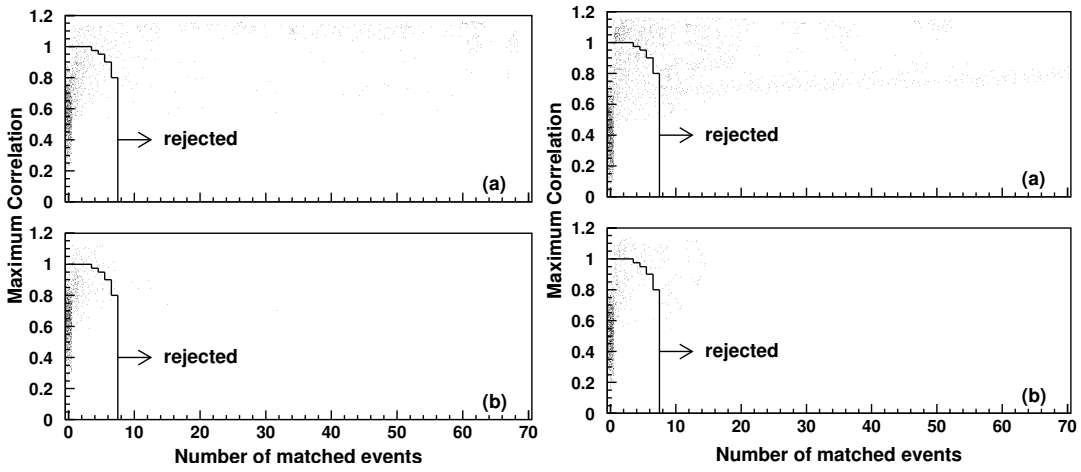

Figure 6.15: FC Fourth Reduction: Estimator r against N_{match} scatter plots for (a) data after FC3, (b) FC MC. Distributions are for SK-I (left) and SK-II (right). The r estimator–N_{match} cut region arrows mark the rejected events.

Stopping Muon Cut

The remaining stopping muons are rejected by tighter criteria than those in the Third Reduction stage. Events satisfying the following criteria are removed:

(1) $NHITA_{in} \geq 5$
$NHITA_{in}$ is the number of hit OD PMTs located within 8 m from the entrance point in a sliding 200 nsec time window from -400 nsec to $+400$ nsec.

This time the entrance position in the OD is estimated by a backward extrapolation from the reconstructed vertex determined by TDC-fit (see Section 7.2.3). Figure 6.16 shows the distributions for $NHITA_{in}$ for the data after FC Fourth Reduction, the FC MC and the final samples.

Invisible Muon Cut

Invisible muon events are caused by cosmic-ray muons with momenta below Cherenkov threshold and the subsequent decay electrons being observed as the triggered event. These events are characterised by a low energy signal from a decay electron and a signal in the OD *before* the trigger timing. Invisible muons are removed by the following cut criteria:

(1) $PE_{tot} < 1000$ p.e.s (500 for SK-II)
PE_{tot} is the total number of p.e.s observed in the ID.

(2) $NHITAC_{early} > 4$
$NHITAC_{early}$ is the maximum number of hit PMTs in an OD hit cluster in a sliding 200 nsec time window from -8800 nsec to -100 nsec.

(3) $NHITAC_{early} + NHITAC_{500} > 9$ if $DIST_{clust} < 500$ cm
$NHITAC_{early} > 9$ otherwise

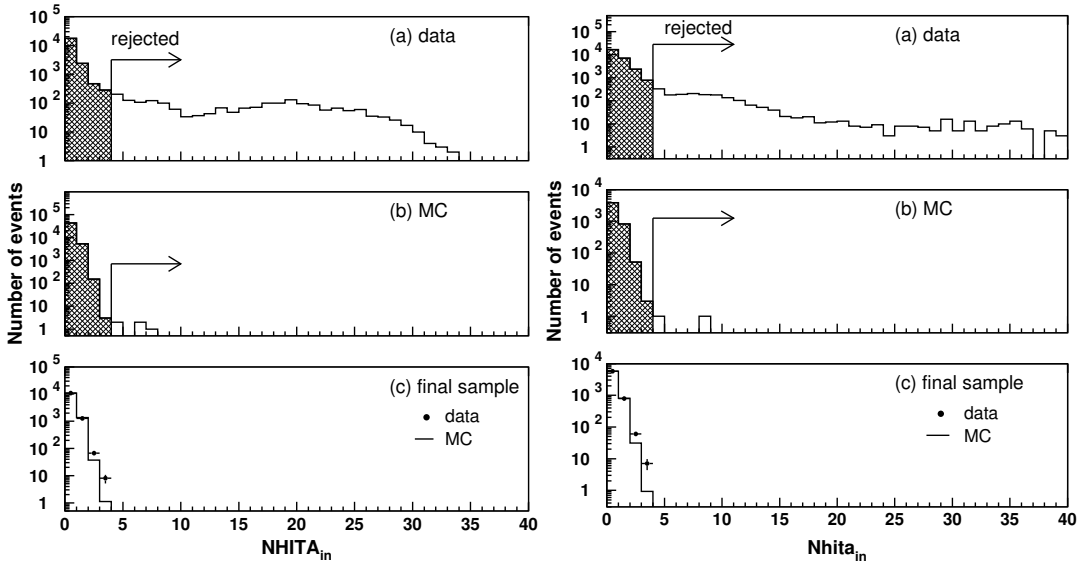

Figure 6.16: FC Fifth Reduction: stopping muon $\mathrm{NHITA_{in}}$ distributions for (a) data after FC4, (b) FC MC, (c) final sample data and MC normalised to the data. Distributions are for SK-I (left) and SK-II (right). The $\mathrm{NHITA_{in}}$ cut criteria arrows mark the rejected events.

$\mathrm{NHITAC_{500}}$ is the number of hit PMTs in the OD hit cluster in a fixed 500 nsec time window from -100 nsec to $+400$ nsec.
$\mathrm{DIST_{clust}}$ is the distance between two OD hit clusters, which are used for the $\mathrm{NHITAC_{early}}$ and the $\mathrm{NHITAC_{500}}$.

Figure 6.17 shows the $\mathrm{NHITAC_{early}}$ distributions for the data after FC Fourth Reduction, the FC MC and the final sample, where the criteria for $\mathrm{DIST_{clust}} > 500$ cm is displayed.

Accidental Coincidence Muon Cut

The remaining accidental coincidence muon events after the Third Reduction are rejected by the following cut criteria:

(1) $\mathrm{PE_{500}} < 300$ p.e.s (150 for SK-II)
$\mathrm{PE_{500}}$ is the total number of p.e.s observed in the ID in a fixed 500 nsec time window from -100 nsec to $+400$ nsec.

(2) $\mathrm{PE_{late}} \geq 20$ p.e.s
$\mathrm{PE_{late}}$ is the maximum number of hit OD PMTs in a 200 nsec sliding time window from $+400$ nsec to $+1600$ nsec.

Figure 6.18 shows the $\mathrm{PE_{late}}$ distributions for the data after FC Fourth Reduction, the FC MC and final samples.

Long-Tail Flasher Cut

This is a stricter version of Flasher Cut than in the FC Third Reduction step. Events satisfying the following criteria are discarded as Flasher events:

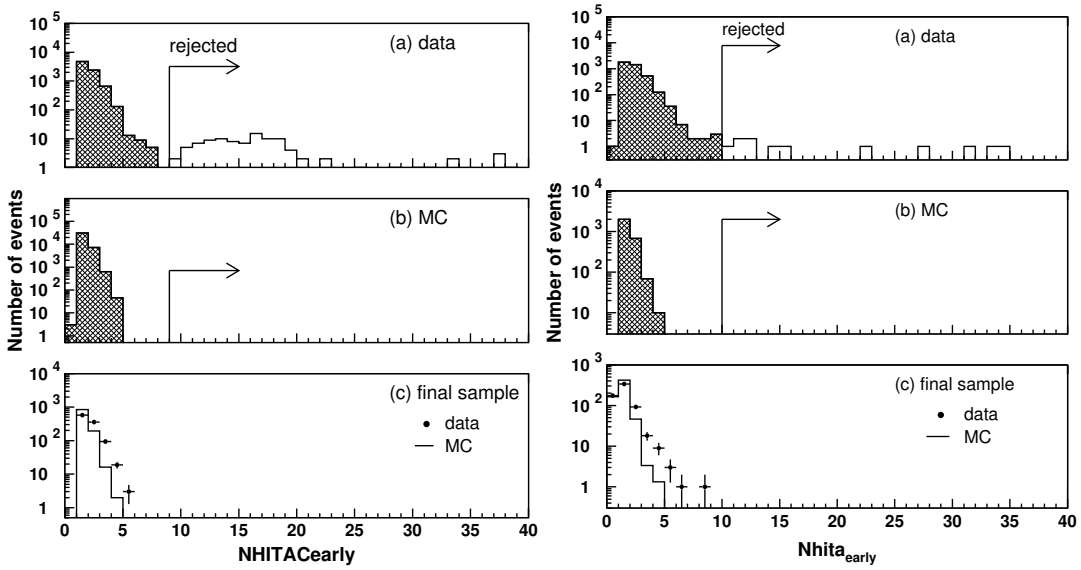

Figure 6.17: FC Fifth Reduction: invisible muon NHITAC$_{\rm early}$ distributions for (a) data after FC4, (b) FC MC, (c) final sample data and MC normalised to the data. Distributions are for SK-I (left) and SK-II (right). The NHITAC$_{\rm early}$ cut criteria arrows mark the rejected events for DIST$_{\rm clust} > 500\,$cm.

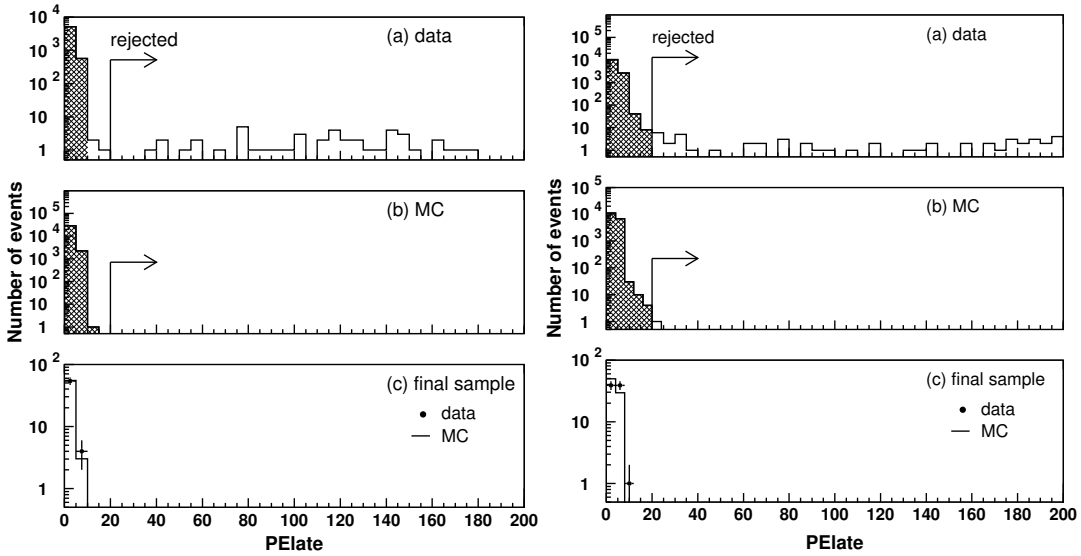

Figure 6.18: FC Fifth Reduction: accidental coincidence muon PE$_{\rm late}$ distributions for (a) data after FC4, (b) FC MC, (c) final sample data and MC normalised to the data. Distributions are for SK-I (left) and SK-II (right). The PE$_{\rm late}$ cut criteria arrows mark the rejected events.

(1) $NMIN_{100} > 5$ if the Goodness of Point-Fit < 0.4
$NMIN_{100}$ is the minimum number of the hit ID PMTs in a sliding 100 nsec time window from +300 nsec to +800 nsec.

From SK-II onwards, in addition to the criteria above, the following extra cuts are applied:

(3) Goodness of point fit < 0.3

(4) $NHITMIN_{100} < 6$

See Section 7.2.1 for an explanation of Point-Fit.

After the FC Fifth Reduction, the FC event rate is ∼16 events/day.

6.2.6 FC Reduction Summary

Finally, the Fully-Contained Fiducial Volume (FCFV) neutrino events are selected by applying the FCFV event cuts:

- Vertex of neutrino interactions should be inside the fiducial volume (2 m from the ID PMT surface).
- The number of hit PMTs in the highest charge OD cluster (NHITAC) should be less than 16 (10 for SK-I).
- Visible energy (E_{vis}) should be greater than 30 MeV.

The detection efficiencies in each reduction step are estimated by the atmospheric neutrino Monte Carlo events as shown in Table 6.1, where FCFV cuts were applied using the true vertex information. The FCFV row shows the detection efficiencies using the reconstructed vertex, and the final row gives the daily event rate for each SK period.

Fully-Contained	Selection Efficiency (%)			
Reduction Step	SK-I	SK-II	SK-III	SK-IV
1st Reduction	100.00	99.97	100.00	100.0
2nd Reduction	100.00	99.92	99.98	99.99
3rd Reduction	99.93	99.78	99.81	99.82
4th Reduction	99.29	99.38	99.30	99.00
5th Reduction	99.26	99.30	99.24	98.95
FCFV	99.25	99.95	99.62	99.19
Event Rate (/day)	8.26±0.07	8.28±0.10	8.41±0.13	8.14±0.09

Table 6.1: The detection efficiency after each FC Reduction step for each of the SK running periods. The efficiencies are shown after the FCFV cuts were applied using the true vertex information. In the FCFV row, the reconstructed vertex is used, and the final row shows the event rate per day.

For the FC events, the main sources of the background are cosmic-ray muons, Flasher events and neutrons from the rock around the detector. The Fiducial Volume cut largely reduces the background from these sources. The estimated contamination of the backgrounds is shown in Table 6.2.

Fully-Contained Background		Background Contamination (%)			
		SK-I	SK-II	SK-III	SK-IV
Cosmic-ray μ	Sub-GeV	0.2	0.2	0.3	0.1
	Multi-GeV	0.3	0.2	0.3	0.1
Flasher PMT	Sub-GeV	0.1	0.4	0.1	0.1
	Multi-GeV	0.5	0.2	0.2	0.1

Table 6.2: Estimated upper limit of the contamination of each background in the FC events. Note that the Cosmic-ray μ are mainly a background for the μ-like sample, while the Flasher PMTs mainly affect the e-like sample.

6.3 Reduction for Partially-Contained Sample

The PC events are separated from FC events by the activity in the OD. PC events require that the number of PMT hits in the highest charge cluster is greater than 15 (9 for SKI):

- NHITAC $>$ 15 (9 for SKI).

Since the PC events inherently require that there be OD activity, the steps for reducing backgrounds are different than those for FC Reduction. There are five reduction steps described here. Note that in the SK-II period, the PMT coverage in the ID was around half of that in the other SK periods, so the numbers for SKII are quoted separately. The reduction stages were modified from the SK-III period and are presented separately where different.

6.3.1 First Reduction

The PC First Reduction aims to reject through-going cosmic ray muons and low energy events. The selection criteria for SK-I and SK-II are as follows:

(1) $PE_{tot} \geq 1000$ p.e.s (≥ 500 for SK-II).
PE_{tot} is the number of p.e.s observed in the ID.

(2) TWIDA ≤ 260 nsec (≤ 170 nsec for SK-II).
TWIDA is the width of the hit timing distribution in the OD PMTs.

(3) NCLSTA ≤ 1 (only for SK-I).
NCLSTA is the number of the hit clusters in the OD.

The PC sample requires that exiting particles, mostly muons, must have a track length in the ID of at least 2 m, which corresponds to a momentum loss of 500 MeV/c for muons. The PE_{tot} cut in Criteria (1) of 1000 p.e.s (500 for SK-II) corresponds to 310 MeV/c for muons. Criteria (2) removes through-going muons. Through-going muon events have a broad hit timing distribution and two hit clusters, around the entrance and exit point in the OD. Figure 6.19 shows the TWIDA distributions for the raw data, the PC atmospheric MC, and the final samples with MC normalised to the data. The OD during SK-II has increased reflectivity and improved quantum efficiency in the OD PMTs, so the TWIDA cut criterion was further tuned for SK-II. The hit clusters for the NCLSTA variable refers to spatial clusters of neighboring hit PMTs.

From SK-III onwards, the segmentation of the OD was used to develop a more efficient through-going muon cut. The PC First Reduction criteria for SK-III onwards:

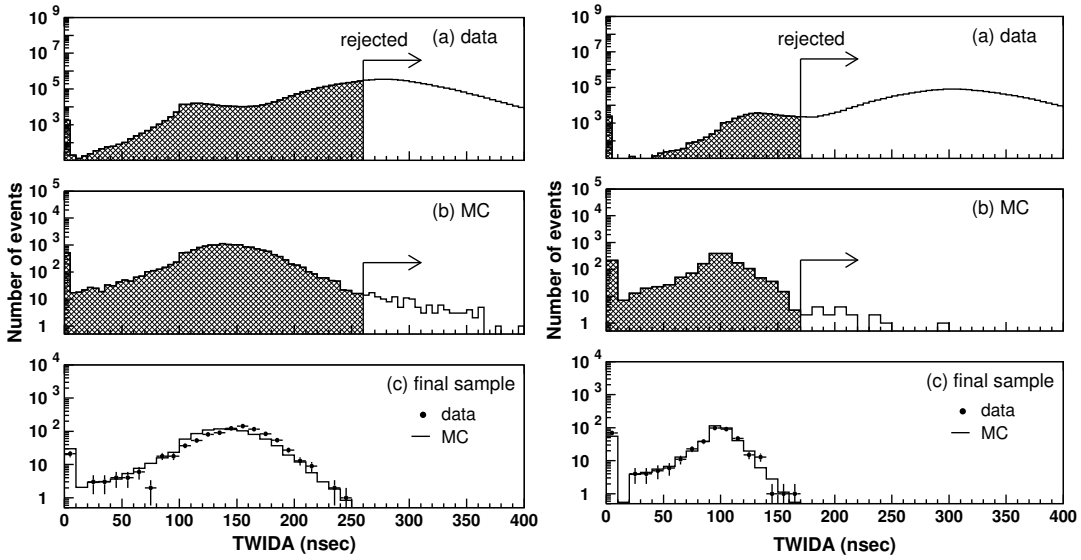

Figure 6.19: PC First Reduction: TWIDA distributions for (a) raw data, (b) PC atmospheric MC with vertex position further than 2 m from the wall, (c) final sample data and MC normalised to the data. Distributions are for SK-I (left) and SK-II (right). The TWIDA cut criteria arrows mark the rejected events.

(1) $\mathrm{PE_{tot}} \geq 1000$ p.e.s

(2) $\mathrm{NHITA_{top}} < 10$ or $\mathrm{NHITA_{bottom}} < 10$
$\mathrm{NHITA_{top}}$ ($\mathrm{NHITA_{bottom}}$) is the number of OD hits in the top (bottom) region.

(3) $\mathrm{NHITA_{endcap}} < 25$ or $\mathrm{NHITA_{side}} < 70$
$\mathrm{NHITA_{endcap}}$ ($\mathrm{NHITA_{side}}$) is the number of OD hits in the top and bottom (side) region.

(4) $\mathrm{ODR_{mean}} < 2100$ cm if OD hits < 20 in 500 nsec time window
$\mathrm{ODR_{mean}}$ is the average distance between all hit pairs.

$$\mathrm{ODR_{mean}} = \frac{1}{N_{\mathrm{pair}}} \sum_{i=1}^{N-1} \sum_{j=i+1}^{N} |\vec{x}_i - \vec{x}_j|.$$

Criteria (2) and (3) remove cosmic-ray muons that pass through two regions in the OD, but pass them if only one region is traversed. Criteria (2) removes the through-going muons which pass through both the top and bottom OD regions. Criteria (3) discards corner clipping muons, which pass through the endcap and side regions. Since through-gonig muons are expected to deposit energy in two regions of the OD, the variable $\mathrm{ODR_{mean}}$ is expected to be larger than a PC event with activity mainly in one region.

The event rate after the PC First Reduction is around $\sim 2 \times 10^4$ events/day.

6.3.2 Second Reduction

In the PC Second Reduction, an algorithm that finds clusters of OD hits is used to remove the remaining through-going and stopping muons. The OD (ID) walls are divided into 11×11

(21×21) patches and the charge observed in each patch is counted. The clusters are formed by looking at the charge gradient to the neighbouring patches, grouping hits into clusters "centred" around the patch with the largest charge in the cluster. The algorithm is illustrated in Figure 6.20.

For SK-I, the PC Second Reduction criteria are:

(1) NCLSTA2 ≤ 1
NCLSTA2 is the number of the OD hit clusters including more than 6 hit PMTs.

(2) $\text{NHITAC}_{\text{min}} < 7$
$\text{NHITAC}_{\text{min}}$ is the minimum number of hit PMTs among top (or bottom) and side regions in the OD hit cluster.

(3) $\text{PE}_{200} > 1000\,\text{p.e.s}$ if NCLSTA2 $= 1$
PE_{200} is the number of the observed p.e.s within 200 cm from the highest charge PMT in the ID hit cluster closest to the OD hit cluster.

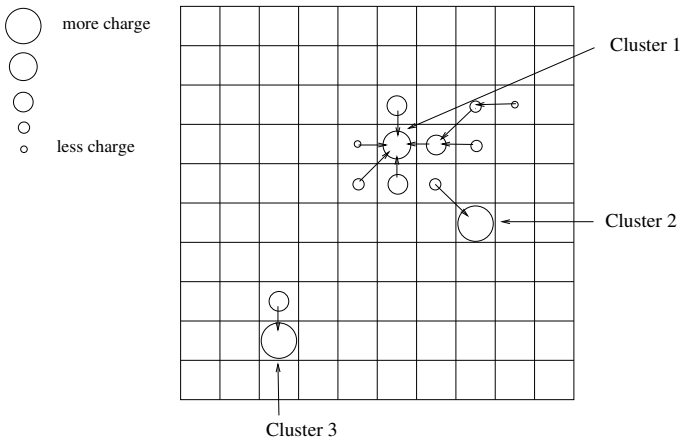

Figure 6.20: A schematic view of the algorithm to find hit clusters in the PC Second Reduction. The circles represent the charge observed in each patch, where the size of the circle is proportional to the number of p.e.s. The arrows represent the vector charge gradient, which point from a patch to the neighbouring patch with the highest charge.

For SK-II, the PC Second Reduction criteria are:

(1) NCLSTA2(2) ≤ 1
NCLSTA2(2) is the number of the 2nd OD hit clusters including more than 10 hit PMTs.

(2) $\text{NHITA}_{\text{endcap}} < 20$ or $\text{NHITA}_{\text{endcap}} < \text{MAX}(\text{NHITA}_{\text{side}})$

$$\text{MAX}(\text{NHITA}_{\text{side}}) = \begin{cases} \exp(5.8 - 0.023 \times \text{NHITA}_{\text{side}}) & \text{if } \text{NHITA}_{\text{side}} < 75 \\ \exp(4.675 - 0.008 \times \text{NHITA}_{\text{side}}) & \text{if } \text{NHITA}_{\text{side}} \geq 75 \end{cases}$$

$\text{NHITA}_{\text{endcap}}$ is the number of OD hit PMTs in the top and bottom region. $\text{NHITA}_{\text{side}}$ is the number of hit OD PMTs in the side region.

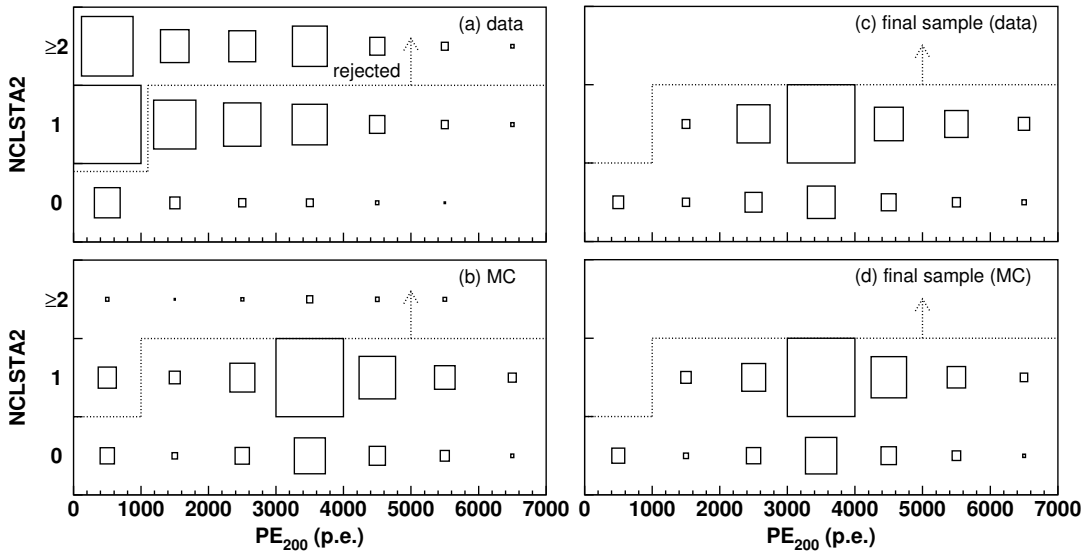

Figure 6.21: PC Second Reduction: NCLSTA2 against PE_{200} scatter plots for (a) data after PC1, (b) PC MC after PC1, (c) final sample data and MC normalised to the data. Distributions are for SK-I. The NCLSTA2–PE_{200} cut region arrows mark the rejected events.

(3) NHITAC2 $< 12 + 0.085 \times PE_{200}$
NHITAC2 is the number of the OD hit PMTs in the 2nd cluster.

Criteria (2) for both SK-I and SK-II reject corner clipping muons, which leave hit PMTs in both the top (or bottom) and side regions in the OD. Criteria (3) for SK-I and SK-II remove stopping muons, using the number of p.e.s in the ID hit cluster located closest to the OD hit cluster.

The event rate after the PC Second Reduction is ∼8000 events/day.

6.3.3 Third Reduction

In the PC Third Reduction, Flasher events and cosmic-ray stopping muons are discarded. The Flasher events are removed by the broad timing distribution expected from a Flasher event, which is the same method as that in the FC Third Reduction.

Flasher events are rejected by requiring the following selection criteria:

(1) $NMIN_{100} \leq 14$
or
$NMIN_{100} \leq 9$ if the number of hit ID PMTs < 800 (400 for SK-II)
$NMIN_{100}$ is the minimum number of hit ID PMTs in a sliding 100 nsec time window from +300 nsec to +800 nsec.

The stopping muon events are removed by the number of hit OD PMTs near the entrance position. The entrance position is estimated by a backward extrapolation from the reconstructed vertex and direction of Point-Fit (see Section 7.2.1). Point-Fit is a simple fitter that assumes a point source for the detected photons. Stopping muons are rejected by requiring the selection criteria, for both SK-I and SK-II:

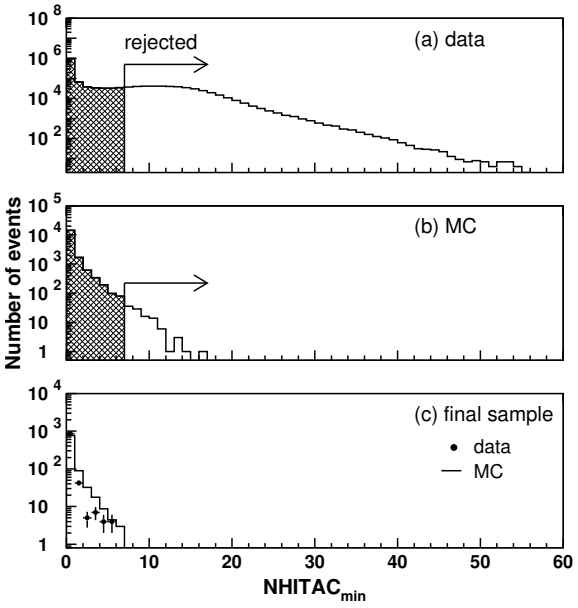

Figure 6.22: PC Second Reduction: $\mathrm{NHITAC_{min}}$ distributions for (a) data after PC1, (b) PC MC after PC1, (c) final sample data and MC normalised to the data. Distributions are for SK-I. The $\mathrm{NHITAC_{min}}$ cut criteria arrows mark the rejected events.

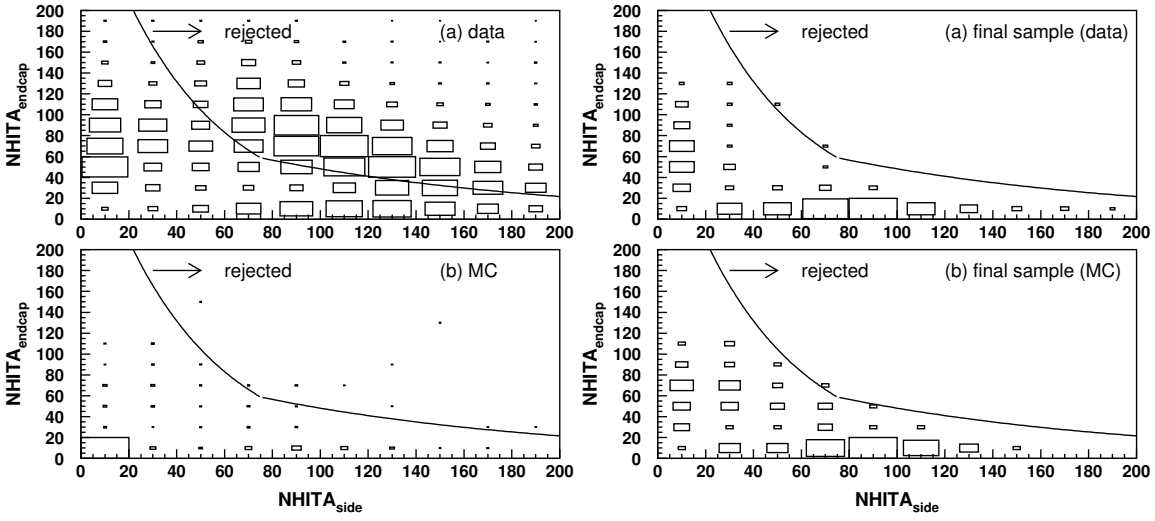

Figure 6.23: PC Second Reduction: $\mathrm{NHITA_{endcap}}$ against $\mathrm{NHITA_{side}}$ scatter plots for (a) data after PC1, (b) PC MC after PC1, (c) final sample data and MC normalised to the data. Distributions are for SK-II. The $\mathrm{NHITA_{endcap}}$–$\mathrm{NHITA_{side}}$ cut region arrows mark the rejected events.

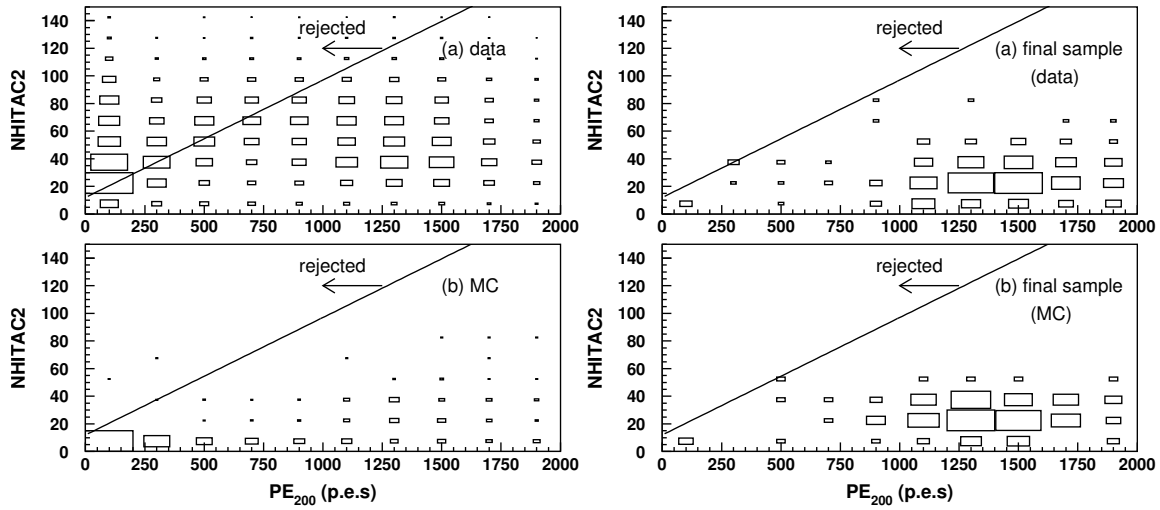

Figure 6.24: PC Second Reduction: NHITAC2 against PE_{200} scatter plots for (a) data after PC1, (b) PC MC after PC1, (c) final sample data and MC normalised to the data. Distributions are for SK-II. The NHITAC2–PE_{200} cut region arrows mark the rejected events.

(2) $NHITA_{in} \leq 10$
$NHITA_{in}$ is the number of hit OD PMTs located within 8 m from the entrance point in a fixed 500 nsec time window.

For SK-III onwards, Criteria (2) is applied at the PC Fifth Reduction stage.

The event rate after the PC Third Reduction is ∼100 events/day.

6.3.4 Fourth Reduction

In the PC Fourth Reduction, cosmic-ray muons that passed the PC Third Reduction due to relatively small OD activity are removed at this stage.

In this reduction stage, two types of event reconstruction fitters are used: Point-Fit and a through-going muon fitter. Point-Fit is described in Section 7.2.1. The through-going muon fitter is also used in the FC Third Reduction. This fitter determines the entrance point as the position of the earliest hit cluster in the ID. For proper PC events, which are initiated inside the ID, the through-going muon fitter cannot determine the entrance point correctly and tends to have worse *goodness* when compared with through-going muons. However, the vertex position and direction can be reasonably well estimated by Point-Fit for both PC events and cosmic-ray muons. The difference in these characteristics are used to reject cosmic-ray muons.

The selection criteria in the PC Fourth Reduction are as follows for SK-I and SK-II:

(1) $\vec{d}_{\rm pfit} \cdot \vec{d}_{\rm PMT} > -0.8$
$\vec{d}_{\rm pfit}$ is the reconstructed direction by Point-Fit, and $\vec{d}_{\rm PMT}$ is the direction from the reconstructed vertex to the earliest saturated PMT.

(2) DCORN > 150 cm
DCORN is the distance from the reconstructed vertex from Point-Fit to the nearest edge of the ID.

(3) TLMU $< 30\,\mathrm{m}$ if Goodness of Through-Going Muon Fit > 0.85
TLMU is the track length of a muon estimated from the entrance and the exit points by the through going muon fit.

Criteria (1) rejects cosmic-ray stopping muons which have their entrance point in the opposite direction to the reconstructed direction by Point-Fit. For PC events, the difference in these directions should be less anti-parallel than for cosmic-ray stopping muons. Criteria (2) attempts to remove corner clipping muons. Criteria (3) discards through-going muons which have a long track length.

SK-III Onwards Cuts

For SK-III onwards a reconstruction fitter is used to classify each event as one of Stopping Muon, Through-Going Muon, Multiple Muon or Corner Clipping Muons. 97% of the background events are classified as either Stopping Muon or Through-Going Muon. On the other hand, 96% of the PC events are categorised as one of the other muon types. There are five possible selection criteria based on the fitter:

(1) $\mathrm{angle_{muon}} < 90^\circ$
$\mathrm{angle_{muon}}$ is the angle between the fitted direction and the vector between the Point-Fit vertex and the centre of the highest charge OD cluster.

(2) $\mathrm{dotprod_{muon}} >$ -0.8
$\mathrm{dotprod_{muon}}$ is a similar variable to $\mathrm{angle_{muon}}$ but using the earliest saturated ID PMT instead of the centre of the highest charge OD cluster.

(3) $\mathrm{length_{muon}} < 17.5\,\mathrm{m}$
$\mathrm{length_{muon}}$ is the length of the fitted muon track. Long track lengths are likely to be produced by cosmic-ray muons.

(4) $\mathrm{goodness_{muon}} < 0.52$
$\mathrm{goodness_{muon}}$ is the goodness from the muon fitter.

(5) $\mathrm{corner_{muon}} \geq 3\,\mathrm{m}$
$\mathrm{corner_{muon}}$ is the distance between the fitted entrance point and the corner of the tank.

The number of these criteria that are required to pass this reduction step depend on the classification of the event from the fitter. In the case the event is classified as Through-Going Muon, then it has to pass 4 of the 5 criteria before being passed. Similarly, if the event is categorised as Stopping Muon, then it has to pass 4 of the 5 criteria including the $\mathrm{dodprod_{muon}}$ criterion with an additional requirement. The event must have $\mathrm{goodness_{muon}} < 0.5$ or $\mathrm{ehit_{muon}} < 10$, where $\mathrm{ehit_{muon}}$ is the number of OD hits located within 8 m from the fitted entrance point in a fixed 500 nsec time window. For the other classifications, 2 of the above 5 criteria have to be passed.

As a final step, low energy background events are removed by requiring the selection:

(1) $\mathrm{PE_{tot}} \geq 2900$ p.e.s
$\mathrm{PE_{tot}}$ is the total number of p.e.s observed in the ID.

$\mathrm{PE_{tot}}$ of $\sim$3000 p.e.s corresponds to a muon momentum of 500 MeV/c, which is safe for PC events as exiting muons must have at least a momentum of 700 MeV/c to reach the OD.

The event rate after the PC Fourth Reduction is $\sim$20 events/day.

6.3.5 Fifth Reduction

In the PC Fifth Reduction stage more elaborate selection criteria specialised for each background source are applied to remove the remaining non-neutrino events to produce the final PC sample. The selections for the SK-I to SK-II period and the SK-III to SK-IV period are different, and have been presented separately here.

SK-I and SK-II Reduction Selections

Low Energy Event Cut

The following selection criteria reject the remaining low energy background events:

(1) $\mathrm{PE_{tot}} \geq 3000$ p.e.s (1500 for SK-II)
$\mathrm{PE_{tot}}$ is the total number of p.e.s observed in the ID.

Again, this requirement corresponds to a muon momentum of 500 MeV/c, where at least a momentum of 700 MeV/c is necessary to reach the OD. This is a safe cut that will remove a lot of the low energy backgrounds.

Through-Going Muon Cut: OD Clusters

At this stage, there are three sets of selection criteria that attempt to remove the remaining through-going muons by considering particular properties of these background events. The first set of cuts make use of the OD hit cluster information obtained by the algorithm in the PC Second Reduction (see Section 6.3.2). Events which seem to have two OD clusters, from the expected entrance and exit points of a through-going muon, are removed. The following selection criteria reject through-going muons:

(1) $\mathrm{DIST_{clust}} \leq 20$ m
$\mathrm{DIST_{clust}}$ is the distance between the highest charge OD hit cluster and the second highest one.

(2) $\mathrm{PEAC_{2nd}} < 10$ p.e.s
$\mathrm{PEAC_{2nd}}$ is the number of p.e.s detected in the second highest charge OD hit cluster.

(3) NCLSTA5 < 2
NCLST5 is the number of OD hit clusters which contain more than 9 hit PMTs.

In criterion (3), the same clustering algorithm as that in the PC Second Reduction is used, but with different parameters. The OD wall is divided into 6×6 instead of 11×11 in the PC Fifth Reduction to avoid the boundary effect of the patches.

Through-Going Muon Cut: Geji

The second set of through-going muon cuts aims to remove "Geji" muon events. Some cosmic-ray muon events enter at the edge of the top of the detector, pass parallel to and along the ID wall, and exit through the edge at the bottom. The result is a "centipede"-like track (*geji* in Japanese)

along the ID wall. Since the light collection efficiency around the edge of the OD is relatively not so good and since the reconstruction tools do not perform so well at the detector boundaries, these events pass the prior reduction steps. The reduction selection criteria that rejects these events is:

(1) $\mathrm{NHITA_{top}} < 7$ and $\mathrm{NHITA_{bottom}} < 7$
$\mathrm{NHITA_{top}}$ ($\mathrm{NHITA_{bottom}}$) is the maximum number of hit OD PMTs in a 8 m radius sphere centered at the top (bottom) edge.

(2) $\mathrm{PEA_{top}} < 10$ p.e.s and $\mathrm{PEA_{bottom}} < 10$ p.e.s
$\mathrm{PEA_{top}}$ ($\mathrm{PEA_{bottom}}$) is the number of p.e.s in OD detected in the same sphere as that for the $\mathrm{NHITA_{top}}$ ($\mathrm{NHITA_{bottom}}$)

(3) TDIFFA $\times\, c/40\,\mathrm{m} < 0.75$ or TDIFFA $\times\, c/40\,\mathrm{m} > 1.5$
TDIFFA is a time interval between the averaged hit timing in the top and the bottom spheres.

Criterion (3) checks that the difference in the timing between the top and bottom is not consistent with a muon passing vertically through the detector.

Through-Going Muon Cut: Fitting

The third set of through-going muon cuts make use of precise reconstruction tools to check the number of hit OD PMTs near the entrance and exit points. The vertex position and the ring direction are reconstructed by a Cherenkov ring pattern based fitter: MS-fit (see Section 7.5). The entrance and the exit points on the detector wall are estimated by extrapolating the fitted information. The selection criteria that remove the remaining through-going muons are:

(1) $\mathrm{NHITA_{in}} < 5$ and $\mathrm{NHITA_{out}} < 5$
$\mathrm{NHITA_{in}}$ ($\mathrm{NHITA_{out}}$) is the number of hit OD PMTs within 8 m from the entrance (exit) point.

(2) TDIFFA $\times\, c/\mathrm{TRACK} < 0.75$ or TDIFFA $\times\, c/\mathrm{TRACK} > 1.5$
TRACK is distance between the entrance and exit point estimated using the vertex position and the ring direction reconstructed by MS-fit.

Stopping Muon Cut: Fitted Entrance Point

Three sets of selection criteria are are applied to reject stopping muons. In the first cut, the reconstructed vertex position and direction using MS-Fit (Section 7.5) are extrapolated backwards to determine the entrance point. The number of hit OD PMTs near the entrance point are counted and used to reject muons that entered through the OD. The first set of reduction criteria that remove stopping muons are:

(1) $\mathrm{NHITA_{in}} < 10$
$\mathrm{NHITA_{in}}$ is the number of OD hit PMTs within 8 m from the reconstructed entrance.

Stopping Muon Cut: Fitted Entrance Angle

In the second stopping muon cut, the Cherenkov ring is reconstructed by two different fitters, TDC-Fit (Section 7.2.3) and MS-Fit (Section 7.5). Then the angle between the reconstructed direction and the OD hit cluster are compared. In the case of a stopping muon event, the opening angle is expected to be large (ideally anti-parallel). However, for a PC event, the angle should be smaller (ideally parallel). The reduction selection that discards stopping muons by comparing this angle are:

(1) $\Theta_{\text{TDC-Fit}} \leq 90^\circ$ or $\Theta_{\text{MS-Fit}} \leq 90^\circ$
$\Theta_{\text{TDC-Fit}}$ ($\Theta_{\text{MS-Fit}}$) is the opening angle between the direction to the OD hit cluster and the ring direction reconstructed by TDC-fit (MS-fit).

Stopping Muon Cut: Stopping Muon Fit

In the third stopping muon cut, the vertex and direction are estimated by Stopping Muon Fit. This fitter estimates the entrance position as the earliest hit cluster in the ID. For PC events, the fitting is not so successful as the vertex is typically not on the wall. However, if the *Goodness* of the Stopping Muon Fit is > 0, then the charge inside a 42° cone facing the entrance position is checked. Less than 60% of the charge should be within this cone. Then the selection criteria for rejecting stopping muons are:

(1) If the *Goodness* of Stopping Muon Fit > 0

(2) $\text{PE}_{\text{cone}}/\text{PE}_{\text{tot}} < 0.6$
PE_{cone} is the number of p.e.s observed by ID PMTs located inside a 42° cone facing the entrance position.
PE_{tot} is the total number of p.e.s observed in the ID.

(3) $\text{NHITA}_{\text{in}} \leq 6$
NHITA_{in} is the number of hit OD PMTs within 8 m from the entrance position.

Cable Hole Muon Cut

There are four veto scintillation counters placed over the cable holes on the top of the detector. Unlike the FC event selection, a PC event may activate those veto counters. So an additional requirement on the reconstructed direction from TDC-Fit (Section 7.2.3) relative to the direction from the reconstructed vertex to the veto counter is required. If these are anti-parallel, then the event is more likely to be a cosmic-ray muon in origin. If there is a veto counter hit, then the reduction selection requires that the directions are not anti-parallel for a PC event:

(1) If there is one veto counter hit.

(2) $\vec{d}_{\text{ring}} \cdot \vec{d}_{\text{veto-vertex}} > -0.8$
$\vec{d}_{\text{ring}}$ is the reconstructed ring direction by TDC-fit, and $\vec{d}_{\text{veto-vertex}}$ is the direction from the reconstructed vertex to the hit veto counter.

Corner Clipping Muon Cut: Evis Track

Most of the corner clipping muon events are rejected in the PC Second and Third Reduction steps. In this reduction step, the remaining corner clipping muon events are removed. The corner clipping muon events have a small hit cluter in the ID, so the vertices are occasionally mis-reconstructed inside the ID. As a result, the track length from the vertex to the exit point reconstructed by MS-fit (Section 7.5) is large, while the track length which is estimated by the visible energy using the energy loss of muons $\sim$2 MeV/cm is small. This cut is applied in SK-II. The reduction selection criteria that rejects corner clipping events are the following:

(1) $\mathrm{TRACK_{Evis}} > \mathrm{TRACK} - 1500$ if $\mathrm{TRACK} > 15\,\mathrm{m}$
$\mathrm{TRACK_{Evis}}$ is the estimated track length from the visible energy and an energy loss of $\sim$2 MeV/cm
TRACK is the track length from the vertex to the exit point estimated from the vertex point and the direction by MS-fit.

When the PC event is properly reconstructed $\mathrm{TRACK_{Evis}} \approx \mathrm{TRACK}$, so Criterion (1) should hold. In the case of a corner clipping event, TRACK may be reconstructed large and be longer than $\mathrm{TRACK_{Evis}}$, even after subtracting 15 m.

SK-III and SK-IV Reduction Selections

The PC Reduction for SK-III onwards was modified to improve the efficiency. For the following reduction steps there are two types of cut: *Hard Cuts* and *Soft Cuts*. PC events are required to pass all of the Hard Cuts, while they may fail the Soft Cuts once only.
The Hard cuts are:

(1) Through-Going Muon Cut: OD Clusters

(2) Through-Going Muon Cut: Geji

(3) Stopping Muon Cut: Fitted Entrance Angle

(4) Cable Hole Muon Cut

(5) Corner Clipping Muon Cut: Edge Distance

Criteria (1)–(4) have already been described for the SK-I and SK-II case.

Corner Clipping Muon Cut: Edge Distance

This is the same criteria that was applied in the PC Fourth Reduction for SK-I and SK-II. This cut avoids clipping muon events by requiring the edge is not too close to the edge of the ID. The reduction selection criteria are:

(1) $\mathrm{DCORN} > 150\,\mathrm{cm}$
DCORN is the distance from the reconstructed vertex from Point-Fit to the nearest edge of the ID.

PC Fifth Reduction Soft Cuts

The soft cuts are:

(1) Through-Going Muon Cut: Fitting

(2) Through-Going Muon Cut: OD Cluster Hits

(3) Stopping Muon Cut: Fitted Entrance Point

(4) Stopping Muon Cut: Stopping Muon Fit

(5) Stopping Muon Cut: Fitted Entrance Strict

(6) Stopping Muon Cut: Point-Fit Angle

(7) Corner Clipping Muon Cut: Evis Track

(8) Decay Electron Cut

Criteria (1), (3), (4), and (7) have been previously described in the reductions for SK-I and SK-II.

Through-Going Muon Cut: OD Cluster Hits

The number of hit OD PMTs in the first and second highest charge clusters are used to remove the remaining through-going muons. The reduction selection critera are:

(1) NCLSTA5(1) < 10 and NCLSTA5(2) < 17
NCLSTA5(1) (NCLSTA5(2)) is the number of hit OD PMTs in the first (second) highest charge cluster.

Stopping Muon Cut: Fitted Entrance Strict

The criteria used here to reject stopping muons considers the number of hit OD PMTs within 8 m of the reconstructed entry point. This criteria was applied during the PC Third Reduction for SK-I and SK-II, but was moved to PC Fifth Reduction for SK-III and SK-IV. In addition the cut is more strict, however it now requires that the vertices fitted by Point-Fit and MS-Fit agree within 15 m. The reduction selection criteria for further removing stopping muons are:

(1) $\mathrm{NHITA_{in}} \leq 6$ if $|\vec{P}_{\text{Point-Fit}} - \vec{P}_{\text{MS-Fit}}| < 15\,\mathrm{m}$
$\mathrm{NHITA_{in}}$ is the number of hit OD PMTs within 8 m from the entrance position.
$\vec{P}_{\text{Point-Fit}}$ ($\vec{P}_{\text{MS-Fit}}$) is the reconstructed vertex position from Point-Fit (MS-Fit)

Stopping Muon Cut: Point-Fit Angle

This reduction step to reject stopping muons uses a selection criteria that was present in the PC Fourth Reduction. However, since this cut was not necessarily required to pass the PC Fourth Reduction, it is applied again in the Fifth Reduction.

(1) $\mathrm{angle_{muon}} < 90^\circ$
$\mathrm{angle_{muon}}$ is the angle between the fitted direction and the vector between the Point-Fit vertex and the centre of the highest charge OD cluster.

Partially-Contained	Selection Efficiency (%)			
Reduction Step	SK-I	SK-II	SK-III	SK-IV
1st Reduction	98.98	98.58	99.09	99.63
2nd Reduction	96.74	93.43	98.52	98.73
3rd Reduction	95.69	92.32	98.51	98.68
4th Reduction	89.86	84.60	97.87	97.42
5th Reduction	88.66	82.63	96.61	96.15
PCFV	80.98	74.80	88.80	86.30
Event Rate (/day)	0.66±0.02	0.65±0.04	0.62±0.03	0.66±0.02

Table 6.3: The detection efficiency after each PC Reduction step for each of the SK running periods. The efficiencies are shown after the PCFV cuts were applied using the true vertex information. In the PCFV row, the reconstructed vertex is used, and the final row shows the event rate per day.

Decay Electron Cut

High energy neutrinos interactions produce pions via DIS interactions. The pions then decay into muons, which further decay into electrons that are tagged as decay electrons associated with the neutrino event. However, high energy cosmic-ray muons decay in flight and no decay electron is observed. The reduction selection that removes these cosmic-ray muon events:

(1) $N_{decaye} \geq 1$ if $E_{vis} > 25\,GeV$
N_{decaye} is the number of tagged decay electrons.

6.3.6 PC Reduction Summary

Summary Finally, the Partially-Contained sample used in analyses are selected by applying these Fiducial Volume (PCFV) cuts:

- Vertex of neutrino interactions should be inside the fiducial volume (2 m from the ID PMT surface).
- The number of hit PMTs in the highest charge OD cluster (NHITAC) should be larger than 15 (9 for SK-I).
- Visible energy (E_{vis}) should be greater than 350 MeV.
(The total observed charge in the ID $>$ 3000 p.e.s (1500 p.e. for SK-II))

The detection efficiency after each PC Reduction stage is estimated with the atmospheric neutrino Monte Carlo, which is summarised in Table 6.3. The final detection efficiency is estimated to be 81%, 74.8%, 88.6% and 1000% for SK-I, SK-II, SK-III and SK-IV, respectively

In the final PC sample, the background events mainly consist of cosmic-ray muons. The final PC sample is checked by eye-scanning the events in an event display. There are few background events, most of which are removed by the fiducial volume cut. However, the presence of background events outside the fiducial volume can lead to some contamination. From the eye-scanning and extrapolation of the background distribution outside the fiducial volume, the systematics for

Partially-Contained	Background Contamination (%)			
Background	SK-I	SK-II	SK-III	SK-IV
Cosmic-ray μ	0.2	0.7	1.8	0.6

Table 6.4: Estimated upper limit of the contamination of cosmic-ray μ in the PC events.

the PC Reduction were estimated. The cosmic-ray muon background contamination in the PC sample is summarised in Table 6.4

The uncertainties of the PC Reduction efficiencies were estimated from the difference between data and Monte Carlo for the cut variables. The uncertainties are estimated to be 2.4%, 4.8%, 0.5% and 1000% for SK-I, SK-II, SK-III and SK-IV, respectively. Due to the improvements of the reduction efficiency for SK-III and SK-IV, there is better agreement between data and MC and a resulting smaller uncertainty.

Chapter 7

Event Reconstruction

7.1 Overview

The extraction of physical properties from the events follows a flow of reconstruction steps:

1. Vertex Reconstruction
   The position of the vertex and a direction is initially fitted assuming a point-like source, then the ring edge is found. Following this the position and direction reconstruction are improved by considering a line source.

2. Ring Counting
   Ring candidates are searched for and tested successively by a likelihood and evaluation functions to determine whether they are real or not. Those that are identified determine the number of reconstructed rings for the event.

3. Particle Identification
   Reconstructed rings are identified to be showering (e-like) or non-showering (μ-like) by considering electron and muon charge pattern distributions and their opening angles.

4. Precise Vertex Fitting (MS-fit)
   The previous vertex fitting is time-based and improves the reconstruction in the direction parallel to the particle direction. The PID and pattern information is used by MS-fit to further improve the vertex and direction reconstruction.

5. Momentum Reconstruction
   The momentum is reconstructed by considering the charge in a cone with a half angle of 70°. Corrections for relative gain between data and MC, scattered photons and light attenuation in water are made.

6. Decay Electron Search
   The muon detection efficiency can be increased by searching for decay electrons from muon decay. These are found and classified into a few different event types.

7. Ring Number Correction
   Some mis-identified rings are found and removed from the final reconstruction.

8. π^0 Fitting
   An algorithm is used to find π^0 events that have been mis-reconstructed as single-ring e-like events.

7.2 Vertex Reconstruction

The vertex reconstruction follows a 3-step process:

- **Point-Fit** gives an initial estimation of the vertex position and ring direction assuming a point-source.
- **Ring Edge Search** locates the opening angle of the ring and improves the direction reconstruction.
- **TDC-Fit** further improves the position and direction by considering a line-source for the photons and accounts for scattering.

7.2.1 Point-Fit

The first step is to find an approximate vertex with a rough fitting assuming a point source. A point vertex, $\vec{A}$, is assumed and the time of flight from $\vec{A}$ to the PMT is subtracted from the hit timing of each PMT, t_i^0 for the i-th PMT, to give the timing residual:

$$t_i = t_i^0 - \left(\frac{n}{c}|\vec{P}_i - \vec{A}|\right) \tag{7.1}$$

where $\vec{P}_i$ is the position of the i-th PMT, and c/n is the speed of light in water. Then to find the best vertex match for $\vec{A}$ the goodness-of-fit is determined by the estimator G_p:

$$G_p = \frac{1}{N}\sum_i \exp\left(-0.5\left(\frac{t_i - t_0}{1.5 \times \sigma}\right)^2\right) \tag{7.2}$$

where N is the number of hit PMTs, t_0 is a free parameter and represents the event timing at the best-fit , t_i is the timing residual (Equation 7.1), σ is the typical timing resolution of a PMT (2.5 ns), and the factor 1.5 is there to improve the performance of the fit. By maximising G_p, a best-fit vertex can be found for $\vec{A}$ with timing t_0.

At this stage the vertex found from point fit, $\vec{A}_0$, is used to estimate the particle direction. The direction from $\vec{A}_0$ to each PMT is weighted by the charge at each PMT, q_i, and summed to give an estimated direction:

$$\vec{d_0} = \sum_i q_i \left(\frac{\vec{P}_i - \vec{A}_0}{|\vec{P}_i - \vec{A}_0|}\right) \tag{7.3}$$

7.2.2 Ring Edge Search

In this stage, the Point Fit estimated vertex, $\vec{A}_0$, and particle direction, d_0, are used to find the outer edge of the Cherenkov ring and improve the reconstruction of the ring direction.

1. A distribution of charge as a function of the opening angle, θ, from the assumed ring direction to the hit PMT is made: $PE(\theta)$. The initial ring direction is taken to be the Point Fit estimation, d_0. The charge in this distribution is corrected for the effects from the water transparency and the PMT acceptance.

2. The outer edge of the Cherenkov ring is found by finding the roots of the second derivative of the $PE(\theta)$ distribution, and satisfying the following conditions:

   - $\left.\frac{d^2PE(\theta)}{d\theta^2}\right|_{\theta_{edge}} = 0$
   - $\theta_{edge} > \theta_{peak}$, where θ_{peak} is the angle at the peak of the $PE(\theta)$ distribution and therefore θ_{edge} is taken to be the angle of the outer edge of the ring.
   - If there are multiple θ_{edge} candidates, the one closest to θ_{peak} is chosen.

   A typical $PE(\theta)$ distribution and it's second derivative is shown in Figure 7.1.

3. The ring direction and θ_{edge} are simultaneously optimised to maximise the estimator $Q(\theta_{edge})$:

$$Q(\theta_{edge}) = \frac{\int_0^{\theta_{edge}} PE(\theta)d\theta}{\sin\theta_{edge}} \times \left(\left.\frac{dPE(\theta)}{d\theta}\right|_{\theta=\theta_{edge}}\right)^2 \times \exp\left(-\frac{(\theta_{edge}-\theta_{exp})^2}{2\sigma_\theta^2}\right) \tag{7.4}$$

   where θ_{exp} is the opening angle of the Cherenkov ring expected from the charge distribution $PE(\theta)$, with angular resolution σ_θ. The ring direction is adjusted around d_0 and the steps are reitterated until $Q(\theta_{edge})$ is maximised.

The numerator in the first factor of Equation (7.4) favours more charge inside the ring, while the denominator enhances $Q(\theta_{edge})$ for narrower rings. The middle factor favours sharper rings and the last factor enhances the estimator if it is close to the expectation.

7.2.3 TDC-Fit

Using the Point-Fit vertex and direction, and the ring information as a starting point, TDC-Fit improves the vertex and ring direction reconstruction. This more precise fitter considers the Cherenkov light as a line-source, estimating the emission point of the Cherenkov for PMTs hit within the ring. For PMTs hit outside the ring the scattering of Cherenkov photons is also considered, and the source point is taken as the assumed vertex. The *time residual*, the estimated timing of the vertex, is calculated as:

$$t_i = \begin{cases} t_i^0 - \frac{1}{c} \times |\vec{X}_i - \vec{O}| - \frac{n}{c} \times |\vec{P}_i - \vec{X}_i| & \text{Hits inside the Cherenkov ring} \\ t_i^0 - \frac{n}{c} \times |\vec{P}_i - \vec{O}| & \text{Hits outside the Cherenkov ring} \end{cases} \tag{7.5}$$

where $\vec{X}_i$ is the estimated point of emission for the Cherenkov photon, $\vec{O}$ is the assumed vertex, n is the refractive index of water and $\vec{P}_i$ is the position of the i-th PMT. From Equation (7.5) it can be seen that the particle is assumed to travel at the speed of light, c, and that the Cherenkov photons take a direct path to the PMT. This scenario is illustrated in Figure 7.2. The mean of the t_i is calculated to give t_0, which is an estimation of the vertex timing.

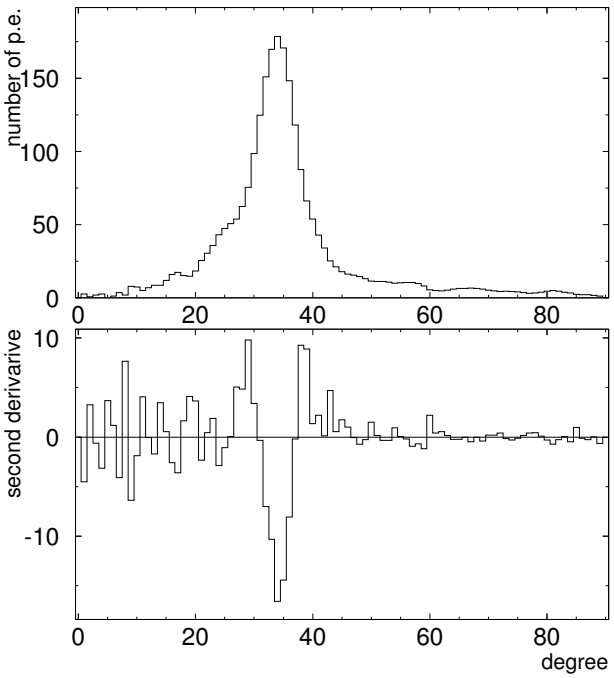

Figure 7.1: A typical $PE(\theta)$ distribution is shown in the upper figure, and the second derivative in the lower figure. The roots of the second derivative are used to find the outer edge of the ring, θ_{edge}.

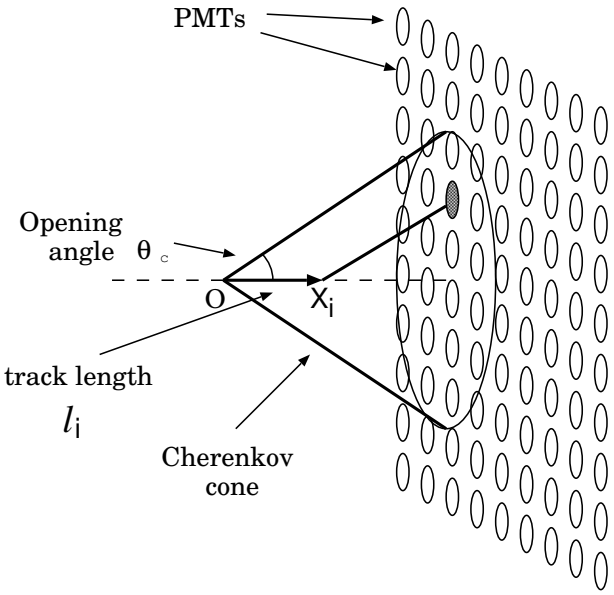

Figure 7.2: Illustration of Cherenkov radiation. The Cherenkov photons are assumed to originate from the track of a charged particle, and are emitted at point X_i to the i-th PMT. The track length from the vertex is given by l_i.

The estimator used to improve the vertex and ring direction is divided into three parts: G_I for PMTs within the ring, G_{O_1} for PMTs outside the ring with an early timing residual ($t_i \leq t_0$), and G_{O_2} for PMTs outside the ring with a late timing residual ($t_i > t_0$). The G_I estimator of the fitting is defined as:

$$G_I = \sum_i \frac{1}{\sigma_i^2} \exp\left(-\frac{1}{2} \cdot \left(\frac{t_i - t_0}{1.5 \cdot \sigma} \right)^2 \right) \tag{7.6}$$

where σ_i is the timing resolution of the i-th PMT and depends on the detected charge, whereas σ is the mean timing resolution for all PMT hits. So G_I gives an estimation of how well the time residual values, t_i, from Equation (7.5) converge to a single vertex time, t_0.

For the PMT hits outside the ring, the estimator depends on the difference between t_i and t_0 and are defined like so:

$$G_{O_1} = \sum_i \frac{1}{\sigma_i^2} \left(\exp\left(-\frac{1}{2} \cdot \left(\frac{t_i - t_0}{1.5 \cdot \sigma} \right)^2 \right) \times 2 - 1 \right) \qquad (\text{for } t_i \leq t_0) \tag{7.7}$$

$$G_{O_2} = \sum_i \frac{1}{\sigma_i^2} \left(\max\left[\exp\left(-\frac{1}{2} \cdot \left(\frac{t_i - t_0}{1.5 \cdot \sigma} \right)^2 \right), G_{scatt}(t_i, t_0) \right] \times 2 - 1 \right) \qquad (\text{for } t_i > t_0) \tag{7.8}$$

where,

$$G_{scatt}(t_i, t_0) = \frac{R_q}{1.5^2} \times \exp\left(-\frac{1}{2} \cdot \left(\frac{t_i - t_0}{1.5 \cdot \sigma} \right)^2 \right) + \left(1 - \frac{R_q}{1.5^2} \right) \times \exp\left(-\frac{t_i - t_0}{60nsec} \right) \tag{7.9}$$

and,

$$R_q = \frac{\sum\limits_{\theta < \theta_c + 3.0} q_i}{\sum\limits_{\theta < 70^\circ} q_i} \tag{7.10}$$

If $t_i \leq t_0$ then this suggests the PMT hit timing is earlier on average than direct light from the assumed vertex, and the estimator G_{O_1} in Equation (7.7) estimates how well these hits converge to t_0. The "$\times 2 - 1$" factor acts as a penalty for a poor fitting. If $t_i > t_0$ then it is possible that the photons arriving at the PMT were scattered, and the estimator G_{O_2} in Equation (7.8) considers this effect. It takes the maximum estimation of either direct light, which is the exponential term, or after considering a degree of scattering, $G_{scatt}(t_i, t_0)$ in Equation (7.9).

G_{scatt} has two terms which depend on the fraction of charge within the ring, R_q in Equation (7.10). The first term is favoured if there is more charge in the ring, and is an estimator for direct light. The second term is stronger with increasing charge outside the ring, and it favours the hits which are less scattered.

Then the three estimators are brought together for all the PMT hits to give the total estimator for the TDC-Fit:

$$G_T = \frac{G_I + (G_{O_1} \text{ or } G_{O_2})}{\sum\limits_i \frac{1}{\sigma_i^2}} \tag{7.11}$$

The vertex position and ring direction which maximises G_T are taken as the fitted result from TDC-Fit.

7.3 Ring Counting

After the vertex, direction and ring edge of the first Cherenkov ring is found, an algorithm is run to search for possible candidates for other rings.

7.3.1 Ring Candidate Search

The algorithm for searching for other ring candidates applies a method known as a Hough Transform [251]. This technique uses a spherical coordinate system about the reconstructed vertex and draws rings centred on each PMT hit as illustrated in Figure 7.3. These virtual rings assume a 42° cone opening angle, and a circular charge distribution depending on the hit PMT charge is generated. Summing these ring charge distributions on the (Θ, Φ) plane gives peaks where the virtual rings overlap, which correspond to the ring direction of candidate rings. A typical charge distribution is shown in Figure 7.4 and a candidate ring is illustrated as the shaded region in Figure 7.3.

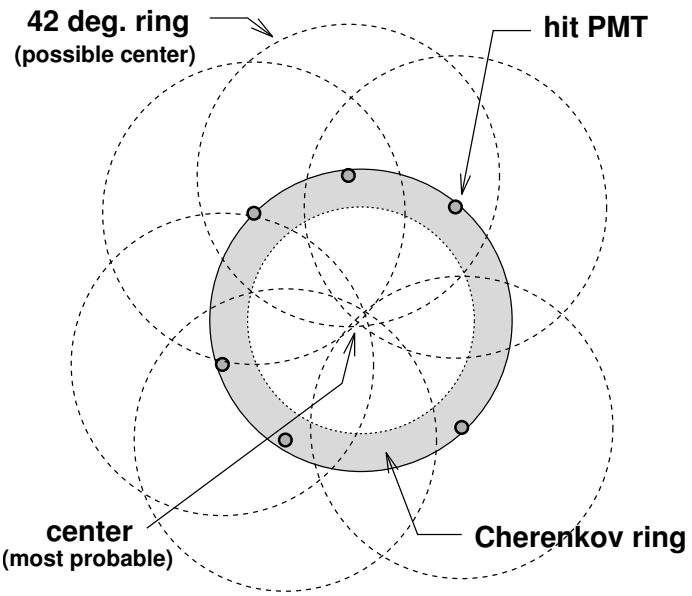

Figure 7.3: Illustration of the Hough Transform. Virtual circles representing Cherenkov rings are drawn around each PMT hit. Points of considerable overlap are likely to be the centre of a real Cherenkov ring, shown as the shaded region.

7.3.2 Ring Candidate Test

The possible candidates for rings are tested by a likelihood function which depends on all the rings already found. When N rings have been identified, and candidates are being tested for the $(N+1)$-th ring, the likelihood that the candidate is a real ring is given by:

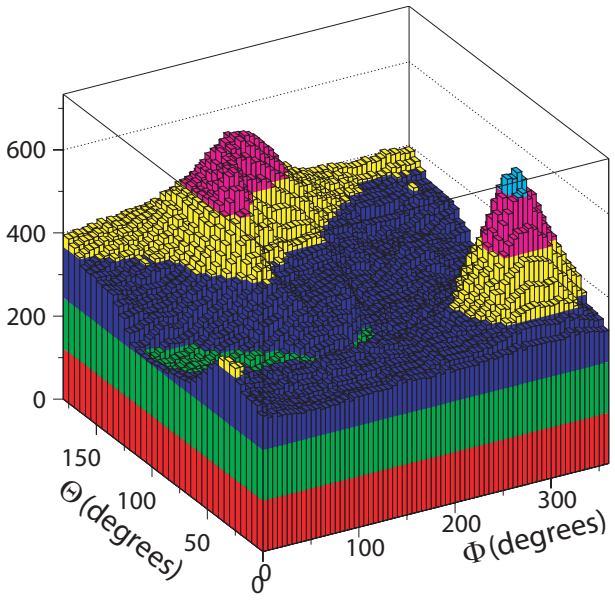

Figure 7.4: The virtual circles from the Hough Transform are actually circular charge distributions, and this is a typical Hough Transform charge distribution. This charge is summed on a (Θ, Φ) plane, the peaks are where there is considerable charge overlap and represent directions that are likely to be the centre of real Cherenkov rings.

$$\mathcal{L}_{N+1} = \sum_i \log(prob(q_i^{\text{obs}}, \textstyle\sum_{n=1}^{N+1} \alpha_n \cdot q_{i,n}^{\text{exp}})) \tag{7.12}$$

where the probability function is defined as:

$$prob(q_i^{\text{obs}}, q_i^{\text{exp}}) = \begin{cases} \dfrac{1}{\sqrt{2\pi}} \exp\left(-\dfrac{(q_i^{\text{obs}} - q_i^{\text{exp}})^2}{2\sigma^2} \right) & (\text{for } q_i^{\text{exp}} > 20 \text{ p.e.}) \\ \text{Single p.e. and Poisson convolution} & (\text{for } q_i^{\text{exp}} < 20 \text{ p.e.}) \end{cases} \tag{7.13}$$

The likelihood in Equation (7.12) compares the charge observed, q_i^{obs}, on the i-th PMT against the summed charge expected on the PMT from the N identified rings and the $(N{+}1)$-th ring being tested, $\alpha \cdot q_{i,n}^{\text{exp}}$ for the n-th ring. The likelihood is maximised by varying the α_n factors $(1 \leq n \leq N+1)$, with a lower momentum constraint.

The probability function in Equation (7.13) measures how closely the expected charge from all the considered rings matches the observed charge by a Gaussian distribution when $q_i^{\text{exp}} > 20$ p.e. In the case $q_i^{\text{exp}} < 20$ p.e. the probability is determined from the convolution of a single photoelectron distribution and a Poisson distribution.

If none of the $(N{+}1)$-th ring candidates satisfy $\mathcal{L}_{N+1} \geq \mathcal{L}_N$, the algorithm is finalised and the number of rings is determined to be N. In the case $\mathcal{L}_{N+1} \geq \mathcal{L}_N$, the $(N{+}1)$-th ring is put through six evaluation functions:

F_1 : The difference $\mathcal{L}_{N+1} - \mathcal{L}_N$ is corrected by considering the total charge of the event. If the difference is larger, the candidate is more likely to be a real ring.

F_2 : The average of the expected charge near the edge of the $(N{+}1)$-th Cherenkov ring, Q_{edge}, excluding the charge expected from the other N rings is calculated. If Q_{edge} is larger, the candidate is more likely to be real.

F_3 : The average of the expected charge outside the (N+1)-th ring, $Q_{\rm out}$, excluding the charge expected from the other N rings is calculated. If the difference $Q_{\rm edge}$-$Q_{\rm out}$ is larger, the candidate is more likely to be real.

F_4 : A residual charge distribution, excluding the residual charge expected from the other N rings is made. Using this, a vector sum $\vec{V} = \sum_i q_i^{\rm res} \cdot \hat{e}_i$ is calculated, where $q_i^{\rm res}$ is the residual charge for the i-th PMT and $\hat{e}_i$ is the unit vector from the reconstructed vertex to the i-th PMT. If $|\vec{V}|$ is larger, the candidate is more likely to be real.

F_5 : The difference in charge between the peak of a candidate ring and the average of inside and outside the ring. If this difference is larger, the candidate is more likely to be real.

F_6 : The azimuthal symmetry about the direction of the ring is considered, where a single-ring event is expected to be more symmetric than a multi-ring event. This evaluation function is only used to separated single and multi ring events.

The weighted sum, F, of these evaluation functions are computed, which constitutes the test for the (N+1)-th ring candidate. If $F \geq 0$, then the (N+1)-th ring is identified as true and the algorithm is repeated to search for the next ring. On the other hand if $F < 0$ for all remaining ring candidates, then the number of rings is determined to be N.

7.4 Particle Identification

After the rings have been identified, a particle identification (PID) algorithm is run. In Super-Kamiokande effectively two types of charge distribution are observed from Cherenkov rings: showering type (e-like), and a non-Showering type (μ-like). The showering events have a diffuse ring due to an electromagnetic shower or multiple scattering and are most likely to be produced by an electron or gamma photon. The non-showering events have a more sharp ring edge and are most likely produced by muons or charged pions.

7.4.1 Estimation of the Particle Type

To estimate the particle type a likelihood is defined assuming a lepton, $\mathcal{L}_l$ ($l = e$ or μ), as the archetype for the showering and non-showering type events. For the n-th ring, the likelihood is defined as:

$$\mathcal{L}_l(n) = \prod_{\substack{i \\ \theta_{i,n} < 1.5\theta_{c,n}}} prob\left(q_i^{\rm obs}, q_{i,n}^{{\rm exp},l} + \sum_{n' \neq n} q_{i,n'}^{{\rm exp},l} \right) \tag{7.14}$$

The product in the likelihood in Equation (7.14) is taken over each PMT which is within 1.5 times the estimated Cherenkov opening angle for the n-th ring, $\theta_{c,n}$. The probability function is the same as that defined in Equation (7.13), which determines how well the expected charge, $q_i^{\rm exp}$, reproduces the charge observed, $q_i^{\rm obs}$, in the i-th PMT. Here, the expected charge of the n-th ring is calculated assuming a lepton type l ($l = e$ or μ), $q_{i,n}^{{\rm exp},l}$, and adding the charge from all

the other rings where $n' \neq n$. The details of these lepton charge distributions is described in the following sections. $\mathcal{L}_l$ is maximised by varying the direction of the n-th ring and its Cherenkov opening angle, while all the other rings are kept fixed.

The probability of a ring being identified as like a particular lepton considers both the charge pattern and opening angle of the ring for single-ring events. For multi-ring events, only the pattern is considered. For the probability contribution from the charge distribution of the ring, the above likelihood is taken in the form of a χ^2:

$$\chi^2_l(n) = -2\ln\mathcal{L}_l(n) - \text{constant} \tag{7.15}$$

Then the pattern probability is defined as:

$$P_l^{\text{pattern}}(n) = \exp\left(-\frac{1}{2}\frac{\left(\chi^2_l(n) - \chi^2_{min}\right)^2}{\sigma^2_{\mathcal{L}_l}}\right) \tag{7.16}$$

where the above mentioned minimum χ^2 is taken as the minimum of the electron or muon assumption, $\chi^2_{min} = \min[\chi^2_e, \chi^2_\mu]$. $\sigma_{\mathcal{L}_l}$ characterises how well the likelihood was calculated and is $\sqrt{2N_{PMT}}$, where N_{PMT} is the number of PMTs that were used in the calculation of $\mathcal{L}_l$.

The probability from the Cherenkov opening angle, generally for the n-th ring is:

$$P_l^{\text{angle}}(n) = \exp\left(-\frac{1}{2}\frac{\left(\theta_{c,n} - \theta_n^{\text{exp},l}\right)^2}{\sigma^2_\theta}\right) \tag{7.17}$$

where $\theta_{c,n}$ is the reconstructed Cherenkov opening angle of the n-th ring, $\theta_n^{\text{exp},l}$ is the expected opening angle for particle type l ($l = e$ or μ), σ_θ is the resolution of the estimated Cherenkov angle.

Then the total probability of the ring being identified as lepton l is the product of the pattern and opening angle probabilities:

$$P_l^{\text{total}}(n) = P_l^{\text{pattern}}(n) \times P_l^{\text{angle}}(n) \tag{7.18}$$

noting that $P_l^{\text{angle}}(n)$ is not used for multi-ring events due to insufficient reconstruction of the Cherenkov opening angle when many rings are involved. The ring is identified as μ-like when the total probability $P_\mu^{\text{total}}(n) > P_e^{\text{total}}(n)$ and vice-versa for the e-like case.

7.4.2 Expected Charge Distribution: Electrons

The expected charge distributions, in photoelectrons (p.e.), produced by an electron were prepared in advance by using a Monte Carlo simulation. The expected charge distribution, $Q_e^{\text{exp}}(p_e, \theta)$, is generated assuming a hypothetical spherical surface of radius $R^{\text{sph}} = 16.9$ m (same as the radius of the Inner Detector), with the charge collected on a 50 cm diameter circular area which represents a PMT surface (equivalent to the 20 inch $\sim$ 50 cm diameter PMT). $Q_e^{\text{exp}}(p_e, \theta)$ is calculated as a function of electron momentum, p_e (MeV/c), and the opening angle, θ, from the electron direction.

The expected charge on the i-th PMT due to the n-th ring is calculated using $Q_e^{\text{exp}}(p_e, \theta)$ like so:

$$q^e_{i,n} = \alpha_{n,e} \times Q_e(p_e, \theta_{i,n}) \times \left(\frac{R^{\text{sph}}}{r_i}\right)^{1.5} \times \exp\left(-\frac{r_i}{\lambda}\right) \times f(\Theta_i) \tag{7.19}$$

where

$q^e_{i,n}$	:	Expected charge (p.e.) for the i-th PMT due to the n-th ring
$\alpha_{n,e}$	:	Normalisation factor
$\theta_{i,n}$	:	Opening angle between the n-th ring direction and the direction from the vertex to the i-th PMT
r_i	:	Distance from the vertex to the i-th PMT
Θ_i	:	Angle of photon arriving direction relative to the i-th PMT's facing direction (acceptance angle)
$f(\Theta_i)$	:	Correction function of the PMT acceptance
λ	:	Attenuation length of light in water (see Section 5.1.4)

The factor $(R^{\rm sph}/r_i)^{1.5}$ takes into account the r_i dependence of the intensity of the Cherenkov light, in effect translating the expected charge in a sphere to the SK geometry. The index 1.5 was tuned by a Monte Carlo study.

7.4.3 Expected Charge Distribution: Muons

The expected charge distribution, in photoelectrons (p.e.), produced by a muon is calculated analytically by the following equation:

$$q^{\mu}_{i,n} = \left(\alpha_{n,\mu} \times \frac{\sin^2\theta_{i,n}}{r_i \left(\sin\theta_{i,n} + r_i \frac{d\theta}{dx}|_{x=x_i} \right)} + q_i^{\rm knock} \right) \times \exp\left(-\frac{r_i}{\lambda}\right) \times f(\Theta_i) \qquad (7.20)$$

where

$q^{\mu}_{i,n}$	:	Expected charge (p.e.) for the i-th PMT due to the n-th ring
$\alpha_{n,\mu}$	:	Normalisation factor
$q_i^{\rm knock}$	:	Observed charge (p.e.) for the i-th PMT due to the knock-on electrons
x	:	Distance from the vertex along the muon trajectory
x_i	:	Distance from the vertex to the Cherenkov emission point for the i-th PMT
$r_i, \theta_{i,n}, \lambda, \Theta_i, f(\Theta)$	:	Same quantities as in Equation (7.19)

The numerator $\sin^2\theta$ in Equation (7.20) is proportional to the number of emitted Cherenkov photons in the direction $\theta_{i,n}$ (compare Equation (3.3)). The denominator $r_i(\sin\theta + r_i\frac{d\theta}{dx})$ comes from the area that Cherenkov photons are emitted towards, which can be readily understood from Figure 7.5 showing a schematic view of Cherenkov photon emission. When the muon loses energy, the Cherenkov opening angle also changes and therefore the area subtended by the angle does as well. The charge contribution from knock-on electrons is $q_i^{\rm knock}$ and was estimated by a Monte Carlo simulation.

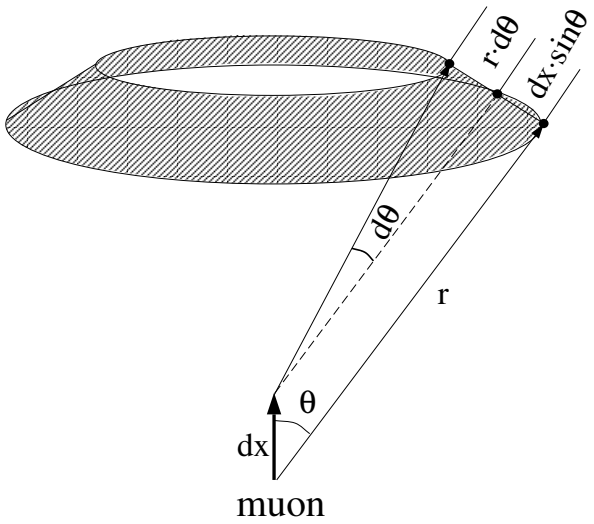

Figure 7.5: lllustration of Cherenkov radiation from a muon. Due to the energy loss in water, the Cherenkov opening angle, θ, changes as the muon momentum changes. When the muon propagates by dx, Cherenkov photons are emitted into the region $dx \cdot \sin\theta + r \cdot d\theta$.

7.4.4 Expected Charge Distribution: Scattered Light

The scattered light that hits the PMTs can be distinguished from direct photons by using the timing information. The *time residual*, t'_i, for the i-th PMT as defined in Equation (7.5) is used to determine the "off timing" by the criteria:

$$t_{peak} - 30\text{nsec} < t'_i < t_{peak} + 2\sigma_i + 5\text{nsec} \qquad \text{(Direct photons)} \tag{7.21}$$

$$t_{peak} + 2\sigma_i + 5\text{nsec} < t'_i \qquad \text{(Scattered photons)} \tag{7.22}$$

where t_{peak} is the time at the peak position of the time residual distribution, and σ_i is the measured timing resolution as a function of observed charge (p.e.).

The charge due to the scattered photons, q_i^{scatt}, is estimated from the "Off timing" PMTs and added to the expected charge for the i-th PMT:

$$q_i^{\text{exp},l} = q_i^{l,\text{direct}} + q_i^{\text{scatt}} \tag{7.23}$$

where the label l denotes the lepton type and is either e or μ.

7.4.5 Performance of PID

The PID efficiency for single-ring events is shown in Figure 7.6.

7.5 Precise Vertex Reconstruction (MS-Fit)

The vertex fitter described earlier in Section 7.2.3, TDC-Fit, is a timing based fitter and mainly improves the vertex reconstruction along the direction parallel to the particle direction. MS-Fit improves the vertex reconstruction by including the ring pattern information. At this stage, the vertex is refitted with MS-Fit adjusting the vertex position and particle direction using the PID likelihood, while simultaneously using TDC-Fit to modify the vertex in the direction parallel to the particle direction using the timing information. This is an iterative process and continues until the changes in the vertex position and the particle direction is less than 5 cm and 0.5°, respectively. The vertex resolution for single-ring events is approximately 30 cm.

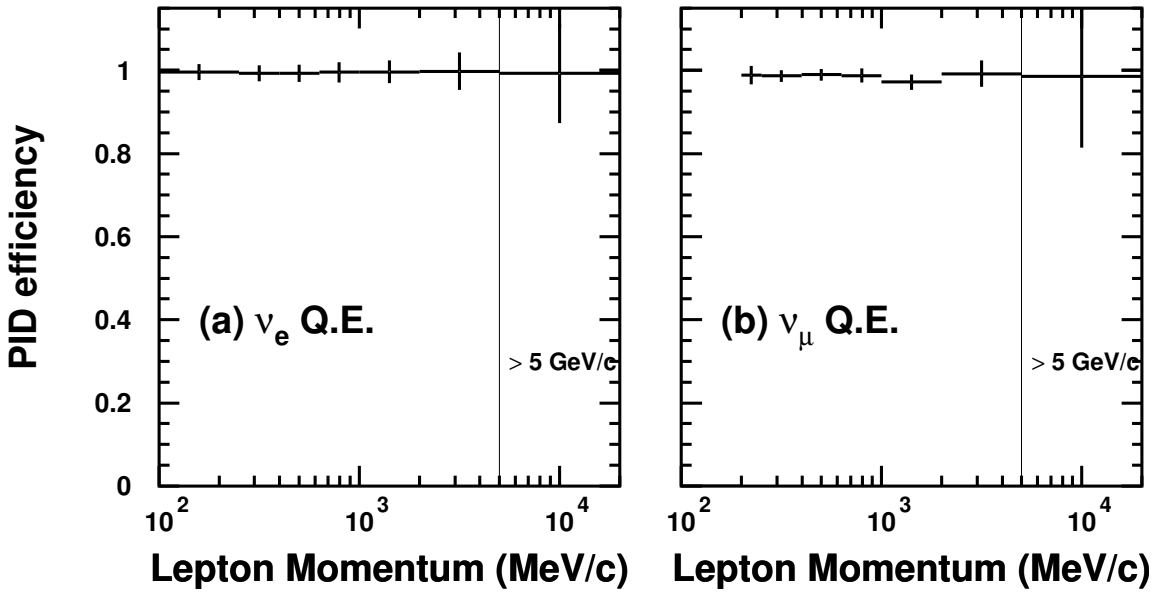

Figure 7.6: The PID efficiency for CC quasi-elastic single-ring events as a function of charged lepton momentum for (a) ν_e and (b) ν_μ.

MS-Fit	Resolution (cm)				Angular Resolution (°)			
Event type	SK-I	SK-II	SK-III	SK-IV	SK-I	SK-II	SK-III	SK-IV
FC Sub-GeV								
Single-Ring e-like	31.2	35.6	31.1	31.5	3.1	3.2	3.0	3.0
μ-like	23.8	30.3	23.9	23.5	1.9	2.1	1.9	1.9
FC Multi-GeV								
Single-Ring e-like	33.5	34.3	33.4	33.5	1.2	1.3	1.2	1.2
μ-like	24.8	26.9	25.1	23.7	0.8	1.0	0.8	0.8
Multi-Ring μ-like	67.4	111.8	73.8	87.8				
PC	53.6	62.8	52.6	67.0	1.0	1.2	0.9	0.9

Table 7.1: The vertex and angular resolution of MS-Fit. The resolution is defined as the width where 68 % of the events are included.

7.6 Decay Electron Search

The selection efficiency of μ-like events can be improved by requiring the detection of the electron produced by the muon decay (decay electron). After the primary event, the presence of a *decay electron* is searched for. The electrons found in this way are classified depending on the following criteria:

- Sub-event type
  Decay electrons observed as a separate event (sub-event) as shown in Figure 7.7.

- Primary-event type
  Decay electrons observed in the same event as the primary event.

- Split type
  Decay electrons that appear at the end of the primary event timing window, and therefore their energy deposition is split between the primary event and the sub-event.

For the Sub-event type decay electrons, the following criteria are required:

1. The time interval from a primary event(Δt) is $< 30\,\mu$sec.

2. The total number of hit PMTs is greater than 50 (25 for SK-II).

3. The goodness of vertex fit is greater than 0.5.

4. The number of hit PMTs in a 50 nsec time window is greater than 30 (15 for SK-II).

5. The total number of photoelectrons is less than 2000 (1000 for SK-II).

6. The number of hit PMTs in a 50 nsec time window (N_{50}) is greater than 60 (30 for SK-II).

noting that the numbers are different for the SK-II period due to the difference in the phototube coverage.

For the Primary-event type decay electrons, another peak is searched for in the primary event time window after the initial main event. Further required conditions are:

7. The number of hit PMTs in a 30 nsec time window is greater than 40 (20 for SK-II). (for the Primary-event type and Split type)

8. $0.1\,\mu\text{sec} < \Delta\text{t} < 0.8\,\mu\text{sec}$ or $1.2\,\mu\text{sec} < \Delta\text{t} < 30\,\mu\text{sec}$. (for all types)

N_{50}=60 (30 for SK-II) corresponds to about $\sim$11 MeV of electron energy. Criterion (1.) rejects the gamma emission from a μ^- capture on ^{16}O nuclei. The decey electron reconstruction is not so efficient around 1 μsec and Criterion (8.) rejects the decays around this timing. The efficiency of detecting these electrons are 80 % and 63 % for μ^+ and μ^-, respectively.

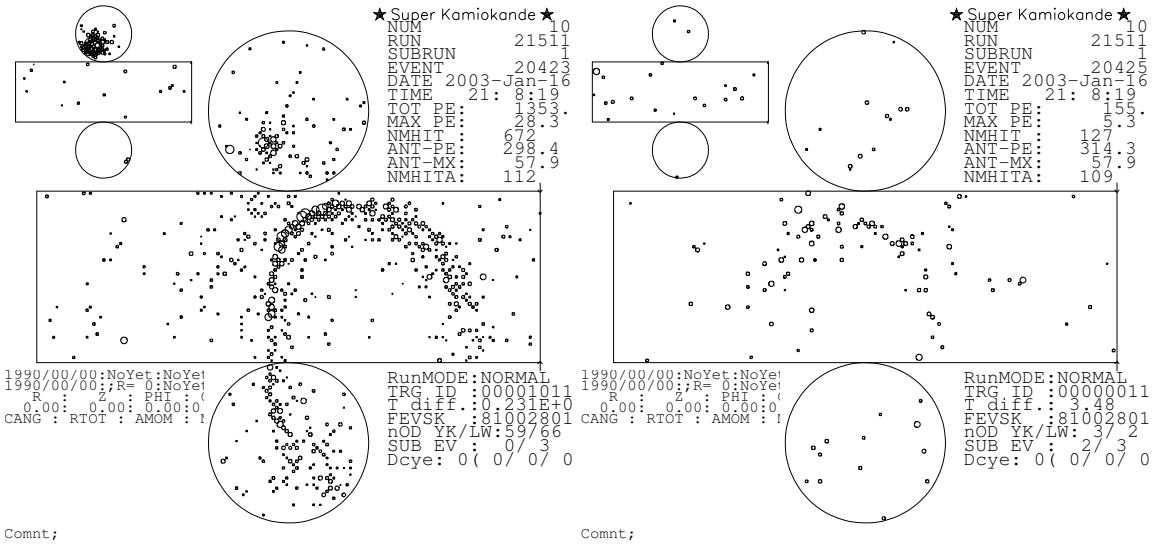

Figure 7.7: An event display of a Sub-event type decay electron where the time difference between the two events is $\sim$3.5 μsec. The primary event (cosmic ray stopping muon) is shown on the left and the following decay electron event on the right.

7.7 Momentum Reconstruction

The momentum is estimated by considering the relationship between the number of observed Cherenkov photons inside a cone with a half opening angle of 70° and the momentum of the particles. In the reconstruction, the momentum for individual rings is determined by separating the observed charge (p.e.) in each hit PMT into the charge contribution from each ring. The separation of the observed charge is carried out based on the expected charge distribution from each ring as a function of the opening angle θ and uniform in azimuthal angle ϕ. The observed charge (p.e.) in the i-th PMT from the n-th ring is estimated as:

$$q_{i,n}^{\rm obs} = q_i^{\rm obs} \times \frac{q_{i,n}^{\rm exp}}{\sum_{n'} q_{i,n'}^{\rm exp}} \tag{7.24}$$

where $q_i^{\rm obs}$ is the total observed charge in the i-th PMT, and $q_{i,n}^{\rm obs}$ is the fractional charge from the n-th ring in the i-th PMT. The expected charge is $q_{i,n}^{\rm exp}$, and the sum of n' is over all the identified rings.

To calculate the charge inside the 70° cone, the charge in each PMT is corrected for the light attenuation in water and the acceptance of the PMT as follows:

$$RTOT_n = \frac{G_{\rm MC}}{G_{\rm data}} \left[\alpha \times \sum_{\substack{\theta_{i,n}<70^\circ \\ -50{\rm nsec}<t_i<250{\rm nsec}}} \left(q_{i,n}^{\rm obs} \times \exp\left(\frac{r_i}{L}\right) \times \frac{\cos\Theta_i}{f(\Theta_i)} \right) - \sum_{\theta_{i,n}<70^\circ} S_i \right] \tag{7.25}$$

where

α : Normalisation factor

$G_{\rm data}$, $G_{\rm MC}$: Relative PMT gain parameter for data and Monte Carlo simulation

$\theta_{i,n}$: Opening angle between the n-th ring direction and the i-th PMT direction

Θ_i : Angle of photon arriving direction relative to the i-th PMT facing direction

t_i : TOF subtracted hit timing of the i-th PMT position

L : Light attenuation length in water

r_i : Distance from the vertex position to the i-th PMT

$f(\Theta)$: Correction function for the PMT acceptance

S_i : Expected charge (p.e.) for the i-th PMT from scattered photons

To reject the effect from muon decay electrons, the summation is restricted to be within the time window from -50 nsec to +250 nsec around the peak of the TOF subtracted hit timing distribution. The time variation of observed data is corrected for the attenuation length in water, L, by the continuous measurement of cosmic ray through-going muons (Section 5.1.4). The momentum resolution is approximately given by:

$$\sigma_p = \begin{cases} 0.6 + \frac{2.6}{\sqrt{p(\mathrm{GeV}/c)}}\ \% & \text{for electron} \\ 1.7 + \frac{0.7}{\sqrt{p(\mathrm{GeV}/c)}}\ \% & \text{for muon} \end{cases} \tag{7.26}$$

The resolution is defined as the 1 σ width of the Gaussian fit.

7.8 Ring Number Correction

Some of the rings are mis-identifited and have low momentum or are overlapped with other reconstructed rings. So at this stage rings that match either of the following 2 sets of criteria are deemed to be mis-identified and are removed from the reconstruction.

The procedure compares the i-th reconstructed ring with the j-th identified ring, where $i \neq j$. The first set of criteria remove the i-th ring if it is of low momentum and overlapping with a larger momentum ring. The second set removes the i-th ring if it has a very low momentum fraction.

(1-1) $p_i < p_j$; $i \neq j$
where p_i is the momentum of i-th ring.

(1-2) $\theta_{ij} < 30^\circ$
where θ_{ij} is the angle between the i-th and j-th ring directions.

(1-3) $p_i \cos\theta_{ij} < 60\,\mathrm{MeV/c}$
where $p_i \cos\theta_{ij}$ is the momentum of i-th ring projected perpendicularly to j-th ring.

or

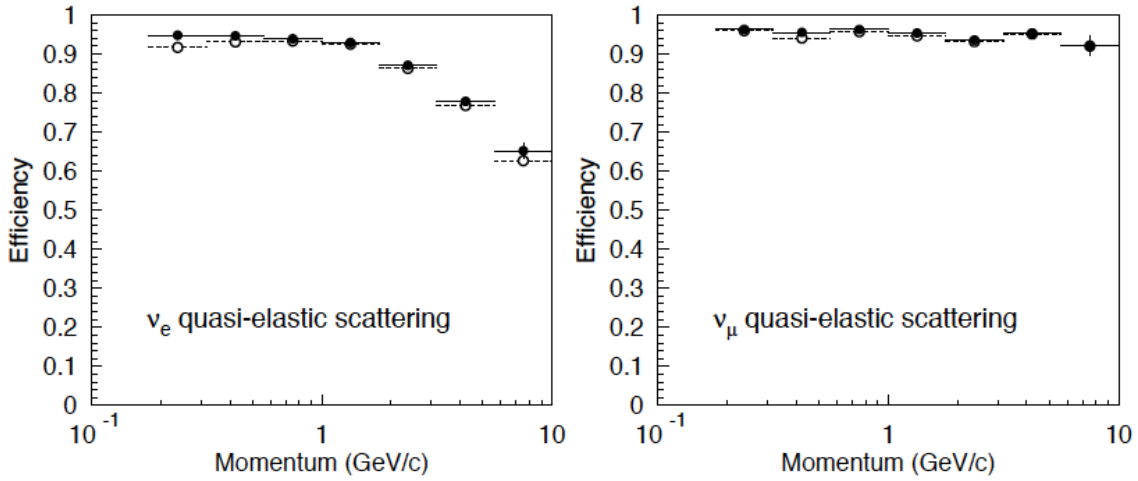

Figure 7.8: Reconstruction efficiency for single-ring events as a function of momentum before and after the ring number correction. The left figure shows the ν_e events and ν_μ on the right. The efficiency before the ring number correction is shown by the white points, and the final result by the black points.

(2-1) $p_i < 40\,\mathrm{MeV/c}$

(2-2) $p_i/p_{\mathrm{tot}} < 0.05$
where p_{tot} is the total momentum for all rings.

After removing poorly reconstructed rings by one of either of the two sets of criteria above, the resulting ring counting efficiency for single-ring events can be seen in Figure 7.8

7.9 π^0 Reconstruction

A π^0 produced from an interaction immediately decays into two γs, which can be reconstructed as a π^0 by the algorithm described in Section 5.3.2. However, if one of the γ from π^0 decay is missed by the reconstruction, the event may sometimes be classified as a single-ring e-like event. This mis-identification may occur for the following reasons:

1. The energies of the two γs are considerably asymmetric and the energy of the second γ ($\mathrm{E}_{\gamma 2}$) is too small to be reconstructed as a ring.

2. The rings of the two γs overlap and are reconstructed as one ring when the opening angle between the two γs is small.

The relationship between the momentum of the second γ and the opening angle between the two γs is shown in Figure 7.9. Figure 7.9 also shows the momentum distribution of the expected NC single π^0 events, with the hatched region showing events mis-identified as single-ring e-like. The mis-identified events amount to 33% of the NC single π^0 events.

The π^0 fitter assumes the existence of two overlapping rings and compares the observed charge distribution with the expected charge distribution of two γs. The direction of the more

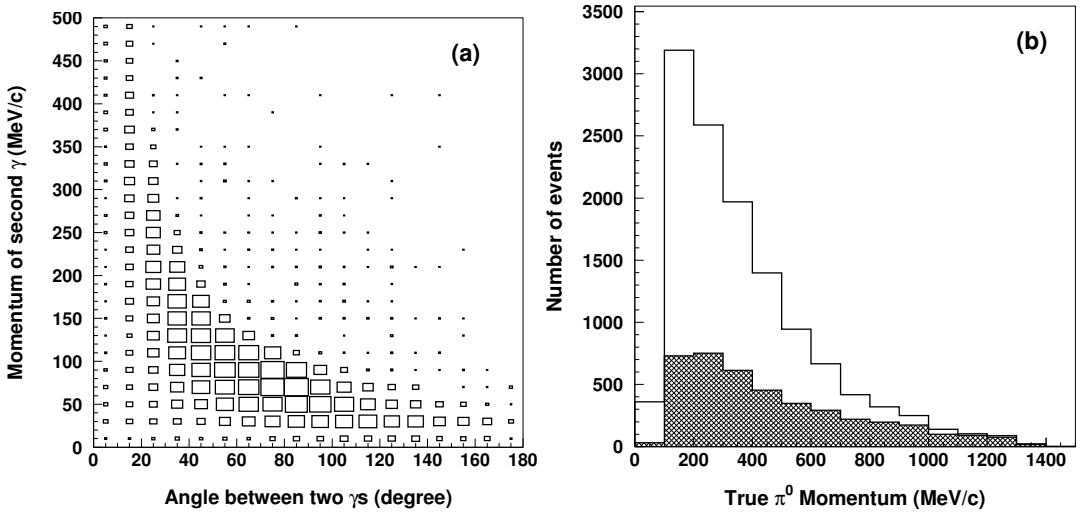

Figure 7.9: (a) A scatter plot of the true momentum of the second gamma against the true opening angle between two gammas for NC1π^0 events in the atmospheric Monte Carlo events. (b) Distribution of the true π^0 momentum for NC1π^0 events in the atmospheric Monte Carlo events. The hatched region shows the NC1π^0 mis-identified as single-ring e-like events.

energetic γ is fixed in the direction from the precise vertex reconstruction, and the second γ is searched for by varying its direction and the energy shared between the two γs until a best-fit combination is found. The two gamma-rays are assumed to be emitted from one vertex.

The expected charge distribution for the i-th PMT is calculated as follows:

$$q_i^{\mathrm{exp},\pi} = \alpha_e \times Q_\pi^{\mathrm{exp}}(\theta_i, p_\gamma, r_i) \times \left(1 - \frac{r_i}{\sqrt{r_i^2 + R_{PMT}^2}}\right) \times \frac{1}{\exp(r_i/L)} \times f(\Theta_i) + q_i^{\mathrm{scatt}} \qquad (7.27)$$

where

α_e	:	Normalisation factor
Q_π^{exp}	:	Expected photon distribution from a gamma-ray as a function of θ_i, p_γ and r_i
θ_i	:	Opening angle between the i-th PMT direction and the ring direction
p_γ	:	Initial gamma-ray momentum
r_i	:	Distance from the vertex to the i-th PMT
R_{PMT}	:	Radius of a PMT$\sim$25 cm
L	:	Light attenuation length in water
$f(\Theta_i)$	:	Correction for the PMT acceptance as a function of the photon incidence angle Θ_i
q_i^{scatt}	:	Expected charge for the i-th PMT from scattered photons

Q^{exp} is the expected photon distribution as a function of opening angle θ_i from the ring direction to the i-th PMT, the initial gamma-ray momentum p_γ and the distance from the vertex to the i-th PMT r_i. The factor $\left(1 - r_i/\sqrt{r_i^2 + R_{PMT}^2}\right)$ corrects for the solid angle, and exp(-r_i/L) accounts for the light attenuation. Note that the charge contribution from scattered hits is already included in Equation (7.27), and q_i^{scatt} is calculated in the same way as that described in Section 7.4.4.

The best-fit configuration of two gamma-rays is determined by a log likelihood method. The likelihood is defined as:

$$\mathcal{L}_\pi = \sum_{i=1} log\left(prob\left(q_i^{\text{obs}}, q_i^{\text{exp},\pi}\right)\right) \tag{7.28}$$

The expected charge from a pion, $q_i^{\text{exp},\pi}$, is optimized by changing the direction and momentum fraction of the second gamma to achieve the maximum likelihood value for $\mathcal{L}_\pi$. The probability function, $prob(q_i^{\text{obs}}, q_i^{\text{exp}})$, is the same as that defined in Equation (7.13) and checks how well $q_i^{\text{exp},\pi}$ matches q_i^{obs}.

After the first fit, the π^0 reconstruction process is re-iterated with finer stepping size to improve the fitting performance for events where two rings are almost overlapped. Such events give a narrow $\mathcal{L}_\pi$ distribution. The maximum likelihood between the first and second fit is chosen as the fitting result.

The invariant mass of the π^0, M_{inv}, is defined as:

$$M_{inv} = \sqrt{2E_{\gamma 1}E_{\gamma 2}(1 - \cos\theta_{\gamma\gamma})}. \tag{7.29}$$

7.10 Upward-Going Muons

The aim of the upward-going muon samples is to analyse neutrino events with very high energy. In the L/E analysis, it is difficult to determine the resolution of these events and they are not included in the present analysis. Figure 7.10 shows the flux of these upward-going muon events against the energy of the primary neutrino.

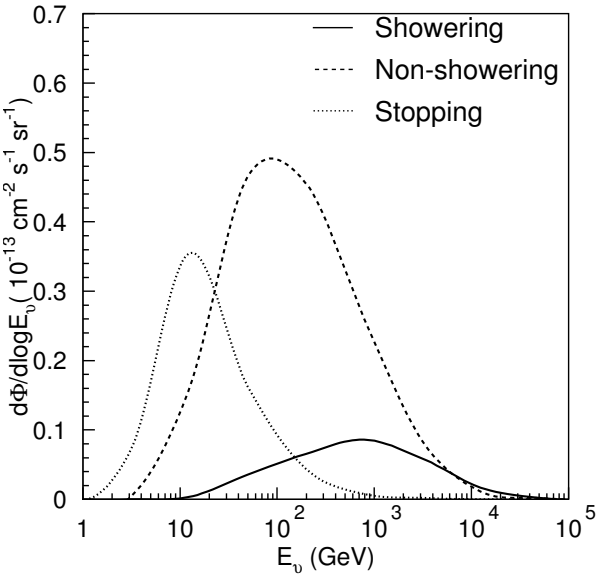

Figure 7.10: Flux of Upward going muon events against energy by event type. The upward muon events are shown by the dotted line for upward stopping, the dashed line for non-showering and the solid line for showering events.

Chapter 8

An Update of the 2-Flavour L/E Analysis

Neutrino Oscillations is a theory where the probability of a neutrino changing from one flavour to another depends on the ratio of the distance travelled by the neutrino and its energy, L_ν/E_ν. The expected oscillatory pattern can be observed by plotting the variable L_ν/E_ν, reproducing the characteristics of Neutrino Oscillations. The L/E survival probability for 2-flavour $\nu_\mu \to \nu_\tau$ oscillations is shown in Figure 8.1, for the typical parameters $\sin^2 2\theta_{23} = 1.0$ and $\Delta m^2_{32} = 2.5 \times 10^{-3}\,\text{eV}^2$. The oscillation parameters were defined as in the following 2-flavour survival probability:

$$P(\nu_\mu \to \nu_\mu) = 1 - \sin^2 2\theta_{23} \sin^2 \left(\frac{1.267 \Delta m^2_{32} L_\nu}{E_\nu} \right). \tag{8.1}$$

The analysis in this chapter aims to reconstruct primarily the first dip, at the region where the oscillation probability reaches its first maximum point. As it can be seen from the figure, the subsequent oscillation maxima are closely spaced together in $\log_{10}(L/E)$. So it is very challenging to achieve a high enough resolution to resolve the second or third oscillation maxima. The Δm^2_{32} parameter characterises the range of L/E values that the deficit in ν_μ occurs; and $\sin^2 2\theta_{23}$ characterises the magnitude of the deficit. The increased sensitivity to Δm^2_{32} of this analysis comes from reconstructing the position of the dip. While sensitivity to $\sin^2 2\theta_{23}$ is achieved by the relative difference of the distribution for no oscillations at low L/E and the averaged oscillations at high L/E, as well as from the depth of the dip.

The L/E Analysis reconstructs the main characteristics of Neutrino Oscillations by selecting a precision sample of data with a good resolution in L/E. This gives it an improved sensitivity to the oscillation parameters, and in particular this analysis has the most discriminating sensitivity to Δm^2_{32} from atmospheric neutrinos. Relying on this advantage, any discrepancy between the Δm^2_{32} for neutrinos and anti-neutrinos was investigated to confirm the CPT symmetry in Neutrino Oscillations in Chapter 9. The strength of the L/E analysis with 3-flavour and matter effects was considered in Chapter 10, while the deviation from pure 3-flavour oscillations in the prescence of Non-Standard Neutrino Interaction (NSI) effects was studied in Chapter 11.

Each of the analyses share the L_ν/E_ν distributions. How these variables are extracted and their treatment are described in this chapter, along with the standard 2-flavour L/E analysis. The L/E data quality, the likelihood analysis method, and the systematic uncertainties are also presented in detail here. So the explanations that follow are relevant to all the analyses presented

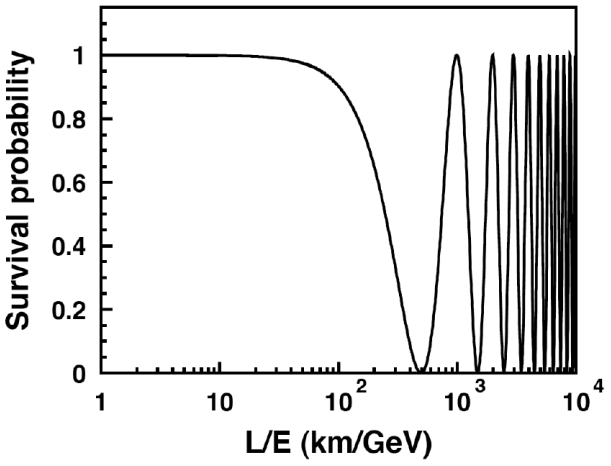

Figure 8.1: L/E survival probability for 2-flavour $\nu_\mu \to \nu_\tau$ oscillations for $\sin^2 2\theta_{23} = 1.0$ and $\Delta m^2_{32} = 2.5 \times 10^{-3}\,\text{eV}^2$. The first oscillation dip is seen at L/E $\sim$500 km/GeV. The subsequent oscillation maxima are closely spaced together in $\log_{10}(L/E)$

in Chapters 9, 10, and 11.

8.1 Dataset and Treatment

For the analyses in this thesis a common dataset was used and divided into samples of interest. The data collected span over 10 years and 4 setups of the detector: SK1 (1489.2 days), SK2 (798.6 days), SK3 (518.084 days) and SK4 (1096.7 days). This data has gone through a process of reduction to remove background events, fully described in Chapter 6. Then the following event samples were collected: Fully-Contained (FC) Single-Ring, FC Multi-Ring, Partially-Contained (PC) Stopping and PC Through-Going. These samples span over a wide range of energies. Depending on the energy, the event topology differs and so the treatment of the data are different for each sample. The details of this selection procedure are written here.

8.1.1 Fully-Contained: Single-Ring (FC1R) and Multi-Ring (FCmR)

The Fully-Contained samples were chosen to select events that remain within the Fiducial Volume of the Inner Detector. Typical energies of FC events may range from some 10s of MeV to around 100 GeV. Firstly, to select the FC events, the following cuts were made:

- Reconstructed vertex is within the Fiducial Volume. Distance from the vertex to the top and bottom ID wall should be > 1.5 m, and to the barrel ID wall should be > 1 m.
- Number of hit PMTs in any cluster in the OD should be < 10 (16) for SK1 (SK2-4).
- Visible energy (E_{vis}) should be > 30 MeV.

The Fiducial Volume defined for FC events used in the L/E distributions was larger than in the Zenith angle analysis or the PC samples. This was done to increases statistics, which were reduced by requiring a high resolution in L_ν/E_ν (Section 8.3).

Then to select the Single-Ring (FC1R) events, which span up to $\sim$10 GeV, the following additional cuts were made:

- The event should be identified as having only one ring.

- The ring should be reconstructed as μ-like and have momentum $p_\mu > 200\,\mathrm{MeV/c}$.

To select the FC Multi-Ring (FCmR) sample, the FC cuts were applied, followed by the following selections:

- The number of rings identified should be > 1.
- The most energetic ring should be reconstructed as μ-like and have momentum $p_\mu > 600\,\mathrm{MeV/c}$ and $E_{\mathrm{vis}} > 600\,\mathrm{MeV}$.

8.1.2 Partially-Contained: PC Stopping And PC Through-Going

The Partially-Contained (PC) sample consisted of events with an outgoing muon that left the Inner Detector (ID) and penetrated into the Outer Detector (OD). There was a special treatment for the energy reconstruction by considering the muon track length and the dE/dx for the muon energy deposited. The details are described in Section 8.2.1. The cuts made to select the PC sample were:

- Vertex is within the Fiducial Volume. Distance from the vertex to the ID wall should be $> 2\,\mathrm{m}$.
- Number of hit PMTs in any cluster in the OD should be > 10 (16) for SK1 (SK2-4).
- Visible energy (E_{vis}) should be $> 350\,\mathrm{MeV}$.
- The total charge deposited in the ID should be > 3000 (1500) photoelectrons for SK1 and SK3-4 (SK2).
- The reconstructed neutrino energy (E_{vis2}) should be $< 50\,\mathrm{GeV}$.

The last cut is related to the resolution cut, discussed in Section 8.3.4; and E_{vis2} is the total energy reconstructed for all outgoing charged particles, explained in Section 8.2.1. Then the PC sample was further divided into PC Stopping and PC Through. PC Stopping consisted of events where the outgoing muon stopped in the OD, while in the PC Through sample the muons passed through the OD and exited the detector. The details of how the events were separated into these two categories is described in Section 8.1.3. To select the PC Stopping events, the following additional cuts were made:

- Must be classified as stopping in the OD. $PE_{\mathrm{anti}} < PE_{\mathrm{exp}}/1.5$.
- The most energetic ring or the second most energetic should be reconstructed as μ-like.

The μ-like cut was made to increase the purity of muon events in this sample. This was not necessary for the PC Through sample which retained a high purity of muons. To select PC Through events, the PC cuts were applied then the following PC separation selection was made:

- Must be classified as passing through the OD. $PE_{\mathrm{anti}} > PE_{\mathrm{exp}}/1.5$.

8.1.3 PC Stopping and Through-Going Separation

The PC sample was separated into two categories. Events in which the muon was expected to have stopped in the OD were classified as *PC Stopping* and those which passed through as *PC Through-Going*. In the case of PC Stopping, the energy of the muon can be reconstructed accurately by considering the path it took and calculating the energy loss from dE/dx. On the other hand, the energy calculated in the PC Through sample was a lower limit for the muon energy.

The separation was made by considering the charge deposited in the OD (PE_{anti}) and comparing it with the expected charge deposition in the OD of a muon exiting the OD (PE_{exp}). Specifically, the charge measured was the maximum number of photoelectrons in a sliding 500 ns window from -400 ns to $+500$ ns from the event time. If the ratio of these charges, $PE_{\text{anti}}/PE_{\text{exp}}$, was less than 0.67 (or 1/1.5) then the event was classified as PC Stopping and PC Through-Going otherwise. A ratio close to 1 would be expected for a PC Through event.

The expected charge, PE_{exp}, was a tuned value since the charge distribution in the OD depends on the structural geometry and the make-up of old and new PMTs in the OD. A MC sample was used to measure the charge deposited in the OD by the method described above, and this value was normalised by the calculated path through the OD for an exiting muon. This formed a distribution of charge/cm and had a peak at the charge/cm for a PC Through event. These peak values were measured for several regions of the OD: Top, Bottom, Barrel, and Edge. So in the analysis, the path through the OD for a PC event could be calculated and multiplied by the tuned peak values to form the variable PE_{exp}. Then the $PE_{\text{anti}}/PE_{\text{exp}}$ ratio was used to classify the event. The distributions of PE_{anti}/PE_{exp} (or $Q_{\text{obs}}/Q_{\text{exp}}$) and the cut position are shown in the left of Figure 8.2.

It was found that due to the charge response in the OD, a significant number of PC Through events were leaking into the PC Stopping sample – enough to cause an asymmetry in a zenith distribution of the PC samples. The effect was that the peak of the $PE_{\text{anti}}/PE_{\text{exp}}$ (or $Q_{\text{obs}}/Q_{\text{exp}}$) distributions pulled away from a ratio of 1 with a variation in the Z coordinate or radius. This was corrected for by fitting the peak of $Q_{\text{obs}}/Q_{\text{exp}}$ against the Z position or radius, and then calculating a correction factor to make the peak of $Q_{\text{obs}}/Q_{\text{exp}} = 1$ at all positions. In the right of Figure 8.2, the top plot shows the asymmetry of $Q_{\text{obs}}/Q_{\text{exp}}$ which was fitted; and the bottom plot shows a heat map of the number of events after applying the correction. A greater number of events is shown by red and fewer events by blue.

The systematics for the PC separation were calculated with the $Q_{\text{obs}}/Q_{\text{exp}}$ distributions. The peak was fitted for data and for MC, then the MC distribution was shifted to make the data and MC peaks match. The percentage of PC Stopping events that changed category was taken as the estimation for the uncertainty in the PC separation.

8.2 Reconstruction of L/E

Neutrino Oscillations have an L/E dependence so it is vital that both the flight path and the energy of the neutrino are reconstructed as accurately as possible. If the resolution is not sufficient, the L/E dependence will average out. This averaging effect can also be seen at large values of L/E, after the first oscillation maximum, where the oscillations become very rapid and it is experimentally difficult to resolve the L/E pattern, as seen in Figure 8.1.

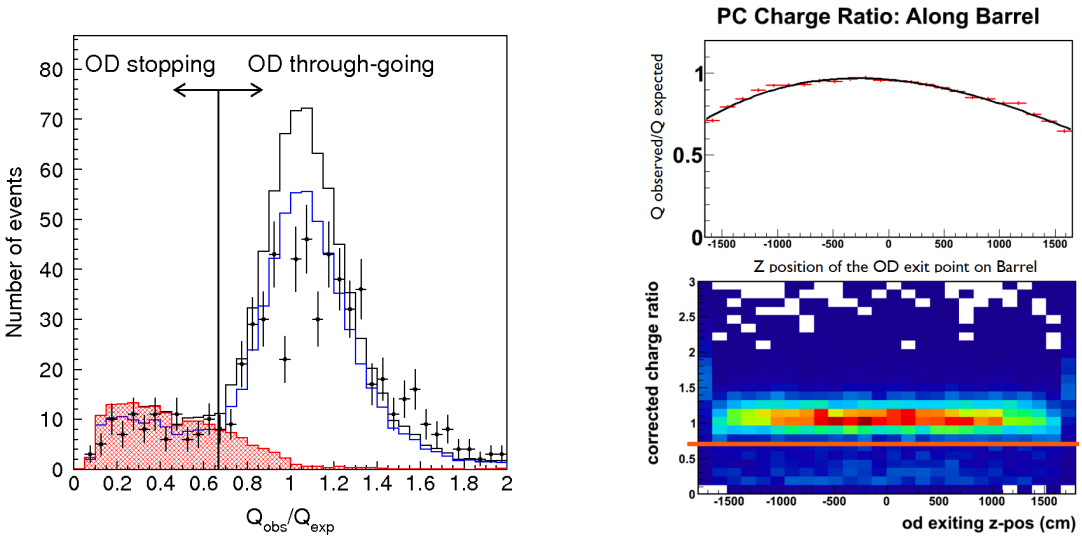

Figure 8.2: The $Q_{\text{obs}}/Q_{\text{exp}}$ ($\equiv PE_{anti}/PE_{exp}$) of PC events penetrating the Barrel section is shown on the left, and figures illustrating the PC charge asymmetry correction on the right. Left: Q_{exp} is the expected charge for a PC Through event, so for a $Q_{\text{obs}}/Q_{\text{exp}}$ ratio of 1, the muon likely exited the OD. This ratio was used to classify the PC events as shown by the cut arrows. The black points are data and the black histogram is the non-oscillated MC, the blue histogram is oscillated MC, and the red hatched histogram are the true stopping events estimated from the MC. Right: the asymmetry of the $Q_{\text{obs}}/Q_{\text{exp}}$ with the Z coordinate along the Barrel region in the top figure; and a heat map of $Q_{\text{obs}}/Q_{\text{exp}}$ after applying the correction to the ratio. A greater number of events is shown by red and fewer events by blue. After the correction, the ratio is flat w.r.t. the Z coordinate, shown by the flat red band.

8.2.1 Neutrino Energy

The neutrino energy calculation was based on the total energy reconstructed for all outgoing charged particles, E_{vis2}. Since various event topologies were expected, the precise energy reconstruction depended on the sample. In particular for PC events, as some of the energy was deposited outside of the ID.

FC Single-Ring

Since the event is fully contained in the Fiducial Volume and only 1 ring was found, the energy reconstruction is rather straight forward. The total visible energy is taken to be the energy of the outgoing muon:

$$E_{\text{vis2}} = E_{\mu}. \tag{8.2}$$

FC Multi-Ring

In the case of FC Multi-Ring events, the energy reconstruction assumes that the most energetic ring was formed by the outgoing muon from a CC interaction. The remaining rings are assumed to be pions if the ring is identified as μ-like and electrons if the ring is e-like. Then the total energy is the summation over all of these rings:

$$E_{\text{vis2}} = E_{\mu} + \sum_{i=2}^{n} (E_{\pi}^{i} \text{ or } E_{e}^{i}). \tag{8.3}$$

Careful treatment is required for the μ-like rings expected to be formed from pions. In the standard reconstruction, the energy of such rings assumes that the source charged particle is a muon, and the Cherenkov energy threshold for the muon is used. So to reconstruct the pion energy, the assumed muon energy is adjusted by considering the difference in the energy threshold for Cherenkov emission.

Whether the particle is a pion or a muon, the visible energy in the ring does not include the energy before the threshold, like so:

$$E_{\text{ring}} = E_{\mu} - E_{\mu}^{\text{th}}, \qquad \text{or} \qquad E_{\text{ring}} = E_{\pi} - E_{\pi}^{\text{th}}, \tag{8.4}$$

where the energy thresholds are defined to be:

$$E_{\mu}^{\text{th}} = 160\,\text{MeV}, \tag{8.5}$$

$$E_{\pi}^{\text{th}} = 212\,\text{MeV}. \tag{8.6}$$

Furthermore, assuming the dE/dx in water is constant and also independent of the energy and the type of particle, then the number of emitted Cherenkov photons is simply proportional to the track length. Then the energy deposited by a muon or pion, estimated from the same ring, is equal:

$$E_{\text{ring}} = E_{\mu} - E_{\mu}^{\text{th}} = E_{\pi} - E_{\pi}^{\text{th}}. \tag{8.7}$$

Then the energy of the pion can be reconstructed:

$$\begin{aligned} E_{\pi} &= (E_{\pi} - E_{\pi}^{\text{th}}) + E_{\pi}^{\text{th}} \\ &= (E_{\mu} - E_{\mu}^{\text{th}}) + E_{\pi}^{\text{th}} \\ &= E_{\mu} + (E_{\pi}^{\text{th}} - E_{\mu}^{\text{th}}). \end{aligned} \tag{8.8}$$

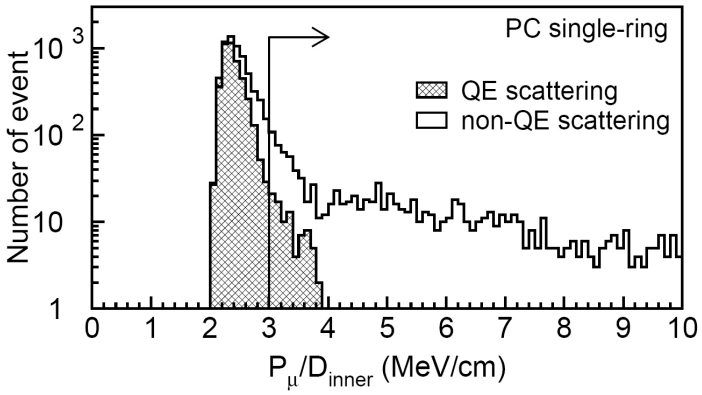

Figure 8.3: Distribution of the momentum of the most energetic muon ring against the track length in the ID, $P_\mu/D_{\rm inner}$. The histograms have been divided into Quasi-Elastic (QE) interactions (hatched) and non-QE interactions using the Atmospheric MC PC Single-Ring sample. Events to the right of the arrow are separated into a muon ring and an electron ring.

Therefore E_π is assumed to be,

$$E_\pi = E_\mu + 52\,\mathrm{MeV}. \tag{8.9}$$

PC Sample

The PC sample consists of events in which the muon escapes the ID and penetrates into the OD. However, the energy for such events can still be accurately reconstructed by considering the path of the muon and the energy deposition, dE/dx, in the OD and the dead region between the ID and OD. Therefore,

$$E_{\rm vis2} = E_{\rm ID} + E_{\rm dead} + E_{\rm OD}. \tag{8.10}$$

For PC events, the incoming neutrinos are quite energetic ($\sim$10 GeV), so there is a significant possibility of collinear outgoing particles being mis-reconstructed as a single ring in the ID. Therefore a correction is made to the number of rings before the energy in the ID, $E_{\rm ID}$, is calculated.

These mis-reconstructed rings can be distinguished by comparing the momentum of the ring, P_μ, against the track length in the ID, $D_{\rm inner}$, as shown in Figure 8.3. A Quasi-Elastic event is a clean single ring CC event in which the proton was below Cherenkov threshold, while a Non-Quasi-Elastic interaction should have multiple rings. A wide tail can be seen in Figure 8.3, which is due to near-parallel pions and/or other particles causing the reconstructed momentum to be considerably larger than what would be expected for a muon ($\sim$2.4 MeV/cm).

This is corrected for by separating the muon rings with suspected overlapping particles. If the most energetic muon ring has $P_\mu/D_{\rm inner} > 3.0\,\mathrm{MeV/cm}$, then the ring is separated into a muon ring with momentum estimated from the track length in the ID and an electron ring. The muon momentum is calculated as $D_{\rm inner} \times dE/dx$, where $dE/dx = 2.4\,\mathrm{MeV/cm}$. Then the expected charge from the muon is subtracted from the overlapped ring, and the remaining charge is used to reconstruct the energy of the electron. Following this separation, the energy in the ID, $E_{\rm ID}$, can be calculated with improved resolution in the same way as the FC sample.

E_{dead} is the energy deposited by the muon in the dead region that is situated between the ID and OD. The energy is estimated by calculating the track length of the muon through the dead region and applying a dE/dx of 2.4 MeV/cm:

$$E_{\text{dead}} = D_{\text{dead}} \times dE/dx, \tag{8.11}$$

where D_{dead} is the track length of the muon in the dead region estimated from the vertex and ring direction.

E_{OD} is the energy deposited by the muon in the OD. The track length, D_{OD}, is estimated in a similar way to that of the E_{dead} case, however a modification is made depending on the PC classification. For OD Through events the track length is taken to be the full length of the muon track through the OD, whereas in the OD Stopping sample the track is assumed to be half this length. Then with a $dE/dx = 2.4\,\text{MeV/cm}$, E_{OD} is estimated as:

$$\begin{array}{lll} E_{\text{OD}} = 0.5\times D_{\text{OD}} \times dE/dx & \text{(for OD Stopping events)}, \\ E_{\text{OD}} = D_{\text{OD}} \times dE/dx & \text{(for OD Through events)}. \end{array} \tag{8.12}$$

Reconstructing E_ν

Once the total energy of all the charged particles, E_{vis2}, has been reconstructed, the neutrino energy is estimated via a fitted polynomial expression as a function of $\log(E_{\text{vis2}})$. The relationship between the neutrino energy, E_ν, and E_{vis2} was determined by fitting the following polynomial with the Monte Carlo:

$$E_\nu^{\text{rec}} = E_{\text{vis2}} \times (a + bx + cx^2 + dx^3), \tag{8.13}$$

where $x = \log(E_{\text{vis2}})$. The energy fitting for each of the event samples from SK4 can be seen in Figure 8.4. The energy resolution of the events in each sample can be seen in Figures 8.5, while the energy resolution against the observed energy is shown in Figure 8.6. These distributions were made from the MC simulation, showing the expected energy reconstruction resolution for the data, which was reconstructed in the same way. Details of the 70% resolution cut used in these figures can be found in Section 8.3.

8.2.2 Neutrino Flight Path Length

To estimate the neutrino flight path length, first the neutrino direction is reconstructed and the zenith angle calculated. The flight length can then be determined from the neutrino incident zenith angle. The details of the direction reconstruction varies for each event sample.

FC Single-Ring

In the FC Single-Ring sample, the neutrino direction is assumed to be simply the reconstructed direction of the muon. Then the *zenith angle* of the neutrino is taken to be:

$$\cos\Theta_\nu^{\text{rec}} = \cos\Theta_\mu, \tag{8.14}$$

where $\cos\Theta_\nu^{\text{rec}}$ and $\cos\Theta_\mu$ are the cosine of the zenith angle of the reconstructed neutrino and muon, respectively.

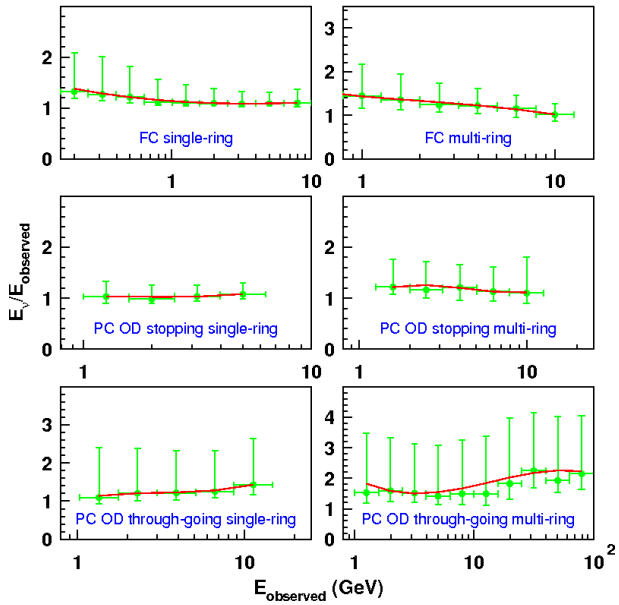

Figure 8.4: E_ν Reconstruction from fitting E_{vis2} to the true neutrino energy estimated by the Monte Carlo. The fitting for each of the event samples is shown, and the PC samples were further divided into single-ring and multi-ring. The fitted result for each SK period is shown in Appendix A.

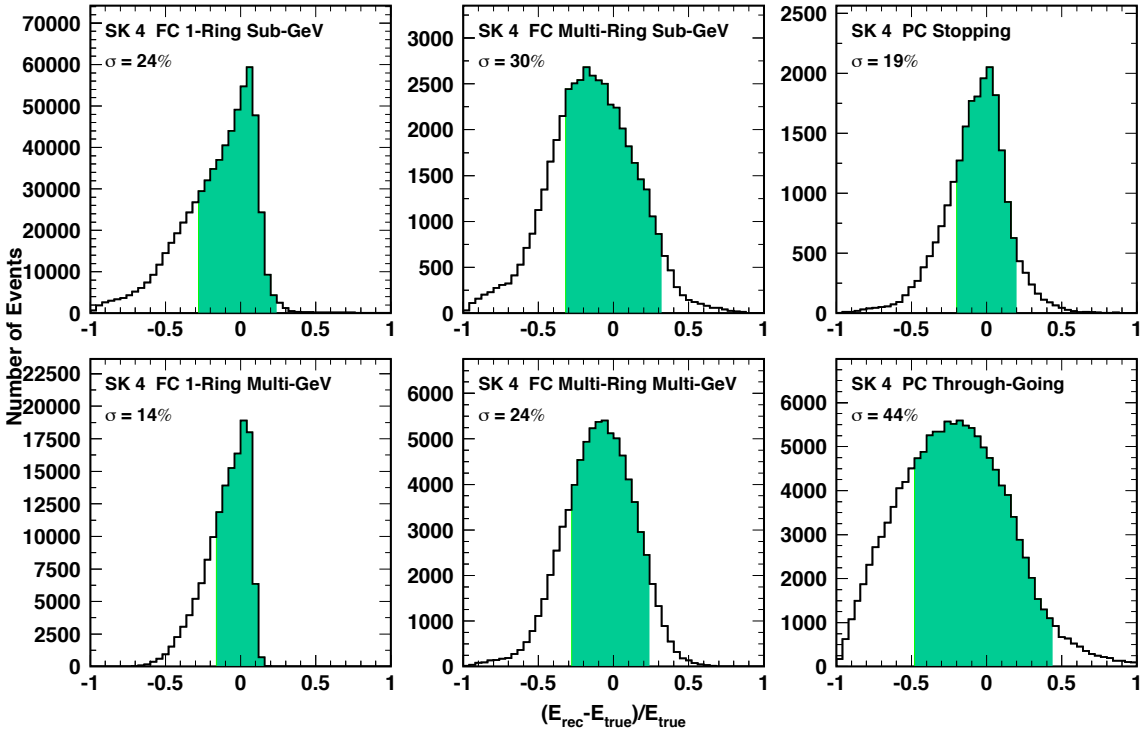

Figure 8.5: L/E Analysis energy resolution for SK4. The difference of the reconstructed and true neutrino energy with respect to the true neutrino energy, estimated by the MC, is shown. Events to the right of zero have been reconstructed with an energy larger than the true energy and vice versa for the left. The black solid histogram is for events satisfying the 70 % resolution cut, and the green shaded area corresponds to 68% of the events. The energy resolution for each SK period is shown in Appendix A.

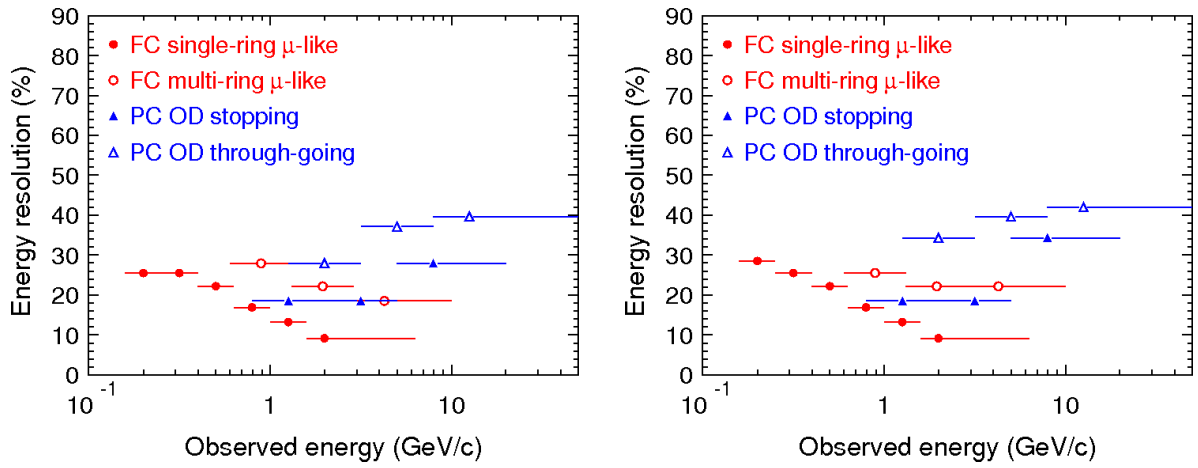

(a) SK1

(b) SK2

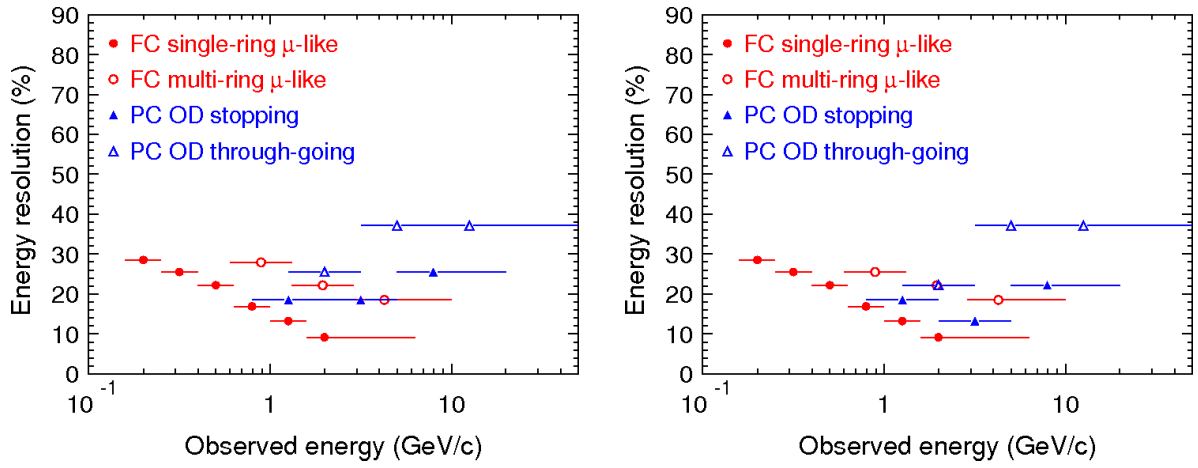

(c) SK3

(d) SK4

Figure 8.6: E_ν Resolution against the lepton momentum (or E_{vis2} for FC multi-ring), estimated with the MC. Each of the event samples are shown by the markers shown in the legend. The energy resolution for the FC samples are quite similar between each SK period, while the resolution for the PC samples vary slightly.

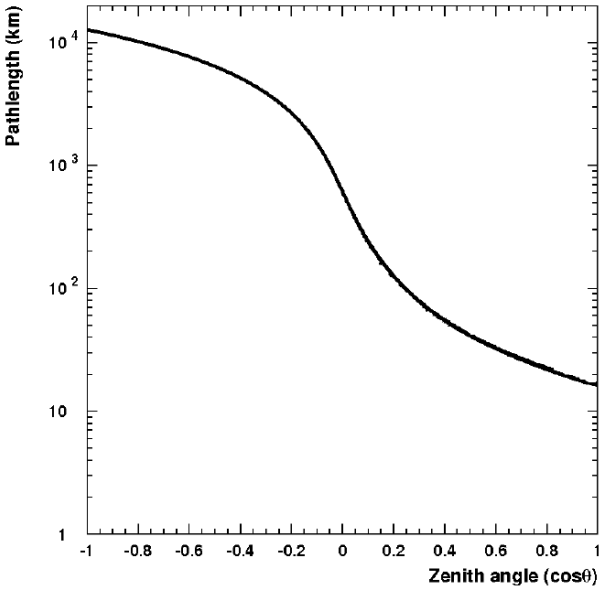

Figure 8.7: Neutrino flightpath through the Earth vs the incoming zenith angle of a neutrino. The flightpath changes rapidly for horizontal events. For upward-going events, the flightpath is so long that uncertainties of production in the atmosphere become negligible.

FC Multi-Ring

For the FC Multi-Ring sample, the neutrino direction is reconstructed as the momentum weighted sum of the directions of all the identified rings. The zenith angle of the neutrino is taken to be:

$$\cos\Theta_\nu^{\rm rec} = \cos\Theta_{\rm sum}, \tag{8.15}$$

$$\vec{d}_{\rm sum} = p_\mu \cdot \vec{d}_1 + \sum_{i=2}^{n} (p_\pi \text{ or } p_e) \cdot \vec{d}_i, \tag{8.16}$$

where the first ring is the muon ring with direction d_1 and momentum p_μ. The other rings are taken to be pions or electrons with momentum p_π or p_e, respectively. d_i is the direction of the i-th ring, with n rings in total. Then $\vec{d}_{\rm sum}$ is their momentum weighted direction summed over all identified rings. From this the summed zenith angle is calculated, $\Theta_{\rm sum}$, giving the zenith angle of the neutrino, $\Theta_\nu^{\rm rec}$.

PC Samples

The reconstruction of the neutrino direction for the PC samples is similar to that of the FC samples. However, for the Multi-Ring events there is an additional weighting factor applied to the most energetic muon ring in the direction calculation. This factor, α, is taken as 2.0 for OD Stopping events and 4.0 for OD Through events. This weighting was optimised to get the best performance for the reconstruction. The zenith angle of the neutrino is calculated like so:

$$\cos\Theta_\nu^{\rm rec} = \cos\Theta_\mu \qquad \text{(for Single-Ring)}, \tag{8.17}$$

$$\cos\Theta_\nu^{\rm rec} = \cos\Theta_{\rm sum} \qquad \text{(for Multi-Ring)}, \tag{8.18}$$

$$\vec{d}_{\rm sum} = \alpha \cdot p_\mu \cdot \vec{d}_1 + \sum_{i=2}^{n} (p_\pi \text{ or } p_e) \cdot \vec{d}_i. \tag{8.19}$$

The angular resolution for several samples is shown in Figures 8.8.

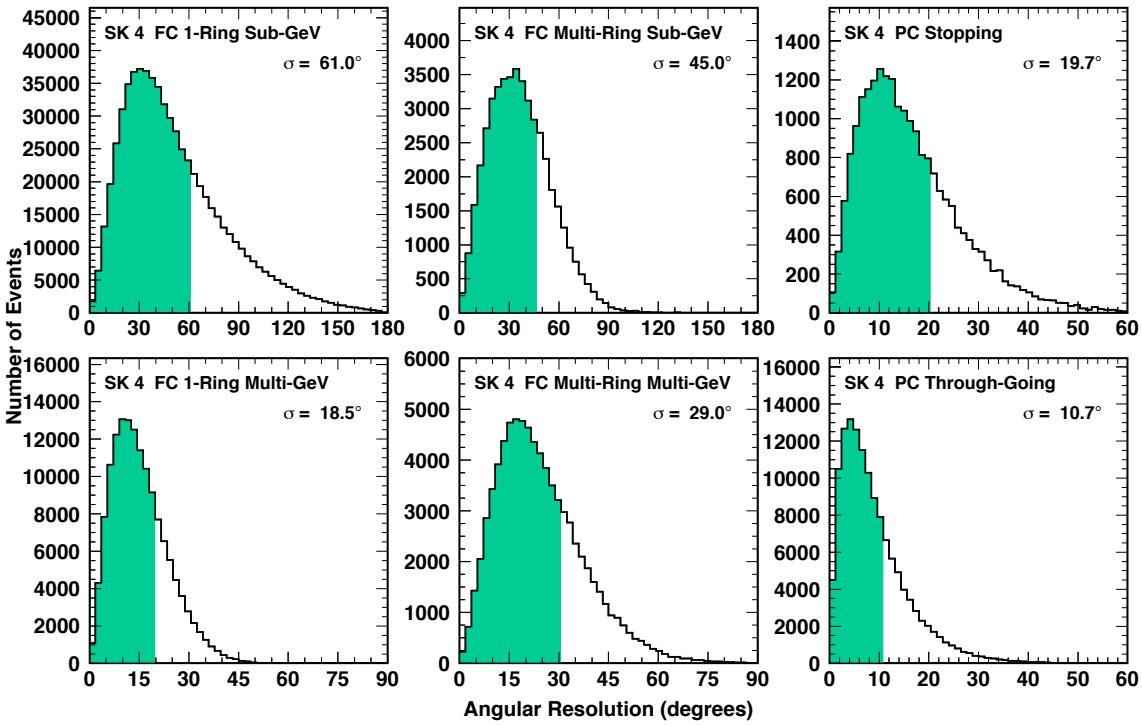

Figure 8.8: Angular resolution in SK4 for the L/E samples, estimated with the MC. The distribution of angles w.r.t. the true neutrino direction is shown. The black solid histogram is for events satisfying the 70 % resolution cut, and the green shaded region corresponds to 68% of events. The angular resolution for each SK period is shown in Appendix A.

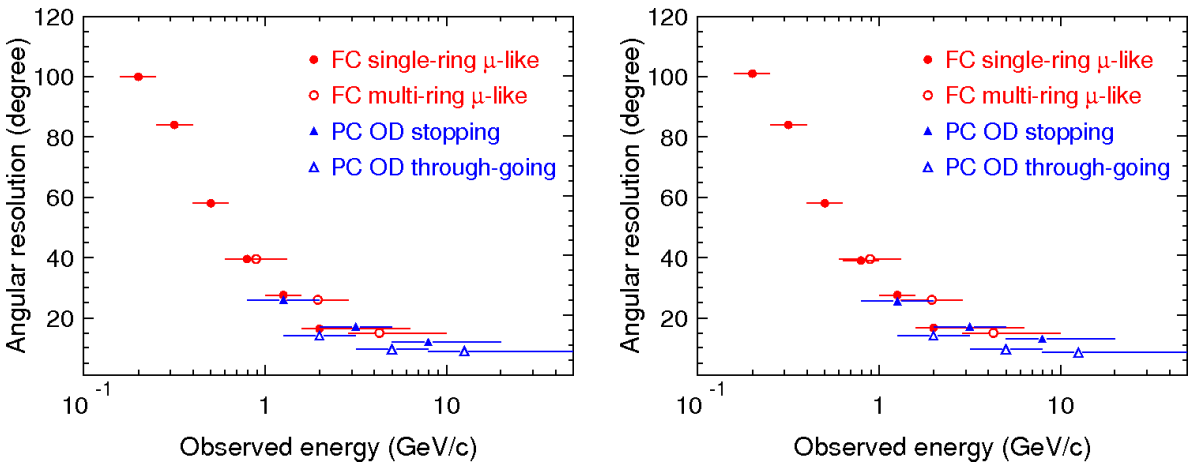

(a) SK1

(b) SK2

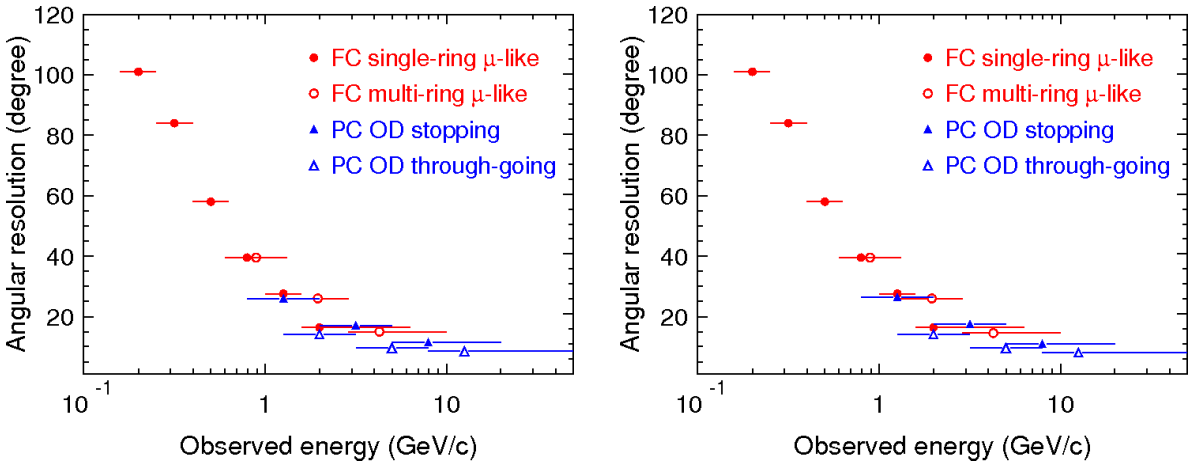

(c) SK3

(d) SK4

Figure 8.9: Angular Resolution against the lepton momentum, estimated with the MC. Each of the event samples are shown by the markers shown in the legend.

Reconstructing L_ν

The flight path length of the neutrino is estimated from the reconstructed zenith angle of the neutrino. For upward-going neutrinos traversing much of the Earth ($\sim 10^4$ km), there is a close relationship between the path length and zenith angle. For horizontal events, the variation of the path length with the zenith angle is rapid (Figure 8.7) and the resolution is expected to be lower than for vertical events. Then for downward-going neutrinos, and for horizontal events as well, the uncertainty in the neutrino production height in the atmosphere (~10 km) is more significant than for upward going neutrinos. The calculation of the flight path length from the zenith angle is based on the Honda flux calculation, and the relationship between these variables can be seen in Figure 8.7. The angular resolution against observed energy is shown in Figure 8.9.

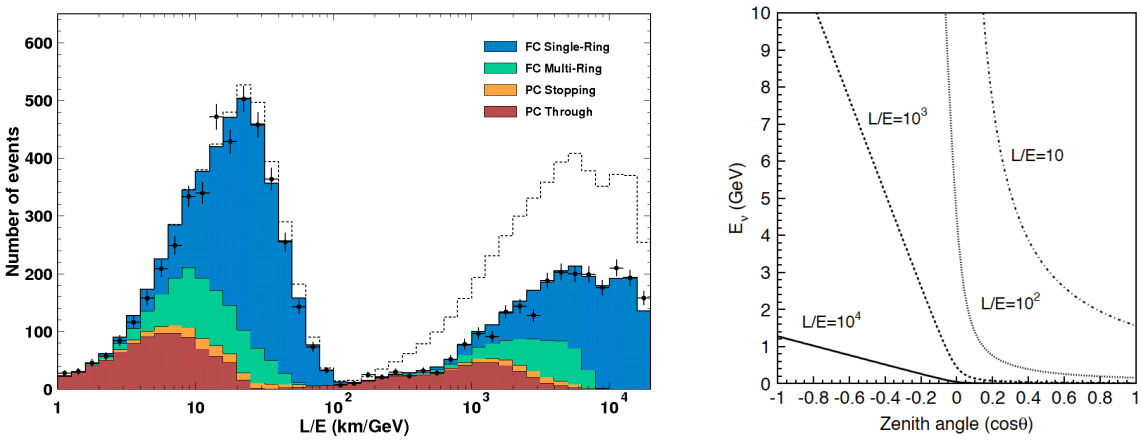

Figure 8.10: The L/E distributions satisfying the 70% resolution cut and oscillated with some typical parameters $(\sin^2 2\theta_{23}, \Delta m^2_{32}) = (1.0, 2.4 \times 10^{-3}\,\text{eV}^2)$ are shown on the left. The contributions from each of the samples is shown and labelled in the legend. The dashed histogram shows the L/E distributions without oscillations. The two bump structure can be understood by studying the L/E contours on the $(\cos\theta, E_\nu)$ plane in the right plot. Just above $L/E = 10^2\,\text{km/GeV}$, the resolution requirements cut out a lot of horizontal events, which can be seen in the right plot of Figure 8.14.

8.3 L/E Event Resolution Cut

As well as improving the reconstruction of L_ν and E_ν as described in the previous sections, the resolution of the quantity L_ν/E_ν was estimated. This was calculated with respect to the neutrino energy and incident zenith angle, for a grid of points in the $(\cos\Theta^{\text{rec}}_\nu, E^{\text{rec}}_\nu)$ parameter space. A resolution map was created to cut out events which were likely to have poor resolution and cause the L/E pattern to become averaged out.

In Figure 8.10, an L/E distribution can be seen on the left, separated by sample, and the L/E contours with respect to neutrino energy and incident zenith angle on the right. The L/E distributions have had a resolution cut applied to them, keeping events that were expected to have a relatively good resolution in L/E. This requirement cuts out many of the low energy events or horizontal-going events.

On the right plot of Figure 8.10, in the region of L/E between 10^2–10^3 km/GeV a narrow band of mostly horizontal events or low energy events are traced. This accounts for the reduced statistics in the L/E plot in this region after the resolution cut was applied. The majority of selected events were either downward-going, L/E between 10–10^2 km/GeV, or upward-going, L/E between 10^3–10^4 km/GeV, with more statistics for lower energy events. This explains the characteristic two-bump structure of the basic L/E distribution.

8.3.1 Estimation of the L/E Resolution

The L/E resolution was estimated using a MC sample equivalent to 100 years of data. The resolution was mostly limited by the reconstruction of the neutrino flight path length. This was dependent on the angular correlation between the incoming neutrino and the measured outgoing lepton direction. For higher energy events, there is a strong correlation between these directions,

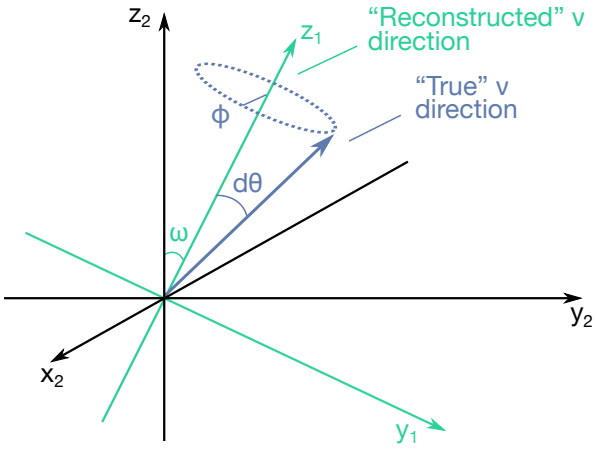

Figure 8.11: The estimation of the L/E resolution considers the angle $d\theta$ between the reconstructed and true neutrino direction, which is where the uncertainty in the flight path comes from. The "reconstructed" direction, ω, was assumed in a loop, and the "true" direction was assumed to be at an angle $d\theta$. Here direction refers to the zenith angle, the incoming neutrino direction. The true directions were rotated through 2π in ϕ w.r.t. the reconstructed direction, sampling 30 steps. Then these true directions were rotated into detector coordinates, assuming ω was in the ZY-plane of the detector.

of about 10°–20°. However, for lower energy events the reconstructed lepton direction can differ considerably from the incoming neutrino direction – upwards of 30° below $E_\nu \sim 1\,\text{GeV}$. See Figure 8.9 for the calculated angular correlation against energy.

To calculate the effect of this on the L/E resolution, a representative sample of 300–1000 events of a particular neutrino energy range was collected. For each of these events, the angle between the reconstructed lepton direction and the true neutrino direction, $d\theta$, was calculated. This gave a distribution of events with a characteristic $d\theta$ for a particular neutrino energy.

In the estimation, a particular reconstructed neutrino zenith direction, ω, was assumed as shown in Figure 8.11. Then the "true" neutrino direction was assumed to be at an angle $d\theta$ from this reconstructed direction, and rotated through 2π in ϕ with respect to the reconstructed direction[1] as depicted in Figure 8.11. In this ϕ rotation, 30 steps were sampled, giving 9000–30000 test events for a given reconstructed E_ν^{rec} and $\cos\Theta_\nu^{\text{rec}}$.

The "reconstructed" direction was assumed to be at a zenith angle, ω, in the ZY-plane of the detector, and the "true" neutrino directions were rotated about the x-axis to match the ZY axes in the detector coordinates — a rotation from the first set of coordinates (green) to the second set of coordinates (black) in Figure 8.11. Then from this assumed "true" neutrino direction, the flight path length was determined, and the quantity $(L/E)_{\text{true}}/(L/E)_{\text{rec.}}$ was calculated.

8.3.2 Definition of the L/E Resolution

This process was repeated for each point on the $(\cos\Theta_\nu^{\text{rec}}, E_\nu^{\text{rec}})$ parameter space, producing a $(L/E)_{\text{true}}/(L/E)_{\text{rec.}}$ distribution at each point. From the distributions, two quantities were calculated: the peak of the distribution, and the estimated resolution from that peak. The peak was defined as the ratio of the $(L/E)_{\text{true}}/(L/E)_{\text{rec.}}$ distribution containing the most test events in a ±25% window from that ratio. Once the peak was found, the resolution was defined as the plus-or-minus-percentage of the peak value that contained 68% of the test events. For example, if the peak was found at a ratio of 1.0, and 68% of the test events were within a ratio of 0.7–1.3 (1.0±30%), then the resolution was defined as 30%.

[1] In this estimation of the L/E resolution, the neutrino flux was assumed to be uniform in ϕ. This estimation produced a value to cut by depending on the reconstructed E_ν and $\cos\Theta$ of the event, and the geometry of the Earth. The L/E resolution estimated here was only used for data screening. Since the data and simulation was treated in the same way in the analysis, it introduced no bias in the results.

A sample of $(L/E)_{\text{true}}/(L/E)_{\text{rec.}}$ distributions from the $(\cos\Theta_\nu^{\text{rec}}, E_\nu^{\text{rec}})$ parameter space for SK1 FC1R MC events can be seen in Figure 8.12. The numbers in the top right of each panel show the neutrino energy and zenith angle in black and calculated resolution in red. The red dashed lines represent the calculated "peak" of these asymmetrical ratio distributions. While the grey shaded regions represent the range of 68% of the test events. Generally, the higher energy events had better resolution due to the stronger angular correlation; and the upward- or downward-going events had better resolution than the horizontal events. For the low energy and horizontal events there was no clear "peak," as the test events were distributed over a wide range range of ratios. In such cases, the shaded region representing 68% of events can extend much beyond the apparent peak.

Figure 8.13 shows heatmaps of the peaks on the left and the resolution on the right, over the $(\cos\Theta_\nu^{\text{rec}}, E_\nu^{\text{rec}})$ parameter space. The third dimension is represented by the colour gradient. The main deficit of ν_μ was in upward-going samples, so it was more important to have a higher resolution in L/E in the upward-going direction. In the L/E analysis, the estimation on the L/E resolution was taken for $\cos\Theta \leq 0$, and reflected at $\cos\Theta = 0$ for $\cos\Theta > 0$.

8.3.3 L/E Shift

The L_ν/L_ν^{rec} and E_ν/E_ν^{rec} had asymmetric distributions, resulting in a shift of $(L_\nu/E_\nu)/(L_\nu^{\text{rec}}/E_\nu^{\text{rec}})$ from unity. This shift was different for each sample and the effect of it was a reduction in resolution and a smearing of the L/E information. This shift was corrected for and the L/E variable was reconstructed as:

$$(L_\nu^{\text{rec}}/E_\nu^{\text{rec}})' = \delta_{L/E} \cdot (L_\nu^{\text{rec}}/E_\nu^{\text{rec}}), \tag{8.20}$$

where $\delta_{L/E}$ was taken as the L/E (true/rec.) peak during the L/E resolution calculation, shown in the left of Figure 8.13, after reflecting the upward-going values to the downward-going direction. Provided the event has sufficient resolution, the shift in $\delta_{L/E}$ should bring the reconstructed L/E closer to the true value.

8.3.4 L/E Resolution Cut

Since the resolution calculation considers a large sample of possible origins of a reconstructed event, it gives an estimation of the reliability of the L/E value at a given point of $(\cos\Theta_\nu^{\text{rec}}, E_\nu^{\text{rec}})$. A larger resolution means that a larger range of true L/E values could produce that event. While a smaller resolution means that the reconstructed L/E will be closer to the true value, despite the uncertainty in the topology of the event. The selection of the L/E resolution to be within 70% was determined by a study to maximise the sensitivity to distinguish neutrino oscillations from other hypotheses in 2004 [9]. Or in other words, the 70% resolution requirement gives a good balance between improved L/E shape and retaining statistics.

Distributions for the true L/E over reconstructed L/E ratios are shown in the left of Figure 8.14 for each event sample. These distributions were made from the analysis MC, and the truth information refers to the source of the simulated event. The solid black histogram has had the <70% resolution cut applied, and has a tighter distribution than without the resolution cut in dashed blue. The resolution contours for each of the event samples in the $(\cos\theta, E_\nu)$ plane can be seen on the right of Figure 8.14. A summary of the events of each of the samples after the <70% resolution cut was applied is shown in Table 8.1. Due to low statistics for high energy events, the resolution for energetic neutrinos ($E_{\text{vis2}} > 10$ GeV for FC Single-Ring, $E_{\text{vis2}} > 50$

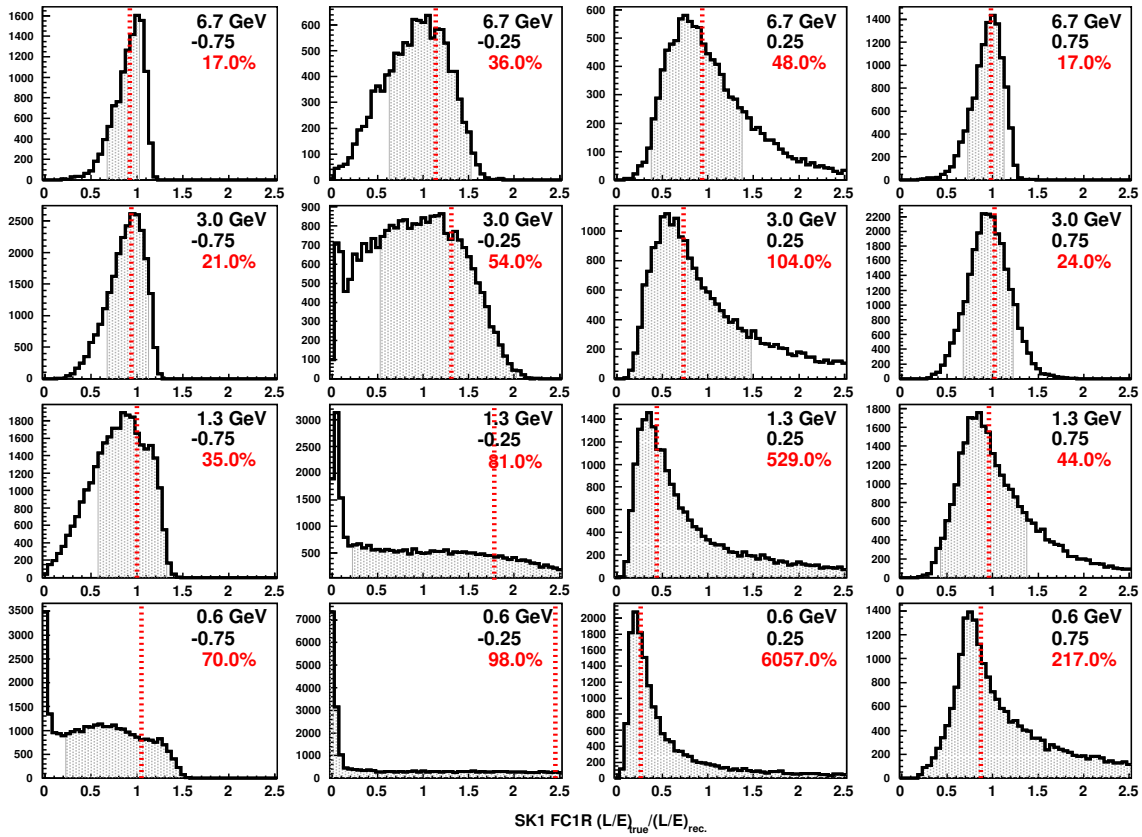

Figure 8.12: The L/E resolution calculation was performed by producing $(L/E)_{\text{true}}/(L/E)_{\text{rec.}}$ distributions for each point in $(\cos\Theta_{\nu}^{\text{rec}}, E_{\nu}^{\text{rec}})$. These plots are samples from this grid, with the reconstructed neutrino energy and assumed zenith written in the top right of each panel. The "peak" was found for these asymmetrical distributions, shown by the red dashed line. The resolution was then calculated from the peak, as the region containing 68% of test events, shown by the grey shaded area. The resolution value is written in red.

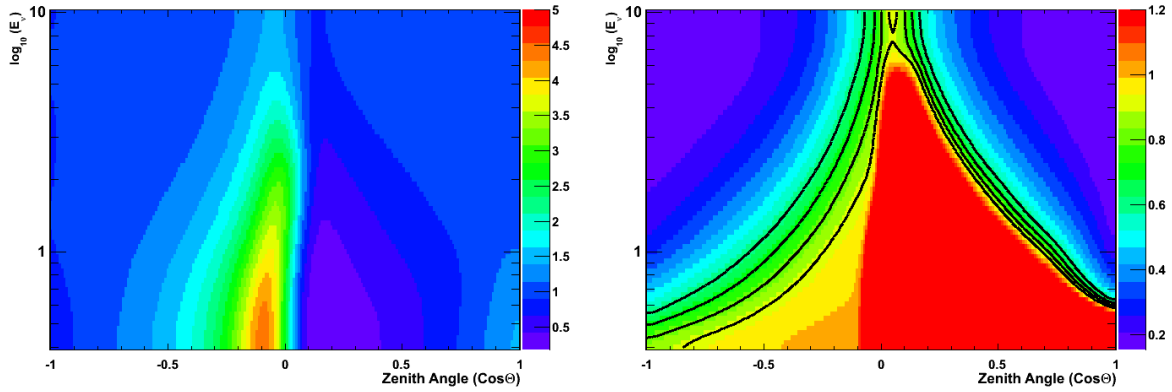

Figure 8.13: Histograms over the ($\cos\Theta$,E_ν) parameter space where the value of the plotted parameter is shown by colour, with the scale shown to the right of each plot. The left plot shows the L/E (true/rec) peaks and the right plot shows the L/E (true/rec) resolution. The peak is close to one for high energy downward-going and upward-going events, and the resolution is high for these events. For horizontal and low-energy events, the L/E ratios are dispersed over a wide range of values and there is no real peak. The resolution is poor in these regions. On the right plot, the contours from the outside inward show 60%, 70%, 80% and 90% resolution. In the analysis, the left half of these plots are reflected in $\cos\Theta = 0$ to the downward direction.

GeV for FC Multi-Ring and PC events) cannot be determined and these events were cut from the analysis (Section 8.1).

8.4 Likelihood Analysis and χ^2 Minimisation

The data were analysed by a binned maximum likelihood technique over 43 L/E bins from $\log_{10}(L/E) = 0.0$ to 4.3. Since the statistics were limited, a likelihood based on Poisson Statistics was used. The bin by bin correlations of systematics from independent sources were considered by using the "Pull Method," [252] which is equivalent to the Covariance Method. The likelihood is then defined:

$$\mathcal{L}(N^{\rm exp}, N^{\rm obs}) = \prod_i \frac{\exp(-N_i^{\rm exp})(N_i^{\rm exp})^{N_i^{\rm obs}}}{N_i^{\rm obs}!} \times \prod_j \exp\left(\frac{\epsilon_j}{\sigma_j^{\rm sys}}\right), \tag{8.21}$$

where $N_i^{\rm obs}$ is the number of events observed in the data in the i-th bin, and $N_i^{\rm exp}$ is the number of events in the i-th bin expected from the Monte Carlo simulation. The $N_i^{\rm exp}$ are adjusted to account for the systematic uncertainties. The 1 sigma value of the j-th systematic is represented by $\sigma_j^{\rm sys}$. While the f_j^i is the fractional change in the i-th bin from a 1 sigma variation of the j-th systematic error, and includes information of the bin-by-bin correlations. Finally ϵ_j are the Pull Terms that adjusts how much the j-th systematic is applied to the MC, and are minimised to reduce the systematic correction. The $N_i^{\rm exp}$ are also adjusted for the particular parameter set of the theory being tested. The Pull Terms modify the MC like so:

$$N_i^{\rm exp} \rightarrow N_i^{\rm exp}\left(1 + \sum_{j=1}^{nsys} f_j^i \cdot \epsilon_j\right), \tag{8.22}$$

Sample Resolution	Data $< 70\%$	MC $< 70\%$	(ν_μ CC)
SK1 (1489.2 days)			
FC			
Single-Ring	1568	2215.5	(98.7 %)
Multi-Ring	421	612.0	(94.0 %)
PC			
Stopping	87	120.3	(93.6 %)
Through-Going	459	684.9	(99.2 %)
SK2 (798.6 days)			
FC			
Single-Ring	865	1206.3	(98.6 %)
Multi-Ring	233	323.0	(93.6 %)
PC			
Stopping	42	58.2	(93.8 %)
Through-Going	212	312.2	(99.2 %)
SK3 (518.084 days)			
FC			
Single-Ring	556	772.3	(98.6 %)
Multi-Ring	160	223.7	(94.3 %)
PC			
Stopping	36	45.8	(94.0 %)
Through-Going	200	275.2	(99.0 %)
SK4 (1096.7 days)			
FC			
Single-Ring	1196	1627.7	(98.4 %)
Multi-Ring	362	488.9	(94.3 %)
PC			
Stopping	71	98.3	(93.7 %)
Through-Going	424	577.7	(99.1 %)

Table 8.1: Summary of events from SK1 to SK4. The left column gives the sample name. The middle columns show the data numbers for events that were expected to have been reconstructed within 70% of the true L/E. The right columns show the same for MC, with an additional column displaying the percentage of ν_μ CC events.

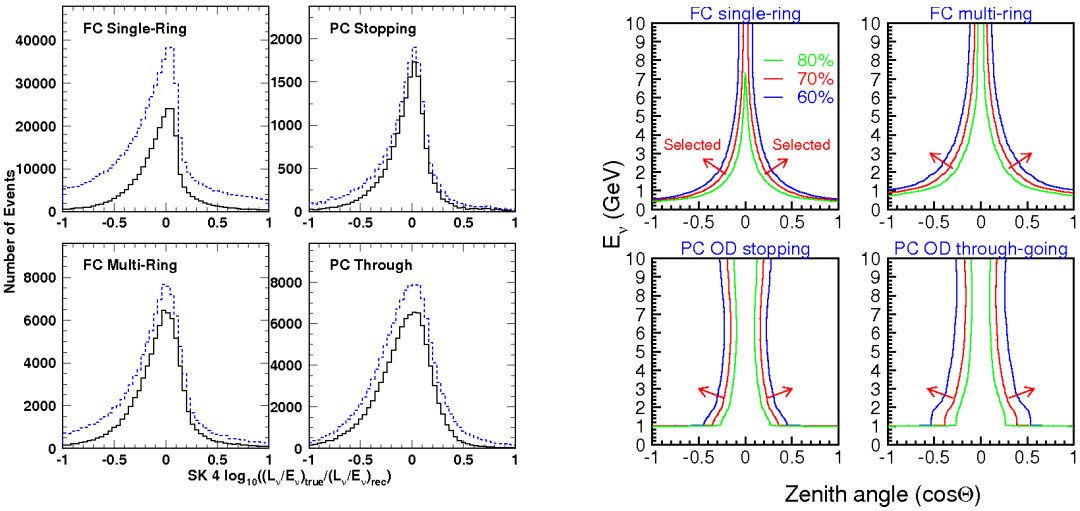

Figure 8.14: $\log_{10}$ of the ratio of True L/E over Reconstructed L/E on the left and the resolution cut contours on the right. On the left, the ratio is shown for each of the four event samples for SK4. The solid black histogram has had the <70% resolution cut applied, while the dashed blue has not. The high resolution samples have a tighter distribution on this L/E true/reconstructed double ratio. On the right, the resolution contours on the ($\cos\theta$,E_ν) plane can be seen for each sample for SK4. The distributions for SK1 to SK3 can be found in Appendix A.

where the sum over the systematic errors combines the contributions of each uncertainty to the i-th bin.

The log likelihood is then defined as a χ^2:

$$\begin{aligned}\chi^2 &\equiv -2\ln\left(\frac{\mathcal{L}(N^{\text{exp}},N^{\text{obs}})}{\mathcal{L}(N^{\text{obs}},N^{\text{obs}})}\right)\\ &= 2\sum_{i=1}^{nbin}\left[N_i^{\text{exp}}\left(1+\sum_{j=1}^{nsys}f_j^i\cdot\epsilon_j\right)-N_i^{\text{obs}}+N_i^{\text{obs}}\ln\left(\frac{N_i^{\text{obs}}}{N_i^{\text{exp}}(1+\sum_{j=1}^{nsys}f_j^i\cdot\epsilon_j)}\right)\right]\\ &\quad+\sum_{j=1}^{nsys}\left(\frac{\epsilon_j}{\sigma_j^{\text{sys}}}\right)^2.\end{aligned} \tag{8.23}$$

The term on the right is like a penalty term. If a large adjustment is made to the MC from the systematics, the χ^2 is increased accordingly.

To minimise over all theoretical parameters along with the systematic parameters would be very computationally intensive. Instead, the pull terms, ϵ, are minimised first. The χ^2 is differentiated with respect to each of the systematic pull terms, with the minimum occurring when the derivative is equal to zero:

$$\frac{\partial\chi^2}{\partial\epsilon_k}=0. \tag{8.24}$$

Considering the derivative of Equation (8.23) with respect to an arbitrary ϵ_k:

$$\frac{\partial\chi^2}{\partial\epsilon_k} = 2\sum_{i=1}^{nbin}\left[N_i^{\exp}f_k^i - N_i^{\text{obs}}\frac{N_i^{\exp}f_k^i}{N_i^{\exp}(1+\sum_{j=1}^{nsys}f_j^i\cdot\epsilon_j)}\right] + 2\frac{\epsilon_k}{(\sigma_k^{\text{sys}})^2} \tag{8.25}$$

$$= \sum_{i=1}^{nbin}\left[N_i^{\exp}f_k^i - \frac{N_i^{\text{obs}}f_k^i}{1+\sum_{j=1}^{nsys}f_j^i\cdot\epsilon_j}\right] + \frac{\epsilon_k}{(\sigma_k^{\text{sys}})^2}, \tag{8.26}$$

where the natural log was expanded to consider only the terms dependent on ϵ and the common factor of 2 was removed by demanding the derivative to be equal to zero. This can then be rewritten as a condition for the epsilon minimum:

$$\frac{\epsilon_k}{(\sigma_k^{\text{sys}})^2} = \sum_{i=1}^{nbin}\left[\frac{N_i^{\text{obs}}}{1+\sum_{j=1}^{nsys}f_j^i\cdot\epsilon_j} - N_i^{\exp}\right]\cdot f_k^i. \tag{8.27}$$

This gives $nsys$ ($k = 1 \to nsys$) linear equations, which can be rearranged into a matrix equation and solved simultaneously. This is done first by adding $\sum_i^{nbin}\sum_j^{nsys}N_i^{\text{obs}}f_j^if_k^i\epsilon_j$ to both sides of the equation:

$$\sum_j^{nsys}\left(\sum_i^{nbin}N_i^{\text{obs}}f_j^if_k^i + \frac{\delta_{jk}}{(\sigma_k^{\text{sys}})^2}\right)\cdot\epsilon_j = \sum_{i=1}^{nbin}\left[N_i^{\text{obs}}\left(\frac{1}{1+\sum_{j=1}^{nsys}f_j^i\cdot\epsilon_j} + \sum_{j=1}^{nsys}f_j^i\cdot\epsilon_j\right) - N_i^{\exp}\right]\cdot f_k^i \tag{8.28}$$

$$= \sum_{i=1}^{nbin}\left[N_i^{\text{obs}}\left(1+S^2-S^3+\cdots\right) - N_i^{\exp}\right]\cdot f_k^i, \tag{8.29}$$

where $S = \sum_{j=1}^{nsys}f_j^i\cdot\epsilon_j$ and the binomial series expansion was used:

$$(1+S)^{-1} = 1 - S + S^2 - S^3 + S^4 - S^5 + \cdots \tag{8.30}$$

The above expansion was used on the first f_j^i term on the RHS of Equation (8.28), cancelling out the second f_j^i term on the RHS. Up to the fifth order, $\mathcal{O}(S^5)$, was considered in the expansion. Equation (8.29) can be more simply expressed in the matrix equation:

$$\sum_j^{nsys}\mathcal{M}_{jk}\cdot\epsilon_j = \mathcal{V}_k, \tag{8.31}$$

where,

$$\left(\sum_i^{nbin}N_i^{\text{obs}}f_j^if_k^i + \frac{\delta_{jk}}{(\sigma_k^{\text{sys}})^2}\right) \longrightarrow \mathcal{M}_{jk}, \tag{8.32}$$

$$\sum_{i=1}^{nbin}\left[N_i^{\text{obs}}\left(1+S^2-S^3+\cdots\right) - N_i^{\exp}\right]\cdot f_k^i \longrightarrow \mathcal{V}_k. \tag{8.33}$$

Therefore Equation (8.31) is solved simultaneously for each k, to obtain the minimised ϵ_k. This was done iteratively, initially inputing $\epsilon_j = 0$ for ($j = 1 \to nsys$) into the $\mathcal{V}_k$. In the next steps the minimum ϵ_k were inserted into $\mathcal{V}_k$, for 10 iterations.

The Pull Method has several advantages over the Covariance Method, especially when the number of bins, N, is greater than the number of systematics, K. The problem of minimising the χ^2 is reduced from inverting an $N \times N$ matrix to inverting a $K \times K$ one. In order to further improve computational efficiency the χ^2 was first minimised over the Pull Terms, ϵ. Minimising Equation 8.23 is equivalent to solving $nsys$ linear equations:

$$\sum_{j=1}^{nsys} \left[\frac{\delta_{jk}}{(\sigma_j^{\text{sys}})^2} + \sum_{i=1}^{nbin} N_i^{\text{exp}} \cdot f_j^i \cdot f_k^i \right] \cdot \epsilon_k = \sum_{i=1}^{nbin} \left[(1 + (f_j^i \cdot \epsilon_j)^2 + \cdots) N_i^{\text{obs}} - N_i^{\text{exp}} \right] \cdot f_k^i. \quad (8.34)$$

8.5 Systematic Uncertainties

The systematic uncertainties used for analysis with the L/E distributions were a subset of the Zenith Analysis systematic errors. The set of uncertainties have been presented in categories relating to the errors in the neutrino flux simulation, neutrino interactions, event reconstruction, and reduction of the raw data and Monte-Carlo. The systematic uncertainties are summarised in Tables 8.2, 8.3, 8.4, and 8.5. The tables show the effect of a 1σ variation of the systematic uncertainty on the relevant distributions, the bestfit ϵ, and the pull column is $(\epsilon_j/\sigma_j)^2$ from Equation (8.23).

8.5.1 Neutrino Flux Uncertainties

The systematic uncertainties in the neutrino flux were estimated by comparing several calculations of the neutrino flux at the Super-Kamiokande Detector. The Honda Flux [16, 165–167] was compared with the Fluka [168, 253] Flux and Bartol Flux [169, 254]. A Super-Kamiokande paper that discusses the flux uncertainties in detail can be found in Reference [109]. The atmospheric neutrino flux uncertainties have been presented in Table 8.2.

Absolute Normalisation (1)

The absolute normalisation depends on the uncertainty in the primary cosmic ray flux and on the differences between the hadronic interaction models used in the flux calculations. In this analysis, the shape of the L/E pattern was the main concern so this parameter was left essentially free, by setting it to 1000%. However, the uncertainty in the normalisation is thought to be around 10%, and the best fit in the L/E analyses in this thesis tends to only require about 6% normalisation (despite being free).

Anti-Neutrino/Neutrino Ratio - $\bar{\nu}_\mu/\nu_\mu$ (3)

The L/E distributions were filled from $(\nu_\mu + \bar{\nu}_\mu)$ samples, so only the uncertainty in the $\bar{\nu}_\mu/\nu_\mu$ ratio was considered. The error in this ratio mainly came from the uncertainty in the π^+/π^- ratio produced from primary cosmic rays, especially below ∼5 GeV. The uncertainty was estimated from the differences in the hadronic interaction model predictions between each of the flux calculations [167–169]. At higher energies, above ∼10 GeV, the uncertainties in the K^+/K^- ratio become more significant. The uncertainty was common for each SK period and was taken to be 6%.

Upward/Downward Going Neutrino Ratio (4)

At low neutrino energies of less than a few GeV, the fluxes of neutrinos are up/down asymmetric. This is due to the rigidity cutoff with the low energy primary cosmic rays being deflected in the geomagnetic field. However, for energies above a few GeV the upward and downward fluxes are for the most part symmetric. This effect can be seen in Figure 1.2. The low energy Zenith distributions at Super-Kamiokande were not substantially affected, as there is a relatively poor angular correlation for low energy neutrino interactions. The uncertainty in the up/down ratio was estimated by comparing the predicted ratios of several flux models. Uncertainties between 0.2% to 0.5% were calculated for several samples as summarised in Table 8.2, which were used to estimate their effect on the analysis distributions.

Horizontal/Vertical Neutrino Ratio (5)

For low energy neutrinos, there is an enhancement of the expected number of horizontal neutrinos, which was implemented in the 3D flux models. This is a characteristic of the 3D nature of the hadronic showers of primary cosmic rays. However this was not seen so clearly in the neutrino zenith distributions due to the relatively weak angular correlation between the incoming neutrino and outgoing lepton below 1 GeV. At larger energies the predicted K/π ratio of hadronic interactions in the atmosphere becomes more significant. So the uncertainty in the horizontal/vertical neutrino ratio was estimated by comparing the 3D calculations of each of the flux models. Uncertainties between 0.1% to 2.3% were estimated for several constituent samples as shown in Table 8.2, which were applied to determine their effect on the analysis distributions.

Neutrino Flight Path Length (6)

The neutrino flight path length can be calculated accurately considering the geometry of the Earth. The main uncertainty came from the neutrino production height in the atmosphere. This was significant for downward-going and horizontal neutrinos where the difference in path length was considerable. In the case of upward-going events, the uncertainty in production height was negligible compared to the path length through the Earth, leading to an uncertainty in the path length of the order of 1%. To estimate this systematic error, the density of the atmospheric structure in the flux simulation was altered by 10% and the difference in the resulting path length calculations were used. Figure 8.15 shows the neutrino flight length against the zenith angle for two different atmospheric densities. The systematic error was taken to be 10%.

Energy Spectrum (7)

At energies relevant to Super-Kamiokande, the spectrum of primary cosmic rays protons, accounting for about ∼75% of the flux, could be fit to a function with a form proportional to E^{γ}, where γ is the spectral index and was found to be -2.74 [109, 255]. This value was a good fit below 100 GeV, above 100 GeV the spectrum was better fit by $\gamma = -2.71$. The primary comic ray helium nuclei, ∼15% of the flux, could be fit with a spectral index of either -2.64 or -2.74. The uncertainty in the energy spectrum was estimated by calculating the flux weighted average of the spectrum index uncertainties [109]. The systematic error was taken to be 5% for all SK configurations.

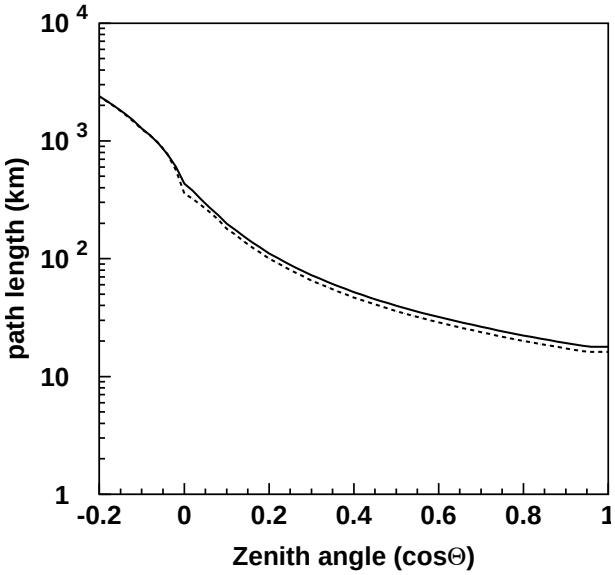

Figure 8.15: Neutrino flight path length against the zenith angle for doward-going and horizontal events. The solid curve shows the standard calculation, and the dashed line was for an atmospheric density structure that was compressed by 10%. The difference tends to zero for upward-going events.

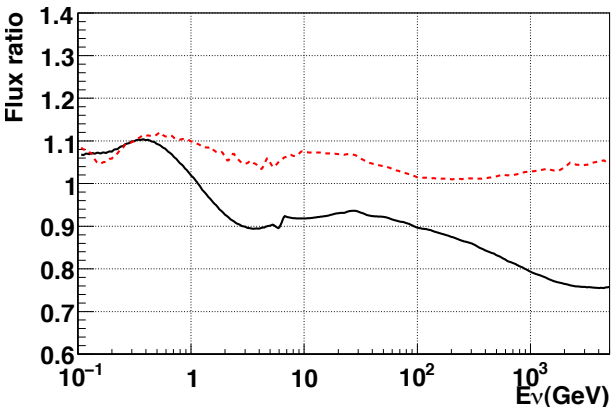

Figure 8.16: The ratio of other flux calculations w.r.t. the Honda flux. The Bartol (solid black) and FLUKA (dashed red) fluxes normalised by the Honda flux are shown.

FC Muli-GeV (8) and PC (2) Sample Normalisation

Although there are already considerations for the systematic uncertainties in the absolute normalisation and for the energy spectrum, as written above, there are further energy-dependent difference between the flux predictions. The differences in the flux of two other calculations with respect to the Honda flux can be seen in Figure 8.16. This can lead to variations within the sample distributions. To consider this effect, the uncertainty in the sample-by-sample relative normalisation for multi-GeV events was taken to be 5%. Both the FC Multi-GeV and PC samples contain Multi-GeV events, so the systematics on these two samples are highly correlated. Another systematic error on the ratio of these two samples was considered to account for further differences. Uncertainties between 0.02% to 0.9% were taken over the SK periods as shown in Table 8.2. The FC Sub-GeV samples were not altered by these uncertainties to avoid double-counting with the other flux errors.

Solar Activity (26)

The solar activity varies over an 11 year cycle, affecting the primary cosmic rays and therefore the atmospheric neutrino flux. To account for the modulation of the solar activity, the change of

the neutrino flux in a ± 1 year period was taken to estimate the uncertainty. This was calculated as 20%, 50%, 20% and 10% for SK1, SK2, SK3 and SK4, respectively. Where these values were the plus or minus percentage shift between high and low solar activity fluxes, to determine the change in the L/E distributions due to the solar activity uncertainty.

8.5.2 Neutrino Interaction Uncertainties

There have been many experiments measuring the cross-sections of neutrino interactions, and several theoretical models based on those results. Where the statistics were abundant, there was generally a good agreement between the theoretical models. However, there can be larger discrepancies when the statistics are limited. A summary of the systematic uncertainties for the neutrino interactions are listed in Table 8.3.

Quasi-Elastic Total Cross-Section (9)

A simulation based on the Smith and Monitz model was used for the CCQE Total Cross-Section for a bound nucleon. To estimate the uncertainty, this model was compared with the Nieves model [215]. The systematic error was taken to be 10%.

Single Meson Production (Total Cross-Section) (10)

To estimate the single meson production cross-section, Pions were used due to their large statistics. This same systematic was then applied to the single meson production of other particles such as η and K. Various experimental results for the $\nu_\mu p \to \mu^- p \pi^+$ interaction were compared against the Monte-Carlo to estimate the systematic error. The uncertainty was set to be 20%. The interactions for charged pion production were better understood than for π^0, so there another uncertainty was estimated for that.

Single Meson Production ($\pi^0/\pi^\pm$) (27)

There was more discrepancy between the interaction models for π^0 due to the poor experimental statistics available. By comparing the Hernandez model and the Rein and Sehgal model for the $\nu_\mu n \to \mu^- p \pi^0$ interaction against the related interactions with an outgoing charged pion, a relative systematic uncertainty of 40% was set for $\pi^0/\pi^\pm$.

DIS (Total Cross-Section) (11)

The agreement between the models and experimental results for the total cross-section for Deep Inelastic Scattering interactions, above a few tens of GeV, was considered to estimate this systematic error. An uncertainty of 5% was set.

Coherent π Production (12)

Generally the Coherent π Production systematic was estimated by comparing the Rein and Sehgal model against experimental results. For NC interactions there was about a 50% agreement, however not much was known about the CC ν_μ interaction so an uncertainty of 100% was set.

ID	Description	Systematics		
		σ %	Best Fit %	Pull
Systematic Errors in Neutrino Flux				
1	Normalisation	–	6.41	0.0000
3	$\bar{\nu}_\mu/\nu_\mu$ Ratio	6.0	0.66	0.0123
4	Up/Down Ratio		0.01	0.0001
	Single-Ring $<$ 400 MeV	0.3		
	Single-Ring $>$ 400 MeV	0.5		
	Single-Ring Multi-GeV	0.2		
	Multi-Ring Sub-GeV	0.2		
	Multi-Ring Multi-GeV	0.2		
	PC	0.2		
5	Horizontal/Vertical		-0.02	0.0003
	Single-Ring $<$ 400 MeV	0.1		
	Single-Ring $>$ 400 MeV	1.9		
	Single-Ring Multi-GeV	2.3		
	Multi-Ring Sub-GeV	1.3		
	Multi-Ring Multi-GeV	1.5		
	PC	1.7		
6	Neutrino Flight Path Length	10.0	0.26	0.0007
7	Energy Spectrum	5.0	-0.98	0.0382
8	Sample Normalisation Multi-GeV			
	SK1	5.0	-3.74	0.5604
	SK2	5.0	-1.61	0.1041
	SK3	5.0	-0.72	0.0208
	SK4	5.0	2.28	0.2076
2	FC Multi-GeV μ / PC			
	SK1	0.6	0.00	0.0000
	SK2	0.5	0.00	0.0000
	SK3	0.9	0.04	0.0016
	SK4	0.02	0.00	0.0000
26	Solar Activity			
	SK1	20.0	0.13	0.0000
	SK2	50.0	0.04	0.0000
	SK3	20.0	0.16	0.0001
	SK4	10.0	-0.48	0.0023

Table 8.2: Neutrino Flux Uncertainties

ID	Description	Systematics		
		σ %	Best Fit %	Pull
Systematic Errors in Neutrino Interactions				
9	QE Scattering Total Cross-Section	10.0	5.10	0.2603
10	Single Meson Production (Total Cross-Section)	20.0	-15.63	0.6108
11	DIS (Total Cross-Section)	5.0	-0.51	0.0102
12	Coherent π Production	100.0	-33.23	0.1104
13	NC/CC Ratio	20.0	2.51	0.0157
21	Nuclear Effect	30.0	1.02	0.0012
24	Axial-Vector Mass (M_A) [QE and Single Meson]	20.0	4.28	0.0458
25	DIS (Bodek Correction)	20.0	17.19	0.7386
27	Single-Meson Production ($\pi^0/\pi^{\pm}$)	40.0	8.66	0.0469

Table 8.3: Neutrino Interaction Uncertainties

NC/CC Ratio (13)

As the NC interactions are less well understood, the NC/CC Ratio systematic uncertainty was taken to be 20%.

Nuclear Effect (21)

Nuclear effects in ^{16}O nuclei affect the angular correlation between the incident neutrino and the emitted mesons in an interaction. The uncertainty concerns the mean free path of hadrons produced in a neutrino interaction. A 30% systematic error was taken by considering the agreement of the model used and experimental results.

Axial-Vector Mass (M_A) for QE and Single Meson Production (24)

There is a dependence on the axial-vector mass, M_A, for quasi-elastic scattering and single meson production. In the simulation $M_A = 1.21\,\mathrm{GeV/c}$ was set. There is about a 10% uncertainty on the value of M_A. The systematic uncertainty on interactions due to this was estimated by comparing the Q^2 spectrum for $M_A = 1.11\,\mathrm{GeV/c}$ and $M_A = 1.21\,\mathrm{GeV/c}$. The systematic error was taken to be 20% in the analysis.

8.5.3 Event Reconstruction Uncertainties

There are many algorithms that reconstruct physical variables from raw charge and timing data on the PMTs, or likelihoods that separate events into different classifications. In these uncertainties, the performance of these likelihoods or the accuracy of the algorithm outputs are estimated.

Ring Counting (16)

The algorithm for finding and separating the rings in an event are described in Section 7.3. A likelihood function divides the events into Single-Ring and Multi-Ring classifications. This classification can be affected by several uncertainties such as water transparency and the detector calibrations. The systematic error was estimated by comparing the data and Monte Carlo ring

counting likelihood distributions. This was done for multiple samples and the 1σ estimations have been listed in Table 8.4.

Particle Identification - Single-Ring (17) and Multi-Ring (18)

The particle identification (PID) into e-like and μ-like events is determined by a likelihood algorithm as described in Section 7.4. The uncertainty in the PID was estimated by comparing these likelihood distributions between the data and Monte Carlo. The classification of the PID algorithm determines the number of e-like and μ-like events, and so determines the μ-like events available to the L/E Analysis. The systematic error was calculated for multiple samples, which have been presented in Table 8.4.

Energy Calibration (19)

The energy reconstruction and uncertainty are studied in the energy scale calibration, which primarily uses four sources to cover a wide energy range, as explained in Section 5.3. The systematic uncertainty in the absolute energy scale for SK1, SK2, SK3, and SK4 were 1.1%, 1.7%, 2.7%, and 2.3%, respectively.

Up-Down Asymmetry of the Energy Calibration (20)

The up/down asymmetry of the energy calibration was determined by comparing the decay electron events from cosmic ray muons. These decay electrons have a nearly uniform momentum in all directions and have vertices distributed throughout the fiducial volume of the inner detector, making them an excellent calibration source. The uncertainties for SK1, SK2, SK3, and SK4 were estimated to be 0.6%, 0.6%, 1.3%, and 0.3%, respectively.

PC Stopping and PC Through-Going Categorisation (23, 28, 29)

PC events were separated into stopping and through-going classifications, by comparing the charge deposited in the OD with the expected charge of a muon that completely passed through the OD. Since the OD has a non-uniform response, due to the geometry and distribution of old and new PMTs, the charge expectation was a tuned value. The PC systematics were estimated by comparing the data and MC, shifting the MC distribution to match the data more closely and then observing the percentage of PC Stopping events that change category. Further details are written in Section 8.1.3. The PC separation uncertainties have been listed in Table 8.4

8.5.4 Reduction Uncertainties

The basic data trigger is rather simple and further steps are required to reduce the raw data to the events that are interesting for analysis, and remove as many background events as possible. These uncertainties estimate the efficiency of these reduction processes.

FC Reduction (14)

The reduction for fully-contained (FC) events was carried out as described in Section 6.2. The systematic uncertainty in the FC reduction was estimated by comparing the reduction distributions between data and Monte Carlo for variations in the cut values. The uncertainties for SK1,

ID	Description	SK1			SK2		
		σ %	Best Fit %	Pull	σ %	Best Fit %	Pull
Systematic Errors from Reconstruction							
16	Ring Counting		-0.30	0.0009		-0.35	0.0012
	Single-Ring $<$ 400 MeV	0.7			2.3		
	Single-Ring $>$ 400 MeV	0.7			0.7		
	Single-Ring Multi-GeV	1.7			1.7		
	Multi-Ring Sub-GeV	-4.5			-8.2		
	Multi-Ring Multi-GeV	-4.1			-0.8		
17	Particle ID Single-Ring		-0.02	0.0006		-0.03	0.0008
	Sub-GeV	-0.1			-0.4		
	Multi-GeV	0.2			-0.1		
18	Particle ID Multi-Ring		1.33	0.0177		0.60	0.0036
	Sub-GeV	-3.9			2.2		
	Multi-GeV	-2.9			-3.4		
19	Energy Calibration	1.1	-0.12	0.0118	1.7	-0.39	0.0529
20	Up-Down Asym of E Calib.	0.6	0.13	0.0435	0.6	0.06	0.0111
23	PC Stop/Through Top	46.1	2.08	0.0020	19.37	-0.37	0.0004
28	PC Stop/Through Bottom	22.7	-3.29	0.0210	12.9	-0.40	0.0009
29	PC Stop/Through Barrel	7.01	0.07	0.0001	9.44	0.19	0.0004
ID	Description	SK3			SK4		
16	Ring Counting		-0.73	0.0053		-0.14	0.0002
	Single-Ring $<$ 400 MeV	3.0			-3.0		
	Single-Ring $>$ 400 MeV	0.6			0.6		
	Single-Ring Multi-GeV	1.0			-1.2		
	Multi-Ring Sub-GeV	-2.6			-2.3		
	Multi-Ring Multi-GeV	-2.1			2.4		
17	Particle ID Single-Ring		0.01	0.0000		-0.10	0.0101
	Sub-GeV	-0.4			-0.4		
	Multi-GeV	-0.5			-0.4		
18	Particle ID Multi-Ring		0.39	0.0015		0.99	0.0098
	Sub-GeV	3.1			2.2		
	Multi-GeV	4.5			6.8		
19	Energy Calibration	2.7	0.92	0.1161	2.3	0.77	0.1113
20	Up-Down Asym of E Calib.	1.3	0.25	0.0360	0.3	-0.02	0.0028
23	PC Stop/Through Top	86.6	-4.47	0.0027	43.3	2.19	0.0026
28	PC Stop/Through Bottom	12.1	0.80	0.0044	11.6	-0.16	0.0002
29	PC Stop/Through Barrel	28.7	5.07	0.0312	7.4	0.07	0.0001

Table 8.4: Neutrino Reconstruction Uncertainties

ID	Description	SK1			SK2		
		σ %	Best Fit %	Pull	σ %	Best Fit %	Pull
Systematic Errors from Reduction							
14	FC Reduction	0.2	-0.01	0.0019	0.2	0.00	0.0000
15	PC Reduction	2.4	-0.68	0.0797	4.8	-1.11	0.0531
22	Non-ν Background (μ-like)		0.00	0.0000		0.11	0.0116
	Cosmic-Ray FC Sub-GeV	0.1			0.1		
	Cosmic-Ray FC Multi-GeV	0.1			0.1		
	Cosmic-Ray PC	0.2			0.7		
ID	Description	SK3			SK4		
14	FC Reduction	0.8	-0.01	0.0003	0.3	0.02	0.0066
15	PC Reduction	0.5	0.01	0.0007	1.0	0.09	0.0076
22	Non-ν Background (μ-like)		0.25	0.0613		-0.29	0.0828
	Cosmic-Ray FC Sub-GeV	0.1			0.1		
	Cosmic-Ray FC Multi-GeV	0.2			0.8		
	Cosmic-Ray PC	1.8			4.9		

Table 8.5: Neutrino Reduction Uncertainties

SK2, SK3 and SK4 were 0.2%, 0.2%, 0.8% and 0.3%, respectively, and have been summarised in Table 8.5.

PC Reduction (15)

The reduction for partially-contained (PC) events is explained in Section 6.3. These uncertainties were estimated by considering the performance of the algorithm that determines the number of hits in charge clusters in the outer detector, which calculates the variable called $NHITAC$. FC and PC events are separated by this variable. The effect of varying the cut values on the data and Monte Carlo distributions were also considered. The uncertainties for SK1, SK2, SK3 and SK4 were 2.4%, 4.8%, 0.5% and 1.0%, respectively, and have been summarised in Table 8.5.

Non-Neutrino Background (22)

The non-neutrino background was estimated during the reduction procedure, and mainly comes from from cosmic ray muons for the μ-like samples that are relevant to the L/E Analysis. The uncertainties were estimated for FC Sub-GeV and Multi-GeV samples, as well as PC events, and have been presented in Table 8.5.

8.6 2-Flavour Oscillation L/E Results

The previous sections have described how the L/E variable was reconstructed as accurately as possible, and how the L/E resolution was estimated for a given neutrino energy and zenith angle. For the analysis, the high resolution events were kept – events with an L/E value that was expected to be within 70% of the true L/E. These precise L/E distributions were compared with

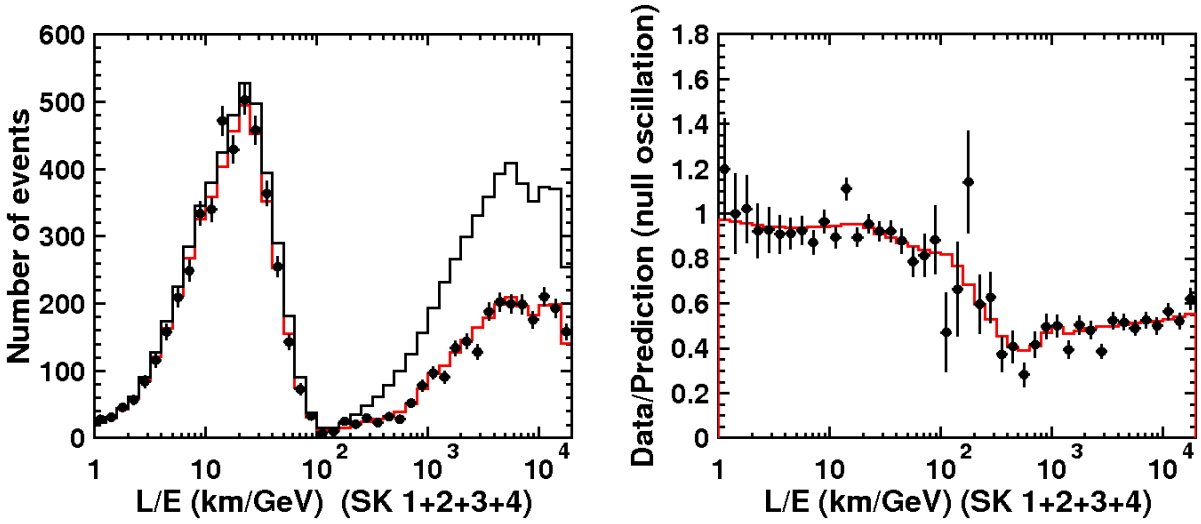

Figure 8.17: The 2-flavour L/E distributions on the left and the L/E distributions normalised by the null oscillation Monte Carlo on the right, for the data from SK1 to SK4. The combined data are shown by the points, and the bestfit oscillated MC in the red solid histogram. The bestfit point was at $(\sin^2 2\theta_{23}, \Delta m^2_{32}) = (1.0, 2.5 \times 10^{-3}\,\mathrm{eV}^2)$. The MC without oscillations is shown in solid black, which has been used to normalise the data and bestfit MC in the right plot.

2-flavour oscillated Monte Carlo through a likelihood analysis, while minimising the contribution from the systematic uncertainties.

The resulting L/E distributions are shown in the left of Figure 8.17. The data consists of the contributions from SK1 (1489.2 days), SK2 (798.6 days), SK3 (518.1 days) and SK4 (1096.7 days), while the Monte Carlo consists of 500 years of simulated data for each detector configuration and each of the fully-contained and partially contained event samples. The combined data is shown in the data points, while the bestfit oscillated Monte Carlo accounting for systematic uncertainties is plotted in the solid red histogram. Also shown for comparison is the Monte Carlo without any oscillations in the solid black histogram. It is clear from this plot that the data cannot be explained without some kind of perturbation such as that introduced by neutrino oscillations. Meanwhile, the oscillated Monte Carlo provides an excellent fit to the data.

In the right of Figure 8.17 the data and bestfit Monte Carlo have been normalised by the non-oscillated Monte Carlo. This brings out some of the more subtle features. A flat distribution around 1 would mean that the data could be described without oscillations. For low values of L/E, the data and MC are distributed around 1, then drop down into a dip at around $L/E \sim (500 \sim 700)\,\mathrm{km/GeV}$. This deficit corresponds to the first point where the oscillation probability is at a maximum. For the oscillated MC the bestfit parameters were:

$$\chi^2 = 171.7/169\,\mathrm{d.o.f}, \tag{8.35}$$

$$\sin^2 2\theta_{23} = 1.000 \pm 0.047, \tag{8.36}$$

$$\Delta m^2_{32} = (2.50 \pm 0.27) \times 10^{-3}\,\mathrm{eV}^2. \tag{8.37}$$

The bestfit systematic errors are summarised in Tables 8.2, 8.3, 8.4, and 8.5. The effect of a 1σ variation of the systematic uncertainty on the relevant distributions is shown in the $\sigma\%$ column. The fraction of the systematic error applied to the bestfit distributions, the ϵ term in

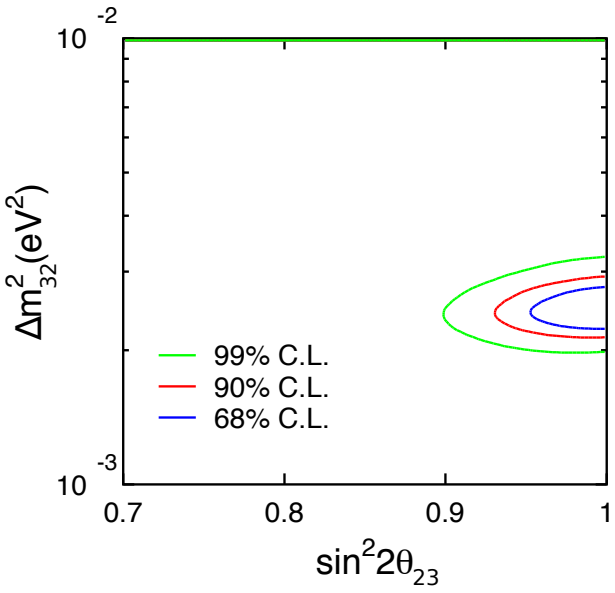

Figure 8.18: 2-Flavour L/E Analysis Oscillation allowed region for the combined dataset from SK1 to SK4. The L/E analysis has more power to constrain the Δm^2_{32} compared to the Zenith Analysis, as it reconstructs the position of the oscillation dip with a high L/E resolution sample. The bestfit point was at $(\sin^2 2\theta_{23}, \Delta m^2_{32}) = (1.0, 2.5 \times 10^{-3}\,\mathrm{eV}^2)$

Equation (8.34), is expressed as a percentage in the Bestfit % column. The value in the pull column is $(\epsilon_j/\sigma_j)^2$ and can be thought of as the contribution of the j-th systematic error to what has been called the penalty term in Equation (8.23). So a large contribution from the systematic uncertainty will result in a poor fit in the χ^2 minimisation.

The contours showing the 2 dimensional allowed regions of the oscillation parameters can be seen in Figure 8.18. Since the global minimum was slightly in the non-physical region ($\sin^2 2\theta_{23}$ = 1.005), the $\Delta\chi^2$ for 68%, 90% and 99% C.L. in the physical region were calculated to be $\Delta\chi^2$ of 2.358, 4.681, and 9.255, respectively, from the global minimum.

The modification to the $\Delta\chi^2$ for a best fit that falls in a non-physical region followed the method described in the 1996 PDG [256]. In this calculation, the $\Delta\chi^2$ between the minimum in the non-physical region and the physical region was used to calculate the number of events that fall in the physical region. For example, if 40% of events fall in the physical region, then the 90% C.L. in the physical region would correspond to the 96% C.L. over the entire range, which is where the effective physical 90% C.L. boundary would be drawn.

The 1 dimensional contours were drawn as slices through the minimum point, and so the above calculated $\Delta\chi^2$ C.L.s for 2 d.o.f. were used. The 1D slices are shown in Figure 8.19. The 1σ (68% C.L.) errors expressed in the bestfit above were calculated from these 1D contours. The 90% C.L. allowed regions were:

$$\sin^2 2\theta_{23} > 0.931, \tag{8.38}$$

$$2.129 \times 10^{-3}\,\mathrm{eV}^2 < \Delta m^2_{32} < 2.918 \times 10^{-3}\,\mathrm{eV}^2. \tag{8.39}$$

8.7 Discussion

The 2-flavour oscillation simulation provides an excellent explanation of the data observed at Super-Kamiokande. The 90% allowed regions presented here are more confined than those previously published with the data from the SK1 period [9]: $\sin^2 2\theta_{23} > 0.90$ and $1.9 \times 10^{-3}\,\mathrm{eV}^2 <$

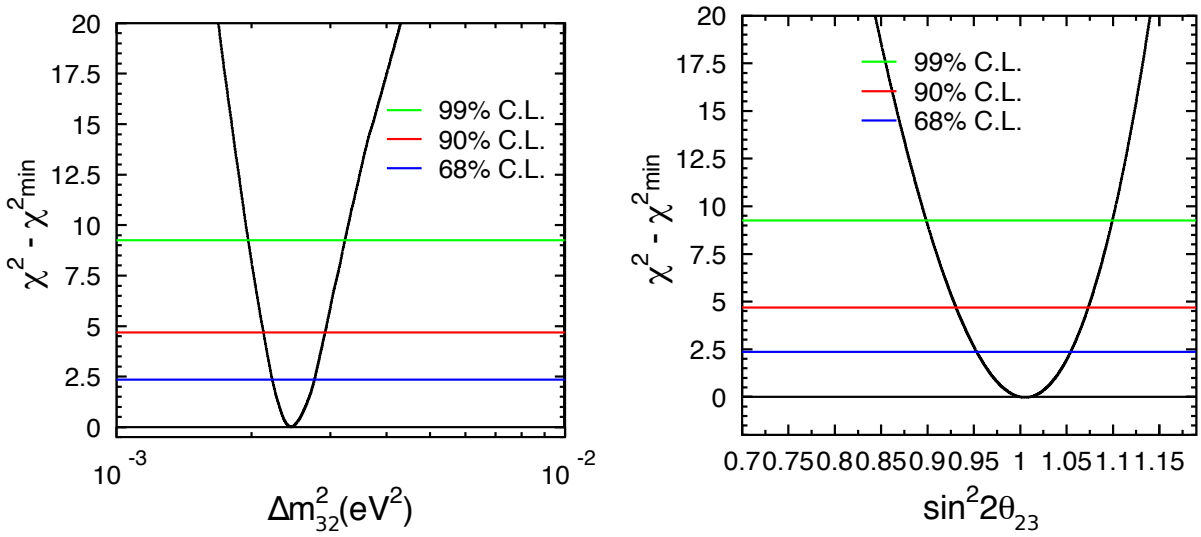

Figure 8.19: 2-Flavour L/E Analysis 1D contours for Δm^2_{32} and $\mathrm{Sin}^2 2\theta_{23}$ for the combined dataset from SK1 to SK4. These were taken as slices through the minimum bestfit point at $(\sin^2 2\theta_{23}, \Delta m^2_{32}) = (1.0, 2.5 \times 10^{-3}\,\mathrm{eV}^2)$

$\Delta m^2_{32} < 3.0 \times 10^{-3}\,\mathrm{eV}^2$. The allowed regions from the SK1 analysis are shown on the left of Figure 8.20. The data in this analysis had 3903 days of data, over double the live time compared to the first result with the SK1 data (1489 days). The result presented here is also in agreement with a later analysis including SK1 and SK2 data [257]: $\sin^2 2\theta_{23} > 0.94$ and $1.85 \times 10^{-3}\,\mathrm{eV}^2 < \Delta m^2_{32} < 2.65 \times 10^{-3}\,\mathrm{eV}^2$. The allowed regions from the SK1+2 analysis are shown on the right of Figure 8.20. However, the bestfit Δm^2_{32} from this analysis ($2.5 \times 10^{-3}\,\mathrm{eV}^2$) was slightly higher than these previous analyses ($2.4 \times 10^{-3}\,\mathrm{eV}^2$ for SK1, $2.2 \times 10^{-3}\,\mathrm{eV}^2$ for SK1+2), and the 90% C.L. constraint on $\sin^2 2\theta_{23}$ was slightly more relaxed compared to the SK1+2 result. By comparing the 2D oscillation allowed regions from each SK period alone, as in Figure 8.21, it can be seen that the SK3 and SK4 data relax the constraint on $\sin^2 2\theta_{23}$ and the SK4 data favours a larger Δm^2_{32}. The results from each SK period, and each analysis, were statistically consistent with one another.

The L/E distributions over the null oscillation prediction for each SK period are shown in Figure 8.22. It seems that for SK3 and SK4 the data at large L/E have more of a tendency to be at 0.5 or slightly above, which could result in a little more relaxed constraint on $\sin^2 2\theta_{23}$. As for Δm^2_{32}, an argument could be made that in the SK4 data the shoulder region before the dip was more strongly pronounced, such that smaller Δm^2_{32} were more suppressed. The bestfit for Δm^2_{32} for SK4 was $2.8 \times 10^{-3}\,\mathrm{eV}^2$, compared to the Δm^2_{32} of $(2.2 \sim 2.4) \times 10^{-3}\,\mathrm{eV}^2$ for SK1, SK2 or SK3. In this analysis, the atmospheric flux was updated to the Honda 2011 flux [16], and the SK1, SK2 and SK3 data and MC were reprocessed with the latest reconstruction software in 2012.

Traditionally, the L/E analysis provided evidence to favour Neutrino Oscillations to explain the ν_μ deficit in the data, and excluded the competing theories of Neutrino Decay and Neutrino Decoherence. The left plot in Figure 8.23 shows the L/E distributions over the null oscillation prediction for SK1+2+3+4, together with the three MC bestfits for each of the theories. As previously shown by the L/E Analysis [9, 257], these competing theories cannot reproduce the

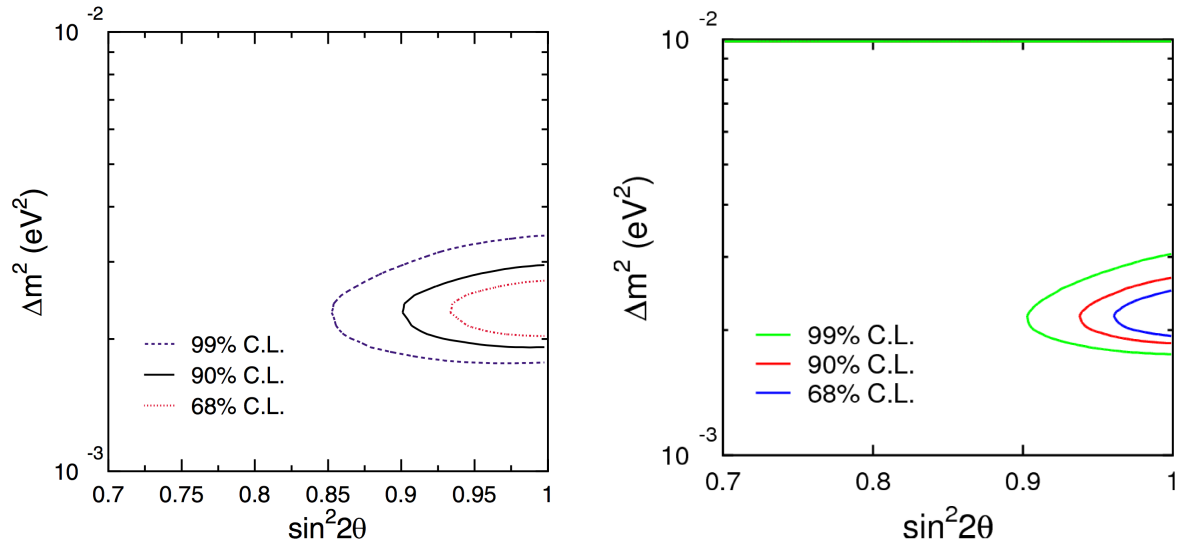

Figure 8.20: Previously published Standard 2-Flavour L/E results for SK1 in 2004 [9] (left) and SK1 and SK2 in 2009 [257] (right). In these plots $\sin^2 2\theta \equiv \sin^2 2\theta_{23}$ and $\Delta m^2 \equiv \Delta m^2_{32}$. The 90% C.L. allowed region for $\sin^2 2\theta_{23}$ was [0.9,1.0] for the SK1 analysis, [0.94,1.0] for SK1+2, and [0.93,1.0] from this thesis. The 90% C.L. allowed region for Δm^2_{32} ($\times 10^{-3}\,\mathrm{eV}^2$) was [1.9,3.0] for SK1, [1.85,2.65] for SK1+2, and [2.13,2.92] from this thesis.

dip in the data, which is a feature of neutrino oscillations. The minimum χ^2 for Neutrino Decay and Decoherence were 187.8/169 d.o.f and 194.8/169 d.o.f, respectively. The bestfit for neutrino oscillations had a minimum χ^2 of 171.1/169 d.o.f, and the $\Delta\chi^2$ for Neutrino Decay and Decoherence from the Oscillation minimum was 16.7 and 23.7, respectively. Taking the square root of the $\Delta\chi^2$ between Oscillations and Decay or Decoherence gave a $4.0\,\sigma$ and $4.8\,\sigma$ difference, respectively, from the oscillation best fit. This is in agreement with past L/E Analysis results, which already excluded these other hypotheses.

Also shown in Figure 8.23, the right plot compares the 2-flavour L/E results presented here with the SK Zenith Analysis, MINOS, and T2K results from 2013 [35]. The 2-flavour L/E Analysis still provides a nice constraint on Δm^2_{32} from the SK data, while the SK atmospheric neutrino analyses constrain the value of $\sin^2 2\theta_{23}$ more than the accelerator experiments, for data up until 2013[2].

Further improved sensitivity to oscillation parameters could be achieved with a more accurate L/E resolution. The L/E analysis with atmospheric neutrinos is limited by the angular correlation of the outgoing lepton direction to the incoming neutrino direction and therefore the inferred ν flight path length. A well-defined path length could be achieved in an accelerator experiment, which could give a better measurement of Δm^2_{32}. Experiments like T2K and MINOS constrain Δm^2_{32} very well.

Improved sensitivity to θ_{23} could be achieved with a very precisely known ν flux. This can be a challenge even for human-made fluxes such as in accelerator experiments producing neutrinos from meson decay, as there is always some uncertainty in the contamination of the beam. The main advantage of a Neutrino Factory is the precisely understood ν beam, produced from the

[2]T2K now provides a better constraint on the atmospheric parameters [258]

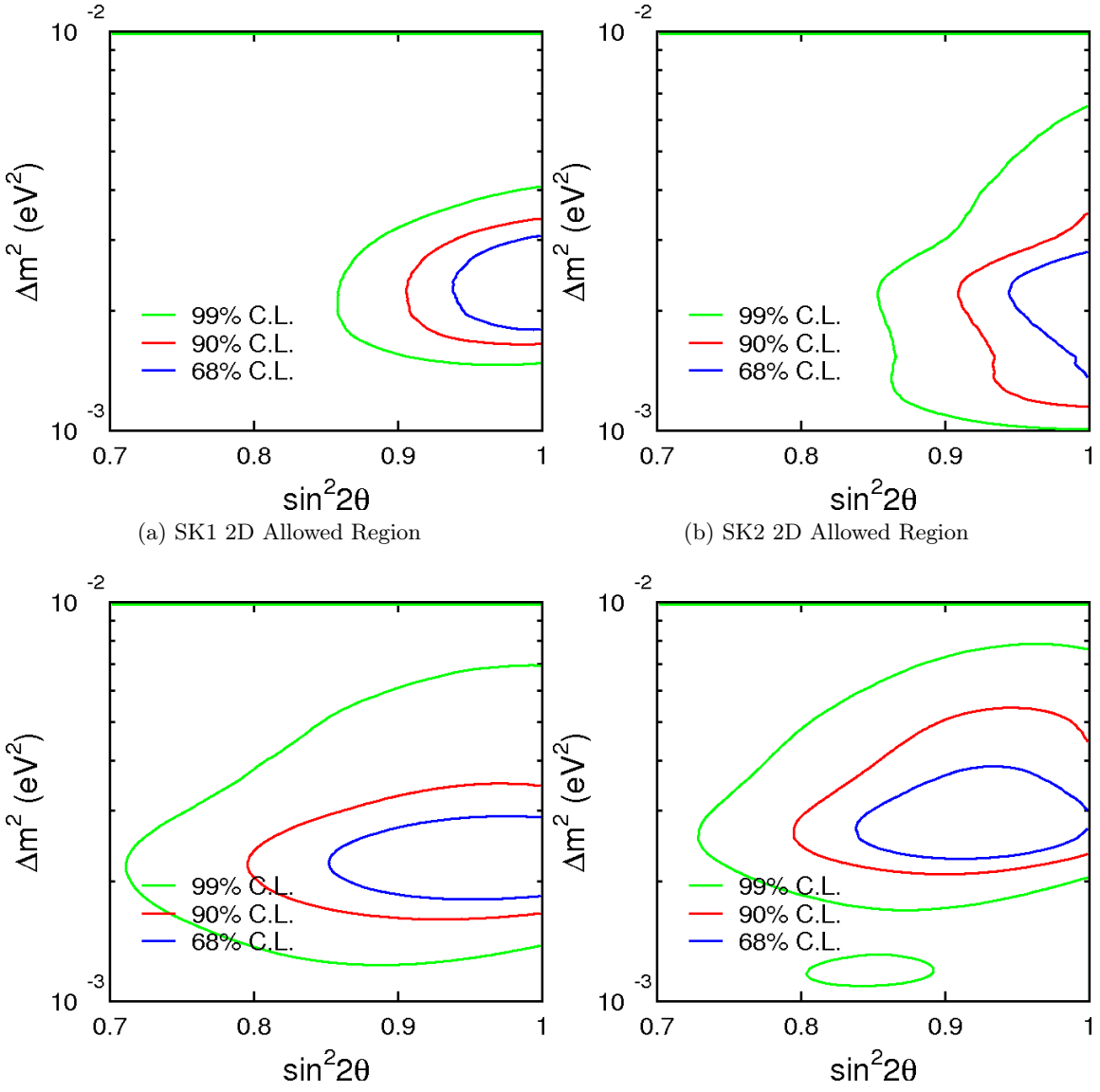

(a) SK1 2D Allowed Region

(b) SK2 2D Allowed Region

(c) SK3 2D Allowed Region

(d) SK4 2D Allowed Region

Figure 8.21: 2-Flavour L/E Analysis oscillation parameter allowed region for each SK period. The SK1 to SK3 data and MC were reprocessed with the latest reconstruction software in 2012. In addition the atmospheric flux was modified to Honda 2011 [16]. So these allowed regions differ from those previously published [9, 257]. The constraint on $\sin^2 2\theta_{23}$ was relaxed by the SK3 and SK4 data, while the SK4 data favours larger Δm^2_{32}. In these plots $\sin^2 2\theta \equiv \sin^2 2\theta_{23}$ and $\Delta m^2 \equiv \Delta m^2_{32}$.

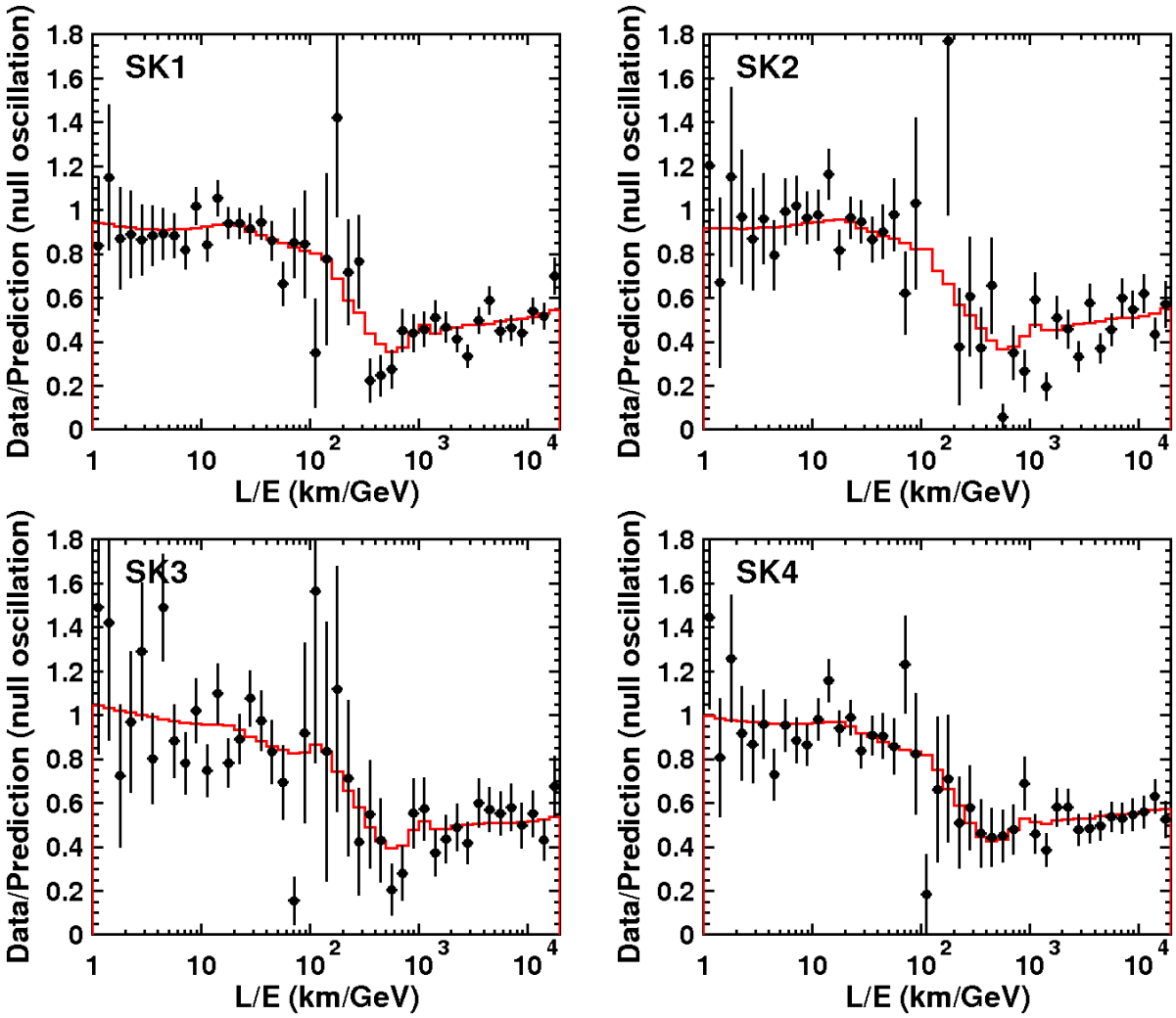

Figure 8.22: 2-Flavour L/E distributions over the null oscillation expectation for each SK period. The dip region is slightly less emphasised in the SK3 and SK4 data leading to a less constrained $\sin^2 2\theta_{23}$. Perhaps the more pronounced shoulder region before the dip in SK4 suppresses smaller Δm^2_{32} values more strongly.

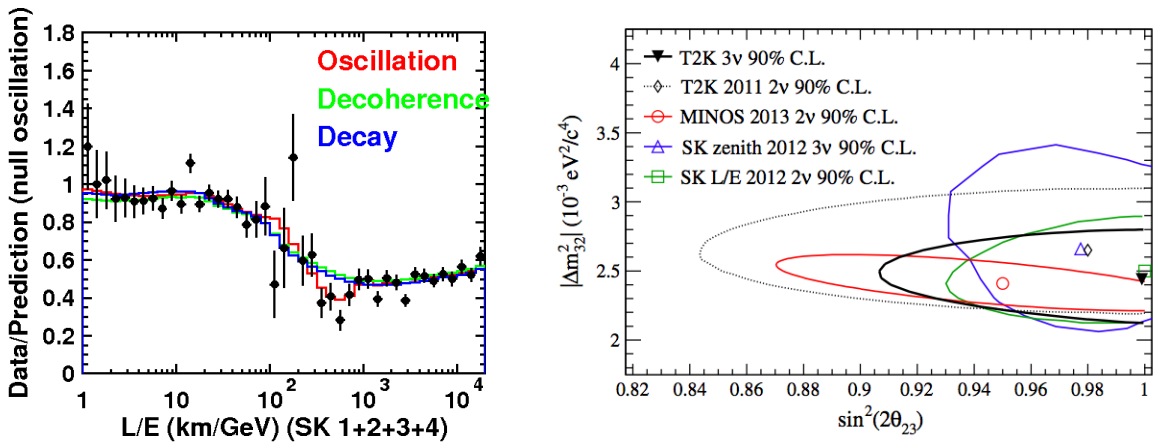

Figure 8.23: Comparison of the 2-Flavour L/E oscillation with Neutrino Decay and Decoherence on the left, and with other experiments on the right [35]. The left plot shows the L/E distributions normalised by the null oscillation prediction. The red curve shows the bestfit for Oscillations, the green for Decoherence and blue for Decay. The right figure compares the 2-Flavour L/E analysis with other experiments measuring the atmospheric oscillation parameters.

decay in flight of accelerated muons.

However, these accelerator experiments are tuned to a specific value of L/E, typically at the oscillation maximum probability, to achieve this sensitivity. One advantage of an experiment like SK is that it probes a large range of baselines and energies, so it can potentially discover unexpected effects outside of tuned sensitivity.

The L/E analysis makes use of the same source of atmospheric data as the Zenith analysis, however it is able to provide a more constrained region for Δm^2_{32}. Since the L/E Analysis is specialised to have sensitivity to oscillations, it could be strong for distinguishing sub-dominant effects beyond oscillations.

Chapter 9

Analysis of Neutrino and Anti-Neutrino Oscillation

Neutrino Oscillations is a Lorentz invariant theory, and so should also be CPT invariant. Decades of experiments on the oscillation of flavour ratios of neutrinos during transit have been carried out (Chapter 2), and Neutrino Oscillations has been found to be the dominant explanation of almost all observations. However, up until fairly recently, there had not been comprehensive studies of neutrino and anti-neutrino oscillations separately. In recent years, accelerator experiments have been running in anti-neutrino mode and have been able to directly measure the transitions of anti-muon neutrinos.

Some of the early results [10] implied that the oscillation parameter $\Delta\bar{m}^2_{32}$, measured with anti-neutrinos, could be significantly larger than the equivalent measurement for neutrinos, Δm^2_{32}. Although the tension from these results were later relaxed [11], these early results inspired more interest in the question of whether neutrino flavour transitions truly are CPT symmetric.

Neutrinos only interact weakly, with very small cross-sections, and so their precise properties are difficult to measure. Since neutrinos appear to Oscillate, this implies that neutrinos have mass, yet up until now none of the mass eigenstates of the neutrino have been measured. The fact that neutrinos should have mass at all was a surprise, as the Standard Model originally postulated them to be massless. So the properties of neutrinos are somewhat elusive and the unknowns make them mysterious, as compared with the other known elementary particles. So even properties such as the fundamental CPT symmetry should be checked in neutrinos. If neutrinos were found to break CPT symmetry, this would certainly require explanation and would point towards new physics.

There has been considerable interest in CPT violation in neutrinos [259]. For example, this could arise if the mass of the neutrino and anti-neutrino differ, $m_{\bar{\nu}} \neq m_{\nu}$; or could be allowed by CPT violating terms in the general relativistically Extended Standard Model (SME) [260, 261]. The observation of Neutrino Oscillations is an amplification of the effect of small parameters, such as neutrino masses, through their interference. In the same way, even a small degree of CPT asymmetry may be visible through Neutrino Oscillation measurements. In this analysis however, rather than attempting to directly measure the strength of CPT violating terms; indications of CPT violation could be observed in neutrino oscillations from a measurement of independent parameters for neutrino and anti-neutrino, if the effect is considerable.

The aim of the Neutrino Anti-Neutrino L/E Analysis was either to confirm the CPT symmetry

of neutrinos at the sensitivity of SK, or to measure a discrepancy between neutrinos and anti-neutrinos. This was done by allowing the oscillation parameters for neutrinos and anti-neutrinos to vary independently in the MC. The ν and $\bar{\nu}$ components were then combined before comparing against the data, which were not separated into ν and $\bar{\nu}$. The data were not separated because SK has little power for charge discrimination, as it is a massive water Cherenkov detector, and is not magnetised.

However, the flux of neutrinos has been accurately calculated and constantly improved for over 20 years with any new cosmic ray flux measurements or updated hadronic interaction models. Although the error of the absolute flux is around $\sim$10%, the $\nu/\bar{\nu}$ ratio is accurately known to within a few percent. So the relative ν and $\bar{\nu}$ composition is well understood. These contributions can be oscillated with independent neutrino and anti-neutrino parameters in the MC, to find the parameter set that best matches the data. If there is a significant difference between the oscillations of ν and $\bar{\nu}$, this could be observed as a distortion of the L/E distributions that can be described best by separate ν and $\bar{\nu}$ parameters.

9.1 Analysis Principles

9.1.1 Reconstruction of L/E

The reconstruction in this analysis is mostly similar to that described in the Standard L/E Analysis (Section 8.2). Here, a brief summary of the process follows. Reconstructing the L/E variable as accurately as possible is important to be able to observe the L/E pattern expected for Neutrino Oscillations. Firstly the visible energy was reconstructed (Section 8.2.1), taking some further considerations. These included the reconstruction of the pion energy in multi-ring events; or making use of dE/dx for a reconstructed muon path in PC events and separating rings that were expected to be overlapping. After all these additional considerations, the visible energy may still differ from the true neutrino energy. To account for this, a Monte Carlo sample was used to estimate the neutrino energy for a given visible energy and event classification. This gave a fitted correction factor as a function of the visible energy. Furthermore, careful momentum weighting was used to try to reconstruct the neutrino direction and therefore the flight path more accurately (Section 8.2.2).

The accuracy of the L/E reconstruction was also estimated depending on the reconstructed energy and zenith of the neutrino, such that cuts could be made on the expected L/E resolution (Section 8.3). There was also an offset of $(L/E)_{\text{true}}/(L/E)_{\text{rec.}}$ from unity during the resolution estimation, which was also accounted for (Section 8.3.3).

9.1.2 Neutrino and Anti-Neutrino Oscillations

Since SK does not have much power to distinguish e^- from e^+ or μ^- from μ^+, it is also very difficult to separate ν and $\bar{\nu}$ on an event-by-event basis. Instead, a discrepancy could be looked for statistically by treating the ν and $\bar{\nu}$ independently in the MC simulation. Since the expected observable difference between the parameters was already small, a simple 2-flavour $\nu_\mu \rightarrow \nu_\tau$

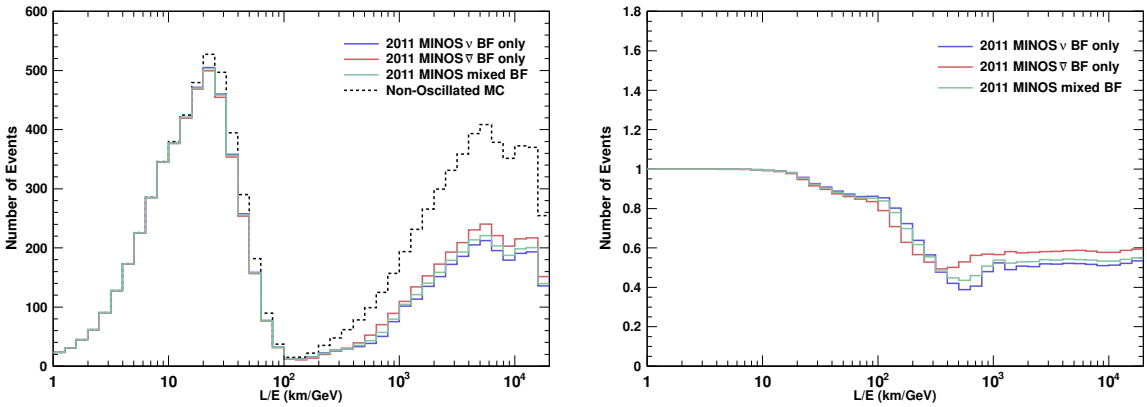

Figure 9.1: Reconstructed L/E plots from the MC assuming the best fit values from the 2011 MINOS best fit values [10], during the period of tension between neutrino and anti-neutrino measurements. The L/E distributions are shown in the left, and have been normalised by the non-oscillated MC on the right. The blue shows the ν and $\bar{\nu}$ oscillated with the 2011 MINOS best fit for neutrino oscillation [262]: $\Delta m^2_{32} = \Delta \bar{m}^2_{32} = 2.32 \times 10^{-3}\,\mathrm{eV}^2$ and $\sin^2 2\theta_{23} = \sin^2 2\bar{\theta}_{23} = 1.00$. The red shows the ν and $\bar{\nu}$ oscillated with the 2011 MINOS best fit for anti-neutrino oscillation [10]: $\Delta m^2_{32} = \Delta \bar{m}^2_{32} = 3.36 \times 10^{-3}\,\mathrm{eV}^2$ and $\sin^2 2\theta_{23} = \sin^2 2\bar{\theta}_{23} = 0.86$. While in the green MC, the ν events were oscillated with $\Delta m^2_{32} = 2.32 \times 10^{-3}\,\mathrm{eV}^2$ and $\sin^2 2\theta_{23} = 1.00$; and the $\bar{\nu}$ events were oscillated with $\Delta \bar{m}^2_{32} = 3.36 \times 10^{-3}\,\mathrm{eV}^2$ and $\sin^2 2\bar{\theta}_{23} = 0.86$. These plots show how the L/E distributions can be used to distinguish between these kinds of oscillation scenarios.

oscillation scenario was assumed with the survival probabilities below:

$$\mathrm{P}(\nu_\mu \to \nu_\mu) = 1 - \sin^2 2\theta_{23} \sin^2 \Big(\frac{1.27\Delta m^2_{32} L}{E}\Big), \tag{9.1}$$

$$\mathrm{P}(\bar{\nu}_\mu \to \bar{\nu}_\mu) = 1 - \sin^2 2\bar{\theta}_{23} \sin^2 \Big(\frac{1.27\Delta \bar{m}^2_{32} L}{E}\Big). \tag{9.2}$$

What this means is that the ν and $\bar{\nu}$ were separated in the MC into two samples and then oscillated independently, keeping track of the oscillation parameters: θ_{23} and Δm^2_{32} for neutrino and $\bar{\theta}_{23}$ and $\Delta \bar{m}^2_{32}$ for anti-neutrino. Then at the analysis stage a $(\Delta m^2_{32}, \theta_{23}, \Delta \bar{m}^2_{32}, \bar{\theta}_{23})$ parameter set was chosen, and the corresponding ν and $\bar{\nu}$ samples were combined to give the L/E distribution to be compared against the data, which were not separated into ν and $\bar{\nu}$.

Figure 9.1 shows how the L/E distributions can be built by oscillating ν and $\bar{\nu}$ independently in the MC. The distributions were made from the reconstructed L/E values. The example parameter sets were based on the best fit results for ν and $\bar{\nu}$ reported by MINOS in 2011 [10, 262], during the period of tension between these measurements. The blue histogram shows ν and $\bar{\nu}$ both oscillated at the ν best fit, which is close to the SK best fit; and the red histogram shows ν and $\bar{\nu}$ both oscillated at the $\bar{\nu}$ best fit. Mixed parameters can be seen in the green histogram, in which the ν events were oscillated at the ν best fit, and the $\bar{\nu}$ events at the $\bar{\nu}$ best fit.

It can be seen that the first slope occurs earlier in the red plot at around L/E$\sim 10^2$ km/GeV, due to the larger $\Delta \bar{m}^2_{32}$, while the magnitude of the oscillations decreases due to the smaller $\sin^2 2\bar{\theta}_{23}$. This is most prominent where the oscillations begin to average at L/E greater than $\sim 10^3$ km/GeV. If the $\bar{\nu}$ truly oscillate independently with parameters such as those reported by MINOS in 2011, the data should be better fitted by the green curve rather than the blue. The MC can be divided into ν and $\bar{\nu}$ reliably, due to the accurate calculation of the neutrino flux and the well-understood $\bar{\nu}/\nu$ ratio.

9.1.3 Neutrino and Anti-Neutrino Flux Ratio

Although there is some discrepancy of the absolute flux between different calculations of the atmospheric neutrino flux at about the $\sim$10% level, the agreement of the anti-neutrino to neutrino ratio is much better. The flux of neutrinos is created by primary cosmic rays bombarding the air molecules in the atmosphere, creating pions and some kaons. These follow decay chains, producing neutrinos at each step.

$$\begin{aligned} \pi^+ &\to \mu^+ + \nu_\mu \\ &\quad \hookrightarrow\ e^+ + \nu_e + \overline{\nu}_\mu, \end{aligned} \tag{9.3}$$

$$\begin{aligned} \pi^- &\to \mu^- + \bar{\nu}_\mu \\ &\quad \hookrightarrow\ e^- + \bar{\nu}_e + \nu_\mu. \end{aligned} \tag{9.4}$$

Kaons also become more relevant towards higher energies. Kaons can decay into muons and neutrinos, or various combinations of pions. These muons and pions can then further decay to produce neutrinos. In pion decay, most of the energy goes to the muon; while in kaon decay the energy is distributed quite evenly over the neutrino and muon, making them more significant at higher energies and the dominant source of neutrinos above 100 GeV.

The meson production by cosmic rays and the subsequent decay chains are the origin of the neutrino anti-neutrino ratios. The uncertainty in this ratio comes from the uncertainty of the

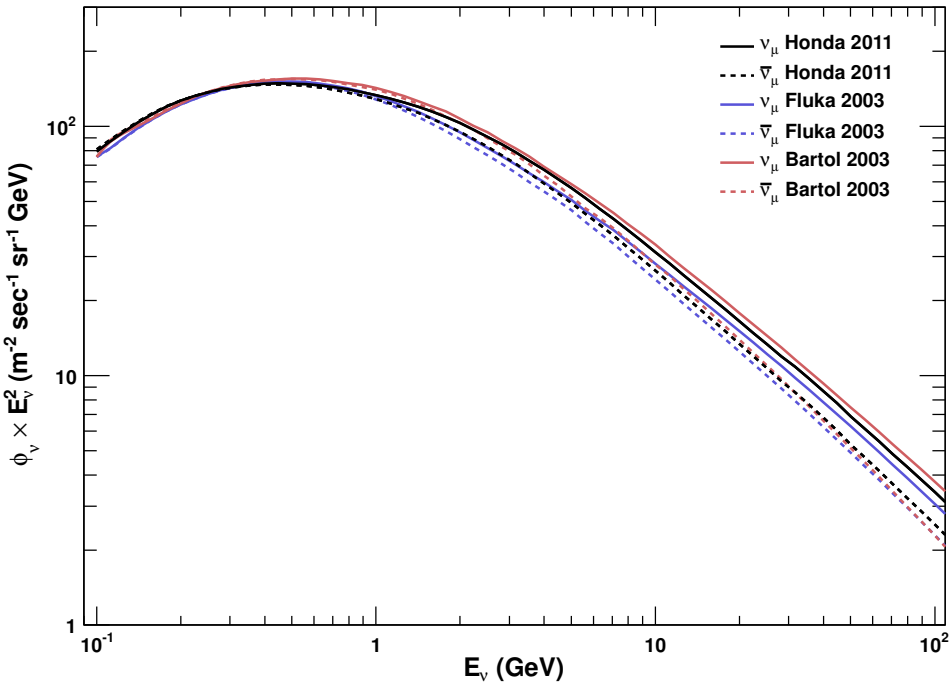

Figure 9.2: The flux of ν_μ and $\bar{\nu}_\mu$ from various flux calculations. Shown in black is Honda 2011 [16]; Fluka 2003 [168] in blue; and Bartol 2003 [169] in red. The ν_μ flux is shown by solid lines, and the $\bar{\nu}_\mu$ by dashed lines. The fluxes are similar, and have been multiplied by E_ν^2 to compress the vertical scale and make the differences more clear. Generally, compared to Honda, the Bartol flux seems slightly larger; and the Fluka flux seems slightly smaller. Except that the Bartol $\bar{\nu}_\mu$ flux falls more rapidly than the other two calculations.

π^+/π^- ratio from pion production by primary cosmic rays. Above ~10 GeV, the uncertainty in the K^+/K^- ratio also becomes more significant. It can also be seen from Equations (9.3) and (9.4), that for a pion decay one ν_μ and one $\bar{\nu}_\mu$ are produced regardless of the π^+/π^- ratio. So a $\bar{\nu}_\mu/\nu_\mu$ ratio of approximately 1 is expected for any given pion. Therefore the predicted ratio is very accurate. This does not hold quite true for kaons, because the energies of the neutrinos from Kaon decay are significantly higher than those of neutrinos produced by the subsequent muon decay. Figure 9.2 shows the ν_μ and $\bar{\nu}_\mu$ fluxes for the Honda 2011 [16], Fluka 2003 [168, 253] and Bartol 2003 [169, 254] calculations. These flux values were very similar, so the fluxes have been multiplied by the square of the neutrino energy, E_ν^2, to shrink the vertical range of the plot and make their differences more apparent.

The neutrino and anti-neutrino fluxes are very similar up to a few GeV, after which the $\bar{\nu}_\mu/\nu_\mu$ ratio decreases, which can be seen more clearly in the left of Figure 9.3. There appears to be a good agreement between the Honda and Fluka fluxes, while the ratio decreases more rapidly in the Bartol flux. This is likely due to an incomplete treatment of the kaon component of the flux in the Bartol 2003 calculation, which becomes increasingly significant towards higher energies.

In the right of Figure 9.3, the $\bar{\nu}_\mu/\nu_\mu$ ratios for Fluka and Bartol have been normalised by the Honda 2011 calculation. It can be seen that these fluxes agree very well, within 3% over most of the energy range, indicated by the inner grey dashed horizontal lines. At most these differ by

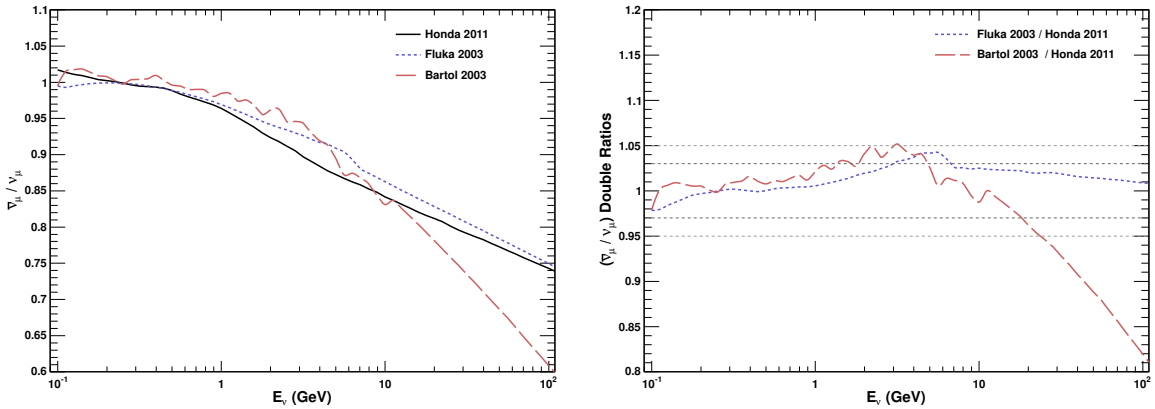

Figure 9.3: The $\bar{\nu}_\mu/\nu_\mu$ ratio of each of the flux models in the left plot, and these ratios normalised to the Honda 2011 ratio on the right for comparison. The flux of $\bar{\nu}_\mu$ is quite similar to ν_μ up until a few GeV, then gradually falls more rapidly. All the fluxes agree well, except that the Bartol ratio falls more rapidly above 10 GeV. This was likely due to an incomplete treatment of the kaon component of the flux, which is more relevant at higher energies. The right plot shows that the fluxes agree within 3% for most of the energy range (inner grey dashed horizontal lines). While at most within about 5% (outer grey dashed lines).

about 5%, marked by the outer grey dashed lines, with the exception being the Bartol flux at higher energies due to the differences in kaon treatment. In the L/E analysis, only events up to 50 GeV were included, as it is very difficult to determine the L/E resolution for energies above this. For the systematic uncertainty on the $\bar{\nu}_\mu/\nu_\mu$ ratio, a conservative estimate of 6% was taken.

Since the $\bar{\nu}_\mu/\nu_\mu$ ratio was well-known, the relative composition of neutrinos and anti-neutrinos in the MC was reliable. So these particle and anti-particle contributions can be oscillated independently to find the combined L/E shape that best matches the data.

9.2 Sensitivity Study for ν and $\bar{\nu}$ Parameters

As a first step of the analysis a sensitivity study was carried out. This was done to determine how accurately the oscillation parameters could be determined by the L/E distributions, when the ν and $\bar{\nu}$ are oscillated independently. It was also used to consider extensions to the Standard L/E Analysis (Chapter 8).

Although the ν and $\bar{\nu}$ fluxes are quite similar, with the ν flux being about $\sim$10% higher, the event rate of $\bar{\nu}$ at SK is much less than for ν, and is about 20-30% of the total events. This meant that the $\bar{\nu}$ distributions would have considerably less influence on the final L/E analysis distribution than the ν contribution. So less sensitivity was expected for $\bar{\nu}$.

9.2.1 Increasing Statistics with a Second Resolution Sample

In the Standard L/E Analysis, there was a requirement for events to have a high resolution in L/E (See Section 8.3). Quantitatively, the requirement was that the resolution of the L/E variable was within 70% of the expected true value. This $<$70% resolution cut discarded a lot of the more horizontal events and lower energy events, which can be seen in the contour plot in

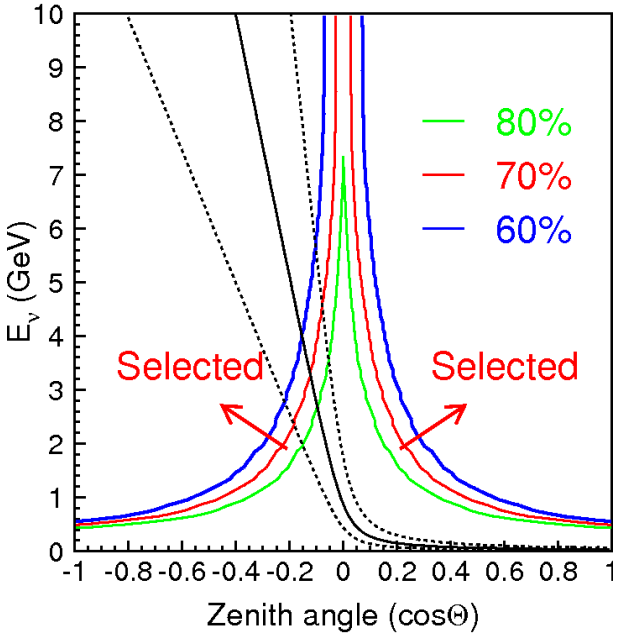

Figure 9.4: L/E resolution contour on the $(\cos\theta, E_\nu)$ plane. The coloured lines show the region of this parameter space that was cut by these resolution requirements. It can be seen that typically low energy and horizontal events were cut by imposing a higher L/E resolution condition. The precise sample selected by the Standard L/E Analysis is shown in red. By considering a second resolution sample outside of 70% the statistics could be increased. The black line shows the contour for maximum oscillation probability, and the dashed black lines for half-maximum oscillation probability.

Figure 9.4.

Of course, to reconstruct the L/E pattern precisely this cut was necessary. However, to increase the available statistics for the $\bar{\nu}$ parameter sensitivity, the addition of a second resolution sample was considered. What this means is that the precise sample (<70% resolution) analysis bins were kept, and additional bins were added for a sample made up from a resolution range that was previously discarded.

The ranges considered were 70-80%, 70-90% and 70-100% resolution. L/E distributions of these second resolution samples can be seen in Figure 9.5. The blue and green distributions correspond to the precise sample, and the orange and red distributions correspond to each of the resolution ranges mentioned above. It can be seen that the second samples each cover a range in L/E previously discarded by the Standard L/E Analysis. The resolution of these samples are relatively poor compared to the precise sample, however the additional information from these L/E distributions could help constrain the allowed region for $\bar{\nu}$.

9.2.2 Analysis Bins

The treatment of the data and MC binning from each of the SK periods was different from that of the Standard L/E Analysis. In the Standard case, the L/E distributions from each of the SK periods had separate analysis bins. For this analysis, the bins from each SK period were merged. This gave increased statistics for each bin, and reduced the risk of unstable effects due to low-statistics bins.

As with the Standard analysis, the precise L/E distributions were divided into 43 bins in $\log_{10}(L/E)$. Previously there were 43 bins for each of SK1 to SK4, or 172 bins in total. Analysing the χ^2 with merged bins compressed the 172 bins into 43 bins, or one combined L/E distribution.

As mentioned in Section 9.2.1, additional bins were added for a second resolution sample. Since these secondary samples cover a different region in L/E, it is not a good idea to naively use the same 43 L/E bins as the precise sample. So the average L/E distribution of ∼400 MC

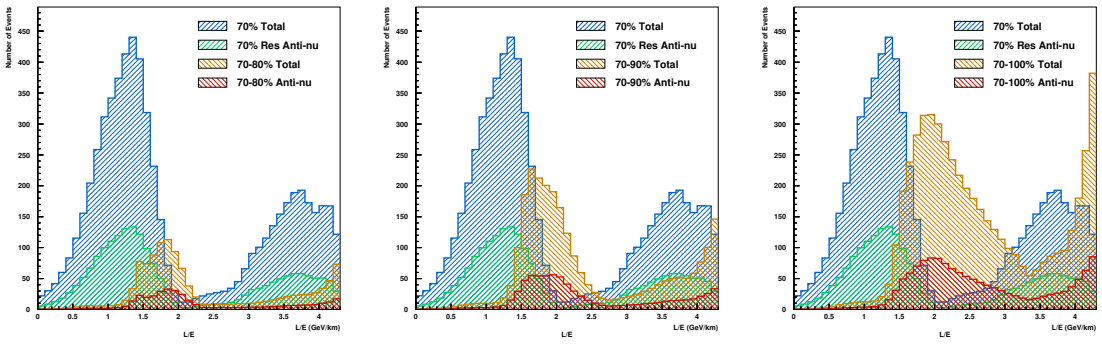

(a) 70-80 % Sample (b) 70-90 % Sample (c) 70-100 % Sample

Figure 9.5: Second Sample Distributions. The L/E Analysis estimates the accuracy of the reconstruction of the L/E variable. The Standard L/E Analysis, discussed in Chapter 8, required that L/E be reconstructed within 70% of the true value. This corresponds to the blue hatched histogram in each of the plots above. The orange hatched histograms show the L/E distributions of possible second samples in an extended resolution range. The green and red hatched histograms show the anti-neutrino contribution for the precise sample and second resolution sample, respectively.

samples of differing oscillation parameters was taken to give an idea of the region in L/E covered by the second sample. The L/E bin where all bins beyond had 5+ or 6+ events per bin was found. These positions are marked by lines in Figure 9.6, where the blue line marks where all following bins have 5 or more events, and the green line for 6 or more events per bin.

To compare the addition of each of these second samples to the analysis, the same binning was used for all the second samples. Since the most strict requirement was from the 70-80% sample, where bins 11 to 43 had 6 or more events, these bins were chosen for the second sample. In other words, the L/E bins 11 to 43 were used in the χ^2 analysis for the second resolution sample. These bins for SK1 to SK4 were, of course, also merged giving 33 additional analysis bins. So the total number of analysis bins used was $43 + 33 = 76$.

9.2.3 Sensitivity with the Second Resolution Sample

After merging the L/E bins for SK1 to SK4, then introducing more bins for a second resolution sample, the sensitivity study was carried out. To scan the relevant parameter space 21 parameters were taken for each of Δm^2_{32}, θ_{23}, $\Delta\bar{m}^2_{32}$, and $\bar{\theta}_{23}$. Where the bar denotes the oscillation parameters applied to the anti-neutrinos in the MC. This gave a parameter space of about 200,000 points (21^4).

The MC was fitted against dummy data with the following input oscillation parameters: $(\Delta m^2_{32}, \theta_{23}, \Delta\bar{m}^2_{32}, \bar{\theta}_{23}) = (2.1 \times 10^{-3} eV^2, 1.0, 2.1 \times 10^{-3} eV^2, 1.0)$. The resulting sensitivity considering the addition of each of the 70-80%, 70-90%, and 70-100% resolution samples can be seen in Figure 9.7. For each of these possibilities, the sensitivity to ν remained the same, but the 70-90% resolution sample marked by the solid line gave the best sensitivity for $\bar{\nu}$. So the 70-90% second resolution sample was chosen for the final analysis.

It can be seen that generally there was reduced sensitivity for $\bar{\nu}$ compared to that of ν,

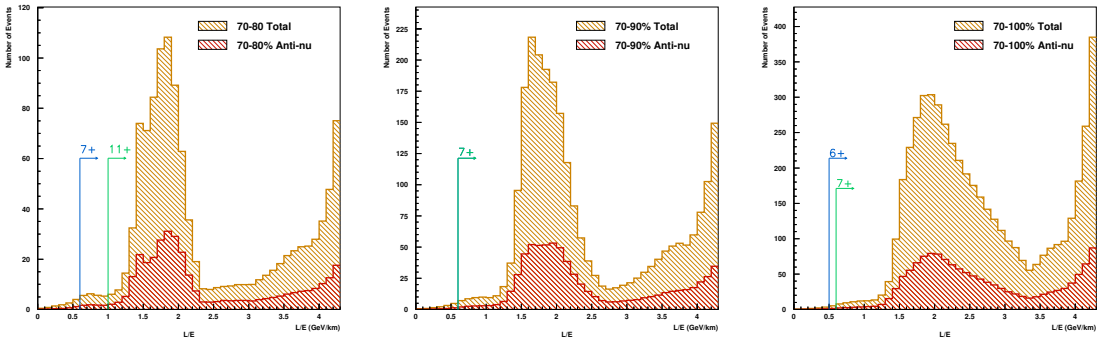

(a) 70-80 % Sample (b) 70-90 % Sample (c) 70-100 % Sample

Figure 9.6: Second Sample Binning. The average L/E distribution for ∼400 MC sets with varying oscillation parameters was used to estimate the bins covered by the second resolution sample. The blue line in each plot above marks where all following bins have more than 5 events per bin, and the green for 6+ events. The 70-80% sample provided the most constrained binning, so bins 11-43 were used for the second sample.

however the addition of the second sample gave a reasonable improvement considering the low statistics available.

These allowed regions were drawn by marginalising over the parameters not under consideration. For example, for the neutrino allowed region all the anti-neutrino parameters were marginalised over. For one particular ν parameter set, this was done by scanning over all the $\bar{\nu}$ parameter sets and finding the minimum χ^2. Then the minimum χ^2 for the next ν parameter set was found, and so on to build up the 2D χ^2 distribution. The corresponding procedure was also done for drawing the anti-neutrino allowed region. This practice was also used for the final analysis. The confidence levels (C.L.) used were for a distribution of two variables and taken to be $(68\%, 90\%, 99\%) = (2.3, 4.61, 9.21)$.

The allowed regions for the $\bar{\nu}$ parameters in this treatment should be larger, as any applied effect by the $\bar{\nu}$ oscillation can be more easily counteracted by the ν oscillation. However, in the global analysis of all the parameters, the best fit could come from a particular combination of neutrino and anti-neutrino parameters. These parameters need not be the same if anti-neutrinos do indeed appear to oscillate differently from neutrinos.

9.3 Likelihood Analysis and χ^2 Minimisation

As with the Standard L/E Analysis, a binned maximum likelihood based on Poisson statistics was used. The "Pull Method" [252] was implemented for minimising the systematics and considering the bin-by-bin correlations of the independent errors. The differences in the χ^2 treatment now include additional bins from the Second Sample discussed in Section 9.2.1, the bin merging briefly mentioned in Section 9.2.2, and some other small changes. A much more full description of the basic concepts of the likelihood was discussed for the Standard L/E Analysis in Section 8.4.

The treatment of the χ^2 was a little complicated, as the systematics needed to be considered for each SK period individually. The systematics for the Second Sample were also considered

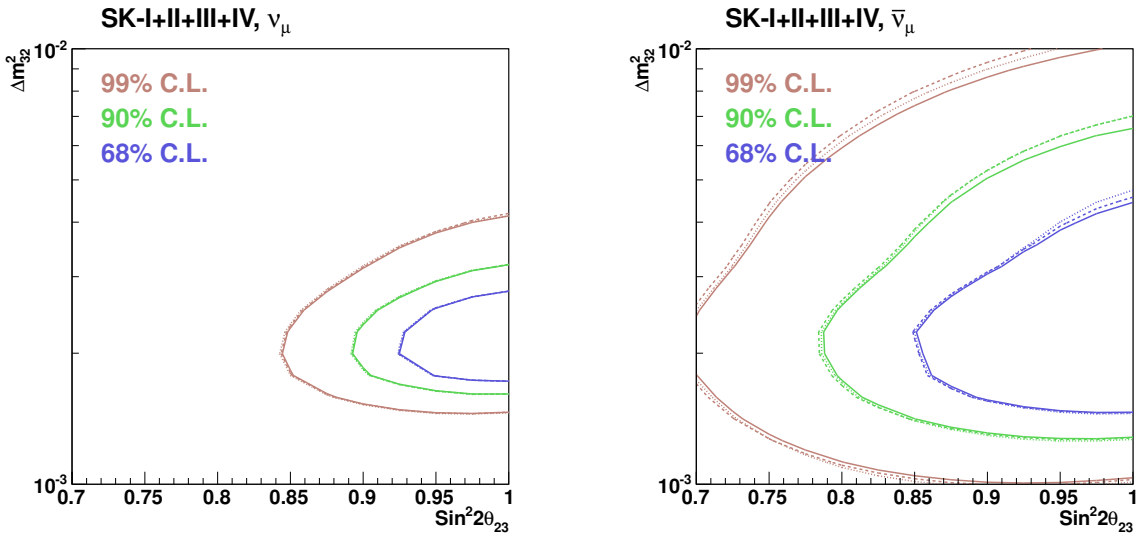

Figure 9.7: Sensitivity for each of the Second Sample Regions. The solid curves show the $\Delta\chi^2$ after adding the 70–90 % resolution sample to the 70 % precise resolution sample. The dashed curves show the $\Delta\chi^2$ after adding 70–80 % sample, and the dotted curves after adding the 70–100 % sample. Very little difference can be observed in the neutrino case, however the addition of the 70–90 % sample has consistently better sensitivity than the other samples for anti-neutrino.

in the same way. This allowed the systematics to be properly minimised before the χ^2 for the parameter set was calculated. At the χ^2 calculation stage, the bins for SK1 to SK4 were merged, after applying the appropriate adjustment from the systematics.

As a reminder the definition of the χ^2 was:

$$\begin{aligned}\chi^2 &\equiv -2\ln\left(\frac{\mathcal{L}(N^{exp},N^{obs})}{\mathcal{L}(N^{obs},N^{obs})}\right)\\ &= 2\sum_{i=1}^{nbin}\left[N_i^{exp}\left(1+\sum_{j=1}^{nsys} f_j^i\cdot\epsilon_j\right) - N_i^{obs} + N_i^{obs}\ln\left(\frac{N_i^{obs}}{N_i^{exp}(1+\sum_{j=1}^{nsys} f_j^i\cdot\epsilon_j)}\right)\right]\\ &\quad + \sum_{j=1}^{nsys}\left(\frac{\epsilon_j}{\sigma_j^{sys}}\right)^2. \end{aligned} \tag{9.5}$$

In the Standard L/E Analysis *nbin* corresponded to the 43 L/E analysis bins for each SK period, side-by-side, giving 172 bins in total. For the $\nu\bar{\nu}$ L/E Analysis, the first 172 bins were for the Precise Sample (L/E resolution $< 70\%$). Following this were the 33 Second Sample L/E bins for each SK period, giving an additional 132 analysis bins, or $172 + 132 = 304$ bins in total. As mentioned in the previous section, the Second Sample chosen had the 70-90% resolution range.

So the systematics were minimised over the 304 bins, so that errors specific to each SK period could be considered. However, as mentioned, the bins were merged at the χ^2 calculation stage. The 172 Precise Samples bins were merged into 43, and the 132 Second Sample bins were merged into 33 bins, giving $43+33 = 76$ bins in the final χ^2. Note that this treatment slightly differs from the definition written in Equation (9.5), as there was summing in each sample over bins with the

same L/E value. In this way, the systematics could be considered properly while improving the stability of the χ^2 for low statistics bins.

9.4 Neutrino Anti-Neutrino Analysis

The sensitivity study was helpful to determine the structure of the analysis. However, since there were 4 free Oscillation parameters compared to only 2 in the Standard L/E Analysis, the parameter space quickly grows very large. In the sensitivity study there were 21 values for each parameter leading to a parameter space of about 200,000 (21^4) points, since every parameter combination was considered.

In the Standard analysis, a 201×201 parameter space could be scanned comfortably on one CPU. In order to scan a more reasonable number of ν and $\bar{\nu}$ parameters, the analysis was extended to work over many CPUs. In the final analysis 41 points for each parameter were considered, giving 2.8 million sets, and was scanned over 100∼200 CPUs.

The parameter space consisted of 41 points in each of $\sin^2 2\theta_{23}$ and $\sin^2 2\bar{\theta}_{23}$ from 0.7 to 1.2, in which values above 1.0 were non-physical. For Δm^2_{32} and $\Delta \bar{m}^2_{32}$, 41 points each from 10^{-2} to 10^{-3} were scanned with logarithmically spaced intervals. Since it was computationally intensive to scan a more fine grid with 4 free parameters, the 1D χ^2 for each parameter were fitted with a spline function to calculate the confidence intervals and central value. In these distributions, the other parameters were marginalised out over the physical region of the parameters.

9.5 Systematic Uncertainties

The systematic uncertainties used for analysis with the L/E distributions were a subset of the Zenith Analysis systematic errors. The set of uncertainties have been presented in categories relating to the errors in the neutrino flux simulation, neutrino interactions, event reconstruction, and reduction of the raw data and Monte Carlo. Since the Neutrino Anti-Neutrino L/E Analysis made use of an additional resolution sample, the bin-by-bin contribution of those systematics had to be estimated for the new samples. This corresponded to extending the f^i_j in Equation 9.5 to account for the new bins introduced by the second resolution sample. Then the systematics were minimised simultaneously over the two resolution samples.

The uncertainties summarised here have the same definitions and discussion as the Standard L/E Analysis. Refer to Section 8.5 for further details. The systematic errors from the best-fit MC from this analysis are summarised in Tables 9.1, 9.2, 9.3, and 9.4. These uncertainties have also been displayed graphically in Figure 9.14 for the estimates; and in Figure 9.15 for the best fit values. Further discussion of the systematics was written together with the results in Section 9.6.

9.6 Neutrino Anti-Neutrino Results

As written above, the analysis was expanded to include two resolution samples. A precise sample with a resolution within 70%, in which the L/E variable was expected to have been reconstructed within 70% of the true L/E value; and a second resolution sample with an expected resolution between 70%–90%.

ID	Description	Systematics		
		σ %	ϵ % (σ)	Pull
Systematic Errors in Neutrino Flux				
1	Normalisation	–	6.51	0.0000
3	$\bar{\nu}_\mu/\nu_\mu$ Ratio	6.0	0.39 (0.065)	0.0043
4	Up/Down Ratio		0.00 (0.000)	0.0000
	Single-Ring $<$ 400 MeV	0.3		
	Single-Ring $>$ 400 MeV	0.5		
	Single-Ring Multi-GeV	0.2		
	Multi-Ring Sub-GeV	0.2		
	Multi-Ring Multi-GeV	0.2		
	PC	0.2		
5	Horizontal/Vertical		0.01 (0.010)	0.0001
	Single-Ring $<$ 400 MeV	0.1		
	Single-Ring $>$ 400 MeV	1.9		
	Single-Ring Multi-GeV	2.3		
	Multi-Ring Sub-GeV	1.3		
	Multi-Ring Multi-GeV	1.5		
	PC	1.7		
6	Neutrino Flight Path Length	10.0	0.92 (0.092)	0.0086
7	Energy Spectrum	5.0	-0.89 (-0.178)	0.0315
8	Sample Normalisation Multi-GeV			
	SK1	5.0	-3.54 (-0.708)	0.5016
	SK2	5.0	-2.54 (-0.508)	0.2583
	SK3	5.0	-1.35 (-0.270)	0.0729
	SK4	5.0	0.94 (0.188)	0.0355
2	FC Multi-GeV μ / PC			
	SK1	0.6	0.02 (0.033)	0.0009
	SK2	0.5	0.00 (0.000)	0.0000
	SK3	0.9	0.05 (0.056)	0.0029
	SK4	0.02	0.00 (0.000)	0.0000
26	Solar Activity			
	SK1	20.0	2.00 (0.100)	0.0100
	SK2	50.0	-3.25 (-0.065)	0.0042
	SK3	20.0	-0.25 (-0.013)	0.0002
	SK4	10.0	-0.34 (-0.034)	0.0012

Table 9.1: Neutrino Flux Uncertainties

ID	Description	Systematics		
		σ %	ϵ % (σ)	Pull
Systematic Errors in Neutrino Interactions				
9	QE Scattering Total Cross-Section	10.0	5.17 (0.517)	0.2676
10	Single Meson Production (Total Cross-Section)	20.0	-15.60 (-0.780)	0.6084
11	DIS (Total Cross-Section)	5.0	-0.46 (-0.092)	0.0085
12	Coherent π Production	100.0	-22.88 (-0.229)	0.0524
13	NC/CC Ratio	20.0	0.19 (0.010)	0.0001
21	Nuclear Effect	30.0	0.37 (0.012)	0.0001
24	Axial-Vector Mass (M_A) [QE and Single Meson]	20.0	3.85 (0.193)	0.0371
25	DIS (Bodek Correction)	20.0	16.55 (0.828)	0.6845
27	Single-Meson Production ($\pi^0/\pi^\pm$)	40.0	11.08 (0.277)	0.0767

Table 9.2: Neutrino Interaction Uncertainties

9.6.1 Neutrino Anti-Neutrino L/E Analysis Best Fit

After minimising the χ^2 for 2.8 million parameter sets, the best fit MC L/E distributions together with the L/E data can be seen in Figure 9.8. In the left plot, the precise sample is represented by the black points for data and the red histograms for MC; and the second sample by the blue points for data and the magenta histograms for MC. The solid histograms show the best fit, while the dashed histograms have not been oscillated. The precise sample looks very similar to the Standard L/E Analysis case; while the L/E values were more smeared in the 70%–90% resolution distributions, leading to some deficit prior to the first oscillation peak. The data was reconstructed in the same way, so this effect can be seen in the data too. The plot on the right shows the same information, but shows the contribution from the anti-neutrino distributions in the green (precise sample) and red (second sample) hatched histograms.

The bestfit in the physical region corresponded to the following parameters:

$$\chi^2 = 69.02/71\,\text{d.o.f}, \tag{9.6}$$

$$\sin^2 2\theta_{23} = 1.00 \pm 0.04, \tag{9.7}$$

$$\Delta m^2_{32} = \left(2.43^{+0.32}_{-0.21}\right) \times 10^{-3}\,\text{eV}^2, \tag{9.8}$$

$$\sin^2 2\bar{\theta}_{23} = 1.00 \pm 0.08, \tag{9.9}$$

$$\Delta \bar{m}^2_{32} = \left(2.44^{+0.56}_{-0.33}\right) \times 10^{-3}\,\text{eV}^2, \tag{9.10}$$

where the errors represent 1σ (68% C.L. for 1 d.o.f.), and the bar denotes the oscillation parameters applied to the anti-neutrino simulated distributions. The central values stated here were calculated from the minimum of a well-fitted spline function to the $\Delta\chi^2$ in 1D with all other parameters marginalised out. Considering only the scanned points, the best fit was found at: $(\sin^2 2\theta_{23},\ \Delta m^2_{32},\ \sin^2 2\bar{\theta}_{23},\ \Delta\bar{m}^2_{32}) = (1.00,\ 2.37 \times 10^{-3}\,\text{eV}^2,\ 1.00,\ 2.51 \times 10^{-3}\,\text{eV}^2)$. The best fit distributions were plotted from this parameter set. In these analyses, any reference to "marginalising out" a parameter means that the parameter was allowed to be free and the value that had the minimum contribution to the χ^2 was used.

The bestfit L/E distributions after normalising by the null oscillation prediction to reveal the L/E oscillation pattern can be seen in Figure 9.9. Again the precise sample looks very similar to

ID	Description	SK1			SK2		
		σ %	ϵ % (σ)	Pull	σ %	ϵ % (σ)	Pull
Systematic Errors from Reconstruction							
16	Ring Counting		-2.42 (-0.242)	0.0587		-0.50 (-0.050)	0.0025
	Single-Ring $<$ 400 MeV	0.7			2.3		
	Single-Ring $>$ 400 MeV	0.7			0.7		
	Single-Ring Multi-GeV	1.7			1.7		
	Multi-Ring Sub-GeV	-4.5			-8.2		
	Multi-Ring Multi-GeV	-4.1			-0.8		
17	Particle ID Single-Ring		-0.02 (-0.020)	0.0004		-0.09 (-0.090)	0.0077
	Sub-GeV	-0.1			-0.4		
	Multi-GeV	0.2			-0.1		
18	Particle ID Multi-Ring		0.28 (0.028)	0.0008		0.52 (0.052)	0.0027
	Sub-GeV	-3.9			2.2		
	Multi-GeV	-2.9			-3.4		
19	Energy Calibration	1.1	-0.38 (-0.345)	0.1195	1.7	-0.34 (-0.200)	0.0402
20	Up-Down Asym of E Calib.	0.6	0.05 (0.083)	0.0072	0.6	0.09 (0.150)	0.0213
23	PC Stop/Through Top	46.1	1.85 (0.040)	0.0016	19.37	-0.30 (-0.015)	0.0002
28	PC Stop/Through Bottom	22.7	-3.23 (-0.142)	0.0203	12.9	-0.32 (-0.025)	0.0006
29	PC Stop/Through Barrel	7.01	0.30 (0.043)	0.0018	9.44	-0.85 (-0.090)	0.0081
ID	Description	SK3			SK4		
16	Ring Counting		1.50 (0.150)	0.0226		3.66 (0.366)	0.1341
	Single-Ring $<$ 400 MeV	3.0			-3.0		
	Single-Ring $>$ 400 MeV	0.6			0.6		
	Single-Ring Multi-GeV	1.0			-1.2		
	Multi-Ring Sub-GeV	-2.6			-2.3		
	Multi-Ring Multi-GeV	-2.1			2.4		
17	Particle ID Single-Ring		0.00 (0.000)	0.0000		-0.09 (-0.090)	0.0075
	Sub-GeV	-0.4			-0.4		
	Multi-GeV	-0.5			-0.4		
18	Particle ID Multi-Ring		0.32 (0.032)	0.0010		-0.95 (-0.095)	0.0090
	Sub-GeV	3.1			2.2		
	Multi-GeV	4.5			6.8		
19	Energy Calibration	2.7	0.91 (0.337)	0.1148	2.3	0.04 (0.017)	0.0003
20	Up-Down Asym of E Calib.	1.3	0.10 (0.077)	0.0060	0.3	-0.05 (-0.167)	0.0258
23	PC Stop/Through Top	86.6	-4.31 (-0.050)	0.0025	43.3	2.18 (0.050)	0.0025
28	PC Stop/Through Bottom	12.1	0.78 (0.064)	0.0042	11.6	-0.19 (-0.016)	0.0003
29	PC Stop/Through Barrel	28.7	8.48 (0.295)	0.0873	7.4	0.14 (0.019)	0.0003

Table 9.3: Neutrino Reconstruction Uncertainties

ID	Description	SK1			SK2		
		σ %	ϵ % (σ)	Pull	σ %	ϵ % (σ)	Pull
Systematic Errors from Reduction							
14	FC Reduction	0.2	-0.01 (-0.050)	0.0031	0.2	0.00 (0.000)	0.0005
15	PC Reduction	2.4	-0.15 (-0.063)	0.0038	4.8	-2.63 (-0.548)	0.3000
22	Non-ν Background (μ-like)		0.00 (0.000)	0.0000		0.11 (0.110)	0.0123
	Cosmic-Ray FC Sub-GeV	0.1			0.1		
	Cosmic-Ray FC Multi-GeV	0.1			0.1		
	Cosmic-Ray PC	0.2			0.7		
ID	Description	SK3			SK4		
14	FC Reduction	0.8	-0.01 (-0.013)	0.0001	0.3	0.02 (0.067)	0.0036
15	PC Reduction	0.5	0.01 (0.020)	0.0007	1.0	0.06 (0.060)	0.0036
22	Non-ν Background (μ-like)		0.29 (0.290)	0.0843		-0.21 (-0.210)	0.0455
	Cosmic-Ray FC Sub-GeV	0.1			0.1		
	Cosmic-Ray FC Multi-GeV	0.2			0.8		
	Cosmic-Ray PC	1.8			4.9		

Table 9.4: Neutrino Reduction Uncertainties

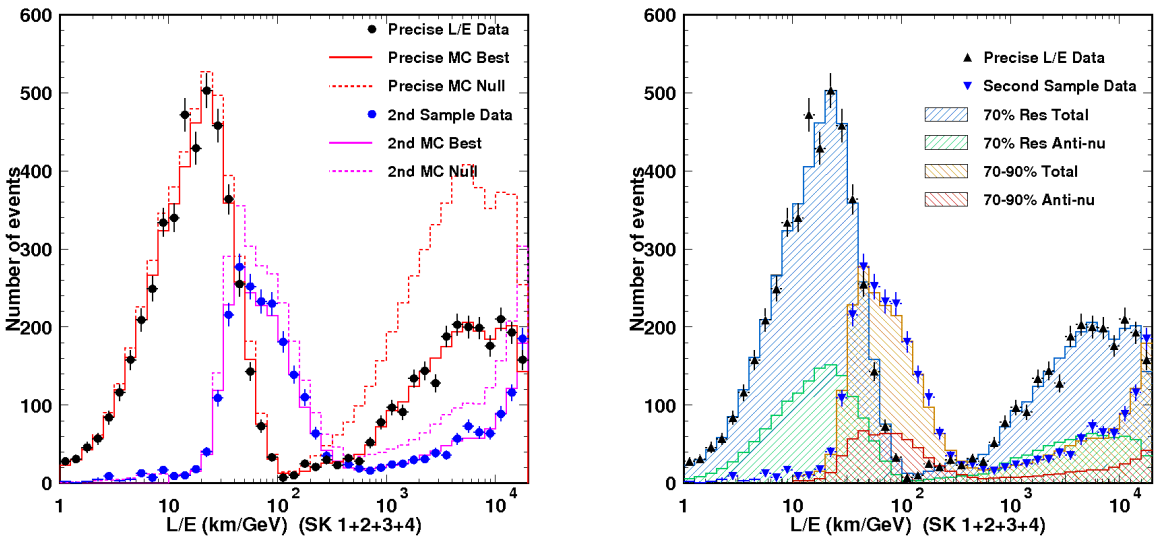

Figure 9.8: Neutrino Anti-Neutrino L/E bestfit distributions. The left plot shows precise sample with black points for data, red solid histogram for the bestfit MC and dashed red for MC without oscillations; and the second sample with blue points for data, magenta solid histogram for the bestfit, and dashed magenta for MC without oscillations. The right plot shows the same information but showing the contribution from anti-neutrinos in the green hatched (precise sample) and red hatched (second sample) histograms.

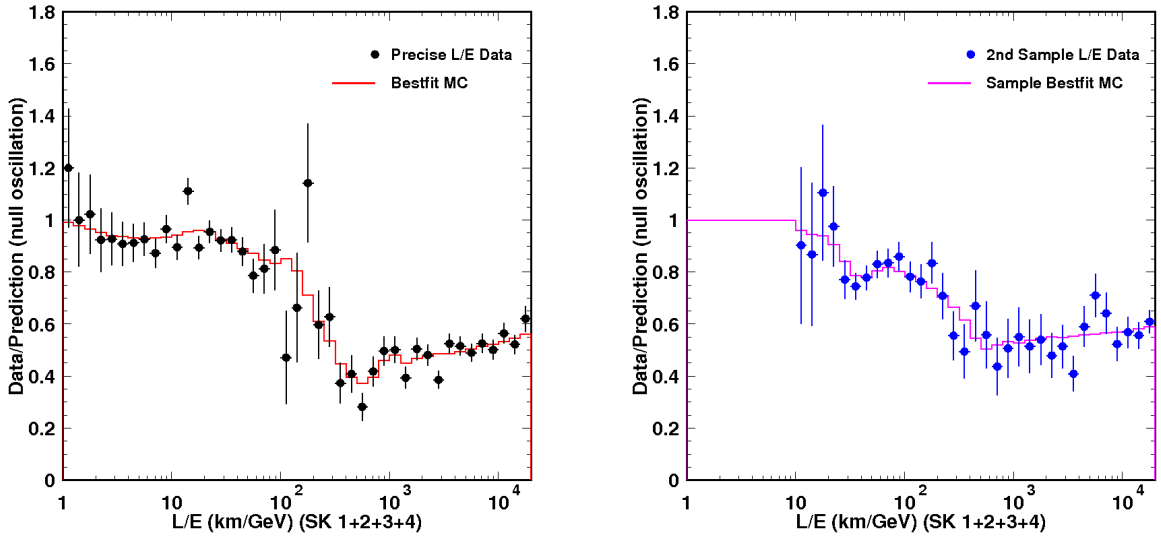

Figure 9.9: Neutrino Anti-Neutrino L/E bestfit and data normalised by the non-oscillated Monte Carlo, for the precise sample on the left and the second resolution sample on the right. The left plot was similar to the Standard L/E case. The right plot shows more smearing of the deficit, but the lowest point in the MC seems to correspond to the oscillation maximum. There was good agreement between data and MC and a clear departure from unity, even for the second sample.

the Standard L/E Analysis case. As expected, the L/E shape was smeared in the second sample distribution. However, it looks like the lowest point in the bestfit distribution corresponds to the position with maximum oscillation probability. The smearing introduces some deficit before the oscillation maximum, while the averaging of oscillations at high L/E values looks similar to the precise sample case. There was a good agreement between the MC and data in the second sample, and disagreement with the non-oscillated case, suggesting that these distributions should contribute to constrain the oscillation parameters.

The 2D allowed regions can be seen in Figure 9.10. Here the $\Delta\chi^2$ was drawn from the global minimum in the physical region and the 68%, 90% and 99% C.L. correspond to a $\Delta\chi^2$ of 2.30, 4.61, and 9.21, respectively. In the ν plot, the $\bar{\nu}$ parameters were marginalised out, and vice versa for the $\bar{\nu}$ plot. Due to the smaller statistics of $\bar{\nu}$ events, the $\bar{\nu}$ allowed region was significantly larger than for ν. Since ν and $\bar{\nu}$ cannot be separated on an event-by-event basis, the ν and $\bar{\nu}$ parameters were measured in a combined distribution. So the larger statistics of the ν events gave it more power to define the overall distribution. The ν and $\bar{\nu}$ allowed regions were overlapping, and no significant discrepancy between the two sets of oscillation parameters could be seen.

The 1D allowed regions for $\sin^2 2\theta_{23}$ for neutrinos and anti-neutrinos are shown in Figure 9.11. The same is shown for Δm^2_{32} in Figure 9.12. In these 1D distributions the 68%, 90% and 99% C.L. correspond to a $\Delta\chi^2$ of 1.00, 2.71, and 6.63, respectively, and the undisplayed parameters were marginalised out. The 1σ (68% C.L.) errors above were calculated from a spline function

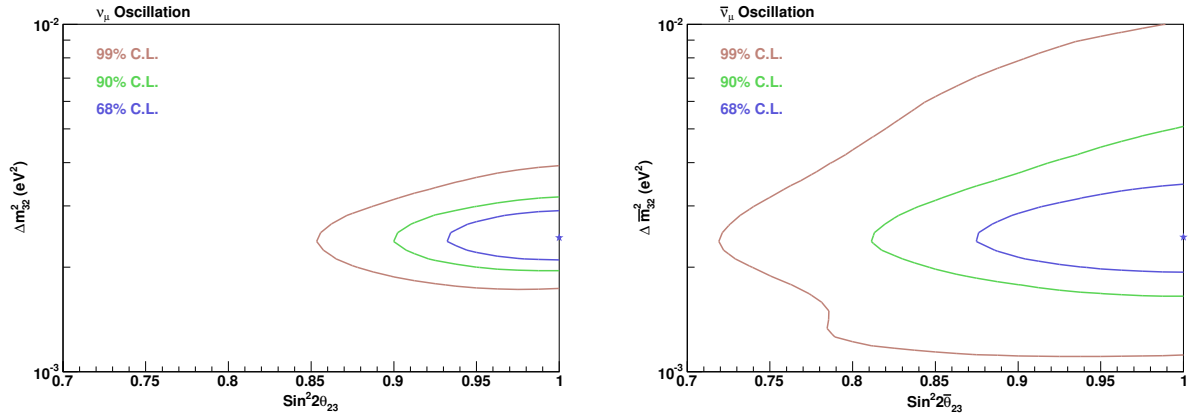

Figure 9.10: 2D allowed region contours for the neutrino oscillation parameters on the left and the anti-neutrino parameters on the right. These allowed regions were overlapping, and no discrepancy between these parameters could be seen. The best fit points found from the 1D distributions are shown by the stars.

smoothly fitted to the $\Delta\chi^2$ points. Additionally, the 90% C.L. allowed regions were:

$$\sin^2 2\theta_{23} > 0.93, \tag{9.11}$$

$$\sin^2 2\bar{\theta}_{23} > 0.86, \tag{9.12}$$

$$2.07 \times 10^{-3}\,\text{eV}^2 < \Delta m^2_{32} < 2.96 \times 10^{-3}\,\text{eV}^2, \tag{9.13}$$

$$1.89 \times 10^{-3}\,\text{eV}^2 < \Delta \bar{m}^2_{32} < 3.63 \times 10^{-3}\,\text{eV}^2. \tag{9.14}$$

The vertical coloured lines in Figures 9.11 and 9.12 indicate the positions where the 1D $\Delta\chi^2$ fitted functions cross the 68% and 90% confidence levels. These positions were taken as the confidence intervals of the oscillation parameters represented by the data. The minimum of the fitted curve was also found to give a more representative central value for the parameter, and is indicated by the light blue downward triangle in the Figures. These central values were quoted as the best fit above, and are marked by the stars in Figure 9.10. Although the scanned parameter space had limited granularity, the measured points in the 1D $\Delta\chi^2$ seemed to follow a smooth simple line and so could be interpolated accurately.

9.6.2 Analysis With Forced Normal Oscillations

In addition to the ν and $\bar{\nu}$ independent oscillation analysis, another analysis with the ν and $\bar{\nu}$ parameters forced to be the same was carried out. This allowed the ν and $\bar{\nu}$ oscillation parameters to be compared with the normal oscillation case, in the same analysis setting. The stability of the analysis after the addition of the second resolution sample and the merging of the bins in the χ^2, can be seen by comparing with the Standard 2F L/E Analysis. The best fit was found at:

$$\chi^2 = 69.08/73\,\text{d.o.f}, \tag{9.15}$$

$$\sin^2 2\theta_{23} = 1.00 \pm 0.03, \tag{9.16}$$

$$\Delta m^2_{32} = \left(2.43^{+0.21}_{-0.15}\right) \times 10^{-3}\,\text{eV}^2. \tag{9.17}$$

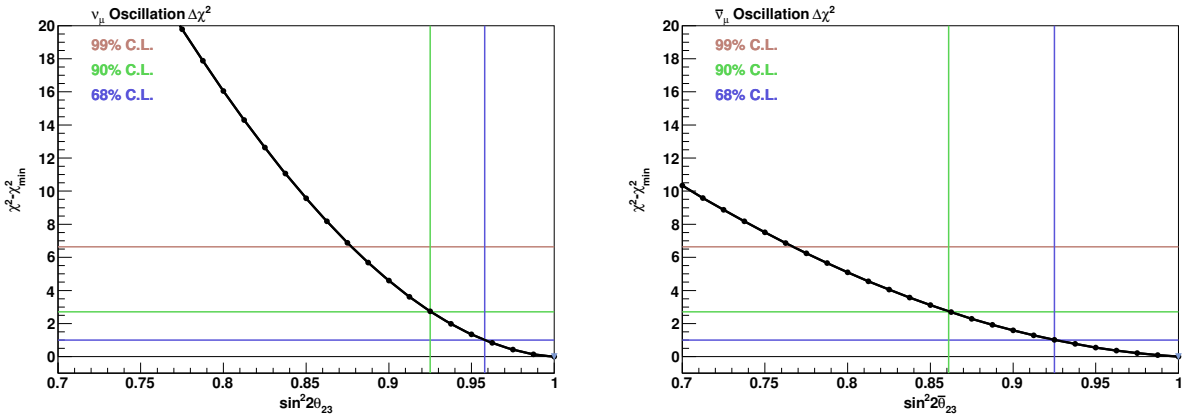

Figure 9.11: $\sin^2 2\theta$ contours for neutrinos on the left and anti-neutrinos on the right. The undisplayed parameters were marginalised out. The points show the scanned parameters, which were smoothly fitted with a spline function as shown by the curve. The fitted curve was used to calculate the 1D 68% and 90% C.L. allowed regions, as well as the minimum point indicated by the light blue triangle.

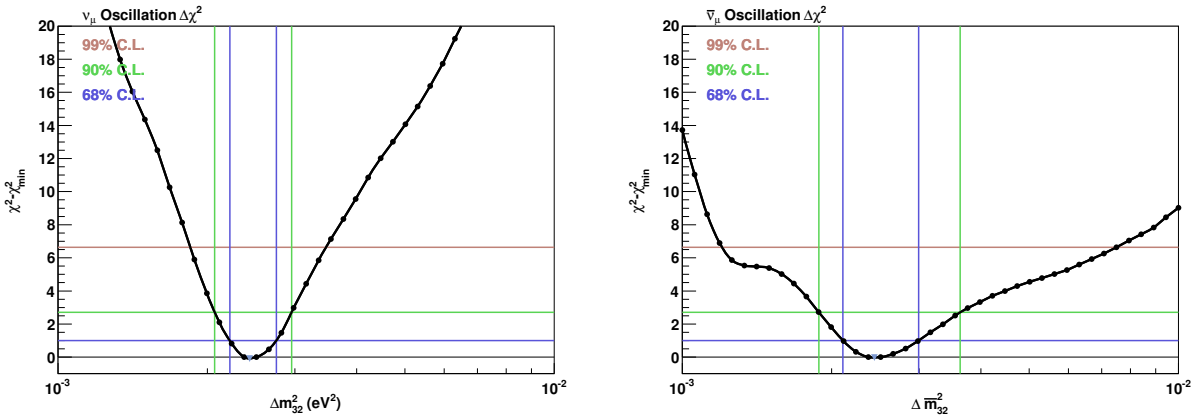

Figure 9.12: Δm^2_{32} contours for neutrinos on the left and anti-neutrinos on the right. The undisplayed parameters were marginalised out. The points show the scanned parameters, which were smoothly fitted with a spline function as shown by the curve. The fitted curve was used to calculate the 1D 68% and 90% C.L. allowed regions, as well as the minimum point indicated by the light blue triangle.

The 90% C.L. allowed regions were found to be:

$$\sin^2 2\theta_{23} > 0.95, \tag{9.18}$$

$$2.19 \times 10^{-3}\,\text{eV}^2 < \Delta m^2_{32} < 2.79 \times 10^{-3}\,\text{eV}^2. \tag{9.19}$$

The 1σ and 90% C.L. regions were calculated from the 1D plots shown in Figure 9.13. The undisplayed parameter was marginalised out. The 2D allowed regions from normal oscillations is shown in the left of Figure 9.16. The allowed regions from this analysis specified in Equations (9.18) and (9.19) seem to be a little more confined than that of the Standard 2-flavour L/E Analysis, written in Equations (8.38) and (8.39). However, this was mostly due to the different procedure used to define the 90% C.L. allowed ranges. In the standard analysis case, a cross-section at the best fit point was used to define the 90% C.L. range for 2 DOF. It can be seen in Figure 9.16 that the 2D allowed regions were very similar, which is discussed in Section 9.7.1.

9.6.3 Systematic Uncertainties

The contribution from the systematic errors were minimised during the χ^2 fitting, and the best fit values are summarised in Tables 9.1, 9.2, 9.3, and 9.4. The 1σ estimates for each of the systematic uncertainties has been displayed graphically in Figure 9.14; and the best-fit values relative to these 1σ estimates in Figure 9.15. Although the normalisation was essentially free in this analysis, as the shape is the main concern with the L/E distributions, the estimate of 10% has been shown. Relative to this, $0.65\,\sigma$ of the normalisation systematic was used in the best fit. If a penalty was included from this term, the χ^2 would increase by 0.42, which would still result in an excellent fit between MC and data.

The contributions from most systematics were below $0.5\,\sigma$, while all of them were below $1\,\sigma$. This perhaps suggests that the estimated magnitudes of the systematic uncertainties were conservative, and that the pulls from these errors were not used too much in the best fitting distribution. A very relevant uncertainty to this analysis was the $\bar{\nu}_\mu/\nu_\mu$ ratio, conservatively estimated at 6%, and its contribution at the best fit was only 0.39% ($0.065\,\sigma$). So the difference between ν and $\bar{\nu}$ was largely defined by the ν and $\bar{\nu}$ oscillation parameters rather than the systematic uncertainty. The larger contributions came from a few systematics such as the Multi-GeV normalisation, or interaction uncertainties like the quasi-elastic total cross-section, single meson production total cross-section, or DIS Bodek correction. Although, the $1\,\sigma$ estimates for these were not too large at 5%, 10%, 20% and 20%, respectively.

9.6.4 Analysis Summary

No discrepancy between ν and $\bar{\nu}$ oscillation parameters was found. Despite allowing the additional freedom for ν and $\bar{\nu}$ parameters to oscillate independently, the best fit for these parameters was essentially identical to the normal oscillation case. The allowed regions between particle and anti-particle oscillation parameters were overlapping, with the $\bar{\nu}$ regions being larger due to the lower statistical significance of the anti-neutrino events to influence the distributions. It has been shown that, within the sensitivity of this analysis, neutrino oscillations appears to be CPT symmetric.

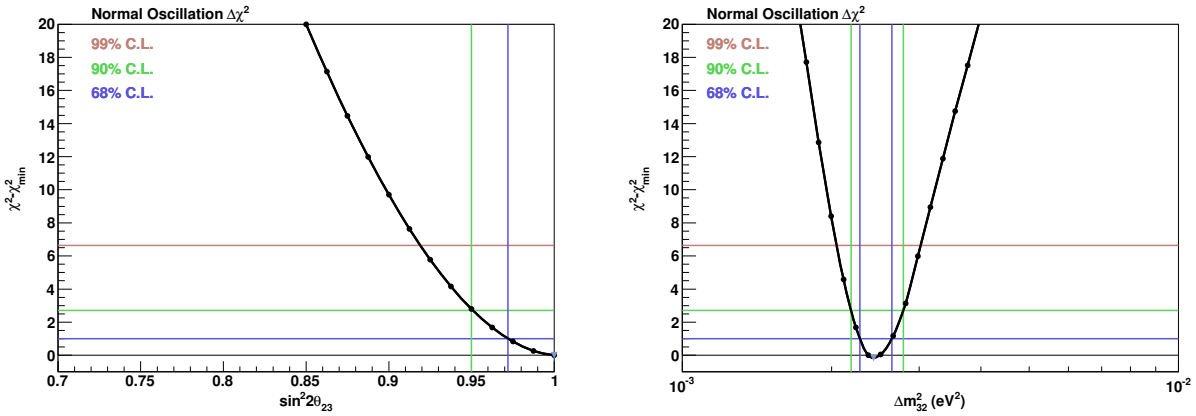

Figure 9.13: $\sin^2 2\theta_{23}$ and Δm^2_{32} 1D Contours for Normal Oscillation, in which the ν and $\bar{\nu}$ parameters were forced to be the same. The undisplayed parameter was marginalised out. The points show the scanned parameters, which were smoothly fitted with a spline function as shown by the curve. The fitted curve was used to calculate the 1D 68% and 90% C.L. allowed regions, as well as the minimum point indicated by the light blue triangle.

9.7 Discussion

9.7.1 Comparisons Between The L/E Analyses

Comparisons of the various L/E Analyses are shown in the right plot of Figure 9.16. It can be seen that the ν, $\bar{\nu}$ and normal oscillation parameters all trace out overlapping regions. The best fit points were all nearly identical, as indicated by the overlapping green and black stars, and red circle. The Standard 2F Analysis is depicted in the grey hatched region, which covers almost the same area as the normal oscillation analysis here. It looks like the forced normal analysis in this chapter has a slightly better constraint on $\sin^2 2\theta_{23}$ from the additional statistics of the second sample, providing a better distinction between the non-oscillated and average oscillated bins. This corresponds to the difference in the event numbers observed at low and high L/E, which largely accounts for the sensitivity of the L/E analysis to the $\sin^2 2\theta_{23}$ parameter.

The shared region between the normal oscillation and standard analysis suggest that the analysis is still stable with the modifications introduced in this chapter. While the second resolution sample gave increased sensitivity to sub-dominant effects such as in independent anti-neutrino oscillations or non-standard interactions. The bin merging in the χ^2 also increases the stability in lower statistics bins. At the L/E values near the position of maximum oscillation probability, the statistics were reduced due to the precise resolution requirements. So the improved stability of the χ^2 in these regions was preferable.

9.7.2 Fit in The Non-Physical Region

There was a very slightly better fit in the non-physical region with a $\Delta\chi^2 = 68.60$ and the following parameters: ($\sin^2 2\theta_{23}$, Δm^2_{32}, $\sin^2 2\bar{\theta}_{23}$, $\Delta\bar{m}^2_{32}$) = (0.91, $2.51 \times 10^{-3}\,\text{eV}^2$, 1.20, $2.37 \times 10^{-3}\,\text{eV}^2$). This may be an indication that the $\bar{\nu}$ parameters could have slightly more influence on the L/E distributions if the $\bar{\nu}$ events had a little more statistical significance. However, it is likely that this effect was simply a fitting artefact from the best fit point being located in

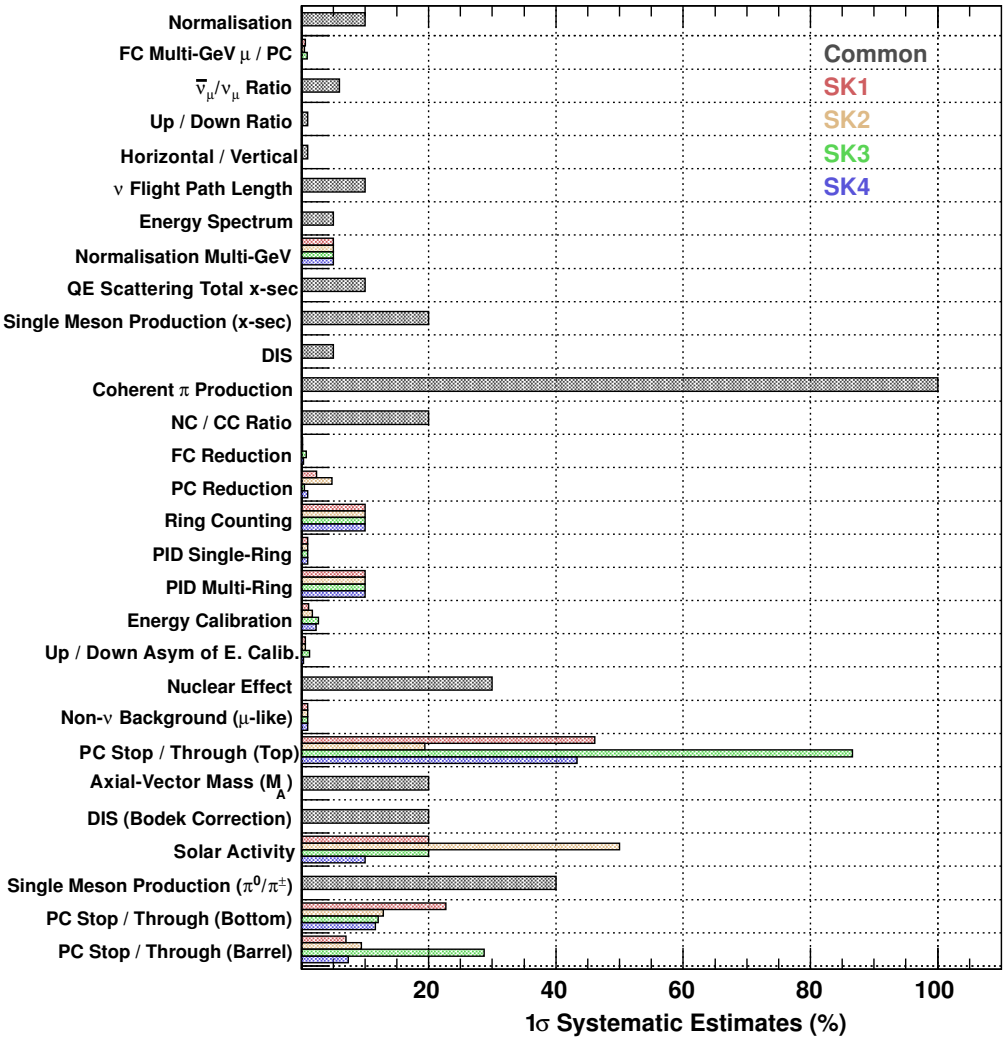

Figure 9.14: Estimates of the systematic errors

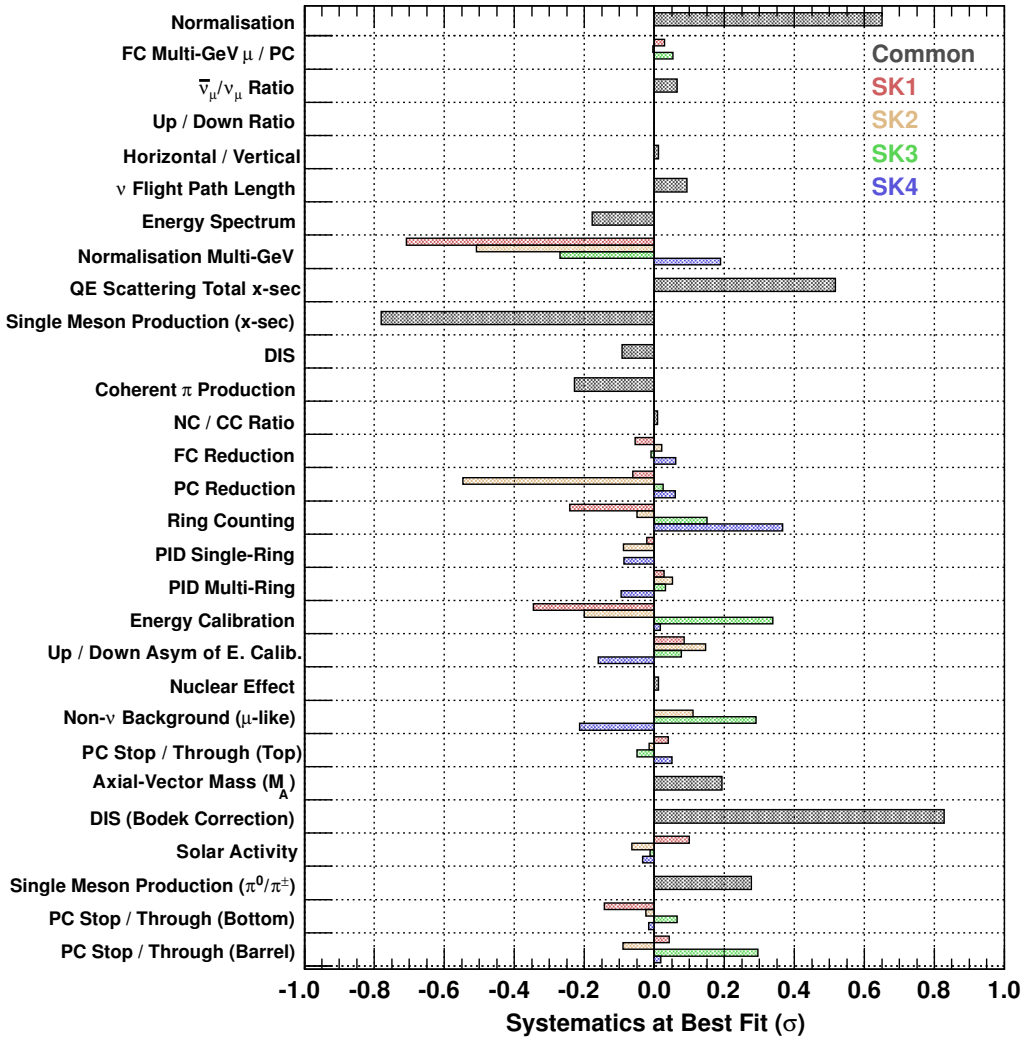

Figure 9.15: Systematics at Best Fit Neutrino Anti-Neutrino Analysis

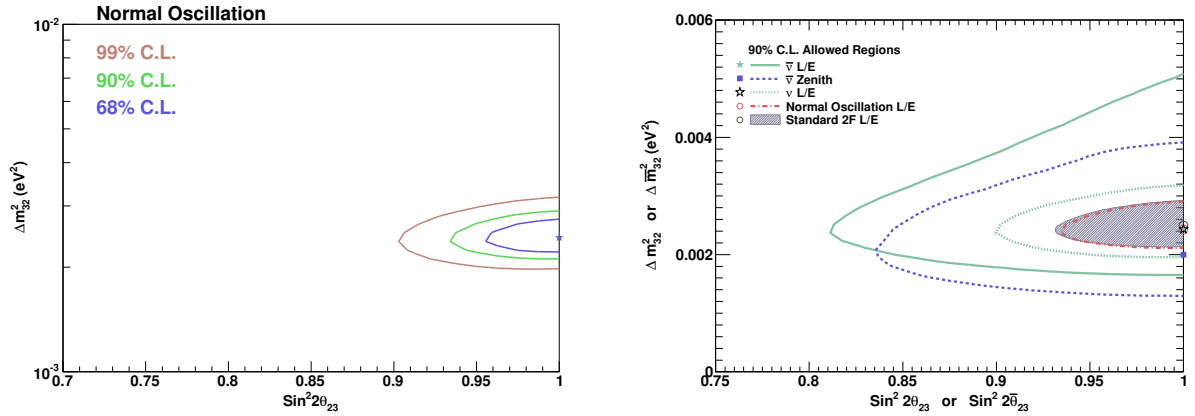

Figure 9.16: 2D allowed region contours for Normal Oscillation on the left, and comparisons of the various L/E analyses in linear scale on the right. In the Normal Oscillation, the ν and $\bar{\nu}$ parameters were forced to be the same. The 90% C.L. from this analysis is shown by the dash-dotted red line in the right plot. The region is very similar to the Standard 2F L/E analysis in shaded grey. The L/E and Zenith $\bar{\nu}$ have comparable regions, with the Zenith result shifted to lower $\Delta\bar{m}^2_{32}$. All parameter regions were in agreement with each other.

between the scanned parameter points, at $\Delta m^2_{32} = 2.43 \times 10^{-3}\,\text{eV}^2$. In this case, the additional power of the $\bar{\nu}$ distributions in the non-physical region could be selected to define a better fitting total $\nu + \bar{\nu}$ distribution.

9.7.3 Comparisons With Other Analyses

A similar $\bar{\nu}$ allowed region was obtained from an anti-neutrino Zenith analysis [12], although it was shifted to smaller Δm^2. This can also be seen in the right plot of Figure 9.16. The $\sin^2 2\bar{\theta}_{23}$ was more confined in the Zenith analysis, perhaps due to greater statistics giving more power to distinguish between the non-oscillated and averaged oscillation bins. Generally the L/E analysis has more sensitivity than the Zenith analysis to the Δm^2 parameter for normal oscillations, due to locating the poisition of the "dip" from the first point of maximum oscillation probability. However, when considering the $\bar{\nu}$ parameters between these analyses, the range extended by $\Delta\bar{m}^2_{32}$ was quite comparable. Both the Zenith and L/E analyses showed neutrinos and anti-neutrino allowed regions that were in agreement, and no evidence for a discrepancy between particle and anti-particle oscillation parameters was observed.

In Figure 9.17, comparisons of the anti-neutrino measurements from SK and MINOS can be seen. The original discrepancy between the $\bar{\nu}$ data (dotted red) and ν data (shaded grey) reported by MINOS in 2011 [10] is also shown for comparison. Their best fit for $\bar{\nu}$ at that time is indicated with the red filled circle, which was excluded at the 90% C.L. by the L/E analysis in green, as well as the Zenith analysis [12] in dashed blue. An updated result from the MINOS $\bar{\nu}$ data in 2012 [11] is traced by the dash-dotted grey contour, which also excludes the earlier best fit point at the 90% C.L. However, the SK analyses gave better constraints on $\sin^2 2\bar{\theta}_{23}$, with the SK data up until 2012. The L/E analysis essentially measures the same oscillation parameters for ν and $\bar{\nu}$, indicated by the overlapping filled and hollow stars. These best fits were close to the ν best fit from MINOS, shown by the open circle, while the Zenith analysis preferred a slightly smaller value for $\Delta\bar{m}^2_{32}$.

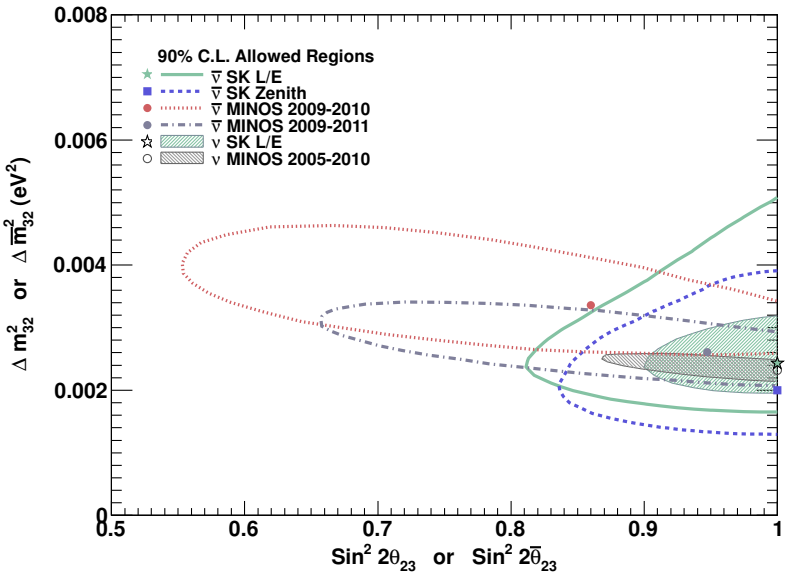

Figure 9.17: Comparisons of various neutrino and anti-neutrino oscillation parameter measurements at the 90% C.L. and in linear scale. The dotted red contour shows the first $\bar{\nu}$ result from MINOS [10] in 2011, which was distinct from the ν data in the shaded grey region. An updated result from MINOS in 2012 [11] is shown in the dash-dotted grey contour. Results from SK with data until around 2012 are also shown. The L/E $\bar{\nu}$ contour is drawn in the green solid line, and just excluded the MINOS 2011 best fit. Similarly for the Zenith measurement [12] in dashed blue. In addition, the L/E neutrino region has been overlaid (marginalised over $\bar{\nu}$) in the shaded green contour. The ν and $\bar{\nu}$ best fits from L/E were overlapping (filled and open stars), and close to the MINOS ν best fit (open circle). All measurements for ν and $\bar{\nu}$ were in agreement from 2012.

9.7.4 The Result and Prospects

All of these results suggest that neutrino oscillations are CPT symmetric, when considering simple 2 flavour vacuum oscillations. Otherwise, any CPT asymmetry present must be very small. The initial surprise on the discrepancy in simple oscillation parameters between neutrino and anti-neutrino has subsided. However, there is still a possibility for a degree of CP-asymmetry in neutrino oscillations. This effect is commonly characterised by the δ_{cp} parameter in full 3-flavour oscillations. As the determination of this parameter requires a very accurate measurement of ν and $\bar{\nu}$ oscillations, it is at the limit of the sensitivity of present day experiments.

Accelerator experiments such as T2K [37] and MINOS [43] are beginning to confine the allowed region of δ_{cp}. T2K, MINOS+ and NOνA [154] will continue to improve these constraints. Meanwhile Hyper-Kamiokande [147], the proposed successor to Super-Kamiokande, will aim to further improve neutrino measurements with much greater statistics.

So there is still considerable interest to make neutrino and anti-neutrino measurements independently. Further sensitivity could be achieved by having much better charge discrimination of outgoing leptons, and therefore the power to distinguish neutrino from anti-neutrino. The India-based Neutrino Observatory, INO [263], has a part of its design to have a magnetised atmospheric neutrino detector on a 50 kT scale. There is also interest to make measurements of CPT violation in neutrinos at INO [264]. In addition, designs for Neutrino Factories [147] have the advantage of a very precisely understood neutrino flux from the decay of accelerated muons and a detector with excellent charge discrimination.

Chapter 10

3-Flavour L/E Analysis

It has been common in neutrino oscillation experiments to approximate the neutrino flavour transition probabilities with 2-flavour models. Since the two mass square differences ($\Delta m^2_{21} \sim 7.6 \times 10^{-5}\,\text{eV}^2$ and $\Delta m^2_{31} \sim 2.5 \times 10^{-3}\,\text{eV}^2$) differ by nearly 2 orders of magnitude, and the parameter that allows cross-mixing between these 2-flavour schemes (θ_{13}) was considered to be small, these approximations were very accurate.

However, since 2012 it has been shown that θ_{13} is non-zero, and not so small. This was first indicated by T2K [39], and unambiguously observed by the reactor experiment Daya Bay in March 2012 [14], with a significance of $5.2\,\sigma$, and shortly afterwards confirmed by the reactor experiments RENO [41] and Double CHOOZ [42]. The reactor experiments made their measurement by observing the disappearance of ν_μ (into ν_e) at a distance of around $\sim$1 km. In addition, in 2013 the accelerator experiment T2K made the first observation of ν_e appearance from a ν_μ beam, with $7.2\,\sigma$ significance [37].

One of the principle characteristics of neutrino oscillations is that the transition probability depends on the quantity L/E. However, up until now there has not been a 3-flavour oscillation analysis considering this characteristic. The analysis presented in this chapter is the first attempt to study the L/E dependence with 3-flavour oscillations. It has been shown that in 2-flavours, the L/E analysis provides strong constraints on the oscillation parameters, with the most confining measurement of Δm^2_{31} from atmospheric neutrinos. This L/E characteristic has also been successful at excluding competing theories for the flavour transitions observed in atmospheric neutrinos.

The aim of this analysis was to confirm that the L/E analysis still provides a meaningful measurement under the presence of 3-flavour effects, such as transitions through matter and $\nu_\mu \leftrightarrow \nu_e$ mixing through oscillations. As this is the first 3-flavour L/E analysis, measurements on the neutrino mass hierarchy and the octant of θ_{23} were made. However, the sensitivity to these parameters was thought to be small, especially since this analysis does not have tuned sensitivity to them. For the same reason, the influence of δ_{cp} was not considered. However, the transition probabilities were updated to include 3-flavour oscillations and matter effects. To achieve this, the non-scanned oscillation parameters were set at the best fit from global solar oscillation parameter results [32], and from measurements of θ_{13} in early 2012 [14, 41]. At this time, θ_{13} was found to be around $\sin^2\theta_{13} = 0.025$.

In recent years, with measurements on the last remaining oscillation parameter θ_{13}, we have been closing in on the final formulation of neutrino oscillations. So it is preferable to carry out analyses with the more accurate 3-flavour probabilities. Through doing this, more significant

measurements on the atmospheric parameters θ_{23} and Δm^2_{31} can be obtained from the L/E analysis – free from any concerns from making 2-flavour approximations.

Super-Kamiokande (SK) has an impressive data set of atmospheric neutrinos spanning over 10 years, and a wide range of neutrino energies and baselines. This makes analyses at SK ideal for scanning the whole parameter space of atmospheric oscillation parameters. Not only can these analyses make precision and significant measurements of these parameters, but they can potentially observe additional effects that may not be visible in an experiment with tuned sensitivity. In addition, the updates in this analysis also serve as a precursor to considering the effects of Non-Standard Neutrino Interactions (NSI) in a 3-flavour framework, which will be discussed in Chapter 11.

10.1 Moving from 2-Flavours to 3-Flavours

Since Δm^2_{31} and Δm^2_{21} differ by about 1.5 orders of magnitude, Neutrino Oscillations can be decoupled into two 2-flavour regimes to a good approximation. For the analysis of atmospheric neutrinos, Δm^2_{31} ($\approx \Delta m^2_{32}$) was most significant and could accurately describe the data with $\nu_\mu \to \nu_\tau$ oscillaitons [30, 31]. Whereas Δm^2_{21} could be probed with solar and reactor neutrinos [32]. As greater statistics were collected and early evidence for non-zero θ_{13} emerged, some analyses were carried out considering 3 flavours, such as the 3-flavour zenith analysis at SK [15]. This is the first L/E analysis to take into account 3-flavour effects.

10.1.1 Treatment of Oscillation Probabilities

The ν_μ deficit in the Standard L/E Analysis discussed in Chapter 8 was described well by the 2-flavour probability:

$$P(\nu_\mu \to \nu_\tau) = \sin^2 2\theta_{23} \sin^2 \left(\frac{1.27 \Delta m^2_{32} L_\nu}{E_\nu} \right), \tag{10.1}$$

while in this analysis, the neutrino oscillations were treated with the following Hamiltonian:

$$H_{\alpha\beta} = \frac{1}{2E} U_{\alpha j} \begin{pmatrix} 0 & 0 & 0 \\ 0 & \Delta m^2_{21} & 0 \\ 0 & 0 & \Delta m^2_{31} \end{pmatrix} U^\dagger_{k\beta} \pm V_{MSW}, \tag{10.2}$$

where U is the Unitary Lepton Mixing Matrix:

$$U = \begin{pmatrix} 1 & 0 & 0 \\ 0 & c_{23} & s_{23} \\ 0 & -s_{23} & c_{23} \end{pmatrix} \begin{pmatrix} c_{13} & 0 & s_{13} \\ 0 & 1 & 0 \\ -s_{13} & 0 & c_{13} \end{pmatrix} \begin{pmatrix} c_{12} & s_{12} & 0 \\ -s_{12} & c_{12} & 0 \\ 0 & 0 & 1 \end{pmatrix}, \tag{10.3}$$

and where $c_{ij} \equiv \cos\theta_{ij}$ and $s_{ij} \equiv \sin\theta_{ij}$. Notice that the CP-term, $e^{\pm i\delta_{cp}}$, has been omitted in this analysis. Matter effects were included in Equation (10.2), in the V_{MSW} term:

$$V_{MSW} = \sqrt{2} G_F N_e(\vec{r}) \begin{pmatrix} 1 & 0 & 0 \\ 0 & 0 & 0 \\ 0 & 0 & 0 \end{pmatrix}, \tag{10.4}$$

where $G_F = 1.166 \times 10^{-5}$ GeV^{-2} is the Fermi constant, and N_e the ambient electron number density calculated along the neutrino path from production to the detector.

In the L/E distributions, ν_μ events were selected and form the bulk of the data analysed. The Standard L/E Analysis considered only the 2-flavour survival probability $P(\nu_\mu \to \nu_\mu)$. Now that 3-flavour effects were being considered, mixing between ν_μ and ν_e must also be considered. Oscillation probabilities were also applied to the few remaining ν_e events for completeness. The probabilities were modified as follows:

$$P(\nu_\mu) = P(\nu_\mu \to \nu_\mu) + P(\nu_e \to \nu_\mu)\frac{\Phi(\nu_e)}{\Phi(\nu_\mu)}, \tag{10.5}$$

$$P(\nu_e) = P(\nu_e \to \nu_e) + P(\nu_\mu \to \nu_e)\frac{\Phi(\nu_\mu)}{\Phi(\nu_e)}, \tag{10.6}$$

where $\Phi(\nu_\mu)$ and $\Phi(\nu_e)$ are the flux of ν_μ and ν_e, respectively, taken from looking up flux tables on an event-by-event basis.

To calculate the probabilities, the hamiltonian in Equation (10.2) was diagonalised to get the effective eigenvalues $\hat{H} = \mathrm{diag}(E_1, E_2, E_3)$ and used to form an evolution matrix for constant matter density:

$$S^j_{\beta\alpha}(t, t_0) = \sum_{i=1}^{3} (U'_{\alpha i})^* U'_{\beta i} e^{-iE_i L} \qquad (\alpha,\, \beta = \mathrm{e},\, \mu,\, \tau), \tag{10.7}$$

where L is equivalent to $t - t_0$ and U' is the Lepton Mixing Matrix in matter. These amplitudes, $S^j_{\beta\alpha}$, were calculated for the j-th region of constant matter density through the earth. In the simulation, the interior of the Earth was divided into five regions of constant matter density using the PREM model [160]. The trajectory of the neutrino through these matter regions was determined and $S^j_{\beta\alpha}$ was calculated for each region traversed. Then the probability for the $\alpha \to \beta$ transition was computed from the $S^j_{\beta\alpha}$ as follows:

$$P_{\alpha\beta} = |S^J_{\beta\alpha} \cdots S^2_{\beta\alpha} S^1_{\beta\alpha}|^2, \tag{10.8}$$

for J regions of constant matter density traversed.

10.1.2 Flavour Flux Re-Weighting

In order to consider the mixing between ν_μ and ν_e, the events in the MC needed to be re-weighted to the corresponding flavour. This was done so that all of the reconstruction in the MC was for the neutrino of the flavour observed, but the origin of the neutrino could be assumed to be of a different flavour.

Event-by-event, the expected flux for ν_μ and ν_e were checked at the particular neutrino energy and direction of the event, and whether it was a neutrino or anti-neutrino. These flux weight variables $\Phi(\nu_\mu)$ and $\Phi(\nu_e)$ were found by looking up flux tables, provided by the Honda 2011 flux calculation [16]. The ratio of the fluxes could be used to re-weight the ν_μ flux to the ν_e flux with the ratio $\frac{\Phi(\nu_e)}{\Phi(\nu_\mu)}$, or vice-versa.

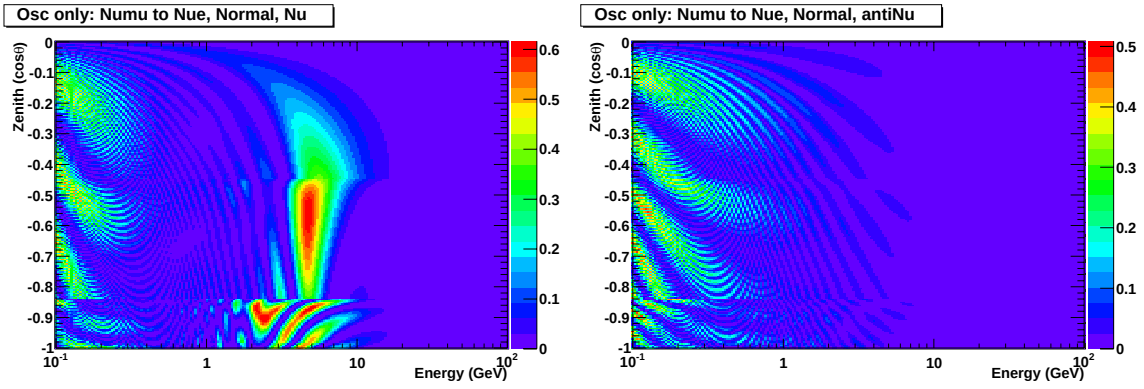

(a) $P(\nu_\mu \to \nu_e)$ Normal Hierarchy

(b) $P(\bar{\nu}_\mu \to \bar{\nu}_e)$ Normal Hierarchy

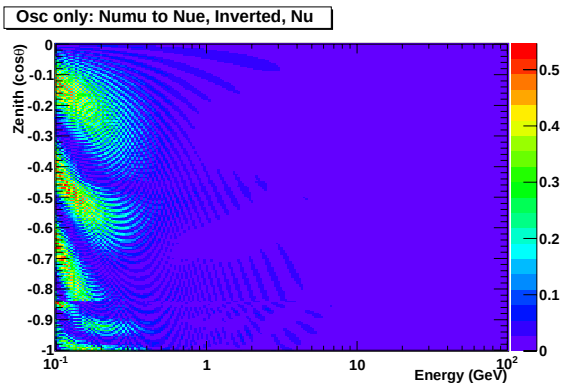

(c) $P(\nu_\mu \to \nu_e)$ Inverted Hierarchy

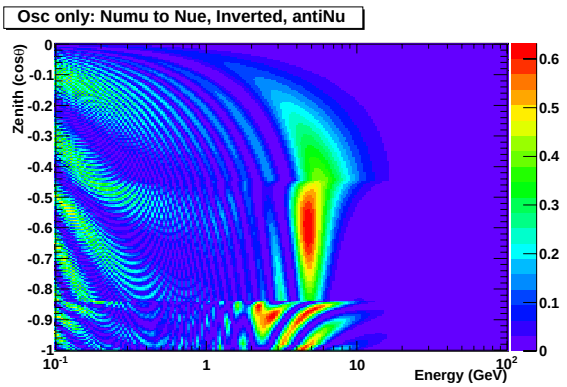

(d) $P(\bar{\nu}_\mu \to \bar{\nu}_e)$ Inverted Hierarchy

Figure 10.1: Oscillation probabilties for $\nu_\mu \to \nu_e$ and $\bar{\nu}_\mu \to \bar{\nu}_e$ for Normal and Inverted Hierarchies. The oscillation parameters were taken as global fit values from an analysis after Neutrino 2012: $\Delta m^2_{21} = 7.62 \times 10^{-5}\, eV^2$, $\Delta m^2_{31} = 2.55 \times 10^{-3}\, eV^2$, $\sin^2\theta_{23} = 0.613$, $\sin^2\theta_{12} = 0.320$, and $\sin^2\theta_{13} = 0.0246$. The effect of the resonance term can be seen at $\sim$5 GeV for neutrinos in the Normal Hierarchy (a), and anti-neutrinos for the Inverted Hierarchy (d)

10.2 Neutrino Mass Hierarchy

One of the remaining pieces of the Neutrino Oscillation model to be determined is the ordering of the neutrino mass hierarchy. Whether the neutrino masses are arranged naturally in increasing mass as ν_1, ν_2, ν_3 in the Normal Hierarchy or as ν_3, ν_1, ν_2 in the Inverted Hierarchy.

The Inverted Hierarchy was simulated to a good approximation by changing the sign of the Δm^2_{31} parameter in the Unitary Lepton Matrix written in Equation (10.4). The possibility of measuring the mass hierarchy comes from a resonance term in the interactions with matter, causing an enhancement in the $P(\nu_\mu \to \nu_e)$ probability for neutrinos in the Normal Hierarchy case, and for anti-neutrinos in the Inverted Hierarchy case. The resonance occurs for upward-going events at around $\sim$5 GeV, and can be seen in Figure 10.1. Since the mass hierarchy is unknown, the analysis was carried out for each case and the results compared.

10.3 Analysis Method

The analysis method used a χ^2 based on Poisson Statistics and is very similar to the Standard L/E Analysis (Chapter 8) with all the improvements made in the Neutrino Anti-Neutrino Analysis (Chapter 9.1). Specifically, the improvements were the merging of the bins from SK1 to SK4 during the χ^2 calculation to have increased stability for bins with few events; and the addition of a Second Resolution Sample. For details, refer to Section 9.2. This analysis was built on top of the previous analyses described, so the verifications and the details written earlier about the analysis techniques apply here also. The main addition to the analysis in this chapter was a modification of the probabilities to take into account 3-flavour oscillations and matter effects.

The parameter space scanned over was 201 points in Δm^2_{31} from $1 \times 10^{-3}\,\mathrm{eV}^2$ to $1 \times 10^{-2}\,\mathrm{eV}^2$ with logarithmically spaced intervals, and 51 linearly spaced points in $\sin^2\theta_{23}$ from 0.2 to 0.8. To include the effects from the other flavours the remaining parameters were set as $\Delta m^2_{21} = 7.66 \times 10^{-5}\,\mathrm{eV}^2$, $\sin^2\theta_{12} = 0.304$, and $\sin^2\theta_{13} = 0.025$ for both hierarchies. These parameters were set by global solar oscillation parameter results [32], and $\sin^2\theta_{13}$ by the earliest measurements in 2012 from Daya Bay [14] and RENO [41].

10.4 Results

The atmospheric oscillation parameters in the MC were varied over the parameter space, and for each parameter set the L/E distributions were calculated and compared with data. In this analysis, the L/E MC distributions were determined with 3-flavour oscillation probabilities.

10.4.1 3-Flavour Results

After scanning the whole parameter space, the points in $(\Delta m^2_{31}, \sin^2\theta_{23})$ with the minimum χ^2 were $(2.60 \times 10^{-3}\,\mathrm{eV}^2, 0.55)$ for the Normal Mass Hierarchy and $(2.45 \times 10^{-3}\,\mathrm{eV}^2, 0.54)$ for the Inverted case. The minimum χ^2 for the Normal Hierarchy was 69.56/73 while the Inverted case was 69.44/73. So a very good fit of the Monte-Carlo to the data was found for both mass hierarchies, with neither scenario being favoured over the other.

The bestfit L/E distributions have been drawn in Figure 10.2, for both hierarchies. As suggested by the minimum χ^2 values, a very good fit can be seen for both cases. So the histograms for both hierarchies appear to be overlapping in the figure, after the systematics have been minimised in their contribution to get the best fit to the data. As expected, there was a large discrepancy between the bestfit MC and the MC assuming no oscillations (Null Oscillation MC).

The bestfit L/E distributions in Figure 10.2 were divided through by the null oscillation expectation, giving the distiribtions in Figure 10.3. This gave an idea of the relative change of the distributions caused by oscillations for a particular value of L/E. The largest deficit was seen at around $\sim$500 km/GeV where you would expect maximum oscillation for $\Delta m^2_{32} \approx 2.5 \times 10^{-3}\,\mathrm{eV}^2$. Even with $\sin^2\theta_{13} = 0.025$, the oscillation minimum "dip" was seen as clearly as in the 2-flavour case, suggesting that the L/E Analysis is a good method to study the oscillations in detail. For large L/E, the oscillations are very rapid and there is an average reduction in the flux. Again, very little difference was seen in the distributions between the mass hierarchies. For comparison, the corresponding distribution in the 2-Flavour Standard L/E Analysis was also drawn.

The analysis was carried out by inputting $\sin^2\theta_{23}$, as opposed to the double angle variable $\sin^2 2\theta_{23}$ that is often used in 2-flavour models, to potentially observe any difference in the θ_{23}

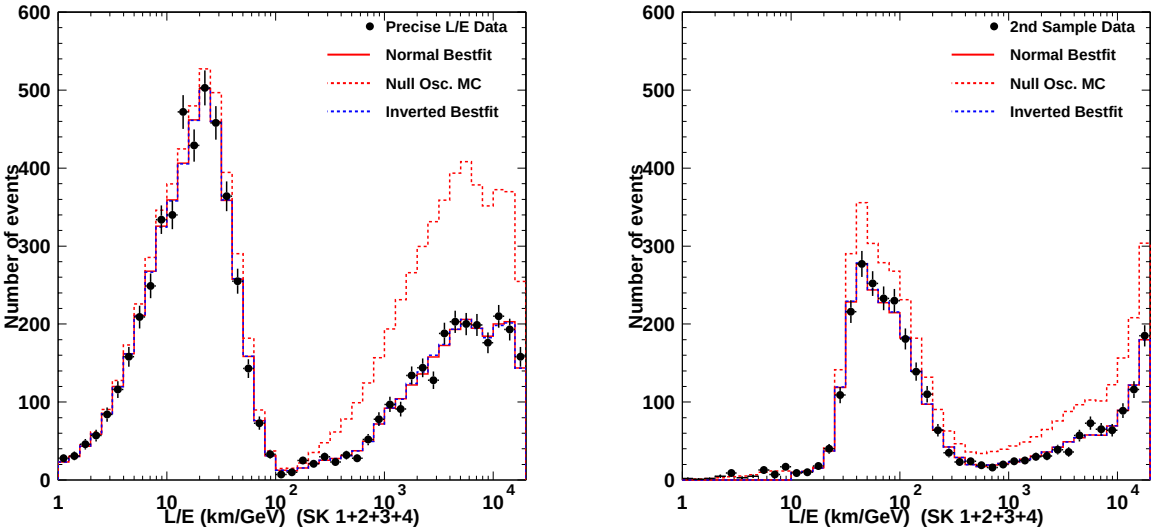

Figure 10.2: L/E bestfit distributions for the 3-Flavour L/E Analysis, for the precise resolution sample on the left and second resolution sample on the right. The red solid histogram shows the bestfit for Normal Hierarchy and the blue dashed histogram for the Inverted case. The red dashed histogram shows the MC L/E distribution with no oscillations applied. Since a very good fit was obtained for both hierarchies, very little discrepancy can be seen between them and the histograms were essentially overlapping.

octants. The resulting allowed region can be seen in Figure 10.4, for Δm^2_{31} against $\sin^2\theta_{23}$. The first immediate observation was that the contours were considerably symmetric across $\sin^2\theta_{23} = 0.5$ and that neither octant was significantly favoured over the other. The best fit points for both hierarchies were for $\sin^2\theta_{23} > 0.5$. However, looking at the 1-dimensional contours drawn by integrating out the other parameter in Figure 10.5, it can be seen that the χ^2 distribution was very flat about $\sin^2\theta_{23} = 0.5$. This suggests that any value close to $\sin^2\theta_{23} = 0.5$ could have been favoured by this analysis.

In the 2D parameter space (Figure 10.4), it appears that the contours for the Normal Hierarchy were shifted very slightly up and to the right compared to the Inverted case. Here the $\Delta\chi^2$ was drawn from the global minimum and the 68%, 90% and 99% C.L. correspond to a $\Delta\chi^2$ of 2.30, 4.61, and 9.21, respectively. This effect can be seen more clearly in the 1D plots in Figure 10.5. In these 1D distributions the 68%, 90% and 99% C.L. correspond to a $\Delta\chi^2$ of 1.00, 2.71, and 6.63, respectively. The 1σ errors (68% C.L.) and 90% C.L. allowed regions were calculated from the 1D distributions. The bestfit parameters with 1σ errors were:

$$\sin^2\theta_{23} = 0.55^{+0.07}_{-0.13}, \quad \text{and} \quad \Delta m^2_{31} = (2.60^{+0.22}_{-0.21}) \times 10^{-3}\,\text{eV}^2 \quad \text{Normal Hierarchy}, \tag{10.9}$$

$$\sin^2\theta_{23} = 0.54^{+0.07}_{-0.12}, \quad \text{and} \quad \Delta m^2_{31} = (2.45^{+0.25}_{-0.16}) \times 10^{-3}\,\text{eV}^2 \quad \text{Inverted Hierarchy}, \tag{10.10}$$

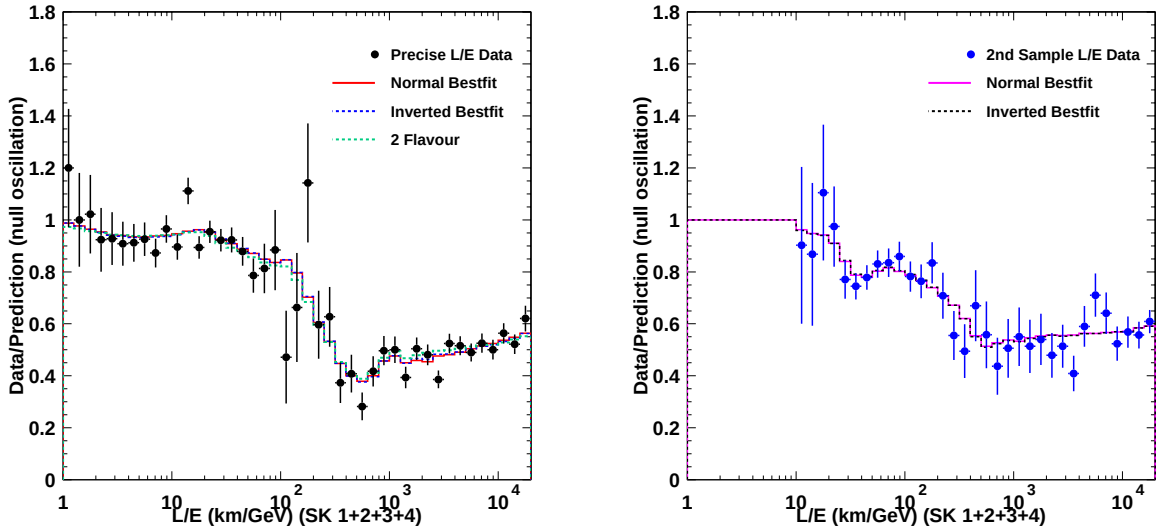

Figure 10.3: L/E bestfit MC over the null oscillation expectation for the 3-Flavour L/E Analysis. The left plot shows the precise resolution sample with the red solid histogram for Normal Hierarchy and the blue dashed histogram for the Inverted case. As expected from the L/E distributions in Figure 10.2, these two histograms were essentially overlapping here as well. Also drawn for comparison in the green dashed histogram is the bestfit from the 2-Flavour Standard L/E Analysis (see Chapter 8). A small difference can be observed between the 2-Flavour and 3-Flavour case. The right plot shows the second resolutions sample, where very little difference can be observed between the two mass hierarchies.

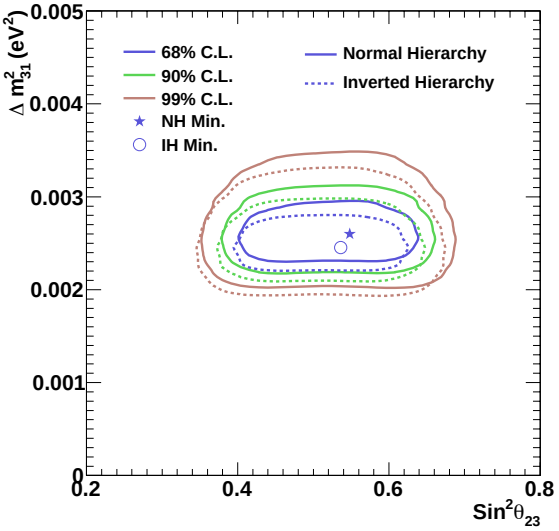

Figure 10.4: Oscillation parameter allowed regions for the 3-Flavour L/E Analysis, this time compared against the single-angle parameter $\sin^2\theta_{23}$. The solid contours show the result from the 3-Flavour Normal Neutrino Mass Hierarchy assumption, and the dashed lines for the Inverted case. The star shows the Normal Hierarchy minimum point, and the circle the Inverted Hierarchy minimum. All the contours look quite symmetric about $\sin^2\theta_{23} = 0.5$. The Normal Hierarchy contours appear to be very slightly shifted up and to the right compared to the Inverted Hierarchy case.

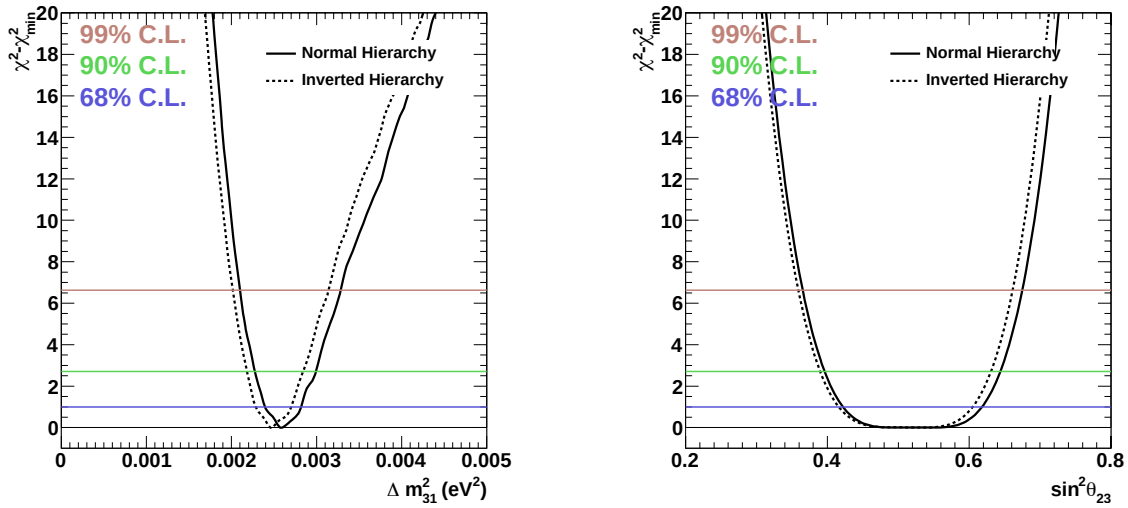

Figure 10.5: 1-Dimentional allowed regions from the 3-Flavour L/E Analysis. In each of these plots the other parameter was integrated out. The solid histogram is for the Normal Hierarchy case, and the dashed histogram for Inverted. The confidence levels have been marked by the horizontal lines. For both parameters, slightly larger values were favoured for Normal Hierarchy compared to the Inverted case.

and the 90% C.L. allowed ranges were:

$$0.396 < \sin^2\theta_{23} < 0.644, \quad \text{and} \quad 2.275 \times 10^{-3}\,\text{eV}^2 < \Delta m^2_{31} < 2.995 \times 10^{-3}\,\text{eV}^2 \quad \text{Normal,} \tag{10.11}$$

$$0.390 < \sin^2\theta_{23} < 0.631, \quad \text{and} \quad 2.182 \times 10^{-3}\,\text{eV}^2 < \Delta m^2_{31} < 2.842 \times 10^{-3}\,\text{eV}^2 \quad \text{Inverted.} \tag{10.12}$$

These allowed ranges were calculated with a smooth spline function that fitted the scanned $\Delta\chi^2$ points well. In this way, the 68% and 90% C.L. ranges were more accurately calculated from the interpolation.

The data were fit equally well by both the Normal and Inverted Mass Hierarchy hypotheses. So there was no evidence to favour one over the other. The only difference observed was that in the Normal Hierarchy case, slightly larger Δm^2_{31} or $\sin^2\theta_{23}$ were preferred by the best fit. For $\sin^2\theta_{23}$, no significant asymmetry was seen around 0.5 to show any preference for a particular octant. However, for both hierarchies the 90% C.L. extends slightly further above 0.5 than it does below 0.5. Since the main purpose of this analysis was to determine if an L/E analysis is still meaningful in a 3-flavour formalism, this issue was not investigated in detail.

10.4.2 Comparison With The 2-Flavour L/E Results

The official result from the L/E analysis was determined from a 2-flavour analysis, as described in Chapter 8. Any L/E analysis performed by a neutrino oscillation experiment has been done in 2-flavours. The results in this chapter are the first attempt to make an L/E measurement with 3-flavour oscillations and matter effects. Here, the 3-flavour results are compared with those from the 2-flavour analysis.

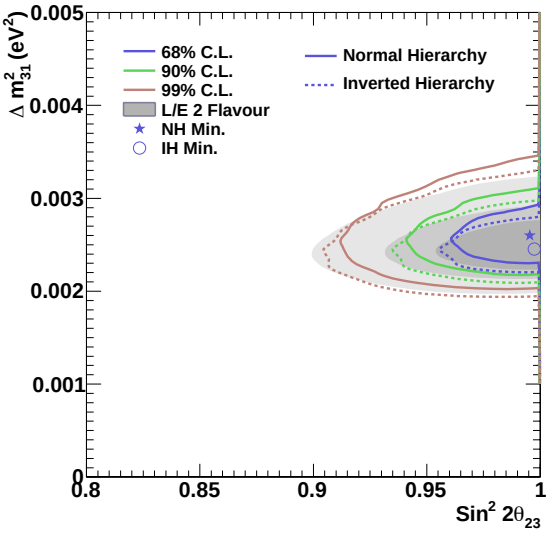

Figure 10.6: Oscillation parameter allowed regions against the double angle parameter, $\sin^2 2\theta_{23}$, to compare the allowed parameter space between the 3-Flavour L/E Analysis and the 2-Flavour Standard L/E Analysis. The solid contours show the result from the 3-Flavour Normal Neutrino Mass Hierarchy assumption, and the dashed lines for the Inverted case. The 3 gray shaded regions show the equivalent allowed regions from the Standard L/E Analysis. The star shows the Normal Hierarchy minimum point, and the circle the Inverted Hierarchy minimum.

Analyses in 2-flavours generally characterise oscillations with the double angle parameter, $\sin^2 2\theta_{23}$. For comparison, the points in the 3-flavour analysis between $\sin^2\theta_{23} = 0.2 \rightarrow 0.5$ were converted to the double angle equivalent. The allowed regions in this parameter space are shown in Figure 10.6. Looking at these allowed regions, the Inverted Hierarchy contours seemed very similar to those of the 2-Flavour analysis. Whereas slightly larger Δm^2 was favoured in the Normal Hierarchy case, and the shift of $\sin^2\theta_{23}$ to larger values resulted in the apparently more constrained region in $\sin^2 2\theta_{23}$ shown here. The minimum points in $(\Delta m^2_{31}, \sin^2 2\theta_{23})$ were $(2.60 \times 10^{-3}\, eV^2, 0.991)$ for Normal Hierarchy and $(2.45 \times 10^{-3}\, eV^2, 0.995)$ for the Inverted case.

The Standard L/E Analysis does not include some modifications present in this analysis, such as the merging of the analysis bins during the χ^2 calculation, or the second resolution sample. However, in the Neutrino Anti-Neutrino Analysis, an analysis assuming normal oscillation was carried out. In that analysis the neutrino and anti-neutrino parameters were forced to be the same, and the analysis included these modifications. It was shown in Figure 9.16 that the allowed regions for normal oscillation were almost identical to the Standard L/E regions. As these modifications were made to increase sensitivity to sub-dominant effects.

The comparable allowed regions to the 2-Flavour Standard L/E Analysis support this analysis and indicate that the extension to 3-Flavours was successfully implemented. The differences suggest that more accurate Oscillation parameters and allowed regions can be obtained with the added information from 3-flavour effects, omitted in the 2-flavour assumption.

10.4.3 3-Flavour L/E Systematic Uncertainties

The $1\,\sigma$ estimates of the systematic uncertainties were the same for all L/E analyses and can be seen in Figure 9.14, and the minimised systematics at the best fit for this analysis can be seen in Figure 10.7 for Normal Hierarchy, and Figure 10.8 for Inverted Hierarchy. For both hierarchies, the best fit systematic errors were all below $1\,\sigma$, with most being below $\sim 0.4\,\sigma$. This suggests that the estimates of the systematics were quite conservative. Despite the slight over-estimation of the errors, the contribution of the systematics to the fitting was minimal.

The shape of these systematic pull distributions was very similar for each hierarchy, and

also for the Neutrino Anti-Neutrino Analysis (Figure 9.15), with only slight differences in the magnitude of each uncertainty. The contribution to the χ^2 from the systematics for the Neutrino Anti-Neutrino Analysis was[1] $\Sigma \left(\frac{\epsilon}{\sigma}\right)^2 = 3.84$ and 3.60 from the Standard 2F Analysis; while for the 3-Flavour Normal and Inverted Hierarchy these contributions were 3.31 and 3.54, respectively. So the 3-Flavour analyses were slightly less dependent on the uncertainties to achieve their best fit, with the 3F Normal Hierarchy fit requiring the smallest contribution from systematics.

Details of the bestfit systematic uncertainties can be seen in Table 10.3 for the neutrino flux; Table 10.2 for neutrino interactions; Table 10.4 and 10.5 for the reconstruction in normal and inverted hierarchy, respectively; and Table 10.6 and 10.7 for the reduction in normal and inverted hierarchy, respectively.

Since a very good fit was achieved for these 3-flavour analyses, with small contributions from the systematic uncertainties, the 3-Flavour L/E distributions appear to be an excellent representation of the data. So the 3-Flavour L/E Analysis is great for investigating the atmospheric neutrino oscillation parameters, with the least assumptions of all the analyses in this thesis.

10.5 Discussion

10.5.1 Comparisons Between L/E Analyses

In order to take a closer look at the difference between each of the L/E analyses, ratios of the L/E distributions between the analyses and Normal and Inverted Hierarchies are shown in Figure 10.9. The left plot in the figure was drawn for the precise resolution sample, and for the second resolution sample on the right. In the ratio plots, the blue line depicts the ratio of Inverted/Normal hierarchy for the precise sample and magenta for the second resolution sample. Very little difference could be observed in these ratios.

A small difference of about ∼2% between the hierarchies was seen in the precise samples at around 1,200∼4,000 km/GeV. This was the region of the resonance coming from the sign of the Δm^2 and the MSW matter effect, which can be seen in Figure 10.1. The resonance was expected to occur at a zenith of -0.49 to -0.65 equivalent to path lengths of about 6,200∼8,500 km, and energies of around 4.2∼5.2 GeV. This corresponds to an L/E range of about 1,200∼2,050 km/GeV. There was also some resonance expected at a zenith of around -0.9, corresponding to an L/E range of about 2,400∼4,800 km/GeV. Although small, some difference was seen in the L/E bins corresponding to the matter resonance. Unfortunately, there was no way to determine whether this difference occurred for neutrinos or anti-neutrinos, which would be necessary to clearly distinguish the mass hierarchy. At SK the neutrino events in the data are more statistically significant than anti-neutrinos, so a larger difference from the resonance would be expected in the case of Normal Hierarchy (in which the resonance occurs for neutrinos) than Inverted (resonance in anti-neutrinos). However, the difference in the Normal and Inverted fits were not significant enough to favour one over the other. A very small variation was seen in the second resolution sample, but it was less than a ∼1% effect.

Also shown in the left of Figure 10.9 is the L/E ratio between the 3-Flavour and 2-Flavour analyses. There appeared to be a distinctive peak at around 2000 km/GeV. This could be due to the averaging treatment in the Standard 2-Flavour analysis. For an oscillation phase greater than 2π, the oscillation phase $\sin^2(1.27L/E)$ term was replaced with 0.5. This averaging treatment

[1] The sum here is over all the systematic uncertainties.

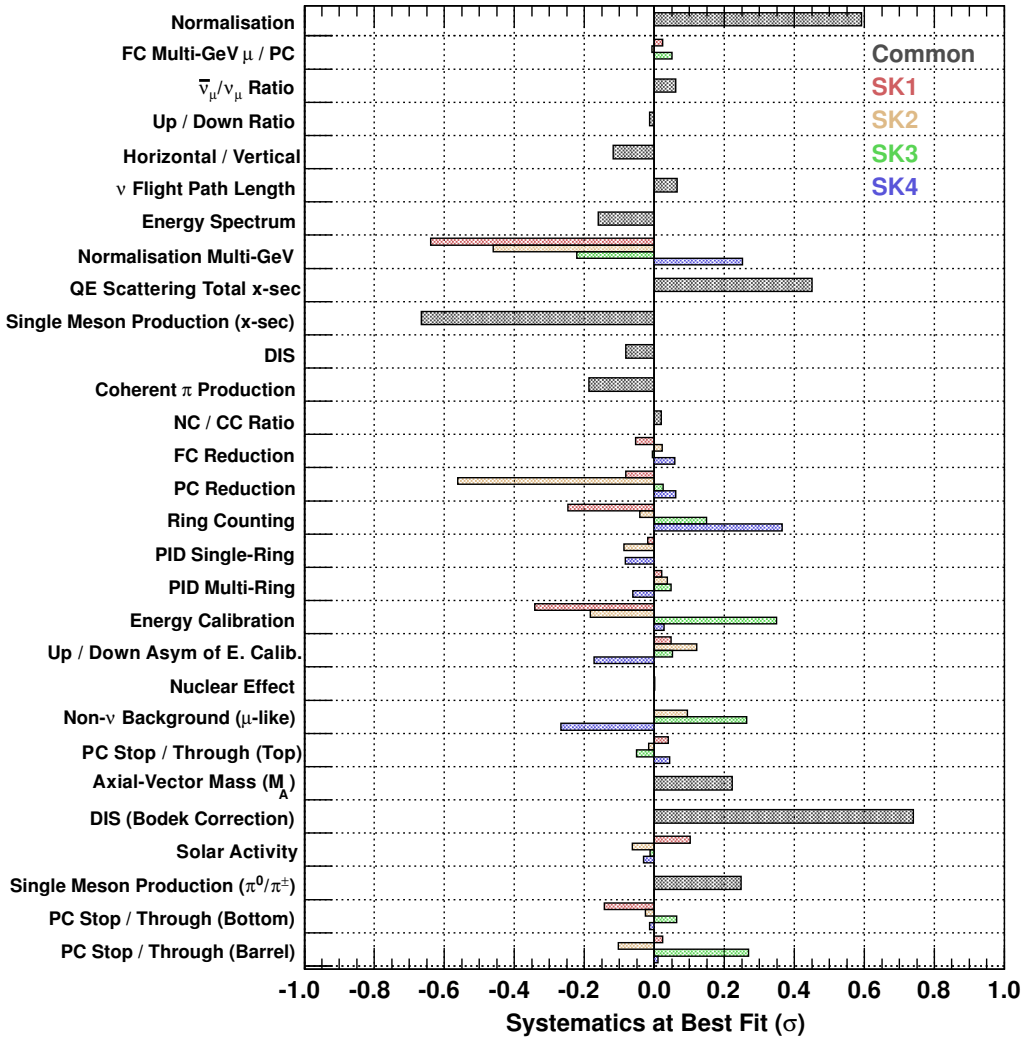

Figure 10.7: Systematics at Best Fit 3-Flavour L/E Analysis, Normal Hierarchy

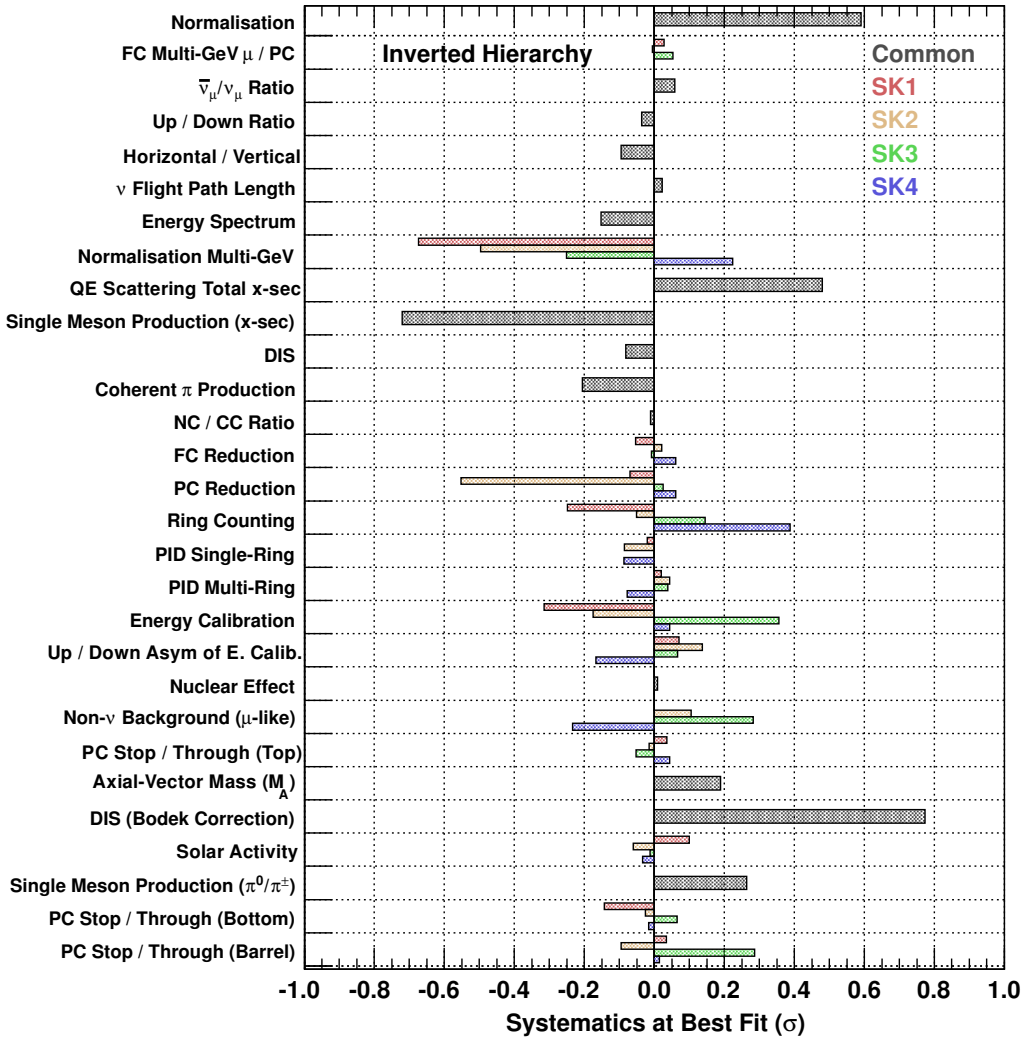

Figure 10.8: Systematics at Best Fit 3-Flavour L/E Analysis, Inverted Hierarchy

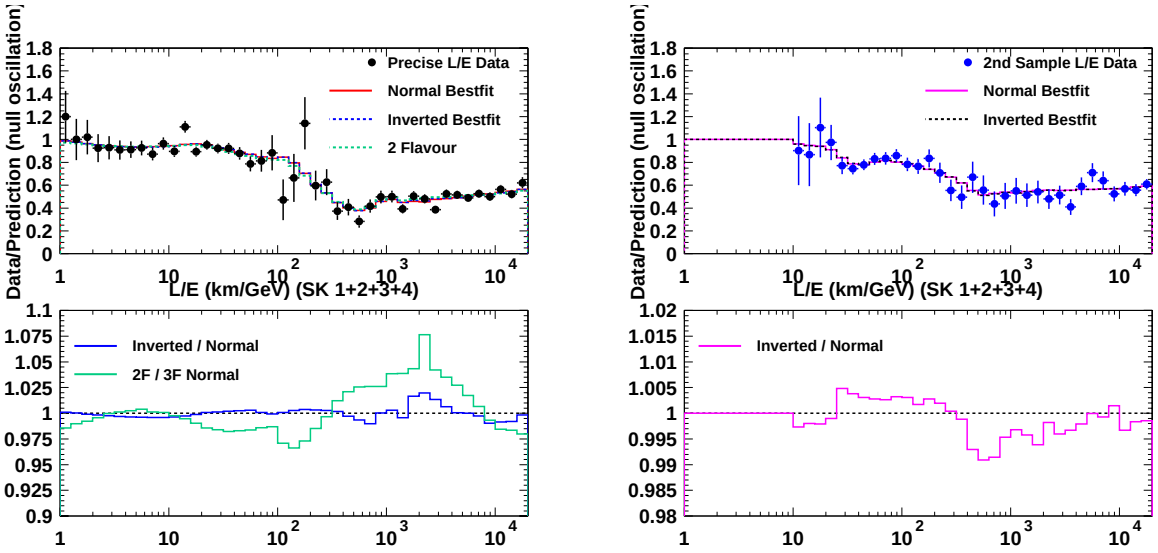

Figure 10.9: The top plots show the L/E distributions for the precise resolution sample on the left, and the second resolution sample on the right. The corresponding lower plots show some ratios of the distributions.

would take effect at an L/E just over 2,000 km/GeV. This could cause a more abrupt discrepancy in the relevant bin, as there was no explicit averaging treatment in the 3-Flavour L/E Analysis. The statistics in the MC were too high to explain the difference. There was 500 years of simulated data per SK period, or 2000 years in total, which was normalised to around 10 years live time. So the ∼150 events in the bin in question, when converted back to the MC statistics, corresponds to $1/\sqrt{150 \times 200} = 0.6\%$, or less than 1 event. However, in the data itself a fluctuation of $1/\sqrt{150} \sim 8\%$ could be expected, and these MC sets were fitted against this same data. Considering the data in the L/E distribution in Figure 10.2, considerable fluctuation can be seen around L/E 1,000∼4,000 km/GeV. In this particular case, the Standard MC was found to be above the data point in the L/E∼2,000 km/GeV bin, and the 3F Normal Hierarchy MC was below it. This is visible with a close inspection of Figure 10.9 at the relevant bin, and clearly both fitted values are allowed by the data point. Otherwise, some difference was expected from properly considering 3-flavour and matter effects. With fewer assumptions, the 3-flavour simulation should be a better representation of neutrino oscillations.

A comparison of the bin-by-bin χ^2 can be seen in Figure 10.10. These distributions were very similar between the mass hierarchies, and no bins distinguishing the hierarchies were found.

10.5.2 Comparisons With Other Analyses

Figure 10.11 shows some comparisons of the L/E Oscillation Analysis results against other measurements of the same parameters. The left plot compares against the 3-Flavour Zenith Analysis, the official 3-flavour result from the Super-Kamiokande Collaboration. There was relatively more asymmetry over $\sin^2\theta_{23}$ in the Zenith Analysis, compared to the symmetrical shape from the L/E Analysis. The Zenith minimum points were also fairly distant from $\sin^2\theta_{23} = 0.5$, changing octant with hierarchy, whereas a minimum close to 0.5 was favoured in this analysis. In

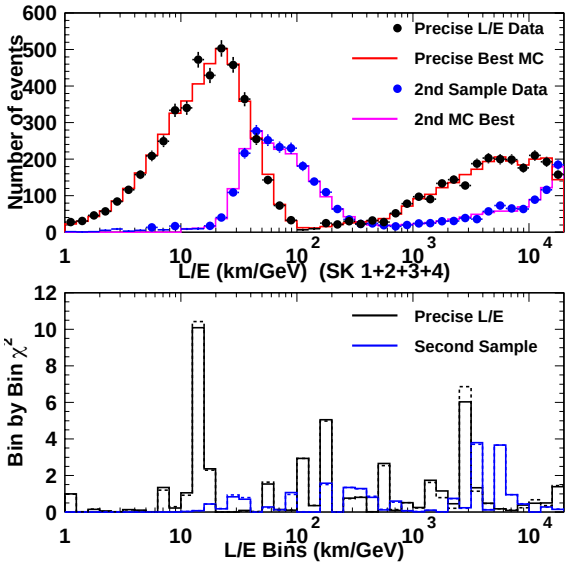

Figure 10.10: The bin-by-bin χ^2 distributions are shown in the lower left plot, with the corresponding L/E distributions shown above. The precise sample is shown by the black histogram, the second resolution sample in blue, where the solid curves are for the Normal Hierarchy and the dashed for Inverted. Not much difference was observed, but a few bins contributing to a small difference in the χ^2 can be seen.

the Zenith analysis, one octant was clearly preferred at about the 68% C.L., depending on the neutrino mass hierarchy. In the L/E case, the $\Delta\chi^2$ distributions were quite flat for $\sin^2\theta_{23}$, for both hierarchies. It is likely that the Zenith Analysis has better sensitivity for determining a difference in the octant of $\sin^2\theta_{23}$, as some difference was expected from the electron neutrino sample at low energies (less than 1 GeV) [265]. However, due to the less precise reconstruction of the L/E variable in such samples, electron samples and low energy samples (below ~1 GeV by the L/E resolution requirement) were excluded from the L/E analysis.

Both analyses saw little difference between the Normal and Inverted Mass Hierarchy assumptions. However, the Zenith Analysis does see a switch in the $\sin^2\theta_{23}$ octant of the best fit from each hierarchy when $\sin^2\theta_{13}$ was fixed [266], which was not seen with the L/E distributions. The 3-Flavour L/E analysis suggests a more constrained region for Δm^2_{31}. It should be noted that the Zenith Analysis scans over δ_{cp}, however this parameter was not included in the 3-Flavour L/E calculation. Inclusion of δ_{cp} could, perhaps, lead to a slightly more relaxed allowed region.

The right plot in Figure 10.11 shows the allowed regions from multiple analyses from 2012, with Δm^2_{31} plotted against $\sin^2 2\theta_{23}$. The 2-Flavour L/E Analysis gave a slightly more constrained region in Δm^2 than the 2-Flavour Zenith equivalent. A similar trend seems to be visible in the 3-flavour variations of the analyses, with the Zenith Analysis allowing a larger range of Δm^2 values, particularly at smaller $\sin^2 2\theta_{23}$. The slightly narrower allowed region of Δm^2 from the L/E analyses was thought to come from considering the neutrino energy on an event-by-event basis, as opposed to the energy range binning used in the Zenith analyses. The 2012 MINOS results were more sensitive to Δm^2 than SK, but their allowed range of $\sin^2 2\theta_{23}$ was quite large.

A comparison of the best fit points and allowed regions for the 2-Flavour and 3-Flavour L/E and Zenith analyses from 2012 can be seen in Table 10.1. The 2F L/E Analysis favoured larger Δm^2 compared to the 2F Zenith, and the 3F L/E favoured a slightly smaller value than the 3F Zenith. The 3F Zenith Analysis saw a small difference in the $\sin^2\theta_{23}$ octant between the mass hierarchies, and the 3F L/E Analysis saw a little difference in the Δm^2_{31} between the hierarchies.

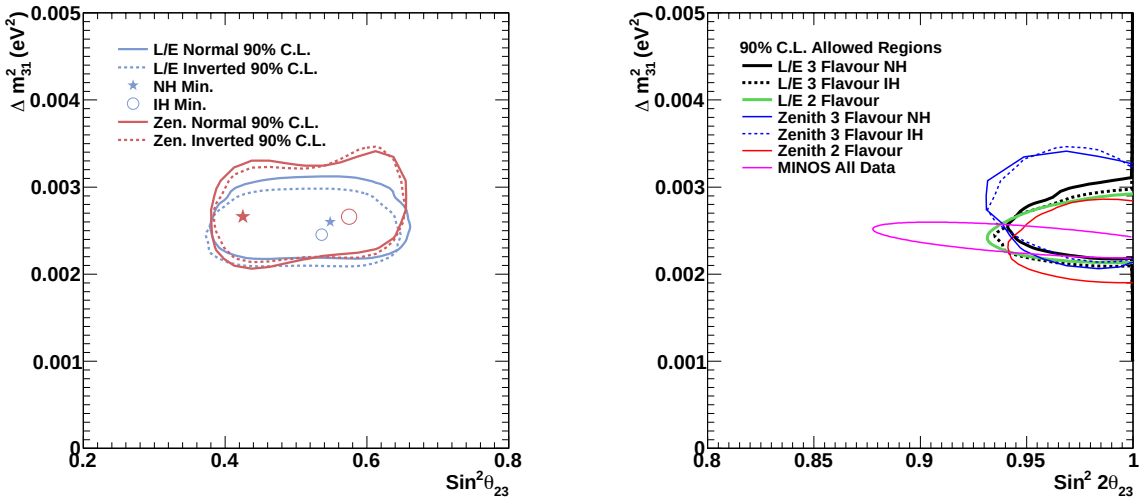

Figure 10.11: The left plot shows a comparison of the 2D 90% C.L. allowed region measured with the L/E Analysis in blue, compared with the Zenith Analysis in red. The minimum point for the Normal Hierarchy is shown with a star, Inverted with a circle, where blue is for L/E and red for Zenith. The L/E contours were quite symmetric horizontally, while a slight skew was seen for Zenith, as well as a flip of the minimum point with mass hierarchy. The right plot compares the 90% C.L. of the L/E, Zenith and Minos Analyses in 2012.

10.5.3 Improved Sensitivity

The main purpose of the analysis in this chapter was to attempt to do an L/E analysis with 3-flavours and matter effects, and to check whether the analysis was stable under the influence of these additional considerations. The analysis appeared to be reliable, and so more significant measurements of the atmospheric oscillation parameters could be made, as there were fewer assumptions. However, this analysis did not have much sensitivity to the neutrino mass hierarchy, or to the octant of θ_{23}.

In terms of an L/E analysis, as mentioned earlier, the main sensitivity to the mass hierarchy was in the L/E range 1,200∼4,000 km/GeV. Greater statistics or finer granularity in this range could perhaps reveal the sign of Δm^2_{31}. In this analysis, at least, the measurement of $\sin^2\theta_{23}$ was mostly symmetrical around $\sin^2\theta_{23} \sim 0.5$. Some sensitivity to the octant could be achieved with lower energy events, in which the L/E resolution is low. So an L/E analysis is not a good choice to measure the octant of θ_{23}. Hyper-Kamiokande [147], the proposed successor to Super-Kamiokande, will have much better sensitivity to smaller observations by collecting much greater statistics.

However, for further improved sensitivity to the mass hierarchy, event-by-event separation of neutrino and anti-neutrino would be preferable. This can be achieved either by accelerator experiments with a high purity of either neutrinos or anti-neutrinos, or with a precisely understood flux; or with a detector with strong charge discrimination. For accelerators, T2K [37] and NOνA [154] are improving sensitivity to these remaining parameters with dedicated ν_μ or $\bar{\nu}_\mu$ beam time. For a precisely understood neutrino beam flux, the Neutrino Factory [142] has been proposed. For massive-scale charge discrimination, the India-based Neutrino Observatory

(INO) [263] are planning to build a 50 kt atmospheric neutrino detector that is magnetised. This would have much improved sensitivity to the mass hierarchy, as well as other measurements that differ for neutrino and anti-neutrino, such as δ_{cp}.

10.5.4 The 3-Flavour L/E Result

The 3-Flavour L/E analysis faithfully calculated the oscillation probabilities, with fewer assumptions than the 2-flavour analyses. It reconstructed one of the key defining features of oscillations, which is its dependence on the L/E variable. This allowed the reconstruction of the first oscillation maximum, and clear regions of average oscillations and no oscillations, leading to a very accurate measurement of the atmospheric Δm^2_{31}. This is the best measurement of the parameter that can currently be achieved from atmospheric neutrinos. Accelerator experiments can make more confined measurements with a well defined human-made flux and baseline, however atmospheric neutrinos can probe a much wider range of energies and baselines, and have much greater sensitivity to matter effects. This is also the first attempt to make an oscillation measurement by its L/E characteristic in 3-flavours and including matter effects.

So the measurement made in this thesis is very significant, as it considers a wide range of the oscillation parameter space; 3-flavour effects; and matter effects. It is important to have these wide-ranging measurements, in conjunction with precise observations with tuned-sensitivity to a smaller range of the parameter space. One of the main strengths of an experiment like Super-Kamiokande is that it can potentially observe unexpected effects outside the tuned sensitivity of other experiments. One such possibility is the observation of Non-Standard Neutrino Interactions, which is the topic of the following chapter.

2-Flavour Analysis	$\sin^2 2\theta_{23}$	(90% C.L.)	$\Delta m^2(eV^2, 1\sigma)$	χ^2
2F L/E Standard Analysis	1.00	> 0.931	$(2.5 \pm 0.27) \times 10^{-3}$	171.7 / 169
2F Zenith Analysis	0.99	> 0.96	$(2.3^{+0.16}_{-0.22}) \times 10^{-3}$	555.0 / 478
3-Flavour Analysis	$\sin^2 \theta_{23}$	(90% C.L.)	$\Delta m^2(eV^2, 1\sigma)$	χ^2
3F L/E Normal	0.548	0.396 – 0.644	$(2.60^{+0.22}_{-0.21}) \times 10^{-3}$	69.56 / 73
3F L/E Inverted	0.536	0.390 – 0.631	$(2.45^{+0.25}_{-0.16}) \times 10^{-3}$	69.44 / 73
3F Zenith Normal	0.425	0.391 – 0.619	$(2.66^{+0.15}_{-0.40}) \times 10^{-3}$	556.7 / 477
3F Zenith Inverted	0.575	0.393 – 0.630	$(2.66^{+0.17}_{-0.23}) \times 10^{-3}$	555.5 / 477

Table 10.1: Oscillation Parameter Results Summary

ID	Description		Normal Hierarchy		Inverted Hierarchy	
		σ %	ϵ % (σ)	Pull	ϵ % (σ)	Pull
Systematic Errors in Neutrino Interactions						
9	QE Scattering Total Cross-Section	10.0	4.50 (0.450)	0.2029	4.80 (0.480)	0.2305
10	Single Meson Production (x-sec)	20.0	-13.33 (-0.667)	0.4442	-14.42 (-0.721)	0.5195
11	DIS (Total Cross-Section)	5.0	-0.41 (-0.082)	0.0066	-0.41 (-0.082)	0.0066
12	Coherent π Production	100.0	-18.70 (-0.187)	0.0350	-20.56 (-0.206)	0.0423
13	NC/CC Ratio	20.0	0.39 (0.020)	0.0004	-0.22 (-0.011)	0.0001
21	Nuclear Effect	30.0	0.02 (0.001)	0.0000	0.29 (0.010)	0.0001
24	Axial-Vector Mass (M_A)	20.0	4.45 (0.223)	0.0494	3.79 (0.190)	0.0360
25	DIS (Bodek Correction)	20.0	14.80 (0.740)	0.5472	15.48 (0.774)	0.5990
27	Single-Meson Production ($\pi^0/\pi^{\pm}$)	40.0	9.89 (0.247)	0.0611	10.53 (0.263)	0.0693

Table 10.2: Neutrino Interaction Uncertainties

ID	Description		Normal Hierarchy		Inverted Hierarchy	
		σ %	ϵ % (σ)	Pull	ϵ % (σ)	Pull
Systematic Errors in Neutrino Flux						
1	Normalisation	–	5.92	0.0000	5.91	0.0000
3	$\bar{\nu}_\mu/\nu_\mu$ Ratio	6.0	0.36 (0.060)	0.0037	0.35 (0.058)	0.0035
4	Up/Down Ratio		-0.01 (-0.010)	0.0002	-0.04 (-0.040)	0.0013
	Single-Ring $<$ 400 MeV	0.3				
	Single-Ring $>$ 400 MeV	0.5				
	Single-Ring Multi-GeV	0.2				
	Multi-Ring Sub-GeV	0.2				
	Multi-Ring Multi-GeV	0.2				
	PC	0.2				
5	Horizontal/Vertical		-0.12 (-0.120)	0.0138	-0.09 (-0.090)	0.0090
	Single-Ring $<$ 400 MeV	0.1				
	Single-Ring $>$ 400 MeV	1.9				
	Single-Ring Multi-GeV	2.3				
	Multi-Ring Sub-GeV	1.3				
	Multi-Ring Multi-GeV	1.5				
	PC	1.7				
6	Neutrino Flight Path Length	10.0	0.65 (0.065)	0.0043	0.23 (0.023)	0.0005
7	Energy Spectrum	5.0	-0.80 (-0.160)	0.0259	-0.76 (-0.152)	0.0234
8	Sample Normalisation Multi-GeV					
	SK1	5.0	-3.19 (-0.638)	0.4078	-3.37 (-0.674)	0.4540
	SK2	5.0	-2.30 (-0.460)	0.2119	-2.48 (-0.496)	0.2465
	SK3	5.0	-1.11 (-0.222)	0.0494	-1.26 (-0.252)	0.0630
	SK4	5.0	1.26 (0.252)	0.0636	1.12 (0.224)	0.0498
2	FC Multi-GeV μ / PC					
	SK1	0.6	0.01 (0.017)	0.0006	0.02 (0.033)	0.0007
	SK2	0.5	0.00 (0.000)	0.0001	0.00 (0.000)	0.0000
	SK3	0.9	0.05 (0.056)	0.0025	0.05 (0.056)	0.0028
	SK4	0.02	0.00 (0.000)	0.0000	0.00 (0.000)	0.0000
26	Solar Activity					
	SK1	20.0	2.05 (0.103)	0.0105	1.99 (0.100)	0.0099
	SK2	50.0	-3.16 (-0.063)	0.0040	-3.04 (-0.061)	0.0037
	SK3	20.0	-0.25 (-0.013)	0.0002	-0.24 (-0.012)	0.0001
	SK4	10.0	-0.31 (-0.031)	0.0009	-0.33 (-0.033)	0.0011

Table 10.3: Neutrino Flux Uncertainties

ID	Description	SK1			SK2		
		σ %	ϵ % (σ)	Pull	σ %	ϵ % (σ)	Pull
Systematic Errors from Reconstruction - Normal Hierarchy							
16	Ring Counting		-2.47 (-0.247)	0.0610		-0.41 (-0.041)	0.0017
	Single-Ring $<$ 400 MeV	0.7			2.3		
	Single-Ring $>$ 400 MeV	0.7			0.7		
	Single-Ring Multi-GeV	1.7			1.7		
	Multi-Ring Sub-GeV	-4.5			-8.2		
	Multi-Ring Multi-GeV	-4.1			-0.8		
17	Particle ID Single-Ring		-0.02 (-0.020)	0.0004		-0.09 (-0.090)	0.0076
	Sub-GeV	-0.1			-0.4		
	Multi-GeV	0.2			-0.1		
18	Particle ID Multi-Ring		0.20 (0.020)	0.0004		0.37 (0.037)	0.0014
	Sub-GeV	-3.9			2.2		
	Multi-GeV	-2.9			-3.4		
19	Energy Calibration	1.1	-0.38 (-0.345)	0.1165	1.7	-0.31 (-0.182)	0.0337
20	Up-Down Asym of E Calib.	0.6	0.03 (0.050)	0.0022	0.6	0.07 (0.117)	0.0147
23	PC Stop/Through Top	46.1	1.81 (0.039)	0.0015	19.37	-0.32 (-0.017)	0.0003
28	PC Stop/Through Bottom	22.7	-3.26 (-0.144)	0.0206	12.9	-0.33 (-0.026)	0.0007
29	PC Stop/Through Barrel	7.01	0.17 (0.024)	0.0006	9.44	-0.97 (-0.103)	0.0106
ID	Description	SK3			SK4		
16	Ring Counting		1.49 (0.149)	0.0221		3.65 (0.365)	0.1332
	Single-Ring $<$ 400 MeV	3.0			-3.0		
	Single-Ring $>$ 400 MeV	0.6			0.6		
	Single-Ring Multi-GeV	1.0			-1.2		
	Multi-Ring Sub-GeV	-2.6			-2.3		
	Multi-Ring Multi-GeV	-2.1			2.4		
17	Particle ID Single-Ring		0.00 (0.000)	0.0000		-0.08 (-0.080)	0.0069
	Sub-GeV	-0.4			-0.4		
	Multi-GeV	-0.5			-0.4		
18	Particle ID Multi-Ring		0.48 (0.048)	0.0023		-0.62 (-0.062)	0.0038
	Sub-GeV	3.1			2.2		
	Multi-GeV	4.5			6.8		
19	Energy Calibration	2.7	0.94 (0.348)	0.1217	2.3	0.07 (0.030)	0.0008
20	Up-Down Asym of E Calib.	1.3	0.07 (0.054)	0.0026	0.3	-0.05 (-0.167)	0.0295
23	PC Stop/Through Top	86.6	-4.45 (-0.051)	0.0026	43.3	1.88 (0.043)	0.0019
28	PC Stop/Through Bottom	12.1	0.78 (0.064)	0.0041	11.6	-0.17 (-0.015)	0.0002
29	PC Stop/Through Barrel	28.7	7.72 (0.269)	0.0724	7.4	0.08 (0.011)	0.0001

Table 10.4: Neutrino Reconstruction Uncertainties for Normal Hierarchy

ID	Description	SK1			SK2		
		σ %	ϵ % (σ)	Pull	σ %	ϵ % (σ)	Pull
Systematic Errors from Reconstruction - Inverted Hierarchy							
16	Ring Counting		-2.49 (-0.249)	0.0619		-0.51 (-0.051)	0.0026
	Single-Ring $<$ 400 MeV	0.7			2.3		
	Single-Ring $>$ 400 MeV	0.7			0.7		
	Single-Ring Multi-GeV	1.7			1.7		
	Multi-Ring Sub-GeV	-4.5			-8.2		
	Multi-Ring Multi-GeV	-4.1			-0.8		
17	Particle ID Single-Ring		-0.02 (-0.020)	0.0004		-0.09 (-0.090)	0.0074
	Sub-GeV	-0.1			-0.4		
	Multi-GeV	0.2			-0.1		
18	Particle ID Multi-Ring		0.19 (0.019)	0.0004		0.44 (0.044)	0.0019
	Sub-GeV	-3.9			2.2		
	Multi-GeV	-2.9			-3.4		
19	Energy Calibration	1.1	-0.35 (-0.318)	0.0990	1.7	-0.30 (-0.176)	0.0309
20	Up-Down Asym of E Calib.	0.6	0.04 (0.067)	0.0049	0.6	0.08 (0.133)	0.0188
23	PC Stop/Through Top	46.1	1.67 (0.036)	0.0013	19.37	-0.30 (-0.015)	0.0002
28	PC Stop/Through Bottom	22.7	-3.25 (-0.143)	0.0205	12.9	-0.33 (-0.026)	0.0007
29	PC Stop/Through Barrel	7.01	0.24 (0.034)	0.0012	9.44	-0.89 (-0.094)	0.0090
ID	Description	SK3			SK4		
16	Ring Counting		1.45 (0.145)	0.0211		3.88 (0.388)	0.1502
	Single-Ring $<$ 400 MeV	3.0			-3.0		
	Single-Ring $>$ 400 MeV	0.6			0.6		
	Single-Ring Multi-GeV	1.0			-1.2		
	Multi-Ring Sub-GeV	-2.6			-2.3		
	Multi-Ring Multi-GeV	-2.1			2.4		
17	Particle ID Single-Ring		0.00 (0.000)	0.0000		-0.09 (-0.090)	0.0076
	Sub-GeV	-0.4			-0.4		
	Multi-GeV	-0.5			-0.4		
18	Particle ID Multi-Ring		0.38 (0.038)	0.0015		-0.78 (-0.078)	0.0061
	Sub-GeV	3.1			2.2		
	Multi-GeV	4.5			6.8		
19	Energy Calibration	2.7	0.96 (0.356)	0.1270	2.3	0.10 (0.043)	0.0019
20	Up-Down Asym of E Calib.	1.3	0.09 (0.069)	0.0044	0.3	-0.05 (-0.167)	0.0277
23	PC Stop/Through Top	86.6	-4.49 (-0.052)	0.0027	43.3	1.89 (0.044)	0.0019
28	PC Stop/Through Bottom	12.1	0.78 (0.064)	0.0042	11.6	-0.18 (-0.016)	0.0003
29	PC Stop/Through Barrel	28.7	8.22 (0.286)	0.0820	7.4	0.11 (0.015)	0.0002

Table 10.5: Neutrino Reconstruction Uncertainties for Inverted Hierarchy

ID	Description	SK1			SK2		
		σ %	ϵ % (σ)	Pull	σ %	ϵ % (σ)	Pull
Systematic Errors from Reduction - Normal Hierarchy							
14	FC Reduction	0.2	-0.01 (-0.050)	0.0029	0.2	0.00 (0.000)	0.0005
15	PC Reduction	2.4	-0.20 (-0.083)	0.0067	4.8	-2.69 (-0.560)	0.3150
22	Non-ν Background (μ-like)		0.00 (0.000)	0.0000		0.09 (0.090)	0.0088
	Cosmic-Ray FC Sub-GeV	0.1			0.1		
	Cosmic-Ray FC Multi-GeV	0.1			0.1		
	Cosmic-Ray PC	0.2			0.7		
ID	Description	SK3			SK4		
14	FC Reduction	0.8	0.00 (0.000)	0.0000	0.3	0.02 (0.067)	0.0035
15	PC Reduction	0.5	0.01 (0.020)	0.0006	1.0	0.06 (0.060)	0.0037
22	Non-ν Background (μ-like)		0.26 (0.260)	0.0696		-0.27 (-0.270)	0.0716
	Cosmic-Ray FC Sub-GeV	0.1			0.1		
	Cosmic-Ray FC Multi-GeV	0.2			0.8		
	Cosmic-Ray PC	1.8			4.9		

Table 10.6: Neutrino Reduction Uncertainties for Normal Hierarchy

ID	Description	SK1			SK2		
		σ %	ϵ % (σ)	Pull	σ %	ϵ % (σ)	Pull
Systematic Errors from Reduction - Inverted Hierarchy							
14	FC Reduction	0.2	-0.01 (-0.050)	0.0029	0.2	0.00 (0.000)	0.0004
15	PC Reduction	2.4	-0.17 (-0.071)	0.0048	4.8	-2.65 (-0.552)	0.3057
22	Non-ν Background (μ-like)		0.00 (0.000)	0.0000		0.11 (0.110)	0.0111
	Cosmic-Ray FC Sub-GeV	0.1			0.1		
	Cosmic-Ray FC Multi-GeV	0.1			0.1		
	Cosmic-Ray PC	0.2			0.7		
ID	Description	SK3			SK4		
14	FC Reduction	0.8	-0.01 (-0.013)	0.0001	0.3	0.02 (0.067)	0.0037
15	PC Reduction	0.5	0.01 (0.020)	0.0007	1.0	0.06 (0.060)	0.0037
22	Non-ν Background (μ-like)		0.28 (0.280)	0.0797		-0.23 (-0.230)	0.0546
	Cosmic-Ray FC Sub-GeV	0.1			0.1		
	Cosmic-Ray FC Multi-GeV	0.2			0.8		
	Cosmic-Ray PC	1.8			4.9		

Table 10.7: Neutrino Reduction Uncertainties for Inverted Hierarchy

Chapter 11

Analysis of NSI with Oscillation in the ν_μ–ν_τ Sector

Non-Standard Neutrino Interactions (NSI) are a class of interactions of neutrinos that rely on some mechanism outside of the Standard Model. The type of NSI that this analysis was concerned with was Neutral-Current (NC) Matter NSI, which allows for the possibility of non-standard neutral current interactions of neutrinos with matter during transit. This is the type of NSI that atmospheric neutrinos at SK would be most sensitive to, and could be observed by variations in the neutrino flavours observed, while retaining the expected total neutrino flux. This is a similar type of observation as neutrino oscillations, but with different dependencies on neutrino properties. NSI could potentially occur at the creation or detection of the neutrino, which would be CC Matter NSI. However, any neutrinos that interacted by such mechanisms before reaching SK, would disappear or change form and not be observed in the detector. This results in a reduced sensitivity to such effects, and so CC Matter NSI have not been considered here.

As NSI theories are numerous, and it is difficult to favour one model over another, the analysis in this thesis takes a model-independent approach. In this way, the strength of NC Matter NSI can be characterised by terms such as $\varepsilon_{\mu\tau}$, which allows for flavour transitions between ν_μ and ν_τ during transit. This analysis simply observes the potential for such interactions allowed by the data, without being restricted to the mechanisms of any one model. Measurements of such parameters can be taken as input or constraints by theorists who wish to propose an NSI model.

Pure NSI has already been ruled out to explain the ν_μ deficit in atmospheric neutrinos [57, 59, 60], so NSI were expected to be sub-dominant at best. This analysis makes use of a hybrid model of 3-Flavour Neutrino Oscillations that allows for NSI. Neutrino Oscillations are widely accepted as the dominant mechanism for flavour transitions in neutrinos. So this analysis could potentially observe some NSI in conjunction with Oscillations, or characterise the amount of NSI that is potentially allowed by the data in the presence of Oscillations.

This is the first analysis of atmospheric neutrino data, that allows for 3-flavour oscillations and NC matter NSI in the $\mu\tau$–sector. The model in this analysis is sensitive to the expected Δm^2_{31} dependence on the $\varepsilon_{\mu\tau}$ NSI term, which was not observed in the 2-flavour hybrid models used in the past [45, 57]. This includes the SK Zenith NSI analysis [73], which also used a 2-flavour model in the $\mu\tau$–sector. So the results in this analysis should be the most meaningful measurements on these NSI parameters, at least from atmospheric neutrinos.

There are many advantages to an analysis of neutrinos created by cosmic rays in the at-

mosphere. Since the vast majority of these neutrinos pass through the entire Earth, the whole atmosphere of the Earth acts as a source of neutrinos for Super-Kamiokande. This provides a wide range of neutrino energies, and baselines that extend from ∼10 km to over 10,000 km. More importantly, these baselines are filled with the Earth's crust, mantle, and core, providing an excellent setting to potentially observe matter effects generated by NSI. In addition, the L/E Analysis gives the best constraint on Δm^2_{31} from atmospheric neutrinos, making it an ideal choice for this Δm^2_{31}–dependent measurement.

11.1 NSI Background and Treatment

Non-Standard Neutrino Interactions (NSI) refer to a collection of non-standard interactions postulated to be possible. For this analysis, the interest is in NC Matter NSI that could have an influence on the flavour ratios observed at SK. Examples of categories of NSI are Flavour Changing Neutral Current (FCNC) [61–64], and Lepton Non-Universality (NU) [65]. These can be illustrated as:

$$\nu_\alpha + f \longrightarrow \nu_\beta + f \qquad \text{(FCNC)}, \tag{11.1}$$

$$\nu_\alpha + f \text{ and } \nu_\beta + f \text{ amplitudes differ} \qquad \text{(NU)}. \tag{11.2}$$

In FCNC, there are non-standard NC interactions with fermions in matter that can result in a flavour change. As represented in Equation (11.1), through a NC interaction of a neutrino of flavour "α" with a fermion, f, a transition to flavour "β" is allowed. In NU, the NC forward scattering amplitudes are allowed to be different between flavours, represented in Equation (11.2).

It has already been shown that NSI alone cannot describe the full energy range of atmospheric neutrino data [57, 59, 60]. So NSI can be investigated as a sub-dominant effect, with a hybrid model including both Neutrino Oscillations and NSI. In such a model, the Hamiltonian for $\nu_\alpha \to \nu_\beta$ can be written as:

$$H_{\alpha\beta} = \frac{1}{2E} U_{\alpha j} \begin{pmatrix} 0 & 0 & 0 \\ 0 & \Delta m^2_{21} & 0 \\ 0 & 0 & \Delta m^2_{31} \end{pmatrix} U^\dagger_{k\beta} \pm V_{MSW} \pm \sqrt{2} G_F N_f(\vec{r}) \begin{pmatrix} \varepsilon_{ee} & \varepsilon^*_{e\mu} & \varepsilon^*_{e\tau} \\ \varepsilon_{e\mu} & \varepsilon_{\mu\mu} & \varepsilon^*_{\mu\tau} \\ \varepsilon_{e\tau} & \varepsilon_{\mu\tau} & \varepsilon_{\tau\tau} \end{pmatrix}, \tag{11.3}$$

where the first term is the vacuum oscillation term; the second is from MSW matter effects on electrons; and the third allows for NSI. While U is the Unitary Lepton Mixing Matrix, $G_F = 1.166 \times 10^{-5}$ GeV^{-2} is the Fermi constant, and N_f the fermion number density, taken to be down-quarks, calculated along the neutrino path from production to the detector. Details of the oscillation term were written in Section 10.1.1. The additional interaction potentials are positive for neutrinos and negative for anti-neutrinos. So the dominant mechanism for the flavour transitions come from the vacuum oscillation term, while allowing for possible non-standard transitions between flavours by NC interactions with matter in a model-independent way. These transitions are characterised by the $\varepsilon_{\alpha\beta}$ parameters, which are like coupling constants for the strength of the NSI.

In this thesis, NSI in the $\mu\tau$–sector were of interest, as these would have the largest effect on atmospheric neutrinos. In this case, $\varepsilon_{\mu\tau}$ would represent possible FCNC interactions, while the quantity $\varepsilon_{\tau\tau} - \varepsilon_{\mu\mu}$ would represent NU. Here, $\varepsilon_{\mu\mu} = 0$ was set, allowing NU to be considered with the $\varepsilon_{\tau\tau}$ parameter. These are general quantities that could be used to constrain non-standard theories of NC neutrino interactions with matter. In general, these matter NSIs depend

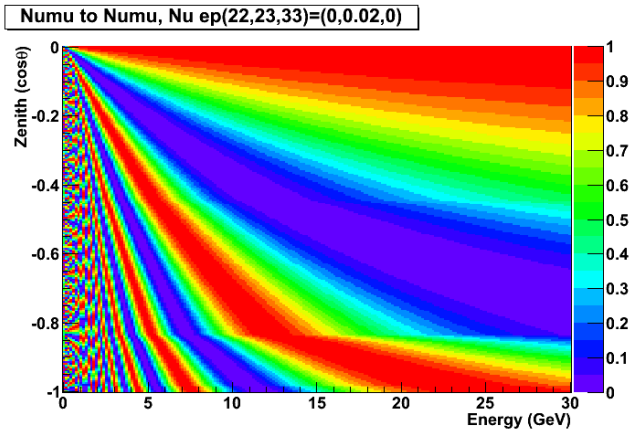

(a) $P(\nu_\mu \to \nu_\mu)$ Neutrino $\varepsilon_{\mu\tau} = 0.02$

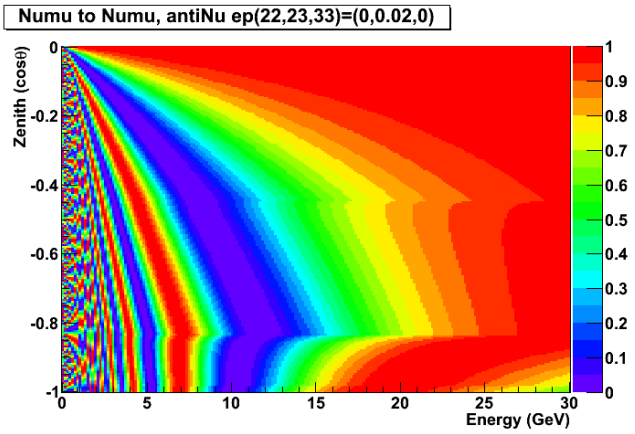

(b) $P(\bar{\nu}_\mu \to \bar{\nu}_\mu)$ Anti-Neutrino $\varepsilon_{\mu\tau} = 0.02$

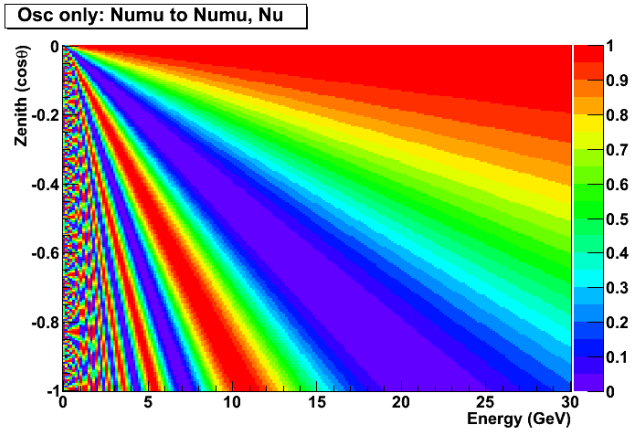

(c) $P(\nu_\mu \to \nu_\mu)$ Neutrino, Oscillation only

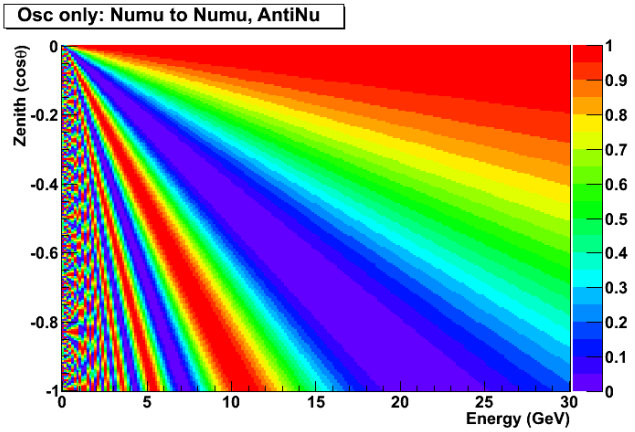

(d) $P(\bar{\nu}_\mu \to \bar{\nu}_\mu)$ Anti-Neutrino, Oscillation only

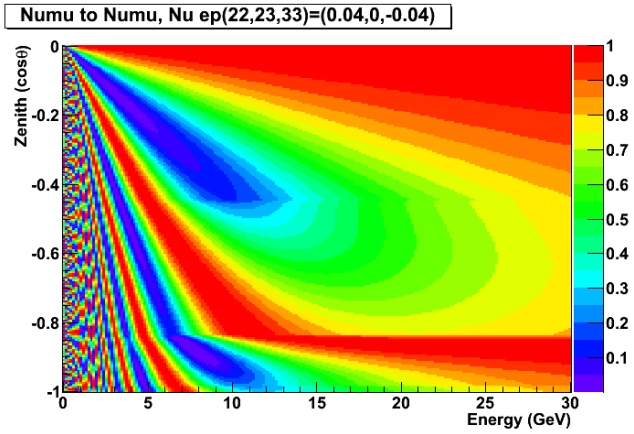

(e) $P(\nu_\mu \to \nu_\mu)$ Neutrino $\varepsilon_{\tau\tau} - \varepsilon_{\mu\mu} = 0.08$

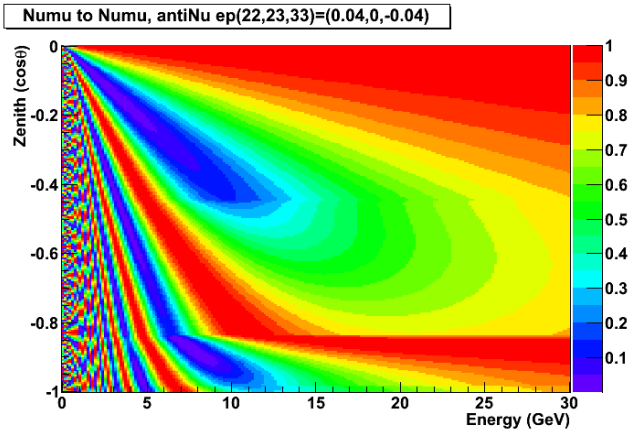

(f) $P(\bar{\nu}_\mu \to \bar{\nu}_\mu)$ Anti-Neutrino $\varepsilon_{\tau\tau} - \varepsilon_{\mu\mu} = 0.08$

Figure 11.1: $P(\nu_\mu \to \nu_\mu)$ survival probabilities for neutrinos and anti-neutrinos and various NSI parameters. In the above, 2-flavour oscillations were assumed with the parameters $(\sin^2\theta_{23}, \Delta m^2_{31}) = (0.5, 2.1 \times 10^{-3}\,\mathrm{eV}^2)$

on the density of matter on the neutrino flight path, while not showing the E^{-1} dependence seen in neutrino oscillations [45]. Details of the derivation of Equation (11.3) were written in Section 1.5.1. An idea of the effect of these NSI parameters can be found in Figure 11.1.

11.2 Assumptions in This Analysis

For the NSI analysis in this thesis, the NSI terms $\varepsilon_{\mu\tau}$ and $\varepsilon_{\tau\tau}$ were varied while the remaining NSI terms were set to zero. Atmospheric neutrinos are sensitive to the quantity $(\varepsilon_{\tau\tau} - \varepsilon_{\mu\mu})$, sometimes referred to as ε', which was probed with the $\varepsilon_{\tau\tau}$ parameter while setting $\varepsilon_{\mu\mu} = 0$. Or in other words, in this analysis $\varepsilon_{\tau\tau} \equiv \varepsilon'$.

The NSI interactions were assumed to be with down-quarks in the transition probability calculation. This means that the matter density calculated along the neutrino flight path was the expected density of down-quarks. This is a normalisation, one used in some of the first NSI analyses with atmospheric neutrinos, and the convention followed here. So the strength of the NSI parameters measured here should be interpreted with this down-quark normalisation in mind. The values reported here could be re-weighted to any other normalisation. A common normalisation used in more recent years is the electron-number density, in which case the strength of NSI can be compared to the strength of the MSW matter effect. Here, the density of down-quarks was simply assumed to be three times the expected number density of electrons.

The $\mu\tau$–oscillation terms, Δm^2_{31} and $\sin^2\theta_{23}$, were allowed some freedom, while the remaining oscillation parameters were set at the best fit from a global analysis [44] published after the Neutrino 2012 conference. Specifically, the values were fixed at $\Delta m^2_{21} = 7.62 \times 10^{-5}\, eV^2$, $\sin^2\theta_{12} = 0.320$, and $\sin^2\theta_{13} = 0.0246$. Normal neutrino mass hierarchy was assumed.

11.3 3-Flavour Oscillation and NSI Results

A four-dimensional parameter space was scanned including 23 parameters each for $\varepsilon_{\mu\tau}$ and $\varepsilon_{\tau\tau}$, and 13 parameters each for Δm^2_{31} and $\sin^2\theta_{23}$. The NSI ranges ran from -0.32 to -0.001 and 0.001 to 0.32, with logarithmic steps. With an additional parameter corresponding to zero NSI also included. The oscillation ranges were $(1.5 \to 4.5) \times 10^{-3}\,\mathrm{eV}^2$ for Δm^2_{31}, and $0.2 \to 0.8$ for $\sin^2\theta_{23}$. This formed a 4D parameter space of around ∼90,000 points, that took over 24 hours to calculate the χ^2 running on ∼200 CPUs. This analysis was computationally intensive, so a much finer parameter space could not be scanned without the processing time quickly growing to many days and weeks (e.g. doubling the number of each parameter would then take more than 2 weeks to run).

11.3.1 Best Fit and Allowed Regions

After scanning the above parameter space, the bestfit point was found at:

$$\chi^2 = 69.94/71\,\mathrm{d.o.f}, \tag{11.4}$$

$$\varepsilon_{\mu\tau} = \left(1.0^{+07.9}_{-12.2}\right) \times 10^{-3}, \tag{11.5}$$

$$\varepsilon_{\tau\tau} = \left(5.6^{+24.8}_{-33.3}\right) \times 10^{-3}, \tag{11.6}$$

$$\sin^2\theta_{23} = 0.55^{+0.07}_{-0.13}, \tag{11.7}$$

$$\Delta m^2_{31} = \left(2.5^{+0.4}_{-0.2}\right) \times 10^{-3}\,\mathrm{eV}^2, \tag{11.8}$$

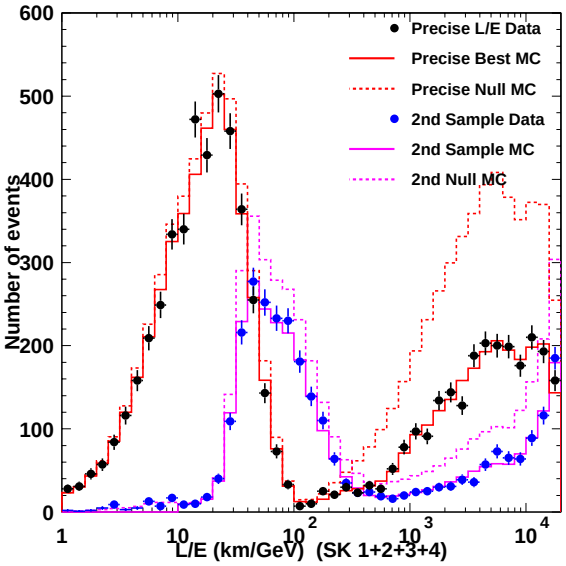

Figure 11.2: The bestfit L/E distributions for the 3-Flavour Oscillation and NSI analysis. Since the bestfit point is close to pure oscillations, these distributions are very similar to the 3-flavour pure oscillation case. The precise resolution samples are drawn in red, and the second resolution sample in magenta. The dashed histograms show the respective null-oscillation Monte Carlo. The points are for data, black for the precise sample and blue for the second resolution sample.

where the errors correspond to 1σ (68% C.L. for 1 d.o.f.). The bestfit L/E distributions can be seen in Figure 11.2, and these have been normalised by the null oscillation expectation in Figure 11.3. As the minimum point was very close to zero NSI, these distributions do not differ much from pure 3-Flavour neutrino oscillations. For illustration, the bestfit L/E over null oscillation plots were compared with a few NSI parameters with a fit just outside the 99% C.L. in Figure 11.4. These distributions do not have any pulls from systematics, and show the differences of the probability calculation. All of the plots have oscillations at the minimum point $\sin^2\theta_{23} = 0.55$ and $\Delta m^2_{32} = 2.5 \times 10^{-3}\,\mathrm{eV}^2$, with only the stated NSI parameters varied. The green curve corresponds to the best fit parameters.

The 2D allowed region of the NSI parameter space, with the oscillation parameters marginalised out, can be seen on the left of Figure 11.5; and the 2D oscillation parameter allowed region with the NSI parameters marginalised out on the right. As noted previously, any mention of marginalisation in this thesis means that the marginalised parameters were minimised over. Here the $\Delta\chi^2$ was drawn from the global minimum and the 68%, 90% and 99% C.L. correspond to a $\Delta\chi^2$ of 2.30, 4.61, and 9.21, respectively. The 1D $\Delta\chi^2$ distributions for $\varepsilon_{\mu\tau}$ and $\varepsilon_{\tau\tau}$ can be seen in Figure 11.6, where the undisplayed parameters were marginalised out. The 1D distributions for the oscillation parameters with the undisplayed parameters marginalised out can be seen in Figure 11.7. The 68%, 90% and 99% C.L. correspond to a $\Delta\chi^2$ of 1.00, 2.71, and 6.63, respectively. These distributions were used to calculate the 68% and 90% C.L. allowed regions. The scanned points were well-fitted with a smooth spline interpolated curve, and the position where the $\Delta\chi^2$ crossed the C.L. boundaries was found, as shown by the intersecting lines in Figure 11.6 and 11.7. The 90% C.L. allowed regions were:

$$-1.97 \times 10^{-2} < \quad \varepsilon_{\mu\tau} \quad < 1.45 \times 10^{-2}, \tag{11.9}$$

$$-4.54 \times 10^{-2} < \quad \varepsilon_{\tau\tau} \quad < 4.47 \times 10^{-2}, \tag{11.10}$$

$$0.39 < \quad \sin^2\theta_{23} \quad < 0.65, \tag{11.11}$$

$$2.21 \times 10^{-3}\,\mathrm{eV}^2 < \quad \Delta m^2_{31} \quad < 3.15 \times 10^{-3}\,\mathrm{eV}^2. \tag{11.12}$$

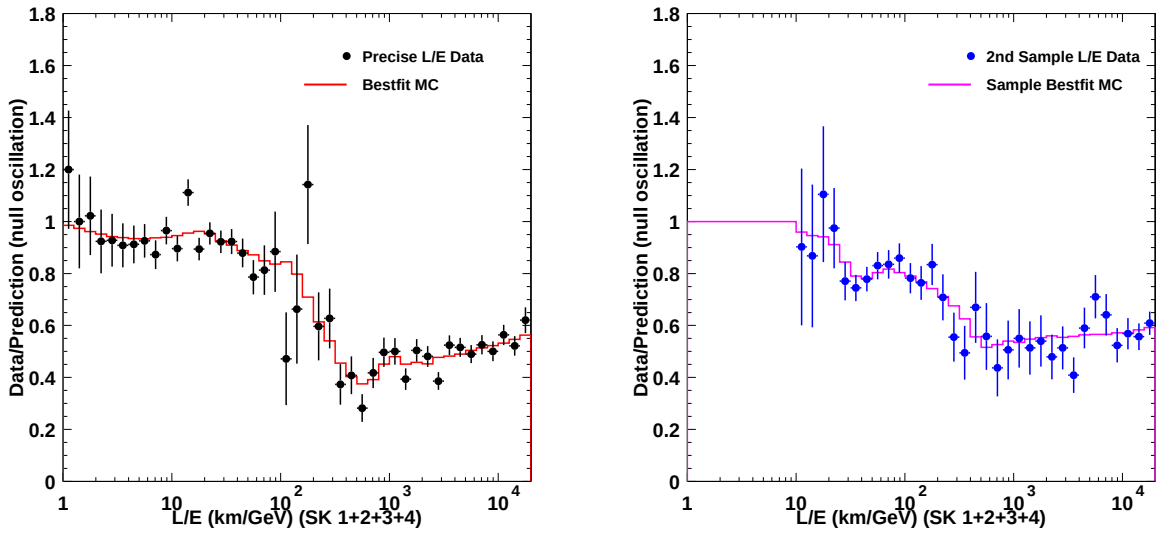

Figure 11.3: The NSI bestfit L/E distributions normalised by the null oscillation expectation, for the precise resolution sample on the left and the second resolution sample on the right. These are similar to the 3-flavour pure oscillation case.

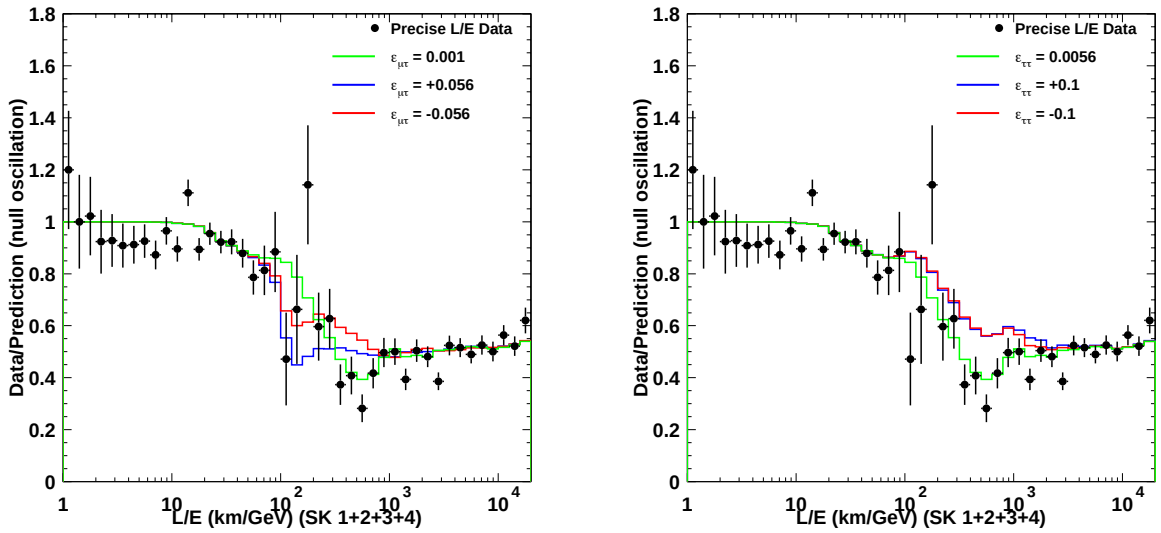

Figure 11.4: Bestfit L/E distribution in green compared with various $\varepsilon_{\mu\tau}$ parameters on the left and various $\varepsilon_{\tau\tau}$ parameters on the right. The blue histograms show an increase in the parameter and the red histograms show a decrease. These parameters were chosen just outside the 99% C.L. boundary to demonstrate considerable variation in the distributions from the NSI parameters. The systematic pulls have not been applied to these distributions, only the survival and transition probabilities.

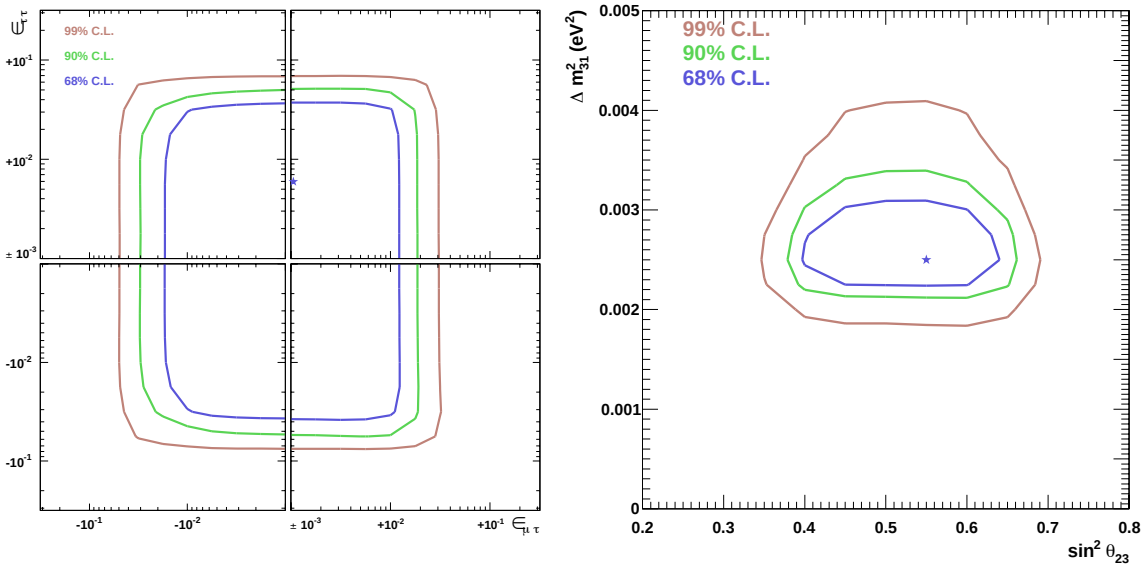

Figure 11.5: The 2D allowed regions for the NSI parameters on the left, and oscillation parameters on the right. The undisplayed parameters from the 4D parameter space have been marginalised out. In the left plot, the $\varepsilon_{\mu\tau}$ was drawn on the x-axis and $\varepsilon_{\tau\tau} \equiv \varepsilon'$ on the y-axis. The axes were drawn in log scale, with the right panels for positive $\varepsilon_{\mu\tau}$, and the left panels for negative $\varepsilon_{\mu\tau}$; postive $\varepsilon_{\tau\tau}$ on the top, and negative $\varepsilon_{\tau\tau}$ on the bottom. The bestfit point is indicated by a star on the top right panel. In the right plot, the oscillation parameter space with the single-angle $\sin^2\theta_{23}$ is shown. The Δm^2_{31} allowed region was slightly elongated to higher values, due to the influence of the $\varepsilon_{\mu\tau}$ NSI parameter.

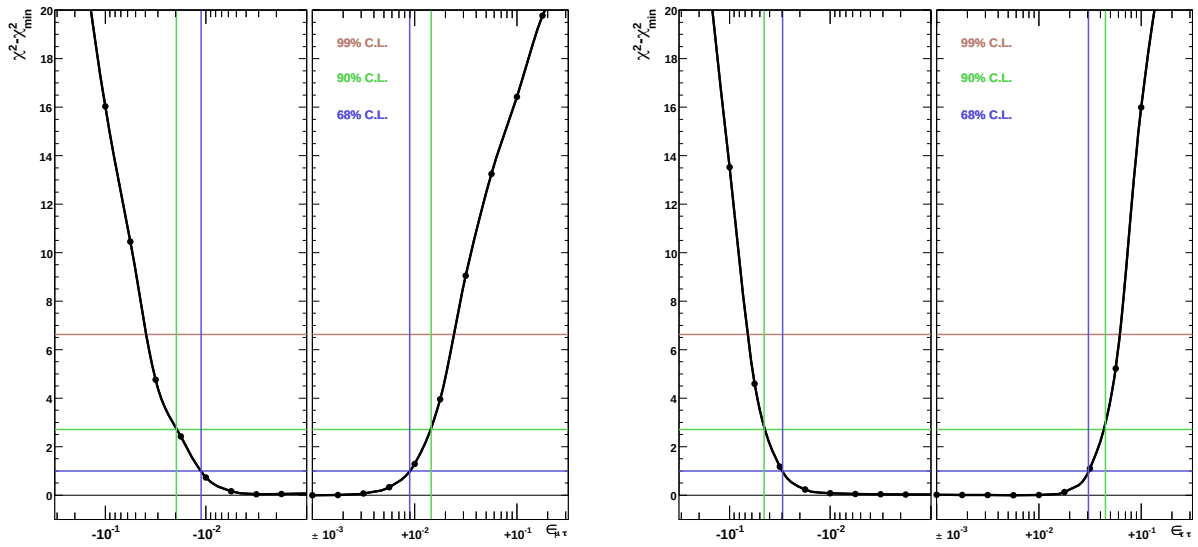

Figure 11.6: The 1D allowed regions for the NSI parameters, $\varepsilon_{\mu\tau}$ in the left plot and $\varepsilon_{\tau\tau}$ in the right, with the undisplayed parameters marginalised out. The NSI parameters are drawn in log scale, with positive values on the right panels and negative values in the left panels. The points show the scanned points, which have been fitted with a spline function to find the C.L. boundaries. The calculated C.L. intervals have been shown by the intersecting lines. These distributions were flat around the minimum.

11.3.2 The $\varepsilon_{\mu\tau}$ and Δm^2_{31} Dependence

Considering the 1D plots in Figure 11.6, the $\Delta\chi^2$ distributions were very flat around the minimum, suggesting a considerable range of NSI parameters fitted the data equally well. When the magnitude of the parameters were slightly larger than 10^{-2}, NSI was rapidly disfavoured. These distributions show that the allowed region for $\varepsilon_{\mu\tau}$ was slightly more relaxed in the negative direction, while $\varepsilon_{\tau\tau}$ was fairly symmetrical. Assuming normal hierarchy, for negative $\varepsilon_{\mu\tau}$ larger values of Δm^2_{31} are allowed for neutrinos, and smaller values for anti-neutrinos. The data appear to have slightly more allowance for this scenario, rather than the opposite tendency. In other words, there was more allowance for $\varepsilon_{\mu\tau}$ with the opposite sign of Δm^2_{31}, and this means more leeway for a larger effective Δm^2_{31} for neutrinos and smaller for anti-neutrinos.

In Figure 11.7, it can be seen that the allowed region for $\sin^2\theta_{23}$ was very similar to that of pure 3-Flavour oscillations. However, in the presence of NSI, the allowed values for Δm^2_{31} were considerably relaxed. Especially, a greater range of larger Δm^2_{31} was allowed, as seen in the right of Figures 11.5 and 11.7. This corresponds to the less restricted region for negative $\varepsilon_{\mu\tau}$, and to the statistics being dominated by neutrino, rather than anti-neutrino. These distributions demonstrate that the presence of NC matter NSI in nature could allow for a discrepancy in the observation of Δm^2_{31} between neutrino and anti-neutrino by an analysis assuming pure vacuum oscillations alone. The effect of the $\varepsilon_{\mu\tau}$ parameter on the Δm^2_{31} region can be seen in Figure 11.8. For normal hierarchy, a negative value for $\varepsilon_{\mu\tau}$ favours larger Δm^2_{31}; while positive values favour smaller Δm^2_{31}. The data consisted of combined neutrino and anti-neutrino contributions, but was statistically dominated by neutrinos, which is the reason for this observed trend.

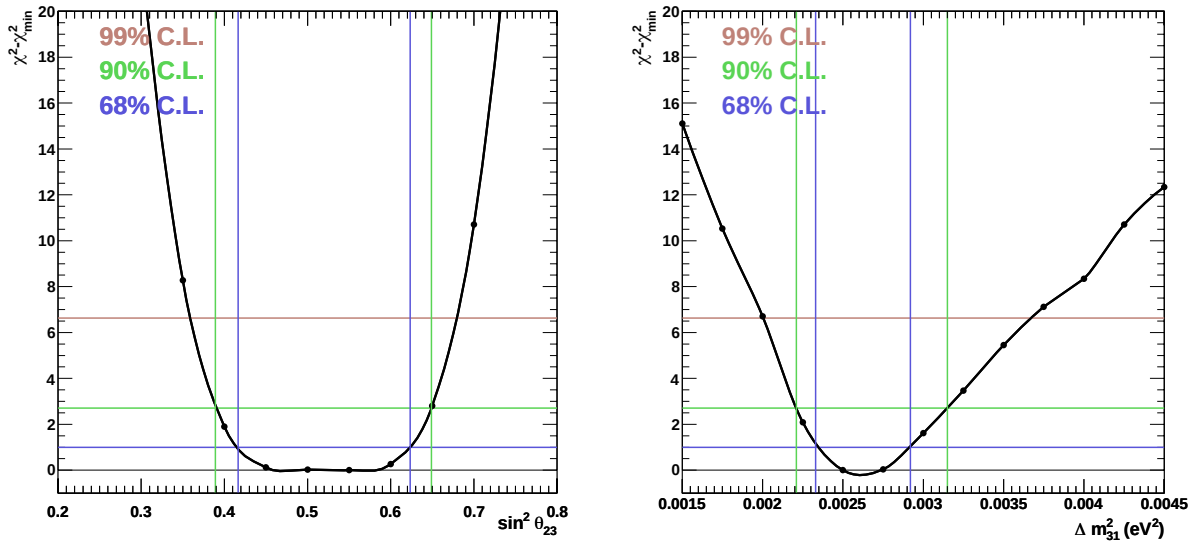

Figure 11.7: The oscillation 1D allowed regions from the 4D NSI analysis. $\sin^2\theta_{23}$ is shown on the left, and Δm^2_{31} on the right. The $\sin^2\theta_{23}$ regions was similar to the pure oscillation case. However, the Δm^2_{31} allowed region was enlarged, particularly in the positive direction due to the effect of the $\varepsilon_{\mu\tau}$ NSI parameter.

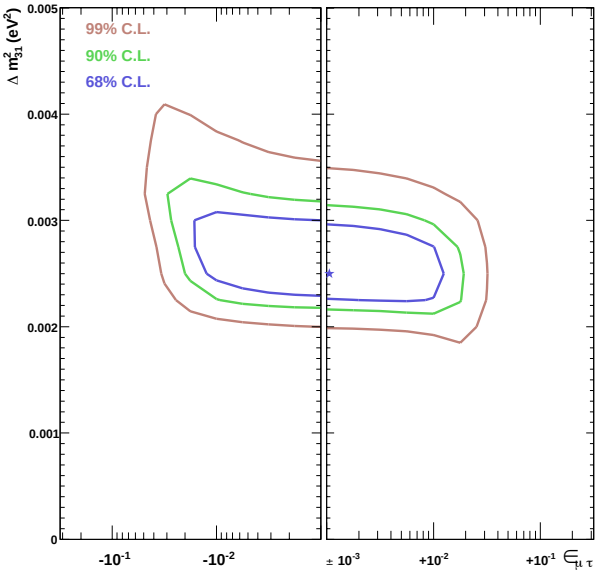

Figure 11.8: The 2D Δm^2_{31} vs $\varepsilon_{\mu\tau}$ allowed region. The $\varepsilon_{\mu\tau}$ parameter is drawn in log scale, with positive values on the right panel and negative values in the left panel. The bestfit point is indicated by a star on the right panel. Larger values of Δm^2_{31} are allowed as $\varepsilon_{\mu\tau}$ becomes more negative.

11.3.3 3F Oscillation and NSI Systematic Uncertainties

The $1\,\sigma$ estimates for the systematic uncertainties were the same for all of the L/E analyses, and has been shown in Figure 9.14. The contribution from these systematics, minimised in the fitting, have been drawn in Figure 11.9. These values have been displayed as the fraction of the $1\,\sigma$ estimates that were actually used in the best fit. As in the other L/E analyses, the pulls for the systematic errors were all below $1\,\sigma$, and most were below $0.5\,\sigma$. The shape of these distributions, of which systematics contribute, were very stable across all the analyses, with only small differences in the magnitude of each error seen. The contribution of the uncertainties to the χ^2 was[1] $\Sigma\left(\frac{\epsilon}{\sigma}\right)^2 = 3.32$. This was essentially the same contribution as seen in the 3-flavour normal hierarchy analysis, and was a minimal dependence on the systematic errors.

The observation of very similar uncertainties was likely due to the L/E data being common between all the analyses, and because the best fits were very close to pure normal neutrino oscillations. Despite allowing for considerable freedom for independent neutrino and anti-neutrino parameters, or additional NSI flavour transitions, the best fits were for essentially pure oscillations. A very nice fit was found from this parameter space, with the minimum point having non-zero NSI. However, as it is clear from the allowed regions, this result was consistent with zero NSI. Neutrino Oscillations appears to be stable and the best description of atmospheric neutrino observations, even in the presence of flavour transitions allowed by NSI.

11.4 Discussion

11.4.1 Comparisson With Atmospheric NSI Measurements

There has been a few analyses of NSI in the $\mu\tau$–sector of atmospheric neutrinos. Most of them have taken a phenomenological approach, depending on officially published data from experiments like SK or MACRO. Since pure NSI had already been ruled out to explain the ν_μ deficit in atmospheric neutrinos [57, 59, 60], analyses had to involve hybrid models of oscillations and NSI. All of these analyses relied on a 2-flavour model [45, 57], including a first measurement of atmospheric data with the SK Zenith distributions [73].

These 2-flavour hybrid models provided stringent constraints on the allowed NSI parameters. Some of the 90% C.L. allowed regions for $\varepsilon_{\mu\tau}$ have been written below for comparison [45, 73]:

$$-1.97\times10^{-2} < \quad \varepsilon_{\mu\tau} \quad < 1.45\times10^{-2} \qquad \text{(L/E, this thesis)}, \tag{11.13}$$

$$-1.3\times10^{-2} < \quad \varepsilon_{\mu\tau} \quad < 1\times10^{-2} \qquad \text{(2004 Gonzalez-Garcia)}, \tag{11.14}$$

$$\quad |\varepsilon_{\mu\tau}| \quad < 1.1\times10^{-2} \qquad \text{(2011 Mitsuka, SK Zenith)}. \tag{11.15}$$

For $\varepsilon_{\mu\tau}$, the constraints from these past analyses appear to be more confined than the results of this analysis. However, it should be noted that these past analyses made use of 2-flavour hybrid models to probe various new physics, and so are not directly comparable with this analysis. There has been some controversy over these 2-flavour atmospheric analyses, which exclude the complications of traversing the mantle and core [13]. This may lead to unrealistically constrained allowed regions. The treatment in this thesis implemented a 3-flavour model, removing some of the symmetries seen in simpler models.

[1] The sum here is over all the systematic uncertainties.

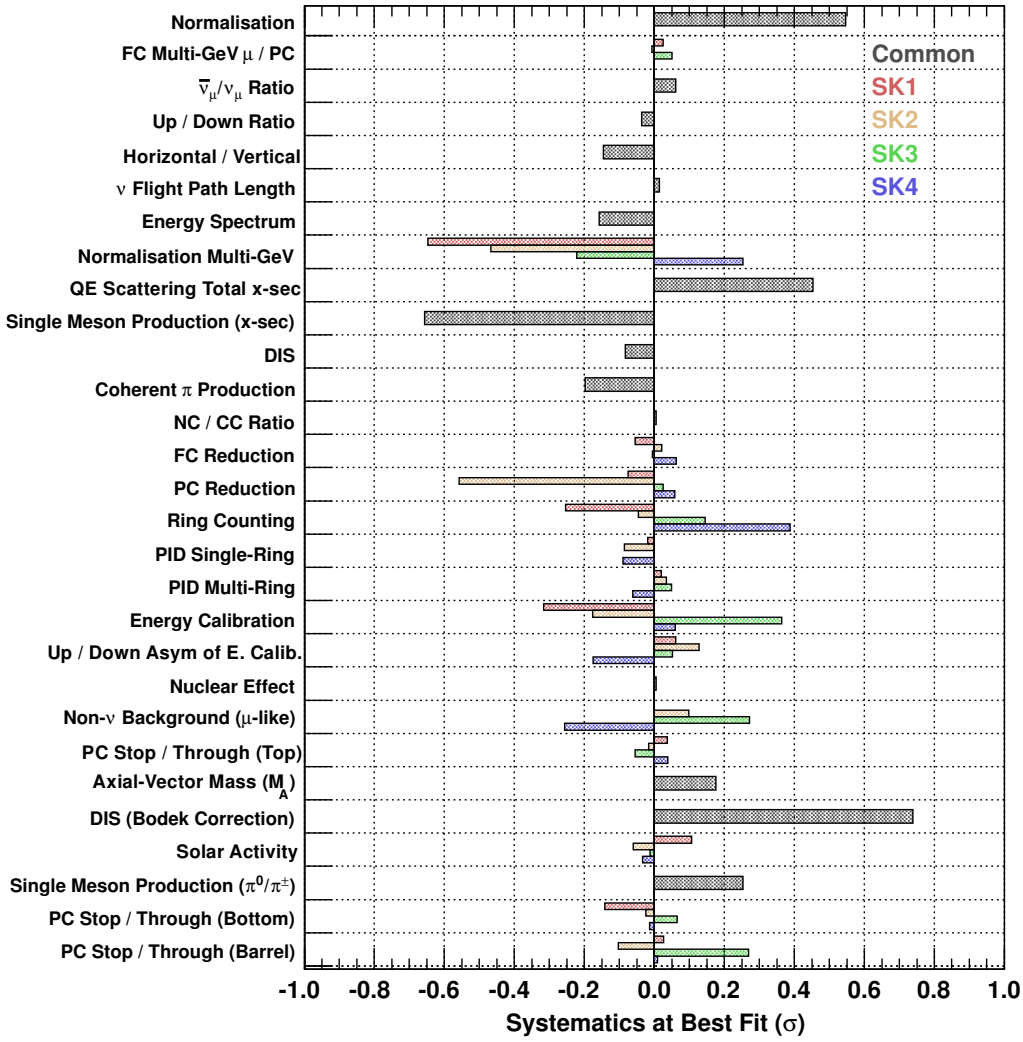

Figure 11.9: Systematics at the best fit for the 3F Oscillation and NSI L/E Analysis

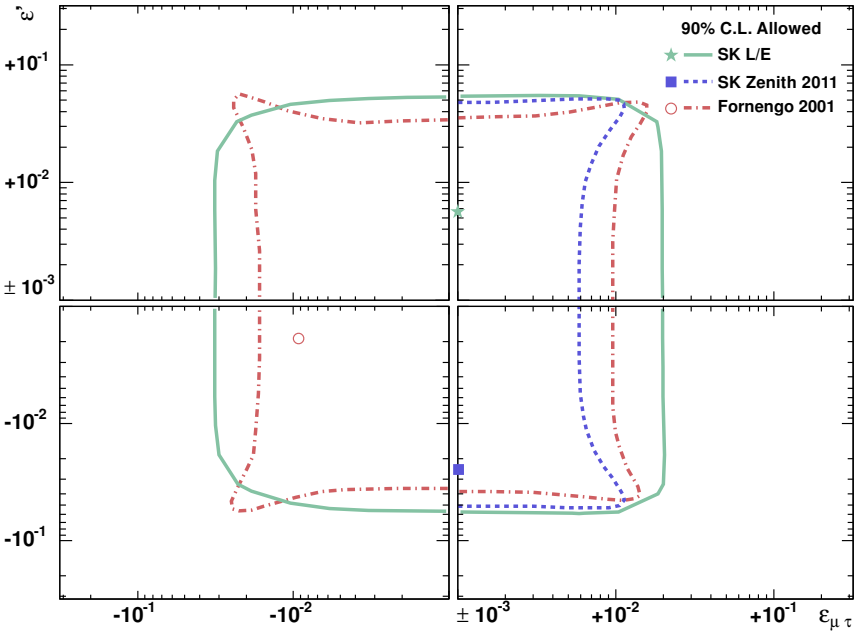

Figure 11.10: Comparison of NSI measurements on the $\varepsilon_{\mu\tau} \times \varepsilon'$ plane, where $\varepsilon' \equiv (\varepsilon_{\tau\tau} - \varepsilon_{\mu\mu})$. The results from this analysis are shown in solid green; the 2-flavour SK Zenith NSI measurement [73] in dashed blue; and an NSI phenomenological study of atmospheric neutrinos by Fornengo et.al. in dash-dotted red [57]. Only the L/E analysis properly considers 3-flavour effects, so these measurements are not directly comparable.

The Δm^2_{31} dependence on $\varepsilon_{\mu\tau}$, as seen this analysis in Figure 11.8, was not observed in these past models. In the 2-flavour SK Zenith NSI analysis [73], the oscillation parameter space was overlapping with and without NSI, which was shown in the left of Figure 1.13. So a 3-flavour approach should give a more accurate representation of the effect of these NSI parameters. The L/E NSI allowed regions have been compared with the SK Zenith NSI analysis [73] and the phenomenological analysis by Fornengo et.al. [57] in Figure 11.10. The 2D allowed regions for the 2004 Gonzalez-Garcia analysis [45] were not available, so the comparison was made with the 2001 Fornengo analysis, which made use of a similar analysis approach.

The 2-flavour models seem to observe more shape on the $\varepsilon_{\mu\tau} \times \varepsilon'$ plane, where $\varepsilon' \equiv (\varepsilon_{\tau\tau} - \varepsilon_{\mu\mu})$. Particularly, the $\varepsilon_{\mu\tau}$ parameter was considerably constrained for small values of ε'. This behaviour was not seen in the L/E analysis, leading to larger allowed regions for $\varepsilon_{\mu\tau}$. However, with fewer assumptions in this analysis, the L/E ranges should be more reliable.

Some of the 90% C.L. allowed regions for ε' have been written below for comparison [45, 73]:

$$-4.54 \times 10^{-2} < \quad \varepsilon' \quad < 4.47 \times 10^{-2} \qquad \text{(L/E, this thesis)}, \tag{11.16}$$

$$|\varepsilon'| \quad < 2.9 \times 10^{-2} \qquad \text{(2004 Gonzalez-Garcia)}, \tag{11.17}$$

$$-4.9 \times 10^{-2} < \quad \varepsilon' \quad < 4.9 \times 10^{-2} \qquad \text{(2011 Mitsuka, SK Zenith)}. \tag{11.18}$$

Again, the Gonzalez-Garcia analysis was very restrictive on this parameter, while the Zenith range was quite similar to that measured by the L/E distributions. The slightly more confined region from the L/E analysis comes from scanning negative values of $\varepsilon_{\mu\tau}$, which were omitted

from the Zenith analysis. In Figure 11.10, a subtle tendency of the ε' allowed range to become narrower with increasingly negative $\varepsilon_{\mu\tau}$ can be seen in both the L/E and Fornengo analyses. The best fit points of each analysis were in different quadrants of the parameter space. Generally, the $\Delta\chi^2$ were fairly flat, with some of the 2-flavour analyses having shallow dips away from zero NSI. Without a consistent and statistically significant non-zero measurement of these parameters, all of these results are consistent with no observation of NSI.

Although the 2-flavour analyses report more confined allowed regions and had more structure over the parameter space than was visible in this analysis, the L/E 3-flavour oscillation and NSI result should be the most realistic and reliable. It has considered 3-flavour effects and accurately simulates the neutrino flight path through matter, including the mantle and core. The expected characteristic dependence of $\varepsilon_{\mu\tau}$ on Δm^2_{31} was seen in the L/E analysis, but not in the previous analyses, making this result the current best measurement of $\varepsilon_{\mu\tau}$ and ε' from atmospheric neutrinos.

11.4.2 Comparisson With MINOS Measurements

In Figure 11.11, the 90% C.L. allowed regions on the $\varepsilon_{\mu\tau} \times \Delta m^2_{31}$ parameter space has been shown. Displayed on the plot are the results from several analyses: 3F Oscillation and NSI L/E; a phenomenological analysis of the MINOS distributions by Mann et.al. in 2010 [13]; and a 2013 measurement by MINOS Collaboration [69]. Since these MINOS related measurements made use of an electron number density normalisation for their calculation, the magnitudes of the $\varepsilon_{\mu\tau}$ have been re-scaled to match the L/E NSI analysis normalisation. The electron number density is 3 times less than the down-quark number density used in this analysis, which allows much larger values of $\varepsilon_{\mu\tau}$ to describe the same strength of NSI. Specifically, the Mann and MINOS $\varepsilon_{\mu\tau}$ values were scaled by 1/3 in Figure 11.11.

Each of these analyses have assumed normal mass hierarchy, and so see the same trend of allowing larger Δm^2_{31} with increasingly negative $\varepsilon_{\mu\tau}$. It is clear that this effect is much more pronounced in the L/E NSI analysis. This is likely due to the much greater sensitivity to matter effects from atmospheric neutrinos, which would be relatively weaker at the fixed ∼730 km baseline through the crust in the MINOS experiment. MINOS is essentially insensitive to the $\varepsilon_{\tau\tau}$ and 3-flavour effects [68, 69], while an analysis with atmospheric neutrinos should take these factors into account. However, MINOS does gain sensitivity due to the event-by-event neutrino and anti-neutrino separation.

After considering 3-flavour effects, the L/E analysis still provides strong constraints on $\varepsilon_{\mu\tau}$, favouring a steeper angle through the parameter space. In particular, the best fit points from the Mann and MINOS analyses were excluded at the 90% C.L., and the best fit from the L/E analysis had close to zero NSI. Quantitatively, the 90% C.L. allowed range for $\varepsilon_{\mu\tau}$ measured by MINOS was:

$$-0.20 < \quad \varepsilon_{\mu\tau} \quad < 0.07, \tag{11.19}$$

$$-6.7 \times 10^{-2} < \quad \varepsilon_{\mu\tau} \quad < 2.3 \times 10^{-2} \qquad \text{(divided by 3)}, \tag{11.20}$$

where the second line has scaled the magnitudes to the d-quark normalisation. The MINOS result allowed just over 3 times larger $\varepsilon_{\mu\tau}$ in the negative direction; while the positive range was only slightly larger than the L/E result.

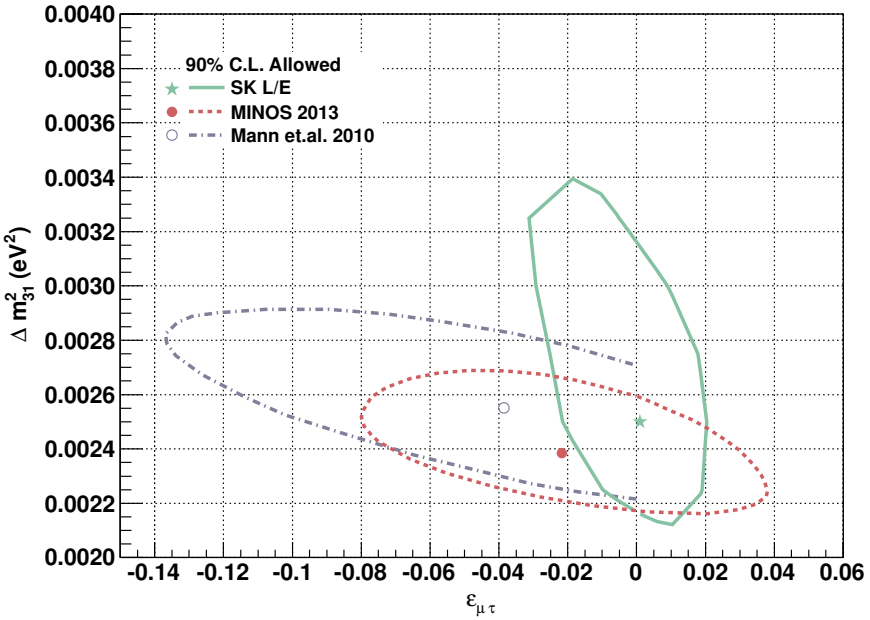

Figure 11.11: Comparison of NSI measurements on the $\varepsilon_{\mu\tau} \times \Delta m^2_{31}$ parameter space. The results from this analysis are shown in solid green; a 2010 NSI phenomenological study of MINOS distributions by Mann et.al. in dash-dotted grey [13]; and a 2013 MINOS NSI measurement of data in dashed red [69]. The MINOS related regions have been re-scaled to match the L/E NSI normalisation. The L/E region is much more confined in $\varepsilon_{\mu\tau}$, and takes a steeper angle through the parameter space.

11.4.3 Improving the Sensitivity to NSI

The analysis in this thesis has included 3-flavour effects, which can largely alleviate the controversy over the highly constraining 2-flavour measurements from atmospheric neutrinos. However, this analysis has not yet considered the effect of $\varepsilon_{e\tau}$, which has been shown [66] to relax the limits on $\varepsilon_{\tau\tau}$ even up to $\mathcal{O}(1)$, which can be seen in Figure 1.10. This analysis was already computationally intensive, but given time, the effect of the $\varepsilon_{e\tau}$ parameter could be studied with the same model used in this analysis (the other NSI parameters were simply set to 0).

Atmospheric neutrinos have great sensitivity to matter effects such as NSI, and accelerator experiments often have detectors with good charge discrimination to separate neutrino and anti-neutrino on an event-by-event basis. These are the best advantages of these experiments. An experiment like Hyper-Kamiokande [147], the proposed successor to SK, will be able to collect much greater statistics, improving sensitivity to many measurements. However, there is a planned atmospheric neutrino experiment which will have a 50 kT magnetised detector: INO [263]. This experiment could have considerably more sensitivity by applying both of these advantages. The other difficulty would be decoupling standard and non-standard physics, which could perhaps be better resolved with a precision beamline experiment like the Neutrino Factory [142], which also has magnetised detectors as a part of some of its designs, and potentially baselines in the order of many thousands of kilometres.

11.4.4 The 3-Flavour Oscillation and NSI L/E Result

Atmospheric neutrinos have unparalleled sensitivity to matter effects such as those seen in NC NSI, due to the huge neutrino flight paths through the Earth – including the mantle and core. This property has given this analysis potentially the best sensitivity to $\mu\tau$–sector NSI. This is the first analysis of this variety of NSI to include 3-flavour effects and an accurate treatment of matter effects using atmospheric neutrino data.

These results go a long way to resolve some of the controversy on the highly constrained results from 2-flavour NSI atmospheric analyses. While the constraints from this analysis are less strong as those from previous measurements, the NSI parameters are still strongly confined when including 3-flavour effects. Since this analysis involved less assumptions, and has been extensive in the scanned parameter space, these results are perhaps the most significant measurements on $\mu\tau$–sector NSI – at least from atmospheric neutrinos.

The best fit was close to zero-NSI, and these results were consistent with no observation of NSI. Strong constraints have been put on the $\varepsilon_{\mu\tau}$ and $\varepsilon' \equiv (\varepsilon_{\tau\tau} - \varepsilon_{\mu\mu})$ NSI parameters. Since this analysis was model independent, these constraints can be used to define, restrict or exclude any number of models including non-standard NC interactions of neutrinos with matter. So these measurements are highly valuable to theorists. Another implication of these results is that Neutrino Oscillations have been shown to be robust, even in the presence of 3-flavour $\mu\tau$–sector NSI.

ID	Description	Systematics		
		σ %	ϵ % (σ)	Pull
Systematic Errors in Neutrino Interactions				
9	QE Scattering Total Cross-Section	10.0	4.53 (0.453)	0.2056
10	Single Meson Production (Total Cross-Section)	20.0	-13.13 (-0.657)	0.4313
11	DIS (Total Cross-Section)	5.0	-0.41 (-0.083)	0.0069
12	Coherent π Production	100.0	-19.81 (-0.198)	0.0392
13	NC/CC Ratio	20.0	0.11 (0.006)	0.0000
21	Nuclear Effect	30.0	0.16 (0.005)	0.0000
24	Axial-Vector Mass (M_A) [QE and Single Meson]	20.0	3.51 (0.175)	0.0307
25	DIS (Bodek Correction)	20.0	14.79 (0.739)	0.5465
27	Single-Meson Production ($\pi^0/\pi^\pm$)	40.0	10.15 (0.254)	0.0644

Table 11.1: Neutrino Interaction Uncertainties

ID	Description	SK1			SK2		
		σ %	ϵ % (σ)	Pull	σ %	ϵ % (σ)	Pull
Systematic Errors from Reduction							
14	FC Reduction	0.2	-0.01 (-0.056)	0.0031	0.2	0.00 (0.021)	0.0005
15	PC Reduction	2.4	-0.18 (-0.076)	0.0057	4.8	-2.68 (-0.557)	0.3107
22	Non-ν Background (μ-like)		0.00 (0.000)	0.0000		0.10 (0.098)	0.0097
	Cosmic-Ray FC Sub-GeV	0.1			0.1		
	Cosmic-Ray FC Multi-GeV	0.1			0.1		
	Cosmic-Ray PC	0.2			0.7		
ID	Description	SK3			SK4		
14	FC Reduction	0.8	0.00 (-0.006)	0.0000	0.3	0.02 (0.063)	0.0039
15	PC Reduction	0.5	0.01 (0.026)	0.0007	1.0	0.06 (0.059)	0.0035
22	Non-ν Background (μ-like)		0.27 (0.272)	0.0740		-0.26 (-0.256)	0.0656
	Cosmic-Ray FC Sub-GeV	0.1			0.1		
	Cosmic-Ray FC Multi-GeV	0.2			0.8		
	Cosmic-Ray PC	1.8			4.9		

Table 11.2: Neutrino Reduction Uncertainties

ID	Description	Systematics		
		σ %	ϵ % (σ)	Pull
Systematic Errors in Neutrino Flux				
1	Normalisation	–	5.46	0.0000
3	$\bar{\nu}_\mu/\nu_\mu$ Ratio	6.0	0.37 (0.062)	0.0038
4	Up/Down Ratio		-0.04 (-0.036)	0.0013
	Single-Ring $<$ 400 MeV	0.3		
	Single-Ring $>$ 400 MeV	0.5		
	Single-Ring Multi-GeV	0.2		
	Multi-Ring Sub-GeV	0.2		
	Multi-Ring Multi-GeV	0.2		
	PC	0.2		
5	Horizontal/Vertical		-0.15 (-0.146)	0.0212
	Single-Ring $<$ 400 MeV	0.1		
	Single-Ring $>$ 400 MeV	1.9		
	Single-Ring Multi-GeV	2.3		
	Multi-Ring Sub-GeV	1.3		
	Multi-Ring Multi-GeV	1.5		
	PC	1.7		
6	Neutrino Flight Path Length	10.0	0.15 (0.015)	0.0002
7	Energy Spectrum	5.0	-0.79 (-0.158)	0.0248
8	Sample Normalisation Multi-GeV			
	SK1	5.0	-3.24 (-0.648)	0.4195
	SK2	5.0	-2.33 (-0.467)	0.2178
	SK3	5.0	-1.11 (-0.222)	0.0493
	SK4	5.0	1.27 (0.253)	0.0642
2	FC Multi-GeV μ / PC			
	SK1	0.6	0.02 (0.025)	0.0006
	SK2	0.5	0.00 (-0.007)	0.0000
	SK3	0.9	0.05 (0.051)	0.0026
	SK4	0.02	0.00 (0.000)	0.0000
26	Solar Activity			
	SK1	20.0	2.13 (0.107)	0.0114
	SK2	50.0	-3.05 (-0.061)	0.0037
	SK3	20.0	-0.24 (-0.012)	0.0001
	SK4	10.0	-0.33 (-0.033)	0.0011

Table 11.3: Neutrino Flux Uncertainties

ID	Description	SK1			SK2		
		σ %	ϵ % (σ)	Pull	σ %	ϵ % (σ)	Pull
Systematic Errors from Reconstruction							
16	Ring Counting		-2.54 (-0.254)	0.0643		-0.45 (-0.045)	0.0021
	Single-Ring $<$ 400 MeV	0.7			2.3		
	Single-Ring $>$ 400 MeV	0.7			0.7		
	Single-Ring Multi-GeV	1.7			1.7		
	Multi-Ring Sub-GeV	-4.5			-8.2		
	Multi-Ring Multi-GeV	-4.1			-0.8		
17	Particle ID Single-Ring		-0.02 (-0.018)	0.0003		-0.09 (-0.086)	0.0073
	Sub-GeV	-0.1			-0.4		
	Multi-GeV	0.2			-0.1		
18	Particle ID Multi-Ring		0.20 (0.020)	0.0004		0.35 (0.035)	0.0012
	Sub-GeV	-3.9			2.2		
	Multi-GeV	-2.9			-3.4		
19	Energy Calibration	1.1	-0.35 (-0.316)	0.0999	1.7	-0.30 (-0.176)	0.0310
20	Up-Down Asym of E Calib.	0.6	0.04 (0.061)	0.0037	0.6	0.08 (0.128)	0.0165
23	PC Stop/Through Top	46.1	1.69 (0.037)	0.0014	19.37	-0.31 (-0.016)	0.0003
28	PC Stop/Through Bottom	22.7	-3.20 (-0.141)	0.0199	12.9	-0.32 (-0.025)	0.0006
29	PC Stop/Through Barrel	7.01	0.19 (0.026)	0.0007	9.44	-0.97 (-0.103)	0.0105
ID	Description	SK3			SK4		
16	Ring Counting		1.45 (0.145)	0.0210		3.88 (0.388)	0.1503
	Single-Ring $<$ 400 MeV	3.0			-3.0		
	Single-Ring $>$ 400 MeV	0.6			0.6		
	Single-Ring Multi-GeV	1.0			-1.2		
	Multi-Ring Sub-GeV	-2.6			-2.3		
	Multi-Ring Multi-GeV	-2.1			2.4		
17	Particle ID Single-Ring		0.00 (-0.001)	0.0000		-0.09 (-0.089)	0.0080
	Sub-GeV	-0.4			-0.4		
	Multi-GeV	-0.5			-0.4		
18	Particle ID Multi-Ring		0.49 (0.049)	0.0024		-0.62 (-0.062)	0.0038
	Sub-GeV	3.1			2.2		
	Multi-GeV	4.5			6.8		
19	Energy Calibration	2.7	0.98 (0.364)	0.1326	2.3	0.14 (0.060)	0.0036
20	Up-Down Asym of E Calib.	1.3	0.07 (0.051)	0.0026	0.3	-0.05 (-0.175)	0.0307
23	PC Stop/Through Top	86.6	-4.71 (-0.054)	0.0030	43.3	1.64 (0.038)	0.0014
28	PC Stop/Through Bottom	12.1	0.79 (0.065)	0.0042	11.6	-0.16 (-0.014)	0.0002
29	PC Stop/Through Barrel	28.7	7.71 (0.268)	0.0721	7.4	0.06 (0.009)	0.0001

Table 11.4: Neutrino Reconstruction Uncertainties

Chapter 12

Conclusion

The Standard L/E analysis was updated to include over 10 years of atmospheric neutrino data, up until summer 2012. This analysis provided the strongest constraint on Δm^2_{31} from atmospheric neutrinos, by accurately reconstructing L/E, a characteristic quantity from Neutrino Oscillations, and by selecting a sample of data with precise resolution in L/E. This made it an ideal approach for making Δm^2_{31}–dependent measurements (Chapter 8).

Sensitivity to sub-dominant effects was improved by the addition of a second resolution sample, and by merging the SK1–SK4 analysis bins at the χ^2 calculation stage, while properly estimating the systematics for each detector configuration separately. By allowing for independent neutrino and anti-neutrino oscillations in the simulation, there was no evidence for different Δm^2_{32} and $\sin^2 2\theta_{23}$ between neutrinos and anti-neutrinos, as expected by CPT symmetry (Chapter 9).

The first 3-Flavour L/E Analysis was performed, removing the assumptions from a 2-flavour analysis. The parameters of interest that were varied were $\sin^2\theta_{23}$ and Δm^2_{31}, which the L/E analysis is primarily sensitive to. The other oscillation parameters were fixed at the values: $\Delta m^2_{21} = 7.66 \times 10^{-5}\, eV^2$, $\sin^2\theta_{12} = 0.304$, and $\sin^2\theta_{13} = 0.025$ for both hierarchies. The L/E Analysis was confirmed to be a proper method for studying Neutrino Oscillations, even with the inclusion of 3-flavour and matter effects. In addition, the Standard 2-Flavour L/E Analysis was confirmed to be an excellent approximation for Oscillations. While the constraint on Δm^2_{31} by the 3-flavour zenith angle analysis was substantially weakened, that from 3-Flavour L/E was not affected much (Chapter 10). The allowed oscillation parameters at the 90% C.L. for each neutrino mass hierarchy were:

$$0.396 < \sin^2\theta_{23} < 0.644, \quad \text{and} \quad 2.275 \times 10^{-3}\,\text{eV}^2 < \Delta m^2_{31} < 2.995 \times 10^{-3}\,\text{eV}^2 \quad \text{(Normal)},$$
$$0.390 < \sin^2\theta_{23} < 0.631, \quad \text{and} \quad 2.182 \times 10^{-3}\,\text{eV}^2 < \Delta m^2_{31} < 2.842 \times 10^{-3}\,\text{eV}^2 \quad \text{(Inverted)}.$$

Included in this thesis was the first analysis of 3-Flavour Neutrino Oscillations with Neutral-Current Non-Standard Neutrino Interactions of atmospheric data in the $\mu\tau$–sector. The extensive baselines across the Earth, including the mantle and core, and wide range of available energies make atmospheric neutrinos have unparalleled sensitivity to matter neutrino NSI. The best fit was close to zero-NSI, and was consistent with no observation of NSI (Chapter 11). Strong constraints have been put on the following NSI parameters at the 90% C.L. (down-quark normalisation):

$$\begin{aligned} -1.97 \times 10^{-2} < \quad & \varepsilon_{\mu\tau} & < 1.45 \times 10^{-2}, \\ -4.54 \times 10^{-2} < \quad & \varepsilon' \equiv (\varepsilon_{\tau\tau} - \varepsilon_{\mu\mu}) & < 4.47 \times 10^{-2}. \end{aligned}$$

These measurements are model independent constraints that can be used to define, restrict or exclude any number of models including non-standard NC interactions of neutrinos with matter. Since this result has properly considered 3-flavour and matter effects, it is much stronger and reliable than past 2-flavour measurements with atmospheric neutrinos. With access to much greater baselines and more dense matter than accelerator experiments, this result is currently the most significant and realistic measurement in the world.

Finally, the implication of these results is that Neutrino Oscillations have been shown to be robust, even in the presence of independent neutrino and anti-neutrino oscillations or 3-flavour $\mu\tau$–sector NSI.

Appendix A

L/E Analysis Distributions

The energy fitting for each of the event samples from SK1 to SK4 can be seen in Figure A.1. The energy resolution for several samples is shown in Figures A.2 and A.3. The angular resolution for several samples is shown in Figures A.4 and A.5. Distributions for the true L/E over reconstructed L/E ratios are shown in Figure A.6. The resolution contours for each of the event samples in the ($\cos\theta$,E_ν) plane can be seen on the right of Figure A.7.

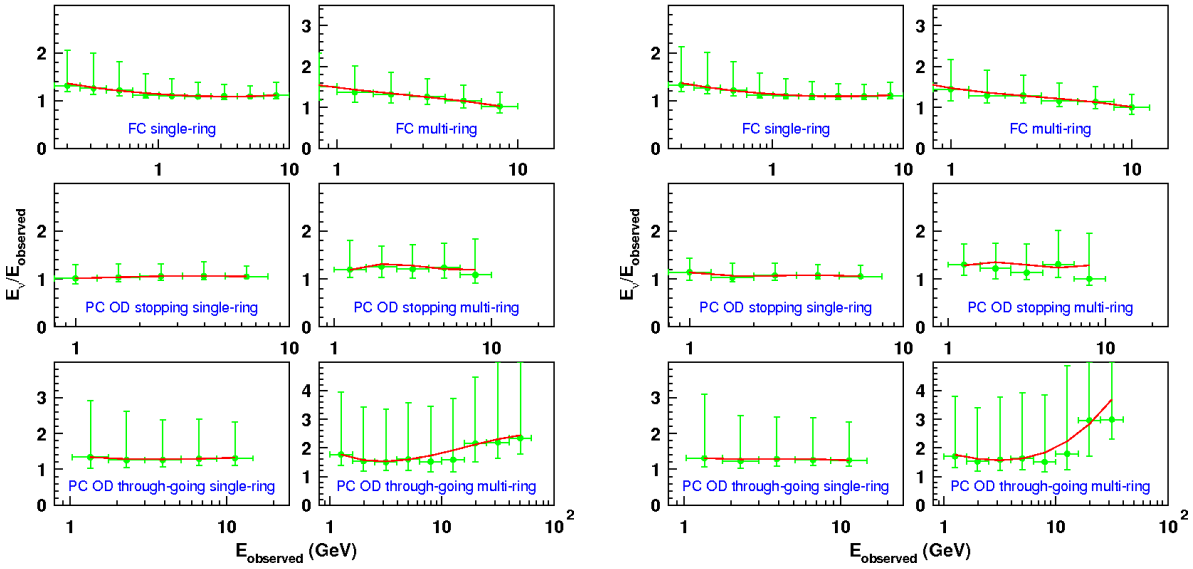

(a) SK1

(b) SK2

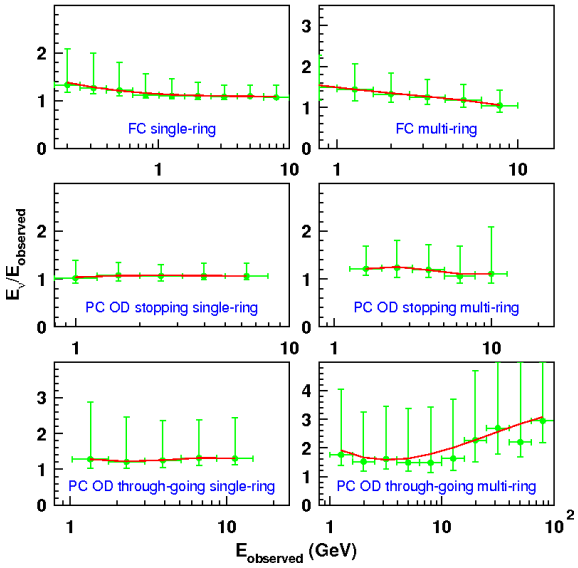

(c) SK3

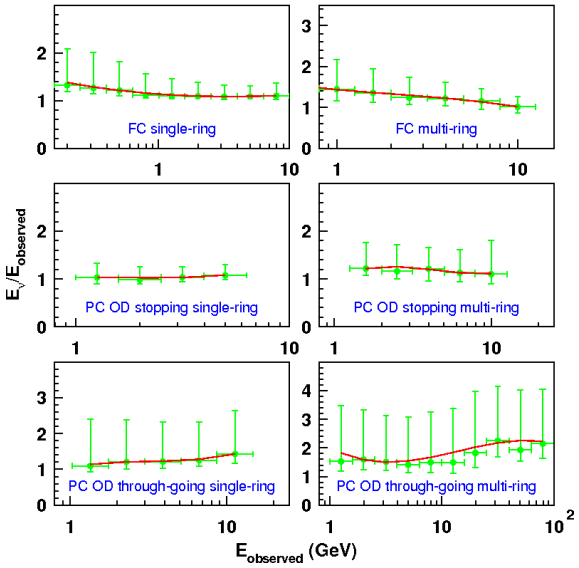

(d) SK4

Figure A.1: E_ν Reconstruction from fitting E_{vis2} to the true neutrino energy estimated by the Monte Carlo. The fitting for each of the event samples is shown, and the PC samples were further divided into single-ring and multi-ring. The fitted result for each SK period is shown.

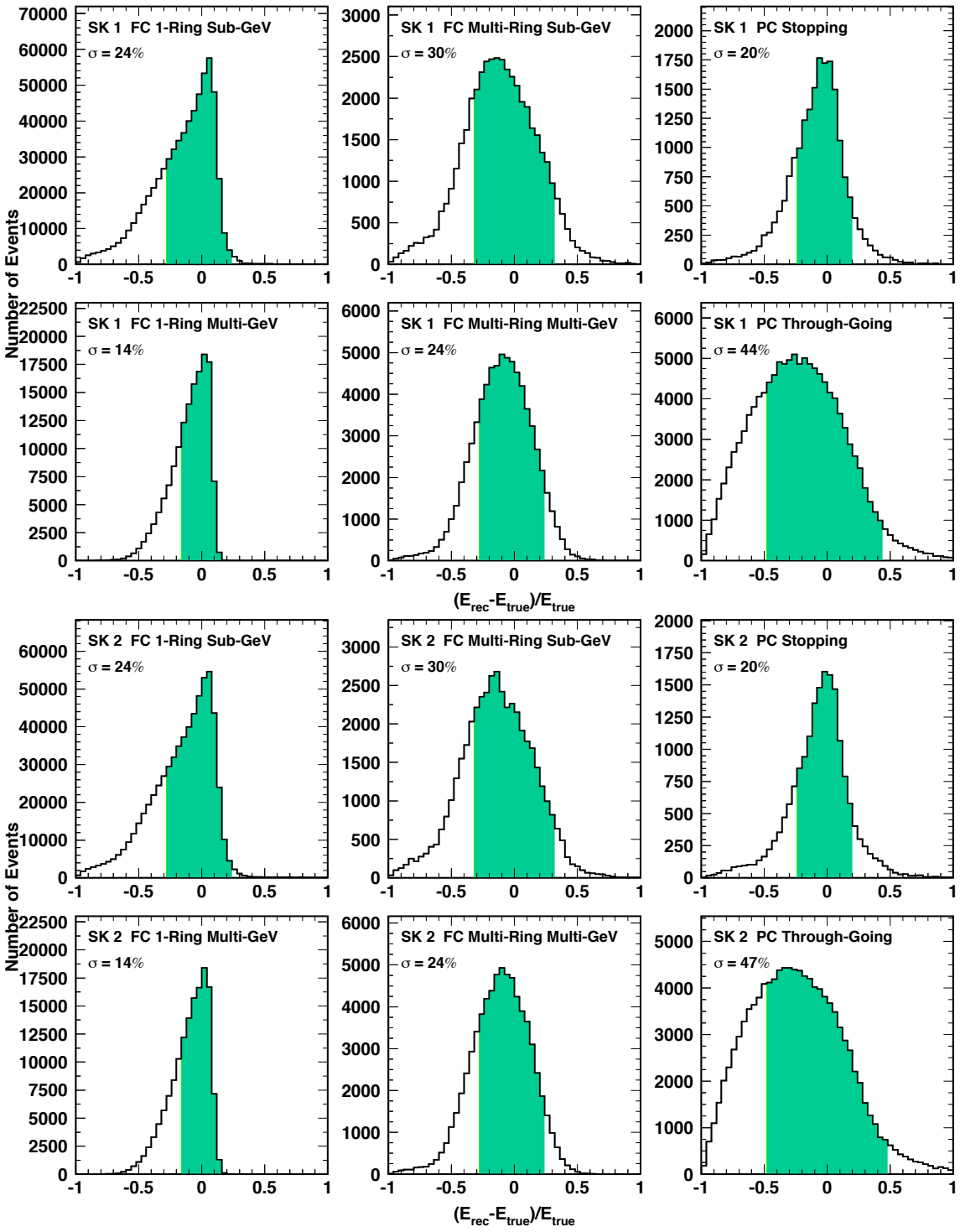

Figure A.2: L/E energy resolution for SK1 and SK2. The difference of the reconstructed energy and the true energy with respect to the true energy is shown. Events to the right of zero have been reconstructed with an energy larger than the true energy and vice versa for the left. The black solid histogram is for events satisfying the 70 % resolution cut, and the green shaded area corresponds to 68% of the events.

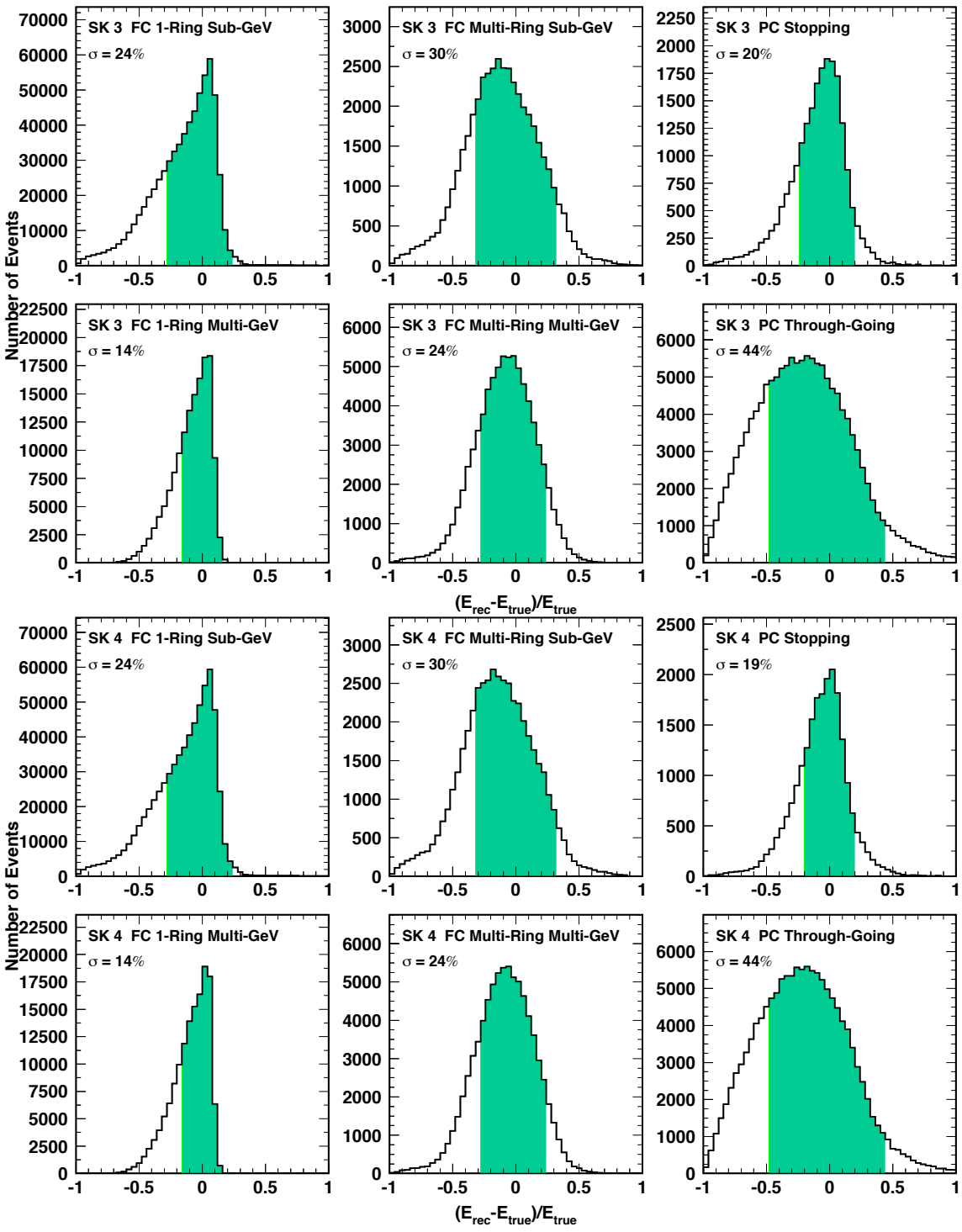

Figure A.3: L/E energy resolution for SK3 and SK4. The difference of the reconstructed energy and the true energy with respect to the true energy is shown. Events to the right of zero have been reconstructed with an energy larger than the true energy and vice versa for the left. The black solid histogram is for events satisfying the 70 % resolution cut, and the green shaded area corresponds to 68% of the events.

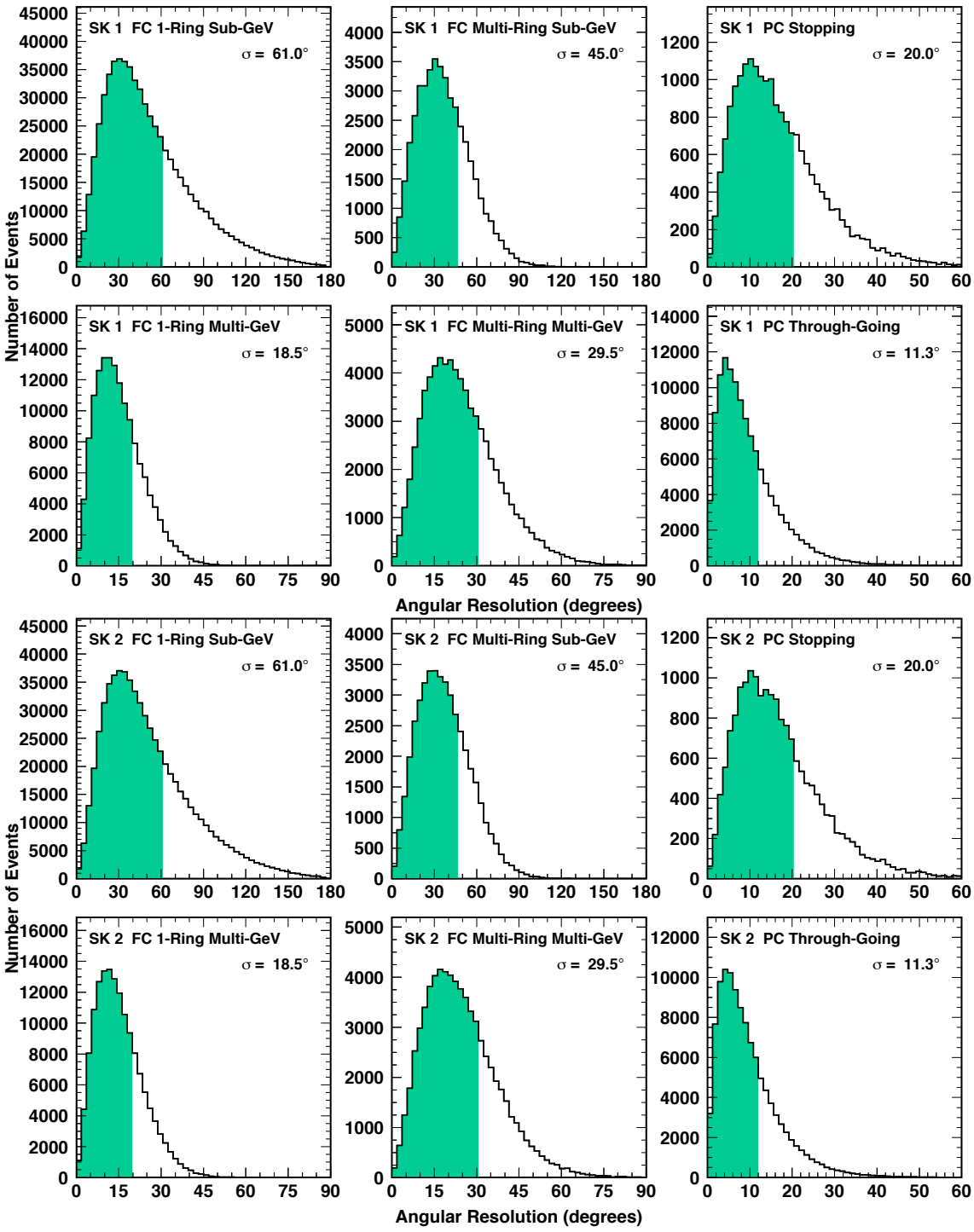

Figure A.4: Angular resolution in SK1 and SK2 for the L/E samples. The distribution of angles w.r.t. the true neutrino direction is shown. The black solid histogram is for events satisfying the 70 % resolution cut, and the green shaded region corresponds to 68% of events.

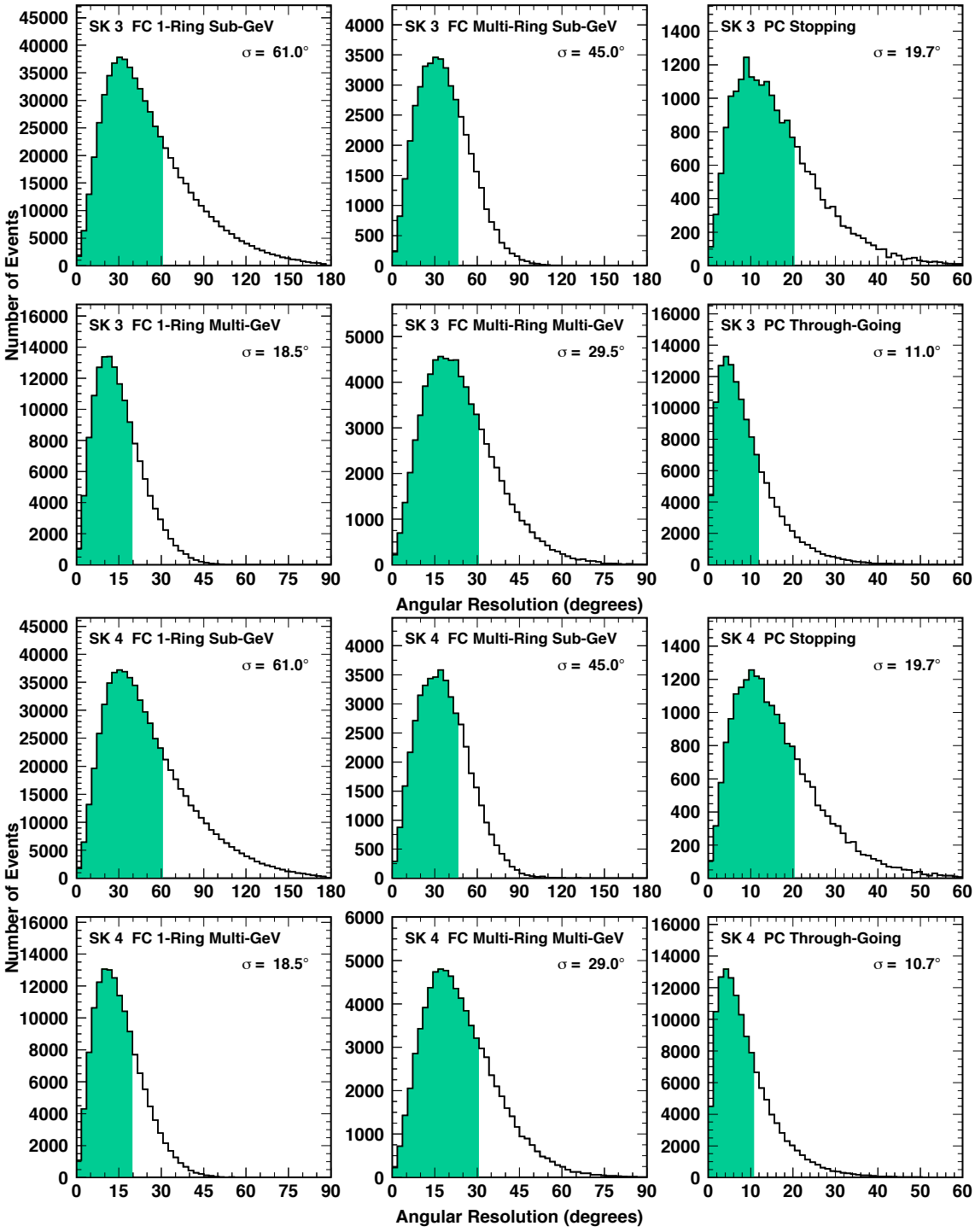

Figure A.5: Angular resolution in SK3 and SK4 for the L/E samples. The distribution of angles w.r.t. the true neutrino direction is shown. The black solid histogram is for events satisfying the 70 % resolution cut, and the green shaded region corresponds to 68% of events.

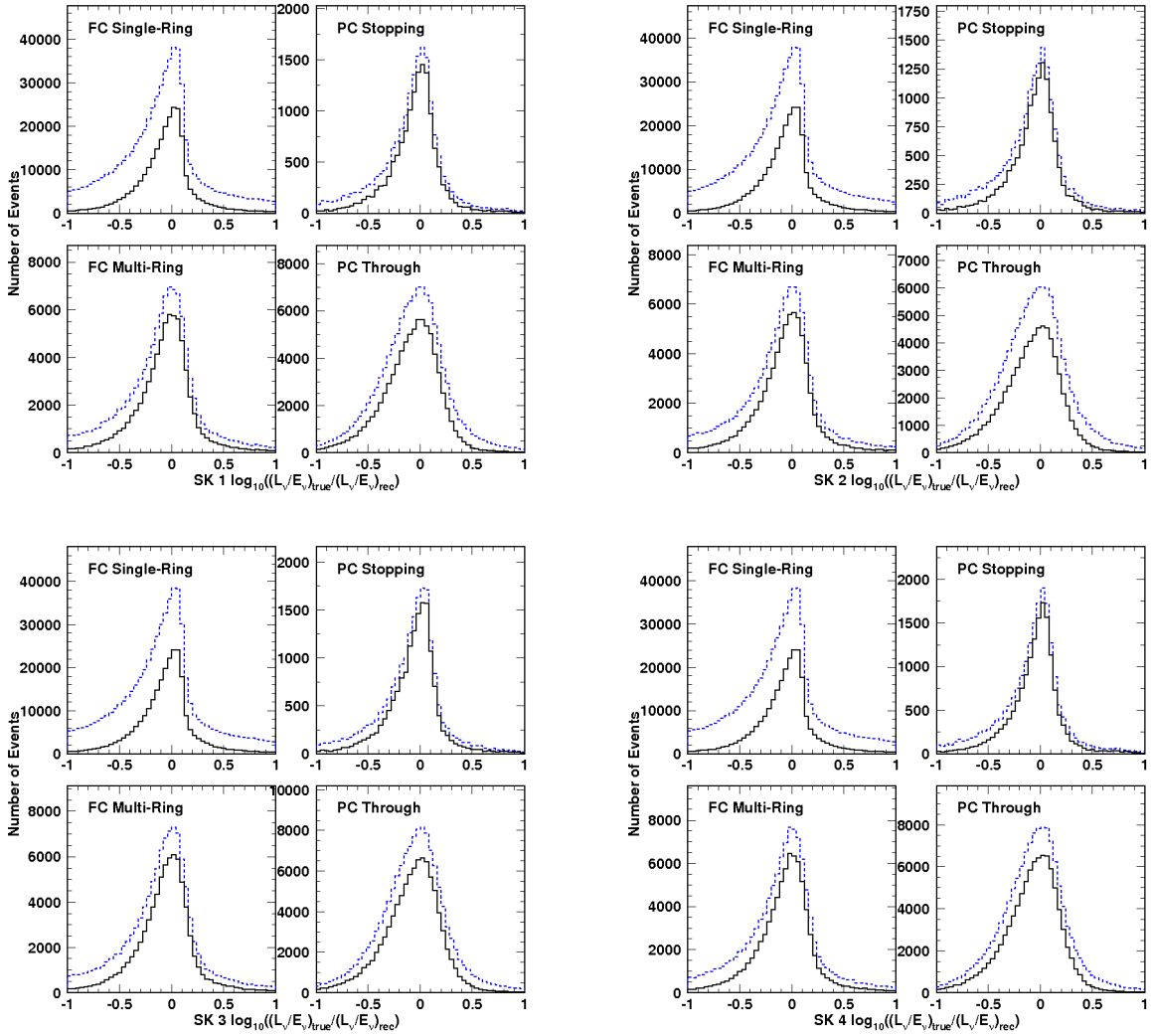

Figure A.6: $\log_{10}$ of the ratio of True L/E over Reconstructed L/E, in sets of plots for SK1 to SK4 as labelled in the x-axis. Within each set, the ratio is shown for each of the four event samples. The solid black histogram has had the <70% resolution cut applied, while the dashed blue has not. The high resolution samples have a tighter distribution on this L/E true/reconstructed double ratio.

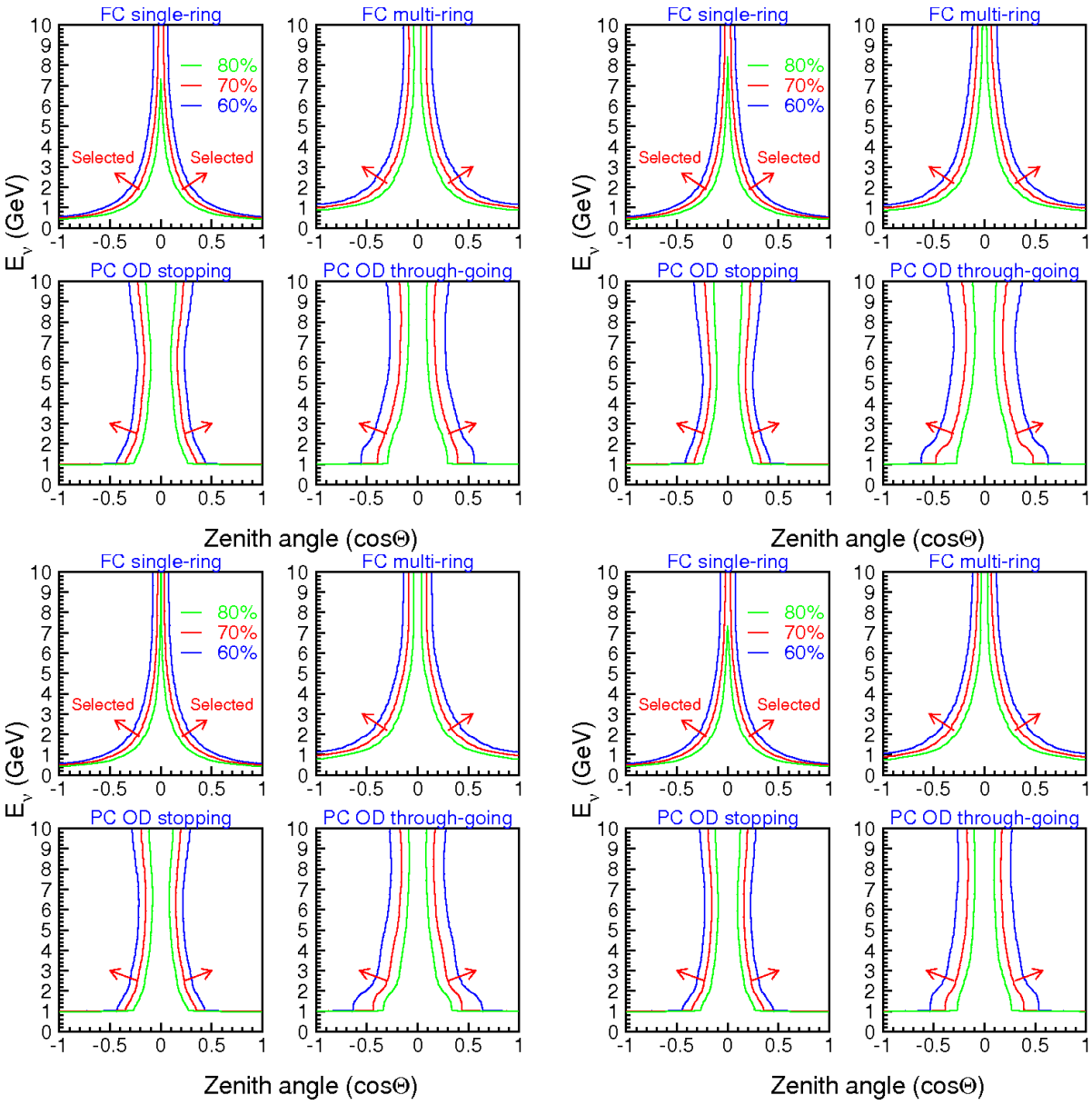

Figure A.7: L/E Resolution Cut by Sample

Bibliography

[1] C. Sutton, *Spaceship Neutrino* (Cambridge University Press, UK, 1992).

[2] W. Pauli, Phys. Today **31N9**, 27 (1978).

[3] F. Reines and C. L. Cowan, Phys. Rev. **92**, 830 (1953).

[4] F. Reines and C. L. Cowan, Nature **178**, 446 (1956).

[5] G. Danby *et al.*, Phys.Rev.Lett. **9**, 36 (1962).

[6] K. Kodama *et al.*, Phys.Lett. **B504**, 218 (2001).

[7] Z. Maki, M. Nakagawa, and S. Sakata, Prog.Theor.Phys. **28**, 870 (1962).

[8] V. Gribov and B. Pontecorvo, Phys.Lett. **B28**, 493 (1969).

[9] Y. Ashie *et al.*, Phys.Rev.Lett. **93**, 101801 (2004).

[10] P. Adamson *et al.*, Phys.Rev.Lett. **107**, 021801 (2011).

[11] P. Adamson *et al.*, Phys.Rev.Lett. **108**, 191801 (2012).

[12] K. Abe *et al.*, Phys.Rev.Lett. **107**, 241801 (2011).

[13] W. Mann, D. Cherdack, W. Musial, and T. Kafka, Phys.Rev. **D82**, 113010 (2010).

[14] F. An *et al.*, Phys.Rev.Lett. **108**, 171803 (2012).

[15] R. Wendell *et al.*, Phys. Rev. **D81**, 092004 (2010).

[16] M. Honda, T. Kajita, K. Kasahara, and S. Midorikawa, Phys.Rev. **D83**, 123001 (2011).

[17] T. Gaisser, *Cosmic Rays and Particle Physics* (Cambridge University Press, UK, 1990).

[18] F. Soler, C. D. Froggatt, and F. Muheim, (2009), Neutrinos in particle physics, astrophysics and cosmology. Proceedings, 61st Scottish Universities Summer School in Physics, SUSSP61, St. Andrews, UK, August 8-23, 2006.

[19] M. Apollonio *et al.*, Phys. Lett. **B466**, 415 (1999).

[20] L. Wolfenstein, Phys. Rev. **D17**, 2369 (1978).

[21] L. Wolfenstein, Phys. Rev. **D20**, 2634 (1979).

[22] S. P. Mikheev and A. Y. Smirnov, Sov. J. Nucl. Phys. **42**, 913 (1985).

[23] J. Davis, Raymond, D. S. Harmer, and K. C. Hoffman, Phys. Rev. Lett. **20**, 1205 (1968).

[24] M. Altmann *et al.*, Phys.Lett. **B616**, 174 (2005).

[25] J. N. Abdurashitov *et al.*, J. Exp. Theor. Phys. **95**, 181 (2002).

[26] Y. Fukuda *et al.*, Phys.Rev.Lett. **77**, 1683 (1996).

[27] K. Hirata *et al.*, Phys.Lett. **B205**, 416 (1988).

[28] Y. Fukuda *et al.*, Phys.Lett. **B335**, 237 (1994).

[29] R. Becker-Szendy *et al.*, Phys.Rev. **D46**, 3720 (1992).

[30] T. Kajita, Nucl. Phys. Proc. Suppl. **77**, 123 (1999).

[31] Y. Fukuda *et al.*, Phys. Rev. Lett. **81**, 1562 (1998).

[32] K. Abe *et al.*, Phys.Rev. **D83**, 052010 (2011).

[33] Q. Ahmad *et al.*, Phys.Rev.Lett. **89**, 011301 (2002).

[34] S. Abe *et al.*, Phys.Rev.Lett. **100**, 221803 (2008).

[35] K. Abe *et al.*, Phys.Rev.Lett. **111**, 211803 (2013).

[36] D. G. Michael *et al.*, Phys. Rev. Lett. **97**, 191801 (2006).

[37] K. Abe *et al.*, Phys.Rev.Lett. **112**, 061802 (2014).

[38] Y. Abe *et al.*, Phys.Rev.Lett. **108**, 131801 (2012).

[39] K. Abe *et al.*, Phys.Rev.Lett. **107**, 041801 (2011).

[40] P. Adamson *et al.*, Phys.Rev.Lett. **107**, 181802 (2011).

[41] J. Ahn *et al.*, Phys.Rev.Lett. **108**, 191802 (2012).

[42] Y. Abe *et al.*, Phys.Rev. **D86**, 052008 (2012).

[43] P. Adamson *et al.*, Phys.Rev.Lett. **110**, 171801 (2013).

[44] D. Forero, M. Tortola, and J. Valle, Phys.Rev. **D86**, 073012 (2012).

[45] M. Gonzalez-Garcia and M. Maltoni, Phys.Rev. **D70**, 033010 (2004).

[46] R. Mohapatra and J. Valle, Phys.Rev. **D34**, 1642 (1986).

[47] D. Wyler and L. Wolfenstein, Nucl.Phys. **B218**, 205 (1983).

[48] L. J. Hall, V. A. Kostelecky, and S. Raby, Nucl.Phys. **B267**, 415 (1986).

[49] J. Schechter and J. Valle, Phys.Rev. **D22**, 2227 (1980).

[50] L. J. Hall and M. Suzuki, Nucl.Phys. **B231**, 419 (1984).

[51] R. Barbieri, L. J. Hall, and A. Strumia, Nucl.Phys. **B445**, 219 (1995).

[52] G. G. Ross and J. Valle, Phys.Lett. **B151**, 375 (1985).

[53] J. R. Ellis *et al.*, Phys.Lett. **B150**, 142 (1985).

[54] S. Bergmann, H. Klapdor-Kleingrothaus, and H. Pas, Phys.Rev. **D62**, 113002 (2000).

[55] M. Fukugita and T. Yanagida, Phys.Lett. **B206**, 93 (1988).

[56] M. Gonzalez-Garcia and J. Valle, Phys.Lett. **B216**, 360 (1989).

[57] N. Fornengo, M. Maltoni, R. Tomas, and J. Valle, Phys.Rev. **D65**, 013010 (2002).

[58] M. Gonzalez-Garcia *et al.*, Phys.Rev.Lett. **82**, 3202 (1999).

[59] P. Lipari and M. Lusignoli, Phys.Rev. **D60**, 013003 (1999).

[60] N. Fornengo, M. Gonzalez-Garcia, and J. Valle, JHEP **0007**, 006 (2000).

[61] M. Guzzo, A. Masiero, and S. Petcov, Phys.Lett. **B260**, 154 (1991).

[62] E. Roulet, Phys.Rev. **D44**, 935 (1991).

[63] V. D. Barger, R. Phillips, and K. Whisnant, Phys.Rev. **D44**, 1629 (1991).

[64] S. Bergmann, Nucl.Phys. **B515**, 363 (1998).

[65] J. Valle, Phys.Lett. **B199**, 432 (1987).

[66] A. Friedland, C. Lunardini, and M. Maltoni, Phys.Rev. **D70**, 111301 (2004).

[67] A. Friedland and C. Lunardini, Phys.Rev. **D72**, 053009 (2005).

[68] M. Blennow *et al.*, Eur.Phys.J. **C56**, 529 (2008).

[69] P. Adamson *et al.*, Phys.Rev. **D88**, 072011 (2013).

[70] J. Kopp, P. A. Machado, and S. J. Parke, Phys.Rev. **D82**, 113002 (2010).

[71] M. Gonzalez-Garcia and M. Maltoni, Phys.Rept. **460**, 1 (2008).

[72] C. Biggio, M. Blennow, and E. Fernandez-Martinez, JHEP **0908**, 090 (2009).

[73] G. Mitsuka *et al.*, Phys.Rev. **D84**, 113008 (2011).

[74] J. N. Bahcall, A. M. Serenelli, and S. Basu, Astrophys.J. **621**, L85 (2005).

[75] J. N. Bahcall and C. Pena-Garay, New J. Phys. **6**, 63 (2004).

[76] P. Anselmann *et al.*, Phys.Lett. **B285**, 376 (1992).

[77] R. Davis, Prog. Part. Nucl. Phys. **32**, 13 (1994).

[78] B. Cleveland *et al.*, Astrophys.J. **496**, 505 (1998).

[79] R. Davis, Int.J.Mod.Phys. **A18**, 3089 (2003).

[80] W. Hampel *et al.*, Phys. Lett. **B447**, 127 (1999).

[81] P. Anselmann *et al.*, Phys.Lett. **B285**, 390 (1992).

[82] J. Abdurashitov *et al.*, Phys.Rev. **C60**, 055801 (1999).

[83] M. Altmann *et al.*, Phys.Lett. **B490**, 16 (2000).

[84] K. Hirata *et al.*, Phys.Rev. **D44**, 2241 (1991).

[85] K. Hirata *et al.*, Phys.Rev.Lett. **58**, 1490 (1987).

[86] J. Hosaka *et al.*, Phys.Rev. **D73**, 112001 (2006).

[87] S. Fukuda *et al.*, Phys.Rev.Lett. **86**, 5651 (2001).

[88] Y. Fukuda *et al.*, Phys.Rev.Lett. **82**, 1810 (1999).

[89] S. Fukuda *et al.*, Phys.Lett. **B539**, 179 (2002).

[90] M. Smy *et al.*, Phys.Rev. **D69**, 011104 (2004).

[91] A. Renshaw *et al.*, Phys.Rev.Lett. **112**, 091805 (2014).

[92] J. Boger *et al.*, Nucl. Instrum. Meth. **A449**, 172 (2000).

[93] Q. Ahmad *et al.*, Phys.Rev.Lett. **87**, 071301 (2001).

[94] B. Aharmim *et al.*, Phys.Rev. **C72**, 055502 (2005).

[95] Q. Ahmad *et al.*, Phys.Rev.Lett. **89**, 011302 (2002).

[96] S. Ahmed *et al.*, Phys.Rev.Lett. **92**, 181301 (2004).

[97] G. Alimonti *et al.*, Astropart.Phys. **16**, 205 (2002).

[98] C. Arpesella *et al.*, Phys.Rev.Lett. **101**, 091302 (2008).

[99] C. Arpesella *et al.*, Phys.Lett. **B658**, 101 (2008).

[100] G. Bellini *et al.*, Phys.Rev. **D82**, 033006 (2010).

[101] G. Bellini *et al.*, Phys.Rev.Lett. **108**, 051302 (2012).

[102] F. Reines *et al.*, Phys.Rev.Lett. **15**, 429 (1965).

[103] C. Achar *et al.*, Physics Letters **18**, 196 (1965).

[104] K. Daum *et al.*, Z.Phys. **C66**, 417 (1995).

[105] M. Aglietta *et al.*, Europhys.Lett. **8**, 611 (1989).

[106] Y. Fukuda *et al.*, Phys. Lett. **B436**, 33 (1998).

[107] Y. Fukuda *et al.*, Phys. Lett. **B433**, 9 (1998).

[108] S. Fukuda *et al.*, Phys. Rev. Lett. **85**, 3999 (2000).

[109] Y. Ashie *et al.*, Phys.Rev. **D71**, 112005 (2005).

[110] Y. Fukuda *et al.*, Phys.Rev.Lett. **82**, 2644 (1999).

[111] K. Abe *et al.*, Phys.Rev.Lett. **110**, 181802 (2013).

[112] M. C. Sanchez *et al.*, Phys. Rev. **D68**, 113004 (2003).

[113] W. Allison *et al.*, Nucl.Instrum.Meth. **A376**, 36 (1996).

[114] M. Ambrosio *et al.*, Nucl.Instrum.Meth. **A486**, 663 (2002).

[115] M. Ambrosio *et al.*, Eur. Phys. J. **C36**, 323 (2004).

[116] M. Apollonio *et al.*, Phys. Lett. **B420**, 397 (1998).

[117] M. Apollonio *et al.*, Eur. Phys. J. **C27**, 331 (2003).

[118] A. Piepke, Nucl. Phys. Proc. Suppl. **91**, 99 (2001).

[119] K. Eguchi *et al.*, Phys.Rev.Lett. **90**, 021802 (2003).

[120] T. Araki *et al.*, Phys. Rev. Lett. **94**, 081801 (2005).

[121] K. Inoue, Nucl.Phys.Proc.Suppl. **235-236**, 249 (2013).

[122] F. Ardellier *et al.*, (2006), hep-ex/0606025.

[123] M. Ahn *et al.*, Phys.Rev.Lett. **90**, 041801 (2003).

[124] E. Aliu *et al.*, Phys.Rev.Lett. **94**, 081802 (2005).

[125] M. H. Ahn *et al.*, Phys. Rev. **D74**, 072003 (2006).

[126] P. Adamson *et al.*, Phys.Rev. **D82**, 051102 (2010).

[127] E. K. Akhmedov *et al.*, JHEP **0404**, 078 (2004).

[128] Y. Itow *et al.*, (2001), hep-ex/0106019.

[129] K. Abe *et al.*, Nucl.Instrum.Meth. **A659**, 106 (2011).

[130] K. Abe *et al.*, Phys.Rev. **D85**, 031103 (2012).

[131] K. Abe *et al.*, Phys.Rev. **D88**, 032002 (2013).

[132] A. Aguilar-Arevalo *et al.*, Phys.Rev. **D64**, 112007 (2001).

[133] G. Mention *et al.*, Phys.Rev. **D83**, 073006 (2011).

[134] C. Giunti and M. Laveder, Phys.Rev. **C83**, 065504 (2011).

[135] A. Aguilar-Arevalo *et al.*, Phys.Rev.Lett. **98**, 231801 (2007).

[136] A. Aguilar-Arevalo *et al.*, Phys.Rev.Lett. **105**, 181801 (2010).

[137] A. Aguilar-Arevalo *et al.*, Phys.Rev.Lett. **110**, 161801 (2013).

[138] R. Acquafredda *et al.*, JINST **4**, P04018 (2009).

[139] N. Agafonova *et al.*, Phys.Lett. **B691**, 138 (2010).

[140] T. Adam *et al.*, JHEP **1210**, 093 (2012).

[141] N. Agafonova *et al.*, (2014), 1401.2079.

[142] S. Geer, Phys. Rev. **D57**, 6989 (1998).

[143] A. Blondel *et al.*, Acta Phys. Polon. **B37**, 2077 (2006).

[144] A. Cervera *et al.*, Nucl. Phys. **B579**, 17 (2000).

[145] I. D. S. of the Neutrino Factory, Neutrino Factory: Specification of Baseline, http://www.hep.ph.ic.ac.uk/ids/docs/index.html, 2008.

[146] P. Zucchelli, Phys. Lett. **B532**, 166 (2002).

[147] K. Abe *et al.*, (2011), 1109.3262.

[148] A. Rubbia, Acta Phys.Polon. **B41**, 1727 (2010).

[149] M. Diwan *et al.*, (2003), hep-ex/0306053.

[150] A. Rubbia, J.Phys.Conf.Ser. **171**, 012020 (2009).

[151] M. Wurm *et al.*, Astropart.Phys. **35**, 685 (2012).

[152] A. de Bellefon *et al.*, (2006), hep-ex/0607026.

[153] D. S. Ayres *et al.*, (2004), hep-ex/0503053.

[154] F. Jediný, J.Phys.Conf.Ser. **490**, 012019 (2014).

[155] T. Ishida, (2013), 1311.5287.

[156] Y. Fukuda *et al.*, Nucl. Instrum. Meth. **A501**, 418 (2003).

[157] I. Frank and I. Tamm, C.R.Acad.Sci.URSS **14**, 109 (1937).

[158] H. Kume *et al.*, Nucl.Instrum.Meth. **205**, 443 (1983).

[159] A. Suzuki *et al.*, Nucl.Instrum.Meth. **A329**, 299 (1993).

[160] A. Dziewonski and D. Anderson, Phys.Earth Planet.Interiors **25**, 297 (1981).

[161] Y. Takeuchi *et al.*, Phys.Lett. **B452**, 418 (1999).

[162] T. Tanimori *et al.*, IEEE Trans.Nucl.Sci. **36**, 497 (1989).

[163] S. Yamada *et al.*, IEEE Trans. Nucl. Sci. **57**, 428 (2010).

[164] H. Nishino *et al.*, Nucl. Instrum. Meth. **A610**, 710 (2009).

[165] M. Honda, T. Kajita, K. Kasahara, and S. Midorikawa, Phys.Rev. **D64**, 053011 (2001).

[166] M. Honda, T. Kajita, K. Kasahara, and S. Midorikawa, Phys.Rev. **D70**, 043008 (2004).

[167] M. Honda *et al.*, Phys.Rev. **D75**, 043006 (2007).

[168] G. Battistoni, A. Ferrari, T. Montaruli, and P. Sala, Astropart.Phys. **19**, 269 (2003).

[169] G. Barr *et al.*, Phys.Rev. **D70**, 023006 (2004).

[170] L. Volkova, Sov.J.Nucl.Phys. **31**, 784 (1980).

[171] T. Sanuki *et al.*, Astrophys.J. **545**, 1135 (2000).

[172] J. Alcaraz *et al.*, Phys.Lett. **B490**, 27 (2000).

[173] W. Webber, R. Golden, and S. Stephens, *Proceedings of the 20th International Cosmic Ray Conference, Vol. 1* (Moscow Nauka, Moscow, 1987).

[174] E. Seo *et al.*, Astrophys.J. **378**, (1987).

[175] P. Pappini *et al.*, *Proceedings of the 23rd International Cosmic Ray Conference, Vol. 1* (University of Calgary, Calgary, 1993).

[176] M. Boezio *et al.*, Astrophys.J. **518**, 457 (1999).

[177] W. Menn *et al.*, Astrophys.J. **533**, (2000).

[178] M. J. Ryan, J. F. Ormes, and V. K. Balasubrahmanyan, Phys. Rev. Lett. **28**, 985 (1972).

[179] K. Asakimori *et al.*, Astrophys.J. **502**, (1998).

[180] I. Ivanenko *et al.*, *Proceedings of the 23rd International Cosmic Ray Conference, Vol. 2* (University of Calgary, Calgary, 1993).

[181] Y. Kawamura *et al.*, Phys. Rev. **D40**, 729 (1989).

[182] A. Apanasenko *et al.*, Astroparticle Physics **16**, 13 (2001).

[183] `http://modelweb.gsfc.nasa.gov/atmos/us_standard.html`.

[184] `http://www.ngdc.noaa.gov/IAGA/vmod/igrf.html`.

[185] K. Hänssgen and J. Ranft, Computer Physics Communications **39**, 37 (1986).

[186] S. Roesler, R. Engel, and J. Ranft, Phys.Rev. **D57**, 2889 (1998).

[187] M. Motoki *et al.*, Astroparticle Physics **19**, 113 (2003).

[188] P. Achard *et al.*, Phys.Lett. **B598**, 15 (2004).

[189] S. Haino *et al.*, Phys.Lett. **B594**, 35 (2004).

[190] T. Sanuki *et al.*, Phys.Lett. **B541**, 234 (2002).

[191] O. Allkofer *et al.*, Nucl.Phys. **B259**, 1 (1985).

[192] S. Matsuno *et al.*, Phys.Rev. **D29**, 1 (1984).

[193] K. Niita *et al.*, Radiat. Meas. **41**, 1080 (2006).

[194] M. G. Catanesi *et al.*, Astropart. Phys. **29**, 257 (2008).

[195] M. G. Catanesi *et al.*, Astropart. Phys. **30**, 124 (2008).

[196] Y. Hayato, Nucl.Phys.Proc.Suppl. **112**, 171 (2002).

[197] G. Mitsuka, Ph.D. thesis, Tokyo U., 2009, Study of Non-Standard Neutrino Interactions with Atmospheric Neutrino Data in Super-Kamiokande.

[198] C. Llewellyn Smith, Phys.Rept. **3**, 261 (1972).

[199] R. Smith and E. Moniz, Nucl.Phys. **B43**, 605 (1972).

[200] S. Barish *et al.*, Phys.Rev. **D16**, 3103 (1977).

[201] S. Bonetti *et al.*, Nuovo Cim. **A38**, 260 (1977).

[202] M. Pohl *et al.*, Lett.Nuovo Cim. **26**, 332 (1979).

[203] N. Armenise *et al.*, Nucl.Phys. **B152**, 365 (1979).

[204] A. Mukhin *et al.*, Sov.J.Nucl.Phys. **30**, 528 (1979).

[205] S. Belikov *et al.*, Z.Phys. **A320**, 625 (1985).

[206] J. Brunner *et al.*, Z.Phys. **C45**, 551 (1990).

[207] R. Gran *et al.*, Phys.Rev. **D74**, 052002 (2006).

[208] F. Sanchez *et al.*, *Proceedings of the Fifth International Workshop on Neutrino-Nucleus Interactions in the Few-GeV Region(NuInt07)* (Fermilab, Chicago, 2007), `http://conferences.fnal.gov/nuint07/`.

[209] A. Aguilar-Arevalo *et al.*, Phys.Rev.Lett. **100**, 032301 (2008).

[210] J. Reich *et al.*, Nucl.Instrum.Meth. **A440**, 535 (2000).

[211] H. Abele, Nucl.Instrum.Meth. **A440**, 499 (2000).

[212] P. E. Bosted, Phys.Rev. **C51**, 409 (1995).

[213] E. Brash, A. Kozlov, S. Li, and G. Huber, Phys.Rev. **C65**, 051001 (2002).

[214] A. Bodek, S. Avvakumov, R. Bradford, and H. S. Budd, (2007), 0708.1827.

[215] J. Nieves, J. E. Amaro, and M. Valverde, Phys.Rev. **C70**, 055503 (2004).

[216] H. Nakamura and R. Seki, Nucl.Phys.Proc.Suppl. **112**, 197 (2002).

[217] C. H. Albright, C. Quigg, R. Shrock, and J. Smith, Phys.Rev. **D14**, 1780 (1976).

[218] L. Ahrens *et al.*, Phys.Rev.Lett. **56**, 1107 (1986).

[219] D. Rein and L. M. Sehgal, Annals Phys. **133**, 79 (1981).

[220] D. Rein, Z.Phys. **C35**, 43 (1987).

[221] K. S. Kuzmin, V. V. Lyubushkin, and V. A. Naumov, Mod.Phys.Lett. **A19**, 2815 (2004).

[222] C. Berger and L. Sehgal, Phys.Rev. **D76**, 113004 (2007).

[223] S. Singh, M. Vicente-Vacas, and E. Oset, Phys.Lett. **B416**, 23 (1998).

[224] M. Gluck, E. Reya, and A. Vogt, Eur.Phys.J. **C5**, 461 (1998).

[225] A. Bodek and U. Yang, Nucl.Phys.Proc.Suppl. (2003), arXiv: hep-ex/0308007.

[226] P. Musset and J. Vialle, Phys.Rept. **39**, 1 (1978).

[227] J. E. Kim, P. Langacker, M. Levine, and H. Williams, Rev.Mod.Phys. **53**, 211 (1981).

[228] S. Barlag *et al.*, Z.Phys. **C11**, 283 (1982).

[229] T. Sjostrand, (1994), pythia 5.7 and jetset 7.4 physics and manual, CERN-TH-7112-93, Revised Version.

[230] D. Rein and L. M. Sehgal, Nucl.Phys. **B223**, 29 (1983).

[231] M. Hasegawa *et al.*, Phys.Rev.Lett. **95**, 252301 (2005).

[232] R. D. Woods and D. S. Saxon, Phys.Rev. **95**, 577 (1954).

[233] C. De Jager, H. De Vries, and C. De Vries, Atom.Data Nucl.Data Tabl. **14**, 479 (1974).

[234] L. Salcedo, E. Oset, M. Vicente-Vacas, and C. Garcia-Recio, Nucl.Phys. **A484**, 557 (1988).

[235] G. Rowe, M. Salomon, and R. H. Landau, Phys.Rev. **C18**, 584 (1978).

[236] D. Ashery *et al.*, Phys.Rev. **C23**, 2173 (1981).

[237] C. Ingram *et al.*, Phys.Rev. **C27**, 1578 (1983).

[238] B. Martin and M. Pidcock, Nucl.Phys. **B126**, 266 (1977).

[239] B. Martin and M. Pidcock, Nucl.Phys. **B126**, 285 (1977).

[240] J. Hyslop, R. Arndt, L. Roper, and R. Workman, Phys.Rev. **D46**, 961 (1992).

[241] D. Sparrow, AIP Conf.Proc. **123**, 1019 (1984).

[242] H. Bertini, Phys.Rev. **C6**, 631 (1972).

[243] S. Lindenbaum and R. Sternheimer, Phys.Rev. **105**, 1874 (1957).

[244] R. Brun, F. Carminati, and S. Giani, (1994), CERN Program Library Long Writeup.

[245] C. Zeitnitz and T. Gabriel, Nucl.Instrum.Meth. **A349**, 106 (1994).

[246] M. Nakahata *et al.*, J.Phys.Soc.Jap. **55**, 3786 (1986).

[247] E. Bracci *et al.*, (1972), CERN-HERA-72-01.

[248] A. Carroll *et al.*, Phys.Rev. **C14**, 635 (1976).

[249] P. Haenggi, R. Viollier, U. Raff, and K. Alder, Phys.Lett. **B51**, 119 (1974).

[250] M. Yamada *et al.*, Phys.Rev. **D44**, 617 (1991).

[251] E. R. Davies, *Machine Vision: Theory, Algorithms, Practicalities* (Morgan Kaufmann Publishers Inc., San Francisco, CA, USA, 2004).

[252] G. Fogli *et al.*, Phys.Rev. **D66**, 053010 (2002).

[253] Y. Tserkovnyak, R. Komar, C. Nally, and C. Waltham, Astropart.Phys. **18**, 449 (2003).

[254] G. Barr, T. Gaisser, S. Robbins, and T. Stanev, Phys.Rev. **D74**, 094009 (2006).

[255] T. Gaisser and M. Honda, Ann.Rev.Nucl.Part.Sci. **52**, 153 (2002).

[256] R. M. Barnett *et al.*, Phys. Rev. **D54**, 1 (1996).

[257] F. Dufour, , Precise Study of the Atmospheric Neutrino Oscillation Pattern Using Super-Kamiokande I and II.

[258] K. Abe *et al.*, Phys.Rev.Lett. **112**, 181801 (2014).

[259] I. S. Tsukerman, (2010), 1006.4989.

[260] D. Colladay and V. A. Kostelecky, Phys. Rev. **D58**, 116002 (1998).

[261] V. A. Kostelecky, Phys. Rev. **D69**, 105009 (2004).

[262] P. Adamson *et al.*, Phys.Rev.Lett. **106**, 181801 (2011).

[263] S. Goswami, Nucl. Phys. Proc. Suppl. **188**, 198 (2009).

[264] A. Chatterjee, R. Gandhi, and J. Singh, JHEP **06**, 045 (2014).

[265] C. Ishihara, Ph.D. thesis, Tokyo U., 2010, Full three flavor oscillation analysis of atmospheric neutrino data observed in Super-Kamiokande.

[266] Y. Itow, Nucl. Phys. Proc. Suppl. **235-236**, 79 (2013).